Falko P. Netzer
Alessandro Fortunelli *Editors*

Oxide Materials at the Two-Dimensional Limit

Springer

Springer Series in Materials Science

Volume 234

Series editors

The Springer Series in Materials Science covers the complete spectrum of materials physics, including fundamental principles, physical properties, materials theory and design. Recognizing the increasing importance of materials science in future device technologies, the book titles in this series reflect the state-of-the-art in understanding and controlling the structure and properties of all important classes of materials.

More information about this series at http://www.springer.com/series/856

Falko P. Netzer · Alessandro Fortunelli
Editors

Oxide Materials at the Two-Dimensional Limit

Springer

Editors
Falko P. Netzer
Institute of Physics
Karl-Franzens University
Graz
Austria

Alessandro Fortunelli
ICCOM
National Research Council
Pisa
Italy

Foreword

The structure of ultrathin films of oxides has attracted considerable attention in recent years, both from an experimental as well as from a theoretical perspective. This is documented by an exponential increase in published original papers in the field within the last decade. Originally driven by semiconductor device research, where the famous amorphous silica film on top of silicon played an important role, via the thin insulating oxide films in storage devices, it has become obvious that the detailed structure of oxide films will influence the properties with respect to transport and electronic structure decisively. The latest account on ultrathin oxide films has been edited a few years ago by Gianfranco Pacchioni and Sergio Valeri entitled "Oxide Ultrathin Films: Science and Technology" and it collected chapters mainly on applications of ultrathin films in a number of important technological areas, such as electronic devices or heterogeneous catalysis.

The present book approaches the topic with 13 chapters from a different, more fundamental angle by focusing on the structural aspects of ultrathin oxide films, however, not without pointing out relations to applications. To this end, Falko Netzer and Alessandro Fortunelli have put together an impressive list of chapters addressing a number of important fundamental issues in ultrathin oxide film research. Netzer and Surnev introduce in the beginning structure concepts for two-dimensional materials, based on their own experience mainly on examples involving transition metal oxides. Fortunelli and collaborators address in Chap. 2 the electronic structure of nanostructured oxides by particularly pointing out the fruitful collaboration of experiment and theory in this area of research. I would like to stress that this is an important factor in the success of the field and its fast expansion, since the interplay between theory and experiment has helped to proceed faster, and direct research towards the decisive scientific issues. The third chapter by Pacchioni underlines the fact that the structure of ultrathin oxide films is considerably more flexible than bulk oxides, which leads to interesting new physical phenomena, for example, upon adsorption on those surfaces, to stabilization of the adsorbate via a polaronic distortion of the ultrathin film. While Pacchioni's chapter mainly deals with simple oxides, in the following chapter Luches and D'Addato

concentrate on reducible ultrathin oxide films. Wu and Castell report studies on a
variety of ultrathin oxide films on Au (111) as a substrate and discuss the large
variety of observed structures, which is another manifestation of the structural
richness of such systems. Again, in the following sixth chapter by Rocca and
collaborators flexibility is addressed via studies of phonons in thin oxide films. This
connects beautifully Chaps. 4–6 and provides a basis for understanding. Noguera
and Goniakowski outline their pioneering work with respect to the influence of
electrostatics and polarity in two-dimensional oxide films. Together with the dis-
cussion on vibrational properties, those aspects are of fundamental importance in
rationalizing the observed structural phenomena. In the subsequent two chapters,
specific aspects of catalysis are touched upon. One, by Matolin and collaborators
from the angle of a specific system, namely, ceria grown on Cu (111), a system that
has provided an interesting playground for evidencing the importance of defects
and charge transfer in rare earths oxide films, and, the other one, through a col-
laboration between Pacific Northwest National Laboratory, Brookhaven National
Laboratory, and Weaver at Florida State University, on catalytic chemistry
involving oxide nanostructures. Chapter 10 by Risse deals with charge transfer
effects in ultrathin oxide films, an interesting and important aspect for metal sup-
ported oxide films, a topic the author has studied in detail by a specific experimental
technique, i.e., ultrahigh vacuum compatible EPR spectroscopy. The following two
chapters extend the discussion towards oxide interfaces. Chapter 11 by Shluger and
Bersuker deals with a specific system, namely Si and two-dimensional oxides films
grown on top of this substrate. In particular, they stress the importance of under-
standing the defect structure of those systems. This was a question raised at the
outset of the field, when oxide films on Si were recognized as crucial in semi-
conductor device physics. Chapter 12 by Demkov addresses the question of
two-dimensional oxide interfaces from a more general point of view. Widdra and
Förster extend the discussion on oxide structures and properties to concepts con-
necting bulk structures and novel interfaces and they use once again perovskite
ultrathin films as an example.

In summary, this book will provide the reader with a marvelous introduction into
the fundamentals of ultrathin oxide films, which has been put together by the editors
carefully in a well-balanced way. The reader is lead from the fundamentals of
ultrathin film physics to the applications, and in this sense the book closes a circle
from the outset of the field demanding an understanding of thin oxide films in
device production to the creation of new concepts and systems that will provide the
scientific community with a wide playground for the years to come. I wish the book
success in every aspect.

Berlin, Germany   Hajo Freund

Preface

The development of new materials has always had a dramatic influence on the world. Consider for example the discovery of bronze, a copper-tin alloy, or of metallic iron, which have given name to their respective ages in ancient time periods. Today, the influence of new materials is not quite as dramatic but still significant, modifying many aspects of human life style. New materials are typically introduced following discoveries in fundamental science. In recent times, it has become clear that not only a new chemical composition may form a new material, but also that reduced size and dimensionality of a known compound can produce novel properties generating a new material behavior. The most recent and perhaps the most popular demonstration is provided by an ultrathin two-dimensional form of carbon, graphene: the discovery of some of its peculiar properties in 2004 has set off a revolution in materials science that is still developing. In fact, the study of two-dimensional materials has been recently hailed as "one of the hottest topics in physics."[1] Prompted by the advent of graphene, a multitude of other atom-thick two-dimensional materials have been introduced in the last decade, with big or even bigger technological payoff promise.

Oxide materials are ubiquitous on earth and in modern science and technology. They feature a huge variety of composition and structure parameters and thus of physical and chemical properties. This variety can be even enhanced by adding reduced dimensionality as a further degree of freedom, and indeed two-dimensional oxides have been actively investigated in various fields of science and technology in the last two to three decades, writing a story going in parallel with the development of carbon two-dimensional materials. This book is devoted to such oxide materials in two dimensions or at the two-dimensional limit, that is, ultrathin oxide films comprising only one or a few atom-thick layers. Typically, two-dimensional materials are derived from *van der Waals* solids, i.e., layered solids with strong

---

[1]See the feature article "Beyond Graphene" by R.F. Service, *Science* 348, 490 (2015).

intra-layer but weak inter-layer interactions; the latter is the result of chemical bond saturation within the layers. This means that when deposited on a substrate for applied use, the two-dimensional layers feature weak overlayer–substrate coupling. Oxides rarely belong in this category, and strong coupling to the environment is rather typical: on a substrate, strong oxide–overlayer/substrate coupling is a rule rather than an exception. The latter is particularly true for transition metal oxides grown on metal surfaces as substrates, where strong oxide–metal interactions occur. This determines the oxide–metal interface as a major descriptor of two-dimensional oxide behavior, which is of particular relevance and besides the two-dimensional confinement as a prominent factor in generating novel materials properties.

The book collects contributions addressing the physical and chemical behavior of quasi-two-dimensional oxides from a fundamental viewpoint but with a look at promising applications, trying to provide a balanced sight from both experimental and theoretical sides, and a comprehensive overview of the present status of the field. The atomic geometry and electronic structure, the influence of the support on two-dimensional oxide overlayers and the properties of oxide–metal and oxide–oxide interfaces, the phonon structure, and the catalytic chemistry are the major topics covered in the thirteen chapters of this book. The topic of two-dimensional oxide materials is relevant to many different scientific and technological areas, and one of our main goals in this book is to show how several basic concepts and physical phenomena transversally underlie such varied fields, with a belief that realizing and appreciating such common grounds can promote interdisciplinary efforts and trigger and accelerate further progress and developments.

Finally, we would like to warmly thank all our colleagues and authors for their support and efforts, for sharing the spirit of this initiative, and producing top-level chapters which perfectly fit into a common scheme; without their contributions this book could not have been realized. We are convinced that the study of two-dimensional oxide materials will continue to be an ongoing active scientific endeavor and an active area of condensed matter research. We strongly hope that this book will provide stimulus in this direction.

Graz, Austria   Falko P. Netzer
Pisa, Italy   Alessandro Fortunelli

Contents

Contributors

Aravind Asthagiri William G. Lowrie Department of Chemical and Biomolecular Engineering, The Ohio State University, Columbus, OH, USA

Giovanni Barcaro CNR IPCF, Consiglio Nazionale Delle Ricerche, Pisa, Italy

Gennadi Bersuker The Aerospace Corporation, Los Angeles, CA, USA

Martin R. Castell Department of Materials, University of Oxford, Oxford, UK

Alexander A. Demkov Department of Physics, University of Texas, Austin, TX, USA

David A. Dixon Department of Chemistry, The University of Alabama, Tuscaloosa, AL, USA

Zdenek Dohnálek Institute for Integrated Catalysis, Pacific Northwest National laboratory, Richland, WA, USA

Sergio D'Addato Istituto Nanoscienze, CNR, Modena, Italy; Dipartimento di Scienze Fisiche, Informatiche e Matematiche, Università degli Studi di Modena e Reggio Emilia, Modena, Italy

Alessandro Fortunelli CNR-ICCOM, Consiglio Nazionale Delle Ricerche, Pisa, Italy

Kurt D. Fredrickson Department of Physics, University of Texas, Austin, TX, USA

Stefan Förster Surface Science Group, Institute of Physics, Martin-Luther-Universität Halle-Wittenberg, Halle, Germany

Jacek Goniakowski CNRS, Institut Des Nanosciences de Paris, Paris, France; Institut des NanoSciences de Paris, Sorbonne Universités, Paris, France

Bruce D. Kay Institute for Integrated Catalysis, Pacific Northwest National laboratory, Richland, WA, USA

Kristy J. Kormondy Department of Physics, University of Texas, Austin, TX, USA

Paola Luches Istituto Nanoscienze – CNR, Modena, Italy

Vladimír Matolín Faculty of Mathematics and Physics, Charles University in Prague, Praha 8, Czech Republic

Iva Matolínová Faculty of Mathematics and Physics, Charles University in Prague, Praha 8, Czech Republic

Josef Mysliveček Faculty of Mathematics and Physics, Charles University in Prague, Praha 8, Czech Republic

Fabio Ribeiro Negreiros Centro de Ciências Naturais e Humanas, Universidade Federal do ABC, Santo André, SP, Brazil

Falko P. Netzer Surface and Interface Physics, Institute of Physics, Karl-Franzens University Graz, Graz, Austria

Claudine Noguera CNRS, Institut Des Nanosciences de Paris, Paris, France; Institut des NanoSciences de Paris, Sorbonne Universités, Paris, France

Gianfranco Pacchioni Dipartimento di Scienza dei Materiali, Università di Milano Bicocca, Milano, Italy

Thomas Risse Berlin Joint EPR Laboratory, Institute for Chemistry and Biochemistry, Freie Universität Berlin, Berlin, Germany

Mario Rocca Dipartimento di Fisica dell'università di Genova, IMEM-CNR, Unità Operativa di Genova, Genoa, Italy

José A. Rodriguez Chemistry Department, Brookhaven National Laboratory, Upton, NY, USA

Roger Rousseau Institute for Integrated Catalysis, Pacific Northwest National laboratory, Richland, WA, USA

Letizia Savio IMEM-CNR, Unità Operativa di Genova, Genoa, Italy

Luca Sementa CNR-ICCOM, Consiglio Nazionale Delle Ricerche, Pisa, Italy

Alexander L. Shluger Department of Physics and Astronomy, University College London, London, UK

Darío J. Stacchiola Chemistry Department, Brookhaven National Laboratory, Upton, NY, USA

Svetlozar Surnev Surface and Interface Physics, Institute of Physics, Karl-Franzens University Graz, Graz, Austria

Iorwerth Owain Thomas Department of Physics, Durham University, Durham, UK

Stefan Vajda Materials Science Division and Center for Nanoscale Materials, Argonne National Laboratory, Argonne, IL, USA; Department of Chemical and Environmental Engineering, Yale University, New Haven, CT, USA; Institute for Molecular Engineering (IME), The University of Chicago, Chicago, IL, USA

Luca Vattuone Dipartimento di Fisica dell'università di Genova, IMEM-CNR, Unità Operativa di Genova, Genoa, Italy

Matthew B. Watkins School of Mathematics and Physics, University of Lincoln, Brayford Pool, Lincoln, UK; Department of Physics and Astronomy, University College London, London, UK

Jason F. Weaver Department of Chemical Engineering, University of Florida, Gainesville, FL, USA

Wolf Widdra Surface Science Group, Institute of Physics, Martin-Luther-Universität Halle-Wittenberg, Halle, Germany

Chen Wu School of Materials Science and Engineering, State Key Laboratory of Silicon Materials, Zhejiang University, Hangzhou, China

Chapter 1
Structure Concepts in Two-Dimensional Oxide Materials

Falko P. Netzer and Svetlozar Surnev

Abstract The atomic structures of two-dimensional oxide systems are investigated with the aim to unravel trends in their complex structural behavior and to identify the major structure-determining descriptors. Categories of oxide structures are introduced, and the important role of the various degrees of freedom of the metal-oxide interface parameters for 2-D structure formation and stability is highlighted with the help of prototypical examples.

1.1 Introduction

Ultrathin films of metal oxides constitute a new class of materials, whose properties deviate from and are often not shared by their respective bulk counterparts [1, 2]. The film thicknesses, at which these deviations from bulk behavior occur, are not uniquely defined and may depend on the particular material and on the physical or chemical properties under consideration. In this chapter, we will be very restrictive and address oxide "films" that are at the two-dimensional (2-D) limit, i.e. oxide materials consisting of only one atomic layer or one single-polyhedron thick layer. In this limit of single layers, the behavior of the oxides approaches that of true 2-D systems. For practical and experimental purposes, the oxide monolayers are typically supported on a solid substrate: convenient substrates are metal single crystal surfaces. The surface science of metal single crystal surfaces is well established, they are easy to prepare in atomically clean form, and their conducting character is beneficial for the use of experimental methodologies involving charged particle probes. Of course, oxide monolayers on metal single crystal surfaces cannot be considered as systems of practical reality, but have to be regarded as model systems

F.P. Netzer (✉) · S. Surnev
Surface and Interface Physics, Institute of Physics, Karl-Franzens University Graz,
Universitätsplatz 5, 8010 Graz, Austria
e-mail: falko.netzer@uni-graz.at

S. Surnev
e-mail: svetlozar.surnev@uni-graz.at

for fundamental studies of scientific endeavor. Studies on model systems are an inherent and essential component of the scientific analytical approach. They allow for a close coupling of experiments with theory, thus creating a platform for a detailed atomic understanding of the properties in low-dimensional complex solids.

The science of 2-D materials has seen a veritable hype during the last decade, which was prompted by the discovery of graphene, and many 2-D materials beyond graphene have been introduced since [3]. Most of these 2-D materials are derived from *van der Waals* solids, that are layered solids characterized by strong intra-layer but weak inter-layer interactions; the latter occur because the layers are internally bond saturated. When depositing these 2-D layers on a substrate, the overlayer-substrate interactions are typically weak. This is in contrast to oxides supported on metal surfaces, where strong interfacial interactions are often encountered, in particular in the case of transition metal oxide overlayers. This strong interfacial coupling of a nanoscale oxide to a metal surface creates a new combined system, an oxide-metal hybrid system, with novel and often unprecedented physical and chemical properties as compared to its individual constituents [4–6]. For oxide overlayers at the 2-D limit, the behavior of the oxide-metal hybrid system is largely determined by the interactions at the interface: in a way, a 2-D oxide layer on a metal may be regarded as a model system or even as an expression of the true oxide-metal interface.

Several degrees of freedom contribute to the interfacial interactions, amongst them structural, electronic and chemical, corresponding to the atomic geometry, the mixing of electronic energy levels including charge transfer, and to the chemical bonding at the interface. In this chapter, we will concentrate on the aspects of atomic structure, which is a key property to which many other properties are related. In a formally reductionist approach, the influence of parameters such as lattice (mis)match and symmetry, electronic effects as well as chemical affinities and bonding at the interface on the oxide overlayer structure will be treated separately, keeping however in mind the interplay and the intricately interwoven balance of these parameters in determining the atomic geometry of the 2-D oxide layer. Structure concepts in 2-D will be highlighted in comparison to bulk structure motifs, and the effects of stabilizing particular structures in 2-D, such as polarity compensation, strain release, charge transfer and finite size effects will be identified. The chemical bonding at the interface as a result of the local epitaxial relationship and the influence of the surface energy and the adhesion energy of the overlayer in the total energy balance [7] will also be points of discussion.

Bulk oxide structures may be visualized from two different viewpoints: (i) as a stacking sequence of layers, for example the rock salt structure in [111] direction can be seen as a sequence of alternating hexagonal planes of oxygen (anions) and metal atoms (cations) (Fig. 1.1a); or (ii) as the combination of metal-oxygen polyhedral coordination blocks, connected and nested via shared corners, edges and planes of the polyhedra; the cubic arrangement of metal-oxygen octahedra in the ReO_3 structure (the parent structure of the perovskite oxides) via the connection of corners is an example for the latter (see Fig. 1.1b). The 2-D structures discussed here will be categorized accordingly, trying to use the most intuitive and pictorial

Fig. 1.1 **a** Representation of the rock salt structure (RS) as a stack of hexagonal cation and anion layers in the [111] direction. **b** Cubic ReO_3 structure, consisting of corner sharing ReO_6 octahedra (*red* O atoms) (Color figure online)
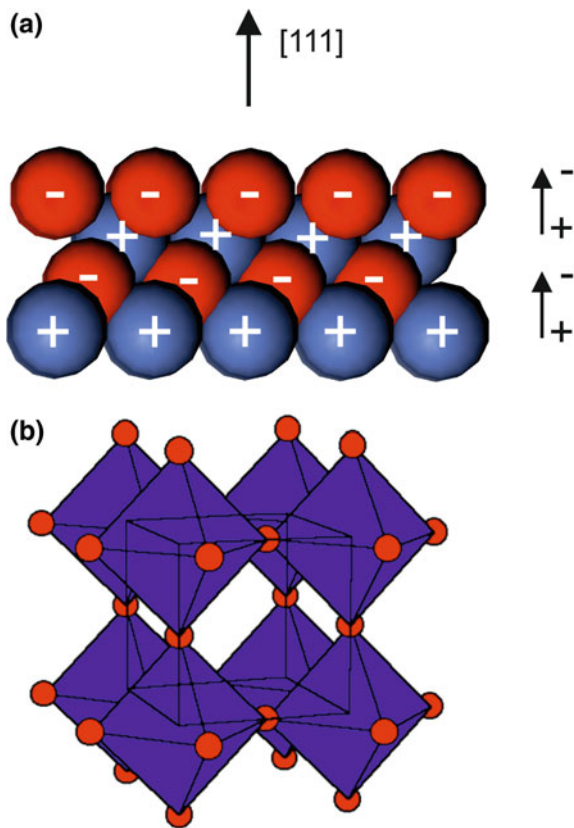
representation for the description. The chemistry at the interface depends on the affinities of the involved elements to each other and to oxygen. The interfacial interactions may be divided into strong and weak, creating so called reactive interfaces, with interdiffusion or chemical reaction of the constituents, or non-reactive and abrupt interfaces, respectively. If the metal surface is intended to provide mainly a rigid support for the 2-D oxide layer, noble metal surfaces of group VIII or Ib are typically chosen, thus providing abrupt, but not necessarily chemically inert interfaces. In the case of weak oxide-metal interactions, incommensurate oxide overlayers are frequently observed. They lead to characteristic patterns in the low-energy electron diffraction (LEED) diagrams or in scanning tunneling microscopy (STM) images due to the Moiré superposition effect of mismatched lattices and are easily identified, as discussed further below. Subtle variations of the interface chemistry modify the oxide-metal hybrid system and allow one to tune some of the properties to a certain extent: for a given oxide overlayer, completely different structure concepts may be encountered on different metal substrate surfaces. However, also here the intermixing and balance of geometrical, electronic and chemical degrees of freedom may be pronounced.

External thermodynamic parameters during the fabrication of 2-D oxide systems such as temperature and oxygen pressure, i.e. the chemical potential of oxygen μ_O, have a profound influence on the stoichiometry and the oxidation state of the growing oxide phase. It has to be mentioned that most experimental investigations of 2-D oxide systems employ the so called surface science approach, that is preparation using physical vapor deposition methods in ultrahigh vacuum (UHV) and in situ characterization of the oxide deposits [8, 9]. Thin film growth is inherently a non-equilibrium kinetic process. However, kinetic effects leading to the stabilization of meta-stable oxide structures tend to be more important in 2-D than in the 3-D case, as a result of more flexibility in the structural components and in phase composition. The discussion of 2-D oxide phase diagrams will give an impression of phase complexities in some oxide-metal systems and of the interplay between thermodynamic versus kinetic effects.

As argued above, 2-D oxides on metal surfaces are interesting model systems for the study of the emergent properties of low-dimensional solids, however quasi-2-D oxide layers exist already in a number of present-day technologies, and promising applications in new device elements of the upcoming nanotechnologies may be envisioned. 2-D oxides are used as catalytic materials, in solid oxide fuel cells and gas sensors, as corrosion protection layers, and in nano-electronic and spintronic devices [10]. As multifunctional systems, they are of interest in biocompatibility applications, in solar energy cells and the multi-ferroic properties of some oxide systems may eventually be used for novel ways of information storage. Turning on to a different subject, the particular geometry of 2-D oxide layers at the interface between metal substrate and oxide overlayer phases is important in mediating the epitaxial growth of oxide thin films. The flexibility of their low-dimensional structures may provide graded interfaces between dissimilar substrate and film materials and may thus enable the epitaxial growth by adjusting symmetry and lattice mismatch. The fields of interest and applications of 2-D oxide systems are thus diverse and wide open and new developments yet unforeseen may well be at hand.

The organization of this chapter is as follows. In Sect. 1.2, 2-D structure categories are introduced, which allow us to identify common trends in the complex variety of oxide-metal systems. The various structure types will be introduced and analysed in the different subsections. In Sect. 1.3, the focus is on the reactivity of interfaces, and this will lead us on the road of increasing complexity from binary oxides to ternary oxide layers. In Sect. 1.4, we address finite size effects in stabilizing 2-D oxide structures, whereas in Sect. 1.5 the influence of the interface chemistry in terms of the affinities of the chemical constituents of the interface on the 2-D oxide structure type is examined. In Sect. 1.6, the thermodynamic stability and kinetic effects of formation of 2-D oxide structures is at the basis of the presented surface phase diagrams. Here, a selected 2-D oxide phase diagram in the form of a projection of the stability regions of phases onto the relevant parameter space is discussed. In Sect. 1.7, the role of the interface bonding subjected to the local epitaxial relationship in lattice and symmetry mismatched systems, leading to mesoscopic nanopattern formation, is investigated. Finally, a brief synopsis in Sect. 1.7 concludes the chapter. Throughout the sections, it is attempted to identify

benchmark or prototypical oxide-metal systems to illustrate the 2-D structure concepts and their major stabilizing agents: within the framework of the reductionist approach these are the release or minimization of strain, the compensation of polarity, electronic charge transfer and local bonding at the interface, which will be conceptually treated as separate effects. As the focus of this chapter is on concepts, a comprehensive bibliographic referencing by listing the available information of reported oxide-metal systems according to their structure types is not undertaken.

1.2 Structure Elements of 2-D Oxide Systems on Metal Surfaces

The cubic rock salt structure (RS), which is the structural basis of the stable 3d transition metal (TM) monoxides VO, MnO, FeO, CoO and NiO, provides a useful starting ground for deriving structure elements of 2-D oxide systems. Many different structure motifs of 2-D oxides can be created by and related to simple RS structure blocks, with modifications as a result of interface and dimensionality effects. The most stable surface of RS is the non-polar (100) plane, which is a square arrangement of oxygen anions and metal cations in a single charge compensated plane. Planar oxide monolayers of RS (100)-type with square symmetry and modifications or reconstructions thereof provide stable structures for a number of TM oxide systems (see Sect. 1.2.1). The hexagonal monolayer analog of the RS (100) plane is not a structure element of RS, but it can be derived from the hexagonal boron nitride (BN) structure, by replacing B and N by metal and oxygen. Indeed, this structure has been found for some 2-D oxide layer systems. Uniaxial structure motifs, with two-fold symmetry properties, have also been observed in planar, or quasi-planar oxide single layers—the latter display a weak corrugation or rumpling of anion or cation sites in a preferred direction, but the deviation from planarity is less than in the bilayer structures mentioned below. Uniaxial structure formation requires a change of lattice symmetry across the interface (e.g. a hexagonal overlayer lattice on a square substrate) or the presence of local metal-oxygen (M–O) coordination spheres of different type, e.g. square and triangular units, within the overlayer (also discussed in Sect. 1.2.1).

In [111] direction, the RS consists of stacks of hexagonal bilayers of oxygen and metal planes (see Fig. 1.1a). These bilayers are polar, with a finite dipole moment perpendicular to the planes, and they are unstable in the bulk due to a diverging electrostatic energy, unless there is charge compensation at the surfaces [11, 12]. In 2-D, however, they may become stable structure elements, because additional mechanisms of polarity compensation become operative. Hexagonal O–M–O trilayer structures may also be derived from the [111] RS stacking sequence: they are stable charge compensated unpolar slabs and have been observed to form on several

2-D oxide systems at higher chemical potentials of oxygen, i.e. under more severe oxidizing conditions. The bilayer and trilayer structures are analyzed in Sect. 1.2.2.

More complex 2-D structures, comprising different connectivities of M–O building blocks and metal cations with different oxygen coordination spheres, and thus different oxidation states, have been detected for the early TM oxides, such as Ti and V oxides; this is the reflection of the comparable stability of different oxidation states of the metal cations. In Sect. 1.2.3, examples of such oxide systems with complexity in oxidation states are introduced and discussed. Furthermore, the formation of complicated quasi-2-D networks of alumina with unusual Al–O surroundings is mentioned here.

Elastic strain, as a result of the epitaxial lattice mismatch at the interface, and its reduction is an important issue in oxide overlayer structure considerations. In 2-D systems, the strain term in the total energy balance may become a decisive factor in promoting novel structure elements that are not stable in 3-D bulk systems. It is therefore appropriate at this point to recall some basic facts. The lattice mismatch **m** is defined by

$$\mathbf{m} = (\mathbf{b} - \mathbf{a})/\mathbf{a} \tag{1.1}$$

with **b** the lattice constant of the overlayer and **a** that of the substrate. Traditionally, the lattice constants of the bulk systems have been taken to evaluate **m** [13, 14]. While this is a reasonable approximation for the substrate surface, it is not so for the 2-D overlayer. The lattice constant of an isolated 2-D layer is contracted with respect to the bulk value. In a somewhat hand-waving argument, this may be understood by the picture of bond strength conservation involving the coordination number [15]: a M–O dimer has a smaller bond length than a 2-D M–O layer, which in turn has smaller bond lengths than the 3-D solid, in sympathy with the increase of the coordination number. Thomas and Fortunelli [16] have investigated, using a density functional DFT + U method, the lattice parameter of NiO(100) on Ag(100) and have compared it to the free standing NiO monolayer. Accordingly, the isolated NiO monolayer has a Ni–Ni spacing of 2.8 Å, which is shrinked by approximately 5 % from the experimental NiO bulk value (2.95 Å). If the NiO monolayer is deposited on a metal surface, the oxide-metal bonding increases the coordination number again and the contraction is partly reversed. The calculations predict that a NiO monolayer on Ag(100) is compressed by 2 %, whereas on Pd(100) a compression of NiO of 3.6 % is predicted [17]. The interfacial strain is thus significantly smaller than the 7 % estimate based on the lattice mismatch as calculated using the respective bulk lattice constants. Thus, in some formally strongly lattice mismatched overlayer-substrate systems—if using bulk lattice parameters for the estimate—the actual lattice mismatch and the corresponding strain can be much less, if the low dimensionality of the overlayer is taken into account.

1.2.1 Planar Oxide Monolayers

Here the term "planar" is used to indicate that the metal and oxygen atoms are located essentially in a single plane, although the surface does not necessarily have to be completely flat, but can be corrugated or rumpled, with the centre of gravity of the anion or cation species slightly offset. Of course, the distinction between single layer and bilayer, where anions and cations are considered to belong to separate *layers*, is somewhat arbitrary, but so is the entire categorization, which is merely a pedagogical construct to facilitate the discussion. In the first part of this subsection, oxide single layer structures that can be derived from a RS (100)-type plane are investigated.

RS (100)-type structures. The simplest structure motif in this context is a single (100) plane of a metal oxide with monoxide MO stoichiometry. This geometry is adopted by the NiO(100)1 × 1 monolayer phase on Ag(100) [18, 19]. Figure 1.2 presents STM images of a NiO(100)1 × 1 island on Ag(100), obtained from a surface prepared by deposition of 2/3 of a monolayer of Ni in 1×10^{-6} mbar O_2 on the Ag surface at room temperature followed by annealing at 600 K in oxygen. The NiO island in Fig. 1.2a shows a morphology reflecting the square symmetry of the (100) plane, whereas the high resolution image in Fig. 1.2b reveals the square mesh of bright protrusions, which have been associated with the Ni atoms according to the DFT calculations [18]. The NiO surface displays a mosaic pattern of brighter and darker contrast regions (Fig. 1.2a). This has been interpreted in terms of local regions, where the NiO forms patches of a bilayer structure, with the brighter STM contrast stemming from the monolayer and the darker from the bilayer regions. The formation of bilayer patches is a way to release the residual interfacial strain—we recall from above that the NiO monolayer is 2 % contracted on the Ag(100). The bilayer has a slightly expanded lattice (due to the higher coordination) and thus improves the elastic energy balance. The darker contrast in the STM image of the bilayer region is due to the lower density of states around the Fermi energy of the
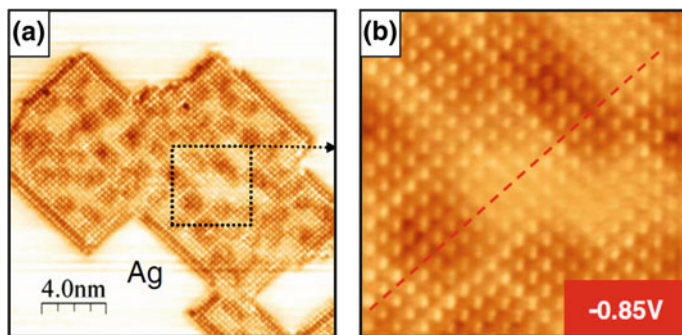
Fig. 1.2 STM images of a NiO(100)1 × 1 island embedded in Ag(100). **a** (20×20 nm^2); sample bias voltage $V_S = -0.85$ V; tunneling current $I_T = 0.5$ nA. **b** (5×5 nm^2); $V_S = -0.85$ V; $I_T = 0.5$ nA; image FFT filtered. Adapted from [19]

bilayer as compared to the monolayer, which is metallic as a result of the interaction with the metal surface [16, 18, 19]. The NiO island in Fig. 1.2 is embedded into the Ag substrate rather than located on top, and this is the majority configuration on this surface. The DFT calculations [18] have found that the embedded (1 × 1) monolayer structure gains stability by the Ni–Ag bonding and the formation of a bilayer rim at the island boundaries. Figure 1.3 gives a schematic model of a NiO(100)1 × 1 island embedded into the Ag(100) surface. In this context, it is of interest to note that the (100)1 × 1 phase has not been detected for MnO on Ag(100) in the 2-D monolayer limit. The MnO(100)1 × 1 phase is observed in the form of 3-D islands [20–22], but for the monolayer only a (2 × 1) structure has been observed for MnO on Ag(100) [20], as discussed below. Presumably, the higher strain as a result of the larger lattice mismatch of MnO precludes the formation of a (100)1 × 1 wetting layer on Ag(100).

A more complex structure system, which may be traced back to the RS (100)-type motif, is the c(4 × 2) structure observed for several TM oxides on Pd(100). The c(4 × 2) structure has been reported for NiO_x [23, 24], CoO_x [25] and MnO_x [26], and is theoretically predicted for FeO_x [27], and it thus seems to constitute a more general 2-D structure concept. Figure 1.4 illustrates the structural ingredients of the c(4 × 2) phase for the example of CoO_x on Pd(100) [28]. The STM image of Fig. 1.4a shows the c(4 × 2) periodicity with respect to the Pd(100) surface, where the c(4 × 2) and the primitive rhombic unit cells are indicated and labeled A and B. Two types of defects are visible on the image with darker and brighter contrast, presumably due to missing cations and adsorbate species, respectively. The LEED pattern in Fig. 1.4b with sharp spots confirms that the surface is well ordered, the c(4 × 2) (A) and the primitive (B) unit cells are also drawn. The high-resolution STM image (Fig. 1.4c) reveals that the structure is characterized by large bright maxima defining the c(4 × 2) unit cell and smaller and less-bright protrusions in a zig-zag line following the ⟨011⟩ Pd substrate directions. Alternatively, the c(4 × 2) unit cell may also be spanned by the dark depressions in between the bright spots.
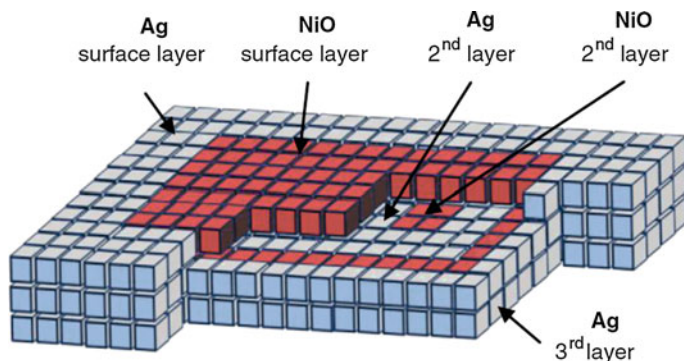
Fig. 1.3 Schematic model of a NiO(100)1 × 1 island embedded in Ag(100); *blue* Ag atoms; *red* NiO. Reproduced with permission from [19] (Color figure online)
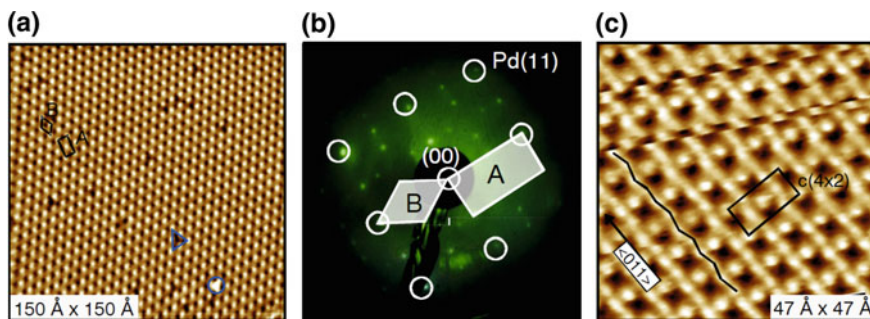
Fig. 1.4 CoO$_x$/Pd(100) c(4 × 2) phase: **a** STM image (15 × 15 nm^2); V$_S$ = +1 V; I$_T$ = 0.1 nA. **b** LEED pattern (electron energy 104 eV). **c** Atomically resolved STM image (4.7 × 4.7 nm^2); V$_S$ = +0.08 V; I$_T$ = 0.1 nA. The characteristic features, i.e. the rectangular c(4 × 2) unit cell and the zig-zag chain of atoms, are highlighted. Reproduced with permission from [28]

According to the DFT calculations, the Co atoms are imaged as maxima in the STM, whereas the O atoms are imaged dark [25].

The c(4 × 2) structure may be modeled by a RS (100) plane, into which 1/4 of cation vacancies has been introduced, defining the c(4 × 2) unit cell and a formal M$_3$O$_4$ stoichiometry. This is shown for Mn$_3$O$_4$ supported on Pd(100) in Fig. 1.5: the square RS (100)-type lattice is given by the Mn atoms (light gray) and O atoms (red), the circles denote the Mn vacancies, the dashed lines trace the 2-D unit cell, and the solid zig-zag line indicates the Mn lateral displacements in the relaxed structure model [29], as discussed below. Franchini et al. [26, 29] have investigated the Mn$_3$O$_4$ c(4 × 2) structure in detail with standard and generalized DFT, considering different adsorbate registries to the Pd substrate as well as different magnetic ordering models. The most stable adsorbate configuration was generally found with the Mn atoms located above the Pd hollow sites and the O atoms on top of Pd

Fig. 1.5 Top view of the geometrical model of the c (4 × 2) Mn$_3$O$_4$ phase on Pd (100) (*red* O atoms; light *grey* Mn atoms; *small green spheres* Pd atoms underneath). *Dashed lines* indicate the 2-D unit cell, full line the Mn lateral displacements, *circles* highlight the position of vacancies. Adapted from [29]
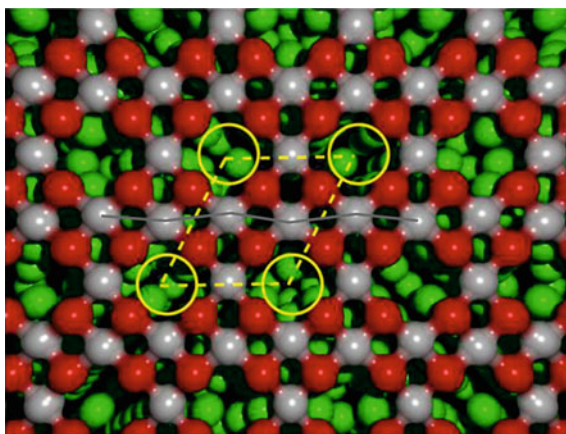
surface atoms (RH1 model), but depending on the choice of the functionals in the calculations antiferromagnetic (AFM2) or ferromagnetic (FM) order was predicted as the lowest energy ground state. However, using the HSE hybrid functional approach a slight preference for the FM configuration as the thermodynamic ground state was obtained [26]. In order to validate this result, experimentally accessible quantities, namely STM images and phonon frequencies, have been simulated for the RH1-AFM2 and RH1-FM models and compared to the measured values. Figure 1.6 shows the optimized geometrical structure for the RH1-FM and RH1-AFM2 magnetic configurations. In both models, there is a significant in-plane lattice distortion with large lateral displacements of Mn and O species, particularly around the Mn vacancies. These distortions are a means to relax the interfacial strain in the overlayer and are reminiscent of a 2-D polaronic distortion. However, whereas the RH1-FM model leads to a flat surface, the RH1-AFM2 model gives a vertical bucking between the oxygen atoms. These geometrical differences are, however, difficult to evaluate in the experimental STM images. There are two types of Mn atoms in the structure, which may be loosely associated with Mn^{2+} and Mn^{3+} species, which have different densities of states (DOS) and magnetic moments and, significantly, which are distinctly different for the two magnetic structure models. The DOS are reflected in the STM contrast and thus allow us to distinguish between
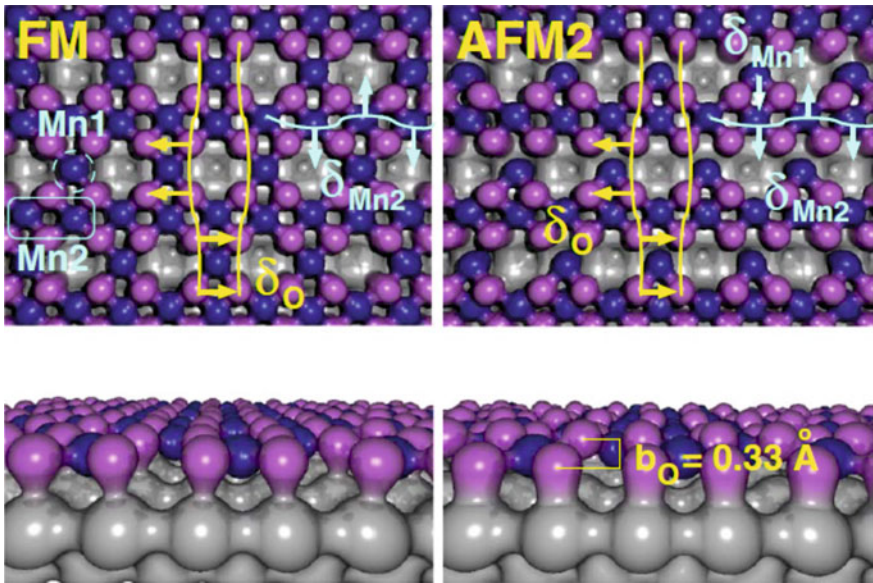
Fig. 1.6 Optimized geometrical structure for the c(4 × 2) Mn_3O_4 RH1 model in FM (*left*) and AFM2 (*right*) magnetic configuration (*light grey* Pd substrate atoms; *pink* O atoms; *blue* Mn atoms). Two distinct Mn species are distinguishable: Mn1 sandwiched between two vacancies and two Mn2 atoms, forming the *zig-zag lines* as highlighted. Strain is indicated by the *arrows*. Note the vertical buckling b_O between oxygen atoms in the AFM2 model. Reproduced with permission from [26]

the models: it turns out that only the RH1-FM model gives the correct contrast in the STM simulations, which is compatible with the experimental image (see Fig. 1.7).

The phonon structure is a highly diagnostic means in the analysis of complex oxide phases [5]. HREELS experiments have established that the phonon loss spectrum of the Mn_3O_4 c(4×2) surface has a single pronounced peak at 44 meV [29]. The DFT calculations for the FM structure found a single dipole active phonon mode in perfect agreement with this experimental value. This phonon mode results from the antiphase and out-of-plane vibrations of the O and Mn sublattices perpendicular to the surface, a mode that is typical of the ideal MnO(100) surface, thus giving overall credence to the (100)-type derived structure model of the c(4×2) structure.

The STM and phonon measurements in conjunction with the DFT calculations support a ferromagnetic model as the lowest energy ground state of the c(4×2) structure. However, an independent experimental confirmation would still be desirable. Altieri et al. have performed X-ray magnetic circular dichroism (XMCD) experiments of the Mn_3O_4 c(4×2) phase [30]. The experiments have been carried out on a c(4×2) Mn_3O_4 phase on a stepped Pd(1 1 21) surface, a vicinal to Pd (100), because the overlayer can be prepared in a virtually defect-free single domain structure on this surface (see Sect. 1.4). A clear magnetic anisotropy in the temperature and field dependent Mn $L_{2,3}$ XMCD spectra has been detected, but the sample remained paramagnetic down to 8K, the lowest temperature attainable in the experiments. Thus, a ferromagnetic state could not be confirmed, perhaps the temperature in the experiment was still too high. The observed magnetic anisotropy with its easy axis perpendicular to the surface has been related to a largely unquenched orbital moment as revealed by XMCD sum rule analysis [30]. A model considering the effects of the crystal field acting on the Mn cations in the c(4×2) Mn_3O_4 structure, where the Mn vacancies hole dope the 3d states, has been
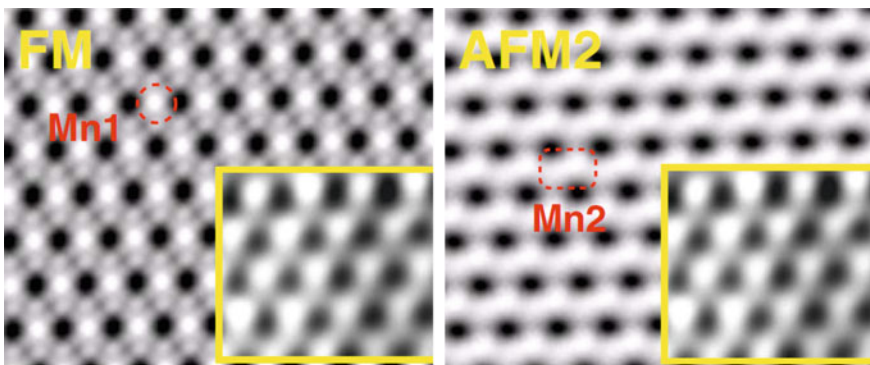
Fig. 1.7 Simulated STM images of the RH1-FM and RH1-AFM c(4×2) Mn_3O_4 structures compared with the experimental STM image (reproduced in the *inserts*). Mn atoms appear as bight maxima, the O atoms are not seen. Reproduced with permission from [26]

proposed to account for this perpendicular magnetic anisotropy. This is in accord with the proposed geometry and structure model of the c(4 × 2) phase. Although the problem of ferromagnetism in c(4 × 2) Mn_3O_4 remains an open question, the XMCD measurements of Altieri et al. have demonstrated that 2-D oxide systems may indeed support interesting magnetic behavior.

Hexagonal monolayer structures. A hexagonal oxide monolayer can be realized within the planar BN structure, if boron and nitrogen are replaced by metal and oxygen species. Goniakowski and Noguera have derived this structure (they called it graphite-like B_k structure) from theoretical considerations of polarity compensation for the MgO(111) monolayer on Ag(111) [31], and their model is consistent with the experimental observations of MgO(111) thin films on Ag(111) by Kiguchi et al. [32] (see also Chap. 7 by Noguera and Goniakowski). For ZnO monolayers on Ag(111), Tusche et al. [33] have proposed the hexagonal BN-type structure on the basis of surface X-ray diffraction and STM results, emphasizing the depolarization character of this structure, which is accompanied by a significant lateral expansion of the lattice constant and a reduced Zn–O bond length within the ZnO sheets. For film thicknesses exceeding 3–4 ML, a transition to the bulk wurtzite structure has been observed [33]. The hexagonal planar structure has also been reported for ZnO on Pd(111) [34]. A (6 × 6) structure has been detected in the STM and LEED experiments, which has been rationalized by DFT calculations in terms of a Zn_6O_6 coincidence structure of the BN-type. This structure is thermodynamically the most stable phase over a large range of oxygen chemical potentials for the monolayer and for coverages up to 4 ML, but converges to the bulk wurtzite structure for thicker films [34].

Uniaxial monolayer structures. The (2 × 1) structures reported for NiO and MnO on Ag(100) at the monolayer stages of growth fit into this category [18, 20]. Figure 1.8 shows STM images of the MnO(2 × 1) phase on Ag(100) [20]: the oxide grows in elongated stripes along the high symmetry ⟨110⟩ directions of the substrate (Fig. 1.8a), with bright and dark lines separated by twice the Ag lattice constant, which define the ×2 order parameter. The peculiar growth pattern in form
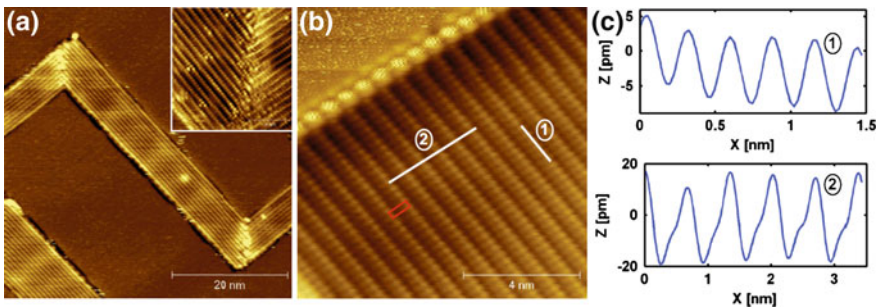
Fig. 1.8 High-resolution STM images of the MnO(2 × 1) structure on Ag(100): **a** $V_S = -1.9$ V; $I_T = 0.1$ nA; **b** $V_S = -1.0$ V; $I_T = 0.1$ nA. The *insert* in (**a**) shows a domain boundary between two orthogonal (2 × 1) stripes. **c** Line scans along the lines 1 and 2 of image (**b**). Adapted from [20]

of narrow oxide stripes is due to a symmetry breaking kinetic growth phenomenon, which has been ascribed to the asymmetric attachment and diffusion energies of ad-atoms at the (2 × 1) island boundaries [20]. The high-resolution STM image of the (2 × 1) structure in Fig. 1.8b reveals the atomic maxima along the bright lines and at the upper left hand corner a MnO–Ag island edge, which is decorated by bright blobs due to an electronic contrast phenomenon at the island boundary. The STM line scans in Fig. 1.8c, following the lines indicated in (b), give measured corrugations of ∼10 and ∼40 pm along and across the (2 × 1) lines, respectively. The DFT calculated model of the MnO(2 × 1) structure on Ag(100) is depicted in Fig. 1.9a. The Mn atoms (blue) are distinguished by threefold oxygen (red) coordination or, alternatively, O–Mn–O zig-zag lines; the condensation of either of these structure elements into a 2-D structure and superimposing it onto the square Ag substrate yields a quasi-hexagonal network with alternating Mn–O up and down zig-zag rows. These rows form the ×1 lines of the (2 × 1) structure, whereby the protruding O atoms are imaged bright in the STM, as shown by the simulated STM image in Fig. 1.9a, left panel. The (2 × 1) structure is polar and its total energy as calculated by DFT is only at a local minimum: it is thus a meta-stable phase, with
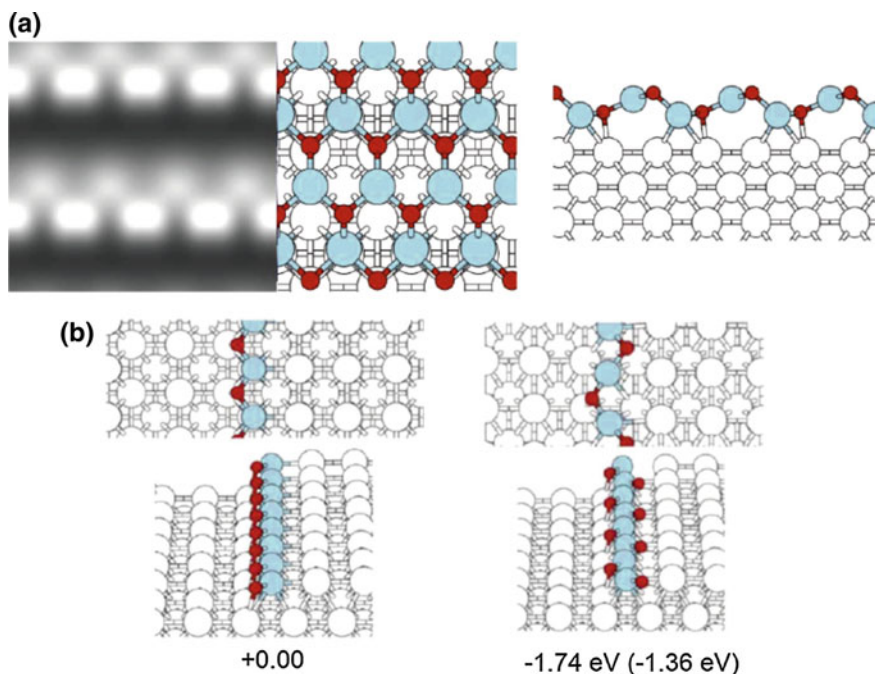
Fig. 1.9 **a** Structural model (*top* and *side views*) and simulated STM image at a bias +1.0 V of the (2 × 1) phase of MnO on Ag(100) (*blue* Mn atoms; *red* O atoms). **b** Growth of a MnO stripe on the border of a step on Ag(100): the structure and energetics of the (100)1 × 1-like stripe (*left*) against the (2 × 1)-like stripe (*right*) are compared, as derived from a DFT + U approach (U = 4.5 eV) or B3PW91 (*in parenthesis*). Adapted from [20] (Color figure online)

the MnO(100)1 × 1 phase being the thermodynamically stable ground state. The (2 × 1) phase, which in the case of MnO/Ag(100) is the predominant phase observed experimentally for the monolayer, must therefore be kinetically stabilized during growth. Obermüller et al. [20] have investigated theoretically the stability of MnO line elements at Ag step edges (see also Chap. 2 by Fortunelli et al.). Figure 1. 9b shows (1 × 1)-type (left) and (2 × 1)-type (right) MnO stripes at the border of a silver step on Ag(100), comparing their relative stabilities: the (2 × 1)-like pattern is more stable than the (1 × 1)-like pattern, by a significant amount of >1.30 eV per MnO unit, mainly due to the cancelation of polarity. The kinetic nucleation of the (2 × 1) structure motif at Ag step edges is thus favorable, and once nucleated, the (2 × 1) structure continues to grow into the two-dimensional layer.

The (6 × 1) NiO structure on Rh(111)-type surfaces [35, 36] illustrates the formation of a uniaxial structure via the incorporation of Ni–O coordination spheres of different symmetry, namely triangular threefold coordinated and quadratic fourfold coordinated oxygen units. Both structure elements are related to the RS (100) and RS (111) surface orientations. The combination of these structure units leads to the development of troughs and ridges along the [110] surface direction. Figure 1.10 displays a high-resolution STM image of the (6 × 1) structure (upper part) and the DFT derived structure model (lower part); the triangular and quadratic oxygen units are colored dark and bright red, respectively [36]. The structure may be viewed as containing Ni–O sheets with quadratic O coordination, which are connected via Ni atoms contributing to the triangular O coordination units: this leads to a complex line pattern in STM (see Fig. 1.10), which however has been reproduced rather well in the DFT simulations [36]. The calculations of the phase stability diagram for monolayer-thick NiO layers on Rh(111) demonstrated that

Fig. 1.10 STM image and corresponding model of the NiO(6 × 1) structure on Rh (111). Adapted from [36]
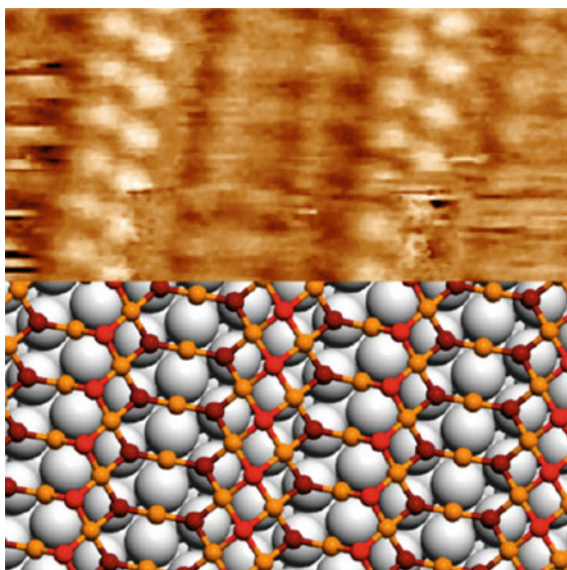
within the range of experimentally accessible oxygen potentials the (6×1) with a Ni_5O_5 stoichiometry is the most stable phase. Another example of a uniaxial surface oxide has been reported for NiO on Pt(111) by Hagenbach et al. [37], where a (7×1) structure with a pattern of bright lines in the STM has been observed. The tentative structure model of Hagenbach et al. employed again a combination of square and triangular Ni–O units [37].

1.2.2 Oxide Bilayer and Trilayer Structures

Hexagonal oxide bilayers. Hexagonal oxide bilayer structures may be derived from three structure motifs: (i) a stacking of densely packed hexagonal planes of cations and anions, as in the RS (111)-type stacking sequence (Fig. 1.11a); (ii) a honeycomb lattice of hexagons sharing sides (Fig. 1.11b); and (iii) a kagomé lattice, containing hexagons that are interconnected through their vertices and create triangles defined by the connection points (Fig. 1.11c). While the latter two lattices have been encountered only on hexagonal substrate surfaces, e.g. fcc (111)-type metal surfaces, the first structure has been reported on both hexagonal (111) and square (100) substrates.

The FeO(111) wetting layer on Pt(111) is a benchmark system of the *RS (111)-type bilayer* structure on a hexagonal substrate surface [38–43]. This bilayer is composed of the close packed oxygen layer forming the outer surface and the Fe layer at the Pt interface. As a result of the significant lattice mismatch, the overlayer is almost incommensurate and displays a characteristic Moiré modulation in the STM images [38, 39, 41, 42]; in fact, up to four different high-order coincidence structures and concomitant Moiré patterns have been reported, depending on the exact FeO coverage [41]. The FeO bilayer cannot grow much beyond two monolayers and, for higher coverages, is transformed into a Fe_3O_4(111) island phase [41]. This is due to the polar character of the FeO bilayer, which precludes further 3-D growth. The Fe–O interlayer distance of the bilayer has been measured by X-ray photoelectron diffraction by Kim et al. [40] and a compression of about 50 % relative to bulk FeO has been detected. This interlayer contraction is a way to
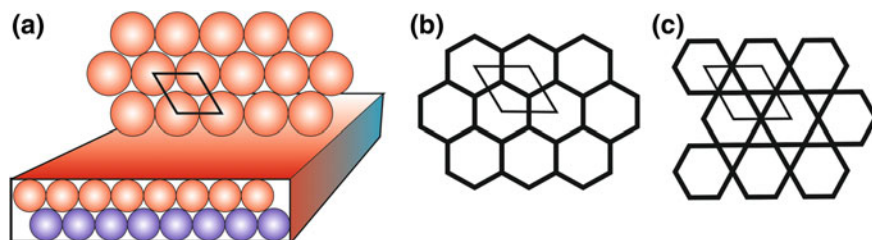
Fig. 1.11 Schematic drawings of: **a** hexagonal RS (111)-type bilayer; **b** honeycomb lattice; **c** Kagomé lattice

reduce the surface dipole and the electrostatic energy and thus adds to the stability of the bilayer. The screening of the FeO surface dipoles by the proximity of the Pt substrate is another mechanism to reduce the polarity in this 2-D system. A very similar FeO(111) bilayer geometry as for FeO/Pt(111) has been reported recently also on a Pd(111) substrate [44], with very similar STM fingerprints; it appears that the chemical nature of the substrate has only a minor influence on the details of the FeO(111) overlayer structure.

Whereas the growth of a hexagonal oxide bilayer on a hexagonal substrate is intuitively persuasive, it is more interesting on a square (100) substrate. The FeO c(2 × 10) on Pt(100) [45] and c(8 × 2) on Pd(100) [46] phases, the CoO c(10 × 2) phase on Ir(100) [47], or the CoO (9 × 2) phase on Pd(100) [48] can be interpreted in terms of a RS (111)-type structure. Here, the CoO (9 × 2) structure on Pd(100) is discussed as a prototypical example [28, 48]. Figure 1.12 displays STM images of the CoO (9 × 2) coincidence structure at different magnifications [28]. The structure is characterized by lines of elongated rod-like maxima along the substrate [0–11] direction (Fig. 1.12a, b—dashed line in b), which can be resolved into atomic protrusions along the orthogonal [011] direction at higher magnification (Fig. 1.12c). These [011] lines of maxima are laterally undulated (indicated by the thin solid line in panel c) and show a significant contrast modulation with four brighter and four darker maxima; the latter is also recognized in the self-correlation plot of the STM image (d). The CoO (9 × 2) structure has been modeled in DFT by a (111)-type bilayer as shown in Fig. 1.13, with the O plane at the surface and the Co plane at the Pd interface [48]. In the relaxed geometry, the bilayer becomes significantly distorted, with strong height modulations in both Co and O sublattices, which tend to interpenetrate each other to reduce the polarity of the bilayer and the interfacial strain. These height modulations are reflected in the atomic contrast modulations seen in the STM image (Fig. 1.12c), which have been reproduced well by the respective DFT simulations [48].
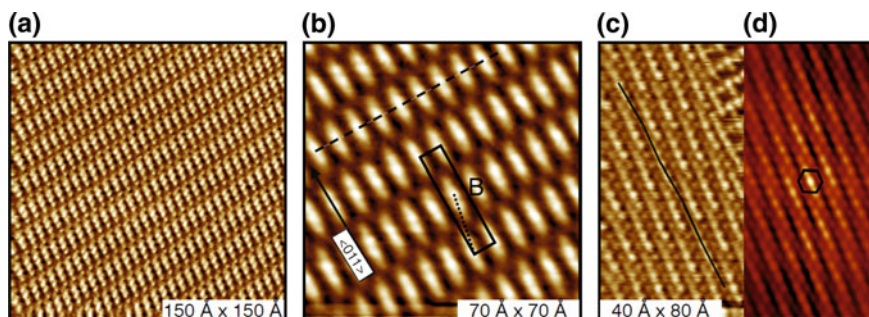
Fig. 1.12 **a–c** STM images of the CoO (9 × 2) coincidence phase on Pd(100) (**a** (15 × 15 nm^2); V_S = +0.01 V; I_T = 1.0 nA. **b** (7 × 7 nm^2); V_S = +1.0 V; I_T = 0.1 nA. **c** (4 × 8 nm^2); V_S = +0.01 V; I_T = 1.0 nA). The *rectangular* (9 × 2) unit cell of the coincidence mesh is indicated in (**b**). **d** Self-correlation image of the STM image of panel (**c**); here the *quasi-hexagonal* cell of the CoO lattice is highlighted. Reproduced with permission from [28]
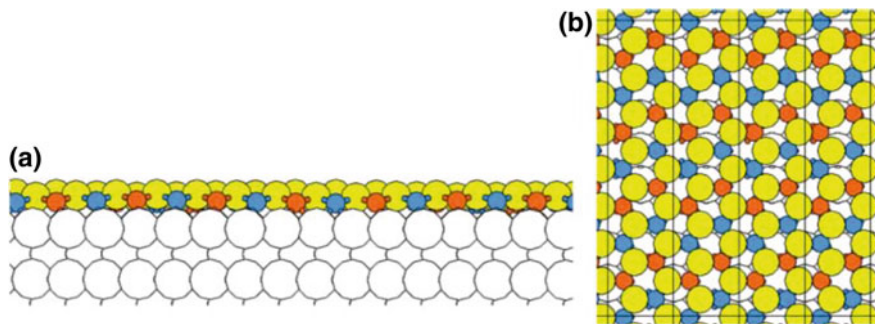
Fig. 1.13 **a** Side view of the (9 × 2) bilayer structure showing the Pd–Co–O stacking. **b** Top view of four unit cells of the (9 × 2) structure. Pd atoms are depicted in *white*, O atoms in *yellow* and Co atoms in *blue* and *red*, reflecting the AFM3 magnetic ordering of the CoO layer. Reproduced with permission from [48]

The CoO (9 × 2) phase has been found in the experiments to coexist frequently with the Co_3O_4 c(4 × 2) structure at the same Pd surface. This is in agreement with the DFT calculations, which predict a similar thermodynamic stability of the two phases, with only a slight preference for the (9 × 2) [48]. The STM images of Fig. 1.14 show an interesting aspect of the coexisting (9 × 2) (left) and c(4 × 2) (right) Co-oxide monolayer phases: the two phases are separated by a well-defined 1-D interface boundary, with a smooth transition from one structure into the other. In the c(4 × 2) structure of Fig. 1.14a (right), the dark depressions form the primitive unit cell and are due to the Co cation vacancy holes of this structure (see
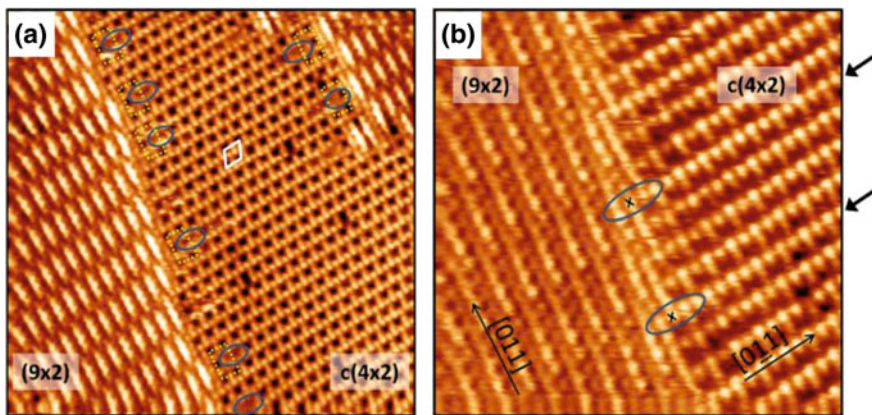
Fig. 1.14 STM images of the Co oxide (9 × 2) (*left*) and c(4 × 2) (*right*) monolayer structures coexisting on Pd(100), displaying a smooth 1-D interface. **a** [(15 × 15 nm^2); V_S = +0.08 V; I_T = 0.6 nA]. The *ellipses* at the c(4 × 2) side of the interface indicate regions with a modified arrangement of dark vacancies. **b** [(8 × 8 nm^2); V_S = +0.01 V; I_T = 1.0 nA]. The *crosses* inside the ellipses at the interface mark bright protrusions apparently belonging to both (9 × 2) and c(4 × 2) structures. Reproduced with permission from [48]

Sect. 1.2.1). Close to the (9 × 2) boundary, the pattern of dark depressions is altered as highlighted by the elipses in the figure, shifting from rhombic to square. Although the exact atomic structure of the region at the c(4 × 2)/(9 × 2) interface cannot be recognized, it has been speculated that additional Co species may have been introduced, leading to a local reduction of the Co_3O_4 c(4 × 2) stoichiometry towards the CoO (9 × 2) stoichiometry and contributing to the smooth boundary. This has been confirmed by the DFT calculations [48].

Moreover, at this point it is worth addressing an interesting technical problem. The interpretation of STM images of oxide materials relies on the identification and assignment of contrast features to atomic species. The oxide community has learnt that this requires, apart from the most simple systems, the help of theoretical simulations. In the case of the c(4 × 2) M_3O_4 phases, it has been generally accepted that the M cations are imaged as bright protrusions [25, 26, 29, 48]. At the (9 × 2)/c(4 × 2) 1-D interface in Fig. 1.14b, there are bright features marked by crosses, which are a continuation of the c(4 × 2) lines but apparently also belong to the (9 × 2) structure. This would suggest that the bright STM protrusions of the (9 × 2) structure can be identified also with Co species, as in the c(4 × 2) structure. This, however, is difficult to reconcile with the bilayer structure model. Gragnaniello et al. [48] have gone into an extensive DFT study of the problem, and found that, while indeed the Co species are imaged bright in the c(4 × 2) structure, the bright maxima in the (9 × 2) structure are located at the oxygen sites: this is the result of the complex interaction of electronic and geometrical degrees of freedom contributing to the STM contrast in this strongly distorted bilayer oxide. The simulations of the 1-D interface revealed that the bright protrusions highlighted by the crosses in Fig. 1.14b are identified as bright oxygen protrusions, thus providing a consistent picture of the interface and of the structural assignment of both 2-D Co oxide phases [48].

The first layer of vanadium oxide on Pd(111) displays a *hexagonal honeycomb lattice*, as recognised from the STM image of Fig. 1.15a. This V surface oxide has
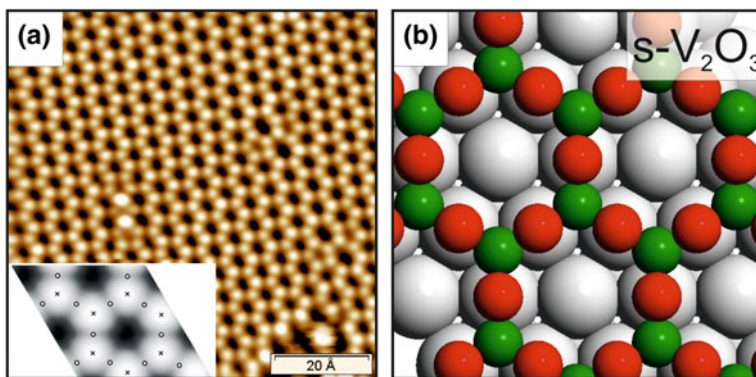
Fig. 1.15 STM image of the honeycomb surface-V_2O_3 (2 × 2) phase on Pd(111) (**a**) and respective DFT model (**b**) (*green* V; *red* O; *grey* Pd). The *insert* in (**a**) displays the DFT simulated STM contrast. Adapted from [54]

been grown under moderately oxidizing conditions [49], it forms a simple (2×2) superstructure and has been interpreted in terms of a bilayer with V_2O_3 stoichiometry [50, 51]. According to the DFT analysis, the V atoms are situated in three-fold hollow Pd sites and the O atoms are on-top of Pd surface sites (see the model in Fig. 1.15b), with the O layer ~ 0.7 Å outside the V plane [51, 52]. This *surface*-V_2O_3 phase is polar and cannot grow beyond the first layer. With increasing oxide coverage, a sequence of other complex phases has been observed [50, 53], until the oxide overlayer converges to the bulk V_2O_3 phase, which is the stable compound under the thermodynamic conditions of typical surface science growth experiments. It has to be stressed that the surface s-V_2O_3 honeycomb geometry is a particular 2-D phenomenon and not a structure element of the V_2O_3 bulk corundum structure.

The Ti_2O_3 bilayer on Pt(111) [55, 56] is related to the *surface*-V_2O_3 phase on Pd (111), but it features an interesting structural difference: it forms a *kagomé lattice*, which can be discerned in the experimental STM image of Fig. 1.16a and the respective STM simulation (Fig. 1.16b). The kagomé lattice with a lattice constant of ~ 6 Å, as derived from LEED and STM measurements, is incommensurate with the Pt lattice; overall it is less dense than a corresponding honeycomb lattice. It could be speculated that the reason for the Ti_2O_3 forming the kagomé lattice on Pt (111) may be due to the poor fit of Ti–O bond distances onto the Pt lattice, the result of which is a less dense incommensurate structure. In the case of V_2O_3 on Pd(111), the V–O bonds fit exactly onto the (2×2) structure formed by the denser honeycomb lattice. Finally, it is noted that the $(\sqrt{7} \times \sqrt{7})R19.1°$ vanadium oxide layer on Rh(111), which can been grown under highly oxidizing conditions, displays also a kagomé lattice pattern—see Fig. 1.18a. However, this phase with a formal V_3O_9 stoichiometry is not strictly a bilayer structure but more complex, and is better discussed in terms of a local building block picture in Sect. 1.2.3.

Hexagonal oxide trilayers. A hexagonal O–M–O trilayer slab may be cut out of the RS structure perpendicular to the [111] direction. The slab is apolar and stable from the electrostatic point of view and corresponds formally to a MO_2
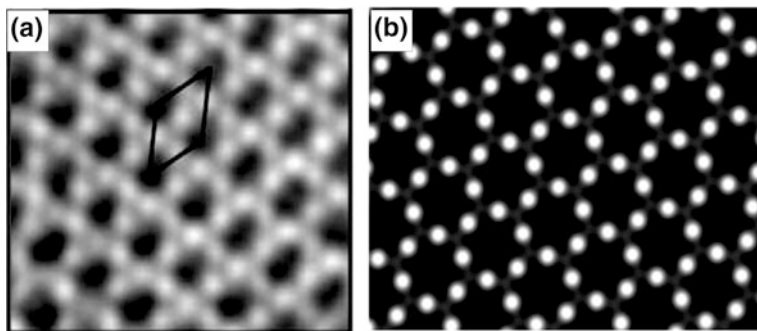
Fig. 1.16 STM image of the Ti_2O_3 kagomé phase on Pt(111) (**a** $(3 \times 3$ nm^2); $V_S = -0.4$ V; $I_T = 1.06$ nA) and theoretically simulated STM image at V $= -0.4$ V (**b**). Adapted from [56]

stoichiometry. The oxygen layer at the interface is however shared with the metallic substrate and the real oxidation state is thus somewhat lower, e.g. $MO_{2-\delta}$. Hexagonal trilayer structures have been proposed for the intrinsic surface oxides of some group VIII metals such as Ru [57] or Rh [58]. The hexagonal $VO_{2-\delta}$-hex phase on Pd(111) [50], the hex-$MnO_{2-\delta}$ phases on Pd(100) [29], the hex-CoO_x phase on Pd(100) [28], and the $c(8 \times 2)$ $CoO_{2-\delta}$ structure on Ir(100) [59] have also been interpreted within this trilayer structure concept. Apart from the last $CoO_{-\delta}$/Ir system, the other hetero-trilayers form incommensurate overlayers. An interesting case is the $FeO_{2-\delta}$ trilayer on Pt(111). It has been observed after oxidation of the FeO(111) bilayer at high oxygen pressures [60]. This trilayer phase is of catalytic relevance, since it has been shown to be the active surface in the low temperature oxidation of CO [61, 62]. Recently, Zeuthen et al. [44] have presented an STM view of an intermediate stage of the oxidation, performed with atomic oxygen, of the FeO(111) bilayer on Pd (111). We recall that the FeO(111) bilayer on Pd(111) is isostructural with the one on Pt(111). Figure 1.17a, b displays STM images, in which O–Fe–O islands (bright contrast) coexist with O-adatom line dislocations, the latter are formed during the initial stages of the oxidation. Panel (c) gives a schematic picture of the structural changes during the bilayer-trilayer transformation [44].

Hexagonal trilayers of 2-D oxides may also be derived from the fluorite structure in [111] direction: this is the case for ceria monolayers on metal surfaces, where generally ceria (111)-type O–Ce–O hexagonal structures have been reported [63–67]. However, the CeO_2 (111) surface is the most stable surface termination of bulk CeO_2, and the occurrence of related structures in monolayer systems does not require the presence of low-dimensional effects for their stabilization.

1.2.3 Complex Binary Oxide Structures

As mentioned above, the term "complex" is used here to indicate that the structures under consideration contain various structure elements of different symmetry, a combination of different M–O building blocks, or different oxidation states. The TM elements at the left of the Periodic Table, such as Ti, V, or W provide flexible oxidation states and a variety of M–O coordination spheres that can support several oxides of this category. The phase diagram of 2-D V-oxides on Pd and Rh surfaces is particularly rich in such complex structure systems, as discussed below.

Figure 1.18a shows an STM image of the $(\sqrt{7} \times \sqrt{7})R19.1°$ structure of V-oxide on Rh(111), a phase that can be fabricated under highly oxidizing growth conditions. The pattern corresponds to a hexagonal kagomé lattice, but simple models failed to account for the experimental facts. The structure was difficult to analyze, but eventually has been resolved by a combination of electronic and vibrational energy level spectroscopies and extensive DFT modeling [68]. Accordingly, the structure is composed of quadratic pyramidal VO_5 building blocks, which have four oxygen atoms in the basal plane attached to the substrate, the V atom in the center and a vanadyl V = O group at the apex (see Fig. 1.18c). These VO_5 units are joined
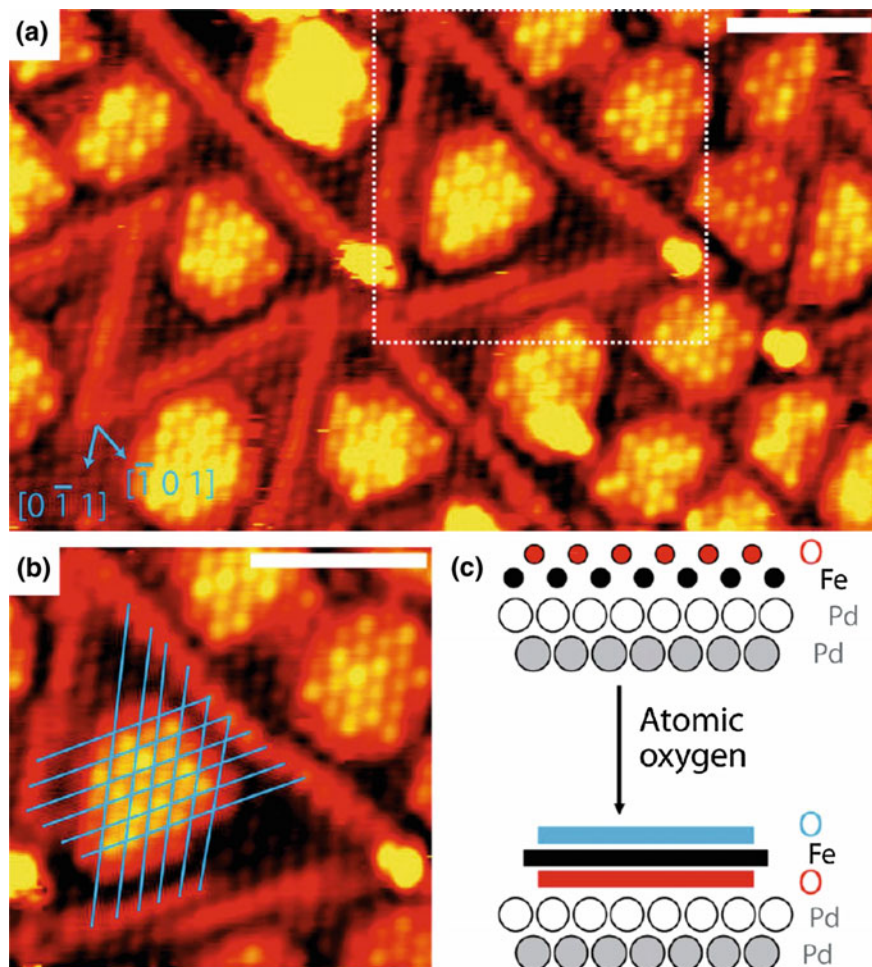
Fig. 1.17 **a**, **b** STM images (scale bars are 2.5 nm; $V_S = 0.30$ mV; $I_T = 229$ nA) showing O–Fe–O trilayer islands coexisting with O-adatom dislocations. Images were obtained after 300 s of O exposure at $p(O_2) = 1 \times 10^{-7}$ mbar at 300 K. **b** Enlargement of the area indicated by the *dotted square* in (**a**). Guidelines mark the Fe positions of the pristine FeO film that coincide with the protrusions on the O–Fe–O islands. **c** Proposed structural changes upon formation of O–Fe–O trilayer islands. Reproduced with permission from [44]

together in a corner sharing way to generate the $\sqrt{7}$ unit cell as indicated in Fig. 1.18b. This model has been substantiated by the very characteristic phonon frequency of the V = O group in the high-resolution electron energy loss (HREELS) spectra [68]. The formal stoichiometry according to this model corresponds to V_3O_9 or VO_3, which would violate the maximum possible oxidation state of V atoms of +5. Therefore, the structure requires charge transfer from the Rh(111) substrate to the oxide layer to enable its stability. An intriguing feature of the $(\sqrt{7} \times \sqrt{7})R19.1°$
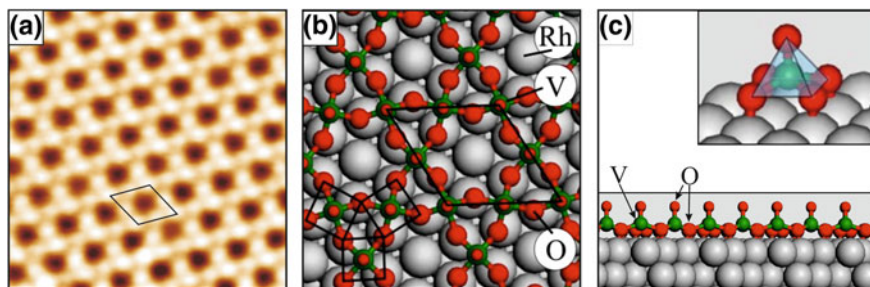
Fig. 1.18 a High-resolution STM image of the $(\sqrt{7} \times \sqrt{7})R19.1°$ V_3O_9 phase on Rh(111) $(5 \times 5$ nm$^2)$; **b** DFT structure model, *top view* (*green* V; *red* O; *grey* Rh). **c** Structure model, *side view*; the *insert* shows a detailed view of the pyramidal $O_4V = O$ units. Adapted from [70, 71]

V_3O_9 model is that its VO_5 building blocks can also explain the formation of the $(\sqrt{13} \times \sqrt{13})R13.8°$ V-oxide structure, which has been frequently found in coexistence with the $(\sqrt{7} \times \sqrt{7})R19.1°$ phase at the same surface. A simple rearrangement of the VO_5 pyramids can generate a $(\sqrt{13} \times \sqrt{13})R13.8°$ unit cell with a V_6O_{18} content, which breaks down again to the formal VO_3 stoichiometry [68]. The formation of such highly oxidized V-oxide phases is not restricted to the Rh substrate, but has also been observed on Pd(111), where a (4×4)-V_5O_{14} monolayer phase has been detected [53, 54, 69]. The V_5O_{14} layer is oxygen terminated on both sides and forms an open hexagonal network with V atoms in an unusual tetrahedral O coordination, which interacts with the Pd surface alternately with one or two oxygen atoms of the VO_4 tetrahedra [54]. Again, charge transfer from the metal across the interface to the oxide via the anchoring O atoms is necessary to stabilize this structure. The highly oxidized V-oxide phases on Rh(111) and Pd(111) provide prototypical examples of how the electronic metal-oxide interface coupling enables unusual oxidation states and new structure concepts in 2-D oxide systems.

The $(\sqrt{7} \times \sqrt{7})R19.1°$ V_3O_9 phase on Rh(111) can be reduced to a $(5 \times 3\sqrt{3})$-rect structure [72]. Figure 1.19a shows a larger scale STM image of islands of this rectangular structure, for sub-monolayer coverage, and the insert presents a high-resolution STM image displaying an intriguing pattern. The DFT derived structure model, given in Fig. 1.19b, contains two major structure elements: the highly oxidized quadratic VO_5 pyramids introduced above, and more reduced hexagonal V_6O_6 ring structures, joined together in a complicated way to generate the $(5 \times 3\sqrt{3})$-rect unit cell, with a $V_{13}O_{21}$ stoichiometry content. The STM image calculated from this model in the insert of Fig. 1.19b reproduces in detail all the features of the experimental image contrast in Fig. 1.19(a—insert), and thus gives credence to this complex structure model. Further reduction of the $(5 \times 3\sqrt{3})$-rect leads to a (9×9) structure, in which all the VO_5 units are reduced and the structure is formed by a complicated network of V_6O_6 hexagons [72]. The overall stoichiometry of this (9×9) phase on Rh(111) is reduced to V_2O_3.

From the phase diagram of Ti-oxides on Pt(111), which contains a number of reduced phases [56], the so called zig-zag-like phase is selected here for the
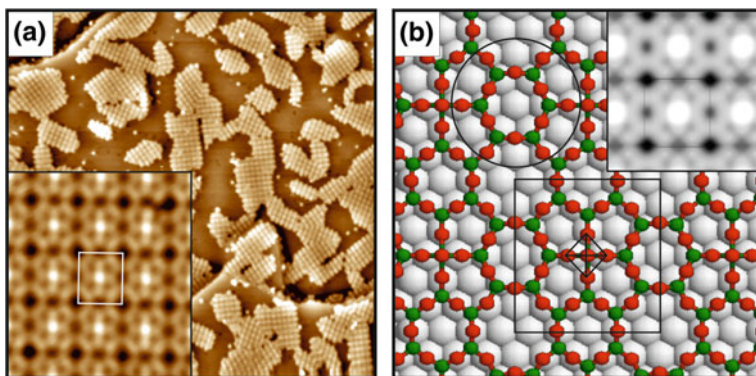
Fig. 1.19 a STM images of the $(5 \times 3\sqrt{3})$-rect V-oxide phase on Rh(111) (main frame: $(100 \times 100 \text{ nm}^2)$; $V_S = +2.0$ V; $I_T = 0.1$ nA; *insert* $(3.3 \times 3.3 \text{ nm}^2)$; $V_S = +2.0$ V; $I_T = 0.1$ nA). **b** DFT model of the $(5 \times 3\sqrt{3})$-rect $V_{13}O_{21}$ phase (*green* V; *red* O). The *insert* shows a DFT simulated STM image. Adapted from [71]

discussion [73]. The zig-zag phase (see STM image of Fig. 1.20a) is formed by three-atom wide stripes separated by dark troughs running along the $\langle 1-10 \rangle$ substrate directions and with a zigzag pattern of atomic protrusions on their surface. The structure displays a rectangular unit cell and is incommensurate with the Pt substrate. The DFT model of Fig. 1.20b is based on a Pt–Ti–O stacking, a Ti_6O_8 stoichiometry, and contains Ti atoms coordinated to four O atoms (labeled as Ti_4) and Ti atoms coordinated to three O atoms (labeled as Ti_3), with a ratio of Ti_4/Ti_3 equal to two. The Ti_4 give rise to the brighter zig-zag contrast whereas the dark
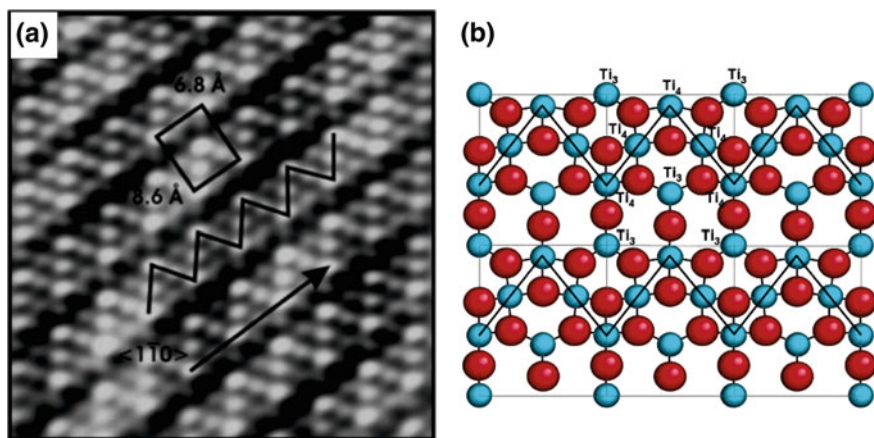
Fig. 1.20 a STM image of the TiO_x-zig-zag phase on Pt(111) [$(6 \times 6 \text{ nm}^2)$; $V_S = +0.1$ V; $I_T = 1.5$ nA]. **b** Top view of the proposed DFT model (*blue* Ti atoms; *red* O atoms). Adapted from [73] (Color figure online)

troughs are formed by bridging oxygens that connect the Ti_4 and Ti_3 atoms [73]. The DFT analysis of the driving force for the formation of this zig-zag structure motif suggested that the oxide/metal interaction is only weakly directional although important for the stability of the phase, and that the tendency to form a closed-packed hexagonal Ti layer is frustrated by the lack of Ti atoms at the established Ti coverage. Consequently, the Ti atoms arrange themselves into close-packed stripes separated by bridging oxygen atoms. There are two non-equivalent Ti atoms in the stripes, both in terms of O coordination and Pt sites, which cause the different contrast in the STM.

An ordered tungsten oxide monolayer film has been fabricated on Pt(111) by Li et al. [74] using a non-conventional preparation methodology: $(WO_3)_3$ clusters, generated in the gas phase by direct thermal sublimation of WO_3, have been deposited onto the Pt surface and their condensation has been initiated by thermal annealing. The surface induced opening of the $(WO_3)_3$ rings leads to the formation of zig-zag chains, which assemble into a 2-D W oxide wetting layer with a $c(4 \times 2)$ superstructure. According to the DFT analysis, the oxide layer is bonded to the Pt surface both via part of the oxygen atoms and by one half of the W atoms, which become reduced to the +5 oxidation state; the latter is in agreement with the signatures in the XPS core level spectra. The other 1/2 of the W atoms remains in the +6 oxidation state and forms tungstyl W=O groups pointing along the surface normal and creating the zig-zag structure that appears in the STM image. The interface layer is slightly buckled and contains both O atoms and W atoms, the latter in 5+ and 6+ oxidation states, whereas the tungstyl oxygens form an open quasi-hexagonal outer surface layer. The $c(4 \times 2)$ structure corresponds to a coverage (=W/Pt surface atom) of 0.5; increasing the coverage to form a denser oxide monolayer was investigated at the theoretical level, but was found energetically unfavorable. Instead, the formation of a second layer of clusters on top of the 2-D monolayer sheet has been suggested, and this has indeed been observed experimentally in the form of a (3×3) second layer superstructure [74].

The ultrathin layers of alumina that form on Ni–Al alloy single crystal surfaces by selective oxidation may be mentioned in this context of complex oxide structures. Taking the AlO_x double bilayer formed by high temperature oxidation of the Ni_3Al (111) surface as an example, this structure is built up by an Al–O–Al–O stacking sequence, with a complex combination of square and triangular Al–O arrangements at the surface and a hole at the corners of the $(\sqrt{67} \times \sqrt{67})R12.2°$ unit cell, reaching down to the Ni_3Al substrate interface [75]. The analog oxide layer on NiAl(110) has been rationalized by a similar structure concept, with an $Al_4O_6Al_6O_7$ stoichiometry, O atoms arranged in squares and triangles and Al atoms in between slightly below, but almost coplanar with the oxygen layer [76]. This oxide film also has another O and Al layer at the interface with the substrate. The oxidation of both Ni–Al substrate surfaces is self-limited to the double bilayer AlO_x thickness in the absence of metal impurities. However, the presence of metal nanoparticles on the alumina surface can promote further oxidation and a thickening of the alumina film [77, 78]. This may be of importance and has to be taken into account, if the alumina films are intended to be used as inert substrates for metal particles in model catalyst studies.

1.3 Reactive Interfaces—Ternary Oxides: Increasing the Complexity

If the chemical interactions between the constituents of the interface are strong, interdiffusion can be initiated and eventually a new interfacial compound can be formed, thus creating a so-called reactive interface. The growth of CaO on Mo(001) may be cited as an example [79, 80]. Crystalline Ca oxide films have been prepared after reactive evaporation of Ca in oxygen atmosphere onto a Mo(001) surface followed by annealing to 1000 K. At low film thickness (≤2 ML) a considerable interdiffusion of Mo atoms into the oxide overlayer has been detected by Auger electron spectroscopy, which was accompanied by the formation of a sharp (2 × 2) LEED pattern. With the help of DFT calculations, the oxide phase at the interface has been interpreted as a Ca_3MoO_4 ternary oxide, where 25 % of Ca cations are replaced by Mo in the RS structure [80]. In contrast to CaO, the ternary molybdate has a smaller lattice constant as a result of the smaller size of the Mo cations as compared to Ca cations and consequently a negligible lattice mismatch with the Mo (001) surface: the interdiffusion of Mo and the formation of this ternary phase may therefore be regarded as a chemical means to reduce the interfacial strain. A further driving force for the formation of this mixed oxide has been ascribed to the higher oxygen content of the new phase due to the presence of Mo atoms and to the formation of an oxidized Mo plane at the interface [80].

The concept of the reactive interface has been employed by Denk et al. [81] as an unconventional approach to fabricate ternary metal tungstates at the 2-D limit. A Cu(110) surface with a (2 × 1) surface oxide reconstruction has been covered by a monolayer of cyclic $(WO_3)_3$ clusters, the latter deposited via a molecular beam from the gas phase, and the interfacial chemical reaction has been initiated by temperature treatment at 600 K, as schematically illustrated in Fig. 1.21a. The resulting well-ordered oxide monolayer has been fully characterized experimentally by a combination of diverse surface science techniques and has been interpreted with the help of DFT calculations as a $CuWO_4$ ternary layer. The complex structure model, which is shown in Fig. 1.21b, corresponds to a sequence of three sublayers with stacking O–W–O/Cu from the Cu interface and contains W atoms with a tetrahedral oxygen coordination. This structure is significantly different from the bulk wolframite structure of $CuWO_4$ [83], although the three-layer stacking sequence (O–W–O/Cu) is somewhat reminiscent of the O–W–O–Cu stacking in the wolframite structure, which however contains W with an octahedral oxygen coordination. On the other hand, the scheelite structure, in which other metal tungstates with larger cations crystallize [84, 85], does have a tetrahedral W–O coordination. The 2-D $CuWO_4$ structure on Cu(110) may therefore be regarded somewhat superficially as a combination of wolframite and scheelite structure elements.

The preparation method of $CuWO_4$ as outlined above, namely the surface reaction between a well-ordered 2-D surface oxide and a layer of $(WO_3)_3$ clusters, is
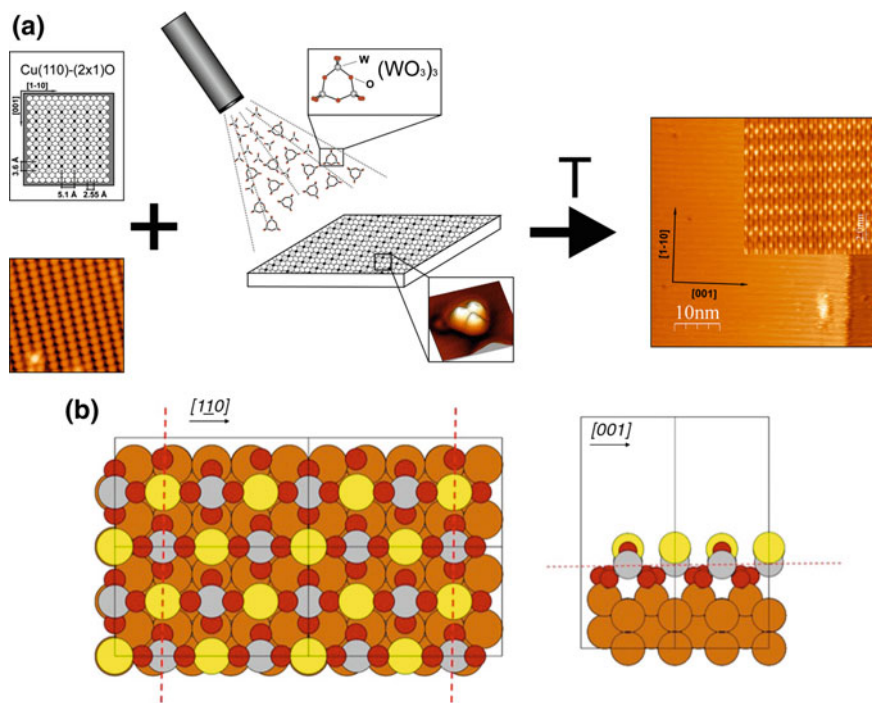
Fig. 1.21 a Schematic illustration of the formation of a surface Cu-tungstate phase: a Cu(110) 2×1-O surface oxide is covered by $(WO_3)_3$ clusters from the gas phase and an interfacial reaction is initiated by T treatment to yield an ordered $CuWO_4$ layer (*right panel*). **b** DFT derived structure model, *top* and *side views* (*brown* Cu substrate atoms; *grey* W atoms; *red* O atoms; *yellow* Cu atoms in the top surface layer). Adapted from [81, 82]

not particular to the Cu-tungstate phase, but appears to be of a more general validity. For example, Ni-tungstate $NiWO_4$ on Ni(110) has been fabricated by chemical reaction of NiO/Ni(110) with $(WO_3)_3$ clusters [86], and a surface Fe-tungstate phase has been generated by the interfacial reaction of the FeO(111) bilayer phase on Pt(111) (see Sect. 1.2.2) with $(WO_3)_3$ clusters [87]. The first step in the latter interface reaction between FeO(111)/Pt(111) and $(WO_3)_3$ clusters has been observed by Li et al. [88], who found evidence for the dissociation of the clusters into WO_3 monomers in their STM images. The related DFT calculations revealed that the dissociation is accompanied by significant restructuring of the FeO (111), with the Fe ions being pulled on top of the surface and bonded to the WO_3 fragments [88].

1.4 Finite Size Effects

Finite size effects are ubiquitous in nanoscale materials [89–91]. A suitable concept for the investigation of finite size effects in oxide nanostructure research is to use the regular step arrangement of a vicinal metal surface as a model template. Schoiswohl et al. [92] have examined the growth structures of 2-D V oxide layers on a vicinal Rh (15 15 13)Rh(15 15 13) surface and have compared them with those on a flat Rh (111) surface. It was found that while similar V–O building units as on the Rh(111) surface develop as a function of the chemical potential of oxygen on the (111) terraces of the vicinal Rh surface, the effects of limited terrace size and strain relief at the step edges lead to a rearrangement of building blocks and the stabilization of novel oxide structures that are not observed on the extended (111) surface [92].

A striking consequence of finite size effects has been encountered during the growth of Mn-oxide on a Pd(1 1 17)Pd(1 1 17) surface [93], a vicinal of Pd(100). We recall that on Pd(100) a Mn_3O_4 c(4 × 2) monolayer is formed [26], in which the creation of Mn vacancies in the c(4 × 2) array provides a means to relax interfacial strain (see Sect. 1.2.1). The strain relief in the c(4 × 2) Mn-oxide layer is however incomplete, and the Mn_3O_4 phase on Pd(100) is a domain structure, characterized by relatively small ordered c(4 × 2) domains separated by disordered domain boundaries [94]; the latter obviously are a consequence of strain relief. On Pd(1 1 17), however, a perfectly ordered c(4 × 2) Mn_3O_4 monolayer surface has been obtained, with the step-terrace structure of the vicinal surface in a perfect superlattice (see Fig. 1.22) [93, 95]. The latter is not the case on the clean Pd(1 1 17) surface, where the step-terrace structure is much less regular: the Mn-oxide overlayer obviously stabilizes a regular step-terrace arrangement of the Pd substrate. The quantitative evaluation of the superlattice parameters of this surface by spot-profile analysis LEED (SPA-LEED) yielded a surprising result: the Pd(1 1 17) surface had undergone a massive reconstruction and had rearranged into a Pd(1 1 21) surface under the influence of the c(4 × 2) Mn_3O_4 oxide overlayer growth [93]. DFT calculations elucidated the physical origin of the stabilization mechanism of particular terrace sizes in terms of "magic widths" of the Mn_3O_4 stripes, with particular stable oxide stripes occurring if full c(4 × 2) unit cells can be accommodated on the Pd terraces. The structural details of the most stable $Mn_{14}O_{20}$/Pd(1 1 21) nanostripe showed substantial relaxation and a buckling of the oxide layer at the boundaries, i.e. at the step edges, which is a clear consequence of limited size effects [93, 95].

1.5 Interface Chemistry

The strong chemical affinities between the elements constituting the interface are at the root of the reactive interface formation, as discussed in Sect. 1.3. Here we will include the affinity to oxygen and examine, how these affinities reflect on the type of particular oxide structure formed on different metal substrates. Prototypical
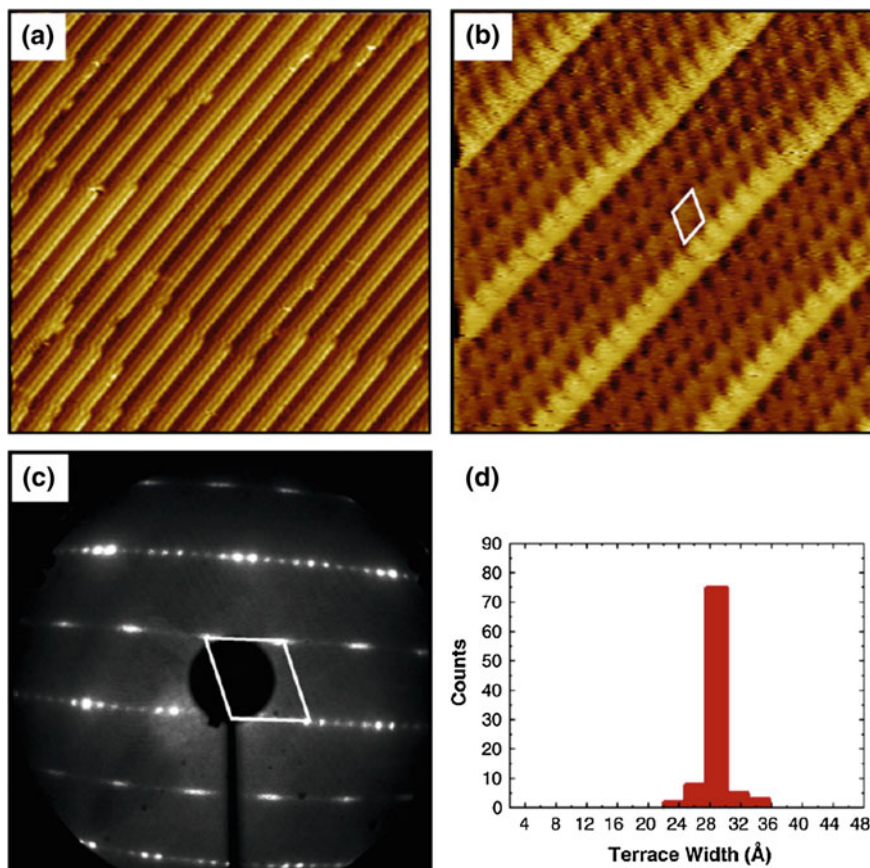
Fig. 1.22 a, **b** STM images of the c(4 × 2) Mn-oxide/Pd(1 1 21) surface (**a** (40 × 40 nm^2); V_S = +1.5 V; I_T = 0.1 nA; **b** (10 × 10 nm^2); V_S = −0.2 V; I_T = 0.1 nA); a primitive c(4 × 2) unit cell is indicated in (**b**). **c** LEED pattern of the c(4 × 2) surface (electron energy = 120 eV). **d** Terrace width distribution of the c(4 × 2) oxide surface. Reproduced with permission from [95]

examples are difficult to find, because the chemical effects are in general strongly mixed up with elastic and electronic effects, so that the chemistry, as defined here, is difficult to single out. A few systems, however, may be discussed in terms of showing these interface chemistry aspects.

The highly oxidized V-oxide monolayers show a (4 × 4) structure on Pd(111) and a ($\sqrt{7}$ × $\sqrt{7}$)R19.1° structure on Rh(111) surfaces, which are formed by different V–O coordination units and somewhat different stoichiometries. The (4 × 4) structure on Pd(111) is an open network structure of VO_4 units with tetrahedral V–O coordination and a formal $VO_{2.8}$ stoichiometry, whereas the ($\sqrt{7}$ × $\sqrt{7}$)R19.1° structure on Rh(111) is built up by quadratic VO_5 pyramids with a formal VO_3 stoichiometry [96]. It is noted that the (4 × 4) V-oxide is thus only slightly O

deficient with respect to the $(\sqrt{7} \times \sqrt{7})R19.1°$ phase. Closer inspection of the proposed structure models shows, however, that the interface of the $(\sqrt{7} \times \sqrt{7})R19.1°$ structure is considerably denser in oxygen: the pyramidal VO_5 units of the $(\sqrt{7} \times \sqrt{7})R19.1°$ structure are attached to the Rh surface via four oxygen atoms of their basal plane, whereas the tetrahedral VO_4 units of the (4×4) phase are bonded alternately via only one or two oxygen atoms to the Pd substrate. The difference in surface lattice constants beween Rh(111) and Pd(111) is relatively small (~ 2.2 %), so that the elastic strain is unlikely to be the decisive factor in determining these different oxide structures. It has been proposed that the higher affinity of Rh towards oxygen may be the cause for the structural difference of these highly oxidized V-oxide structures on Rh(111) and Pd(111) substrate surfaces [96]; this is an interface chemistry effect in the sense discussed here.

The Co-oxide monolayer grows on Ir(100) in a c(10×2) structure, which has been interpreted in terms of a hexagonal RS (111)-type bilayer [97] (see Sect. 1.2.2). The Co-oxide monolayer however displays a different structure, if the substrate is chemically modified by deposition of a pseudomorphic Co monolayer as an interlayer on top of the Ir(100) surface: in this latter case, an RS (100)-like c(4×2) Co_3O_4 vacancy structure is formed [98] (see Sect. 1.2.1). Gubo et al. have analyzed the stability of the two systems by ab initio thermodynamic phase diagrams and found that, while the c(10×2) structure is thermodynamically most stable over a wide range of oxygen chemical potentials on the bare Ir(100) surface, the c(4×2) structure becomes more stable on the Co/Ir(100) support. The strength of the interface chemical bonding between the oxide oxygen and the Co atoms of the support interlayer has been made responsible for the formation of this c(4×2) oxide structure [98]; in the latter structure, the overlayer-substrate bonding appears to be more specific and directional than in the c(10×2) phase, which is less commensurate.

The first monolayer of W-oxide on Pt(111), displaying a c(4×2) structure with zig-zag line motif of W–O chains condensed into a 2-D network, is anchored to the Pt surface by strong W–Pt and O–Pt bonds [74]. In contrast, W-oxide on Ag(100) forms an extended first wetting layer with square symmetry that is incommensurate to the substrate: this creates a characteristic Moiré modulation pattern in the STM images [21]. The interesting aspect of this W-oxide monolayer is that it is rotationally disordered in different domains, that is the registry of the WO_x layer is in a random azimuth orientation with respect to the Ag(100) surface directions; this becomes apparent from a varying Moiré signature in different domains, but is also most simply seen in the LEED pattern. Figure 1.23 shows a LEED pattern of the WO_x/Ag(100) surface: the bright outer spots are the integer order reflections of the Ag substrate, whereas the weak ring-like intensity is from the rotationally disordered domains of the WO_x overlayer. There are indications that there is some preferential orientation of domains rotated 45° with respect to Ag(100) surface lattice, but the rotational disorder is clearly apparent. Although the exact atomic structure of the WO_x monolayer on Ag(100) has not yet been resolved, the
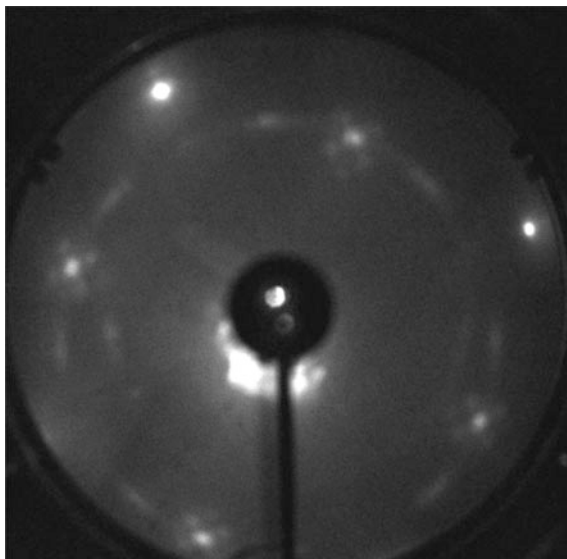
orientational randomness of the WO$_x$ overlayer indicates that the surface potential
is flat and that the chemical interactions across the interface are not pronounced.
This is in line with the weak chemical affinitiy of silver to tungsten and oxygen.

1.6   Surface Phase Diagrams

Elements with several atomic oxidation states of comparable stability may exhibit a
very complex oxide structure behavior as a function of external growth parameters,
and an impression of such structural complexities may be obtained from the surface
phase diagram. The term is used here as the projection of the regions of stable
phases onto the relevant parameter space, which is in most cases the chemical
potential of oxygen μ_O and the metal atom surface concentration as expressed by
the surface coverage; notice that the metal atom surface concentration not only
determines the actual oxide coverage of the surface, but also influences the stoi-
chiometry of the growing oxide phase due to kinetic effects. This definition of phase
diagram is different from the one in the thermodynamic sense, where the total
energy of a phase versus a particular parameter, e.g. μ_O, is presented. Complex
phase diagrams have been reported for V-oxides on Pd(111) [50] or Rh(111) [68,
72] surfaces, Ti-oxides on Pt(111) [55, 56], or Mn-oxides on Pd(100) [94]. The
latter is a benchmark system and the surface phase diagram for a given metal
coverage as a function of μ_O is illustrated in Fig. 1.24. Nine different 2-D Mn-oxide
phases have been detected as a function of μ_O. The phases in the different regions of
the μ_O (e.g. "oxygen-rich", etc.) are structurally related to each other and often
occur in coexistence at the surface. It should be mentioned at this point that the
latter constitutes a considerable problem for the experimental characterization of the
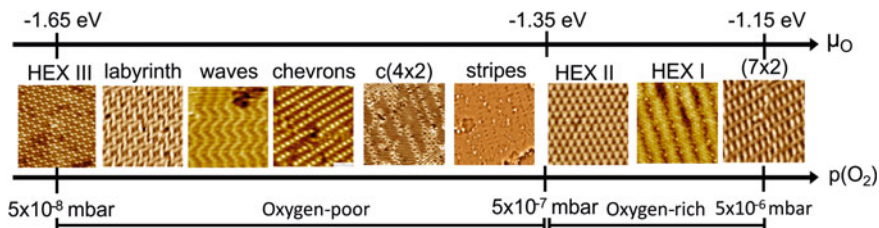
Fig. 1.24 Schematic phase diagram of 2-D Mn-oxides on Pd(100), presented as a function of the oxygen pressure p_{O2} and of the oxygen chemical potential μ_O. The nominal coverage of Mn on the surface is 0.75 ML. Adapted from [94]

different phases, since subtle variations in the thermodynamic parameters, often below the control of the experimenter, may drive the system into a different structure. It is therefore a challenge in these systems with multi-structure phase diagrams to reproducibly prepare a particular phase, which sometimes even cannot be prepared as a single phase at the surface. This is detrimental for the structure characterization, since a combination of several experimental techniques is often necessary, including area averaging techniques besides the space-resolved STM, to unravel a complex oxide structure. In the "oxygen-rich" regime of the MnO_x/Pd (100) phase diagram (Fig. 1.24), hexagonal trilayer MnO_2-type structures are observed (Sect. 1.2.2), in the "intermediate" region the $c(4 \times 2)$ Mn_3O_4 phase is central (Sect. 1.2.1), with the other phases related to it by a vacancy propagation mechanism [5, 29], whereas in the "oxygen-poor" region (left part of the diagram), the atomic details of the reduced structures are mostly lacking for the reasons mentioned above.

The importance of kinetic stabilization in surface oxide phase diagrams cannot be underestimated—see the discussion of Fortunelli et al. in Chap. 2. It appears that kinetic effects in 2-D systems are more prominent than in 3-D bulk systems. This may be related to the enhanced flexibility of 2-D oxide structures in terms of geometric stiffness, which depends on the O-coordination number [2]—with less flexibility for higher O-coordination—as well as in terms of allowing for different metal-oxygen building blocks and their variable connectivities.

1.7 Pattern Formation

The mismatch of lattice constant and symmetry across a hetero-epitaxial interface may lead to the formation of a mesoscopic corrugation pattern at the surface. This has been demonstrated for a nanostripe pattern of a NaCl monolayer on a Cu(110) surface [99]. NaCl is not an oxide, but a dielectric material, and similar effects are expected to occur on other 2-D dielectric systems, including oxides. Indeed, very recently the formation of a nanostripe pattern has been observed for a 2-D layer of CeO_2 on Cu(110) [100]. NaCl grows in the form of quadratic RS (100) monolayers
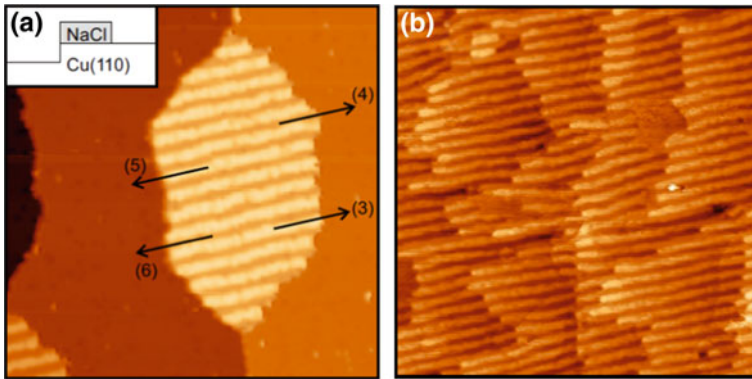
Fig. 1.25 **a** STM image of a NaCl monolayer island on Cu(110) located at an upper step edge (as illustrated by the cartoon in the *insert*) [(81 × 81 nm^2); V$_S$ = −1.75 V; I$_T$ = 0.03 nA]. **b** STM image of 1 ML NaCl on Cu(110) [(111.5 × 115.5 nm^2); V$_S$ = +1.0 V; I$_T$ = 0.1 nm]. Adapted from [99]

on Cu(110), as on most other noble metal surfaces. Figure 1.25a shows an STM image of an individual NaCl island at a step edge, and Fig. 1.25b of the full NaCl monolayer on Cu(110): the pattern of dark and bright stripes with a periodicity distance of ∼40 Å and a corrugation of ∼1.2 Å is clearly apparent. The formation of this pattern has been interpreted with the help of DFT calculations as the result of the frustration of the overlayer-substrate chemical bonding produced by the epitaxial mismatch. In regions of a favorable epitaxial relationship the Cu–Cl covalent bonding is strong and the overlayer-substrate distance is short; conversely, in regions of poor epitaxial match the Cu–Cl bonding is weak and the overlayer-substrate distance is long. This leads to a chemically induced periodic modulation of the overlayer topography and a geometric rumpling of the surface, and thus to the observed stripe pattern in the STM. This is a true 2-D effect: simulations of NaCl bilayers were conducted, but the experimental corrugation could not be reproduced, because the interaction of the first interfacial NaCl layer with the second NaCl layer competes with that with the support, reducing substantially the topographic corrugation at the surface [99]. The formation of such anisotropic template surfaces, produced by the epitaxial lattice and symmetry mismatch in a hetero-epitaxial 2-D dielectric-metal system, may be of interest for the growth of hierarchical superstructures or for the engineering of periodic strain on oxide surfaces [100], with associated heterogeneous surface properties.

1.8 Synopsis

Oxide materials at the 2-D limit, supported on metal surfaces, exhibit a fascinating, sometimes confusing complexity of geometries and phases. We have analyzed this structural behavior of 2-D oxides with the aim to understand and reduce the

complexity by tracing down common structure motifs and trends. To identify the physical origin driving oxide phases into a particular structure and atomic geometry, we have attempted to isolate the major physical parameters that drive a system into a particular phase, employing a reductionist approach. This is, of course, somewhat simplistic, since the various degrees of freedom—geometric, electronic, chemical, magnetic—are intimately coupled and interwoven. However, it is a useful approach for a categorical discussion and of pedagogical advantage.

To categorize oxide structures, we have chosen either a stacking layer representation, e.g. using a sequence of oxygen and metal layers, or a description by combining and nesting the individual M–O coordination building blocks, the selection being made somewhat arbitrarily with the purpose of easy perception. A variety of structure concepts have been identified and their characteristic parameters have been discussed. To illustrate the major oxide structure categories, benchmark systems have been chosen for the presentation. The main body of this chapter has been devoted to describe and analyze structure types of binary oxide systems, where most of the surface science based work has been undertaken hitherto, but the way towards more complex ternary oxide systems has been indicated.

Interfaces play an important role in hetero-epitaxial thin film growth. The more so for the behavior of 2-D overlayers, where the parameters of the interface become decisive in determining the properties of the whole system. The geometry and the electronic/chemical interactions at the interface have therefore been emphasized throughout the treatise as a major structure determining aspect. Finite size effects are present in all nanoscale systems, but are particularly prominent at low dimensionality. In this context, we have investigated the consequence of the steps of vicinal metal substrate surfaces for the formation of oxide overlayers and their influence on the stability of structures. The interplay of thermodynamic and kinetic effects is responsible for the structural richness of some oxide surface phase diagrams, where several different phases can coexist at the surface after preparation under closely related conditions. Such multitude of oxide structures of similar stability may be regarded as a structurally degenerated ground state, which is conceptually interesting because it illustrates most evidently the flexibility of structure building blocks of oxides at the 2-D limit. Experimentally, it is difficult to handle, since area averaging techniques cannot be applied. The epitaxial lattice and symmetry misfit at the interface between a metal and a dielectric layer may give rise to the formation of a periodic anisotropy at the surface of oxides and the spontaneous appearance of mesoscopic stripe patterns. This supports the notion of a local chemical bonding concept at the interface, as the stripe pattern has been ascribed to the frustration and the local variation of the interfacial bonding due to the epitaxial mismatch.

The study of structures of 2-D oxide systems, which span the range from a single plane of a bulk crystal to novel structure types containing unusual metal oxidation states in metal-oxygen coordination spheres with atypical connectivities, has been an evolving field of research during the last one and a half decades that has benefitted enormously from the progress in area-resolving experimental methodologies (e.g. the scanning probe techniques) and advanced density functional theory techniques (see the Chap. 2 by Fortunelli et al.). It was the close combination of

experiment and theory that has enabled the remarkable advances in this field and has led to an atomic picture of very complex oxide phases, and a glimpse of this close coupling between experiment and theory has been given in this chapter. Due to the concentration on structure aspects, local probe techniques have been in the foreground of the present description, but the connection with complementary area averaging techniques, e.g. electron spectroscopies, has been crucial for the progress in the field.

What are the further perspectives for the years to come? The path towards more complexity is already preordained and the study of ternary oxides and beyond is on the way. The magnetic structures of 2-D oxides have been addressed during their theoretical modeling, but experimental investigations are still sparse; we expect more to come. Most studies of 2-D oxides have been performed on systems supported on metal surfaces; the structure of 2-D oxides on oxide substrates is largely unexplored. In view of their high interest in catalytic chemistry, 2-D oxide systems supported on oxides substrates are an emerging active area of research. The combination of 2-D oxides with other 2-D materials (e.g. oxides supported on graphene, BN and the like) has been barely attempted so far. Such combinations may be of interest from the point of view of weakly interacting systems, where the intrinsic 2-D oxide character may be preserved due to the expected weaker influence of the interface to the substrate. The materials science of 2-D oxides is a wide open field and we expect new phenomena and materials´ properties to be discovered.

References

1. Pacchioni G, Valeri S (eds) (2012) Oxide ultrathin films: science and technology. Wiley-VCH, Weinheim
2. Freysoldt C, Rinke P, Scheffler M (2007) Ultrathin oxides: bulk-oxide-like model surfaces of unique films? Phys Rev Lett 99:086101
3. Butler SZ, Hollen SM, Cao L et al (2013) Progress, challenges, and opportunities in two-dimensional materials beyond graphene. ACS Nano 4:2898–2926
4. Netzer FP, Allegretti F, Surnev S (2010) Low-dimensional oxide nanostructures on metals: hybrid systems with novel properties. J Vac Sci Technol B 28:1–16
5. Surnev S, Fortunelli A, Netzer FP (2013) Structure-property relationship and chemical aspects of oxide-metal hybrid nanostructures. Chem Rev 113:4314–4372
6. Netzer FP (2010) "Small and beautiful"—the novel structues and phases of nano-oxides. Surface Sci 604:485–489
7. Campbell CT (2006) Transition metal oxides: extra thermodynamic stability as thin films. Phys Rev Lett 96:066106
8. Valeri S, Benedetti S (2012) Synthesis and preparation of oxide ultrathin films. In: Pacchioni G, Valeri S (eds) Oxide ultrathin films: science and technology. Wiley-V-CH, Weinheim, pp 1–26

9. Grinter DC, Thornton G (2012) Characterization tools of ultrathin oxide films. In: Pacchioni G, Valeri S (eds) Oxide ultrathin films: science and technology. Wiley-V-CH, Weinheim, pp 27–46

10. Pacchioni G (2012) Two-dimensional oxides: multifunctional materials for advanced technologies. Chem Eur J 18:10144–10158

11. Tasker PW (1979) The stability of ionic crystal surfaces. J Phys C: Solid State Phys 12:4977–4984

12. Goniakowski J, Finocchi F, Noguera C (2008) Polarity of oxide surfaces and nanostructures. Rep Prog Phys 71:016501

13. Lüth H (1993) Surfaces and interfaces of solids. springer series in surface sciences 15, Springer, Berlin

14. Brune H (1998) Microscopic view of epitaxial metal growth: nucleation and aggregation. Surf Sci Rep 31:121–230

15. Pauling L (1947) Atomic radii and interatomic distances in metals. J Am Chem Soc 69:542–553

16. Thomas IO, Fortunelli A (2010) Analysis of the electronic structure of ultrathin NiO/Ag(100) films. Eur Phys J B75:5–13

17. Barcaro G, Thomas IO, Fortunelli A (2010) Validation of density-functional versus density-functional + U approaches for oxide ultrathin films. J Chem Phys 132:124703

18. Steurer W, Allegretti F, Surnev S et al (2011) Metamorphosis of ultrathin Ni oxide nanostructures on Ag(100). Phys Rev B 84:115446

19. Steurer W, Surnev S, Fortunelli A, Netzer FP (2012) Scanning tunneling microscopy imaging of Ni(100)1 × 1 islands embedded in Ag(100). Surface Sci 606:803–807

20. Obermüller T, Steurer W, Surnev S et al (2013) Kinetic asymmetry in the growth of two-dimensional Mn oxide nanostripes. Phys Rev B 88:235410

21. Obermüller T (2015) Growth of transition metal oxides in 2D layers: probing and tuning the properties of matter at the atomic scale. PhD thesis, University of Graz

22. Müller F, de Masi R, Reinicke DK et al (2002) Epitaxial growth of MnO/Ag(001) films. Surface Sci 520:158–172

23. Schoiswohl J, Agnoli S, Xu B et al (2005) Growth and thermal behaviour of NiO nanolayers on Pd(100). Surface Sci 599:1–13

24. Agnoli S, Sambi M, Granozzi G et al (2005) Experimental and theoretical study of a surface stabilized monolayer phase of nickel oxide on Pd(100). J Phys Chem B 109(17197):17204

25. Allegretti F, Parteder G, Gragnaniello L et al (2010) Strained c(4 × 2) CoO(100)-like monolayer on Pd(100): experiment and theory. Surface Sci. 604:529–533

26. Franchini C, Zabloudil J, Podloucky R et al (2009) Interplay between magnetic, electronic, and vibrational effects in monolayer Mn_3O_4 grown on Pd(100). J Chem Phys 130:124707

27. Fortunelli A (2015), private communication

28. Gragnaniello L, Agnoli S, Parteder G et al (2010) Cobalt oxide nanolayers on Pd(100): the thickness-dependent structural evolution. Surface Sci 604:2002–2011

29. Franchini C, Podloucky R, Allegretti F et al (2009) Structural and vibrational properties of two-dimensional Mn_xO_y layers on Pd(100): experiments and density functional calculations. Phys Rev B 79:035420

30. Altieri S, Allegretti F, Steurer W et al (2013) Orbital anisotropy in paramagnetic manganese oxide nanostripes. Phys Rev B 87:241407(R)

31. Goniakowski J, Noguera C, Giordano L (2004) Using polarity for engineering oxide nanostructures: structural phase diagram in free and supported MgO(111) ultrathin films. Phys Rev Lett 93:215702

32. Kiguchi M, Entani S, Saiki K et al (2003) Atomic and electronic structure of an unreconstructed polar MgO(111) thin film on Ag(111). Phys Rev B 68:115402

33. Tusche C, Meyerheim HL, Kirschner J (2007) Observation of depolarized ZnO(0001) monolayers: formation of unreconstructed planar sheets. Phys Rev Lett 99:026102

34. Weirum G, Barcaro G, Fortunelli A et al (2010) Growth and surface structure of zink oxide layers on a Pd(111) surface. J Phys Chem C114:15432–15439

35. Parteder G, Allegretti F, Wagner et al (2008) Growth and oxidation of Ni nanostructures on stepped Rh surfaces. J Phys Chem C112:19272–19278

36. Franz T, Zabloudil J, Mittendorfer F et al (2012) Deformed surface oxides: uncommon structure of a (6×1) NiO surface oxide on Rh(111). J Phys Chem Lett 3:186–190

37. Hagenbach Ch, Shantyr R, Neddermeyer H et al (2006) Pressure-dependent Ni-O phase transitions and Ni oxide formation on Pt(111): an in situ STM study at elevated temperatures. Phys Chem Chem Phys 8:1575–1583

38. Galloway HC, Benitez JJ, Salmeron M (1994) Growth of FeO_x on Pt(111) studied by tunneling microscopy. J Vac Sci Technol, A 12:2302–2307

39. Galloway HC, Sautet P, Salmeron M (1996) Structure and contrast in scanning tunneling microscopy of oxides: FeO monolayer on Pt(111). Phys Rev B 54:R11145–R11148

40. Kim YJ, Westphal C, Ynzunza RX et al (1997) Interlayer interactions in epitaxial oxide growth: FeO on Pt(111). Phys Rev B 55:R13448–R13451

41. Ritter M, Ranke W, Weiss W (1998) Growth and structure of ultrathin FeO films on Pt(111) studied by STM and LEED. Phys Rev B 57:7240–7251

42. Ranke W, Ritter M, Weiss W (1999) Crystal structures and growth mechanism for ultrathin films of ionic compound materials: FeO(111) on Pt(111). Phys Rev B 60:1527–1530

43. Weiss W, Ranke W (2002) Surface chemistry and catalysis on well-defined epitaxial iron-oxie layers. Progr Surface Sci 70:1–151

44. Zeuthen H, Kudernatsch W, Peng G et al (2013) Structure and stoichiometry of oxygen-rich ultrathin FeO(111) films grown on Pd(111). J Phys Chem C117:15155–15163

45. Shaikhutdinov Sh, Ritter M, Weiss W (2000) Hexagonal heterolayers on a square lattice: a combined STM and LEED study of FeO(111) on Pd(100). Phys Rev B 62:7535–7541

46. Kuhness D (2015) Synthesis of low dimensional ternary oxide $FeWO_x$ and $MnWO_x$ nanostructures on single crystal metal surfaces. PhD thesis, University of Graz

47. Ebensperger C, Gubo M, Meyer W et al (2010) Substrate-induced structural modulation of a CoO(111) bilayer on Ir(100). Phys Rev B 81:235405

48. Gragnaniello G, Barcaro G, Sementa L et al (2011) The two-dimensional cobalt oxide (9x2) phase on Pd(100). J Chem Phys 134:184706

49. Surnev S, Vitali L, Ramsey MG et al (2000) Growth and structure of ultrathin vanadium oxide layers on Pd(111). Phys Rev B 61:13945–13954

50. Surnev S, Kresse G, Ramsey MG et al (2001) Novel interface-mediated metastable oxide phases: vanadium oxides on Pd(111). Phys Rev Lett 87:86102

51. Kresse G, Surnev S, Ramsey MG et al (2001) First-principles calculations for V_xO_y grown on Pd(111). Surface Sci 492:329–344

52. Sambi M, Petukhov M, Domenichini B et al (2003) A photoelectron diffraction study of the surface-V_2O_3 (2×2) layer on Pd(111). Surface Sci 529:L234–L238

53. Surnev S, Kresse G, Sock M et al (2001) Surface structures of ultrathin vanadium oxide films on Pd(111). Surface Sci 495:91–196

54. Surnev S, Sock M, Kresse G et al (2003) Unusual CO adsorption sites on vanadium oxide—Pd(111) "inverse model catalyst" surfaces. J Phys Chem B 107:4777–4785

55. Sedona F, Rizzi GA, Agnoli S et al (2005) UltrathinTiO$_x$ films on Pt(111): A LEED, XPS, and STM investigation. J Phys Chem B 109:24411–24426

56. Barcaro G, Agnoli S, Sedona F et al (2009) Structure of reduced ultrathin TiO_x polar films on Pt(111). J Phys Chem C113:5721–5729

57. Reuter K, Stampfl C, Ganduglia-Pirovano MV et al (2002) Atomistic description of oxide formation on metal surfaces: the example of ruthenium. Chem Phys Lett 352:311–317

58. Gustafson J, Mikkelsen A, Borg M et al (2004) Self-limited growth of a thin oxide layer on Rh(111). Phys Rev Lett 92:126102

59. Heinz K, Hammer L (2013) Epitaxial cobalt oxide films on Ir(100)—the importance of crystallographic analyses. J Phys: Condens Matter 25:173001

60. Giordano L, Lewandowski M, Groot IMN et al (2010) Oxygen-induced transformations of an FeO(111) film on Pt(111): a combined DFT and STM study. J Phys Chem C114:21504–21509

61. Sun YN, Giordano L, Goniakowski J et al (2010) The interplay between structure and CO oxidation catalysis on metal-supported ultrathin oxide films. Angew Chem Int Ed 49:4418–4421

62. Lewandowski M, Groot IMN, Shaikhutdinov S et al (2012) Scanning tunneling microscopy evidence for the Mars-van Krevelen type mechanism of low temperature CO oxidation on an FeO(111) film on Pt(111). Catal Today 181:52–55

63. Eck S, Castellarin-Cudia C, Surnev S et al (2002) Growth and thermal properties of ultrathin cerium oxide layers on Rh(111). Surface Sci 520:173–185

64. Castellarin-Cudia C, Surnev S, Schneider G et al (2004) Strain-induced formation of arrays of catalytically active sites at the metal-oxide interface. Surface Sci. 554:L120–L126

65. Lu J-L, Gao H-J, Shaikhutdinov S et al (2006) Morphology and defect structure of the $CeO_2(111)$ films grown on Ru(0001) as studied by scanning tunneling microscopy. Surface Sci. 600:5004–5010

66. Staudt T, Lykhach Y, Hammer L et al (2009) A route to continuous ultra thin cerium oxide films on Cu(111). Surface Sci. 603:3382–3388

67. Grinter DC, Ithnin R, Pang CL et al (2010) Defect structure of ultrathin ceria films on Pt (111): atomic views from scanning tunneling microscopy. J Phys Chem C114:17036–17041

68. Schoiswohl J, Sock M, Eck S et al (2004) Atomic-level growth study of vanadium oxide nanostructures on Rh(111). Phys Rev B 69:155403

69. Klein C, Kresse G, Surnev S et al (2003) Vanadium surface oxides on Pd(111): a structural analysis. Phys Rev B 68:235416

70. Schoiswohl J, Surnev S, Netzer FP (2006) Vanadium oxide nanostructures: from zero- to three-dimensional. J Phys: Condens Matter 18:R1–R14

71. Schoiswohl J, Surnev S, Netzer FP (2005) Reactions on inverse model catalyst surfaces: atomic views by STM. Topics Catal 36:91–105

72. Schoiswohl J, Surnev S, Sock M et al (2005) Reduction of vanadium-oxide monolayer structures. Phys Rev B 71:165437

73. Barcaro G, Sedona F, Fortunelli A et al (2007) Structure of a TiO_x zigzag-like monolayer on Pt(111). J Phys Chem C111:6095–6102

74. Li Z, Zhang Z, Kim YK et al (2011) Growth of ordered ultrathin tungsten oxide films on Pt (111). J Phys Chem C115:5773–5783

75. Schmid M, Kresse G, Buchsbaum A et al (2007) Nanotemplate with holes: ultrathin alumina on $Ni_3Al(111)$. Phys Rev Lett 99:196104

76. Kresse G, Schmid M, Napetschnig E et al (2005) Structure of the ultrathin aluminum oxide film on NiAl(110). Science 308:1440

77. Gragnaniello L, Ma T, Barcaro G et al (2012) Ordered arrays of size-selected oxide nanoparticles. Phys Rev Lett 108:195507

78. Chaudhury A, Gragnaniello L, Ma T et al (2013) Alumina-supported array of Co nanoparticles: size-dependent oxidation kinetics? J Phys Chem C117:18112–18119

79. Shao X, Myrach P, Nilius N et al (2011) Growth and morphology of calcium-oxide films grown on Mo(001). J Phys Chem C115:8784–8789

80. Shao X, Nilius N, Myrach P et al (2011) Strain-induced formation of ultrathin mixed-oxide films. Phys Rev B 83:245407

81. Denk M, Kuhness D, Wagner M et al (2014) Metal tungstates atthe ultimate two-dimensional limit: fabrication of a $CuWO_4$ nanophase. ACS Nano 8:3947–3954

82. Ma L, Denk M, Kuhness D et al (2015) Chemical properties of two-dimensional oxide systems: adsorption of $(WO_3)_3$ clusters on $CuWO_4$. Surface Sci. doi:10.1016/j.susc.2015.03. 006

83. Kihlborg L, Gebert E (1970) $CuWO_4$, a distorted wolframite-type structure. Acta Cryst B26:1020–1026

84. Zhang Y, Holzwarth NAW, Williams RT (1998) Electronic band structures of the scheelite materials $CaMoO_4$, $CaWO_4$, $PbMoO_4$, and $PbWO_4$. Phys Rev B 57:12738–12750

85. Kuzmin A, Purans J (2001) Local atomic and electronic structure pf tungsten ions in AWO_4 crystals of scheelite and wolframite types. Radiat Meas 33:583–586

86. Pomp S (2013) Interaction of $(WO_3)_3$ clusters with bare Ni(110) and oxygen reconstructed O-Ni(110) surfaces. Master Thesis, University of Graz

87. Pomp S, Kuhness D, Barcaro G, Sementa L, Mankad V, Fortunelli A, Sterrer M, Netzer FP, Surnev S (2016) Two-dimensional iron tungstate: a ternary oxide with honeycomb geometry. Submitted for publication

88. Li S-C, Li Z, Zhang Z et al (2012) Preparation, characterization, and catalytic properties of tungsten trioxide cyclic trimers on FeO(111)/Pt(111). J Phys Chem C116:908–916

89. Huang WJ, Sun R, Tao J et al (2008) Coordination-dependent surface atomic contraction in nanocrystals revealed by coherent diffraction. Nat Mat 7:308–313

90. Mironets O, Meyerheim HL, Tusche C et al (2008) Direct evidence for mesoscopic relaxations in cobalt nanocrystals on Cu(001). Phys Rev Lett 100:096103

91. Feng W, Meyerheim HL, Mohseni K et al (2013) Misfit-induced modification of structure and magnetism in O/Fe(001)-p(1x1). Phys Rev Lett 110:235503

92. Schoiswohl J, Surnev S, Netzer FP (2007) Vanadium oxide overlayers on vicinal Rh(15 15 13): the influence of surface steps. J Phys Chem C111:10503–10507

93. Franchini C, Li F, Surnev S et al (2012) Tailor-made ultrathin manganese oxide nanostripes: "Magic widths" on Pd(1 1 N) terraces. J Phys: Condens Matter 24:042001

94. Li F, Parteder G, Allegretti et al (2009) Two-dimensional manganese oxide nanolayers on Pd (100): the surface phase diagram. J Phys: Condens Matter 21:134008

95. Li F, Allegretti F, Surnev S et al (2010) Atomic engineering of oxide nanostructure superlattices. Surface Sci 604:L43–L47

96. Schoiswohl J, Sock M, Chen Q et al (2007) Metal supported oxide nanostructures: model systems for advanced catalysis. Topics Catal 46:137–149

97. Ebensperger C, Gubo M, Meyer W et al (2010) Substrate-induced structural modulation of a CoO(111) bilayer on Ir(100). Phys Rev B 81:235405

98. Gubo M, Ebensperger C, Meyer W et al (2012) Tuning the growth orientation of epitaxial films by interface chemistry. Phys Rev Lett 108:066101

99. Wagner M, Negreiros FR, Sementa L et al (2013) Nanostripe pattern of NaCl layers on Cu (110). Phys Rev Lett 110:216101

100. Ma L, Doudin N, Surnev S et al (2015) Ceria on Cu(110): formation of nanostripe strain defects. Unpublished results

Chapter 2
Atomistic and Electronic Structure Methods for Nanostructured Oxide Interfaces

**Giovanni Barcaro, Luca Sementa, Fabio Ribeiro Negreiros,
Iorwerth Owain Thomas, Stefan Vajda and Alessandro Fortunelli**

Abstract An overview is given of methods for the computational prediction of the atomistic and electronic structures of nanoscale oxide interfaces. Global optimization approaches for structure prediction, together with total energy and electronic structure methods are reviewed and discussed. Our aim is to furnish conceptual instruments to select the optimal (i.e., the most accurate and least costly) method for treating a given system, and to understand the potentialities and limi-

G. Barcaro
CNR IPCF, Consiglio Nazionale Delle Ricerche,
Via G. Moruzzi 1, 56124 Pisa, Italy
e-mail: barcaro@pi.ipcf.cnr.it

F.R. Negreiros
Centro de Ciências Naturais e Humanas, Universidade Federal do ABC,
Santo André, SP, Brazil
e-mail: f.ribeiro@ufabc.edu.br

I.O. Thomas
Department of Physics, Durham University, South Road, Durham DH1 3LE, UK
e-mail: iorwerth.thomas@durham.ac.uk

S. Vajda
Materials Science Division and Center for Nanoscale Materials, Argonne National
Laboratory, 9700 South Cass Avenue, Argonne, IL 60439, USA
e-mail: vajda@anl.gov

S. Vajda
Department of Chemical and Environmental Engineering, Yale University,
9 Hillhouse Avenue, New Haven, CT 06520, USA

S. Vajda
Institute for Molecular Engineering (IME), The University of Chicago,
5801 South Ellis Avenue, Chicago, IL 60637, USA

L. Sementa · A. Fortunelli (✉)
CNR-ICCOM, Consiglio Nazionale Delle Ricerche, Via G. Moruzzi 1, 56124 Pisa, Italy
e-mail: alessandro.fortunelli@cnr.it

L. Sementa
e-mail: sementa@pi.ipcf.cnr.it

tations of current approaches. Theoretical modeling of the structural, catalytic, mechanical, optical and magnetic properties of nanoscale oxides is also briefly described. Finally, an outlook on extending computational and experimental investigation from crystalline-like to amorphous oxide ultrathin layers and the challenges to be faced when dealing with these more complex systems is presented. Final remarks conclude the chapter.

Interfaces between an oxide and another material (a metal, a dielectric, a solvent, a polymer, …) are ubiquitous in nature, and are usefully exploited or simply dealt with in a huge number of technological applications. The strong oxygen affinity of many elements (including metals) makes in fact that under ordinary conditions surfaces of materials are typically covered by a protective layer of an oxide of some kind. Often, these are thin layers, and in given cases ultrathin or nanometer-scale layers, i.e., with at least one dimension of the order of few nanometers.

Drawing inspiration from this everyday experience, systems mimicking such 'natural' interfaces or, at the other extreme, new interfacial systems purposely designed and prepared in the laboratory under completely different (e.g., Ultra-High Vacuum, UHV) conditions have been the subject of increasing attention in the scientific community in the last decades, and in this context the sub-field of nanostructured oxides has attracted a substantial amount of studies and efforts [54, 127]. The reasons for this interest are easy to understand. From the point of view of fundamental science, nanoscale oxide systems offer the possibility of an improved, more detailed characterization and in-depth understanding, in addition to a wide playground of novel and unexplored materials. From the point of view of technology, focus on ultrathin or variedly nanostructured systems is encouraged and triggered by the parallel progressive shrinking of device dimensions as required by increasing miniaturization, in addition to the appeal of investigating the novel phenomena exhibited by such systems [54, 84, 127].

In these studies it has been soon realized that, in keeping with a general expectation in nanoscience and nanotechnology, nano-confinement entails the system features which are peculiar and as a norm very different from those of extended systems. Nanoscale dimensions in fact produce a much greater freedom and the relief of many thermodynamic or kinetic constraints enforced upon extended systems by their macroscopic extension and the consequent renormalization of fine interactions into Hamiltonians valid for bulk. In other words, in nanoscale oxides the realm of strongly non-scalable structure/property relationships is explored in which addition of one layer can substantially alter the observed behavior and huge oscillations occur as a function of size. As described in other chapters of this book it has then been found that the atomistic configurations at nanostructured interfaces are sometimes completely apart from those known for bulk oxides (widening of structural degrees of freedom), and that response properties can be greatly affected by the rapid cross-over of dielectric and/or structural characteristics at the interface between two possibly very different materials (widening of both structural and electronic degrees of freedom).

The above considerations also explain the reasons of the great importance of theoretical and computational methods in the field of nanostructured oxide interfaces.

Theory can in fact provide a general framework and a hierarchy of interactions in which to place and analyze the complex empirical phenomenology (see for example the discussion of polarity by Noguera and Goniakowski in this book).

In addition to this original role, computational methods have acquired a continuously increasing (at times dominant) importance. This is also easy to rationalize. Even in those cases (such as those considered in this chapter) in which the presence of a conducting or semi-conducting substrate enables the use of charged-particle probe techniques thus offering great advantages in terms of experimental characterization, the novelty of behavior and the intricacies of these multi-component interfacial systems are such that it is often impossible to comprehend their physics simply on the basis of experimental information combined with general theoretical principles. The availability of *accurate and predictive* computational methods is thus crucial for an in-depth understanding. An accurate and predictive computational modeling can first of all cross-validate and double-check experimental findings, thus supporting experimental analysis and assignment. Additionally, if *accurate*, it can provide a completely independent source of information thus representing an advanced form of characterization with features, advantages and limitations typically very different from, thus complementary to, experiment. New systems can e.g. be conceived, and the existence and properties of these hypothetical systems can then be verified experimentally in a cross-fertilizing synergy. Finally, computational 'gedanken' experiments can be devised which help analyzing and dissecting the basic interactions governing the physics of a class of systems.

The aim of the present chapter is thus to provide an overview of the computational approaches utilized in the field of nanostructured oxide interfaces, with focus on those based on electronic structure methods. Given this methodological character, the topics here discussed transversally underlie many of the other contributions.

Attention will be concentrated on nanostructured oxide interfaces in the form of metal oxide ultrathin films on a conducting or semi-conducting substrate (e.g., a metal single-crystal surface), i.e., films with a thickness of few (1–2) nanometers or 1–10 monolayers (ML)—see Fig. 2.1, which are most familiar to the authors [127]. However, the methods here described possess a more general significance, and can be adapted or adjusted to deal with any kind of nanostructured oxide interfaces (see e.g. the extension to amorphous systems in Sect. 2.4).

The chapter will end with a brief perspective outlook. Here we will make a leap to a further step in science and technology, which will bring us from the model crystalline phases mostly considered in this book toward amorphous materials close to those realized under realistic conditions [84].

The chapter is structured as follows. Given the widening of structural degrees of freedom in nano-oxides and the importance of knowing their atomistic structure to achieve predictive accuracy, we start with reviewing methods for structure
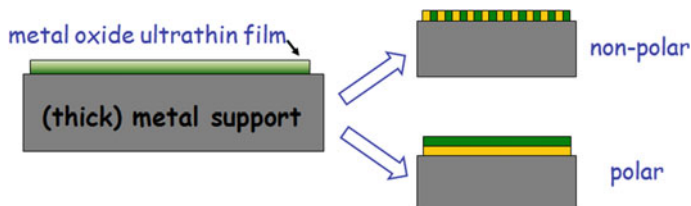
Fig. 2.1 Schematic depiction of metal oxide ultrathin films on metal surfaces

prediction and global optimization (Sect. 2.1). We then describe and briefly discuss approaches for total energy (Sect. 2.2), and electronic states (Sect. 2.3). Also to complement information not contained in other chapters of this book, Sect. 2.4 presents an outlook on and a brief introduction to the topic of amorphous nanoscale oxide interfaces and their potentialities in fields such as heterogeneous catalysis. Few final remarks and considerations then conclude this chapter (Sect. 2.5).

2.1 Structure Prediction Methods

As mentioned in the introduction, low-dimensional oxides may adopt structural configurations that are completely differ from the corresponding bulk motifs. It is therefore of great importance to be able to rigorously determine these configurations to provide a basis for structure/property relationships and surface functionality. Structure determination is however a very difficult task, and in practice often nearly impossible using experimental characterization alone. The number of atomistic structures of nanoscale oxides which have been fully unveiled is thus still somewhat limited. Crucial progress and successful examples have been achieved by combining the multitude of different experimental techniques with extensive calculations [127], see e.g. [78, 89, 112, 135] as pioneering cases. Given the importance of this subject and the common occurrence of a few misconceptions in the literature, we devote this Section to a review of structure prediction methods, i.e., computational methods for efficiently exploring the complex potential energy surface of multi-component systems that can be applied to oxide/metal and oxide/oxide interfaces to reliably predict their structure, providing a general framework in which to comprehend their basic principles.

Structure prediction is tantamount to finding the absolute minimum (the global minimum) of the potential energy surface (PES) of a given system—sometimes subjected to constraints which mimic or correspond to external physical constraints. In the mathematical literature, this problem goes under the name of 'global optimization' (GO) [109]: to find the global minimum of a function $f: \mathfrak{R}^N \to \mathfrak{R}$, defined under suitable conditions. In our case the function f corresponds to the energy of the system (or some form of free energy at finite temperature).
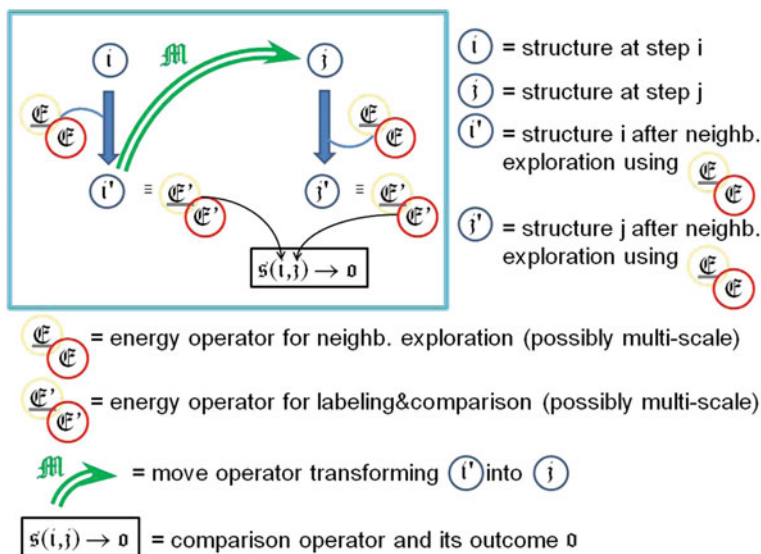
Fig. 2.2 Conceptual scheme of global optimization (GO)

Figure 2.2 illustrates the conceptual scheme of a Global Optimization (GO) approach. The basic ingredients are the following:

- $i \equiv$ structure at step i; $i' \equiv$ structure i after neighborhood exploration using the energy function $\mathbb{E}$
- $j \equiv$ structure at step j; $j' \equiv$ structure j after neighborhood exploration using the energy function $\mathbb{E}$
- $\mathbb{E} \equiv$ energy operator for neighborhood exploration − possibly hierarchical whence $\underline{\mathbb{E}}$
- $\mathbb{E}' \equiv$ energy operator for labeling & comparison − possibly hierarchical whence $\underline{\mathbb{E}'}$
- $\mathbb{M} \equiv$ move operator transforming i into j
- $\mathfrak{s}(i,j) \equiv$ selection/comparison operator, with $\mathfrak{o}$ as its result

This conceptual scheme is based on a few simple rules and ideas:

1. since a global minimum in the PES is sought for, the efficiency of the search is increased if—given a trial configuration—a neighborhood exploration (e.g., a local minimization) is performed before deciding whether to accept or reject the given configuration as meaningful—this neighborhood search is best performed using as the energy operator $\mathbb{E}$ the true physical energy of the system Hamiltonian without any modifications;
2. to label and decide whether to accept or reject the given configuration as meaningful a modified energy operator can be used, e.g., by combining the

energy of the system with other descriptors or order parameters or generalized variables (see the discussion below): this modified energy operator for labeling & comparison is indicated as $\mathfrak{E}'$;

3. both the energy and modified energy operators can be multi-mode (or hierarchical or multi-scale): in these approaches the energy is evaluated in an initial sampling of the phase space using a lower-level, less sophisticated but faster computational approach—indicated as $\underline{\mathfrak{E}}$ or $\underline{\mathfrak{E}'}$ –, and one switches to a higher-level, more accurate but more computationally demanding method—i.e., $\mathfrak{E}$ or $\mathfrak{E}'$ -, only for the energetically promising configurations;

4. in stochastic searches the selection/comparison operator $\mathfrak{s}(\mathfrak{i},\mathfrak{j})$ is often implemented as a Metropolis criterion comparing structure $\mathfrak{i}$ and $\mathfrak{j}$, i.e., by defining a fictitious temperature T and accepting the structure $\mathfrak{j}$ either if its modified energy $\mathfrak{E}'(\mathfrak{j})$ is lower than $\mathfrak{E}'(\mathfrak{i})$ or if the criterion: "$\exp\{[\mathfrak{E}'(\mathfrak{j}) - \mathfrak{E}'(\mathfrak{i})]/k_BT\} < \text{rndm}$" is satisfied, where rndm is a random number between 0 and 1 and k_B is the Boltmann constant—we anticipate that, in practical implementations, an optimal acceptance probability is typically around 50 % (if too low, the search is inexistent, if too high, the search is ineffective);

5. the move operator $\mathfrak{M}$ (i.e., the way to transform structure $\mathfrak{i}$ into structure $\mathfrak{j}$ or simply to generate structures $\mathfrak{j}$ sequentially) is obviously important for the efficiency and thoroughness of the GO algorithm, and will be discussed below, distinguishing between systematic and stochastic sampling techniques;

6. structures $\mathfrak{i}$ and $\mathfrak{j}$ can be either single configurations or *ensembles* of configurations.

A GO search then starts from a given structure $\mathfrak{i}$, locally explores/minimizes its energy $\mathfrak{E}(\mathfrak{i})$, records its modified energy $\mathfrak{E}'(\mathfrak{i})$—possibly multi-scale thus $\underline{\mathfrak{E}'}(\mathfrak{i})$, generates the next structure $\mathfrak{j}$ via the move operator $\mathfrak{M}$, locally explores/minimizes its energy $\mathfrak{E}(\mathfrak{j})$, records its modified energy $\mathfrak{E}'(\mathfrak{j})$—possibly multi-scale thus $\underline{\mathfrak{E}'}(\mathfrak{j})$, performs a selection/comparison $\mathfrak{s}(\mathfrak{i},\mathfrak{j})$ to decide whether to accept the structure $\mathfrak{j}$ or not, and starts the cycle again from structure $\mathfrak{i}$ or $\mathfrak{j}$ depending on the outcome $\mathfrak{o}$ of $\mathfrak{s}(\mathfrak{i},\mathfrak{j})$.

Let us discuss each point (1–6) in more detail.

Point (1) is at the basis of any current GO approach, although it can be recalled that historically the first GO algorithms used simple Monte Carlo sampling without any neighborhood exploration. To make this local neighborhood exploration, the *true physical energy of the system* $\mathfrak{E}$ rather than any modified energy operator $\mathfrak{E}'$ should be used, as this best corresponds to the physics of the problem.

For activated systems, i.e., systems in which the phase space is composed of basins separated by energy barriers appreciably larger than the thermal energy, the local neighborhood exploration is best realized as a local minimization, as in the pioneering basin-hopping algorithm [87]. What this energy minimization step does
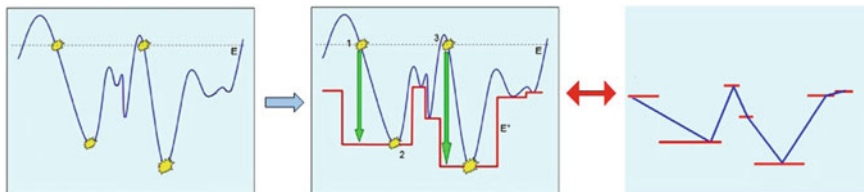
Fig. 2.3 Transformation of the original PES (*leftmost image*) via local minimization into a staircase function (*middle image*) which is tantamount to a phase-space graph (*rightmost image*)

is to associate to each point of the PES the energy of its closest local minimum. In this way, one actually transforms the original PES into a stair-case function, as illustrated in Fig. 2.3. More precisely, the original PES is transformed into a graph in which a volume-let of the phase space is associated to each vertex (see the right most side of Fig. 2.3).

For diffusive systems, i.e., systems with a very flat potential energy landscape in which energy barriers are comparable to the thermal energy, a GO search is meaningless, and the system should be studied using a Molecular Dynamics (MD) approach. It can be noted in passing that a GO search is also meaningless in the opposite régime of glassy systems, i.e., systems with an extremely rugged potential energy landscape in which energy barriers are so high that the system is frozen and will never reach the global minimum. For hybrid systems, i.e., simultaneously exhibiting activated and diffusive degrees of freedom, such as soft matter and biological systems, a GO search is meaningful for the activated degrees of freedom, with the local minimization best replaced by a MD run as a local neighborhood exploration over the diffusive degrees of freedom. A MD run can also be used in activated systems in place of a local minimization to get rid of metastable minima with barriers $\sim k_B T \log_e(A\tau)$, where A is a typical Arrhenius prefactor and τ is the time of the MD run (it can also be recalled that indeed a local minimization is often realized as a simulated annealing with $T \rightarrow 0$). Since an MD run is conducted at a finite temperature, one has the option of using either the average potential energy or the free energy from the MD run for labeling and comparing the given configuration—in either case one realizes a *finite-temperature GO* search. An alternative approach in activated systems corresponds to determining the vibrational eigenvalues $\{\omega_i\}$ of the given local minimum configuration and adding the corresponding zero-point vibrational energies: since some minima are stiffer than others, this can obviously make a difference.

Point (2) brings us a step further by introducing one of the most important tools in terms of efficiency of the search, which is exploiting within GO *structural recognition* or *order parameters* (from the theory of phase transition) or *descriptors*. An order parameter or descriptor is a function 🝚: $\mathfrak{R}^N \rightarrow \mathfrak{R}$, defined in the same configurational space as the energy, let's label it Ⓟ.

Paralleling the energy but offering a different landscape, order parameters can be used to increase the *diversity* of a stochastic search. A common problem of GO is in fact that there are regions of the phase space ('basins') which are wide and contain

very many (similar) structures and thus represent attractors for a stochastic search but which do not necessarily contain the global minimum which instead may reside in a different and much narrower region of the phase space. A stochastic search, such as a basin-hopping random walk, will be likely confined to the wider regions and will only rarely end up in the narrow regions where the global minimum may be located. However, if an order parameter is defined which exhibits different values in the different region of the phase space, it can be used to orient the search toward one or the other of these regions, thus increasing diversity. There are many ways of realizing this. In perhaps the simplest example, a modified energy $\mathbb{E}'$ is defined as a linear combination of $\mathbb{E}$ and $\mathbb{P}$ [108]. Other methods will be mentioned at point (5).

Within systematic sampling, instead, order parameters can be used to achieve the opposite goal of enforcing *constraints* on the search, constraints aimed at reducing its exponential complexity, as will also be discussed at point (5).

Point (4) corresponds to selecting configurations.

This selection/comparison can be based on a relative comparison between structures i and j as in the basin-hopping algorithm [87] or on an absolute comparison between the modified energy: $\mathbb{E}'$(i) or $\mathbb{E}'$(j), and some reference value (reservoir).

It should be recalled that the GO problem is a non-polynomial problem, i.e., its complexity increases as a function of the size of the system not as a power of size but exponentially. This means that the number of local minima accessible to a given system will increase exponentially, thus quickly exceeding the processing capabilities (storage, enumerating, etc.) of any given hardware resources. Most of these configurations will however be at high energy and thus physically irrelevant at any practically interesting, finite temperature (see below the discussion of kinetics and structural dynamics). The selection operator $\mathbb{s}(i,j)$ is thus an expedient tool to discard high-energy configurations as quickly as possible, i.e., to implement *filtering*.

If the selection operator is based on a Metropolis criterion and the neighborhood exploration is a local minimization as in the basin-hopping algorithm [87], then the stochastic search corresponds to a Metropolis Monte Carlo random walk on the staircase-transformed PES (using $k_B T$ as the Monte Carlo parameter), see Fig. 2.3. Here mathematical theorems on random walk can be usefully recalled. One of the most interesting reminds us that for a homogeneous random walk (i.e., on a flat potential energy surface, with no underlying energy bias) the recurrence probability of getting back to any starting point is 1 in 1 dimension (1D case), still finite in the 2D case, and equals zero in the 3D and higher-dimensional cases. This implies that there is no guarantee that a GO search for any higher-dimensional system will be successful. The $k_B T$ value determines the acceptance probability. As mentioned above, the optimal acceptance probability is roughly around 50 %. However, more than a mere numerical value the important point is that acceptance must be such that the system is able to explore those higher-energy configurations that are intermediate steps in the stochastic diffusion between one basin and another (see Fig. 2.3). It can be noted that the typical value of the 'energy barriers' to be so crossed depends on

the features of the PES of the given system but also on the move operator $\mathfrak{M}$, which is discussed at point (5).

Finally, in stochastic searches the selection/comparison operator should also ascertain whether structure $\mathfrak{j}$ is unique, i.e., it has not been already considered in the search, otherwise it does not add information and should be neglected. In "big data" searches (generating millions of configurations each one describing the position of millions of atoms) this can be a non-trivial problem. Applying the standard structure-comparison algorithm between two configurations (based on first rotating the structures into standard inertia-axes orientation and then calculating the distance matrix) to compare structure $\mathfrak{j}$ with all the previously generated structures can be computationally unfeasible. Faster algorithms comparing only a limited set of descriptors to label/indentify a given structure (typically the energy and a few order parameters) and partitioning their values into histograms are computationally more affordable and should be used.

Point (3) can also greatly increase the efficiency of the GO search. The principle is to find an approximation $\underline{\mathfrak{E}}$ to the energy $\mathfrak{E}$ (equivalently $\underline{\mathfrak{E}}'$ and $\mathfrak{E}'$) which is computationally faster, and to use $\underline{\mathfrak{E}}$ (equivalently $\underline{\mathfrak{E}}'$) to select promising configurations, while implementing the higher-level, more accurate but more computationally demanding method for the promising configurations *only*. In other words, candidate configurations are *filtered* via a fast but less precise ('quick-and-dirty') method, so that this approach can be called multi-mode filtering technique [13]. The reasons of the usefulness and importance of filtering have been discussed at point (3), i.e., the non-polynomial character of a GO search. Filtering can be implemented in a multi-mode fashion e.g. by coupling first-principles calculations with analytic potentials [14], or analytic potentials and effective Hamiltonians [17], and so on, i.e., by coupling a theoretical method with its higher neighboring one along the multi-scale hierarchical ladder. It is thus intrinsically and nicely connected with multi-scale modeling [16].

Even when $\mathfrak{E}'$ is taken as the un-modified energy $\mathfrak{E}$ so that order parameters discussed at point (2) are not used directly in the search, an approach which is extremely useful in which multi-mode techniques—point (3)—and structural recognition—point (2)—are synergistically combined is to perform a GO search using the approximate energy $\underline{\mathfrak{E}}$, classify the resulting structures according to an order parameter $\mathfrak{O}$, take the lowest-energy structures from each class (or structural basin) and re-optimizing them using the accurate energy $\mathfrak{E}$. In this approach one thus checks whether the relative ordering of the structural classes or structural motifs is different in the $\underline{\mathfrak{E}}$ or $\mathfrak{E}$ PES, as illustrated in Fig. 2.4 in the case of metal nanoclusters described via quantum-mechanics/empirical-potential approaches [47]. The idea behind this approach is that the approximate energy $\underline{\mathfrak{E}}$ is accurate enough to predict the energy ordering within a given structural motif or basin but not accurate enough to predict the energy ordering among different structural motifs or
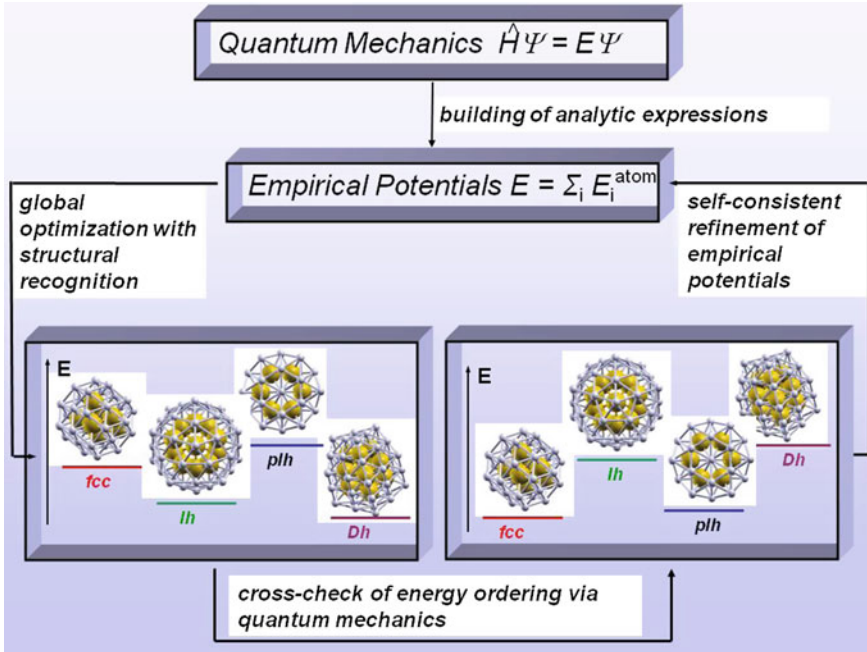
Fig. 2.4 Schematic depiction of an approach combining multi-mode techniques—point (3)—and structural recognition—point (2). Taken with permissions from [16]. Copyright 2012 Springer

basins: the reason for this expectation ultimately derives from perturbation theory: the physical interactions determining the energy ordering within a given structural basins are more homogeneous than when the basic motifs change across basins.

In passing: an approximation $\mathfrak{E}$ to the energy $\mathfrak{E}$ is necessarily based on some sort of analytic interpolation, which in turn is an expression based on some sort of *generalized variables*. Crucial for the accuracy of such an approximation, and thus for its usefulness in the filtering process, is the choice of the generalized variables. Looking in more depth, one easily sees that these generalized variables actually coincide with the order parameters or descriptors introduced above. One fundamental mathematical problem, currently the subject of great efforts in many research groups around the world, is how to find the minimal number of descriptors and their optimal form in an *automated* way (intrinsically this corresponds to a principal-eigenvalue combined with a GO problem).

Point (5)   i.e., the choice of the move operator $\hat{\mathfrak{M}}$, is also obviously important for the efficiency of GO sampling. Moves can be distinguished into stochastic or systematic.

In stochastic moves, one realizes a random perturbation of the system. The simplest option is a random 'shake', i.e., a random move of the coordinates of all atoms, in which the only free parameter is e.g. the modulus or length of the move.

For the degrees of freedom associated with chemical ordering, an exchange of the position of two atoms is the simplest move, but many others can be defined, see [13] for a recent discussion. In fact, there is a wide range of possibilities. The basic problem here is the need to perturb the system in an undetermined way (so that it can explore as many regions of the phase space as possible in an unbiased way) without forcing the system into exceedingly high-energy (thus unphysical, unrealistic) configurations. It is not easy to find the right balance between these opposite requirements of thoroughness and efficiency. One possibility is to combine a random move with structural recognition. One can then analyze the coordination environment of a given atom and perform a move which takes this information into account e.g. trivially by limiting the length of the random move at high coordination numbers or orienting it along certain preferential directions at low coordination numbers or for 5-fold rather than fcc coordination environments. Again, this is nothing but a possible use of order parameters to accelerate the search. This kind of restricted moves is usually expedient for small systems (less than—say—100 atoms). For large systems (more than 100 atoms), a random move which has a collective but not fully disruptive character is a short run of unstable Molecular Dynamics [74, 108], and its use has enabled GO searches on systems with thousands of atoms using analytic potential [46]. So far little explored but in our opinion very promising is an approach based on rough eigenvector-following of vibrational eigenvalues $\{\omega_i\}$ of an approximate Hessian, as first proposed in [96]. This approach has also connections with exploring the saddle-points of the PES, thus structural dynamics [96], and will be discussed in more detail in a future publication.

It should be noted that for open systems or for systems whose stoichiometry is not known, the degrees of freedom associated with chemical composition should also be sampled. In other words, moves in the space of *stoichiometry* or *chemical composition* should also be considered. This implies defining a chemical potential for each of the component species. The simplest example in oxide systems is the free energy of the O_2 molecule in the gas phase [107]. For elements deposited on the support surface, the definition of an appropriate chemical potential can be non-trivial. It can be noted that this point introduces the use of *reservoir* techniques [74] which are not discussed here although they can be very effective.

Systematic moves are also widely used. The basic principle behind such systematic moves is to limit the search by enforcing constraints which reduce the parameter space in such a way that it can be thoroughly sampled. In other words, the aim here is to reduce the number of degrees of freedom of the system in such a way that a systematic sampling becomes computationally affordable. There are several ways in which this can be effected.

One way is to draw from a *database* of previously determined configurations. These can be taken from knowledge on an analogous system, in which case this techniques is called 'system comparison' [47]. This knowledge can be derived from a previous GO search, or from experimental information, e.g., on a systematics based on crystallographic principles or tiling theorems [38], etc.

Another way is to *generate* a database of configurations for the given specific system (which can then be used in successive GO searches).

One effective tool in this respect is to exploit or enforce *group symmetry*, either point group symmetry or translational symmetry, as originally proposed in [50] and discussed in some detail in [16]. Given the exponential increase in the structural freedom of the system as a function of the size of the system, enforcing group symmetry entails a reduction in the system size by the order of the symmetry group, i.e., typically 10–20 in practically useful cases. In this case atoms are grouped into symmetry classes (also called 'symmetry orbits'), i.e., groups of atoms transformed into each other by the operations of the symmetry group. Ultimately, looking in more depth, the existence of rigorous symmetry turns out to be unnecessary. Rather, atom grouping can be more generally realized on the basis of equivalence classes determined by the physics of the system itself, i.e., grouping atoms into sets which share a common physics (e.g., a common coordination environment). This approach has been called 'grouping approach' and is extremely efficient, e.g., enabling GO sampling of the chemical ordering of nanoparticles with thousands of atoms using empirical potentials with a modest computational effort, see [13]. Since recognizing a common physics is once more based on some sort of analytic interpolation or model for the Hamiltonian energy of the system, hence it is necessarily based on order parameters or descriptors or generalized variables introduced at step (2), order parameters can be easily used in the grouping approach. A final step forward presently under investigation is the automated, 'on-the-fly' definition of order parameters that best describe the system under consideration, as recalled at the end of point (3). How to best achieve this further step is an important topic of current research.

Grouping atoms is not the only possible way to reduce the number of degrees of freedom, as it only *correlates* motions of different atoms without constraining them. It can then be complemented by techniques *limiting* the configurational space. This can be realized by defining a lattice, i.e., merging volumes of the phase space into single points (or—more in general—by defining a limited number of possible lattices). To illustrate this point visually thus more efficiently, let us consider an example. Suppose we want to study a system in which an oxide ultrathin film is deposited onto a fcc(111) single crystal surface, and suppose we know e.g. from experimental information or wild guess that this film is composed by four atomic layers in polar M/O/M'/O stacking, exhibits three-fold symmetry and has a (2×2) unit cell, as schematically depicted in Fig. 2.5a, b.

One can then limit the configurational space to a finite number of sites (lattice), such as 4 fcc, 4 hcp, and 4 top sites with respect to the underlying substrate (see Fig. 2.5b). By exploiting three-fold symmetry, for each layer three patterns are permitted: 4 atoms in a fcc(111) epitaxial pattern, 3 atoms along a kagomé pattern, and two atoms giving rise to a honey-comb pattern (see Fig. 2.5c–e). By considering for definitiveness a single metal element in the lowermost layer and two different metal elements in the subsurface layer, a finite number of combinations then results, some of which are exemplified in Fig. 2.6. It should be underlined that
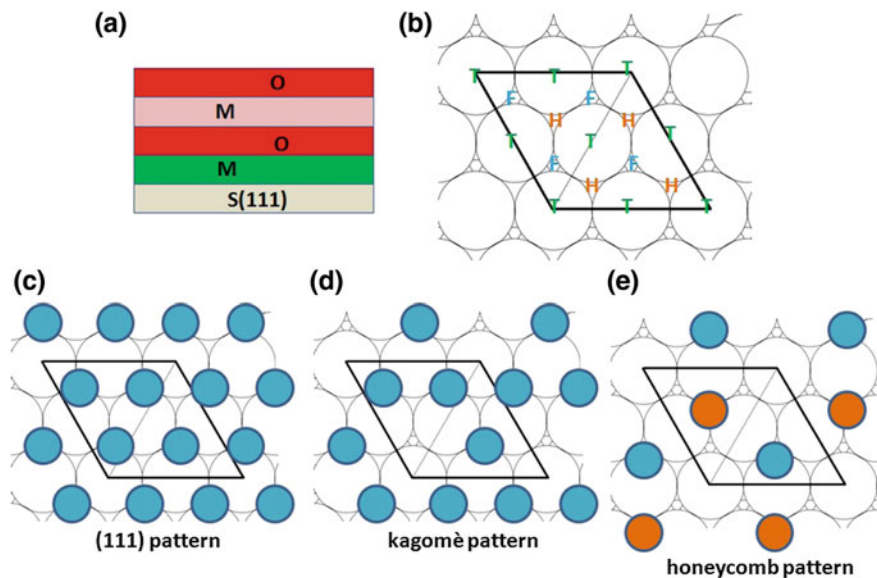
Fig. 2.5 (**a**) Schematics of a tetra-layer polar films on a fcc(111) metal surface; (**b**) adsorption sites on a fcc(111) surface: top(T), hollow fcc (F), hollow hcp (H) (bridge and other sites are not considered); (**c–e**) coverage patterns on fcc(111) consistent with a (2×2), three-fold symmetric unit cell
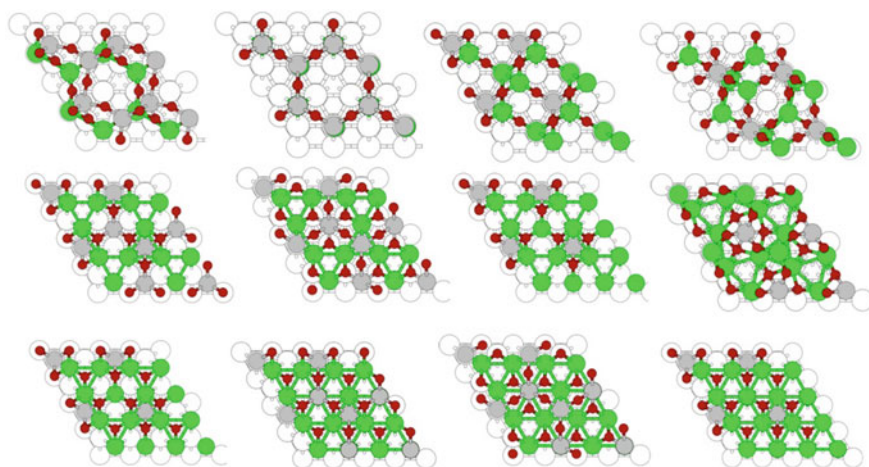
Fig. 2.6 Selected configurations generated by a systematic search of a tetra-layer fcc(2×2) ultrathin ternary films (with further constraints as detailed in the text). Oxide atoms in *gray*, *green*, and *red*; substrate atoms in *white*
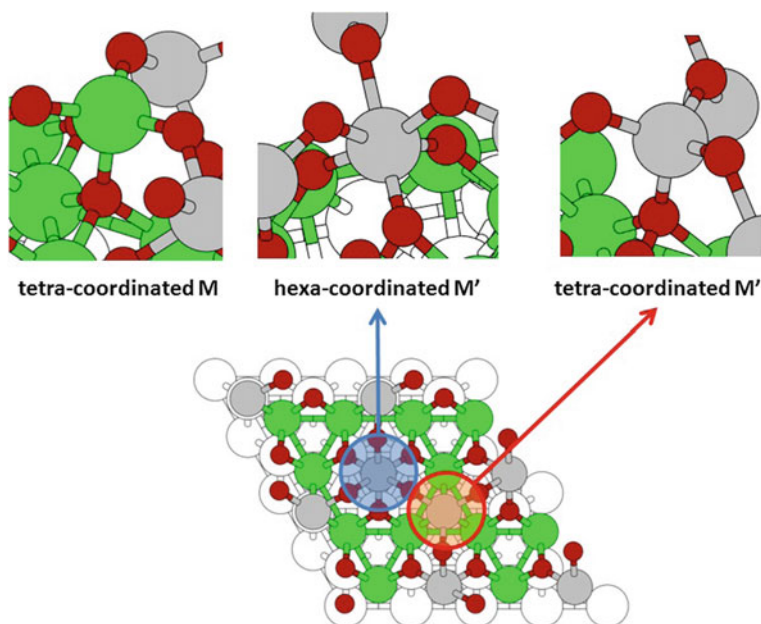
Fig. 2.7 Structural units extracted from an analysis of one of the configurations in Fig. 2.6

both binary and ternary oxides can in this way be generated, as in the example of Fig. 2.6.

Before leaving this point, it is worthwhile underlining that one important side-product of both systematic and stochastic sampling is to generate new structural knowledge which can then be exploited in stochastic and also systematic searches. For example, the configurations generated in Fig. 2.6 can be analyzed, and *basic structural units* can be extracted, as illustrated in Fig. 2.7. These units can then be exploited as building blocks e.g. in stochastic GO searches: this has the advantage that the number of degrees of freedom are reduced by the size of the unit, producing structures which contain many types of such units thus being too complicated and numerous to be tested in a systematic sampling (e.g., the crystallographic or tiling approaches mentioned above). An important question is how to define/recognize structural units. Ultimately, this is once more tantamount to the problem of finding order parameters best describing the given system. In our opinion, the analysis of vibrational modes $\{\omega_i\}$ [96] lends itself to the most promising developments in this respect as building blocks emerge as nearly frozen structural units in low-frequency modes (Unpublished work). A principal value analysis of the Hessian filtered at a given frequency should therefore automatically produce these compact, stable units (as indeed confirmed in exploratory, still unpublished tests).

Point (6)   finally introduces *ensemble* techniques. In these, instead of focusing on a single configuration at a time, a set or ensemble of configurations is

simultaneously investigated. The aim again is to increase the diversity of the GO search, in this case by letting different configurations explore simultaneously different regions of the phase space and exchange information to avoid overlaps in exploring the potential energy surface ("repel" each other). Since the computational effort scales roughly linearly with the dimension of this ensemble whereas the GO problem is non-polynomial, any linear technique achieving a more than linear acceleration in sampling is worth the while. Parenthetically, this viewpoint highlights an intrinsic equivalence between apparently different approaches such as basin-hopping with walkers [108], genetic algorithms [71], and parallel tempering [30] techniques: all these approaches are different implementation of the same basic idea, realized by exploiting structural recognition and order parameters [108], or structure combination [71], or different physical behavior at different temperatures [30], respectively.

The previous overview of GO approaches may seem disproportionate with respect to the limited possibilities realized so far in the field of 2D oxides. However, two points should be underlined. First, any structural search can be classified and understood on the basis of the principles outlined above: from the most simplified, biased, roughest trial-and-error attempts to the most sophisticated systematic or stochastic [135] sampling realized so far. Second, given future advances in hardware, especially at the level of parallel high-performance computing, more and more refined GO searches will become accessible and feasible to an increasing number of researchers in the future: our aim here is to provide a general scheme in which this research can be framed, understood, and thus accelerated. Indeed, it can be recalled as a great success of structural prediction approaches that already in a few cases *new* ultrathin oxide phases and their the atomistic structures have been predicted by theory *prior* to experimental realization, see [15] for one of the possible examples.

To conclude, we add a few considerations on structural dynamics. So far we have considered only the problem of how to predict the lowest-energy configurations of the system. However, of the outmost interest is to investigate and be able to accurately simulate dynamical processes and kinetics. Structural dynamics is very difficult to study especially at the experimental level, but also at the theoretical level due to the need of exploring not just the bottom of energy basins (local minima) but also the critical points (saddle points) connecting minimum-energy configurations [96]. The importance of these processes (e.g. growth!) can however be hardly overestimated, and rigorous information is strongly needed. Unfortunately, the situation in the field of nanoscale oxide interfaces is such that information is available only in a very limited number of cases. Here we will discuss one of these cases: MnO and NiO mono-layer (ML) phases on Ag(100), which have been investigated via a combined experimental and theoretical investigation [97, 125], thus deriving three main points concerning the description of kinetic phenomena (and their interplay with polarity effects).
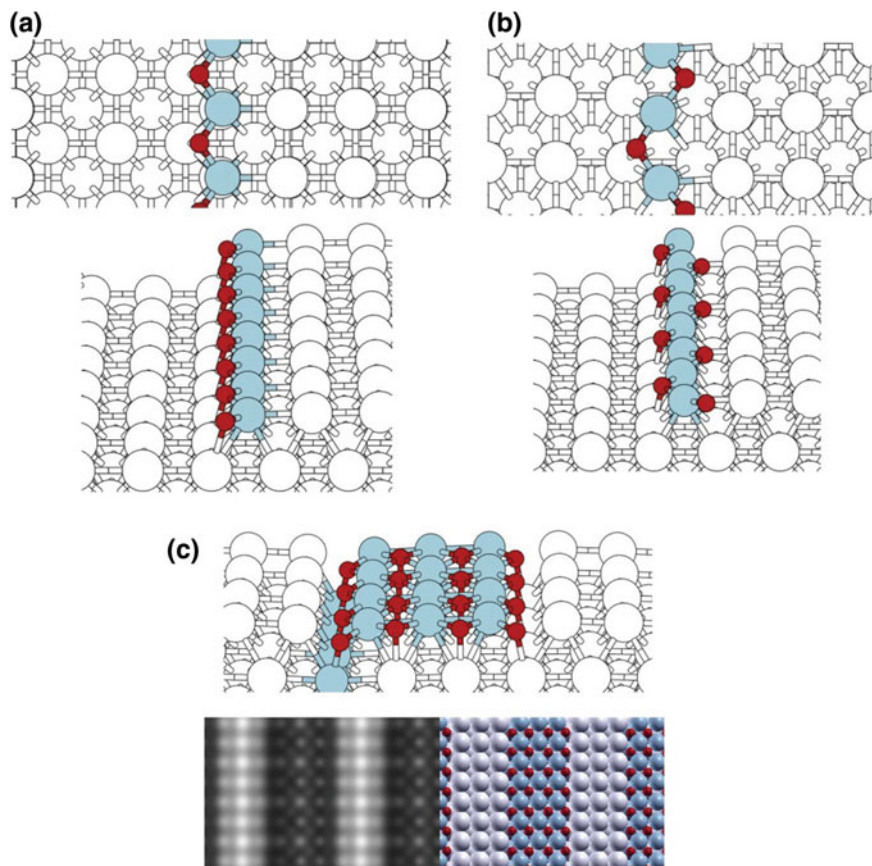
Fig. 2.8 (**a**, **b**) Structural models of the nucleation of the epitaxial (100)/(100) Mo phase (**a**) and a polar precursor phase (**b**) at a step edge of Ag(100). (**c**) Formation of subsurface M atoms at the border of the embedded epitaxial (100)/(100) Mo phase. Taken with permissions from [125]. Copyright 2011 Elsevier

First, the experimental observation in both the MnO/Ag(100) and NiO/Ag(100) systems of the formation of a precursor polar phase which is *thermodynamically less stable* than the epitaxial non-polar (100)/(100) phase has been rationalized via a structural model of nucleation at a Ag(100) step edge, see Fig. 2.8a, b [97, 125]. This represents an example of embedded growth, in which the thermodynamically more stable phase is non-polar but presents polar border along certain directions, and this fact kinetically destabilizes its growth while favoring the formation of a higher-energy polar competitor which exhibits non-polar borders.

Second, the energy barriers for the diffusion of metal atoms (specifically, Mn atoms) during the growth of the precursor polar phase MO/Ag(100) were calculated, finding a strong *diffusional anisotropy* along preferential directions of the oxide island borders (where growth takes place) which gives rise to strongly
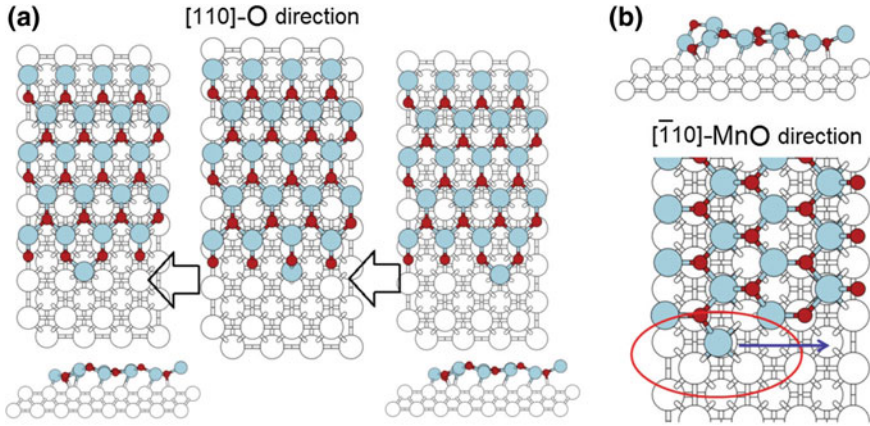
Fig. 2.9 Schematic depiction of the migration (diffusion) of Mn atoms at two different borders of the precursor polar phase of MnO/Ag(100). Taken with permissions from [97]. Copyright 2013 American Physical Society

anisotropic growth and the striking formation of nanostripes of macroscopic length, see Fig. 2.9 [97].

Third, polarity compensation was found to play again a crucial role in determining the atomistic structure of borders of the epitaxial non-polar (100)/(100) phase. Indeed, to compensate the polarity of these borders M atoms prefer to bury in subsurface positions thus rationalizing the experimental observation of dark features at the domain borders, see Fig. 2.8c [125].

These are simple, preliminary examples but with a possible general significance which shall be tested in future studies.

2.2 Total Energy Methods

To investigate the structural properties of a given system what is needed at the computational level is an expression for the total energy. Such an expression depends on both the nuclear and electronic coordinates of the atoms which constitute the chosen system. First-principles methods (i.e., methods which do not introduce parameters other than the basic physical constants) furnish such an expression at the Quantum Mechanical level via a solution to the time-independent many-body Schrödinger equation [37, 90]:

$$H\Psi_i(\vec{r}, \vec{R}) = E_i \Psi_i(\vec{r}, \vec{R}) \tag{2.1}$$

where H is the Hamiltonian operator and E_i and Ψ_i are its eigenvalues (energies) and eigenvectors (wave functions), respectively: Ψ_i depend on both electronic

(r) and nuclear (R) coordinates. In practice, accurate solutions of this equation can only be obtained for systems containing few particles (nuclei and electrons). As a consequence, for larger (realistic systems) one inevitably has to use some sort of approximate approach.

First of all, the so-called Born-Oppenheimer approximation [27] is invoked, which, by taking advantage of the much larger mass of the nuclei with respect to that of the electrons, disentangles the electronic from the nuclear degrees of freedom. Within this approximation, the electrons move on a Potential Energy Surface (PES) generated by the immobile nuclei, whereas residual effects (such as electron-phonon coupling) are treated as perturbations.

2.2.1 Density-Functional Theory (DFT)

To solve the electronic problem at a fixed geometry of the nuclei in the Born-Oppenheimer approximation, many approaches are available. Among them, the most widely employed in the field of metal/oxide hybrid systems is density-functional theory (DFT), as it realizes the best compromise between chemical accuracy and computational effort. By following the original derivation by Kohn and Sham [67, 76], the following coupled single-particle (single-electron) equations have to be solved within DFT:

$$\left(\frac{-\hbar^2}{2m}\nabla^2 + V(r) + \int \frac{\rho(r')}{|r - r'|}dr' + V_{xc}[\rho(r)](r)\right)\varphi_i(r) = \lambda_i\varphi_i(r) \qquad (2.2)$$

where the Hamiltonian operator (in parenthesis) is expressed as a functional form of the electronic density $\rho(r)$ of the system, and $\varphi_i(r)$ and λ_i are single-particle wave functions and energies, respectively. The Hamiltonian operator is the sum of the following contributions (in order from left to right): kinetic energy, external potential due to the nuclear field, electron-electron Coulomb repulsion and the so-called exchange-correlation potential, which is the key-ingredient of DFT as it takes into account in an implicit form all the intricacies associated with the correlated motion of interacting electrons. Although in the form of a single-particle Hamiltonian and thus less computational demanding than the original many-particle Schrödinger equation, DFT is still a first-principles method with an explicit description of the electronic wave function, and can only be used in practice when the size of the system is relatively small, even though advances in software and hardware are continuously extending the scope of systems amenable to accurate DFT modelling.

The central problem in DFT is that the exact functional form of the exchange-correlation term is unknown. Great efforts of current research in the field focus on deriving increasingly accurate approximations to it. This goal is often framed within the so-called Jacob's ladder [103], where a hierarchy of increased

accuracy in principle leads to the limit of the exact form of the xc-functional. The idea behind this approach is that at the lowest level (rung) of the ladder one considers V_{xc} functionals depending only the electron density, while climbing to higher rungs corresponds to introducing first the gradient (first derivative) of the electron density, and then its Laplacian (second derivative). At this point, the expansion of the V_{xc} functional in terms of higher derivatives becomes ineffective because it can be demonstrated that the corresponding series is only weakly convergent. Moreover, it can also be demonstrated via a Taylor series or coupling constant expansion of the correlation energy with respect to the strength of the electron–electron interaction that the presence of a non-local or Hartree-Fock-exchange-type component within V_{xc} is justified [61]. This Fock-type exchange component however does not depend *locally* on the electron density but rather on the density-matrix, i.e., *non*-locally, and thus exhibits quite different features with respect to functionals depending only locally on $\rho(r)$. This leads to the so-called hybrid xc-functionals [18] in which the exchange component of V_{xc} is a mixture of a Hartree-Fock-type term and a term which instead depends only on the density and its gradients.

To summarize the Jacob's ladder schematically:

(i) first rung: the Local Density Approximation (LDA), in which the xc-functional is simply given by the sum of the Slater exchange [41, 118] plus a correlation functional parametrized on accurate results derived for the homogeneous electron gas;

(ii) second rung: the Generalized Gradient Approximation (GGA), in which LDA is corrected via terms which depend on the gradient of the electron density [100–102];

(iii) third rung: meta-GGA, in which GGA are further corrected via terms which depend on the Laplacian of the electron density;

(iv) fourth rung: hybrid xc-functionals, whose exchange consists in a mixture of a GGA-like exchange and the exact (Hartree-Fock) exchange [18];

(v) fifth rung: RPA and post-DFT approaches (see later Sect. 2.2.2).

Although this hierarchy is appealing both aesthetically and from a principles point of view, it is based on an internal DFT criterion, so that in our opinion it may obscure the fundamental physical reasons underlying such a complicated panorama. Let us thus pause to consider in more depth and in a more general framework these reasons, as this can be helpful to guide us in the crucial choice of the most appropriate xc-functional within DFT.

The Kohn-Sham theorems assure us that—for each given system—a model single-particle Hamiltonian does exist which is exact, and provide the same energy as the real system. However, in the few cases in which it has been possible to derive *rigorously* such an exact single-particle Hamiltonian, its form turned out to be extremely complicated [72]. Moreover, a qualitatively different form of the single-electron Hamiltonian is expected for (i) conductive versus (ii) insulating systems. (i) For a metal, in fact, it has been demonstrated that the correct renormalized Hamiltonian is the free electron gas, in which Coulombic interactions are

fully screened and rigorously renormalized to zero (apart from intrinsic instabilities leading to superconductive behavior) [117]. This represents a major issue for approaches based on Hartree-Fock Hamiltonian and exchange, in which the bare, *unscreened* Coulombic interactions are used. When applied to the electron gas, for example, it has been shown that the Hartree-Fock exchange leads to exceedingly wide valence bands and a diverging (infinite) value of the density of states at the Fermi level [75]. This probably reverberates in issues of the Hartree-Fock approach when describing metals or metallic nanoparticles [51] or the metal supports of nanoscale oxides, although at present the situation is not completely clear. It should be noted that such issues are associated with the *long-range tail* of the Coulomb potential, which is also the well-known source of electrostatic divergences [42, 140]. Hybrid DFT xc-functionals inherit these issues of the Hartree-Fock approach, although damped by the mixing of Hartree-Fock exchange with density-based exchange potentials. To cure these issues, one possibility is to use the so-called "range-separated hybrid" xc-functionals [64]. In range-separated hybrid xc-functional the $1/r_{12}$ term in the Hartree-Fock exact exchange is partitioned into a short-range and a long-range component, only the long-range tail of the exchange is screened (in an empirical way). This has the great advantage that the short-term component of the Fock exchange is retained, that is very important and can account for several effects, such as—importantly—Hund coupling in the atomic regions, and therefore atomic magnetism, etc. (ii) Going in fact from delocalized metallic electrons in a flat potential to the opposite extreme of localized electrons in the atomic core regions, one finds a completely different, indeed *opposite* situation. It has been demonstrated that correlation (screening) is asymptotically *irrelevant* for the inner-core orbitals with increasing the atomic number. In other words, for these inner-core, high-electron-density electrons Hartree-Fock represents the correct, renormalized single-particle Hamiltonian [79]. We are thus facing the crux of computational atomistic material science, i.e., the need to keep in the same framework and methodological description delocalized (e.g., metallic) and localized (e.g., core or inner *d*- or *f*-) electrons. This crux corresponds to the antithesis between low-density/low-density-gradient versus high-density/high-density-gradient diversity in the physical reality. In passing: this diversity also undermines Thomas-Fermi or Hohenberg-Kohn density-only approaches with respect to Xα-Slater or Kohn-Sham ones, and it is noteworthy that the difference between Thomas-Fermi and Hartree-Fock kinetic energy density was used as a parameter to monitor the local state of the system and interpolate between the opposite régime of localization and delocalization.

These considerations lead us naturally to "space-dependent" approaches, i.e., approaches in which the analytic dependence of the single-particle Hamiltonian as a function of the density or density matrix *varies in space* [32, 131]. This spatial variation in fact seems necessary to account for the basic issue of computational atomistic material science, i.e., the presence in the system of regions with a different delocalized (e.g., metallic) versus localized (e.g., core or inner *d*- or *f*-orbitals) character.
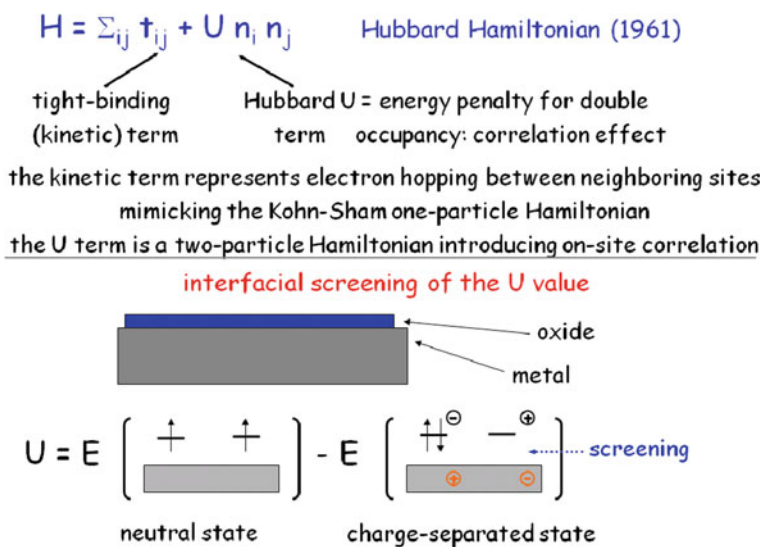
Fig. 2.10 Definition of the Hubbard Hamiltonian. Taken with permissions from [16]. Copyright 2012 Springer

An alternative to the use of hybrid xc-functional comes from the use of the so-called DFT+U method [4]. In this approach, an energy (Hubbard U) term [69] is added to the DFT Hamiltonian in order to introduce an energy penalty for the double occupation of specific orbitals, see Fig. 2.10. This additional term in the Hamiltonian is introduced to improve the description of the *localized* electronic states which characterize many metal oxides, especially those where incomplete *d*-bands are present (transition metal oxides, see the discussion below about NiO), via a term which takes partially into account their correlated motion. Importantly, in a similar way of operation as the short-term component of the Fock exchange in range-separated hybrid xc-functionals discussed above, the Hubbard U term in the DFT+U approach approximately accounts for Hund coupling in the atomic regions, and therefore definitively improves the description of atomic magnetism. Technically, U is an empirical parameter whose value must be determined in some way. The value of U can in principle be evaluated a priori, but a common practice consists in empirically deriving its value by comparison with experiment, see e.g. [12].

An advantage of the DFT+U approach with respect to hybrid xc-functionals is that the U term can be selectively turned on specific atoms, selected not only on the basis of their chemical identity, but also e.g. by their position in space, while keeping a bare LDA/GGA description on those parts of the systems where localization of the electronic states is not needed. In such a way, one easily implements a *space-dependent approach*, that can be expedient to achieve an accurate description of systems exhibiting regions of space with different electron localization/delocalization

features. In the following we will indeed illustrate the advantage of such space-dependent methods using a DFT+U approach.

Let us now see how these very general considerations reverberate in the discussion of our specific systems. A prototype nanostructured-oxide/metal system can be distinguished into three parts, given by: (i) the metal support; (ii) the oxide layer and (iii) the metal/oxide interface. (i) When employing a DFT approach to calculate the total energy of the system, an accurate description of the metal support is often achieved by employing a GGA xc-functional. (ii) Hybrid xc-functionals or DFT+U are instead often beneficial in the description of the oxide layer, especially for those systems with a gap between the highest occupied (HOMO) and the lowest unoccupied molecular orbital (LUMO). Although in metal-supported ultra-thin oxide layers metallization effects often reduce the HOMO-LUMO gap, the introduction of a Hartree-Fock exchange component or a Hubbard term in DFT+U can be of great importance in accurately reproducing not only the total energy of the system, but also other important properties in addition to structural ones, such as electronic quantities: the position of semi-core states, the magnetic moment on the individual metal ions, and the relative energetic stability of the magnetic ordering patterns (ferromagnetic vs. different types of anti-ferromagnetic patterns), see the next section. (iii) The description of the interface between the metal and the oxide is a delicate issue. Sometimes experimental data on specific systems can furnish valuable insight on the best xc-functional for the correct description of this region but unfortunately information of this kind is rare. Nevertheless, at least in few cases it has been possible to obtain such information, and, interestingly, this has shown the usefulness or even the necessity of the *space-dependent approaches* mentioned above. It has been demonstrated in fact that within the DFT+U approach the value of U at the *interface* between an oxide and a metallic surface should be properly *rescaled* in order to take into account the electronic screening by the metal electrons. More specifically, it has been shown [1, 12] that a reduction of the U parameter with respect to the value appropriate to the bulk oxide due to screening of electron-electron interactions by the underlying metal support (see Fig. 2.10) better describes the atomistic and electronic structure at the interface and allows an accurate agreement between theory and experiments. We now discuss these results in detail.

Figure 2.11 reports results from a DFT study on the structure of a single layer Ni_3O_4 grown on Pd(100) [12]. On this oxide, precise LEED (Low Energy Electron Diffraction) data exist which furnish accurate structural parameters on the relative heights of the ions inside the oxide phase. As it can be seen, this oxide is formed by dense stripes of Ni ions (labeled Ni_b) alternating with defective stripes where the density of Ni ions (labeled Ni_a) is one half. Oxygen stripes with the same density as Ni_b stripes separate the metal ion stripes. As illustrated in Fig. 2.11, a pure GGA-DFT approach (U = 0) does not reproduce correctly the relative heights of the ions, overestimating the height of the oxygen stripes. In contrast, when performing a local optimization by turning the Hubbard U term on (with a value of U = 4.0 eV), a much better agreement with the LEED data is achieved. In the same work, it was also shown that the introduction of the Hubbard term is beneficial to correctly
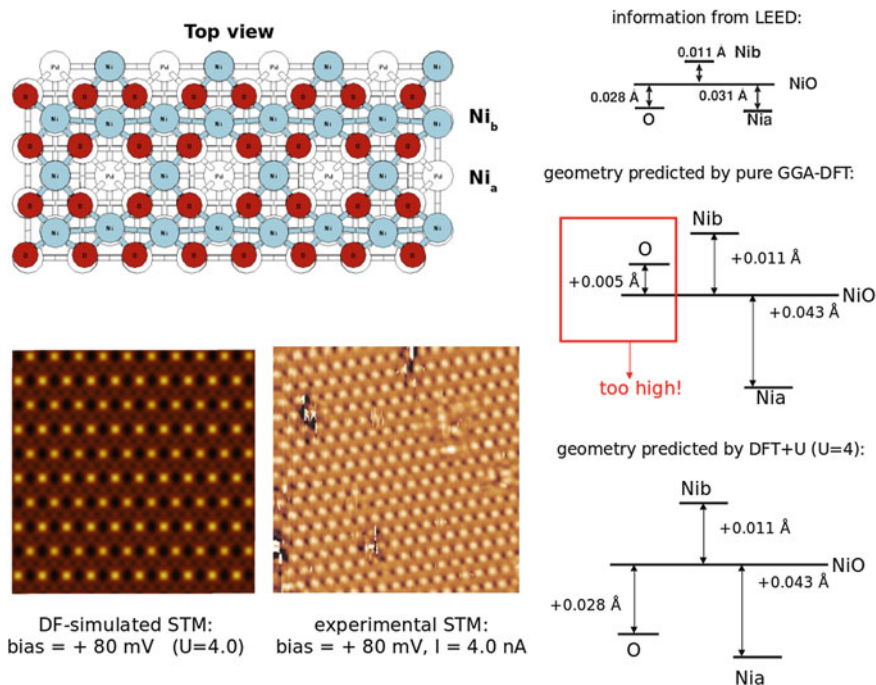
Fig. 2.11 Improved accuracy using the DFT+U approach in Ni_3O_4/Pd(100). Adapted with permissions from [12]. Copyright 2010 American Institute of Physics

reproduce the experimental STM pattern (see Fig. 2.11 for a final comparison between theory and experiment) and the work function of the system. It should be strongly underlined that the proper value of U (around 3.3–4.0 eV) which enables fully exploiting the potentialities of the DFT+U approach is reduced due to metallization (screening) effect with respect to 5.3 eV, the value derived for bulk NiO. This therefore represents one example of a 'space-dependent' approach, whose need is easy to understand: the dielectric characteristics of the system vary from regions with metallic character (no band or HOMO-LUMO gap) to regions with insulating character (wide band gap), thus the screening of Coulomb interactions is different in these different regions and the Hamiltonian should reproduce these different behavior. DFT+U can achieve this simply by modulating the U value for metal atoms in different dielectric environment. As illustrated in Fig. 2.10, in fact, U can be seen as an energy difference associated with the process of moving one electron from a neighboring site onto a site already occupied by another electron: for metal atoms at the oxide/metal interface, the charge-inhomogeneous configuration will be strongly stabilized by the image charges in the underlying metal substrate, thus appreciably reducing the value of U.

So far we have illustrated the advantage of space-dependent methods using a DFT+U approach. However, analogous space-dependent techniques have been

proposed in the context of hybrid xc-functionals. Indeed, the same idea of the original range-separated hybrid xc-functionals, in which the Fock-exchange is partitioned into a short-range and a long-range component, is intrinsically homologous to a space-dependent approach. How can we optimally exploit this idea on the basis of physical considerations? As discussed above, the short-range component of the Hartree-Fock exchange is useful or even necessary to describe the correct renormalized single-particle Hamiltonian in the atomic regions, so accounting for Hund's coupling etc. in much the same way as the DFT+U method. If one is interested in the total energy of the electronic ground state only, the short-range Fock exchange may be sufficient, and one can therefore damp the long-range component and achieve an enormous simplification of painful Coulomb divergencies in periodic systems. However, as we will see in the section, this long-range component of Fock exchange is often important to describe some type of electronic excited states. See e.g. the Rydberg image states discussed in connection with Fig. 2.18. There is nothing mysterious about this. Coulomb electron-electron interactions renormalize to zero in the bulk but not at the surface of an electron gas. Therefore, while the occupied orbitals are only slightly affected by the long-range component of Fock exchange, the virtual or unoccupied orbitals —expanding in regions outside atoms/bonds, i.e., regions of very low electron density—can be significantly affected by the presence of a long-range Coulomb tail. Such tails in general make virtual orbitals more compact and can even create bound state from continuum ones (see Fig. 2.18). Recall that virtual orbitals are a first approximation to excited states, whence the importance of long-range Fock exchange e.g. in TDDFT calculations. As a consequence, there exists a class of range-separated hybrid xc-functionals in which, at variance with the original proposal consisting in damping the long-range Fock component, this component has been optimized for the description of excited states. In our opinion, there is still room for playing around with the admixture of long- and short-range component of Fock exchange and fully exploit the associated degree of freedom [32], before moving to more sophisticated approaches [131]. In the most advanced of these latter approaches, the Hartree-Fock exchange component is modulated by a space-dependent factor, in such a way that different parts of the systems are described by a different combination of Hartree-Fock and GGA exchange [32, 131]. Note that it is precisely the long-range Fock component which is missing in the DFT+U approach, which can thus be seen as a convenient and efficient way to fix Hund's coupling phenomena, but intrinsically misses long-range Coulomb phenomena/effects.

2.2.2 Beyond DFT

So far we have only considered DFT. However, we recall that approaches that go beyond DFT have also been used to describe hybrid metal/oxide systems. Among

them, we mention the Random Phase Approximation (RPA) [98] and the GW approach [98].

RPA has indeed emerged as a powerful and relatively affordable method to predict total energy, also in difficult cases such as molecule/surface [110] or cluster/surface [24] interactions. Being a second-order perturbation method, RPA includes van der Waals forces due to fluctuating dipoles which are not included in DFT approaches based on standard semi-local or hybrid xc-functionals. It should be noted, however, that dispersion forces can be approximately described via alternative (and computationally less demanding) approaches. In these alternative approaches analytic terms are added to the energy expression typically in the form of atom-atom interactions. These terms mimic dispersion interactions and have been shown to be of sufficient accuracy in several instances while their evaluation is computationally negligible (we do not discuss the various possible choices of parameters used in the analytic expressions, ranging from empirically parametrized [62] to theoretically predicted [130]). Therefore, the value of RPA in our opinion is rather to provide data against which to parametrize analytic expressions of dispersion forces and the treatment of complicated cases for which no really accurate DFT xc-functional has been devised so far more than the correct description of long-range dispersion forces.

The GW approach [98] will be briefly introduced in the next Section. Finally, a different path to the solution of the Schrödinger equation passes through methods of statistical integration such as the Quantum Monte Carlo one [23]. Despite the intrinsically high computational demands of these methods, their use is constantly increasing and it can be expected that it will become widespread in the future, especially for those systems and properties for which DFT has known limitations.

Comparison with experiment typically implies the prediction of response properties, i.e., the response of the system to some external force or perturbation. At the lowest order, response properties are then associated with derivatives of the energy with respect to some external driving force. In this context, due to the choice of the Born-Oppenheimer approximation, vibrational properties stand apart from other form of response in that—at least at a rough level of accuracy—they are usually a side-product of a PES exploration. However, a complete and thorough prediction of vibrational spectra passes through a linear-response calculation [57, 104].

2.2.3 The Promising Field of Multi-component Oxides

Before concluding this section, we briefly discuss a topic which in our opinion represents one of the most promising directions for both fundamental and applied future research on nanostructured oxides, i.e., the field of multi-component systems. This means moving from the traditionally investigated binary oxides with stoichiometry A_xO_z, with A a generic element and x, z stoichiometry coefficients, to e.g. ternary oxides with stoichiometry $A_xB_yO_z$, with B an element different from A

and O, and y its stoichiometric coefficient. It can be recalled that an analogous development has occurred in the field of nanostructured metals, where the research on pure metal nanoparticles has been progressively enriched and attention has shifted toward multi-component metal nanoparticles, also called nanoalloys [21, 22]. Several general concepts developed in the field of nanoalloys can then be easily carried over and exploited in the field of ternary, quaternary, etc. oxides, and we believe it worthwhile illustrating three such concepts in the following paragraphs.

First, from previous experience on nanoalloys, it can be expected that in ternary oxides complications will arise connected with the match among the energy scales of the different elements composing the oxide. The presence of multiple length and energy scales is common to any composite system, and must be dealt with care in order to achieve reliable predictions. When multiple elements compose the system, in fact, an absolute accuracy in the description of the properties of each element (rather than a relative accuracy) must be achieved, and this puts much more stringent demands on the theoretical approach. Note that an oxide is already intrinsically a multi-component (binary) system, and examples of issues associated with the energy match between oxygen the A element in A_xO_z nanoscale phases will be described in the next Section.

Second, one of the issues that one encounters in dealing with nanoalloys is how to compare the stability of nanoalloys of a given size but different chemical composition. To this purpose, the concept of mixing energy has been introduced in the nanoalloy field and has turned out to be very useful, see [13, 45, 50, 70] for more details. For a nanoalloy of a given size (i.e., number of atoms) but different chemical composition the mixing energy is defined as:

$$\Delta[N_A, N_B] = E_{alloy}[N_A, N_B] - N_A E_A[N]/N - N_B E_B[N]/N$$

where $E_{alloy}[N_A, N_B]$ is the energy of a nanoalloy cluster composed of N_A atoms of the species A and N_B atoms of the species B, $N = N_A + N_B$ is the total number of atoms in the cluster, $E_A[N]$ is the energy of a pure cluster of N atoms and $E_B[N]$ is the corresponding quantity for the B species. Note that it is assumed that E_{alloy}, E_A, E_B are global minimum energies, i.e., the lowest energies among all possible isomers. The mixing energy $\Delta[N_A, N_B]$ can be easily generalized to ternary oxide nanoparticles thus providing also in this context a measure of how thermodynamically favorable is alloying at the given size and composition. In particular in [39] a definition of mixing energy in terms of constituent pure *oxides* has been employed which could turn to be of general usefulness.

Third, the concept of homotops can be recalled and 'imported' from the nanoalloy field [70]. Homotops are defined as configurations of multi-component systems sharing the same or a very similar structural framework but a different distribution of the atoms of the different elements within this framework, thus a different chemical composition. In the nanoalloy field, one speaks of different realizations of 'chemical ordering' or 'compositional order' in the homotops. Chemical ordering greatly increases the number of degrees of freedom of the system and complicates the associated computational description [13]. To give an idea,

neglecting the reduction due to point group symmetry, for a given structural framework of N atoms of which N_A of species A and N_B of species B, one has $(N_{tot})!/((N_A)!(N_B)!)$ possible different "homotops", a number exponentially increasing with the size of the system. Even the simple description of which phases of chemical ordering are realized is non-trivial, see Figs. 2.5, 2.6 and 2.7 above for an illustration of the associated issues. Finally, for metal alloys, order parameters describing chemical order have been defined for bulk [7] and to a lesser extent also for finite [8] systems: analogous definitions will be needed for ternary and multi-component oxides.

It is noteworthy to underline that the first fully resolved atomistic structure of a ternary oxide ultrathin film over a single crystal metal surface—$CuWO_4$ on Cu (110)—is now finally available [39], which opens exciting perspectives in the field. Although we do not have space to go into details here and we refer the reader to the original publication, we note among the several reasons of interest of this pioneering work: the definition of mixing energy in terms of constituent pure *oxides* recalled above, the outcome from the computational search of different isomers—both structural isomers and chemical ordering homotops [13], the presence of top-most Cu ions in a highly reduced oxidation state thus representing the experimental validation of the prediction discussed below in connection with Fig. 2.14, and the theoretical prediction and experimental observation of a peak in the phonon spectrum around 950 cm^{-1} which resembles that of tungstyls in undercoordinated WO_3-systems, but which is actually originated by a W–O–Cu interfacial vibrational mode (see Fig. 2.4 in [39]).

2.2.4 Practicalities

Passing finally from the above general considerations to technical practicalities, we note that, from a technical point of view, many black-box packages are nowadays available to perform a wide range of structural and electronic simulations within DFT: they range from total energy calculations, to structure optimizations, to the search for saddle points, to response properties, etc. Some of them are open-source codes and they usually come with a graphical interface that allow the users to build up the system of their interest with a modest effort, see as an example [58, 77]. These packages can be used to model a 2D metal/interface if periodic boundary conditions are implemented. When studying a periodic system, a unit cell has to be defined; the Kohn-Sham equations will then be solved on the atoms inside the cell on a grid of k points sampling the Brillouin zone in the reciprocal space; for more details see [75].

Among the computational packages implementing periodic-boundary conditions, a distinction has to be made between those which use localized (Slater-type, Gaussian-type, numerical) basis sets and those using delocalized (mainly plane-waves) basis sets. When adopting a localized-basis-set computational code, all type of xc-functionals can be efficiently evaluated, with the use of an auxiliary

basis set for the expansion of the electron density as an effective technique to achieve linear scaling [43, 48, 49, 114]. Vice versa, as discussed above, the long-range Coulombic tail of hybrid (non-range-saparated) xc-functionals is heavier to evaluate using delocalized basis sets. Within computational codes using delocalized basis sets, the implementation of hybrid xc-functionals is therefore more recent [111]. For completeness of information, the calculations on the Ni_3O_4/Pd (100) system discussed above (see Fig. 2.11) were performed using the Quantum Espresso package and a DFT+U formalism with periodic boundary conditions and plane waves as basis set.

A final point concerns the pseudo-potentials. There are three main types of pseudo-potentials currently implemented in available computational codes: (i) norm-conserving; (ii) ultra-soft; (iii) projector-augmented-waves. (i) Norm-conserving pseudo-potentials (NC-PPs) were derived first historically [63] and obey a strict integral rule which assures that the pseudo-charge (norm) inside a given cut-off radius equals the real charge of the atom. To reduce the computational cost of calculations involving NC-PPs (which necessitates of rich basis sets), (ii) ultra-soft pseudo-potentials (US-PPs) have been derived in the early 1990s [133] by relaxing the strict constraint of the norm conservation. US-PPs allow a significant reduction of the computational demand in terms of basis set dimension. (iii) Projector-augmented-waves pseudo-potentials (PAW-PPs) [20] are a further evolution in the direction of reducing the computational cost of DFT calculations and consist in transforming the rapidly oscillating wavefunctions near the nuclei into smooth wavefunctions which are more computationally convenient, also providing a way to calculate all-electron properties from these smooth wavefunctions.

2.3 Electronic States

For convenience, we will divide this Section into three parts: (Sect. 2.3.1) electronic ground state (occupied orbitals); (Sect. 2.3.2) electronic transport properties; (Sect. 2.3.3) electronic excited states.

2.3.1 Electronic Ground State (Occupied Orbitals)

The electronic ground state corresponds to the lowest-energy solution of the Schrödinger Hamiltonian in the Born-Oppenheimer approximation, and the methods for obtaining this solution have been discussed in the previous Section, however focusing attention on the total energy, while we deal in this Section with electronic ground state observables other than energy. The first question one can ask is whether the DFT occupied orbitals (defining the electronic ground state within DFT—we focus on DFT as the most used approach in this field) of interfacial nanostructured oxides are affected by the presence of the support material and
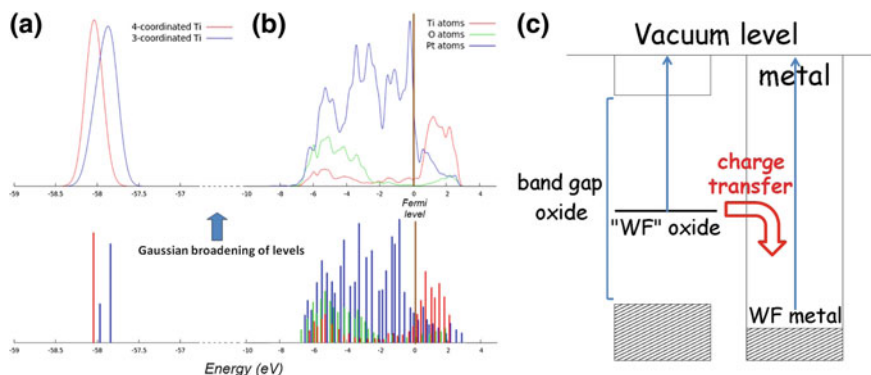
Fig. 2.12 *Left-hand-side* typical PDOS plot specifically corresponding to a TiOx/Pt(111) phase [15]. The one-particle levels are visualized as delta peaks in the lower panel and are Gaussian-broadened in the upper panel. The occupied orbitals are those below the Fermi level, and the virtual ones are those above it. Semicore levels corresponding to the 3s states of Ti atoms lie at low binding energies and exhibit a difference between 3-oxygen-coordinated and 4-oxygen-coordinated Ti cations. The contributions projected on the different atoms are depicted in different colors. *Right-hand-side* interaction between an insulating oxide ultrathin layer (*left*) and a metal substrate (*right*) with the definition of work function for the two component subsystems, and the charge transfer associated with the difference between the two. Adapted with permission from [127]. Copyright 2013 American Chemical Society

nanoscale confinement effects. This is expected on general grounds, and has been actually demonstrated in many cases.

To analyze interface effects on occupied orbitals, it is common to focus on three computational descriptors: (Projected) Density Of States—or (P)DOS, atomic charges, and work function.

The Projected Density Of States (PDOS) is obtained by projecting the Density Of States (given by the sequence of the single-particle energy levels, each weighted with its degeneracy) onto properly chosen atomic components localized on the atoms of the system. One can thus estimate the contribution of a given atomic orbital to a particular state (or band) of the whole system, see Fig. 2.12 and the examples reported below in connection with Fig. 2.13.

Charges on the individual atoms furnish valuable information on the oxidation state and on the flow of charge between the metal support and the oxide overlayer. Values of atomic charges can be calculated according to several different schemes which are implemented in almost all computational codes: Mulliken [95], Lowdin [88], Bader [9], etc.

The work function is a fundamental quantity, which is defined as the energy necessary to bring an electron from the top of the valence band to infinite distance (vacuum level), see the right-hand-side of Fig. 2.12. Its value sensitively depends on several factors (see below), among which the atomistic arrangement of the surface. Comparison of the work function of a metal surface in the absence and in
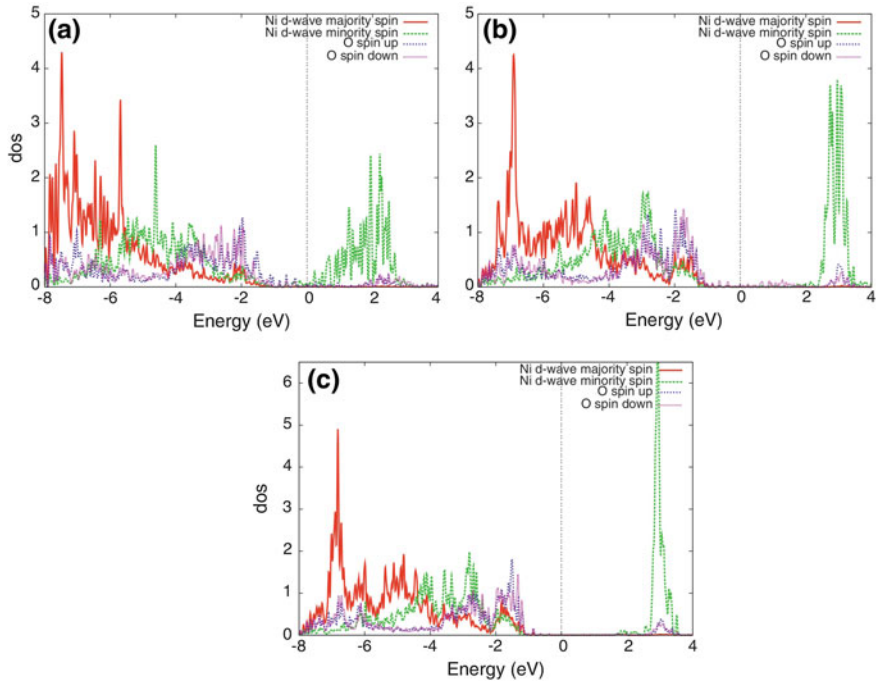
Fig. 2.13 PDOS projected onto three different layers of a 5-layer NiO ultrathin phase deposited on Ag(100): (**a**) interfacial or first layer; (**b**) second layer; (**c**) third or middle layer. Adapted with permissions from [129]. Copyright 2010 Springer

the presence of an oxide overlayer can provide important information on the structural and electronic properties of the deposited oxide.

Let us focus for definitiveness as in the previous section on oxide ultrathin films on a metal substrate. Analyzing the electronic structure of such systems, it is useful to distinguish between: (i) oxides which adopt a polar arrangement with the positive and negative ions at a different height and in which the distances between the metal atoms of the support and the metal cations of the oxide are quite small (such as to form a metallic chemical bond); (ii) oxides which are adsorbed on the metal in a non-polar fashion in which usually distances between metal atoms of the support and metal ions of the oxide are larger. A schematic depiction of these two classes of oxides is given in the right-hand-side of Fig. 2.1.

In category (i), the strong metal-metal chemical bond which is formed between the support and the oxide makes that the electronic structure of the oxide is very different with respect to that of a bulk oxide with the same or similar stoichiometry. One then finds a large contribution around the Fermi level originating from both the metallic states of the support and from the valence/conduction band of the oxide, with a consequent vanishing HOMO-LUMO gap in the oxide layer. A "metallization" of the oxide layer takes place in these systems. From the

methodological point of view, due to metallization, one expects that a DFT/GGA approach is reliable and is able to describe the electronic structure this class of systems, while the introduction of a Hubbard term (or the use of a hybrid xc-functional for the oxide part) should not introduce a qualitative change in the global picture. It is worth noting that in such systems the structure of the oxide overlayer will hardly be stable in absence of the metal support, as the chemical bond and the electrostatic interaction with the metal underneath is an essential ingredient for the stability of the oxide phase.

Systems that fits into this (i)-category are the several TiO_x phases formed on Pt(111) [10]. These have been extensively studied by the authors and reviewed previously [11, 12, 15, 55, 134], so that we do not repeat their discussion here and we refer the reader to these previous reviews.

In category (ii) different effects come into play. First of all, as the distances between the atoms of the metal support and those of the oxide are usually larger than those found within oxide layer, and a real oxide/support chemical bond is not formed. Here a distinction can be made among: (ii-a) oxides of simple metals which exhibit only delocalized states both in the valence and the conduction band, (ii-b) oxides which possess localized states in their valence band, and (ii-c) oxides which possess localized states in both the valence and the conduction band. From the methodological point of view, the introduction of a Hubbard term in the Hamiltonian (or the use of hybrid xc-functionals) is essential for a qualitative description of categories (ii-b) e (ii-c), as localization effects are poorly described by DFT/GGA (local or semi-local xc-functionals). In the case of category (ii-a) oxides, on the contrary, a qualitative picture is satisfactorily achieved using a pure DFT/GGA approach. In oxides of category (ii), metallization effects in general occur as in oxides of category (i), with their extent depending on the relative positions of the bands of the metal support and of the oxide. Since in oxides with localized states the correct position of the bands strongly depends on the choice of the U value, a fine tuning of U is essential to get a reliable description of the system, as also discussed in the previous section.

Let us consider MgO as an oxide of category (ii-a). In ultrathin MgO, an analysis of the PDOS shows that the valence band is mostly formed by the $2p$ states of O atoms, whereas the conduction band is mostly formed by $3s$ states of Mg atoms. When deposited on Ag(100), a charge transfer from the oxide to the metal support is observed (favored by the location of electron-rich O atoms on top of Ag atoms [106]). A charge analysis then shows an increase of electron density on the Ag atoms in direct contact with the oxide accompanied by a remarkable reduction of the work function. This charge transfer mostly affects the first oxide layer in contact with the metal, while from the third oxide layer on the electronic band structure of the bulk oxide is basically restored [40]. These effects are well described at the DFT/GGA level without introducing Hubbard terms.

In the case of an oxide of category (ii-b), as ZnO, an analysis of the PDOS shows that the valence band is mostly formed by $2p$ states of O atoms, but localized $3d$ states of Zn atoms are close in energy, whereas the conduction band is mostly formed by $4s$ states of Zn atoms. When deposited on Ag(111), a weak metal/oxide

interaction takes place with an almost negligible charge transfer and metallization effect, and only a slight increase of the system work function. DFT/GGA describes this system reasonably. Both the bottom of the conduction band and the top of the valence band have in fact a delocalized character (as in MgO). The introduction of Hubbard is however beneficial in improving the description of the localized *3d* band which, when a proper value of the U term is adopted, is shifted to much lower energies and narrowed, although the final description is not entirely satisfactory [12].

Let us finally consider an oxide of category (ii-c), such as NiO, in which both valence and conduction bands have important contributions from the partially occupied *3d* states of Ni atoms. A reliable description of ultrathin NiO phases deposited on Ag(100) requires a careful choice of the U term on the Ni *d*-orbitals. If considered as a free monolayer, NiO exhibits a band gap of about 2 eV at the DFT +U level. When deposited on Ag(100), a metallization effect (with a charge flow from Ag atoms to Ni atoms of the oxide, opposite to the case of MgO) is observed which appreciably reduces the band gap and increases the work function of the system [129]. This is true especially for the first NiO layer in contact with the metal substrate (see Fig. 2.13a for the detailed PDOS), while the electronic structure of the second (Fig. 2.13b) and third (Fig. 2.13c) layer (as parts of a thicker deposition of five layers) present electronic features similar to the free oxide and a band-gap at the Fermi level. The reasons for this different behavior reside in the presence in NiO of incompletely filled *d*-orbitals: these are able to receive electron donation from the metal support, thus closing the band gap and appreciably increasing the work function of the system. In a systematic study in which a comparison among ultrathin monolayer films made of the different metal elements along the first transition metal series and deposited on Ag(100), it was found that the flow (charge transfer) of electrons from the Ag support peaked at Cu, as expected on the basis of the electronegativity of the metal element. In particular for the CuO/Ag(100) monolayer the charge transfer was so strong as to affect even the *atomistic structure* of the oxide, leading to a rumpling inversion [115]. This is nicely illustrated in Fig. 2.14, in which plots of the electronic density difference upon adsorption are reported.

We conclude this section by summarizing for the convenience of the reader the status of knowledge and further considerations on the work function. For ultrathin oxides on metal surfaces this quantity is basically connected with the difference between electron affinity of the metal support and of the oxide overlayer, but—as already mentioned—can be significantly tuned by the atomistic arrangement of the oxide interfacial atoms. In synthesis, this quantity depends on three factors [106, 115]: (a) charge compression, (b) geometric rumpling (polarity), and (c) charge transfer. (a) A charge compression is always exerted by the oxide overlayer on the metal support. This charge compression pushes the metal electrons back into the support, decreases the surface dipole moment and thus as a norm decreases the work function of the system. This effect is particularly strong when the diffuse electronic clouds (*2p* states) of oxygen anions are directly on top of substrate metal
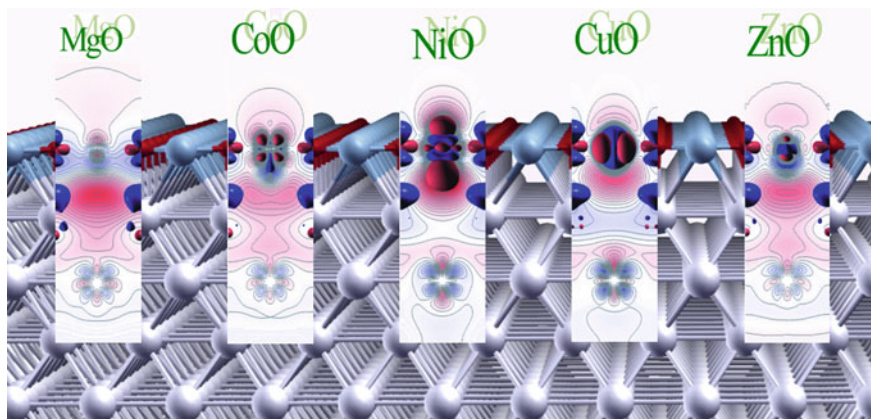
Fig. 2.14 A perspective view of a Ag(100) surface covered by monolayers of various transition metal oxides with the corresponding (superimposed) 2D contour plots of the electronic density difference upon adsorption (*blue* depletion of electron density, *red* increase). Reprinted with permission from [115]. Copyright 2012 American Chemical Society

atoms, as in the case of MgO supported on Ag(100) [106]. On the contrary, when epitaxial relationships are not so precise, as e.g. in the case of (111)/(100) epitaxy or incommensurate phases, this effect is less important. However, in the case of incommensurate or Moiré phases, it can become *locally important* in the more epitaxial regions, as demonstrated in a specific examples [59, 139]. (b) When the oxide is polar (geometric rumpling) as in category (i) phases, the dipole moment generated by the difference in height between the positively charged metal cations and the negatively charged oxygen anions exerts a field on the electrons of the metal underneath thus changing the energy necessary to reach the vacuum level. If the cations are closer to the surface as it often occurs, this effect increases the work function. However, we recall again that for the CuO/Ag(100) monolayer a rumpling inversion has been predicted [115] which leads to a decrease of the work function. Usually, the dipole moment associated with polarity is also diminished by the metallization effect due to the metal support. For the oxides of category (ii), which are non-polar, this contribution is obviously absent. Finally, (c) charge transfer effects can occur, as already discussed above. It can be noted that for non-polar oxides the effects of charge transfer on the work function can go in the same sense of the effects of charge compression, as in the case of MgO deposited on Ag(100), or in the opposite sense, as in the case of NiO on Ag(100) [115], due to the presence of incompletely filled *d*-orbitals with a high relative electron affinity as discussed in the previous paragraph. The delicate balance between these three components finally determines the global value of the work function of the system.

2.3.2 Electronic Transport Properties

Nanostructured systems are known to exhibit conduction properties very different from bulk systems: at an interface, an insulator can turn into a conductor [137] or, vice versa, a conductor can turn into an insulator [25]. Indeed, it is worth recalling that one of the motivations to study ultrathin films grown over a conducting or semi-conducting substrate is their conductive character enabling the use of charged-particle probe and deposition techniques. Modeling electronic transport through nanoscale oxides thus has a wealth of implications.

Let us start from the simulation of Scanning Tunneling Microscopy (STM) experiments. STM is a technique developed in the early '80s, based on the tunneling current which flows between a sharp tip and a conducting or semi-conducting surface at a distance of approximately one nanometer or less. The electronic set-up of the STM system controls the tip position either by maintaining a constant current through the external circuit (constant current mode) or by maintaining a constant height of the tip above the sample (constant height mode). STM images are typically predicted via the Tersoff-Hamann approach [128]. STM is in fact a tunneling transport phenomenon. As such, it is reasonably well described by a zeroth-order method such as Tersoff-Hamann in which conductance is related to the density of states projected onto space (usually a point corresponding to the tip apex) and energy (where one has the ambiguity of integrating from the Fermi level up to the given value of bias potential or of picking the given bias value). This basic approach has been extended by considering realistic shapes of the tip [113]. Being a tunneling phenomenon, it decays exponentially with spatial distance, and is thus roughly speaking dominated by topmost surface atoms. There are however exception to this simple expectation. First, among surface atoms, some atoms can be imagined brighter than others due to the fact that they possess more diffuse electronic states. This occurs for example in polar TiO_x monolayer phases grown on Pt(111) mentioned above where Ti atoms, although being lower in height with respect to O atoms, are imagined at positive bias due to presence of diffuse $3d$ empty states, and among Ti atoms, those are imaged brighter which have the higher oxygen coordination and thus the higher density of unoccupied virtual states [10]. Second, the wave function and experimental conditions can be such that buried interfaces can sometimes be imaged. An example is given in [123], where STM at very low bias allows one to reach a very short distance between the tip and the surface. In these conditions, in regions of the sample characterized by a reduced oxide DOS due to the local formation of an oxide bi-layer instead of a monolayer, conduction is determined by the underlying metallic Ag atoms, which are actually imaged although quite far from the surface (see Fig. 2.15). This picture has later been confirmed by other groups [91], and is very interesting, as it is one of the few cases in which information on *buried interfaces* is achieved.

Before leaving this subsection we stress again that a full treatment of transport properties requires more sophisticated techniques such as a scattering approach involving the calculation of transmission matrix and, subsequently, of the
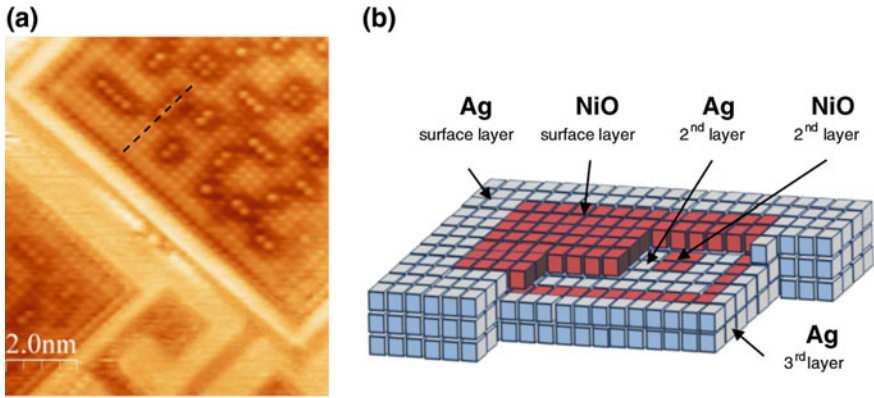
Fig. 2.15 (**a**) STM image at low bias and (**b**) corresponding atomistic scheme of a NiO ultrathin system deposited on the Ag(100) surface. Adapted with permissions from [123]. Copyright 2012 Elsevier

conductance (G) of the investigated system [66]. The conductance (G) at finite temperature through a nanoscale device can be computed within the Landauer-Buttiker linear response formalism [80, 138] by integrating over the energy E the total transmission T(E) computed at a given E [36, 119]. The transmission T(E) is often evaluated in a single-particle approximation, i.e., by using the orbitals of a composite system derived from a previous band structure calculation (typically, a DFT one) and e.g. projecting them onto the orbitals of left and right 'leads' derived from band structure calculations of bulk systems generating by using the leads as unit cells. Without entering into technical details, it can be noted here that even this simplified approach can be computationally tedious, and part of the current research deals with reducing the computational effort by developing efficient sampling algorithm in the k-space. A completely rigorous approach should finally overcome the limitations even of these low-order perturbative approaches and realize a fully many-body simulation of transport.

An example of such a many-body approach can be found in studies of strongly correlated systems involving Mott insulating transitions, typically described using a fermionic Hubbard Model [2]. In systems of this kind, there exists a transition from a metallic state to an insulating state at a critical value of the on-site repulsive interaction U at half-filling. An extensive literature describes how the many-body correlations of strongly correlated systems may be related to the existence of quantum entanglement in their ground states; here we will simply draw the interested reader's attention to Section V.F. of [3] in which results indicating a link between quantum phase transitions and the dominance of multipartite (i.e. involving more than two quantum states) entanglement in one dimensional Hubbard models are reviewed.

The Hubbard model may be solved self-consistently through the use of Dynamical Mean Field Theory, as reviewed in [56] (while extensions of this
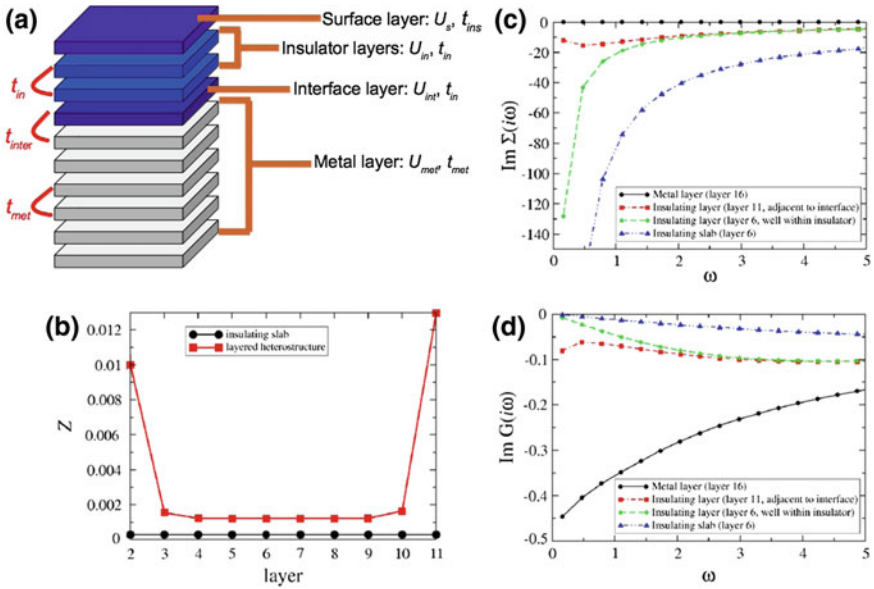
Fig. 2.16 (**a**) A schematic depiction of an inhomogenous Hubbard model for an insulating surface deposited on a bulk metal. Hopping parameters t that represent hopping between layers are depicted in *red*, those for hopping within layers are depicted in black. (**b**–**c**) depict the metalization Z for the insulating region. the self energy, and the Green's function for selected layers as calculated for a slab with 10 insulating layers and 10 metal layers using IDMFT (i) with $t_{met}=1$, $t_{ins}=t_{inter}=0.5\ t_{met}$, $U_{met}=2\ t_{met}$, $U_{int}=20\ t_{met}$, $U_{in}=U_s=20\ t_{met}$ and (ii) an insulating slab with $U=20$ t_{met} and $t=t_{met}$ for all layers. The calculation uses a Lanczos impurity solver [56] with $n_s = 10$ impurities and a fictitious temperature of 0.05 t_{met}

approach to non-equilibrium processes are reviewed in [5]). This approach takes into account quantum fluctuations, and relies on a mapping between the Hubbard model and the Anderson impurity model that is exact in the infinite-dimensional limit but approximate otherwise. In each step of the calculation, the Green's function of the Hubbard model is mapped to an appropriate impurity model, which is then solved. The difference between the initial Green's function and the Green's function of the solved model defines a self-energy that is used to generate a new Green's function for the Hubbard model that is the input of the next step. When the difference between two successive Hubbard Green's functions is less than some cut-off value, the procedure is assumed to have converged to a solution of that accuracy. Nanostructured layered systems are modelled with a Hubbard model whose parameters vary from layer to layer. For a given set of Hubbard U values and hopping parameters t one may calculate the properties of such a system through the use of Inhomogeneous Dynamical Mean Field Theory (IDMFT) [53, 105]. In this approaches, one maps the Hubbard model to a *set* of Anderson impurity models, one for each layer, and introduces the coupling between layers as part of the self-consistency step.

Figure 2.16 shows the results of a preliminary IDMFT calculation performed by the authors using the Lanczos impurity solver of [56]. The model system is that of an insulating layer deposited on a metallic slab, and the metallisation Z of each layer is obtained from the imaginary component of the self-energy $\Im\Sigma(i\omega)$ through the application of the approximate relation [29]:

$$\Im\Sigma(i\omega) \sim \left(1 - \frac{1}{Z}\right)\omega + \cdots$$

to the smallest calculated frequency for that layer. Allowing for finite error introduced by the need of introducing a discretisation of the frequency and hence a fictitious finite temperature in order to perform the calculation, it appears that there exists metallisation of the insulating layers since they all possess a greater value of Z than is present in the calculation for the insulating reference slab, whose deviation from the expected insulating Z of zero can be taken to give some idea of the numerical error. However, this conclusion would be too quick. Examining our plots of the Green's functions and the self-energy and comparing their behaviour with that of metallic and insulating phase Green's functions and self-energies displayed in [105], we find that while the behaviour of layer 11, the layer adjacent to the interface layer, is qualitatively metallic (that is, the Green's function shows signs of beginning to diverge at low frequencies and the self-energy shows signs of tending towards zero as the frequency decreases) the low frequency behaviour of layer 6 is much similar to that of an insulator (that is, the Green's function tends towards zero at low frequencies whereas the self-energy diverges), while tending to be close to that of layer 11 for the larger frequencies shown. If metallization is present in layer 6, then it is possible that the frequency resolution is not sufficient to locate it, with the minimum in the self-energy that metallic systems exhibit occurring below the smallest frequency which we have calculated. Since we appear to be at the point at which numerical noise sets a limit to the resolution of our calculations, it is not possible to increase the resolution further (this also rules out more sophisticated approaches to calculating Z, such as in [6] the use of extrapolations to fictitious temperatures of 0, since we would not be able to reach a resolution where the features required for such an extrapolation to work correctly would be present). As a result, if metallization is present deep within the insulating region then we are likely underestimating its extent. In order to increase the resolution to the required degree, an improved impurity solver such as one utilising the Numerical Renormalisation Group [28] (implemented for IDMFT in [52]) will be required.

As an example, this approach has been applied to systems consisting of a semi-infinite metal joined to a semi-infinite insulator [65] or an insulating layer sandwiched between two semi-infinite metal leads [137]. Metallization was monitored by checking whether a small quasi-particle peak is present in the density of states or, equivalently, whether there is a finite quasi-particle weight. Interestingly, it was found that the insulating layers or the semi-infinite insulator are metallised and that this metallisation (a 'fragile Fermi liquid' in the terminology of [137]) is sensitive to temperature. However, the two groups disagree in their assessment of

the results: Helmes et al. [65] conclude that the Mott insulating layers are basically impenetrable due to the slightness of the metallisation, whereas Zenia et al. [137] hold that, provided that the insulating barrier is not infinite, the metallisation will persist throughout the layer, although it will exponentially attenuate as a function of the distance from the metal. A study of very large systems using a further variational approximation [26] suggests that the latter is the case, with the metallisation decaying exponentially with distance but remaining finite as a result of the tunnelling of evanescent electron wavefunctions from the leads into the insulator. The authors however observe that full Dynamical Mean Field Theory calculations for very large systems will be needed to settle the controversy. Such metalisation might explain why it is possible to produce STM images of relatively thick insulating films deposited on metallic surfaces [93]. One can also ask which characteristics of actually existing nanostructured systems might enhance or suppress the metalisation, since most calculations are carried out using relatively simple models. Furthermore, one might speculate as to the effects of depositing an insulator whose U is very close to the critical value on a metal: would the insulator be pulled into a fully metallic state? Tuning the effects of such metallisation through a judicious choice of metals and insulators could be a means of exploring the physics of Hubbard-type systems close to the critical value of the coupling.

2.3.3 Electronic Excited States (Unoccupied or Virtual Orbitals)

An extension of the possibility of the STM technique into the realm of spectroscopy and thus excited states is represented by Scanning Tunneling Spectroscopy (STS) technique, in which the *derivative of the STM current* is measured. Theoretical simulation of STS spectra is non-trivial. One should in fact consider in principle a fully consistent first-principles treatment of excited states which is usually computationally unfeasible due to the need of sophisticated first-principles methods to properly describe the electronic structure of 2D-confined phases, the large size of the treated systems, and the complications associated with the description of non-equilibrium phenomena occurring in tunnelling spectroscopy.

However, analogously to the simulation of STM images via the Tersoff-Hamann approach, a very simplified possibility to simulate STS spectra can be obtained by approximating the electronic transport matrix elements in terms of the projected density of states (PDOS) of the system as obtained by a band structure DFT calculation. Neglecting tip effects the basic quantity to be evaluated is the system DOS at an energy value (ε) corresponding to the given bias, projected onto a point in space (r) outside the sample roughly corresponding to the tip position. Simulating STS spectra then involves calculating the derivative of the tunnelling current with respect to the applied bias. To this purpose, at a given height that corresponds to the distance of the tip from the surface, and over an energy window

(that depends on the bias spanned by the simulation), one can integrate the PDOS over a grid of proper size around the chosen site. A numerical derivative with respect to the bias (ε in the DOS) of the integrated PDOS finally gives the simulated STS curves [33]. Let us see the results of this extremely simplified approach in a specific case.

In [33] an ultrathin titania z-TO_x/Pt(111) phase was investigated both in the absence and in the presence of deposited Au nanoclusters. STS experiments were conducted and the STS spectra were simulated according to the simplified approach described above supplemented by an analysis of the DFT wave function. Figure 2.17 shows the contribution of the different surface states of the system to the experimental and simulated STS spectra. In more detail, from this analysis Shockley states, basically made of occupied *2p* state of oxygen atoms in the oxide layer, were found to contribute to the STS peaks localized at about −1.0 eV, see Fig. 2.17a, b. These two panels further show at +0.7 eV peaks associated with a resonance state, made by a superposition of unoccupied the *3d*$_z$ orbital of Ti^{3+}/Ti^{4+} species. Finally, when gold clusters are deposited, the strong peak that dominates the experimental curve at negative bias (see Fig. 2.17c) reveals a Tamm state made by a mixture of *5d* states of the gold atoms and platinum atoms from the underneath support. Although very approximate, this approach can then provide at least in some cases interesting insight.

In a zeroth-order approximation, excited states can be taken as the unoccupied or virtual states of a single-electron Kohn-Sham Hamiltonian, as discussed in the previous example. However, this is often not sufficiently accurate, and a more precise description must rely on more advanced methods. DFT encounters two main issues in describing excited states. First, at an interface the correct form of the single-electron potential depends on subtle screening effects, as discussed in more detail below. Second, some excited states possess an intrinsically many-body character which cannot be described as a single-particle electron/hole excitation but involves coupling of many single-electron states as realized e.g. in truly collective phenomena such as plasmonic resonances. More advanced approach such as time-dependent density-functional theory [31] may then be used to describe such complex situations.

To give an example of the first issue, i.e., subtle screening effects at an interface, let us focus on a specific example, and consider a particularly difficult case: that of image states. Image states are surface excited states localized in the potential well created in front of a conductive material, whose origin lies in the Coulomb-like attractive force of the image charge generated in the metal by the presence of the excited electron combined with the repulsive force due to the electronic clouds of surface atoms. These image states fall in the energy gap near the vacuum level and follow approximately a Rydberg-like series determined by the Coulomb-like potential. Although theoretically well understood, their modeling is computationally very demanding. For a reliable description of such states, in fact, it is crucial to achieve an accurate representation of the Coulombic tail of the potential outside the surface. The problem is that many mean-field approaches (as the DDT/GGA) do not predict the correct spatial Coulombic decay of the potential for virtual (unoccupied)
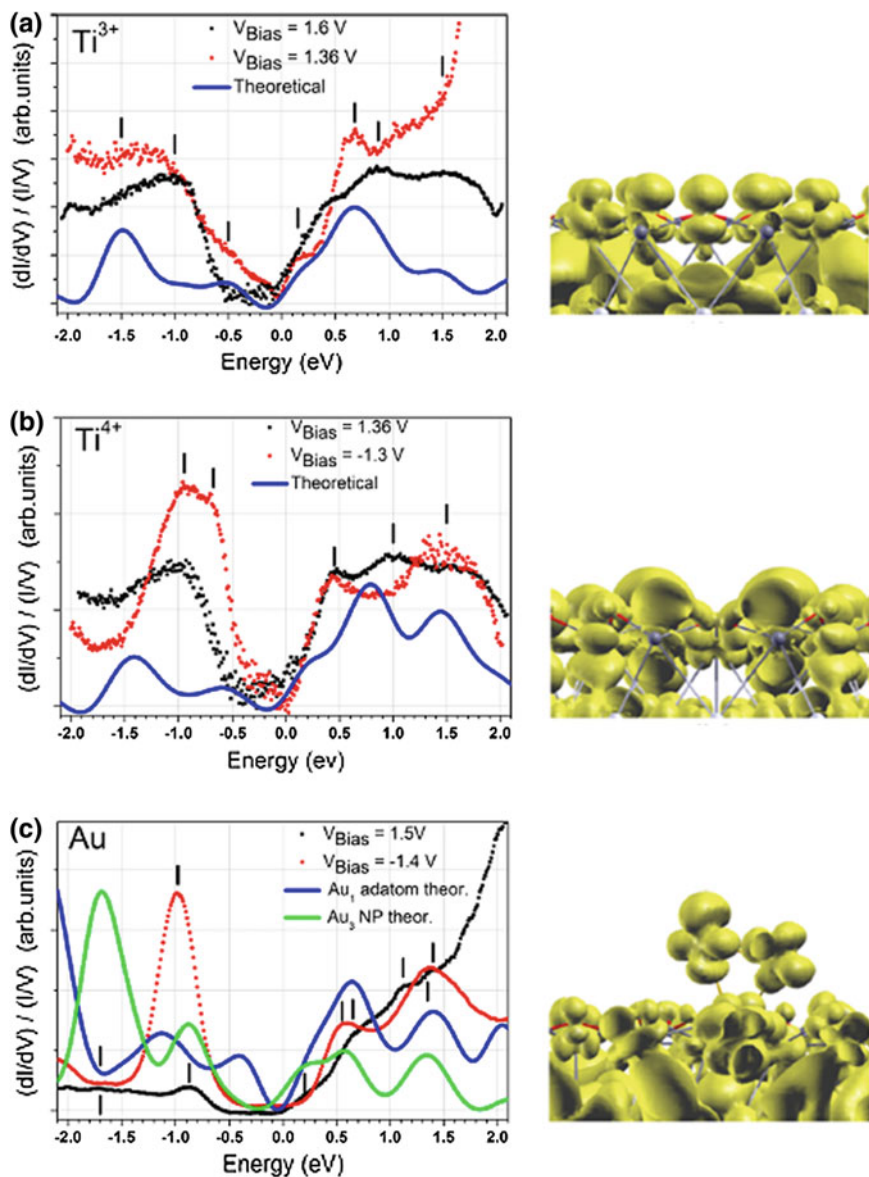
Fig. 2.17 STS experimental and simulated spectra (*left*) and wave function of the states most contributing to STS peaks: occupied Shockley (*top*), resonance (*middle*), and Tamm (*bottom*) states. Adapted with permissions from [33]. Copyright 2012 American Chemical Society

levels and a computationally demanding many-body perturbation theory (MBPT) becomes necessary to describe these electronic excited states. Among MBPT approaches, the most suitable for interfaces systems is the self-consistent solution of
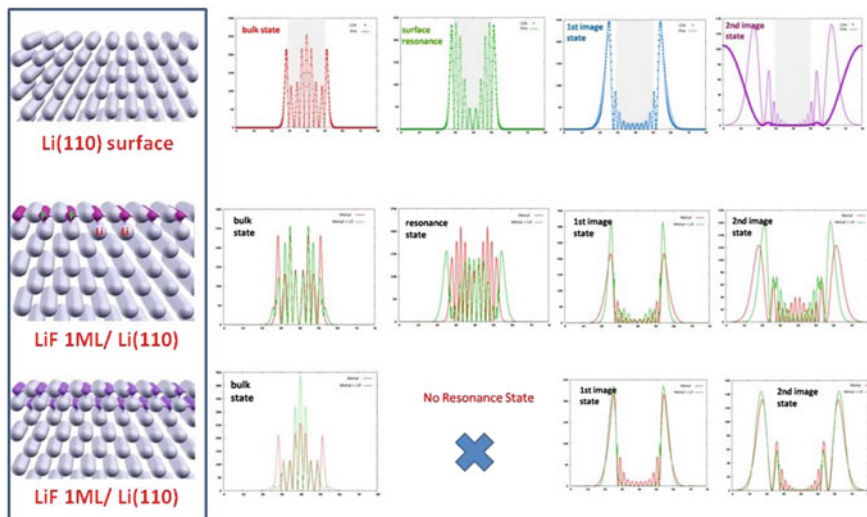
Fig. 2.18 Schematic depiction of the systems (*leftmost column*) and the wave functions of their occupied (*second-leftmost column*) and unoccupied (*last three rightmost columns*) states plotted along an axis perpendicular to the (110) surface. The plots highlight the difference between the LDA (*continuous curves*) and self-consistent GW (*dotted curves*) wave functions. Adapted with permissions from [116]. Copyright 2013 American Chemical Society

the Dyson equation in the so-called GW approximation [98], which corresponds to a modified mean-field problem for the electrons. In this approach, the DFT potential is replaced by a spatially non-local self-energy operator where the bare Coulomb interaction is renormalized by the electronic screening, which, in turn, is calculated using the dielectric response function $\varepsilon(\mathbf{q}, \omega)$. Although this latter function can be approximated using the DFT wave functions, the evaluation of the full energy-dependent description of the screened interaction can be computationally very demanding. A fall-back alternative solution is to resort to different approximations such as the Godby-Needs plasmon-pole approximation (PPA). In this case the dielectric function still retains a dynamical behaviour which is however interpolated on the basis of an explicit calculation of $\varepsilon(\mathbf{q}, \omega)$ at just two frequencies. For a correct theoretical prediction screening effects should be evaluated not simply at zeroth-order level as a perturbative correction but *self-consistently*, with all the in-principle and practical convergence issues that self-consistency entails. Nevertheless, a fully self-consistent GW approach (in the PPA approximation) has been implemented at a fully atomistic level in a pioneering work and applied to the investigation of a Li(110) surface both bare and covered by 1 or 2 atomic layers of LiF [116]. Figure 2.18 shows how the introduction of a self-consistent MBPT appreciably contracts the spatial extent of the system wave functions. Moreover, interestingly it was found that the presence of a resonance excited state at the surface gives rise to a mixing with pure image states and can significantly perturb

the Rydberg series of energy levels. This is interesting and important because it implies that the usual experimental analysis of image state energies to extract e.g. values of the system work function can be *misleading* when such energies are perturbed by the presence of a resonance state, as it can occur when the surface is covered by dielectric ultrathin layers. This picture has been recently confirmed, both in terms of deviation from a hydrogenic Rydberg progression due to the image potential states coupling to and mixing with the conduction band and resonance states at the interface [126].

Finally, we underline that tunneling phenomena and excited states are relevant not only to electron transport but can also give rise to chemical processes. Although we do not have space to go into details here, it can be mentioned that current-induced redox phenomena—i.e., electron capture and successive detachment of an oxygen atom—have been demonstrated in a custom-built surface science apparatus applied to a system in which a Ag(100) surface was covered by an NiO ultrathin film [124]. A strong homogeneous electric field of the order of 1 V/nm triggered dissociative attachment chemical processes reducing the NiO layer to Ni clusters in a resonant phenomenon, thus realizing a "surface-science electrochemical" analogue of STM-induced chemical reductions. It is clear that much exciting work could to be done along these lines.

2.4 Nanoscale Amorphous Oxide Interfaces

The nanoscale oxide interfaces considered typically in this book exhibit a crystalline-like character. Apart from modulations associated with Moiré patterns due to an inconmmensurate mismatch between the oxide and support components, the oxide phase itself can typically be described in terms of translational or quasi-translational symmetry. One of the present most fascinating challenges is however to move from the domain of crystalline-like systems into that of amorphous materials. In real-world applications, in fact, entropic effects and not perfectly controlled operation conditions or on the opposite purposedly created treatment make that the atomistic structure of the oxide is not crystalline but rather amorphous or disordered. Our strong conviction is that the knowledge accumulated on well-characterized model systems will be useful to shed light on these more complex and intricated materials. In this section we will thus briefly provide one such examples, that of ultrathin amorphous oxides recently proposed as supports for catalytic applications, discuss the reasons for its great interest and appeal (both scientific and technological), and mention the associated challenges and opportunities for future research.

In the past decades, thin oxide films (i.e. two-dimensional oxides) with controlled thickness have been widely used in basic research as catalysts support. The oxide supports included crystalline ones, such as MgO, TiO_2, alumina, aluminosilicates [19, 34, 60, 92, 120–122, 132], but more recently amorphous and crystalline 2D films have been prepared by atomic layer deposition (ALD) [136]

and intensively investigated. While studies on single crystal supports greatly advance basic studies, an advantage of the ALD technique is that it can be scaled up to meet the needs posed by technological applications. The catalytic particles studied on such 2D-oxides range from large nanoparticles to ultrasmall sub-nanometer size clusters, metallic as well as metal oxides.

Such 2D oxide phases offer several advantages. For example, thanks their conductance, they facilitate the deposition of charged particles during the fabrication of the catalyst and facilitate charge transfer between the support and the catalytic clusters and nanoparticles. Indeed, by varying the thickness of the oxide film and the choice of the underlying metal and semiconductor carrier, these supports offer a control of the charge state of the catalytic particle, and consequently may allow to fine tune its catalytic properties [73, 99, 122]. Moreover, the effects of the oxide film as a support of catalytic nanoparticles are expected to become increasingly pronounced with shrinking nanoparticle size, especially when the sub-nanometer scale is achieved (ultra-small clusters) in which most of the atoms of the cluster are surface/interface atoms in direct contact with the support, as demonstrated for propylene epoxidation on subnanometer silver clusters and their nanometer size aggregates supported on 3-monolayer-thin ALD alumina created on the top of a naturally oxidized doped silicon chip [35, 86].

Although the morphology and surface termination of the thin oxide films prepared by ALD can be rather complex, these supports offer several advantages for (sub) nanocatalysis, such as stabilization against sintering under reaction conditions of the catalytic particles on the binding sites on their surface, control of their amorphicity versus crystallinity by preparation conditions and annealing. The chemical composition and thickness of the 2D oxides can be readily controlled and in connection with the choice of the base support and the efficiency of charge transfer on the cluster well tunable. The charge/oxidation state of the catalyst can determine catalytic activity as well as selectivity, as shown for example in the oxidation of CO oxidation on twenty atom Pd clusters [73] or 27-atom oxidized Co clusters in the dehydrogenation of cyclohexene [83, 85] or Fischer-Tropsch reaction [84]. ALD synthesis also allows for creating multicomponent mixed oxide films [44] and films made of layers with same or different composition around the catalyst, to fine tuning performance and/or the multifunctionality of the system [81, 82] as shown in Fig. 2.20.

The advantages offered by 2D oxide films are thus tremendous. However the atomistic and electronic structures these films are far from being sufficiently understood, starting from their synthesis to their structure, surface morphology and termination, types of surface defects, binding of the catalytic particles, just to name a few aspects. A detailed understanding of the 2D oxides will necessarily require a significant interdisciplinary experimental and theoretical effort. This challenge can be illustrated with the example of Fig. 2.19, which reports grazing incidence X-ray small angle scattering (GISAXS) data acquired during the growth of an ultrathin alumina film on top of a naturally oxidized Si wafer, using the ALD technique and applying an increasing number of ALD cycles, i.e., cycles with alternating pulses of the gas phase precursor $Al(CH_3)_3$ and water vapor pulse [44]. The GISAXS data indicate that the growth of the film begins with the formation of sub-nanometer size
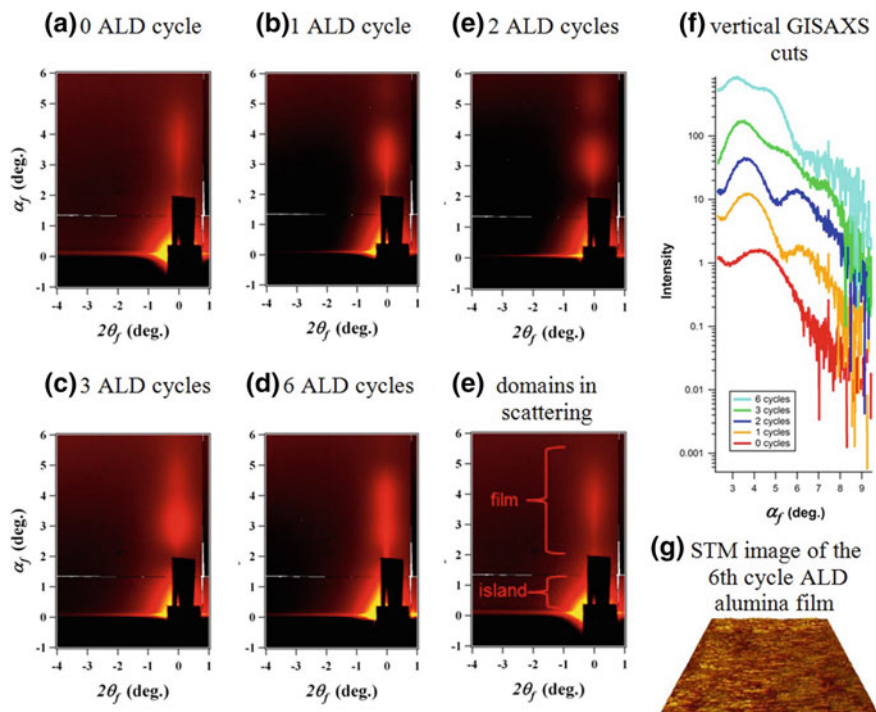
Fig. 2.19 2-dimensional GISAXS images providing information about particle height/film thickness and horizontal dimensions of particles/islands. (**a**) GISAXS pattern collected on naturally oxidized Si wafer used as carrier for the growth of the ALD alumina film (0 ALD cycle). (**b–d**) GISAXS images after applying 1,2, 3 and 6 ALD cycles, respectively. (**e**) Illustration of the domains in GISAXS patterns where information about the film and islands can be extracted from. (**f**) Vertical cuts of GISAXS images shown in a-d for 0, 1, 2,3 and 6 ALD cycles (from *bottom* to the *top*). (**g**) Topographic STM image (adapted with permission from [94]) of the amorphous alumina support layer (500 × 500 nm). (Copyright Elsevier 2011)

Fig. 2.20 Illustration of the fabrication of layers of oxide films below and around the clusters. Adapted with permission from [81]. Copyright 2010 American Chemical Society
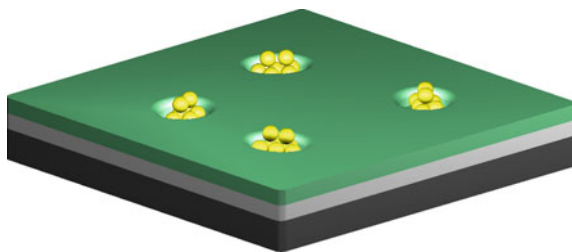
isolated islands. With increasing number of cycles, layers add to the structure, in this case forming a 3 monolayer (∼0.75 nm) thick film after applying 6 cycles of ALD, as determined by circular dichroism. The obtained GISAXS images and the vertical cuts indicate a rather complex evolution of the thickness and structure of the film with increasing number of applied ALD cycles, such as possible variations in

the compactness and density of its individual layers. The resulting 3 ML thick alumina film has a rough surface (see a typical STM image in Fig. 2.19g) and is amorphous, as confirmed by low energy electron diffraction experiments which shows no signs of crystallinity, while possesses various defects and voids [94]. Based on X-ray absorption characterization, this particular film can be best described as a mixture of tetrahedral and octahedral building units with a high degree of hydroxylation [35]. We stress again that this select example provides only a partial description of one type of alumina film fabricated on one support and under single synthesis conditions only, simply to illustrate the opening of a large multiparameter search space for the design of new classes of 2D oxides with tailored properties for use e.g. in catalysis, poised to be explored in joint theoretical and experimental endeavors.

From the theoretical/computational point of view, the first and probably the major issue that such systems pose is the description of their atomistic structure. Clearly, the amorphous character of such systems makes that a traditional global minimum search is meaningless. This however does not implies that energetic considerations are also meaningless. Rather, one will need to consider a statistically weighted ensemble or *set of different realizations* of the system: this set will be large as required by the disordered character of the system but will also be a *finite* set due to energetic constraints which discards meta-stable configurations with insufficient thermodynamic and kinetic stability. In keeping with the X-ray absorption data recalled above, the definition of *structural units* as illustrated in Fig. 2.7 will probably be useful to accelerate production of sensible structural configurations. Moreover, the issue of the presence of hydroxyls on the oxide surface recalled above will probably need to be tackled via the stoichiometry moves mentioned at point (5) in the description of GO approaches. A second issue for computational science is connected with the description of electron transport. It is possible in fact that such a phenomenon plays an important role in determining catalytic activity of nanoscale oxide or semi-conductor systems [68]. If this is the case, the methods discussed in the Section on electronic response properties will turn to be necessary for predicting the catalytic functionality of these systems. Given the outline provided in the Section on total energy method, it is finally likely that some sort of DFT approaches will be accurate enough to describe e.g. ultrathin alumina ALD-deposited on a Si wafer.

2.5 Concluding Remarks

In this chapter, an overview of available computational methods to describe the atomistic and electronic structure of nanostructured oxide interfaces has been presented. Potentialities and limitations have been discussed, with the goal of providing tools for orienting oneself in this complex field.

In terms of atomistic structure, a very general and comprehensive framework in which to understand structure prediction and global optimization has been given,

which should be useful for understanding and framing future studies in which these approaches are expected to become more and more frequent and important, while the problems associated with structural dynamics and kinetic phenomena have only briefly illustrated in a specific case. In terms of electronic structure, for convenience of the reader methods for prediction of total energy have been presented separately from methods for prediction of response properties. For the former, a detailed discussion has been given of the choice of the exchange and correlation functional most appropriate for a given system, while charge distribution and work function, electronic transport and electronic excited states have been discussed in some detail as examples of electronic response properties. Also to complement information not presented in other chapters in this book, a brief introduction to the topic of amorphous (rather than crystalline-like) nanoscale oxides has finally been presented.

From all this material, the challenges still facing the achievement of a predictive computational science of nanoscale (interfacial) oxides should be apparent. In several cases the accuracy of available and computationally affordable approaches is not yet en par with present needs, and the situation will become even worse in going from the crystalline-like extended (translationally invariant) binary oxide phases mostly investigated so far to more complex ternary and amorphous nanomaterials. Nevertheless, these are the present challenges, and the prize to be gained from both the scientific and the technological points of view is enormous.

In our opinion, two are the most likely near-term developments. In terms of structure prediction, hardware advances will soon greatly increase the feasibility of systematic sampling of the potential energy surface using first-principles approaches in conjunction with hierarchical or multi-mode acceleration techniques and automated structure recognition algorithms. These will enable the investigation of complex disordered systems. The next challenge will then be the study of structural dynamics. In terms of total energy methods, a proper development of space-dependent DFT approaches could greatly extend the scope of DFT accurate predictions and delay take-over of higher-level competitors such as RPA or Quantum Monte Carlo. These space-dependent approaches might prove to be sufficiently accurate also for the prediction of response properties, together with the implementation of time-dependent variants of DFT to describe Coulombic interactions in complex electronic states.

Regardless whether these expectations will be fulfilled or not, it is our hope that the present contribution will trigger interest and promote efforts in this fascinating field.

References

1. Altieri S, Finazzi M, Hsieh HH, Havekort MW, Lin HJ, Chen CT, Frabboni S, Gazzardi GC, Rot A, Valeri S (2009) Image charge screening: a new approach to enhance magnetic ordering temperatures in ultrathin correlated oxide films. Phys Rev B 79:174431
2. Altland A, Simons B (2006) Condensed matter field theory. Cambridge University Press, Cambridge
3. Amico L, Fazio R, Osterloh A, Vedral V (2008) Entanglement in many-body systems. Rev Mod Phys 80:517–567
4. Anisimov VI, Zaanen J, Andersen OK (1991) Band theory and Mott insulators: Hubbard U instead of Stoner I. Phys Rev B 44:943
5. Aoki H, Tsuji N, Eckstein M, Kollar M, Oka T, Werner P (2014) Nonequilibrium dynamical mean-field theory and its applications. Rev Mod Phys 86:779–839
6. Arsenault L-F, Sémon P, Tremblay A-MS (2012) Benchmark of a modified iterated peturbation theory approach on the fcc lattice at strong coupling. Phys Rev B 86(085133):1–16
7. Atanasov IS, Hou M (2009) A multi-range order parameter for binary alloy bulk materials and nanoparticles. Eur Phys J D 52:51
8. Atanasov IS, Hou M (2009) Equilibrium ordering properties of Au-Pd alloys and nanoalloys. Surf Sci 603:2639
9. Bader R (1990) Atoms in molecules: a quantum theory. Oxford University Press, New York
10. Barcaro G, Sedona F, Fortunelli A, Granozzi G (2007) Structure of a TiOx zigzag-like monolayer on pt(111). J Phys Chem C 111:6095
11. Barcaro G, Sedona F, Fortunelli A, Granozzi G (2009) Structure of reduced ultrathin TiOx polar films on Pt(111). J Phys Chem C 113:5721–5729
12. Barcaro G, Thomas IO, Fortunelli A (2010) Validation of density-functional versus density-functional+ U approaches for oxide ultrathin films. J Chem Phys 132:124703
13. Barcaro G, Sementa L, Fortunelli A (2014) A grouping approach to homotop global optimization in alloy nanoparticles. Phys Chem Chem Phys 16:24256–24265
14. Barcaro G, Fortunelli A, Rossi G, Ferrando R (2005) Electronic and structural shell closure in AgCu and AuCu nanoclusters. J Phys Chem B 110:23197
15. Barcaro G, Cavaliere E, Artiglia L, Sementa L, Gavioli L, Granozzi G, Fortunelli A (2012) Building principles and structural motifs in TiOx ultrathin films on a (111) substrate. J Phys Chem C 116:13302–13306
16. Barcaro G, Fortunelli A (2012) Functional theory of free and supported metal clusters and nanoalloys. In: Mariscal MM, Oviedo OA, Leiva EPM (eds) Metal clusters and nanoalloys—from modeling to applications. Springer, New York
17. Barcaro G, Fortunelli A, Polak M, Rubinovich L (2011) Patchy multishell segregation in Pd–Pt alloy nanoparticles. Nano Lett 11:1766
18. Becke AD (1993) Density functional thermochemistry. III. The role of exact exchange. J Chem Phys 98:5648
19. Beniya A, Isomura N, Hirata H, Watanabe Y (2014) Morphology and chemical states of size-selected Ptn clusters on an aluminium oxide film on NiAl(110). Phys Chem Chem Phys 16:26485–26492

20. Blochl PE (1994) Projector augmented-wave method. Phys Rev B 50:17953
21. Calvo F (ed) (2013) Nanoalloys: from fundamentals to emergent applications. Elsevier, Amsterdam
22. Mariscal MM, Oviedo OA, Leiva EPM (eds) (2012) Metal clusters and nanoalloys—from modeling to applications. Springer, New York
23. Booth GH, Alavi A (2010) Approaching chemical accuracy using full configuration-interaction quantum Monte Carlo: a study of ionization potentials. J Chem Phys 132:174104
24. Paz-Borbón LO, Barcaro G, Fortunelli A, Levchenko SV (2012) AuN clusters (N = 1–6) supported on MgO(100) surfaces: effect of exact exchange and dispersion interactions on adhesion energies. Phys Rev B 85:155409
25. Borghi G, Fabrizio M, Tosatti E (2009) Surface dead layer for quasiparticles near a mott transition. Phys Rev Lett 102:066806
26. Borghi G, Fabrizio M, Tosatti E (2010) Strongly correlated metal interfaces in the Gutzwiller approximation. Phys Rev B 81(115134):1–10
27. Born M, Oppenheimer JR (1927) On the quantum theory of molecules. Ann Phys 84:457
28. Bulla R, Costi TA, Pruschke T (2008) Numerical renormalisation group method for quantum impurity systems. Rev Mod Phys 80:395–450
29. Caffarel M, Krauth W (1994) Exact diagonalization approach to correlated fermions in infinite dimensions: Mott transition and superconductivity. Phys Rev Lett 72:1545–1548
30. Calvo F (2005) All-exchanges parallel tempering. J Chem Phys 123:124106
31. Casida ME (1995) Time-dependent density-functional response theory for molecules. In: Chong DP (ed) Recent advances in density functional methods, Part I. World Scientific, Singapore
32. Causà M, Colle R, Dovesi R, Fortunelli A, Pisani C (1988) Correlation correction to the Hartree-Fock total energy of solids. II. Phys Scripta 38:194
33. Cavaliere E, Barcaro G, Sementa L, Granozzi G, Fortunelli A, Gavioli L (2014) Experimental and theoretical scanning tunneling spectroscopy analysis of an ultrathin titania film and adsorbed Au nanoparticles. J Phys Chem C 118:14640
34. Chen MS, Goodman DW (2007) Interaction of Au with titania: the role of reduced Ti. Top Catal 44:41–47
35. Cheng L et al (2013) Reaction mechanism for direct propylene epoxidation by alumina-supported silver aggregates: the role of the particle/support interface. ACS Catal 4:32–39
36. Choi HJ, Ihm J (1999) Ab initio pseudopotential method for the calculation of conductance in quantum wires. Phys Rev B 59:2267
37. Cohen-Tannoudji C, Diu B, Laloe F (2006) Quantum mechanics. Wiley-Interscience, Hoboken
38. Demiroglu I, Bromley ST (2013) Nanofilm versus bulk polymorphism in wurtzite materials. Phys Rev Lett 110:245501
39. Denk M, Kuhness D, Wagner M, Surnev S, Negreiros FR, Sementa L, Barcaro G, Vobornik I, Fortunelli A, Netzer FP (2014) Metal tungstates at the ultimate two-dimensional limit: fabrication of a $CuWO_4$ nanophase. ACS Nano 8:3947–3954
40. Schintke S, Messerli S, Pivetta M, Patthey F, Libioulle L, Stengel M, De Vita A, Schneider WD (2001) Insulator at the ultrathin limit: MgO on Ag(001). Phys Rev Lett 87:276801
41. Dirac PAM (1930) Note on exchange phenomena in the Thomas atom. Proc Cambridge Phil Soc 26:376
42. Dovesi R, Pisani C, Roetti C, Saunders VR (1983) Treatment of Coulomb interactions in Hartree-Fock calculations of periodic systems. Phys Rev B 28:5781
43. Dunlap BI, Rosch N, Trickey SB (2010) Variational fitting methods for electronic structure calculations. Mol Phys 108:3167
44. Elam JW, George SM (2003) Growth of ZnO/Al2O3 alloy films using atomic layer deposition techniques. Chem Mater 15:1020–1028

45. Ferrando R, Fortunelli A, Rossi G (2005) Quantum effects on the structure of pure and binary metallic nanoclusters. Phys Rev B 72:085449
46. Ferrando R, Rossi G, Nita F, Barcaro G, Fortunelli A (2008) Interface-stabilized phases of metal-on-oxide nanodots. ACS Nano 2:1849–1856
47. Ferrando R, Fortunelli A, Johnston RL (2008) Searching for the optimum structures of alloy nanoclusters. Phys Chem Chem Phys 10:640–649
48. Fortunelli A, Salvetti O (1991) A simplified representation of the potential produced by a Gaussian charge-distribution. J Comp Chem 12:36
49. Fortunelli A, Salvetti O (1991) Overlapping and non-overlapping integrals in molecular calculations. Chem Phys Lett 186:372
50. Fortunelli A, Velasco AM (1999) Structural and electronic properties of Pt/Fe nanoclusters from EHT calculations. J Mol Struct (Theochem) 487:251–266
51. Apra E, Fortunelli A (2000) Density-functional study of Pt-13 and Pt-55 cuboctahedral clusters. J Mol Struct 501–502:251
52. Freericks JK (2004) Dynamical mean-field theory for strongly correlated inhomogenous nanostructures. Phys Rev B 70(195342):1–14
53. Freericks JK (2006) Transport in multilayered nanostructures: the dynamical mean-field theory approach. Imperial College Press, London
54. Kuhlenbeck H, Shaikhutdinov S, Freund H-J (2013) Well-ordered transition metal oxide layers in model catalysis—a series of case studies. Chem Rev 113:3986–4034
55. Gavioli L, Cavaliere E, Agnoli S, Barcaro G, Fortunelli A, Granozzi G (2011) Template-assisted assembly of transition metal nanoparticles on oxide ultrathin films. Progr Surf Sci 86:59–81
56. Georges A, Kotliar G, Krauth W, Rosenberg MJ (1996) Dynamical mean-field theory of strongly correlated fermion systems and the limit of infinite dimensions. Rev Mod Phys 68:13–125
57. Baroni S, de Gironcoli S, Dal Corso A, Giannozzi P (2001) Phonons and related crystal properties from density-functional perturbation theory. Rev Mod Phys 73:515
58. Giannozzi P, Baroni S, Bonini N et al (2009) QUANTUM ESPRESSO: a modular and open-source software project for quantum simulations of materials. J Phys Condens Matter 21:395502
59. Giordano L, Pacchioni G, Goniakowski J, Nilius N, Rienks EDL, Freund H-J (2007) Interplay between structural, magnetic, and electronic properties in a FeO/Pt(111) ultrathin film. Phys Rev B 76:075416
60. Gragnaniello L et al (2012) Ordered arrays of size-selected oxide nanoparticles. Phys Rev Lett 108:195507
61. Gorling A, Levy M (1997) Hybrid schemes combining the Hartree-Fock method and density-functional theory: underlying formalism and properties of correlation functionals. J Chem Phys 106:2675–2680
62. Grimme S (2006) Semiempirical GGA-type density functional constructed with a long-range dispersion correction. J Comput Chem 27:1787
63. Hamann DR, Schluter M, Chiang C (1979) Norm-conserving pseudopotentials. Phys Rev Lett 43:1494
64. Haunschild R, Scuseria GE (2010) Range-separated local hybrids. J Chem Phys 132:224106
65. Helmes RW, Costi TA, Rosch A (2008) Kondo proximity effect: how does a metal penetrate into a Mott insulator? Phys Rev Lett 101(066802):1–4
66. Hofer WA, Foster AS, Shluger AL (2003) Theories of scanning probe microscopes at the atomic scale. Rev Mod Phys 75:1287
67. Hohenberg P, Kohn W (1964) Inhomogeneous electron gas. Phys Rev 136:864B
68. Hu S et al (2014) Amorphous TiO_2 coatings stabilize Si, GaAs, and GaP photoanodes for efficient water oxidation. Science 344:1005–1009
69. Hubbard PS (1961) Quantum-mechanical and semiclassical forms of the density operator theory of relaxation. Rev Mod Phys 33:249

70. Jellinek J, Krissinel EB (1996) Ni_nAl_m alloy clusters: analysis of structural forms and their energy ordering. Chem Phys Lett 258:283

71. Johnston RL (2003) Evolving better nanoparticles: aenetic algorithms for optimising cluster geometries. Dalton Trans 4193–4207

72. Kais S, Herschbach DR, Handy NC, Murray CW, Laming GJ (1993) Density functionals and dimensional renormalization for an exactly solvable model. J Chem Phys 99:417

73. Kane MD, Roberts FS, Anderson SL (2015) Effects of alumina thickness on CO oxidation activity over Pd-20/Alumina/Re(0001): correlated effects of alumina electronic properties and Pd-20 geometry on activity. J Phys Chem C 119:1359–1375

74. Karewar SV, Gupta N, Caro A, Srinivasan SG (2014) A concentration dependent embedded atom method potential for the Mg–Li system. Comput Mater Sci 85:172–178

75. Kittel C (1996) Introduction to solid state physics, 7th edn. Wiley, Hoboken

76. Kohn W, Sham LJ (1965) Self-consistent equations including exchange and correlation effects. Phys Rev 140:1133A

77. Kokalj A (2003) Computer graphics and graphical user interfaces as tools in simulations of matter at the atomic scale. Comp Mat Sci 28:155

78. Kresse G, Schmid M, Napetschnig E, Shishkin M, Kohler L, Varga P (2005) Structure of the ultrathin aluminum oxide film on NiAl(110). Science 308:1440–1442

79. Kryachko ES, Ludeña EV (1990) Energy density functional theory of many-electron systems. Springer, Berlin

80. Landauer R (1985) Electrical resistance of disordered one-dimensional lattice. Philos Mag 21:863

81. Lee S et al (2010) Oxidative decomposition of methanol on subnanometer palladium clusters: the effect of catalyst size and support composition. J Phys Chem C 114:10342–10348

82. Lee S et al (2009) Selective propene epoxidation on immobilized $Au_{6–10}$ clusters: the effect of hydrogen and water on activity and selectivity. Angew Chem Int Ed 121:1495–1499

83. Lee S et al (2012) Support-dependent performance of size-selected subnanometer cobalt cluster-based catalysts in the dehydrogenation of cyclohexene. ChemCatChem 4:1632–1637

84. Lee S, Lee B, Seifert S, Winans RE, Vajda S (2015) Fischer-Tropsch synthesis at a low pressure on subnanometer cobalt oxide clusters: the effect of cluster size and support on activity and selectivity. J Phys Chem C 119:11210–11216

85. Lee S et al (2012) Oxidative dehydrogenation of cyclohexene on size selected subnanometer cobalt clusters: improved catalytic performance via evolution of cluster-assembled nanostructures. Phys Chem Chem Phys 14:9336–9342

86. Lei Y et al (2010) Increased silver activity for direct propylene epoxidation via subnanometer size effects. Science 328:224–228

87. Li Z, Scheraga HA (1987) Monte Carlo-minimization approach to the multiple-minima problem in protein folding. Proc Natl Acad Sci USA 84:6611–6615

88. Lowdin PO (1955) Quantum theory of many-particle systems. I. Physical interpretations by means of density matrices, natural spin-orbitals, and convergence problems in the method of configurational interaction. Phys Rev 97:1474

89. Lundgren E, Kresse G, Klein C, Borg M, Andersen JN, De Santis M, Gauthier Y, Konvicka C, Schmid M, Varga P (2002) Two-dimensional oxide on Pd(111). Phys Rev Lett 88:246103

90. Mahan GD (2008) Quantum mechanics in a nutshell. Princeton University Press, Princeton

91. Malashevich A, Altman EI, Ismail-Beigi S (2014) Imaging the buried MgO/Ag interface: formation mechanism of the STM contrast. Phys Rev B 90:165426

92. Marsault M, Worz GHA, Sitja G, Barth C, Henry CR (2008) Farad Disc 138:407–420

93. Meyer W, Hock D, Biedermann K, Gubo M, Mu¨ller S, Hammer L, Heinz K (2008) Coexistence of rocksalt and wurtzite structure in nanosized CoO films. Phys Rev Lett 101:016103

94. Molina LM et al (2011) Size-dependent selectivity and activity of silver nanoclusters in the partial oxidation of propylene to propylene oxide and acrolein: a joint experimental and theoretical study. Catal Today 160:116–130

95. Mulliken RS (1955) Electronic population analysis on LCAO-MO molecular wave functions I. J Chem Phys 23:1833
96. Negreiros FR, Aprà E, Barcaro G, Sementa L, Vajda S, Fortunelli A (2012) A first-principles theoretical approach to heterogeneous nanocatalysis. Nanoscale 4:1208–1219
97. Obermüller T, Steurer W, Surnev S, Barcaro G, Sementa L, Stroppa A, Fortunelli A, Netzer FP (2013) Kinetic asymmetry in the growth of two-dimensional Mn oxide nanostripes. Phys Rev B 88:235410
98. Onida G, Reining L, Rubio A (2002) Electronic excitations: density-functional versus many-body Green's-function approaches. Rev Mod Phys 74:601
99. Pacchioni G (2013) Electronic interactions and charge transfers of metal atoms and clusters on oxide surfaces. Phys Chem Chem Phys 15:1737–1757
100. Perdew JP (1985) Accurate density functional for the energy: real-space cutoff of the gradient expansion for the exchange hole. Phys Rev Lett 55:1665
101. Perdew JP, Yue W (1986) Accurate and simple density functional for the electronic exchange energy: generalized gradient approximation. Phys Rev B 33:8800R
102. Perdew JP, Burke K, Ernzerhof M (1996) Generalized gradient approximation made simple. Phys Rev Lett 77:3865
103. Perdew JP, Ruzsinszky A, Tao J, Staroverov V, Scuseria G, Csonka G (2005) Prescription for the design and selection of density functional approximations: more constraint satisfaction with fewer fits. J Chem Phys 123:062201
104. Pisani C, Erba A, Ferrabone M, Dovesi R (2012) Nuclear motion effects on the density matrix of crystals: an ab initio Monte Carlo harmonic approach. J Chem Phys 137:044114
105. Potthoff M, Nolting W (1999) Dynamical mean-field study of the Mott transition in thin films. Euro Phys J B 8:555–568
106. Prada S, Martinez U, Pacchioni G (2008) Work function changes induced by deposition of ultrathin dielectric films on metals: a theoretical analysis. Phys Rev B 78:235423
107. Reuter K, Scheffler M (2002) Composition, structure, and stability of $RuO_2(110)$ as a function of oxygen pressure. Phys Rev B 65:035406
108. Rossi G, Ferrando R (2009) Searching for low-energy structures of nanoparticles: a comparison of different methods and algorithms. J Phys Condens Matt 21:084208
109. Sahimi M, Hamzehpour H (2010) Efficient computational strategies for solving global optimization problems. Comp Sci Eng 12:74–82
110. Schimka L, Harl J, Stroppa A, Grüneis A, Marsman M, Mittendorfer F, Kresse G (2010) Accurate surface and adsorption energies from many-body perturbation theory. Nat Mater 9:741
111. Schimka L, Harl J, Kresse G (2011) Improved hybrid functional for solids: the HSEsol functional. J Chem Phys 134:024116
112. Schnadt J, Michaelides A, Knudsen J, Vang RT, Reuter K, Lægsgaard E, Scheffler M, FBesenbacher F (2006) Revisiting the structure of the p(4×4) surface oxide on Ag(111). Phys Rev Lett 96:146101
113. Schouteden K, Lauwaet K, Janssens E, Barcaro G, Fortunelli A, Van Haesendonck C, Lievens P (2014) Probing the atomic structure of metallic nanoclusters with the tip of a scanning tunneling microscope. Nanoscale 6:2170
114. Scuseria GE (1999) Linear scaling density functional calculations with gaussian orbitals. J Phys Chem A 103:4782
115. Sementa L, Barcaro G, Negreiros FR, Thomas IO, Netzer FP, Ferrari AM, Fortunelli A (2012) Work function of oxide ultrathin films on the Ag(100) surface. J Chem Theor Comput 8:629
116. Sementa L, Marini A, Barcaro G, Negreiros FR, Fortunelli A (2013) Electronic excited states at ultrathin dielectric-metal interfaces. Phys Rev B 88:125413
117. Shankar R (1994) Renormalization-group approach to interacting fermions. Rev Mod Phys 66:129
118. Slater JC (1972) Statistical exchange-correlation in the self-consistent field. In: Lowdin PO (ed) Advances in quantum chemistry. Academic Press, Cambridge

119. Smogunov A, Dal Corso A, Tosatti E (2004) Ballistic conductance of magnetic Co and Ni nanowires with ultrasoft pseudopotentials. Phys Rev B 70:045417

120. Stacchiola DJ et al (2006) Synthesis and structure of ultrathin aluminosilicate films. Angew Chem Int Ed 45:7636–7639

121. Stacchiola DJ, Kaya S, Weissenrieder SJ, Shaikhutdinov SK, Freund H-J (2007), Synthesis and structure of an ultrathin aluminosilicate film. In: Abstracts of Papers, 234th ACS National Meeting, Boston, 19–23 August

122. Sterrer M et al (2007) Control of the charge state of metal atoms on thin MgO films. Phys Rev Lett 98:096107

123. Steurer W, Surnev S, Fortunelli A, Netzer FP (2012) Scanning tunneling microscopy imaging of NiO(100)(1×1) Islands embedded in Ag(100). Surf Sci 606:803

124. Steurer W, Surnev S, Netzer FP, Sementa L, Negreiros FR, Barcaro G, Durante N, Fortunelli A (2014) Redox processes at a nanostructured interface under strong electric fields. Nanoscale 6:10589–10595

125. Steurer W, Allegretti F, Surnev S, Barcaro G, Sementa L, Negreiros FR, Fortunelli A, FNetzer FP (2011) Metamorphosis of ultrathin Ni oxide nanostructures on Ag(100). Phys Rev B 84:115446

126. Suich DE, Caplins BW, Shearer AJ, Harris CB (2014) Femtosecond trapping of free electrons in ultrathin films of NaCl on Ag(100). J Phys Chem Lett 5:3073

127. Surnev S, Fortunelli A, Netzer FP (2013) Structure-property relationship and chemical aspects of oxide-metal hybrid nanostructures. Chem Rev 113:4314–4372

128. Tersoff J, Hamann DR (1985) Theory of scanning tunneling microscope. Phys Rev B 31:805

129. Thomas IO, Fortunelli A (2010) Analysis of the electronic structure of ultrathin NiO/Ag(100) films. E Phys J B 75:5

130. Tkatchenko A, Scheffler M (2009) Accurate molecular Van Der Waals interactions from ground-state electron density and free-atom reference data. Phys Rev Lett 102:073005

131. Tran F, Blaha P (2009) Accurate band gaps of semiconductors and insulators with a semilocal exchange-correlation potential. Phys Rev Lett 102:226401

132. Ulrich S, Nilius N, Freund H-J (2007) Growth of thin alumina films on a vicinal NiAl surface. Surf Sci 601:4603–4607

133. Vanderbilt D (1990) Soft self-consistent pseudopotentials in a generalized eigenvalue formalism. Phys Rev B 41:7892

134. Wu QH, Fortunelli A, Granozzi G (2009) Preparation, characterisation and structure of Ti and Al ultrathin oxide films on metals. Int Rev Phys Chem 28:517–576

135. Weissenrieder J, Kaya S, Lu J-L, Gao H-J, Shaikhutdinov S, Freund H-J, Sierka M, Todorova TK, Sauer J (2005) Atomic structure of a thin silica film on a Mo(112) substrate: a two-dimensional network of SiO4 tetrahedra. Phys Rev Lett 95:076103

136. Xiong G, Elam JW, Feng H et al (2005) Effect of atomic layer deposition coatings on the surface structure of anodic aluminum oxide membranes. J Phys Chem B 109:14059–14063

137. Zenia H et al (2009) Appearance of "fragile" fermi liquids in finite-width mott insulators sandwiched between metallic leads. Phys Rev Lett 103:116402

138. Buttiker M, Imry Y, Landauer R (1985) Generalized many-channel conductance formula with applications to small rings. Phys Rev B 31:6207

139. Wagner M, Negreiros FR, Sementa L, Barcaro G, Surnev S, Fortunelli A, Netzer FR (2013) Nanostripe Pattern of NaCl Layers on Cu(110). Phys Rev Lett 110:216101. doi: 10.1103/PhysRevLett.110.216101

140. Saunders VR, Freyria-Fava C, Dovesi R, Salasco L, Roetti C (1992) On the electrostatic potential in crystalline systems where the charge density is expanded in Gaussian functions. Mol Phys 77(4):629–665. doi: 10.1080/00268979200102671

Chapter 3
Role of Structural Flexibility on the Physical and Chemical Properties of Metal-Supported Oxide Ultrathin Films

Gianfranco Pacchioni

Abstract Ultrathin films of dielectric materials supported on a metal are becoming increasingly interesting for their peculiar and unprecedented properties. One important aspect is that usually two-dimensional materials are much more flexible and easy to structurally modify than the corresponding bulk counterparts. In this paper we discuss this phenomenon with particular attention to its relevance for the adsorption properties of the films. For instance, formation of charged adsorbates is accompanied by substantial local relaxations of the support that are reminiscent of the formation of polarons in dielectric crystals to screen localized charges.

3.1   Introduction

Ultrathin films of insulating materials are attracting an increasing interest due to their extraordinary properties and to the different physico-chemical properties that they exhibit compared to their bulk counterparts. The field has grown very rapidly after the discovery of various materials in form of single layer. Graphene is the prototype of this family systems, but several other examples are known [1]. This has opened new avenues for the study of systems of reduced dimensionality along one of the space directions. Today these systems are called two-dimensional materials and their properties are being studied for a variety of potential applications [2, 3]. However, despite the great excitement and interest on these systems, one should recognize that they are not really new since they have been used in various technologies in the last few decades. For instance, ultrathin silicon dioxide films have been the basis of metal oxide field effect transistors [4], and the microelectronic revolution is largely based on the excellent properties of thin SiO_2 films grown on silicon. The mature applications of two-dimensional oxides (with thickness of 10 nm or less) is not restricted to microelectronic devices. For instance they form under reactive conditions when

G. Pacchioni (✉)
Dipartimento di Scienza dei Materiali, Università di Milano Bicocca,
via R. Cozzi 55, 20125 Milano, Italy
e-mail: gianfranco.pacchioni@unimib.it

91

metals are exposed to oxidizing ambient; the formation of passive films guarantees corrosion protection of metals [5, 6]. Today two-dimensional oxides are studied as ultrathin capacitors [7], for solar energy materials [8], magnetoresistance sensors [9], etc [10].

In the last two decades oxide ultrathin films have become interesting also in the field of heterogeneous catalysis. They have been introduced in order to create model systems able to mimic the properties of real catalysts but at the same time to use electron spectroscopies and scanning tunneling microscopies (STM) to study oxide surfaces at an atomistic level [11–15]. New techniques have been developed to grow epitaxial oxide films, deposit metal nanoclusters, and study their chemistry under well controlled conditions [10]. However, besides oxide ultrathin films that closely resemble the corresponding bulk phases, other examples have been reported where completely different and unexpected properties emerge due to the nanometric vertical dimension of the films. Among these properties, a lot of interest has been attracted by the possibility to selectively charge atomic or molecular species deposited on the surface of an ultrathin film [16, 17]. It has been observed that electrons can spontaneously tunnel through the insulating thin layer as result of the equilibration of the Fermi level of the metal support with the frontier orbitals of the adsorbed species. This may result in charged clusters or molecules supported on oxide thin films with completely different chemistry and catalytic activity [13, 16].

These studies have shown that the charging effect is accompanied by non-negligible structural relaxation in the supported film. This effect turned out to be essential for the stabilization of the charged species and, in general, for the properties of these films. The structural flexibility is an intrinsic and specific property of ultrathin films which is not found on the corresponding solid surfaces. This is the topic of this review. Using some examples taken from the literature we will discuss the role of the easy deformation of two-dimensional insulators for processes where adsorbed species are involved, including some examples of catalytic reactions.

3.2 Polaronic Distortion as Response to the Formation of Charged Adsorbates

Gold atoms exhibit completely different adsorption properties when deposited on bulk MgO or on an ultrathin MgO film: while they remains neutral on MgO(100), they become negatively charged on MgO/Mo(100) or MgO/Ag(100) supports if the MgO film consists of a few monolayers (ML) [18, 19]. The net charge transfer takes place from the metal support to Au through the MgO thin dielectric barrier via spontaneous electron tunneling, provided that the film thickness remains below the mean-free paths of electrons. The charging effect, originally predicted by DFT calculations, has been shown by low-temperature STM experiments [19], providing a clear proof that materials at the nanoscale may behave differently from the

corresponding bulk materials. There is a very important phenomenon associated to the charge transfer which is central for the present discussion. This is the structural relaxation of the films that follows the formation of the charged species.

Let's consider an Ag atom adsorbed on MgO/Mo(100) films [20]. Also in this case the formation of an adsorbed anion has been predicted by DFT which has also shown the occurrence of a non-negligible local relaxation in the MgO top layer. This can be measured by the change in vertical distance, Δz, of a given ion of the surface before and after adsorption of the Ag atom, Table 3.1. We start by adsorbing an Ag atom on an unsupported MgO(100) 3 ML film (here and below we will use 3 ML MgO films with the bottom layer fixed as realistic models of the MgO(100) surface). The displacements of the O or Mg ions to which Ag is bound, Δz, and of the first neighbors are very small (<0.02 Å in absolute value). Now let us consider Ag on the metal supported MgO 3 ML films: the displacements become substantial, $\Delta z = 0.1$–0.2 Å, Table 3.1. In particular, on a MgO/Mo(100) 3 ML film, when Ag is adsorbed on-top of an O^{2-} ion there is a downwards shift of this ion by 0.08 Å; at the same time, the surrounding Mg cations move up by about the same amount. If, however, the negatively charged Ag atom is positioned on-top of a Mg cation, the displacement of this ion from the MgO top layer is quite substantial, 0.23 Å, Table 3.1.

These effects are even more pronounced for Au. Take the Au–MgO distances: on MgO/Mo(100) films the Au–O^{2-} distance, $z_e = 2.76$ Å, is 0.52 Å longer than on the MgO(100) surface; the Au–Mg distance, $z_e = 2.57$ Å, is 0.13 Å shorter than on the bare surface. The formation of a Au anion is accompanied by a very large surface relaxation, which is not observed for the case of Au on MgO(100). In particular, on MgO/Mo(100) 3 ML films the adsorption on Mg is accompanied by an outward displacement of the surface cation by 0.36 Å, while the surrounding O anions do not move significantly. The adsorption on the O anions induces a downward displacement of −0.20 Å, and an outward movement of the neighboring Mg cations by 0.15 Å, Table 3.1 [20].

These geometrical rearrangements are often referred to as polaronic distortion. The polaron concept was first proposed by Lev Landau in 1933 to describe an electron moving in a crystalline dielectric material where the atoms undergo local displacements from their equilibrium positions to effectively screen the charge of the electron. An induced polarization will follow the charge carrier when it is moving through the medium. The carrier together with the induced polarization is considered as one entity, which is called a polaron. Polarons are formed also when

Table 3.1 Local surface relaxation on MgO 3L slabs induced by adsorption of a Ag or Au atoms

		On-top of O		On-top of Mg	
		Δz_O Å	Δz_{Mg} Å	Δz_O Å	Δz_{Mg} Å
Ag	MgO(100)	+0.01	+0.02	−0.02	−0.01
	MgO/Mo(100)	−0.08	+0.09	−0.03	+0.23
Au	MgO(100)	−0.04	+0.03	−0.02	+0.01
	MgO/Mo(100)	−0.20	+0.15	−0.03	+0.36

charge defects form in bulk crystals. The polaronic distortions are very relevant and substantially contribute to the stabilization of charged adsorbed species on ultrathin films. This can be easily demonstrated by a computational experiment. In fact, if the MgO ultrathin film is not allowed to relax after Au deposition, the charge transfer is not observed and the formation of the Au^- species does not occur. Hence, the charge transfer is a direct consequence of the structural deformation of the two-dimensional oxide.

A very similar phenomenon has been observed for Au atoms deposited on 2 ML NaCl films grown on Cu(111) [21]. Using a STM tip it has been possible to add or remove a single electron to or from Au adatoms deposited on NaCl/Cu(111) films, with formation of negatively charged Au^- species near other Au atoms that retain the original neutral state. Interestingly, DFT calculations showed that the formation of the Au^- species is accompanied by a strong relaxation of the NaCl substrate, Fig. 3.1. In particular, the Cl^- ion underneath the adatom is forced to move downward by 0.6 Å and the surrounding Na^+ ions to move upward by 0.6 Å [21], showing that the flexibility of the NaCl thin film substrate is even larger than that of MgO. We will return to this point below when we will compare explicitly the reactivity of ultrathin MgO and NaCl films (see Sect. 3.5).

Formation of negatively charged species is not restricted to Au. Another example which is relevant for our discussion is that of the formation of superoxo species. DFT calculations predicted that O_2 molecules adsorbed on MgO/Mo(100) films will form superoxo radical anions, O_2^-, by the same mechanism described above, electron tunneling from the support [22]. The formation of O_2^- species on MgO/Mo(100) films exposed to oxygen has been confirmed by low temperature Electron Paramagnetic Resonance (EPR) spectra [23], which show that the intensity of the EPR signal decreases with the thickness of the MgO film. For films containing 15 ML of MgO, the EPR signal disappears, in complete agreement with the
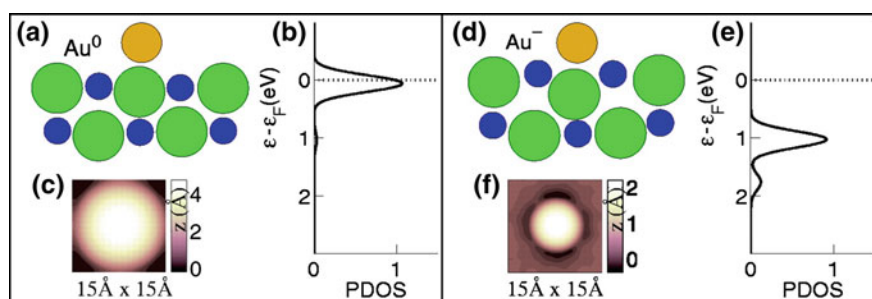

Fig. 3.1 Electronic and geometric properties of the neutral **a–c** and negatively charged **d–f** Au adatom (from DFT calculations). Au, Cl^-, and Na^+ are colored *gold*, *green*, and *blue*, respectively. **b** and **e**: calculated partial density of states of *s*-states at the Au adatom. The 6 *s*-derived state is partially and fully occupied in (**b**) and (**e**), respectively. Simulated STM images are shown in the *Inset*. While little relaxation occurs for the adsorption of a Au^0 species, the Cl^- ion underneath Au^- moves downward by 0.6 Å and the surrounding Na^+ ions move upward by 0.6 Å Adapted from [21] (Color figure online)

model of charge transfer via electron tunneling [13, 16, 19, 24]. Very interesting for the present discussion is the analysis of the g-tensor of the O_2^- species formed on MgO/Mo(100) films, Table 3.2. In fact, this has proven unambiguously that the MgO film undergoes a polaronic distortion in response to the formation of the O_2^- species, providing the first experimental proof of a theoretical prediction.

The EPR experiments were performed under ultrahigh vacuum conditions adsorbing molecular oxygen at 40 K on a 4 ML thick MgO/Mo(100) film [23]. The value of the g-tensor components directly extracted from the experiment are $g_{xx} = 2.002$, $g_{yy} = 2.012$, and $g_{zz} = 2.072$. The reason why this measure is particularly interesting is that similar measurements exist for O_2^- species formed on the surface of MgO polycrystalline materials [25–27]. Here the superoxo species forms by interaction of O_2 with electron-rich sites at the surface of the material.

A comparison of the values of the g-tensor found on the thin MgO/Mo(100) films with those obtained on bulk MgO show that the x- and y-components of the tensor are not too different, while a significantly larger z-component is found on powders compared to thin films, $g_{zz} = 2.091$ on the (100) terrace sites of MgO powders, $g_{zz} = 2.072$ on the terrace sites of MgO/Mo(100), Table 3.2. These differences, which are small but relevant, have been explained with the help of theory. A calculation of the g-tensor was performed for an O_2^- radical adsorbed on a MgO cluster modeling the (100) MgO surface, Table 3.2. When comparing the calculation to the measurement on the MgO powder samples it results that the g_{xx} and g_{yy} components of the tensor are well reproduced while g_{zz} component is considerably underestimated as compared to the experimental values (not surprisingly as detailed studies in literature show that the g_{zz} component is systematically underestimated in all calculations). However, what is relevant here is the trend found when comparing the computed g tensor of O_2^- radicals on terrace, five-coordinated, and edge, four-coordinated, Mg^{2+} sites. This results in a reduction of the g_{zz} component, Δg_{zz}, with decreasing coordination number of the Mg ion, see Table 3.2. What is the implication of this for the discussion of the polaronic distortion in thin films? The value of the g_{zz} tensor measured for the MgO/Mo(100) thin films is closer to that measured on MgO powders and assigned to edges rather than to terraces. But on the thin films the O_2^- superoxo species are clearly formed on the flat terrace sites, and not on the edges. The solution of the problem comes from a calculation which includes the polaronic distortion of the MgO/Mo(100) thin

Table 3.2 Measured and computed g-tensor for O_2^- adsorbed on the surface of MgO/Mo(001) films and MgO powders [23]

	Method	Ref.	Site	g_{xx}	g_{yy}	g_{zz}	Δg_{zz}
MgO powders	Exp	[25]	Terrace	2.002	2.008	2.091	0.000
MgO powders	Exp	[26]	Edge	2.002	2.008	2.077	−0.014
MgO/Mo(100)	Exp	[23]	Terrace	2.002	2.012	2.072	−0.019
MgO(100)	Theory	[27]	Terrace	2.0022	2.0092	2.0639	0.0000
MgO(100)	Theory	[27]	Edge	2.0021	2.0096	2.0527	−0.0112
MgO/Mo(100)	Theory	[23]	Terrace	2.0025	2.0093	2.0560	−0.0089

film. When this is taken into account in the model, what one finds is a reduced g_{zz} component as observed experimentally, with a sizable reduction of the g_{zz} component, Table 3.2 [23].

To understand this effect one has to consider that the shift of the g_{zz} component away from the free electron value is given by $g_{zz} = g_e + 2\left[\lambda^2/(\lambda^2 + \Delta^2)\right]^{1/2}$ with λ being the spin orbit coupling constant and $\Delta = 2\pi_g^y - 2\pi_g^x$ the increase of Δ due to the increased electric field. A more exposed cation, as on the edge sites of the MgO powders or on the terrace sites of the MgO/Mo(100) thin films (polaronic distortion) leads to a reduction in the g_{zz} component. This is exactly what is found both in theory and in experiment. The observed reduction of the g_{zz} component for the MgO thin film is thus a direct proof of the occurrence of a polaronic distortion.

Another way to proof the structural flexibility of oxide films in the ultrathin thickness limit is based on the use of X-ray photoelectron spectroscopy (XPS) line broadening [28]. XPS is widely applied to investigate the electronic structure of materials. It is based on the analysis of the area and the position of photoemission

Fig. 3.2 Experimental Mg 2p XPS spectra of 14 and 1 ML MgO/Ag (100). Reproduced with permission from [28]
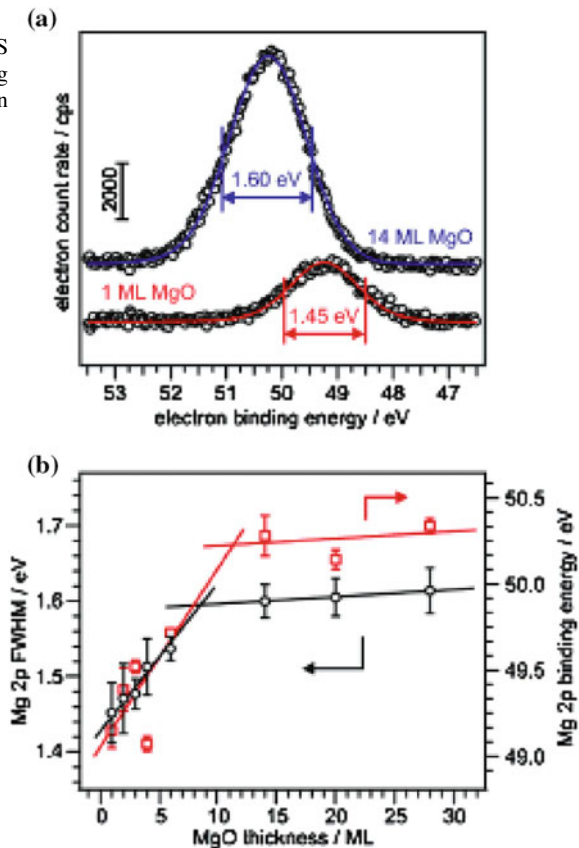
peaks. The flexibility of oxide thin films is intimately connected to the phonon structure of materials. A way of investigating vibrational properties is to look at the broadening in photoelectron spectra. Vibrational excitations lead to broadening in XPS. This broadening is due to the change in the equilibrium nuclear geometry between the initial ground state of a system and the final excited or ionized state. Changes in the initial-state polaronic distortion can significantly affect the final-state changes in bond length. A pronounced decrease of the line widths of MgO ionizations has been observed when single crystals or thick MgO films are compared with results on an ultrathin MgO/Ag(100) films, Fig. 3.2.

In Fig. 3.2 is reported the experimental Mg 2p XPS spectra of 1 and 14 ML MgO/Ag(100). The full width at half maximum (FWHM) of the Mg 2p peak is approximately 1.45 eV in the limit of 1 ML MgO/Ag(100) and reaches a constant value of approximately 1.60 eV for MgO films of 10 ML and thicker. The experimentally observed reduction in the broadening agrees qualitatively with that predicted one based on pure Frank-Condon broadening by theoretical calculations. The changes in the Frank-Condon broadenings for 1 ML MgO from the values of thick MgO films (bulk-like) arise because the equilibrium Mg–O distance r_e is different for bulk and monolayer MgO; this is true for both the ground state and the 2p hole potential curves. The curvature of these potential curves, as measured by ω_e, is different between bulk and monolayer, and provides a measure of the softness of the phonon modes of films of different thickness [28].

Another example of occurrence of polaronic distortion is related to gold atoms adsorption on ultrathin silica films. Crystalline SiO_2 films on Mo(112) have been investigated in detail by experiment and theory [29–31]. The film consists of a single layer of SiO_4 tetrahedra which share three oxygen atoms forming three Si–O–Si bridges with the forth oxygen directly bound to the Mo substrate. This corresponds to an hexagonal two-dimensional film covering the entire surface. The film is interrupted by eight-membered rings along line defects. Spontaneous charging of deposited gold does not occur on SiO_2/Mo(112) films. Both experiments and calculations show that gold atoms deposited at low temperature on these films (10 K) interact very weakly with the surface, diffuse and aggregate to form Au nanoparticles in correspondence of the line defects [32, 33]. The SiO_2 ultrathin films are very unreactive and, being bound to the Mo(112) substrate through an

Fig. 3.3 Preferred adsorption site and structural distortion (*side view*) induced by the adsorption of a Au atom on a Li doped SiO_2/Mo(112) film. Reproduced with permission from [37]
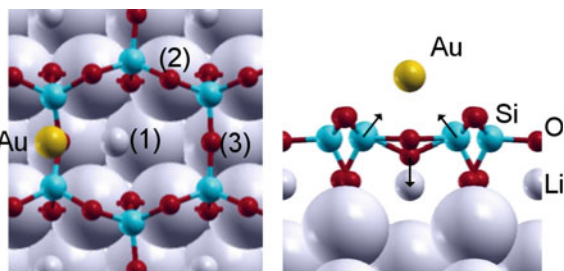
oxygen atom, generate a surface dipole which raises Φ, an effect which acts against the possibility to transfer charge from the Mo metal to the adsorbed gold. However, a possible way to modify the film reactivity is to deposit on the oxide film alkali metal atoms which are easily ionized to form M^+ ions stabilized above the silica film or at the SiO_2–Mo(112) interface, depending on their size. If one deposit Li atoms on this system, the Li atoms diffuse spontaneously to the interface where they form stable Li^+ ions. In these positions the Li ions cannot interact directly with the deposited Au atoms which, because of their size, remain above the surface, Fig. 3.3. The presence of Li^+ ions results in a substantial lowering of the work function Φ. For a coverage corresponding to one interface Li atom per silica ring, $\theta = 1$, the work function change is of about 1 eV. When the Au atoms are deposited on a Li-doped SiO_2/Mo(112) film, the adsorption properties change completely, as shown theoretically [34] and later proven experimentally [35, 36].

Three possible adsorption sites can be identified: (1) Au is adsorbed at the center of the ring, directly above a Li atom at the interface; (2) Au is on-top of a bridging O atom protruding outside the surface; (3) Au is on-top of a bridging O atom lying at the same height as the Si atoms of the film, Fig. 3.3. In (1) the bonding for Au is weak, −0.34 eV, and a partial charge transfer, as measured by the Bader charge (−0.55 e), occurs. In (2) the atom is very weakly bound, −0.18 eV, and almost neutral (Bader charge −0.26 e). However, when Au is in position (3) it becomes strongly bound, $E_b = -1.33$ eV, and negatively charged (Bader charge −0.80 e). With the help of STM images it has been possible to verify that the Au atoms are effectively bound above O sites of the film [35].

It is important to analyze the reasons why the charge transfer occurs only in some specific adsorption sites and not everywhere [37]. Also in this case, this is connected to the strong polaronic distortion which stabilizes the charged state of the Au^- anion. In particular, in the preferred adsorption site, Fig. 3.3, the O atom of the top layer relaxes downwards in direction of the Mo surface by about 0.85 Å, while the two adjacent Si atoms move towards the Au anion by about 0.1 Å, Fig. 3.3. This relaxation strongly stabilizes the 6 s level of Au, which becomes doubly occupied with formation of Au^-. As for MgO/Ag(100), in absence of the polaronic distortion, the charge transfer does not take place, showing that the change in work function alone is not sufficient to induce a charge transfer.

To emphasize the importance of the polaronic distortion, Au atom adsorption has been modeled also on the non-doped SiO_2/Mo(112) film. As we mentioned above, on this system Au forms a very weak bond and remains neutral. However, if the geometry optimization starts from a distorted silica structure as found in Li/SiO_2/Mo(112), one obtains a local minimum where the Au atom is charged. However, this configuration is slightly less stable (by about 0.1 eV) than neutral gold on the undistorted film. The cost to distort the silica structure is +2.95 eV; the Au atom is bound by −2.90 eV to this "distorted" structure, and the final result is a slightly unbound system. This clearly proofs that the lattice distortion is the key ingredient to stabilize the charged state. Of course, this does not form if the position of the metal Fermi level is not above the empty states of the adsorbate, but the two effects go together and one is useless without the other.

3.3 Electrostatic Origin of Rumpling in Supported Oxide Thin Films

So far we have considered the film reconstruction after adsorbed species have been deposited and an electron transfer has taken place via electron tunnelling through the support. However, structural relaxation in supported oxide films can be substantial also without the presence of adsorbed species. Rumpling is defined as the separation between the atomic planes of cations and anions of a monolayer. In general, while the rumpling for unsupported monolayers is negligible [38], it can be relevant when the film is deposited on a metal substrate. In particular, the rumpling of a supported oxide monolayer depends on the electronic properties of the metal substrate [39]. The electronegativity of the support determines the direction and the extent of the charge transfer at the metal/oxide interface. This charge transfer induces an electric field which causes the rumpling of the oxide film. If the oxide film is deposited on a substrate with high electronegativity, the oxide layer transfers electrons to the metal support. As the consequence, the anions in the oxide layer are pushed outwards, Fig. 3.4a, for electrostatic reasons. Viceversa, if the substrate has a low electronegativity electrons flow from the metal to the oxide. In this case are the cations of the oxide layer that are displaced outwards, Fig. 3.4b. Therefore, the
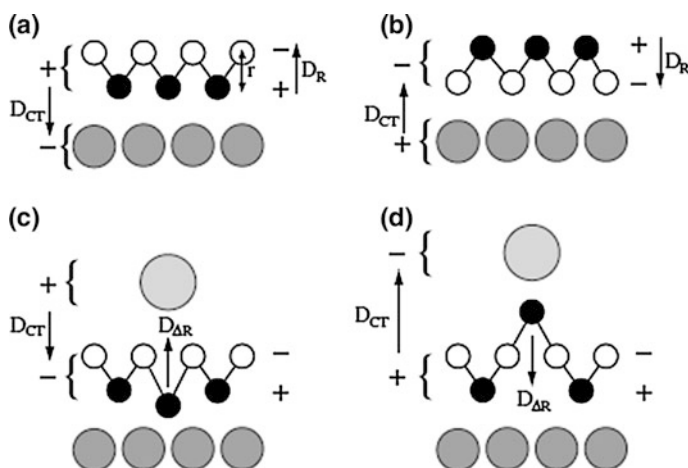
Fig. 3.4 **a** and **b**: schematic representation of the coupling between dipole moments due to the interface charge transfer (D_{CT}) and oxide film rumpling (D_R) in oxide monolayer films (*black circles* cations, *white circles* anions) deposited on a metal substrate (*large gray circles*); **c** and **d**: schematic representation of "direct" (**c**) and "flipped" (**d**) adsorption modes of an adatom (*large circle*) on a supported oxide film. In direct adsorption, the polaronic-like distortion induced by the adatom increases locally the rumpling (distance between planes of anions and cations); in flipped adsorption mode, the distortion locally reduces or inverses the rumpling. Dipole moments due to charging of the adatom (D_{CT}) and to the adsorption-induced structural distortion (D_R) are plotted schematically with *arrows* in the two cases. Reproduced with permission from [40]

rumpling in the supported film can be seen as the structural response to the charge transfer at the metal/oxide interface. The dipole moment associated to the rumpling in the oxide layer (D_R) has the opposite sign and partially compensates that due to charge transfer at the interface (D_{CT}).

As an example, DFT calculations show that when MgO monolayers are adsorbed on electropositive metals (Al and Mg) electrons are transferred from the metal to the oxide inducing a negative rumpling (oxygen closer to the metal surface); when MgO monlayers are deposited on transition metals (Ag, Mo and Pt), characterized by a larger work function, electrons are transferred from the oxide to the substrate, the rumpling is positive, and oxygen relaxes outwards, Fig. 3.4a, b.

A similar electrostatic response can be used to rationalize the surface relaxation induced by atoms or molecules adsorbed on the film when this is accompanied by a charge transfer (see the cases discussed above). The local relaxation which accompanies the charge transfer induces a dipole moment (consequence of the rumpling of the ionic layer) which partially counteracts the dipole moment due to the charge transfer, Fig. 3.4c, d. As a consequence, on a structurally very soft oxide monolayer the same adsorbate can exist in two opposite charge states, stabilized by different displacements of the ions in the films, Fig. 3.4c, d [40].

An example of this behaviour is provided by Au atoms deposited on FeO(111)/Pt(111) ultrathin films. FeO(111) films grown on Pt(111) have been the subject of ultrahigh vacuum investigations in the past [11, 12]. The most peculiar feature of the FeO(111)/Pt(111) system is the periodic variation of the interface structure imposed by the lattice mismatch between FeO(111) and Pt(111), which leads to the formation of a Moiré superlattice with three high-symmetry domains with Fe either in on-top, hcp, or fcc stacking with respect to the interfacial Pt atoms. [13–19] An Au atom deposited on this film becomes negatively charged if the rumpling is reversed locally with respect to the clean surface, with an outwards displacement of a Fe atom, Fig. 3.5a [40, 41]. The Au atom becomes positively charged on FeO(111)/Pt(111) if the oxide rumpling is as in the clean film (oxygens relaxed outwards, Fe ions relaxed towards the Pt surface, Fig. 3.5b). The relative stability of

Fig. 3.5 *Side view* of an Au adatom adsorbed on the FeO (111)/Pt(111) substrate: **a** flipped top-Fe configuration (negatively charged Au); **b** direct top-O configuration (positively charged Au)
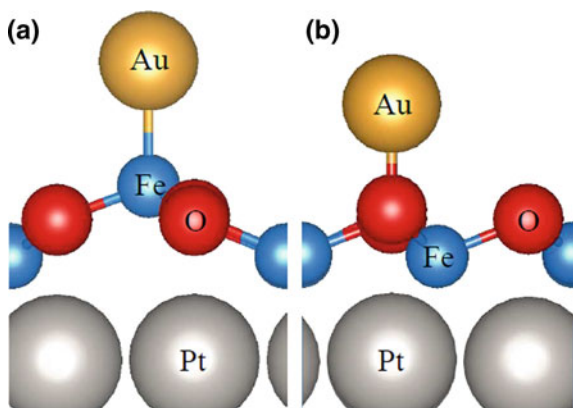
the two charged configurations, −1 or +1, respectively, depends on the alignment of the energy levels of the oxide film and of the adsorbate. If the singly occupied 6 s level of the Au atom falls below the Fermi level of the metal, then an electron is transferred from the FeO/Pt interface to the Au adsorbate that becomes negatively charged; in this case the electron affinity of adsorbed Au is larger than the work function of the metal/oxide interface. If, on the contrary, the singly occupied 6 s level of Au is above the Fermi level, this means that its ionization potential is smaller than the work function of the support and one electron is transferred from the adsorbate to the FeO/Pt interface and a positive charge forms on the Au species. Of the two configurations, only that corresponding the positively charged Au has been observed experimentally [41]. The fact that the other configuration has never been observed could be due to the presence of a kinetic barrier to reverse the local rumpling. This barrier has been investigated theoretically. The most stable adsorption is the Au adatom on the Fe-top site of flipped adsorption, forming an Au anion with zero barrier. In the fcc domain, a low-lying Fe cation cannot be lifted automatically and the barrier of the Au adatom moving from the O-top site of direct adsorption onto the adjacent Fe-top site of flipped adsorption was estimated to be 0.39 eV. Therefore, the Au cation at the O-top site of the fcc domain is metastable and will transform into an Au anion at the Fe-top site by overcoming a barrier of 0.39 eV [42].

A similar effect has been observed for MgO/Ag(100) 2 ML films by adsorbing Au and K atoms, Fig. 3.6 [43]. As described above, Au becomes negatively charged and induces an outward relaxation of the Mg ion to which is bound, Fig. 3.6a. Let's consider the adsorption of a K atom. On a MgO single crystal surface, K is predicted to adsorb very weakly, with a long distance from a surface O ion (2.89 Å) and very little surface relaxation. When K is adsorbed on a MgO/Ag(100) 2 ML film, there is a net change in the adsorption properties. The K atom donates one
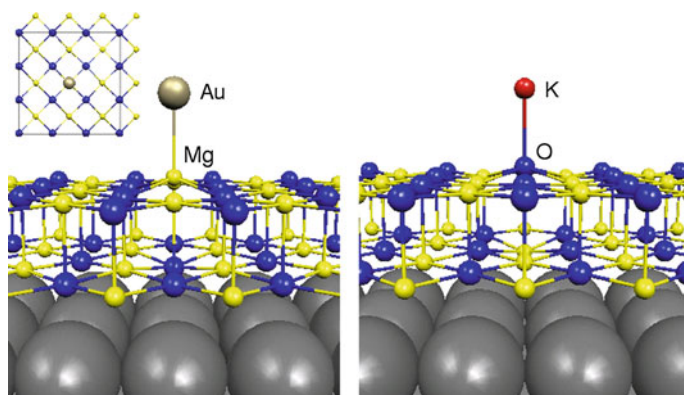

Fig. 3.6 Optimal geometry of **a** a Au atom adsorbed on-top of a Mg cation of a MgO/Ag(100) 2 ML film; **b** a K atom adsorbed on-top of a O anion of a MgO/Ag(100) 2 ML film. In both cases notice the strong relaxation of the surface ion in direct contact with the adsorbate. The *Inset* shows a *top view* of the 3 × 3 supercell used in the calculations. Reprinted with permission from [43]

electron to the support and becomes positively charged. The bonding on-top of oxygen is reinforced, $E_b = -0.43$ eV, and the K-O distance is considerably reduced, from 2.89 to 2.56 Å. The surface oxide anion relaxes outwards by 0.4 Å, Fig. 3.6b, while the Mg ion below it moves by 0.3 Å towards the Ag metal. Thus, adsorption of Au or K atoms leads to opposite structural relaxation of the MgO ultrathin film in order to create a surface dipole that partially screens the dipole moment generated by the charged adsorbates.

In general, the case discussed above of FeO(111)/Pt(111) films can be considered as one example of the more general theory of polarity in reduced dimensionality oxides. It has been shown for instance that one microscopic mechanism of stabilization of polar oxide orientations is based on a strong modification of the structural phase diagram of ionic crystals with rock-salt structure in the bulk phase [44]. At low thickness, films which are either unsupported or are deposited on metal surfaces like the Ag(111) display a graphite-like structure rather than the expected rocksalt one, providing strong evidence of the completely different nature of materials at low-dimensionality [44].

A relevant question from the computational point of view is to which extent the structural deformability of the films depends on the methods used to describe the electronic structure. Normally DFT calculations of ultrathin oxide films on metals are done at the GGA level of theory. In some cases, the description of layers of transition metal oxides with magnetic insulator character is performed using the DFT+U approach implemented by Dudarev et al. which consists in the definition of the effective Hubbard's parameter U [45, 46]. This allows to partly correct for the self-interaction error in DFT. In a recent study the performance of the DFT+U approach has been compared to the more robust hybrid functionals to describe the FeO(111)/Pt(111) films mentioned above [47]. Notice that the problem of describing simultaneously the metal electronic structure and that of a magnetic insulator like FeO is far from being straightforward (for a more detailed discussion see for instance [48]). The DFT+U approach allows one to apply the U correction only to those atoms that are involved in spin localization problems typical of transition metal compounds (Fe ions in this case) while the Pt metal is treated at the

Table 3.3 Structural and electronic characteristics of FeO(111)/Pt(111) as a function of interface lattice register obtained with DFT+U and HSE06 exchange-correlation functionals: relative stability ΔE (eV/FeO) with respect to the most stable Fe-fcc register, FeO adsorption height z(FeO) (Å), rumpling of the oxide film Δz (Å), electron transfer towards the Pt substrate CT(e/FeO) (positive values correspond to a negative charging of Pt), and FeO-induced change of the Pt(111) work function $\Delta\Phi$

			DFT+U					HSE06		
	ΔE	z(FeO)	Δz	CT	$\Delta\Phi$	ΔE	z(FeO)	Δz	CT	$\Delta\Phi$
	eV/FeO	Å	Å	e/FeO	eV	eV/FeO	Å	Å	e/FeO	eV
Fe-fcc	0.00	2.44	0.71	0.35	+0.57	0.00	2.40	0.67	0.40	+0.46
Fe-hcp	0.20	2.48	0.72	0.31	+0.37	0.24	2.49	0.68	0.68	+0.02
Fe-top	0.24	2.78	0.60	0.22	−0.30	0.21	2.72	0.58	0.58	−0.52

As a reference, the calculated Φ for the Pt(111) surface is 5.40 and 5.48 eV in DFT+U and HSE06 approaches, respectively [47]

standard DFT-GGA level. Hybrid functionals, on the other hand, provide a good description of semiconducting oxides but are not particularly suited to treat metallic systems. The HSE06 hybrid functional probably represents the best method available today to treat a mixed metallic/insulator system with an hybrid functional [49]. Table 3.3 reports the results of the DFT+U and HSE06 calculations on the rumpling in the FeO(111)/Pt(111) layers. The results refer to three different orientations of the FeO(111) film with respect to the Pt(111) support.

In general, Table 3.3 shows that the HSE06 approximation leads to relatively small modifications with respect to DFT+U results. In average, the FeO adsorption height z(FeO) and the film rumpling Δz are slightly smaller, whereas the electron transfer towards the metal substrate, CT, is slightly larger. These results show that the rumpling of the film is not connected to the level of computational method used.

3.4 From Structural Flexibility to Chemical Reactivity of Two-Dimensional Oxides

The relationship between charge transfer and film relaxation can have important consequences on the surface reactivity of ultrathin films. We have seen above that the simple adsorption of O_2 molecules can induce a significant polaronic distortion which is essential for the formation O_2^- superoxo species (see Sect. 3.2). Now we discuss a case where the exposure of an untrathin film to an oxygen atmosphere results in major restructuring of the film and in the complete change of its reactivity. This is the case of O_2 adsorption on the FeO(111)/Pt(111) films discussed in the previous section. The catalytic performance of this system in CO oxidation has important consequences for the understanding of how catalysts work under real catalytic conditions.

In the late 70-s, the notion of the so called Strong Metal Support Interaction (SMSI) [50] was introduced. According to this highly debated and often controversial definition, thin oxide films can form under reactive conditions on the surface of a metal particle deposited on an oxide support. Atoms from the oxide surface migrate to the metal particle, and, as a consequence, the metal catalysts becomes encapsulated into the oxide. Usually, this phenomenon leads to a suppression of the reactivity of the system. Recently, an opposite behavior has been reported which is relevant for the present discussion. In particular, it has been demonstrated that thin oxide films on metals may exhibit greatly enhanced catalytic activity, even higher than the metal substrate underneath under the same conditions. We are referring to the work by Sun et al. where CO oxidation has been studied on Pt nanoparticles deposited on the surface of magnetite, Fe_3O_4 [51]. It was observed that for temperatures of about 850 K the Pt particle becomes covered by an ultrathin oxide layer, Fig. 3.7. This layer has exactly the structure and composition of the FeO(111) film grown on a Pt(111) single crystal surface [52].
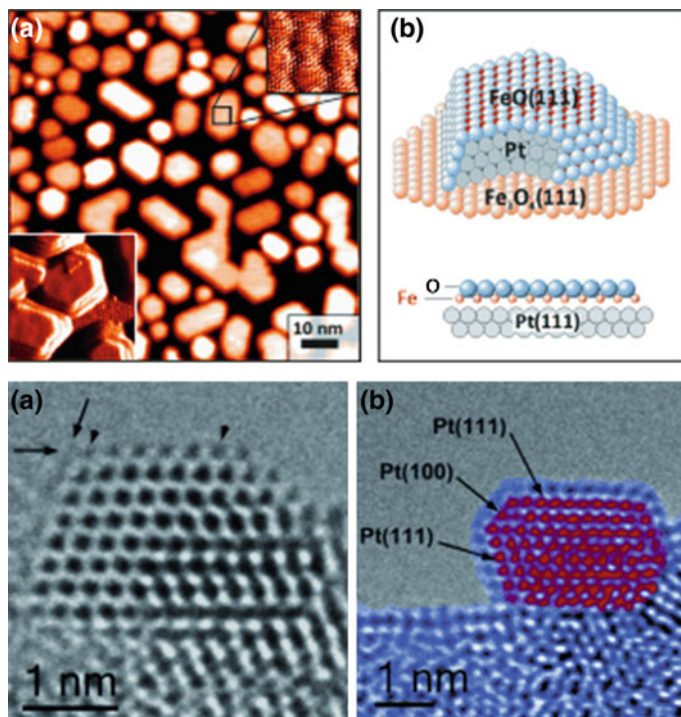
Fig. 3.7 *Top* **a** A typical STM image of a Pt/Fe$_3$O$_4$(111) surface after annealing in vacuum at 850 K. **b** Representation of an encapsulated Pt particle and a cross-view of an FeO(111) monolayer on Pt(111). *Bottom* HRTEM images of Pt particles supported by Fe$_3$O$_4$(111). **a** The *long arrows* indicate the encapsulated layer. **b** Colorized image to illustrate continuous encapsulation layer on different facets of a Pt particle as indicated. Reprinted with permission from [52]

It was suggested that under reaction conditions (an oxygen partial pressure in the mbar range), the unreactive bilayer FeO film reconstructs leading to a tri-layer OFeO film which exhibits an enhanced chemical reactivity [51, 53]. Here we will discuss in some detail the mechanism of this process. At low pressures (below 10^{-3} mbar) the FeO(111)/Pt(111) film is essentially inert towards CO and O$_2$. However, the film undergoes an important reconstruction at higher O$_2$ pressure when it approaches the formal stoichiometry FeO$_2$. The formation of a new phase is shown by thermal desorption spectroscopy (TDS) measurements, Fig. 3.8. The pristine FeO films show a single O$_2$ desorption peak at $\sim$1170 K (see Fig. 3.8). After reconstruction, the O-rich films exhibit a desorption feature at 840 K, clearly indicating that the O-rich film contains two types of O species.

The formation of the new structure is clearly seen in STM images of the film, Fig. 3.9a. The profile line presented in Fig. 3.9c reveals height modulation about 0.6 Å.

Fig. 3.8 (*Top*) Cross and top views of a FeO(111) film on Pt(111). Not all O atoms are shown in the *top view*, for clarity. Unit cells of FeO and Moiré superstructure are also indicated in the high-resolution STM image, (size 6 nm × 6 nm). (*Bottom*) Thermal desorption spectra of a pristine FeO(111) film (*dashed line*) and an O-rich film (*solid line*) produced by exposure to 20 mbar of O_2 at 450 K. The *Inset* shows a LEED pattern of an O-rich film characteristic of the Moiré superstructure. Adapted from [53]
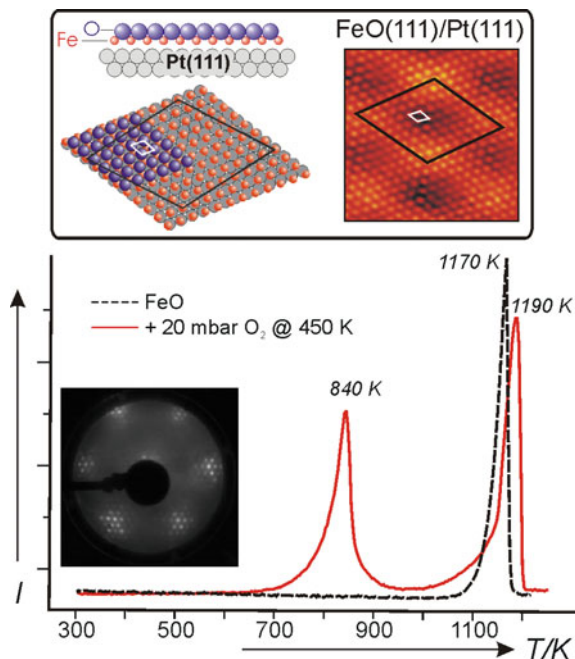
The STM image of a FeO film exposed to high O_2 pressure at 300 K, Fig. 3.9b, shows that a partial surface restructuring occurs under these conditions. The initial FeO and a new phase coexist. The difference in height between the two phases, ~ 0.65 Å, coincides with a Fe–O interlayer distance on FeO(111)/Pt(111), consistent with the formation of additional oxygen layer, see Fig. 3.9d. The process has been studied by DFT calculations with the aim to model the transformation of the FeO bi-layer into a FeO_2 tri-layer under oxygen exposure [53]. Figure 3.10 shows the calculated energy profile for the interaction of an O_2 molecule with the FeO (111)/Pt(111) film (entropic effects have not been considered). By overcoming a small energy barrier O_2 chemisorbs in molecular form on a Fe atom, which is pulled out from the original position in the pristine film. The existence of a small barrier to chemisorbed oxygen explains why the process occurs only at a given oxygen pressure. In the chemisorbed state electrons are transferred from the oxide/metal substrate, and O_2 becomes negatively charged and activated. The elongated O–O bond, 1.46 Å, is typical of O_2^{2-} peroxo species. The electron transfer is the direct consequence of the local inversion of the rumpling in the oxide film, as discussed above. Even more important, this is accompanied by a local reduction of work function ($\Delta\Phi \sim -1.5$ eV). This is an essential point. In fact, Pt(111) has a high work function and as such is difficult to transfer charge to an adsorbate. The local rumpling provides the conditions to activate the O_2 via charge transfer from the support.
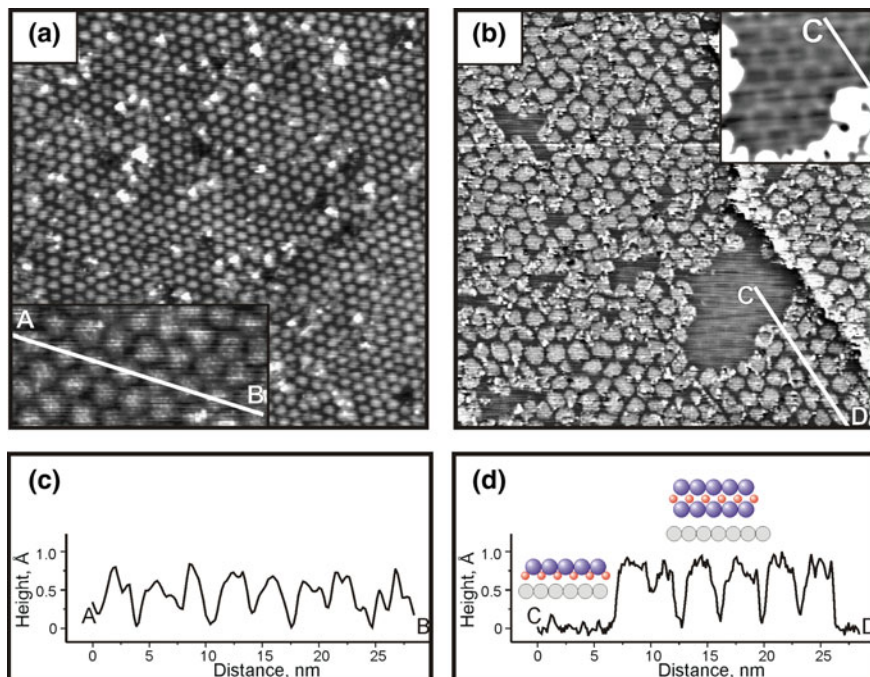
Fig. 3.9 STM images and profile lines of the FeO films exposed to 20 mbar O_2 at 450 K for 10 min **a**, **c** and 2 mbar O_2 at 300 K for 5 h **b**, **d**. The *Insets* show close-ups of the corresponding surfaces. The Moiré superstructure of the pristine FeO film is seen in the *Inset* **b**. Image sizes are 100 nm × 100 nm (**a**) and 50 nm × 50 nm (**b**). Adapted from [53]

Fig. 3.10 (*Top*) Energy profile for the oxidation of the FeO/Pt(111) film upon exposure to O_2 at high oxygen coverage. (*Bottom*) Energy profile for CO oxidation on FeO_2/Pt(111) film at low CO coverage. *Blue* (Fe), *red* (O), *yellow* (C), *gray* (Pt). Adapted from [53]
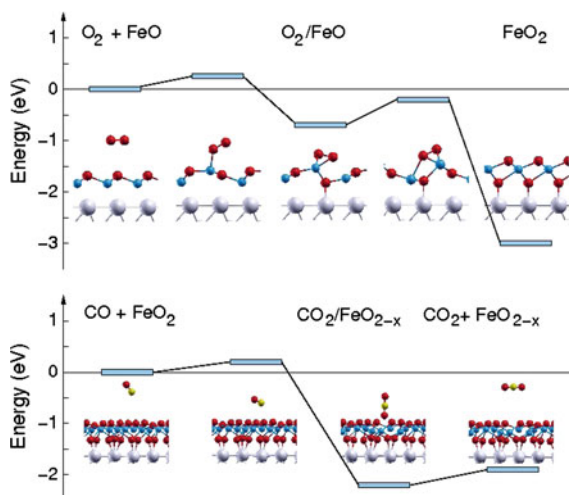
The activation of adsorbed O_2 is followed by the dissociation of the molecule. A second small activation barrier (0.4 eV) leads to the formation of two O ad-atoms, Fig. 3.10a and to the O–Fe–O tri-layer. This mechanism explains why at high O_2 pressure the FeO film transforms into the O–Fe–O tri-layer structure with FeO_2 stoichiometry. The overall process is accompanied by a substantial energy gain. The process is the result of the structural flexibility of the FeO two-layer film. Its reaction and reconstruction occurs with very low barriers and in very mild conditions.

What remains to be explained, is why the new phase is more reactive than Pt in CO oxidation [51]. Also in this case the answer is provided by DFT calculations [53]. The energy profile of the reaction $CO + FeO_2/Pt(111) \rightarrow CO_2 + FeO_{2-x}/Pt(111)$, Fig. 3.10b, shows that the reaction involves the extraction of an oxygen atom from the oxide surface film with formation of a CO_2 molecule leaving behind an oxygen vacancy.

The CO molecule coming from the gas-phase is first physisorbed on the FeO_2/Pt (111) film and then, overcoming a small barrier of ~ 0.2 eV, Fig. 3.10b, binds strongly with the C-end to one O ion in the topmost layer, with formation of a stable CO_2 molecule and an oxygen vacancy. Here there are two important aspects to stress: (1) the global energy barrier for CO oxidation on $FeO_2/Pt(111)$ is lower than the computed barrier on Pt(111), thus explaining the higher reactivity of the oxide film and the fact that the reaction occurs at lower temperatures than those observed for Pt; (2) the key aspect of the entire process is the relatively low formation energy of an oxygen vacancy on the $FeO_2/Pt(111)$ bilayer, 1.3 eV (computed with respect to ½ O_2). This is about one half of the cost to create a vacancy on the pristine single layer FeO film, 2.8 eV. This is in full agreement with the TDS curves shown in Fig. 3.8, where oxygen desorbs from FeO-rich films at much lower temperature than from FeO. Therefore, the easy formation energy of an oxygen vacancy is the key factor in the CO oxidation reaction over FeO films. The reaction proceeds via the Mars-van Krevelen type mechanism and the oxygen vacancies formed by reaction with CO are replenished by the reaction with gas-phase oxygen that restores the original stoichiometry of the film.

The initial step in the overall reaction is the formation of an activated peroxo species on the surface of FeO(111)/Pt(111). We have seen above that formation of O_2^- occurs spontaneously on ultrathin MgO/Ag(100) films due to the low work function of the system. Indeed, it has been suggested theoretically that this should lead to low-temperature CO oxidation on MgO/Ag(100) surface, a result that still needs experimental confirmation [28]. On the contrary, FeO(111)/Pt(111) films exhibit a very high work function, due to the initial high work function of the Pt (111) surface. This makes the electron transfer from the metal/oxide interface to O_2 impossible in absence of surface relaxation. The strong local restructuring of the film upon exposure to oxygen has exactly the function to lower locally the work-function, leading to the transient formation of a peroxo species. The structural flexibility of the oxide layer is therefore the key aspect of the entire reaction.

3.5 Spontaneous Incorporation of Adsorbed Atoms on Ultrathin Films

As a last example of structural flexibility of two-dimensional insulators supported on a metal we discuss the case of spontaneous incorporation of deposited metal atoms into ultrathin film supports. Recently, it has been shown that Co and Cr atoms adsorbed at low temperature on NaCl/Au(111) films result in spontaneous doping and incorporation into the NaCl layer [54, 55]. STM images combined with DFT calculations have revealed that Co and Cr atoms can replace both Na and Cl ions in the topmost layer of the NaCl/Au(111) 2 and 3 ML film. DFT calculations also suggest the possibility for the transition metal atoms to penetrate into the surface layer of the NaCl film and to be stabilized in interstitial sites (interstitial doping) [56].

These results have shown once more the important role of surface reconstruction and deformability of ultrathin films. At the same time, they have also opened several questions. The first, obvious, one is to which extent the properties of a two-layer film differ from those of the corresponding surface of a bulk material. We have seen already that there is ample evidence that often these properties are quite different due to the reduced vertical dimensionality of the films. The second question is if beside NaCl also other materials once grown in form of ultrathin film are in principle capable to incorporate atoms arriving with low kinetic energy on the surface. For instance, we have seen above that Au atoms deposited on MgO/Ag (100) films become negatively charged [16], but do not show any tendency to penetrate into the oxide layers. The third question is related to the role of the metal support and of the metal/insulator interface in determining the properties of two-dimensional insulators. Assuming that these materials can be prepared as free-standing units like graphene, are the properties of the supported or unsupported layers the same? To answer these questions in this last Section we compare the properties of supported and unsupported NaCl ultrathin films with those of the corresponding MgO structures [57]. In particular, we focus on the reactivity with adsorbed Co atoms as these are the atoms that have shown the tendency to spontaneously replace Na and Cl ions in NaCl/Au(111) supports [55].

NaCl is the prototype of ionic crystals and NaCl ultrathin films [58–62] have been used to electronically decouple the metal support from adsorbed atoms (e.g., Ag, Au) [21, 63], molecules [64, 65] or nanostructures (e.g. C_{60}) [66]. MgO is the typical example of ionic oxide and, as we have seen, MgO ultrathin films have been deposited on substrates like Ag(100) or Mo(100) [67–70].

The surface of bulk materials has been modelled by 3 ML NaCl and MgO films where the bottom layer is fixed at the bulk positions. It has been shown in the past that this is a good model of the real bulk surfaces. The properties of these systems have been compared with those of free-standing, fully optimized, 2 ML films. Then, the 2 ML NaCl and MgO films have been deposited on Au(111) and Ag(100) metal supports, respectively. Co atoms have been adsorbed on all these systems. The calculations were performed with the DFT-D2′ method that includes dispersion forces by means of the pair-wise force field implemented by Grimme [71] using a

Table 3.4 Binding energies, E_b (eV), and Bader charge, q (|e|), for a Co atom adsorbed or incorporated on the surface of NaCl and MgO (100) 3 ML films, and on unsupported and supported NaCl and MgO 2 ML films (results obtained at the DFT-D2′ level) [57]

		Anion-top	Hollow	Interstitial
NaCl(100) (3 ML)	E_b	−0.82	−0.90	−1.18
	q	−0.07	−0.06	−0.02
MgO(100) (3 ML)	E_b	−1.66	[a]	−0.29[b]
	q	−0.15	–	0.80[b]
NaCl film (2 ML)	E_b	−0.78	−0.93	−1.36
	q	−0.06	−0.04	−0.03
MgO film (2 ML)	E_b	−1.62	[a]	0.94
	q	−0.03	–	−0.11
NaCl(2 ML)/Au(111)	E_b	−1.06	−2.55	−2.98
	q	0.25	0.44	0.63
MgO(2 ML)/Ag(100)	E_b	−1.45	–	−0.33
	q	−0.09	–	0.60

[a]Co goes to on top of O; [b]Co goes in a Mg substitutional site and displaces the Mg atom which moves to a bridge adsorption site

variant of the original parametrization (DFT-D2′ approach). In DFT-D2′ the C_6 parameters and van der Waals Radii R_0 of Na and Mg ions have been replaced by those of Ne since the size of this atom is closer to that of the Na^+ and Mg^{2+} cations. Further computational details can be found in [56, 57].

We start by discussing the adsorption properties of a single Co atom on NaCl (100) and MgO(100) surfaces. Adsorption on anion-top, hollow and interstitial sites has been considered, Table 3.4.

On NaCl(100) Co is bound by −0.82 eV on-top of Cl and by −0.90 eV on the hollow site. The bonding originates from the mixing of the Co 3d levels with the Cl 3p orbitals but there is little charge transfer (neutral adsorbed Co). When Co occupies an interstitial site between the first and the second NaCl layers, a large geometrical distortion occurs that involves mainly the top NaCl layer; here Co is bound by −1.18 eV, Table 3.4. Thus, the binding energy in the interstitial position is stronger than for adsorption on the surface (this does not mean that spontaneous incorporation of Co is expected since a barrier separates the adsorption on the surface from that below the top NaCl layer). Also in the interstitial site Co remains neutral.

On the MgO(100) surface (modelled by 3 ML films) Co binds on top of O with a binding energy of −1.66 eV, Table 3.4, about twice that found on NaCl(100). The hollow site is not a minimum. Also on MgO the bonding of Co is due to the hybridization of the Co 3d and O 2p valence states, with little charge transfer from MgO to Co (Bader charge −0.15 e). However, things are totally different when Co occupies an interstitial position between the first and the second MgO layers. The site is clearly too small and a strong reconstruction occurs with Co that replaces a Mg lattice ion which is pushed above the surface. The resulting configuration is unstable (about +1.4 eV higher than for Co adsorbed on-top of O). Thus, there are two quite different situations for a Co atom adsorbed on NaCl(100) and MgO(100)
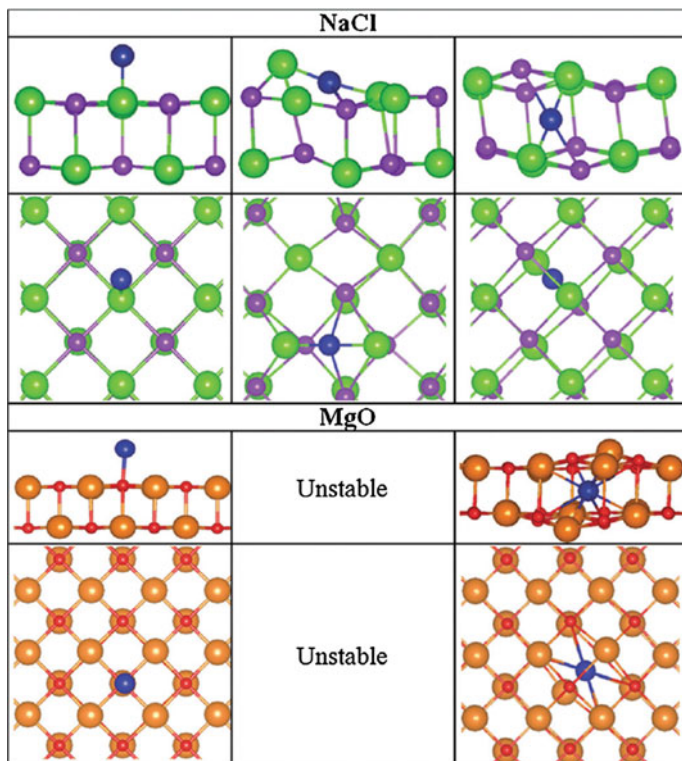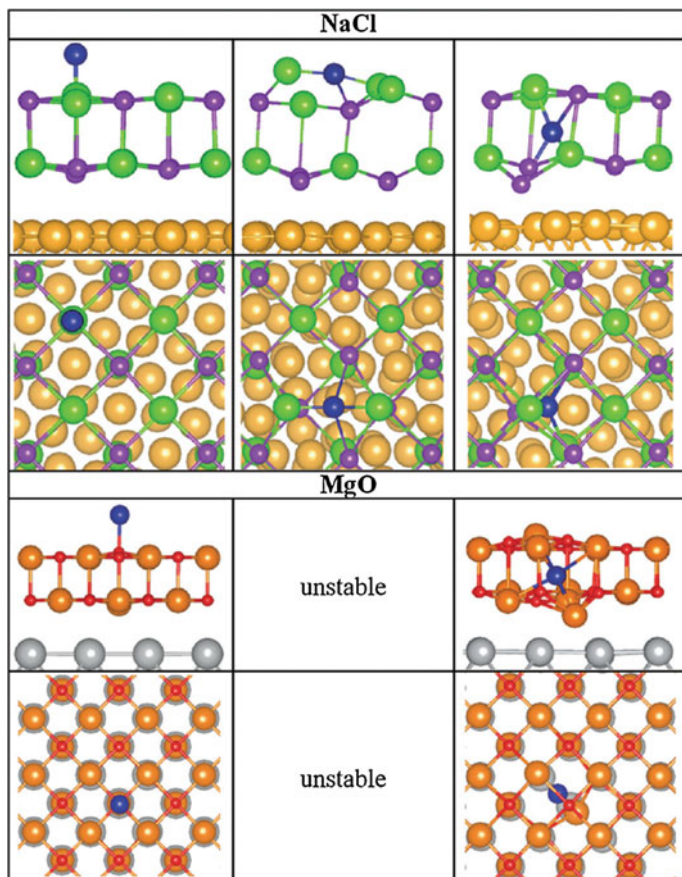
Fig. 3.11 *Side* and *top views* of a Co atom adsorbed on-top of the anion (*top*), in hollow sites (*center*), or in interstitial sites (*bottom*) of free standing NaCl (*left*) and MgO (*right*) 2 ML films (*blue* Co; *green* Cl; *violet* Na; *orange* O; *red* Mg). Reproduced with permission from [57]

surfaces: on NaCl the interstitial site is the most stable site while on MgO is totally unfavourable and only surface adsorption is possible. This result can be explained with the different lattice constants of the two materials, 5.65 Å NaCl, 4.21 Å MgO and the different size of the interstitial sites but also with the different cost required to distort the structures (smaller in NaCl than in MgO).

We consider now Co adsorption on free-standing NaCl and MgO 2 ML films. The order of stability for Co adsorption on NaCl 2 ML film remains interstitial > hollow > on-top of Cl, Table 3.4 and Fig. 3.11 (the adsorption energies on-top of Cl and on hollow sites are comparable, −0.78 and −0.93 eV). However, due to the higher degree of freedom (the 2 ML film is free to relax in all directions) the energy gain is larger, −1.36 eV, when Co atom is in an interstitial position.

On the MgO 2 ML unsupported film there is only one stable Co adsorption site, i.e. on top of O, with E_b = −1.62 eV. The adsorption energy is virtually the same computed for the MgO(100) surface (−1.66 eV for the 3 ML film, Table 3.4). A metastable structure exist when Co is included in the interstitial position. The structure of the 2 ML MgO film undergoes a strong distortion to accommodate the

Fig. 3.12 *Side* and *top* views of a Co atom adsorbed on top of the anion (*top*), in hollow sites (*center*), or in interstitial sites (*bottom*) of NaCl/Au(111) (*left*) and MgO/Ag(100) (*right*) 2L films (*blue* Co; *green* Cl; *violet* Na; *yellow* Au; *orange* O; *red* Mg; *grey* Ag). Reproduced with permission from [57]

Co atom, see Fig. 3.11, in order to release the strain. In this configuration the system is unbound by 0.94 eV, indicating a strong steric repulsion. On both NaCl and MgO 2 ML films the Co atom keeps the same number of electrons it has in the gas-phase and remains essentially neutral. This is not surprising since there are no acceptor states in non-defective NaCl or MgO films to accommodate extra electrons coming from the adsorbed atom. This makes the formation of a cation, Co^{n+}, energetically unfavorable. Therefore, Co adsorption on free-standing NaCl and MgO 2 ML films shows that adsorption sites and properties are the same as for the corresponding bulk surfaces, see Table 3.4. In particular, Co binds on the surface of MgO and shows no tendency to go to interstitial sites; on the contrary, on NaCl the thermodynamically stable structure corresponds to a Co atom adsorbed between the

first and the second NaCl layers. The different behaviour of NaCl and MgO can be attributed to the stronger Madelung potential in the oxide compared to the chloride, which leads to a softer NaCl structure.

As a last point we consider Co adsorption on NaCl and MgO 2 ML films deposited on Au(111) and Ag(100) metals, respectively, Fig. 3.12. In this way we will be able to identify the role of the support in determining the properties of the ultrathin film. The structures of the NaCl/Au(111) and MgO/Ag(100) interfaces has been fully optimized keeping only the two metal bottom layers fixed.

The adsorption properties of Co on NaCl/Au(111) 2 ML films are very different from those of the unsupported NaCl layer. When Co is on-top of Cl, E_b goes from -0.78 eV (unsupported) to -1.06 eV (supported), Table 3.4. The situation changes completely on the hollow site where Co is bound by -2.55 eV, i.e. about three times larger than on the unsupported NaCl 2 ML film, Table 3.4. For both adsorption sites the top NaCl layer undergoes a major reconstruction (see Figs. 3.11 and 3.12). But the reason for the much larger Co adsorption energy on NaCl/Au(111) is related to electronic effects. On NaCl/Au(111) the position of the metal Fermi level is such that the valence electrons of the Co adsorbate are transferred to the Au support, with formation of a Co^{n+} species. The occurrence of a charge transfer is shown also by the Bader charges: on the NaCl 2 ML film the Bader charge on Co is slightly negative, $q = -0.04$ e; on NaCl/Au(111) it is positive, $q = +0.44$ e, Table 3.4. This charge transfer interaction results in a considerable reinforcement of the bond. The occurrence of the charge transfer is even more important when Co in interstitial sites of the NaCl/Au(111) 2 ML film. While on the free-standing 2 ML film Co interstitial is bound by -1.36 eV and is neutral ($q = -0.03$ e), on NaCl/Au(111) the adsorption energy becomes almost -3 eV and the charge is positive, $q = +0.63$ e, Table 3.4. The adsorption is accompanied by a major geometrical relaxation, with displacement of a Na ion in the second NaCl layer towards the Au(111) support, Fig. 3.12. This shows that the supported NaCl/Au(111) 2ML film is even more flexible than the unsupported one, and is able to incorporate the Co atom with a large energy gain. In the interstitial site Co donates one electron to Au forming a Co^+ ion. This leads to a reduction of the steric repulsion and an increase of the electrostatic attraction. The conclusion is that the adsorption energies and bonding modes are totally different on unsupported and supported NaCl/Au(111) 2 ML films. This is due in large part to the possibility to exchange charge with the metal support, an effect which is obviously absent in the free-standing 2 ML films. However, the supported NaCl films also show a greater tendency to distort compared to the unsupported ones, due to the reasons that have been discussed above in connection to the dipole response to the creation of local perturbations, see Fig. 3.4. Once more, the large structural flexibility is at the basis of the unexpected properties of NaCl ultrathin films.

Let us consider now Co on MgO/Ag(100) 2 ML films. Co adsorption on-top of O remains the most stable configuration ($E_b = -1.45$ eV), and the adsorption energy is similar to the unsupported MgO 2 ML case ($E_b = -1.62$ eV). This is not surprising considering that the bonding mechanism does not change; Co binds via covalent polar bonds, and the Bader charges are very close for the three cases examined, MgO(100), MgO 2 ML film, and MgO(2 ML)/Ag(100), Table 3.4. The

presence of the Ag support is irrelevant, and the supported or unsupported MgO films behave essentially in the same way. This is no longer true when the interstitial site is considered. In fact, on the unsupported MgO 2 ML film Co incorporation is highly unfavorable (E_b = +0.94 eV), while it becomes slightly exothermic on MgO/Ag(100) 2 ML films (E_b = −0.33 eV), Table 3.4. The presence of the Ag support leads to an energy gain of about 1.4 eV due to the occurrence of a net charge transfer from Co to the MgO/Ag(100) interface. Co donates 0.6 valence electrons to the Ag metal, forms $Co^{\delta+}$ thus reducing the steric repulsion, with a mechanism similar to that observed for NaCl/Au(111). However, while on NaCl/Au (111) the interstitial site is the most stable one, on MgO/Ag(100) this site is metastable and adsorption on the surface of the film remains clearly preferred (−1.45 eV on-top of O, −0.33 eV interstitial). As mentioned previously, the different behaviour of MgO compared to NaCl in the ultrathin limit is due to the stronger Madelung field in the oxide compared to the chloride.

In conclusion, a comparison of the adsorption properties of Co atoms on NaCl (100) or MgO(100) surfaces, on free-standing 2 ML NaCl and MgO films, and on NaCl/Au(111) and MgO/Ag(100) films provides some interesting indications on the role of the structural flexibility of the ultrathin films and on the differences existing between different highly ionic materials. On one side, on defect-free unsupported films no charge transfer with the adsorbed metal atom is possible, while on the supported films transition metal atoms can exchange charge with the metal support, changing completely the adsorption properties. Furthermore, the supported films are more flexible and easy to distort than the bare materials or the unsupported layers. As a consequence, incorporation of transition metal atoms like Co in the interstitial sites of NaCl becomes favourable. This is also at the basis of the observed replacement of Na or Cl ions in the film, with spontaneous doping of the two-dimensional insulator by simple exposure to a gas of atoms [54, 55].

3.6 Conclusions

In this Chapter we have discussed one particular property of oxides, and more in general of insulating or semiconducting materials, in form of ultrathin films, their structural flexibility. The fact that due to the reduced dimensionality these systems can exhibit quite different properties from their bulk counterparts has been recognized some time ago and has been extensively discussed in the literature [3, 13, 16, 17]. Normally, the emphasis on the peculiarities of two-dimensional insulators is restricted to their electronic properties, like for instance the fact that they do not behave as insulating layers when the thickness is below few nanometers, due to the occurrence of electron tunnelling phenomena to or from the metal support.

Here we have emphasized another important property of low-dimensional oxides, their easy structural deformation. This aspect has been recognized when it has been observed that the formation of charged adsorbates on supported ultrathin films

results in a local surface relaxation, also called polaronic distortion. This distortion is not restricted to the surface ion where the adsorbed species is bound, but also to other neighbouring atoms and can be up to half an angstrom, leading to pronounced corrugation in the surface. Experimental proofs of this important surface modification predicted by DFT calculations have become available in the last few years. The origin of this phenomenon lies in the electrostatic response of the thin supported layer to the formation of a surface dipole induced by the charged adsorbate. The insulating film undergoes a structural relaxation that opposes and compensates the dipole generated by the charged adsorbed species. This effect is also at the basis of the surface rumpling in oxide thin films, even in absence of adsorbates.

The marked flexibility of two-dimensional oxides can be at the basis of their pronounced chemical reactivity. We have analyzed in some detail the case of the formation of new phases in iron oxide films supported on Pt in the reaction of low temperature oxidation of CO. Here the entire catalytic process is dominated by the capability of the solid surface to rearrange under reactive conditions.

Finally, we have seen that adsorbed atoms can even penetrate into insulating thin layers, either by replacing some of the lattice ions, or by becoming incorporated into interstitial sites of the supported film. Comparing NaCl with MgO films we have seen that the structural flexibility is a function of two main parameters: (1) the nature of the bond within the film (stronger bonds in MgO result in a smaller flexibility compared to NaCl which has weaker ion-ion interactions); (2) the metal support has the role on one side to allow electron exchange with the insulating phase and with species adsorbed on it, and on the other side to allow a larger structural flexibility.

For all these reasons two-dimensional insulating materials supported on a metal represent a new class of systems with very interesting properties and often unexpected behaviours. Playing around with the film thickness, nature of the insulator, metal support, and adsorbed species opens a new playground for the design of new materials with useful and unprecedented applications.

References

1. Xu M, Liang T, Shi M, Chen H (2013) Graphene-like two-dimensional materials. Chem Rev 113:3766–3798
2. Osada M, Sasaki T (2012) Two-dimensional dielectric nanosheets: novel nanoelectronics from nanocrystal building blocks. Adv Mater 24:210–228
3. Pacchioni G (2012) Two-dimensional oxides: multifunctional materials for advanced technologies. Chem Europ J 18:10144–10158
4. Gusev EP (2000) Defects in SiO_2 and related dielectrics: science and technology. In: Pacchioni G, Skuja L, Griscom DL (eds), Kluwer, Dordrecht, p 557
5. Olsson COA, Landolt D (2003) Passive films on stainless steels—chemistry, structure and growth. Electrochim Acta 48:1093–1104
6. Costa D, Ribeiro T, Mercuri F, Pacchioni G, Marcus P (2014) Atomistic modelling of corrosion resistance: a first principles study of O_2 reduction on the Al(111) surface covered with a thin hydroxylated alumina film. Adv Mater Interf 1:1300072
7. Ahn CH, Rabe KM, Triscone JM (2004) Ferroelectricity at the nanoscale: local polarization in oxide thin films and heterostructures. Science 303:488–491
8. Granqvist CG (2007) Transparent conductors as solar energy materials: a panoramic review. Solar En Mater Solar Cell 91:1529–1598
9. Parkin SSP, Kaiser C, Panchula A, Rice PM, Hughes B, Samant M, Yang SH (2004) Giant tunnelling magnetoresistance at room temperature with MgO (100) tunnel barriers. Nat Mat 3:862–867
10. Pacchioni G, Valeri S (eds) (2012) Oxide ultrathin films: science and technology. Wiley-VCH, Weinheim
11. Xu X, Goodman DW (1992) New approach to the preparation of ultrathin silicon dioxide films at low-temperatures. App Phys Lett 61:774–776
12. Freund HJ, Kuhlenbeck H, Staemmler V (1996) Oxide surfaces. Rep Progr Phys 59:283–347
13. Freund HJ, Pacchioni G (2008) Oxide ultra-thin films on metals: new materials for the design of supported metal catalysts. Chem Soc Rev 37:2224–2242
14. Surnev S, Ramsey MG, Netzer FP (2003) Vanadium oxide surface studies. Prog Surf Sci 73:117–165
15. Wu QH, Fortunelli A, Granozzi G (2009) Preparation, characterisation and structure of Ti and Al ultrathin oxide films on metals. Int Rev Phys Chem 28:571–576
16. Giordano L, Pacchioni G (2011) Oxide films at the nanoscale: new structures, new functions, and new materials. Acc Chem Res 44:1244–1252
17. Pacchioni G, Freund HJ (2013) Electron transfer at oxide surfaces. The MgO paradigm: from defects to ultrathin films. Chem Rev 113:4035–4072
18. Pacchioni G, Giordano L, Baistrocchi M (2005) Charging of metal atoms on ultra-thin MgO/Mo(100) films. Phys Rev Lett 94:226104
19. Sterrer M, Risse T, Pozzoni UM, Giordano L, Heyde M, Rust HP, Pacchioni G, Freund HJ (2007) Binding of single gold atoms on thin MgO(001) films. Phys Rev Lett 98:096107
20. Giordano L, Baistrocchi M, Pacchioni G (2005) Bonding of Pd, Ag, and Au atoms on MgO (100) surfaces and MgO/Mo(100) ultra-thin films. A comparative DFT study. Phys Rev B 72:115403
21. Repp J, Meyer G, Olsson FE, Persson M (2004) Controlling the charge state of individual gold adatoms. Science 305:493–495
22. Hellman A, Klacar S, Grönbeck H (2009) Low temperature CO oxidation over supported ultrathin MgO films. J Am Chem Soc 131:16636–16637
23. Gonchar A, Risse T, Freund HJ, Giordano L, Di Valentin C, Pacchioni G (2011) Activation of oxygen on MgO: O_2^- formation on thin, metal supported MgO(001) films. Angew Chemie Int Ed 50:2635–2638

24. Frondelius P, Hellman A, Honkala K, Hakkinen H, Gronbeck H (2008) Charging of atoms, clusters, and molecules on metal-supported oxides: a general and long-ranged phenomenon. Phys Rev B 78:085426

25. Pacchioni G, Ferrari AM, Giamello E (1996) Cluster models of O_2^- adsorption on regular and defect sites, and F_s centers of the MgO(100) surface. Chem Phys Lett 255:58–64

26. Chiesa M, Giamello E, Paganini MC, Sojka Z, Murphy DM (2002) Continuous wave electron paramagnetic resonance investigation of the hyperfine structure of $^{17}O_2^-$ adsorbed on the MgO surface. J Chem Phys 116:4266–4274

27. Napoli F, Chiesa M, Giamello E, Preda G, Di Valentin C, Pacchioni G (2010) Formation of superoxo species by interaction of O_2 with Na atoms deposited on MgO powders: a combined continuous-wave EPR (CW-EPR), hyperfine sublevel correlation (HYSCORE) and DFT study. Chem Eur J 16:6776–6785

28. Nelin CJ, Bagus PS, Brown MA, Sterrer M, Freund HJ (2011) Analysis of the broadening of X-ray photoelectron spectroscopy peaks for ionic crystals. Angew Chemie Int Ed 50:1521–3773

29. Weissenrieder J, Kaya S, Lu JL, Gao H, Shaikhutdinov S, Freund HJ, Sierka M, Todorova TK, Sauer J (2005) Atomic structure of a thin silica film on a Mo(112) substrate: a two-dimensional network of SiO_4 tetrahedra. Phys Rev Lett 95:076103

30. Giordano L, Ricci D, Pacchioni G, Ugliengo P (2005) Structure and vibrational spectra of crystalline SiO_2 ultra-thin films on Mo(112). Surf Sci 584:225–236

31. Lu JL, Kaya S, Weissenrieder J, Gao H, Shaikhutdinov S, Freund HJ (2006) Low temperature CO induced growth of Pd supported on a monolayer silica film. Surf Sci 600:L153–L157

32. Ulrich S, Nilius N, Freund HJ, Martinez U, Giordano L, Pacchioni G (2008) Evidence for a size-selective adsorption mechanism on oxide surfaces: Pd and Au atoms on SiO_2/Mo(112). ChemPhysChem 9:1367–1370

33. Ulrich S, Nilius N, Freund HJ, Martinez U, Giordano L, Pacchioni G (2009) Realization of an atomic sieve: silica on Mo(112). Surf Sci 603:1145–1149

34. Martinez U, Giordano L, Pacchioni G (2008) Tuning the work function of ultrathin oxide films on metals by adsorption of alkali atoms. J Chem Phys 128:164707

35. Martinez U, Jerratsch JF, Nilius N, Giordano L, Pacchioni G, Freund HJ (2009) Tailoring the interaction strength between gold particles and silica thin films via work function control. Phys Rev Lett 103:056801

36. Jerratsch JF, Nilius N, Freund HJ, Martinez U, Giordano L, Pacchioni G (2009) Lithium incorporation into a silica thin film: scanning tunneling microscopy and density functional theory. Phys Rev B 80:245423

37. Martinez U, Giordano L, Pacchioni G (2010) Mechanism of charging of Au atoms and nanoclusters on Li doped SiO_2/Mo(112) films. ChemPhysChem 11:412–418

38. Goniakowski J, Noguera C, Giordano L (2004) Prediction of uncompensated polarity in ultrathin films. Phys Rev Lett 93:215702

39. Goniakowski J, Noguera C (2009) Polarization and rumpling in oxide monolayers deposited on metallic substrates. Phys Rev B 79:155433

40. Goniakowki J, Noguera C, Giordano L, Pacchioni G (2009) Adsorption of metal atoms on FeO(111) and MgO(111) monolayers: effects of charge state of adsorbate on rumpling of supported oxide film. Phys Rev B 80:125403

41. Giordano L, Pacchioni G, Goniakowski J, Nilius N, Rienks EDL, Freund HJ (2008) Charging of metal adatoms on ultrathin oxide films: Au and Pd on FeO/Pt(111). Phys Rev Lett 101:026102

42. Ouyang R, Li WX (2011) First-principles study of the adsorption of Au atoms and Au_2 and Au_4 clusters on FeO/Pt(111). Phys. Rev. B 84:165403

43. Giordano L, Pacchioni G (2006) Charge transfers at metal/oxide interfaces: a DFT study of formation of $K^{\delta+}$ and $Au^{\delta-}$ species on MgO/Ag(100) ultra-thin films from deposition of neutral atoms. Phys Chem Chem Phys 8:3335–3341

44. Goniakovski J, Noguera C, Giordano L (2004) Using polarity for engineering oxide nanostructures: structural phase diagram in free and supported MgO(111) ultrathin films. Phys Rev Lett 93:215702
45. Anisimov VI, Zaanen J, Andersen OK (1991) Band theory and mott insulators hubbard-U instead of stoner-I. Phys Rev B 44:943–954
46. Dudarev SL, Botton GA, Savrasov SY, Humphreys CJ, Sutton AP (1998) Electron-energy-loss spectra and the structural stability of nickel oxide: an LSDA+U study. Phys Rev B 57:1505–1509
47. Prada S, Giordano L, Pacchioni G, Noguera C, Goniakowski J (2014) Properties of Pt-supported iron oxide ultra-thin films: similarity of Hubbard-corrected and hybrid density functional theory description. J Chem Phys 141:144702
48. Surnev S, Fortunelli A, Netzer FP (2013) Structure-property relationship and chemical aspects of oxide-metal hybrid nanostructures. Chem Rev 113:4314–4372
49. Heyd J, Scuseria GE, Ernzerhof M (2003) Hybrid functionals based on a screened Coulomb potential. J Chem Phys 118:8207–8215
50. Tauster SJ, Fung SC, Garten RL (1978) Strong metal-support interactions—group-8 noble-metals supported on TiO_2. J Am Chem Soc 100:170–175
51. Sun YN, Qin ZH, Lewandowski M, Carrasco E, Sterrer M, Shaikhutdinov S, Freund HJ (2009) Monolayer iron oxide film on platinum promotes low temperature CO oxidation. J Catal 266:359–368
52. Willinger MG, Zhang W, Bondarchuk O, Shaikhutdinov S, Freund HJ, Schlögl R (2014) A case of strong metal-support interactions: combining advanced microscopy and model systems to elucidate the atomic structure of interfaces. Angew Chem Int Ed 53:1521–3773
53. Sun YN, Giordano L, Goniakowski J, Lewandowski M, Qin ZH, Noguera C, Shaikhutdinov S, Pacchioni G, Freund HJ (2010) The interplay between structure and CO oxidation catalysis on metal supported ultrathin oxide films. Angew Chem Int Ed 49:4418–4421
54. Li Z, Chen HYT, Schouteden K, Lauwaet K, Giordano L, Trioni MI, Janssens E, Iancu V, Van Haesendonck C, Lievens P, Pacchioni G (2014) Self-doping of ultrathin insulating films by transition metal atoms. Phys Rev Lett 112:026102
55. Li Z, Chen HYT, Schouteden K, Janssens E, Van Haesendonck C, Lievens P, Pacchioni G (2015) Spontaneous doping of two-dimensional NaCl films with Cr atoms: aggregation and electronic structure. Nanoscale 7:2366–2373
56. Chen HYT, Giordano L, Pacchioni G (2014) Adsorption properties of two-dimensional NaCl: a density functional theory study of the interaction of Co, Ag, and Au atoms with NaCl/Au (111) ultrathin films. J Phys Chem C 118:12353–12363
57. Chen HYT, Pacchioni G (2014) Properties of two-dimensional insulators: a DFT study of Co adsorption on NaCl and MgO ultrathin films. Phys Chem Chem Phys 16:21838–21845
58. Wagner M, Negreiros FR, Sementa L, Barcaro G, Surnev S, Fortunelli A, Netzer FP (2013) Nanostripe pattern of NaCl layers on Cu(110). Phys Rev Lett 110:216101
59. Repp J, Meyer G, Paavilainen S, Olsson FE, Persson M (2005) Scanning tunneling spectroscopy of Cl vacancies in NaCl films: strong electron-phonon coupling in double-barrier tunneling junctions. Phys Rev Lett 95:225503
60. Cabailh G, Henry CR, Barth C (2012) Thin NaCl films on silver (001): island growth and work function. New J Phys 14:103037
61. Bombis C, Ample F, Mielke J, Mannsberger M, Villagomez CJ, Roth C, Joachim C, Grill L (2010) Mechanical behavior of nanocrystalline NaCl islands on Cu(111). Phys Rev Lett 104:185502
62. Ploigt HC, Brun C, Pivetta M, Patthey F, Schneider WD (2007) Local work function changes determined by field emission resonances, NaCl/Ag(100). Phys Rev B 76:195404
63. Olsson FE, Paavilainen S, Persson M, Repp J, Meyer G (2007) Multiple charge states of Ag atoms on ultrathin NaCl films. Phys Rev Lett 98:176803

64. Kim SH, Jeong HG, Lim SJ, Ham UD, Song YJ, Yu J, Kuk Y (2013) Geometric and electronic properties of porphyrin molecules on Au(111) and NaCl surfaces. Surf Sci 613:54–57

65. Yan S, Ding Z, Xie N, Gong H, Sun Q, Guo Y, Shan X, Meng S, Lu X (2012) Turning on and off the rotational oscillation of a single porphine molecule by molecular charge state. ACS Nano 6:4132–4136

66. Cavar E, Blum MC, Pivetta M, Patthey F, Chergui M, Schneider WD (2005) Fluorescence and phosphorescence from individual C_{60} molecules excited by local electron tunnelling. Phys Rev Lett 95:196102

67. Schintke S, Messerli S, Pivetta M, Patthey F, Libioulle L, Stengel M, De Vita A, Schneider WD (2001) Insulator at the ultrathin limit: MgO on Ag(001). Phys Rev Lett 87:276801

68. Benedetti S, Torelli P, Valeri S, Benia HM, Nilius N, Renaud G (2008) Structure and morphology of thin MgO films on Mo (001). Phys Rev B 78:195411

69. Kiguchi M, Goto T, Saiki K, Sasaki T, Iwasawa Y, Koma A (2002) Atomic and electronic structure of MgO/Ag(001) heterointerface. Surf Sci 512:97–106

70. Chen MS, Goodman DW (2008) Ultrathin, ordered oxide films on metal surfaces. J Phys: Condens Matter 20:264013

71. Grimme S (2006) Semiempirical GGA-type density functional constructed with a long-range dispersion correction. J Comput Chem 27:1787–1799

Chapter 4
Reducible Oxides as Ultrathin Epitaxial Films

Paola Luches and Sergio D'Addato

Abstract This chapter reviews and discusses recent work on two-dimensional films of reducible oxides supported on metal substrates. In general, peculiar chemical and structural phases, different from the bulk ones, can be stabilized depending on the oxygen chemical potential, on kinetic processes and on the specific substrate used. A peculiarity of reducible oxides is that the observed phases can often be reversibly transformed one into the other by applying reducing and oxidizing treatments.

4.1 Introduction

An oxide is defined reducible if it can be easily and reversibly reduced depending on the ambient conditions. Reducibility is linked to the existence of two or more oxidation states with comparable stability for the cations. Prototypical reducible oxides are represented by cerium and titanium oxides, although also other transition metal and rare earth oxides can be considered reducible; among these for example other rare earth oxides, like PrO_x, SmO_x, TbO_x, and other $3d$ metal oxides, like VO_x, MnO_x, FeO_x, CoO_x, but also HfO_x, TaO_x, NbO_x, WO_x and many more.

Indeed, reducibility is very relevant for catalysis, since materials based on reducible oxides can act as oxygen buffers, which can store and release oxygen and/or charge, promoting redox reactions with a unique regeneration ability [1]. Furthermore, reducibility is an important property also in view of the application of oxides in other fields, like for example energy conversion and storage, [1] biomedicine [2] and memories [3]. Reducibility is not only linked to the material capacity of easily

P. Luches (✉) · S. D'Addato
Istituto Nanoscienze – CNR, Via G. Campi 213/a, 41125 Modena, Italy
e-mail: paola.luches@unimore.it

S. D'Addato
e-mail: sergio.daddato@unimore.it

S. D'Addato
Dipartimento di Scienze Fisiche, Informatiche e Matematiche, Università degli Studi di Modena e Reggio Emilia, Via G. Campi 213/a, 41125 Modena, Italy

forming oxygen vacancies but also to the reversibility of the process and to oxygen transport properties within the material.

The influence of reduced dimensionality on the reducibility of an oxide is certainly relevant in view of the optimization of the properties of the material through the understanding of the modifications which arise with confinement. Pronounced changes of the electronic structure of oxides at reduced dimensionality have been widely investigated, and interesting properties have been observed on reducible oxides in particular [4, 5]. In cerium oxide particles of nanometric size the oxygen vacancy formation energy has been found to be greatly reduced and to reach a minimum at a specific size [4], thereby causing a surprisingly enhanced reactivity of catalysts made of metal nanoparticles supported on nanocrystalline cerium oxide [6], possibly also facilitated by easy oxygen transfer to the supported metal nanoparticles [7].

If only one of the dimensions of the considered material is confined to the nanoscale, i.e. if the system under study is a two-dimensional film, several interesting modifications are introduced and intriguing phenomena can take place. The stabilization of metastable structural phases by epitaxy or by the mere spatial confinement, the presence of lattice strain or rumpling, the interaction with the substrate, in terms of charge transfer but possibly also of interfacial atom exchange, the different stability of structural defects, are all expected to determine relevant changes in the electronic structure, which give origin to systems with different properties compared to the corresponding bulk phases.

The studies of two-dimensional reducible oxides are typically carried out on model systems, i.e. on ultrathin films supported on single crystalline substrates, prepared and analyzed in high or ultrahigh vacuum. The investigations aim at identifying interesting aspects on simple systems, which can be analyzed by surface science techniques and understood with the help of theoretical descriptions. A proper modeling of the systems under investigation often represents a crucial step for a complete atomic level understanding of the material properties and potential performances. Only through the fundamental insight of the new properties which arise on simple systems, the much more complex real systems, based on the same materials, can be understood and optimized in their functionality. For example, catalysts made of metal nanoparticles supported on reducible oxides typically involve some degree of encapsulation of the metal within the oxide and the formation of very thin oxide layers on the metal nanoparticle surface, through the so called strong metal-support interaction (SMSI) [8]. Ultrathin oxide layers exposing different facets, with different structures and morphologies can be prepared in the form of model systems to identify the most active species towards the considered reaction. The results of these studies can be used to design the catalysts with an optimized activity and selectivity by finding suitable synthetic routes to maximize the density of required active sites for the chosen specific functionality.

In this chapter recent studies on the properties of ultrathin films of reducible oxides are reviewed, focusing on the aspects which influence the reducibility of the materials at the two dimensional limit. New properties of cerium oxide two-dimensional films are discussed in Sect. 4.2. Section 4.3 reports studies of

titanium oxide two-dimensional films, which are interesting for comparison and for complementing the concepts outlined on cerium oxide based systems. Selected studies of ultrathin films of different reducible transition metal and rare earth oxides are finally reported in Sect. 4.4.

4.2 Cerium Oxide Two-Dimensional Films

The most stable cerium oxide phase is CeO_2, also known as *ceria*, which has a fluorite structure with cerium ions in the 4+ oxidation state. The Ce_2O_3 phase, with an orthorhombic structure (A-type phase), is relatively less stable at ambient conditions. Several additional metastable phases with different stoichiometry can be stabilized in specific conditions [9], among them the Ce_2O_3 bixbyite (c-type) phase deserves a particular relevance, since it can be obtained from the most stable fluorite-type CeO_2 phase by removing 25 % of the oxygen lattice atoms in an ordered way and allowing for a slight structural rearrangement [10].

The (111) surface of the CeO_2 phase is the thermodynamically most stable one, followed by the (100) and (110) surfaces, the latter two being polar [11]. The repeating unit along the (111) direction is an O-Ce-O triple layer, which in the following will be referred to as a monolayer (ML). Cerium oxide ultrathin films exposing the (111) surface can be obtained by epitaxial growth on metallic single crystal substrates with six-fold surface symmetry such as (111) surfaces of cubic structures [12–18], or hcp (0001) surfaces [14, 19, 20]. The lattice mismatch between cerium oxide and most of the metal substrates is quite large and it amounts to approximately 30–40 %. Nevertheless, films with a (111) surface orientation and a very good epitaxial quality have been obtained [15, 17, 21, 22]. The (100) and (110) surface orientation can be stabilized through epitaxy using substrates with a very small lattice mismatch with CeO_2. These are typically non-metallic and include Si [22, 23], YSZ [24] and $SrTiO_3$ [25, 26]. However, most of the studies performed using non metallic substrates focus on thick films of several tens of nm thickness, possibly because of the difficulties in applying surface science techniques, necessary to obtain information at the ultrathin limit, on substrates with low conductivity.

The first and main part of this section will be dedicated to studies of cerium oxide (111) ultrathin films, and the final part to the investigations concerning ultrathin films exposing less stable surfaces. Important aspects connected to reducibility at the two- dimensional limit will be reviewed and discussed, with focus on: (i) structure, morphology and defectivity, (ii) charge transfer and inter-mixing at the interface, (iii) modifications in structure and morphology induced by reduction, (iv) stabilization of metastable structures induced by dimensionality and/or epitaxial constraints.

Pioneering works studying ultrathin cerium oxide films on the Pt(111) surface date back to the mid-nineties and they were motivated by the idea that a deep understanding of ceria-based materials obtained from studies of single crystalline

surfaces and films of different thickness, structure and morphology could help improving the activity of cerium oxide supports in three way catalytic converters [12, 13, 27, 28]. Cerium oxide films were grown either by deposition of metallic cerium followed by post-oxidation [12, 27] or by oxidation of Ce-Pt surface alloys [13, 28]. Already these early works pointed out that ultrathin films in the ML and sub-ML range contain a non negligible Ce^{3+} concentration, while thicker films can be fully oxidized [12, 13]. As will be clearer in the following, this aspect is rather crucial in trying to identify a charge transfer from the metal substrate and/or a dimensionality-induced decrease of oxygen vacancy formation energy induced by the lower average O coordination of Ce ions at the early stages of the growth. The structure of the films was found to be disordered unless thermal treatments at temperatures higher than 700 K, which stabilize the fluorite (111) phase, are performed [12, 13]. Thermally-induced instabilities were observed above 1000 K [12, 13]. Interestingly, films which fully cover the substrate showed a significant activity towards CO oxidation, higher than the one of the bare Pt(111) surface [12]. An important role of the metal-oxide interfacial sites and of non-(111) oriented surfaces was also hypothesized, based on the high activity of films which do not fully cover the substrate [12].

The results of the early studies provided a strong motivation for subsequent works, using more controlled growth procedures, combined with a variety of techniques for surface characterization down to the atomic level. Cerium oxide ultrathin films with the (111) fluorite structure were grown on Pt(111) [17, 21, 28, 29], Rh (111) [15, 16], Ru(0001) [14, 20], Ni(111) [14], Cu(111) [30, 31], Au(111) [32], Pd (111) [33] and Re(0001) [34] substrates. On one side these studies confirmed the enhanced reactivity of bidimensional cerium oxide films compared to the clean substrates and the importance of metal–oxide interface sites [31, 35], on the other they clarified important fundamental aspects linked to the reducibility of low-dimensional supported cerium oxide systems [15, 29, 30].

In general, the studies of ultrathin supported cerium oxide films and islands were motivated by the need to identify the active sites in real catalysts made of metallic nanoparticles supported on cerium oxide. Several works specifically addressed the reactivity of metal-supported cerium oxide systems and towards selected reactions [31, 35–37]. A catalytically active role of the interface between cerium oxide and Rh(111) in CO oxidation was suggested for example by Eck et al., who identified preferential CO adsorption sites near the phase boundaries of the oxide islands [36]. Suchorski et al. showed that the catalytic activity towards CO oxidation of cerium oxide nanoislands on Pt(111) is remarkably increased compared to the bare Pt(111) surface [35]. By comparing systems with different density of step edges they suggested the observed increase to be due to the different electronic properties at the islands perimeter [35]. A similar role for the oxide metal interface, combined with the low dimensionality of cerium oxide, was identified for the CO oxidation reaction and for the water gas shift reaction on the cerium oxide/Cu(111) inverse catalyst model system [31, 37]. Studies of this kind stimulated more accurate work on cerium oxide bidimensional structures and a systematic investigation of the

influence of the preparation conditions and of the substrate used on the structure, morphology, defectivity and reducibility of the obtained systems.

On most substrates post-growth thermal treatments in O_2 have been found to improve the surface morphology, stoichiometry and structure of the cerium oxide terraces obtained [17, 20]. The ultrathin films have relatively large coincidence cells with the underlying metal surface, which give origin to moiré patterns in scanning tunneling microscopy (STM) images [20, 38] or in low energy electron diffraction (LEED) patterns [15]. The coincidence cells with the lowest strain typically involve 5×5 ceria surface cells and 7×7 substrate surface cells (hereafter termed 5:7 coincidence), however at the ultrathin limit smaller coincidence cells, implying a larger strain, can be stabilized. This phenomenon has been observed for example on the Pt(111) substrate, where ultrathin films have a compressed surface structure and an interatomic distance comparable with the 3:4 coincidence cell, while thicker films have the relaxed bulk structure [17, 21, 39]. At the ultrathin limit a contraction of the in plane lattice parameter has been observed also using Rh(111) as a substrate [15], and even on Cu(111) substrates [38]. The evidence for a lattice contraction also on Cu(111), on which cerium oxide could adopt a 3:2 coincidence with the substrate with negligible strain, demonstrates that the tendency for lattice contraction is probably an intrinsic property linked to reduced dimensionality [38].

The deposition of cerium oxide amounts in the ML range typically results in the formation of large flat islands of ML or multi-layer height [15, 17, 20]. Procedures to obtain continuous films of monolayer thickness with almost complete coverage have been identified on the Cu(111) substrate, using low temperature (110 K) growth in O_2 followed by post-annealing in O_2 at 770 K [18]. Ultrathin cerium oxide films grown in strongly oxidizing conditions contain a non-negligible concentration of Ce^{3+} ions on the Pd(111) [33], Pt(111) [17] and Rh(111) substrate [15]. In the latter case a preferential localization of the Ce^{3+} sites at the interface was deduced by comparison of x-ray photoemission spectroscopy (XPS) and valence band resonant photoemission spectroscopy (RESPES) results. RESPES, having a smaller probing depth than XPS, does not show any significant Ce^{3+} concentration on the surface. The non-negligible Ce^{3+} concentration detected by XPS is therefore ascribed to interface sites [15]. This represents a strong evidence of possible charge transfer from the metallic substrate towards the cerium oxide films. This effect can indeed significantly alter the properties of two-dimensional cerium oxide films, however a definite assignment of the origin of reduced interfacial states requires a theoretical description of the system. On the Cu(111) substrate density functional theory (DFT) calculations showed that a very relevant charge transfer from the metal to the oxide takes place, yielding to the reduction of a full layer of interfacial Ce ions [40]. DFT calculations on a 1 ML cerium oxide film supported on Pt(111), instead, evidenced electrostatic interactions between the topmost Pt layer and the interfacial oxygen atoms in the oxide, which cause a significant corrugation of both the film surface and of the interfacial Pt layer [41]. The charge transfer between Pt and Ce ions is significant only in the interfacial sites where the distance between the two atoms is short [41].

Not only the size, but also the shape and surface defects of the terraces of ultrathin cerium oxide films seem to depend on the preparation conditions. On Ru (0001), using high temperature (T > 800 K) growth and post-growth annealing (T ∼ 1000 K) in oxygen atmosphere (P > 10^{-7} mbar), ultrathin films with point defects, linear defects ascribed to grain boundaries and round terrace step edges have been obtained [20]. The presence of grain boundaries, possibly induced by three-dimensional growth mode at the early stages of film formation [20], is not suppressed by room temperature growth followed by annealing of ceria films using a Pt(111) substrate [17]. On this substrate ultrathin films present terraces with straight edges, oriented along the substrate main symmetry directions [17]. Thicker films instead show more rounded terrace edges [17]. This is possibly caused by the stabilization of less stable step edges by the proximity of the metallic substrate in ultrathin films. A detailed characterization of the film step edges for various preparation conditions showed that depending on the heating temperature different step types can be obtained. The different steps are rationalized in terms of stability of the exposed facets and analyzed in terms of electronic properties [42]. One–dimensional electronic states have been found to develop on specific step types, and at domain boundaries as shown in Fig. 4.1, which reports STM images acquired at different sample biases.

The step edges exposed by cerium oxide two-dimensional films show similarities to those exposed by bulk ceria surfaces, although in this case depressions rather protrusions are most frequently observed on the surface [43]. A non-negligible density of point defects has been often detected on ultrathin film terraces [21]. The defects are very similar to the ones formed on bulk surfaces, the most common being surface oxygen vacancies, also imaged as trimers and as linear arrays, and subsurface oxygen vacancies [21]. Defects can also be intentionally induced by electron bombardment of the film surface [44]. A work by Jerratsch et al. identified some degree of delocalization of the charge left after O vacancy formation [44]. The delocalization of charge after O release has been highly debated also on bulk
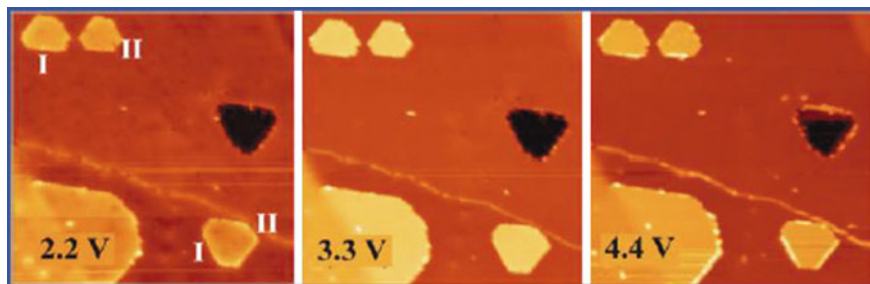
Fig. 4.1 65×65 nm^2 STM topographic images of a 6 ML cerium oxide film grown on Ru(0001) with islands and holes exposing different step edge orientation. Steps indicated as I and domain boundaries show an increased apparent height at 4.4 V sample bias, while steps indicated as II do not change apparent contrast with bias. Reprinted with permission from Nilius et al. [42]. Copyright 2012 American Chemical Society

surfaces [45, 46], and at reduced dimensionality some non negligible degree of delocalization has been clearly identified [5, 47].

Cerium oxide films can be reduced by different procedures, including thermal annealing in vacuum [15, 17, 29, 35], growth of metallic Ce in low oxygen background pressure [14, 16, 48], ion bombardment [49] or exposure to reducing gases [49–51]. Vacuum thermal treatments often induce also a structural and morphological modification, pointed out to be strongly dependent on the initial film thickness [15, 29]. In particular, the temperature at which reduction starts is lower for thinner films, which also show an apparently higher final degree of reduction [15, 29]. Indeed it is difficult to determine the absolute amount of Ce^{3+} ions formed in the different samples by the different treatments, given the unknown shape of the depth profile of O vacancy concentration, and the different depth sensitivity of the techniques used to measure the Ce^{3+}/Ce^{4+} ratio. However, the idea of having a higher density of Ce^{3+} sites in the surface layer after reduction is generally accepted [29]. A dependence of the onset of cerium oxide surface reduction on the growth temperature of the film, and hence on the density of reduced coordination sites, has been observed for films grown on the Cu(111) substrate [38]. A very interesting effect, shown to take place on the surface of a thin ceria film on Rh(111) after reduction, is the formation of an ordered array of surface defects, clearly visible in the STM images (Fig. 4.2), and ascribed to triple oxygen vacancies [52]. The smaller energy for the formation of vacancies at specific sites of the 5:7 coincidence lattice is ascribed to the local surface stress [52].

The surface of reduced ceria films on Pt(111) instead shows a corrugated morphology with bias-dependent features tentatively ascribed to electronic modifications induced by reduction [29]. Interestingly, ultrathin reduced cerium oxide phases show peculiar surface reconstructions (Fig. 4.3), whose origin is still under investigation and appears to be linked to the presence of the underlying substrate [29]. The effect of the heating time and heating rate on the final degree of reduction of the films has been also pointed out to be very important [29]. Some extra-periodicities have been observed also on the Cu(111) substrate after deposition of variable amounts of metallic cerium on a CeO_2 buffer layer, followed by annealing in UHV [53]. Some of them are commonly observed also on the surface of thick films after reduction [54] and correspond to metastable bulk phases such as the Ce_7O_{12} phase and the c-type bixbyite phase.

The full reversibility of the reduction process was demonstrated for ceria films of different thickness on Pt(111) [29]. We note here that this aspect is not trivial, and it is linked to the reducibility of the films. Cerium oxide films on a Si(111) substrate reduced by vacuum thermal treatments under conditions similar to those used in [29], showed a non reversible reduction of Ce ions from the 4+ state to the 3+ state [23]. This process was ascribed to the formation of interface cerium silicate phases which are not reducible [23]. Interfacial atom exchange during growth was also observed using Ni(111) and Cu(111) substrates, and it was shown to have a non-negligible influence on the stoichiometry of the films at the ultrathin limit [14, 31]. On the Au(111) substrate the formation of Au/Ce alloys hinders the good ordering of extended two-dimensional films [32].
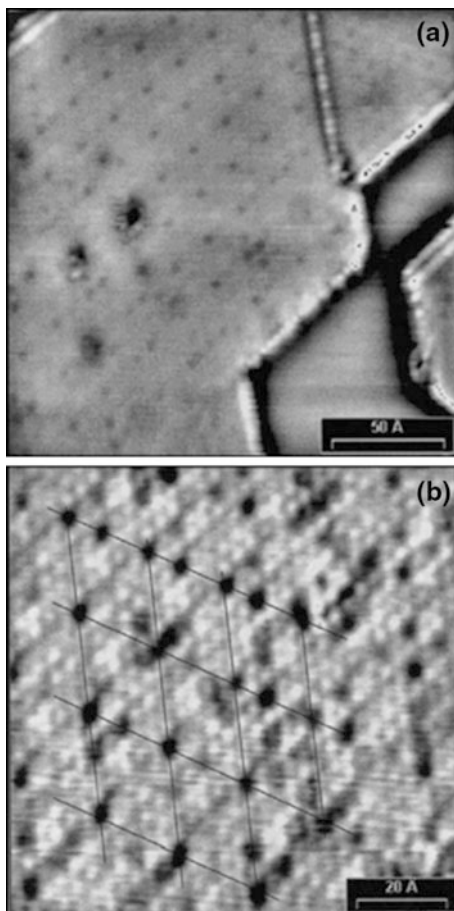
Substoichiometric films were also obtained by evaporation of Ce on Ru(0001) and on Ni(111) in low oxygen pressure $(P_{O_2} \sim 10^{-8}$ mbar$)$ and they were found to have the fluorite structure with a high concentration of oxygen vacancies in at least the topmost oxygen atom layers, compatible with a bixbyite structure rather than with a hexagonal A-type Ce_2O_3 structure [14].

As reported above, several works have shown some degree of reducibility of cerium oxide ultrathin films, which is typically higher than the bulk, but they also evidenced that fully reduced states are very difficult to be achieved [15, 29]. This may be linked to the fact that it is easy to form oxygen vacancies in the fluorite structure up to a certain density, or to the fast (partial) reversibility of the reduction process when high Ce^{3+} concentrations are obtained. The cubic c-type bixbyite phase, with 25 % oxygen vacancies, is in fact unstable in the bulk form and a full cerium oxide reduction may require a transition to the most stable hexagonal A-type phase. A metastable epitaxial cubic c-type Ce_2O_3 phase has been stabilized on the
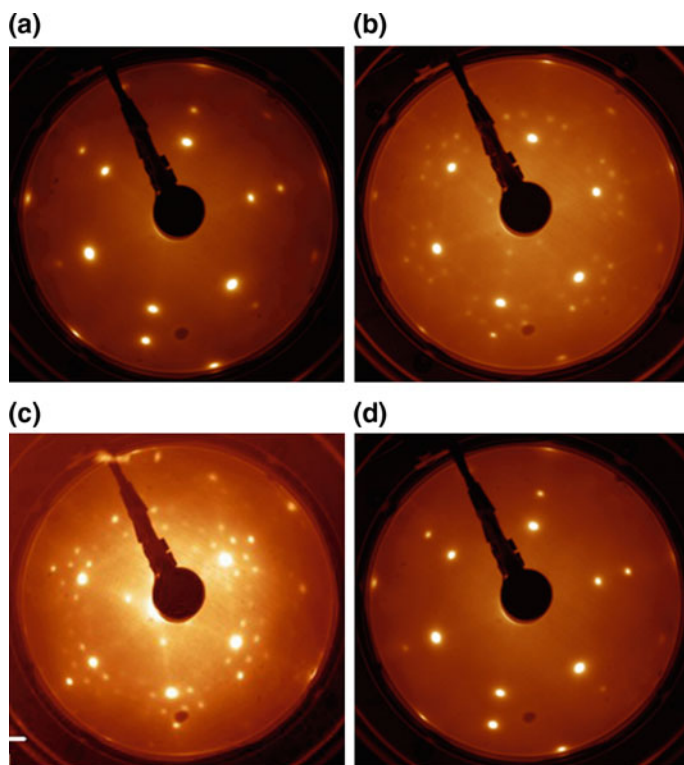
Fig. 4.3 LEED patterns (Ep = 80 eV) of a 2 ML cerium oxide film, **a** as prepared, **b** after intermediate reduction by heating in UHV at 770 K for 30 min ($c_{Ce3+} \sim 40$ %, as measured by XPS), showing the (3×3) and the $9/4(\sqrt{3} \times \sqrt{3})R30°$ phase, **c** after strong reduction by heating in UHV at 1040 K for 15 min ($c_{Ce3+} \sim 60$–80 %) showing the $9/4(\sqrt{3} \times \sqrt{3})R30°$ phase, **d** after re-oxidation by heating in O_2 at 1040 K. Luches et al. [29]. Reproduced by permission of the PCCP Owner Societies

Cu(111) surface by deposition of metallic Ce on a CeO_2 buffer layer followed by 900 K annealing [55]. The film shows a well ordered surface with a (4×4) reconstruction with respect to the $CeO_2(111)$ surface (Fig. 4.4). The reconstruction is ascribed to ordered arrays of quadruple oxygen vacancy clusters and corresponds to the bulk termination of c-Ce_2O_3 [55]. Although the film thickness is as high as a few nm, the influence of the substrate is considered to be determinant for the stabilization of the observed phase, ascribed to the effect of the tetragonal strain induced by the Cu substrate [55]. A phase with a similar c-type bixbyite structure in the form of an ultrathin film was also stabilized on a Cl-passivated Si(111) surface [22].

The exposed works show that ultrathin cerium oxide films offer new opportunities in view of obtaining modifications of the material properties, and in particular for the stabilization of metastable structural phases. This last issue has been investigated also in a rather recent theoretical investigation aimed at identifying the

Fig. 4.4 STM images
showing the different stages
of formation of c-Ce$_2$O$_3$ films
on Cu(111). **a** CeO$_2$ buffer,
b CeO$_2$ buffer with
subsequent metallic Ce
deposition, **c** ordered c-Ce$_2$O$_3$
layer obtained by annealing
(**b**) in vacuum at 900 K. *Inset*
high-resolution image and
surface unit cell (*red
rhombus*) of the c-Ce$_2$O$_3$
layer. Images **a**–**c** are to scale.
Image width **a**, **b** 60 nm,
c 120 nm, *Inset* 6 × 6 nm^2.
Reprinted with permission
from Stetsovych et al. [55].
Copyright 2013, American
Chemical Society (Color
figure online)
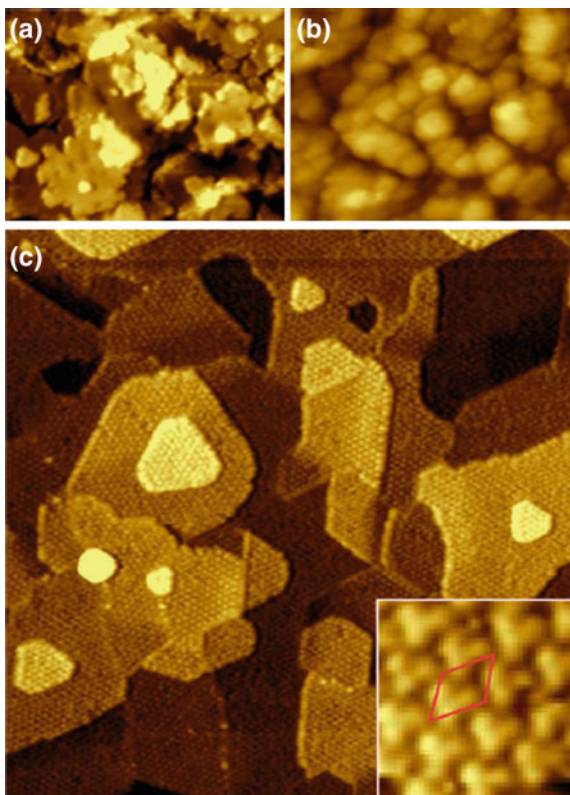
most stable Ce$_2$O$_3$ structures at the ultrathin limit [56]. The work, using simulated
mechanical annealing searches and DFT calculations, shows that different ultrathin
film structures are stable at different values of the in plane lattice parameter and it
identifies in particular a new structure, which does not correspond to any known
bulk crystalline polymorph, which is more stable than the A-type and than the
c-type Ce$_2$O$_3$ structures at specific, relatively large, in-plane lattice parameters
(Fig. 4.5) [56].

As mentioned at the beginning of this section, a few studies have also been
focused on the stabilization of ultrathin cerium oxide films exposing surfaces dif-
ferent from the (111) on metal substrates. For example, the stabilization of cerium
oxide nanoislands exposing (100) facets, with thickness down to 1 ML, has been
shown to be possible using a Cu(111) surface and highly oxidizing growth con-
ditions [57]. The stabilization mechanism invoked is the formation of a copper
oxide with a rectangular unit cell at the interface, which imposes an epitaxial
constraint and shares an O layer with cerium oxide to compensate polarity (Fig. 4.6)
[57]. On the same substrate the presence of an interfacial CeO$_2$(100) layer sup-
porting three dimensional CeO$_2$ nanoislands with (100) surface orientation has also
been observed to coexist with the (111) CeO$_2$ orientation [58].
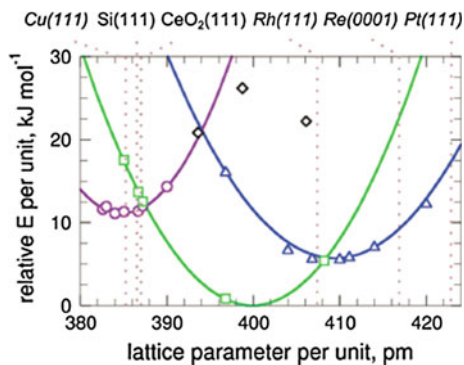
Fig. 4.5 Results of DFT calculations for 4 ML Ce_2O_3 films with different structure: A-type (*circles*), bixbyite (*squares*) NF1 (*triangles*), NF2–4 (*diamonds*). Energies (relative to that of the optimized bixbyite film) and lattice parameters are given per Ce_2O_3 unit. *Vertical dotted lines* indicate lattice parameters of possible supports for film growth (multiplied by 3/2 for transition metals—highlighted by *italics*). Kozlov et al. [56]. Published by The Royal Society of Chemistry

Fig. 4.6 High resolution STM images of $CeO_2(100)$ phases prepared by Ce deposition in 5×10^{-7} mbar of O_2 at 650 K on a copper oxide surface, formed by oxidizing Cu(111) with NO_2 at 600 K. The large-scale images with size 40×40 nm^2 is shown in the derivative mode. Reprinted with permission from Yang et al. [57]. Copyright 2011 American Chemical Society
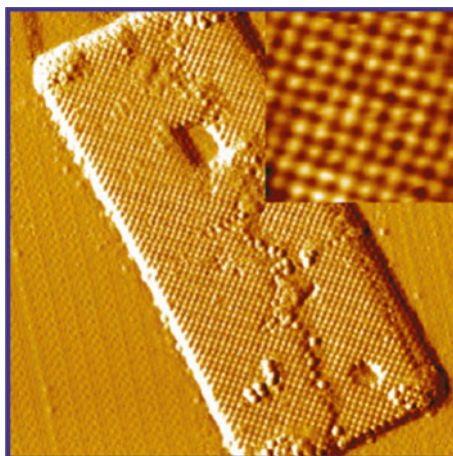
A recent study pointed out the formation of ceria nanocrystallites exposing (100) facets after thermal treatments in vacuum of continuous (111) cerium oxide films grown on Ru(0001) [59]. The nanostructures, of nanometric height and several tens of nm lateral size, compensate their polarity through surface reconstructions similar to those hypothesized for the bulk (100) orientation [11]. Open aspects which may contribute to a better understanding of less stable surfaces, also in view of preparing two-dimensional films with less stable orientation, are the understanding of the mechanisms which preferentially stabilize this phase under highly reducing conditions compared to other phases, and the possible reasons for the existence of the (001) orientation only at relatively large heights of a few nm.

Although studies of cerium oxide films exposing less stable surfaces at the two-dimensional limit are in general rather scarce, they have a great potential interest in view of the expected smaller surface oxygen vacancy formation energy, due to the lower coordination of surface O atoms. Furthermore, the possible formation of new structural phases driven by the compensation of polarity at reduced dimensionality may also open up new perspectives, in analogy with the case of non-reducible oxides [60].

4.3 Titanium Oxide Two-Dimensional Films

Titanium oxide is another case study for reducible oxides. Unlike cerium ions which are stable only in the 3+ and 4+ oxidation states, titanium ions can have different oxidation states, the most common ones being Ti^{2+}, Ti^{3+}, Ti^4, giving rise to various oxides. The most stable oxide is TiO_2, also known as *titania*, which can present different structural phases, the most important ones being rutile, anatase and brookite.

Ultrathin titanium oxide films grown on metal substrates have been the subject of extensive research over the last twenty years, as they can give rise to novel nanostructures and to a rich variety of phases which have been studied using surface science techniques. Stoichiometric and non-stoichiometric phases with different atomic structures can be obtained through the growth on single crystal metal surfaces, using simple experimental procedures: deposition of Ti in a vacuum chamber in controlled pressure of residual oxygen, i.e. reactive deposition, post-oxidation of Ti metal films, reduction in vacuum by heating the films in UHV or in controlled residual hydrogen pressure. A selection of results reported in the literature, with focus on peculiar properties arising at two-dimensions and in particular on reducibility-related issues, are hereby reported and discussed.

Experiments on titanium oxide ultrathin films grown on Cu(100) were carried out by different groups [61–63]. Maeda et al. [61] deposited metallic Ti on the Cu surface previously exposed to O_2 (P = 1 × 10⁻⁶ mbar at T = 330 K), and oxidized the resulting film by post-growth O_2 dosage (P = 1 × 10⁻⁷ mbar at T = 623 K). A two-dimensional growth of an $O^{2-}/Ti^{4+}/O^{2-}$ trilayer with TiO_2 stoichiometry was deduced from XPS data. LEED patterns showed a hexagonal geometry with two domains rotated by 90° with respect to each other, and an in-plane lattice constant of 0.29 nm. The study also indicates that this phase is unstable for coverages beyond a single $O^{2-}/Ti^{4+}/O^{2-}$ trilayer. The model proposed by Maeda et al. [61] for the atomic geometry of the trilayer is analogous to the one deduced for the quasi-hexagonal structure formed by titanium oxide on the oxidized (110) surface of the NiTi alloy [64]. A quasi-hexagonal phase was also observed for titanium oxide films obtained by reactive deposition of Ti (P = 1 × 10⁻⁶ mbar, T = 573 K) on Cu(100) previously saturated with chemisorbed oxygen [63, 65]. The chemisorption resulted in a $(\sqrt{2} \times 2\sqrt{2})$ $R45°$ LEED pattern with Cu missing-row reconstruction. At low Ti coverage (θ_{Ti} < 0.5 ML) the same group observed a LEED pattern with a centred

rectangular unit cell indicated as c-($\sqrt{2}$ × $\sqrt{2}$) $R45°$. STM data showed that the rectangular phase is associated with flat islands of uniform thickness, embedded within the outermost layer of the substrate. The stabilization of this phase is probably favoured by the missing-row reconstruction of the O-Cu(100) surface used as substrate [63, 65]. The quasi-hexagonal phase is observed at $\theta_{Ti} > 0.5$ ML (Fig. 4.7), however when the whole substrate surface is covered by the film ($\theta_{Ti} = 2.0$ ML) a regular hexagonal pattern is visible in the LEED, very similar to the one observed by Maeda et al. [61] An in-deep X-ray photoelectron diffraction (XPD) and LEED intensity analysis of the quasi-hexagonal phase, compared with DFT calculations, confirmed the O-Ti-O trilayer model, allowing to identify also the specific registry of the titanium oxide film with respect to the Cu(100) surface (Fig. 4.7) [65]. Interestingly, DFT provided also information about the electronic properties of the film, showing that the O $2p$ and Cu 4 sp states overlap and that the film does not show an insulating behaviour because of an upshift of the O $2p$ bands and a downshift of the Ti $4s$ states, compared to the case of the ideal unsupported films.

A TiO$_2$ lepidocrocite-like structure was instead obtained at submonolayer coverage when the substrate used for the growth was Ag(100) [66]. Again, LEED, XPD and STM experiments results were compared with the results of DFT calculations. At coverages higher than 1 ML, islands with the rutile (110) surface begin to form [67]. Single domain titania nano-sheets with lepidocrocite structure were also observed when TiO$_2$ films were grown on the (1 × 2) Pt(110) surface [68].

Rutile TiO$_2$ (110) films were also observed to grow on W(100) [69, 70] and O(2 × 1)-W(100) [71] in two orthogonal domains along the W[010] and [001] directions. In the first case, the TiO$_2$ films at coverage values between 5 and 30 ML

Fig. 4.7 a LEED pattern observed on a TiO$_2$ film with the quasi-hexagonal structure on the Cu(001) surface. **b** Atomistic model of the quasi-hexagonal phase of the O-Ti-O trilayer, with a rectangular $p(2 × 7)$ unit cell, showing the registry of the film with the substrate. Reprinted with permission from Atrei et al. [65]. Copyright 2009 American Chemical Society
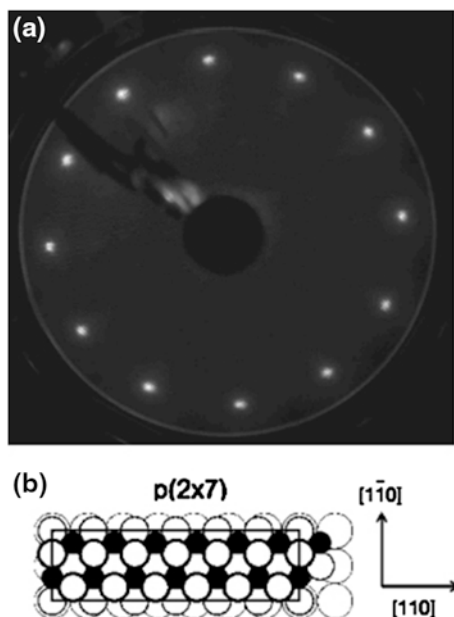
reverted to the bulk structure, and a systematic splitting of the spots in the LEED pattern was attributed to the formation of a stepped surface, probably caused by a strain relaxation mechanism due to the compression of the long axis of the TiO_2 unit cell. In the case of oxygen-reconstructed W(100) surface, STM images showed the formation of titanium oxide islands at low coverage following the orientation of the original missing rows induced by the O(2 × 1) reconstruction (Fig. 4.8). At increasing coverage, the islands extend and become higher, but TiO_2 does not form a continuous film. The presence of point defects on the rutile islands, characteristic of the native rutile TiO_2(110)-(1 × 1) surface was observed in high resolution STM images. TiO_2 was also grown by reactive deposition and annealing on Mo(100) [72, 73]. At coverage values below 10 nm, LEED showed a $(2\sqrt{2} \times \sqrt{2})$ $R45°$ pattern, while STM images showed ordered atomic rows along the [010] and [001] substrate direction. Annealing procedures allowed reduction of the film, with the Ti ions oxidation state changing from Ti^{4+} only, to a mixture of Ti^{4+}, Ti^{3+} and Ti^{2+} valence states, as evidenced by XPS. Similar studies were carried out also on Mo(110) [74, 75], on which films of TiO_2 with (100) orientation or Ti_2O_3(0001) were obtained, depending on the preparation method. In particular the Ti_2O_3(0001) phase was stabilized by initial deposition of a metallic Ti layer on the Mo(110) surface, followed by reactive Ti growth in O_2 in the same conditions, which lead to the formation of the TiO_2(100) phase [74]. STM images evidenced smooth surfaces with distinct flat terraces and well-defined step edges after annealing in O_2 at T = 900–1100 K, while XPS data showed that the oxide films remained partially reduced after the treatment. In contrast, thin films annealed in oxygen at T = 1200 K were fully oxidized but they exhibited a three-dimensional rough surface morphology [75].

Fig. 4.8 STM image of a 0.2 ML film of TiO_x(110) on W(100)-O(2 × 1). An area of TiO_x(110) and an area of the W(100)-O(2 × 1) substrate are indicated. *White lines* are drawn over some of the W (100)-O(2 × 1) rows then duplicated, *in black*, over the TiOx rows to highlight the similar periodicity. The crystal directions correspond to those of the W(100) substrate. Reprinted with permission from Pang et al. [71]. Copyright 2013 American Chemical Society
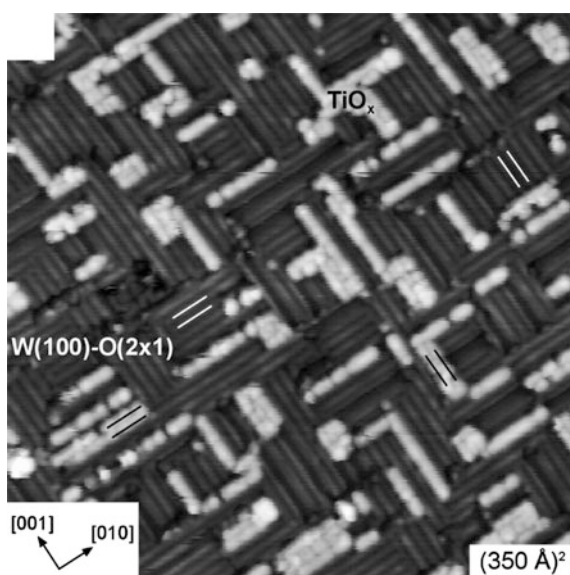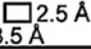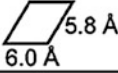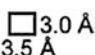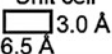
The same group also reported formation of a well-ordered (8 × 2) TiO_x film on Mo(112), obtained by depositing Ti on SiO_2(ML)/Mo(112) followed by oxidation/annealing and a final anneal at 1400 K to completely remove residual Si [76]. This phase shows peculiar properties, including a strong interaction with Au, which allowed a complete wetting of its surface, at variance with other oxide supports [71, 76].

Using a Ni(110) substrate for titanium oxide ultrathin films growth either a quasi-hexagonal phase or (110) rutile rods on a TiO_2 wetting layer could be obtained, depending on the initial titanium coverage [78, 79]. In both cases, XPS and x-ray absorption near edge spectroscopy (XANES) results demonstrated that Ti was fully oxidized. Figure 4.9 gives a summary of the TiO_2 phases reported in [76]. The rutile and wetting layer phases showed a similar behaviour with respect to exposure to water at $P = 10^{-8}$ mbar, which resulted in coadsorption of both molecular water and hydroxyl groups. By dosing water at $P = 10^{-6}$ mbar hydroxylation of the thin films was observed. The process was found to be reversible by annealing at $T = 490$ K. STM images on rutile rods revealed a (1 × 2) reconstruction in some areas, ascribed to a reduced phase, very close to the one observed on the surface of bulk rutile TiO_2(110) single crystals [79]. The (1 × 2) islands disappear completely after annealing at $T = 773$ K in O_2 [79]. Further reduction of the surface could be induced by annealing in UHV at $T = 1110$ K, with observation of {132} and {121} families of crystallographic shear planes. In this respect the behaviour of ultrathin films is analogous to the one of the TiO_2 (110) single crystal surface [80].

The study of titanium oxide films on Pt surfaces is particular relevant, in view of a deeper understanding of the phases formed in oxide-supported metal catalysts as a consequence of SMSI [8]. Experiments of Pt nanoparticles grown on TiO_2(110)

Fig. 4.9 Summary of the TiO_2 phases grown on Ni (110). Reprinted with permission from Papageorgiou et al. [78]. Copyright 2007 American Chemical Society

surface revealed that the (111) oriented Pt islands were encapsulated within TiO_2 regular films after annealing at T = 1100 K with a subsequent change of the catalytic activity [81]. The encapsulation was observed and studied in detail also in the case of Pd on (1 × 2) TiO_2(110) [82]. Some of the structures obtained in these systems were also observed on the reverse catalyst model TiO_x/Pt systems.

Matsumoto et al. used a number of experimental techniques for a complete study of titanium oxide grown on Pt(100) [77, 83]. In particular, two different routes for film synthesis were used: in the first one a Pt_3Ti surface alloy was oxidized with O_3 and annealed at T = 1000 K. The result was a smooth film composed of one layer of Ti_2O_3 with (3 × 5) superstructure, with flat terraces without islands, and with a structure similar to the (1 × 2) strands formed on the reduced TiO_2(110) surface. The second route was reactive deposition of Ti in O_2 (P = 6.7 × 10^{-7} mbar) followed by annealing above 750 K in vacuum. In this case, a (3 × 5) structure could be observed for coverages lower than 1 ML, while a (4 × 3$\sqrt{5}$)$R60°$ structure was obtained after deposition of 2 ML. The proposed model for the observed reconstruction consists of TiO_2 tetragonal nets with some O atoms in the second layer. The (3 × 5) structure was re-obtained after annealing above 950 K in vacuum. At increasing coverage and after annealing a T = 1000 K, TiO_2 clusters were observed, coexisting with Ti_2O_3 (3 × 5) and clean Pt(100) domains. Finally, after further annealing at T = 1300 K the TiO_2 clusters decomposed to form a (2$\sqrt{2}$ × 2$\sqrt{2}$)$R45°$ structure, proposed to be Ti_5O_8, and (3 × 5) domains.

Boffa et al. [84] investigated titanium oxide films grown on Pt(111) for coverages ranging from 1 to 5 ML. Two different structures were obtained depending on the sample pretreatment. In particular, annealing at temperatures between 770 and 970 K in O_2 gave a ($\sqrt{3}$ × $\sqrt{43}$)$R7.6°$ three fold symmetric structure, with TiO_2 stoichiometry and primitive cell 18.2 Å × 18.2 Å size. Annealing in vacuum (820–1120 K) gave a second ordered overlayer with primitive cell of 18.2 Å × 13.9 Å size and Ti_4O_7 stoichiometry. Partial dissolution of Ti in Pt was observed after annealing at high temperatures, reducing the thickness of the films to approximately 1 ML [84].

A systematic work on titanium oxide films grown on Pt(111) was carried out during the last years [85–90]. The study first concentrated in ultrathin layers, with an amount of Ti lower than 1.2 MLE, where 1 MLE corresponds to the surface density of Pt atoms per unit area on the Pt(111) surface. By varying the Ti dose and the annealing conditions (temperature and oxygen pressure) six metastable phases with different long-range order were originally found [85]. The conditions leading to the different phases are summarized in Fig. 4.10.

The different phases are identified by the geometry of the surface structures observed in atomically resolved STM images. Some of the observed structures include reduced titanium ions. Upon thermal treatments the films could undergo some structural transformations while in O_2-rich and O_2-poor conditions reversible film oxidation and reduction were observed (Fig. 4.10). All the identified phases, with the exception of the stoichiometric TiO_2 phase with rectangular surface symmetry, correspond to a film composed of a Ti-O bilayer, with interfacial Ti. The TiO_x phases wet the Pt substrate, and present long-range order with complex

$$\text{Pt(111)} + 0.4 \text{ MLE Ti} + O_2 \xrightarrow{823\,K,\, p_{O_2} = 10^{-3}...10^{-6}\,Pa} k\text{-}TiO_x/\text{Pt(111)} \quad (1)$$

$$\text{Pt(111)} + 0.8 \text{ MLE Ti} + O_2 \xrightarrow{823\,K,\, p_{O_2} = 10^{-5}\,Pa} z\text{-}TiO_x/\text{Pt(111)} \quad (2)$$

$$\text{Pt(111)} + 0.8 \text{ MLE Ti} \xrightarrow{673\,K,\, p_{O_2} < 10^{-8}\,Pa} z'\text{-}TiO_x/\text{Pt(111)} \quad (3)$$

$$\text{Pt(111)} + 0.8 \div 1.2 \text{ MLE Ti} + O_2 \xrightarrow{973\,K,\, p_{O_2} = 10^{-4}\,Pa} rect\text{-}TiO_2/\text{Pt(111)} \quad (4)$$

$$\text{Pt(111)} + 1.2 \text{ MLE Ti} + O_2 \xrightarrow{823\,K,\, p_{O_2} = 10^{-5}\,Pa} w\text{-}TiO_x/\text{Pt(111)} \quad (5)$$

$$\text{Pt(111)} + 1.2 \text{ MLE Ti} \xrightarrow{723\,K,\, p_{O_2} < 10^{-8}\,Pa} w'\text{-}TiO_x/\text{Pt(111)} \quad (6)$$

$$w\text{-}TiO_x \xrightarrow{723\,K,\, p_{O_2} < 10^{-8}\,Pa} w'\text{-}TiO_x \quad (7)$$

$$w'\text{-}TiO_x + O_2 \xrightarrow{823\,K,\, p_{O_2} = 10^{-5}\,Pa} w\text{-}TiO_x \quad (8)$$

$$z\text{-}TiO_x \xrightarrow{673\,K,\, p_{O_2} < 10^{-8}\,Pa} z'\text{-}TiO_x \quad (9)$$

$$z'\text{-}TiO_x + O_2 \xrightarrow{823\,K,\, p_{O_2} = 10^{-4}\,Pa} z\text{-}TiO_x \quad (10)$$

$$z\text{-}TiO_x + O_2 \xrightarrow{973\,K,\, p_{O_2} = 10^{-4}\,Pa} rect\text{-}TiO_2 \quad (11)$$

$$rect\text{-}TiO_2 \xrightarrow{823\,K,\, p_{O_2} < 10^{-8}\,Pa} k\text{-}TiO_x + z\text{-}TiO_x \quad (12)$$

$$k\text{-}TiO_x \xrightarrow{873\,K,\, p_{O_2} < 10^{-8}\,Pa} z'\text{-}TiO_x \quad (13)$$

Fig. 4.10 a Summary of the different ultrathin titanium oxide phases obtained on Pt(111) in different conditions. *k* stands for *kagomè*, *z* for *zig-zag*, *rect* for *rectangular* and *w* for *wagon-wheels*. **b** Summary of the structural and chemical transitions observed to occur under different thermal treatment conditions. The prime symbol indicates a reduced phase. Reprinted with permission from Sedona et al. [85]. Copyright 2005 American Chemical Society

superstructures, observed in LEED patterns. The combination of LEED, XPD and STM data with DFT calculations allowed to identify the atomic geometry of all the studied phases [88]. For instance, the *z*-phase has an incommensurate unit cell with 6.8 Å × 8.6 Å size, and a Ti_6O_8 geometry, while the *z'*-phase has a commensurate unit cell of 16.6 Å × 14.4 Å size (with $Ti_{24}O_{30}$), geometry (Fig. 4.11). Ti *2p* and O*1s* core level XPS and valence band photoemission studies [86] allowed also to separate the observed phases in two main groups: a group of three stoichiometric films (*k', rect* and *rect'*) and a group of sub-stoichiometric films (*z, z' and w*). The valence band photoemission data also revealed some peculiar aspects of the electronic properties, like for instance the mixing of the Ti-Pt states near the Fermi level in the sub-stoichiometric films, a clear indication of the presence of the Pt-Ti interface in this group.

Another interesting phase is the stoichiometric TiO_2 *rect* phase, showing an incommensurate rectangular unit cell of size 3.8 Å × 3.0 Å. STM revealed also that the apparent height of the *rect*- TiO_2 islands can be only explained by a multilayer sequence, with oxygen atoms at the interface with Pt occupying only top and bridge sites, an arrangement similar to the one proposed for *rect* -VO_2 [89]. Recently, other reduced hexagonal phases $h(6 \times 6)$ and $h(9 \times 9)$ were discovered by annealing *z'* phases at high temperature [90].

Fig. 4.11 a Atomically
resolved image of the *z*- and
z'-TiO$_x$ phase on Pt(111).
b Simulated STM image and
structure of the *z'* phase, as
obtained by DFT calculations.
Reprinted with permission
from Barcaro et al. [88].
Copyright 2009 American
Chemical Society
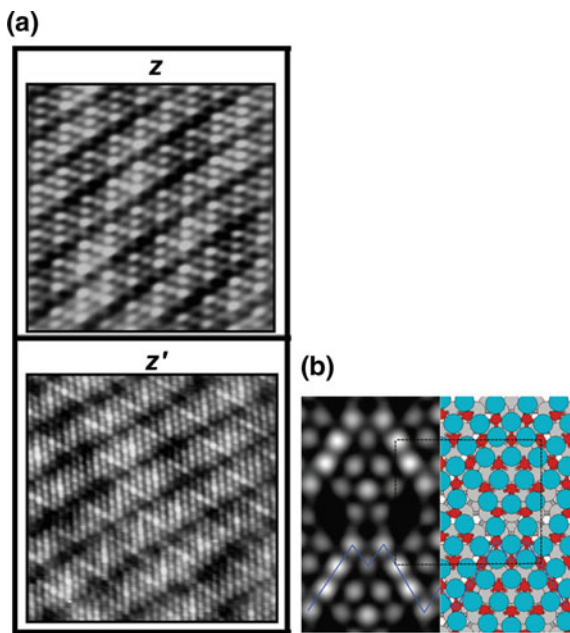
4.4 Two-Dimensional Films of Other Reducible Oxides

4.4.1 Transition Metal Oxide Two-Dimensional Films

Indeed, most transition metals, due to their specific electronic structure, can have
different oxidation states and can form oxides which are reducible. Within the wide
number of studies done in the field of two-dimensional reducible transition metal
oxide films, we will here focus on those reporting aspects strictly related to
reducibility and we will limit to the strictly two-dimensional case, i.e. to films with
thickness of the order or below 1 nm.

A very interesting example of a study of this kind is represented by the work by Li
et al. on manganese oxide two-dimensional films [91]. By STM, LEED and XPS
analyses different low dimensionality phases were identified in films of approxi-
mately 1 ML thickness as a function of the oxygen chemical potential during
preparation on a Pd(100) substrate. Figure 4.12 summarizes the obtained results.
Among the observed structures, some represent the two-dimensional limit of bulk
truncated structures, like the hexagonal structure observed under mildly oxidizing
condition, which recalls the MnO(111) structure. However, most of them do not
resemble any known manganese oxide phase and they are often found in coexistence
on the Pd surface [92].

Also vanadium cations in vanadium oxide can have different oxidation states
(from 2+ to 5+), giving a wide variety of phases. The most important ones are
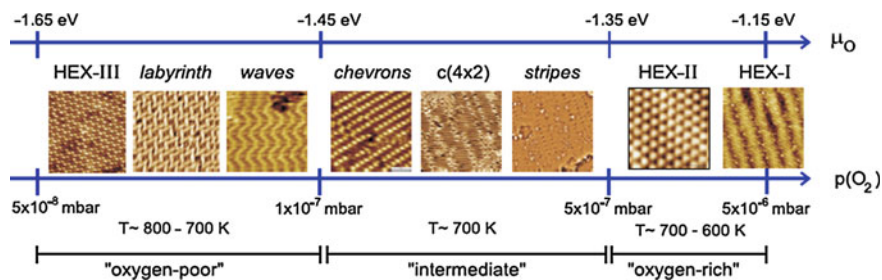
Fig. 4.12 Schematic phase diagram of the two-dimensional Mn oxides, presented as a function of the oxygen pressure $p(O_2)$ and of the oxygen chemical potential μ_O. The nominal coverage of Mn on Pd(100) is 0.75 ML. © IOP Publishing. Reproduced with permission from Li et al. [91]. All rights reserved

V_2O_5, VO_2, V_2O_3 and VO, each one having a different crystal structure and showing a variety of physical and chemical properties [92]. Furthermore, mixed valence oxides can also be formed, with the cations in two possible oxidation states, like for example V^{5+} and V^{4+} in V_6O_{13}. Of peculiar interest is the crystal structure of V_2O_5 (layered orthorhombic), which is essentially composed of zigzag double chains of square VO_5 pyramidal units sharing edges and running along the b direction. The VO_5 pyramid has the vanadium atom in the centre, four oxygen atoms in the basal plane and a vanadyl-type oxygen atom at the apex (see also inset of Fig. 4.13d). The layers of chains are stacked along the [0 0 1] (c) direction. The resulting solid is composed of distorted tetrahedrally coordinated VO_6 unit. The VO_6 unit is also present in the tetrahedral rutile and monoclinic phases of VO_2 which are stable below and above T = 340 K respectively, while the V_2O_3 phase has a corundum structure above 160 K. All these structures can be found in ultrathin films grown either on oxides or on metals, but other phases can also be stabilised by the interaction with the substrate [89, 92].

A systematic work was carried out on vanadium oxide nanostructures and films deposited on Rh(111) by Netzer and co-workers. The experimental results were supported by ab initio DFT calculations in order to obtain complete information the structure and on the thermodynamics of the different phases obtained [89, 93–96]. A phase diagram of the vanadium oxide nanostructures on Rh(111) is reported in Fig. 4.14. Concentrating on the two-dimensional phases, it was found that $(\sqrt{7} \times \sqrt{7})$R 19.1° or $(\sqrt{13} \times \sqrt{13})$R 13.8° structures can be formed under highly oxidative conditions, with $P_{O_2} = 2 \times 10^{-7}$ mbar and by keeping the substrate temperature at 670 K.

As obtained by careful analysis of STM images and by DFT calculations, the $(\sqrt{7} \times \sqrt{7})$R 19.1° nanolayer consists of a V_3O_9 oxide phase with VO_5 square pyramids as building blocks. The same holds for the $(\sqrt{13} \times \sqrt{13})$R 13.8° phase, which has a V_6O_{18} stoichiometry.

By exposing the film to reducing conditions (i.e. to annealing in UHV or in hydrogen atmosphere) reduced two-dimensional phases can be obtained with
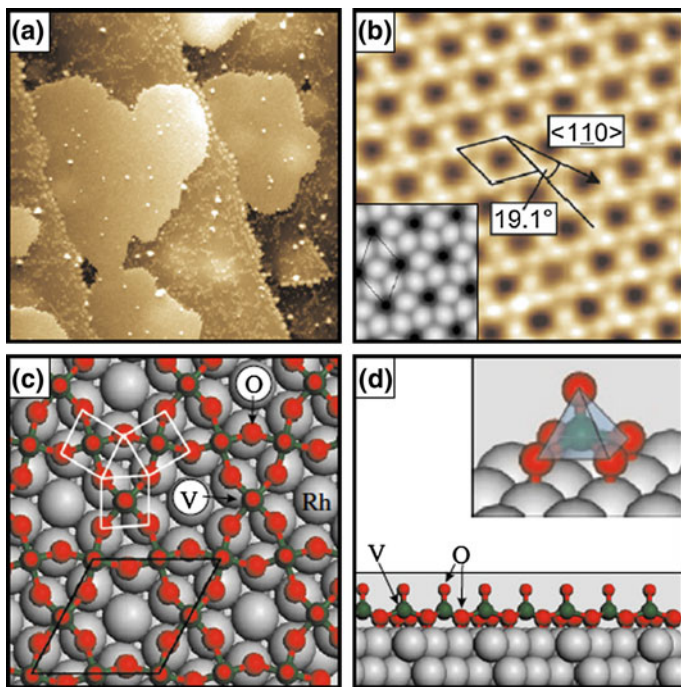
Fig. 4.13 **a** Large scale (100×100 nm^2) and **b** high resolution STM images of the ($\sqrt{7} \times \sqrt{7}$)R 19.1° vanadium oxide nanolayer on Rh(111). *Inset* simulated STM image obtained by DFT calculations. **c** *Top view* and **d** *side view* of the structural model obtained by DFT. *Inset* the VO$_5$ square pyramid constituting the building block of the film. © IOP Publishing. Reproduced with permission from Schoiswohl et al. [89]. All rights reserved

$V_{11}O_{23}$, $V_{13}O_{21}$, V_2O_3 and VO stoichiometry. The reduction process occurs essentially by removing the vanadyl groups.

Zero-dimensional structures could also be obtained by evaporation of small quantities (less than 0.2 ML) of vanadium on O(2×1)-Rh(111) and by flashing at 250 °C in UHV. The obtained structures are identical planar star-shaped V_6O_{12} molecules [96]. It was shown also that under high substrate temperature the clusters can diffuse and assemble in 2-D overlayers with well determined phases, like the (5×5) or the ($5 \times 3\sqrt{3}$)-rect. The different phases are obtained either in oxidizing or in reducing conditions [89].

Another interesting example is the growth of V_2O_y ($y \approx 5$) and V_2O_5 on Au(111) reported by the Freund group [97, 98]. The films were obtained by physical vapour deposition of vanadium, subsequent oxidation under 50 mbar of oxygen at 670 K and annealing in UHV at 470 K. The high oxygen pressure used allowed to obtain a high oxidation state (V^{5+}) even for films thicker than 1 MLE (1 MLE corresponding to the same number of V atoms as one layer of Au(111)), at variance with previous studies, where the standard reactive deposition and post-oxidation procedures gave
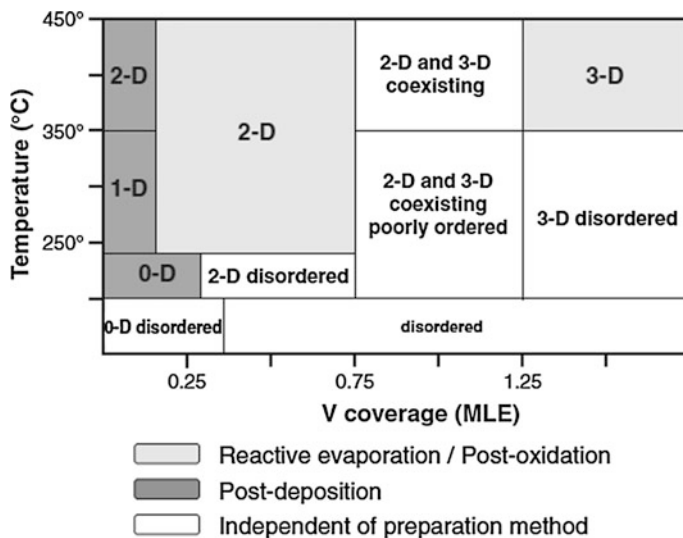
Fig. 4.14 Phase diagram of vanadium oxide nanostructures on Rh(111) as a function of vanadium coverage and of substrate temperature. © IOP Publishing. Reproduced with permission from Schoiswohl et al. [89].

V^{2+}, V^{3+} or V^{4+} states (see for example 89, 93, 99–101). At low coverage, from 0.26 to 1.04 MLE, two different coincidence monolayer structures could be observed by STM and LEED, which are determined by the interaction with the Au(111) substrate. The first structure has a rectangular unit cell, with size 3.6 Å × 15 Å, while the second one (observed at 0.52 MLE of V/Au(111) which correspond to one full layer of oxide film), has a 3.6 Å × 10.8 Å ($\alpha = 60°$) oblique unit cell. In analogy with the case of vanadium oxide monolayers on Rh(111) [89, 93–96], it was supposed that the full monolayer film consists of VO_5 pyramid building blocks sharing corners and edges at their bases, and on the basis of the XPS and XANES measurements it was also shown that the oxidation state in the V cations is close to V^{5+}, characteristic of V_2O_5. Increasing the coverage again to 1.05 MLE, a different structure was observed, which was found to be similar to V_6O_{13} with (001) orientation, while for higher coverage V_2O_5 islands were formed, extending in size and giving rise eventually to V_2O_5 (001) films containing a low number of point defects. These films were composed of large (20 nm size) single crystal domains with some azimuthal disorder (Fig. 4.15) [97].

4.4.2 Rare Earth Oxide Two-Dimensional Films

In analogy with cerium oxide also in other rare earth oxides (REOs), like praseodymium, terbium and samarium oxide the cations can have different oxidation states, and the oxides can be defined as reducible. For samarium oxide the most stable oxidation

Fig. 4.15 STM images of
a 100×100 nm^2,
b 44×20 nm^2 of a film
formed by the oxidation of
1.56 MLE V/Au(111). The
images show the presence of
V$_2$O$_5$(100) islands growing
on V$_6$O$_{13}$(001) film.
Reprinted with permission
from Guimond et al. [97].
Copyright 2008 American
Chemical Society
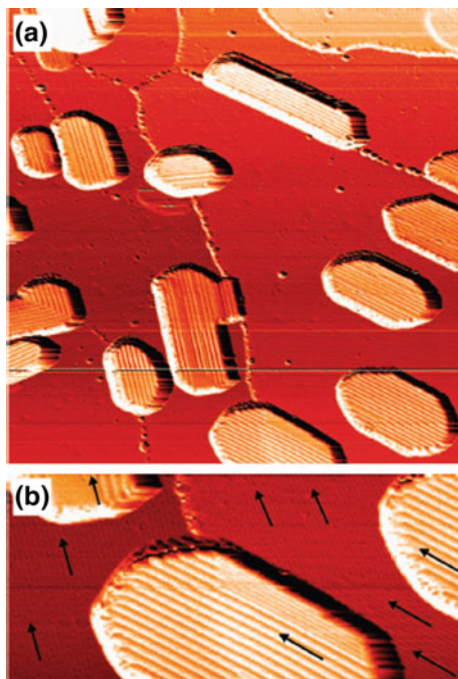
state is Sm$_2$O$_3$, which can form different structural phases. Samarium oxide is the only REO which can also form a monoxide, SmO, with a rock-salt structure, stable under reducing conditions. The most stable valence state for terbium is 3+ , leading to the Tb$_2$O$_3$ phase, however also the dioxide TbO$_2$, as well as intermediate phases like Tb$_4$O$_7$, can form. Praseodymium can be found in the 2+ , 3+ and 4+ oxidation states and the most stable oxides are Pr$_2$O$_3$, PrO$_2$ and Pr$_6$O$_{11}$. The sesquioxides are typically stable in the c-type bixbyite structure, at variance with cerium oxide, for which the hexagonal A-type phase is favoured in the Ce$_2$O$_3$ stoichiometry.

Some studies report the growth of REO in the form of ultrathin films on metallic substrates and point out interesting aspects related to those observed in cerium oxide ultrathin films. Temperature programmed desorption (TPD) allows to monitor oxygen release in these REO films, while in the case of cerium oxide the release is considered to be too fast to be monitored [102, 103].

Samarium oxide in the form of an ultrathin film has been shown to form by controlled oxidation of surface SmRh and SmRu surface alloys, in turn obtained by heating metallic Sm films deposited on Rh(100) and Ru(0001) surfaces respectively, leading to a SmO$_x$ phase [102–104]. On both substrates specific sites for CO absorption have been shown to form at the perimeter of the samarium oxide ultrathin islands, due to the interaction with the underlying metal [102, 103]. A more recent study by Jhang et al. investigated samarium oxide films grown on a Pt(111) substrate by reactive deposition at 600 K followed by annealing in O$_2$ (P $\sim 10^{-7}$ mbar) at 1000 K [105]. In close analogy with cerium oxide films grown

in similar conditions, the LEED pattern for submonolayer coverage shows a
(1.37 × 1.37) structure. Interestingly, for coverages between 1 and 3 ML the LEED
pattern shows additional faint spots in the so called quasi-(3 × 3) superstructure,
very similar to the one observed in reduced ultrathin cerium oxide phases on Pt
(111) (Fig. 4.16) [17, 29]. The authors ascribe these features to a Sm_2O_3(111) phase
with a defective fluorite structure, in which the oxygen vacancies are randomly
distributed within the crystal, and to the formation of a 8:11 coincidence with the
underlying Pt. A similar origin may be invoked also for the LEED pattern of
reduced cerium oxide films, although in the latter case a similar coincidence may be
expected also when the films are oxidized, and the reasons for its appearance only
when the films are reduced are not clear. Reduction by thermal treatments in UHV
at 1000 K for 30 min of the Sm_2O_3 films lead to the coexistence of Sm_2O_3(111)
phase and of a SmO(100) phase, giving a superstructure rotated by 30° with respect
to the (111) spots in the LEED pattern [105]. The reversibility of the structural and
morphological modifications is observed also in this case [105].

Terbium oxide films were prepared with similar methods, i.e. using reactive
deposition and post growth annealing in O_2 [106]. The LEED pattern up to 4 ML
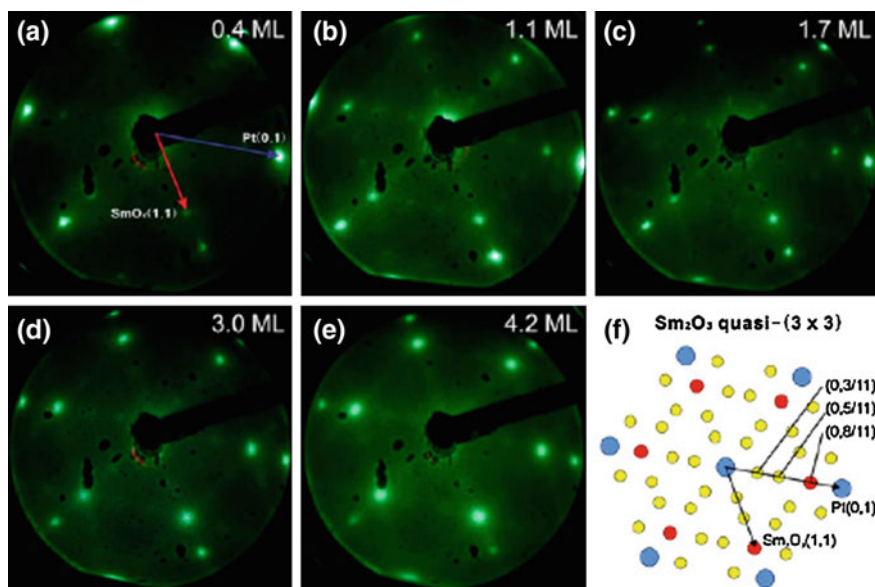
Fig. 4.16 LEED patterns obtained after growing Sm_2O_3(111) films of different coverages on
Pt(111), followed by annealing in 7×10^{-7} mbar of O_2 at 1000 K for 10 min: **a** 0.4 ML of Sm_2O_3
shows a hexagonal (1.37 × 1.37) superstructure in registry with the Pt(111) (1 × 1) spots,
E = 58 eV, **b** 1.1 ML, E = 48 eV, **c** 1.7 ML, E = 56 eV, **d** 3.0 ML, E = 52 eV exhibit a quasi-(3 × 3)
superstructure, **e** 4.2 ML, E = 56 eV; the quasi-(3 × 3) becomes blurry and **f** shows a schematic
representation of the quasi-(3 × 3) pattern that is determined from FFT analysis of a structural
model of superposed, hexagonal Sm and Pt lattices that form a hexagonal (8 × 8) coincidence
lattice with respect to the Sm lattice, i.e. (11 × 11) with respect to the Pt lattice. Reprinted with
permission from Jhang et al. [105]. Copyright 2013 American Chemical Society

thickness shows the (1.32×1.32) structure, compatible with the terbium oxide lattice parameter of the Tb_2O_3 phase in a fluorite structure with disordered oxygen vacancies in close analogy with the case of samarium oxide [107]. In this case however diffraction from possible coincidence superlattices could not be observed. The films could not be oxidized by using thermal treatments in O_2 at $P \sim 7 \times 10^{-7}$ mbar and temperatures from 95 to 1000 K, while plasma-generated atomic oxygen was shown to be effective in oxidizing a film at 300 K to TbO_2 and in generating weakly bound surface O species. The reduced Tb_2O_3 phase could be re-obtained by annealing TbO_2 in vacuum at 1000 K [106].

Praseodymium oxide has been studied only in the form of relatively thick films on Si(111) substrates [107–109]. As for terbium oxide thin films, also in this case, an oxidizing treatment in oxygen plasma was shown to be necessary to oxidize the Pr_2O_3 phase to the PrO_2 fluorite phase [107]. UHV thermal treatments to reduce the PrO_2 phase have been shown to give origin to a phase including a mixture of Pr_6O_{11} and Pr_5O_9, the latter being unstable in the bulk phase [109].

4.5 Conclusions

The studies discussed in this chapter show that reducible oxides at two dimensionality may show important modifications of their properties, and indeed also of the reversible reduction and oxidation processes. Ultrathin films, typically supported on metal substrates, at different degree of reduction show new structural and chemical phases, often unstable in the bulk, which have been deeply characterized by surface science techniques, combined with the extremely important support of theoretical modeling. In some cases the different phases can be reversibly transformed one into the other by reducing and oxidizing treatments. The studies point out interesting challenging aspects, on which future studies might be focused, such as for example the stabilization of phases with less stable surface orientation, or more complex systems such as ternary two-dimensional compounds or mixed oxide phases. We believe that investigations following these lines may open up unexpectedly interesting aspects within the field of reducible oxide based materials.

References

1. Trovarelli A, Fornasiero P (2013) Catalysis by ceria and related materials. Catalytic science, 2nd edn. Imperial College Pr., London
2. Celardo I, Pedersen JZ, Traversa E, Ghibelli L (2011) Pharmacological potential of cerium oxide nanoparticles. Nanoscale 3(4):1411–1420

3. Waser R, Dittmann R, Staikov G, Szot K (2009) Redox-based resistive switching memories—nanoionic mechanisms, prospects, and challenges. Adv Mater 21(25–26):2632

4. Migani A, Vayssilov GN, Bromley ST, Illas F, Neyman KM (2010) Dramatic reduction of the oxygen vacancy formation energy in ceria particles: a possible key to their remarkable reactivity at the nanoscale. J Mater Chem 20(46):10535–10546

5. Cafun JD, Kvashnina KO, Casals E, Puntes VF, Glatzel P (2013) Absence of Ce^{3+} sites in chemically active colloidal ceria nanoparticles. ACS Nano 7(12):10726–10732

6. Carrettin S, Concepcion P, Corma A, Nieto JML, Puntes VF (2004) Nanocrystalline CeO_2 increases the activity of an for CO oxidation by two orders of magnitude. Angew Chem Int Edit 43(19):2538–2540

7. Vayssilov GN, Lykhach Y, Migani A, Staudt T, Petrova GP, Tsud N, Skala T, Bruix A, Illas F, Prince KC, Matolin V, Neyman KM, Libuda J (2011) Support nanostructure boosts oxygen transfer to catalytically active platinum nanoparticles. Nat Mater 10(4):310–315

8. Tauster SJ, Fung SC, Garten RL (1978) Strong metal-support interactions—group-8 noble-metals supported on Tio_2. J Am Chem Soc 100(1):170–175

9. Bevan DJM (1955) Ordered intermediate phases in the system CeO_2-Ce_2O_3. J Inorg Nucl Chem 1:49

10. Skorodumova NV, Simak SI, Lundqvist BI, Abrikosov IA, Johansson B (2002) Quantum origin of the oxygen storage capability of ceria. Phys Rev Lett 89(16):166601

11. Conesa JC (1995) Computer modeling of surfaces and defects on cerium dioxide. Surf Sci 339(3):337–352

12. Hardacre C, Ormerod RM, Lambert RM (1994) Platinum-promoted catalysis by ceria—a study of carbon-monoxide oxidation over Pt(111)/CeO_2. J Phys Chem-Us 98(42):10901–10905

13. Schierbaum KD (1998) Ordered ultra-thin cerium oxide overlayers on Pt(111) single crystal surfaces studied by LEED and XPS. Surf Sci 399 (1):29–38-X

14. Mullins DR, Radulovic PV, Overbury SH (1999) Ordered cerium oxide thin films grown on Ru(0001) and Ni(111). Surf Sci 429(1–3):186–198

15. Eck S, Castellarin-Cudia C, Surnev S, Ramsey MG, Netzer FP (2002) Growth and thermal properties of ultrathin cerium oxide layers on Rh(111). Surf Sci 520(3):173–185

16. Wilson EL, Chen Q, Brown WA, Thornton G (2007) CO adsorption on the model catalyst Pd/$CeO_{2−x}$(111)/Rh(111). J Phys Chem C 111(38):14215–14222

17. Luches P, Pagliuca F, Valeri S (2011) Morphology, stoichiometry, and interface structure of CeO_2 ultrathin films on Pt(111). J Phys Chem C 115(21):10718–10726

18. Staudt T, Lykhach Y, Hammer L, Schneider MA, Matolin V, Libuda J (2009) A route to continuous ultra-thin cerium oxide films on Cu(111). Surf Sci 603(23):3382–3388

19. Xiao WD, Guo QL, Wang EG (2003) Transformation of CeO_2(111) to Ce_2O_3(0001) films. Chem Phys Lett 368(5–6):527–531

20. Lu JL, Gao HJ, Shaikhutdinov S, Freund HJ (2006) Morphology and defect structure of the CeO_2(111) films grown on Ru(0001) as studied by scanning tunneling microscopy. Surf Sci 600(22):5004–5010

21. Grinter DC, Ithnin R, Pang CL, Thornton G (2010) Defect structure of ultrathin ceria films on Pt(111): atomic views from scanning tunnelling microscopy. J Phys Chem C 114(40):17036–17041

22. Flege JI, Kaemena B, Gevers S, Bertram F, Wilkens T, Bruns D, Batjer J, Schmidt T, Wollschlager J, Falta J (2011) Silicate-free growth of high-quality ultrathin cerium oxide films on Si(111). Phys Rev B 84(23):235418

23. Pagliuca F, Luches P, Valeri S (2013) Interfacial interaction between cerium oxide and silicon surfaces. Surf Sci 607:164–169

24. Putna ES, Bunluesin T, Fan XL, Gorte RJ, Vohs JM, Lakis RE, Egami T (1999) Ceria films on zirconia substrates: models for understanding oxygen-storage properties. Catal Today 50 (2):343–352

25. vanWijck MAAM, Verhoeven MAJ, Reuvekamp EMCM, Gerritsma GJ, Blank DHA, Rogalla H (1996) CeO_2 as insulation layer in high T-c superconducting multilayer and crossover structures. Appl Phys Lett 68(4):553–555

26. Overbury SH, Huntley DR, Mullins DR, Ailey KS, Radulovic PV (1997) Surface studies of model supported catalysts: NO adsorption on Rh/CeO_2(001). J Vac Sci Technol A 15 (3):1647–1652

27. Hardacre C, Roe GM, Lambert RM (1995) Structure, composition and thermal-properties of cerium oxide-films on platinum(111). Surf Sci 326(1–2):1–10

28. Berner U, Schierbaum KD (2002) Cerium oxides and cerium-platinum surface alloys on Pt (111) single-crystal surfaces studied by scanning tunneling microscopy. Phys Rev B 65 (23):235404

29. Luches P, Pagliuca F, Valeri S (2014) Structural and morphological modifications of thermally reduced cerium oxide ultrathin epitaxial films on Pt(111). Phys Chem Chem Phys 16(35):18848–18857

30. Matolin V, Libra J, Matolinova I, Nehasil V, Sedlacek L, Sutara F (2007) Growth of ultra-thin cerium oxide layers on Cu(111). Appl Surf Sci 254(1):153–155

31. Yang F, Graciani J, Evans J, Liu P, Hrbek J, Sanz JF, Rodriguez JA (2011) CO oxidation on inverse $CeOx/Cu$(111) catalysts: high catalytic activity and ceria-promoted dissociation of O-2. J Am Chem Soc 133(10):3444–3451

32. Ma SG, Rodriguez J, Hrbek J (2008) STM study of the growth of cerium oxide nanoparticles on Au(111). Surf Sci 602(21):3272–3278

33. Škoda M, Libra J, Šutara F, Tsud N, Skála T, Sedláček L, Cháb V, Prince KC, Matolín V (2007) A resonant photoemission study of the Ce and Ce-oxide/Pd(1 1 1) interfaces. Surf Sci 601(21):4958–4965

34. Grinter DC, Yim CM, Pang CL, Santos B, Mentes TO, Locatelli A, Thornton G (2013) Oxidation state imaging of Ceria island growth on Re(0001). J Phys Chem C 117(32):16509–16514

35. Suchorski Y, Wrobel R, Becker S, Weiss H (2008) CO oxidation on a $CeOx/Pt$(111) inverse model catalyst surface: catalytic promotion and tuning of kinetic phase diagrams. J Phys Chem C 112(50):20012–20017

36. Eck S, Castellarin-Cudia C, Surnev S, Prince KC, Ramsey MG, Netzer FP (2003) Adsorption and reaction of CO on a ceria–Rh(1 1 1) "inverse model catalyst" surface. Surf Sci 536(1–3):166–176

37. Rodriguez JA, Graciani J, Evans J, Park JB, Yang F, Stacchiola D, Senanayake SD, Ma S, Pérez M, Liu P, Sanz JF, Hrbek J (2009) Water-gas shift reaction on a highly active inverse $CeOx/Cu$(111) catalyst: unique role of ceria nanoparticles. Angew Chem Int Ed 48 (43):8047–8050

38. Dvorak F, Stetsovych O, Steger M, Cherradi E, Matolinova I, Tsud N, Skoda M, Skala T, Myslivecek J, Matolin V (2011) Adjusting morphology and surface reduction of CeO_2(111) thin films on Cu(111). J Phys Chem C 115(15):7496–7503

39. Luches P, Pagliuca F, Valeri S, Boscherini F (2013) Structure of ultrathin CeO_2 films on Pt (111) by polarization-dependent X-ray absorption fine structure. J Phys Chem C 117 (2):1030–1036

40. Szabova L, Stetsovych O, Dvorak F, Camellone MF, Fabris S, Myslivecek J, Matolin V (2012) Distinct physicochemical properties of the first ceria monolayer on Cu(111). J Phys Chem C 116(11):6677–6684

41. Spiel C, Blaha P, Suchorski Y, Schwarz K, Rupprechter G (2011) CeO_2/Pt(111) interface studied using first-principles density functional theory calculations. Phys Rev B 84 (4):045412

42. Nilius N, Kozlov SM, Jerratsch JF, Baron M, Shao X, Vines F, Shaikhutdinov S, Neyman KM, Freund HJ (2012) Formation of one-dimensional electronic states along the step edges of CeO_2(111). ACS Nano 6(2):1126–1133

43. Torbrugge S, Cranney M, Reichling M (2008) Morphology of step structures on CeO(2) (111). Appl Phys Lett 93(7):073112

44. Jerratsch JF, Shao X, Nilius N, Freund HJ, Popa C, Ganduglia-Pirovano MV, Burow AM, Sauer J (2011) Electron localization in defective ceria films: a study with scanning-tunneling microscopy and density-functional theory. Phys Rev Lett 106(24):246801
45. Esch F, Fabris S, Zhou L, Montini T, Africh C, Fornasiero P, Comelli G, Rosei R (2005) Electron localization determines defect formation on ceria substrates. Science 309 (5735):752–755
46. Ganduglia-Pirovano MV, Da Silva JLF, Sauer J (2009) Density-functional calculations of the structure of near-surface oxygen vacancies and electron localization on $CeO_2(111)$. Phys Rev Lett 102(2):026101
47. Loschen C, Bromley ST, Neyman KM, Illas F (2007) Understanding ceria nanoparticles from first-principles calculations. J Phys Chem C 111(28):10142–10145
48. Kaemena B, Senanayake SD, Meyer A, Sadowski JT, Falta J, Flege JI (2013) Growth and morphology of ceria on ruthenium (0001). J Phys Chem C 117(1):221–232
49. Pfau A, Schierbaum KD (1994) The electronic-structure of stoichiometric and reduced Ceo_2 surfaces—an Xps, Ups and Hreels. Study Surf Sci 321(1–2):71–80
50. Matolin V, Libra J, Skoda M, Tsud N, Prince KC, Skala T (2009) Methanol adsorption on a $CeO_2(111)/Cu(111)$ thin film model catalyst. Surf Sci 603(8):1087–1092
51. Senanayake SD, Stacchiola D, Evans J, Estrella M, Barrio L, Perez M, Hrbek J, Rodriguez JA (2010) Probing the reaction intermediates for the water-gas shift over inverse $CeOx/Au(111)$ catalysts. J Catal 271(2):392–400
52. Castellarin-Cudia C, Surnev S, Schneider G, Podlucky R, Ramsey MG, Netzer FP (2004) Strain-induced formation of arrays of catalytically active sites at the metal-oxide interface. Surf Sci 554(2–3):L120–L126
53. Duchon T, Dvorak F, Aulicka M, Stetsovych V, Vorokhta M, Mazur D, Veltruska K, Skala T, Myslivecek J, Matolinova I, Matolin V (2014) Ordered phases of reduced ceria as epitaxial films on Cu(111). J Phys Chem C 118(1):357–365
54. Wilkens H, Schuckmann O, Oelke R, Gevers S, Reichling M, Schaefer A, Baumer M, Zoellner MH, Niu G, Schroeder T, Wollschlager J (2013) Structural transitions of epitaxial ceria films on Si(111). Phys Chem Chem Phys 15(42):18589–18599
55. Stetsovych V, Pagliuca F, Dvorak F, Duchon T, Vorokhta M, Aulicka M, Lachnitt J, Schernich S, Matolinova I, Veltruska K, Skala T, Mazur D, Myslivecek J, Libuda J, Matolin V (2013) Epitaxial Cubic Ce_2O_3 films via Ce-CeO_2 interfacial reaction. J Phys Chem Lett 4(6):866–871
56. Kozlov SM, Demiroglu I, Neyman KM, Bromley ST (2015) Reduced ceria nanofilms from structure prediction. Nanoscale 7(10):4361–4366
57. Yang F, Choi Y, Agnoli S, Liu P, Stacchiola D, Hrbek J, Rodriguez JA (2011) CeO_2 < - > $CuOx$ interactions and the controlled assembly of $CeO_2(111)$ and $CeO_2(100)$ nanoparticles on an oxidized Cu(111) substrate. J Phys Chem C 115(46):23062–23066
58. Stetsovych O, Beran J, Dvorak F, Masek K, Myslivecek J, Matolin V (2013) Polarity driven morphology of $CeO_2(100)$ islands on Cu(111). Appl Surf Sci 285:766–771
59. Pan Y, Nilius N, Stiehler C, Freund HJ, Goniakowski J, Noguera C (2014) Ceria nanocrystals exposing wide (100) facets: structure and polarity compensation. Adv Mater Interfaces 1(9):1400404
60. Noguera C, Goniakowski J (2013) Polarity in oxide nano-objects. Chem Rev 113(6):4073–4105
61. Maeda T, Kobayashi Y, Kishi K (1999) Growth of ultra-thin titanium oxide on Cu(100), Fe/Cu(100) and ordered ultra-thin iron oxide studied by low-energy electron diffraction and X-ray photoelectron spectroscopy. Surf Sci 436(1–3):249–258
62. Passeggi MCG, Vergara LI, Mendoza SM, Ferron J (2002) Passivation and temperature effects on the oxidation process of titanium thin films. Surf Sci 507:825–831
63. Finetti P, Caffio M, Cortigiani B, Atrei A, Rovida G (2008) Mechanism of growth and structure of titanium oxide ultrathin films deposited on Cu(001). Surf Sci 602(5):1101–1113
64. Atrei A, Bardi U, Rovida G (1997) Structure and composition of the titanium oxide layers formed by low-pressure oxidation of the Ni94Ti6(110) surface. Surf Sci 391(1–3):216–225

65. Atrei A, Ferrari AM, Finetti P, Beni A, Rovida G (2009) LEED and DFT study of the quasihexagonal TiO_2 structure on Cu(001). J Phys Chem C 113(45):19578–19584

66. Atrei A, Ferrari AM, Szieberth D, Cortigiani B, Rovida G (2010) Lepidocrocite-like structure of the TiO_2 monolayer grown on Ag(100). Phys Chem Chem Phys 12(37):11587–11595

67. Atrei A, Cortigiani B, Ferrari AM (2012) Epitaxial growth of TiO_2 films with the rutile (110) structure on Ag(100). J Phys-Condens Mat 24(44):445005

68. Orzali T, Casarin M, Granozzi G, Sambi M, Vittadini A (2006) Bottom-up assembly of single-domain titania nanosheets on (1 × 2)-Pt(110). Phys Rev Lett 97(15):156101

69. McCavish ND, Bennett RA (2003) Ultra-thin film growth of titanium dioxide on W(100). Surf Sci 546(1):47–56

70. Bennett RA, Mulley JS, Newton MA, Surman M (2007) Spectroscopy of ultrathin epitaxial rutile TiO_2(110) films grown on W(100). J Chem Phys 127(8):084707

71. Pang CL, Grinter DC, Matharu J, Thornton G (2013) A scanning tunneling microscopy study of ultrathin film rutile TiO_2(110) supported on W(100)-O(2 × 1). J Phys Chem C 117 (48):25622–25627

72. Oh WS, Xu C, Kim DY, Goodman DW (1997) Preparation and characterization of epitaxial titanium oxide films on Mo(100). J Vac Sci Technol A 15(3):1710–1716

73. Chen MS, Goodman DW (2008) Ultrathin, ordered oxide films on metal surfaces. J Phys-Condens Mat 20(26):264013

74. Guo Q, Oh WS, Goodman DW (1999) Titanium oxide films grown on Mo(110). Surf Sci 437 (1–2):49–60

75. Lai X, Guo Q, Min BK, Goodman DW (2001) Synthesis and characterization of titania films on Mo(110). Surf Sci 487(1–3):1–8

76. Chen MS, Goodman DW (2004) The structure of catalytically active gold on titania. Science 306(5694):252–255

77. Matsumoto T, Batzill M, Hsieh S, Koel BE (2004) Fundamental studies of titanium oxide-Pt (100) interfaces—I. stable high temperature structures formed by annealing TiOx films on Pt (100). Surf Sci 572(2–3):127–145

78. Papageorgiou AC, Cabailh G, Chen Q, Resta A, Lundgren E, Andersen JN, Thornton G (2007) Growth and reactivity of titanium oxide ultrathin films on Ni(110). J Phys Chem C 111(21):7704–7710

79. Papageorgiou AC, Pang CL, Chen Q, Thornton G (2007) Low-dimensional, reduced phases of ultrathin $TiO_{(2)}$. ACS Nano 1(5):409–414

80. Bennett RA, Poulston S, Stone P, Bowker M (1999) STM and LEED observations of the surface structure of TiO_2(110) following crystallographic shear plane formation. Phys Rev B 59(15):10341–10346

81. Dulub O, Hebenstreit W, Diebold U (2000) Imaging cluster surfaces with atomic resolution: the strong metal-support interaction state of Pt supported on TiO_2(110). Phys Rev Lett 84 (16):3646–3649

82. Bennett RA, Pang CL, Perkins N, Smith RD, Morrall P, Kvon RI, Bowker M (2002) Surface structures in the SMSI state; Pd on (1 × 2) reconstructed TiO_2(110). J Phys Chem B 106 (18):4688–4696

83. Matsumoto T, Batzill M, Hsieh S, Koel BE (2004) Fundamental studies of titanium oxide-Pt (100) interfaces—II. influence of oxidation and reduction reactions on the surface structure of TiOx films on Pt(100). Surf Sci 572(2–3):146–161

84. Boffa AB, Galloway HC, Jacobs PW, Benitez JJ, Batteas JD, Salmeron M, Bell AT, Somorjai GA (1995) The growth and structure of titanium-oxide films on Pt(111) investigated by Leed, Xps, Iss, and Stm. Surf Sci 326(1–2):80–92

85. Sedona F, Rizzi GA, Agnoli S, Xamena FXLI, Papageorgiou A, Ostermann D, Sambi M, Finetti P, Schierbaum K, Granozzi G (2005) Ultrathin TiOx films on Pt(111): A LEED, XPS, and STM investigation. J Phys Chem B 109(51):24411–24426

86. Sedona F, Agnoli S, Granozzi G (2006) Ultrathin wagon-wheel-like TiOx phases on Pt(111): a combined low-energy electron diffraction and scanning tunneling microscopy investigation. J Phys Chem B 110(31):15359–15367

87. Finetti P, Sedona F, Rizzi GA, Mick U, Sutara F, Svec M, Matolin V, Schierbaum K, Granozzi G (2007) Core and valence band photoemission spectroscopy of well-ordered ultrathin TiOx films on Pt(111). J Phys Chem C 111(2):869–876
88. Barcaro G, Agnoli S, Sedona F, Rizzi GA, Fortunelli A, Granozzi G (2009) Structure of reduced ultrathin TiOx polar films on Pt(111). J Phys Chem C 113(14):5721–5729
89. Schoiswohl J, Surnev S, Netzer FP, Kresse G (2006) Vanadium oxide nanostructures: from zero- to three-dimensional. J Phys-Condens Mat 18(4):R1–R14
90. Barcaro G, Cavaliere E, Artiglia L, Sementa L, Gavioli L, Granozzi G, Fortunelli A (2012) Building principles and structural motifs in TiOx ultrathin films on a (111) substrate. J Phys Chem C 116(24):13302–13306
91. Li F, Parteder G, Allegretti F, Franchini C, Podloucky R, Surnev S, Netzer FP (2009) Two-dimensional manganese oxide nanolayers on Pd(100): the surface phase diagram. J Phys-Condens Mat 21(13):134008
92. Surnev S, Ramsey MG, Netzer FP (2003) Vanadium oxide surface studies. Prog Surf Sci 73 (4–8):117–165
93. Surnev S, Kresse G, Ramsey MG, Netzer FP (2001) Novel interface-mediated metastable oxide phases: vanadium oxides on Pd(111). Phys Rev Lett 87(8):086102
94. Schoiswohl J, Sock M, Eck S, Surnev S, Ramsey MG, Netzer FP, Kresse G (2004) Atomic-level growth study of vanadium oxide nanostructures on Rh(111). Phys Rev B 69 (15):155403
95. Schoiswohl J, Surnev S, Sock M, Eck S, Ramsey MG, Netzer FP, Kresse G (2005) Reduction of vanadium-oxide monolayer structures. Phys Rev B 71(16):165437
96. Schoiswohl J, Kresse G, Surnev S, Sock M, Ramsey MG, Netzer FP (2004) Planar vanadium oxide clusters: two-dimensional evaporation and diffusion on Rh(111). Phys Rev Lett 92 (20):206103
97. Guimond S, Gobke D, Romanyshyn Y, Sturm JM, Naschitzki M, Kuhlenbeck H, Freund HJ (2008) Growth and characterization of ultrathin V(2)O(y) (y approximate to 5) films on Au (111). J Phys Chem C 112(32):12363–12373
98. Guimond S, Sturm JM, Gobke D, Romanyshyn Y, Naschitzki M, Kuhlenbeck H, Freund HJ (2008) Well-ordered V2O5(001) thin films on Au(111): growth and thermal stability. J Phys Chem C 112(31):11835–11846
99. Petukhov M, Rizzi GA, Granozzi G (2001) Spectroscopic and structural characterisation of a VOx (x approximate to 1) ultrathin epitaxial film on Pt (111). Thin Solid Films 400(1–2):154–159
100. Petukhov M, Rizzi GA, Granozzi G (2001) Ultrathin film growth and spectroscopic characterization of VOx (0.8 <= x <= 1.3) on Pt(111). Surf Sci 490(3):376–384
101. Surnev S, Kresse G, Sock M, Ramsey MG, Netzer FP (2001) Surface structures of ultrathin vanadium oxide films on Pd(111). Surf Sci 495(1–2):91–106
102. Jiang ZQ, Zhou WP, Tan DL, Zhai RS, Bao XH (2004) Evidence for perimeter sites over SmOx-modified Rh(100) surface by CO chemisorption. Surf Sci 565(2–3):269–278
103. Kuriyama T, Kunimori K, Nozoye H (1998) Interaction of CO with the SmOx/Ru(001) interface. Surf Sci 402(1–3):178–181
104. Zhu JF, Ma YS, Zhuang SX (2009) Exploring the role of samarium in the modification of rhodium catalysts through surface science approach. Surf Sci 603(10–12):1802–1811
105. Jhang JH, Schaefer A, Cartas W, Epuri S, Baeumer M, Weaver JF (2013) Growth and partial reduction of Sm$_2$O$_3$(111) thin films on Pt(111): evidence for the formation of SmO(100). J Phys Chem C 117(41):21396–21406
106. Cartas W, Rai R, Sathe A, Schaefer A, Weaver JF (2014) Oxidation of a Tb$_2$O$_3$(111) thin film on Pt(111) by gas-phase oxygen atoms. J Phys Chem C 118(36):20916–20926
107. Schaefer A, Gevers S, Zielasek V, Schroeder T, Falta J, Wollschlager J, Baumer M (2011) Photoemission study of praseodymia in its highest oxidation state: the necessity of in situ plasma treatment. J Chem Phys 134(5):054701

108. Gevers S, Weisemoeller T, Schaefer A, Zielasek V, Baumer M, Wollschlager J (2011) Structure of oxygen-plasma-treated ultrathin praseodymia films on Si(111). Phys Rev B 83 (19):193408
109. Wilkens H, Gevers S, Rohe S, Schaefer A, Baumer M, Zoellner MH, Schroeder T, Wollschlager J (2014) Structural changes of ultrathin cub-PrO2(111)/Si(111) films due to thermally induced oxygen desorption. J Phys Chem C 118(6):3056–3061

Chapter 5
Ultrathin Oxide Films on Au(111) Substrates

Chen Wu and Martin R. Castell

Abstract The Au(111) surface is an excellent substrate for the growth of ultrathin oxide films. Although it is chemically relatively inert, the high electronegativity of Au tends to give rise to strong interactions between the oxide film and the substrate via charge transfer processes. Many new surface oxide structures with unique properties have been observed in ultrathin film form that have no analogues as bulk crystal terminations.

Abbreviations

2D	Two-dimensional
3D	Three-dimensional
AES	Auger electron spectroscopy
CVD	Chemical vapor deposition
FCC	Face centered cubic
HCP	Hexagonal close packing
LEED	Low-energy electron diffraction
MBE	Molecular beam epitaxy
ML	Monolayer
PVD	Physical vapor deposition
RHEED	Reflection high energy electron diffraction
RLAD	Reactive-layer-assisted deposition
RT	Room temperature
SMSI	Strong metal-support interactions
STM	Scanning tunneling microscopy
STS	Scanning tunneling spectroscopy

C. Wu (✉)
School of Materials Science and Engineering, State Key Laboratory
of Silicon Materials, Zhejiang University, 310027 Hangzhou, China
e-mail: chen_wu@zju.edu.cn

M.R. Castell (✉)
Department of Materials, University of Oxford, Parks Road,
Oxford OX1 3PH, UK
e-mail: martin.castell@materials.ox.ac.uk

TMAA   Trimethyl acetic acid
TPD   Thermal programmed desorption
UHV   Ultrahigh vacuum
XPS   X-ray photoelectron spectroscopy

5.1 Introduction

Ultrathin oxide films consist of only a few monolayers (MLs) of oxide material with a typical thickness ranging between 1 and 2 nm. They are of extensive interest in the context of new technologies and fundamental research. Oxide ultrathin films can be incorporated into various advanced technologies including plasma display panels, microelectronic devices and metal-oxide catalysts [1–3]. For these applications, ultrathin films provide novel properties, decreased component size for device miniaturization, and significantly increased surface-to-volume ratios for enhanced catalytic performance.

One of the difficulties in the study of native oxide surfaces is that many of them are electrically insulating, and therefore do not lend themselves to be characterized with electron-based probes such as X-ray photoelectron spectroscopy (XPS), scanning tunneling microscopy (STM), or low-energy electron diffraction (LEED). However, this problem can be circumvented through the growth of very thin oxide films on metal substrates. Oxide thin films also provide model surfaces, since a much wider range of oxides can be grown in the form of thin layers than are available as bulk crystals [4]. Ultrathin films can have novel surface structures which do not correspond to the thermodynamically favored terminations of bulk crystals [5]. For example, polar planes of some bulk oxides have been considered to be unstable since the repeat unit of the stacking sequence perpendicular to the surface has a non-zero dipole moment. Alternating cationic and anionic layers of the bulk crystal leads to an infinite surface energy. The polarity is usually compensated by various surface mechanisms including substoichiometry, reconstruction and molecular adsorption [6]. However, in principle, a stoichiometric and unreconstructed polar surface can be achieved in ultrathin films because there is no macroscopic dipole. New structures of ultrathin films also arise due to the strong template effect of the substrate, which opens up the opportunity for fabricating a broad variety of epitaxial oxide materials with novel physical and chemical properties.

Noble metal crystal surfaces serve as an important type of substrate for ultrathin oxide film growth due to their relatively simple preparation procedures, chemical stability, and high electrical conductivity that eliminates charging effects. Oxides grown on metal substrates can be considered as inverse models for catalytic oxide-supported metal nanoparticles. The complexity of real-world catalyst materials tend to hinder in-depth investigations of their active sites and reaction mechanisms. However, inverse model catalysts with ordered oxide structures deposited on metal substrates allow for the exploration of some fundamental steps in

heterogeneous catalysis using a variety of surface science tools. An oxide/metal system that has attracted much attention is that of oxide-supported Au nanoparticles which acts as an excellent catalysts in the conversion of CO into CO_2 at remarkably low temperatures (200 K) [7, 8]. Another important area is the catalytic activity of the Au/oxide systems towards the water-gas shift reaction ($H_2O + CO \rightarrow H_2 + CO_2$) [9, 10]. Au catalysts supported on a variety of oxides are also active for many other reactions such as NO reduction, selective oxidation of propene to propene oxide and the production of ethyl acetate from ethanol, etc. [11–13]. The unique catalytic properties of oxide-supported Au catalysts have also stimulated extensive studies into inverse model catalysts that consist of oxide thin films supported on Au single crystal substrates, and recent research indicates that such inverse systems are catalytically active themselves. Excellent performance has been reported for CeO_x and TiO_x nanoparticles grown on Au(111) with respect to the water-gas shift reaction [14, 15]. A further example is CO oxidation promoted by Fe_2O_3 or TiO_2 nanoclusters grown on Au(111) [16, 17]. The catalytic activity for both Au/oxide and oxide/Au systems has stimulated research into the Au-oxide interaction. To gain a better understanding of this system, the growth of oxide thin films on Au(111) can provide some valuable insights.

5.2 Preparation and Characterization Methods

5.2.1 Thin Film Growth

The growth of oxide ultrathin films on noble metal substrates usually involves evaporation of the component materials onto the substrate. Since the oxide generally possesses a higher sublimation temperature than the corresponding metal, thermal evaporation of the metal is often carried out either from an electron-beam evaporator or an effusion cell. The evaporation is sometimes carried out in an oxidizing atmosphere. An alternative method is to evaporate the metal in UHV and then post-anneal the sample in an oxidizing gas environment using, for example O_2 or NO_2. This latter method tends to be the most widely-used process for the formation of oxide thin films [18–22]. The oxidation process may vary for different methods, e.g. in reactive-layer-assisted deposition (RLAD), Ti is evaporated onto a Au(111) substrate pre-deposited with a layer of H_2O or N_2O and post-annealing then gives rise to TiO_x structures [23, 24]. RLAD has also been reported for the CeO_x/Au(111) system where a pre-deposited H_2O or NO_2 layer was used [25]. Oxidation of an alloy substrate such as Ti–Au has also been reported in the preparation of TiO_2 crystallites on Au(111) [26]. Recently, chemical vapor deposition (CVD) has been used to sublime gaseous titanium tetrasopropoxide. The Ti $(OC_3H_7)_4$ precursor decomposes on the Au(111) substrate and forms an ultrathin TiO_x film [27]. CVD has also been used to deposit Mo clusters using $Mo(CO)_6$ as a precursor followed by oxidation in NO_2 to form MoO_3 on Au(111) [28].

5.2.2   Thin Film Characterization

The conductive nature of the Au substrate allows various surface characterization techniques to be used that involve electrons, enabling in-depth investigation of the ultrathin films. Classical techniques for surface structure determination involve electron diffraction at different energies. Both LEED and reflection high energy electron diffraction (RHEED) provide convenient ways to determine the crystallinity and periodicity of the oxide films. Atomically resolved surface structure images can be obtained by STM. Meanwhile, scanning tunneling spectroscopy (STS) provides information on the local electronic properties of the films. Apart from structural investigations, determination of the chemical composition of the film is often also necessary. Electron-based spectroscopy including XPS, Auger electron spectroscopy (AES) and ultra-violet photoelectron spectroscopy (UPS) are surface sensitive, and are extremely useful in understanding the chemistry of the oxide films and the substrate-film charge transfer [29]. Theoretical analysis of proposed atomic models and prediction of the electronic structure can be carried out using density function theory (DFT). DFT is also used for calculation of the charge transfer at the substrate-film interfaces and the work function of the films.

5.3   Structural Features of the Oxide Films

5.3.1   The Au(111) Substrate Reconstruction

The nature of the substrate surface plays an important role in the determination of the film structure. The surface atoms of the clean substrate metal are not usually located in the positions of a simple bulk termination. This is because the atoms on the surface have a lower coordination number compared with those in the bulk [30]. The surface relaxes or reconstructs to minimize the surface free energy. Relaxation involves a subtle adjustment of the layer spacings perpendicular to the surface, but the periodicity or the symmetry parallel to the surface remains unchanged. A reconstruction refers to the rearrangement of the surface atoms to form a structure that differs from the bulk crystallographic planes.

Unreconstructed Au(111) planes consist of hexagonal lattices, as Au has a face centered cubic (fcc) crystal structure. For the reconstructed Au(111) surface, a complex structure consisting of paired rows is observed, as shown in the STM images in Fig. 5.1. The bright lines are boundaries between unfaulted fcc and faulted hexagonal close packed (hcp) stacking [31]. This faulting arises because the surface atomic bonds undergo a uniaxial contraction by 4 % along the $\langle 1\bar{1}0 \rangle$ direction and the surface therefore contains more atoms than a bulk (111) plane. For every 22 atoms along the $\langle 1\bar{1}0 \rangle$ direction in the bulk there are 23 surface atoms, resulting in a $(22 \times \sqrt{3})$ unit cell. This reconstruction is also sometimes erroneously called the $(23 \times \sqrt{3})$ reconstruction because of the 23 atoms in the surface
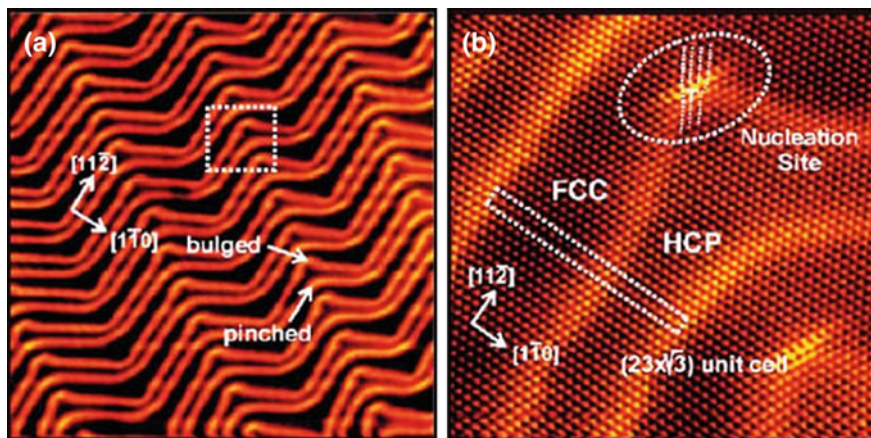
Fig. 5.1 STM images showing **a** large scale herringbone reconstruction of the Au(111) surface (Image size: 80.2 × 79.5 nm^2) and **b** atomically resolved $(22 \times \sqrt{3})$ unit cells on Au(111) (Image size: 14.1 × 13.5 nm^2; $V_s = -0.04$ V; $I_t = 1.55$ nA) [32, 33]

layer, however reconstructions should always refer to the bulk crystallography, and hence $(22 \times \sqrt{3})$ is the correct expression. Long-range forces on this surface further complicate matters in which the lowest energy configuration involves a periodic change in the direction of the reconstruction, and this results in a zig-zag appearance that is called the herringbone reconstruction.

5.3.2 Structure of the Oxide Films

A variety of oxide thin films have been fabricated on the Au(111) surface including TiO$_x$ [18, 23, 24, 27], FeO$_x$ [22, 34], VO$_x$ [35–38], CoO [39–41], MoO$_3$ [28, 42, 43], MgO [19, 44–46], CeO$_x$ [25], ZnO [47] and BaO$_x$ [48]. The growth of ultrathin oxide films on the Au(111) surface usually lifts the herringbone reconstruction due to the strong interaction between the film and the substrate. This effect has been observed in various systems including TiO$_x$/Au(111) and MoO$_3$/Au(111) [18, 27, 49]. For cases where there is less than a monolayer coverage of the oxide, the herringbone lines wind around the oxide islands without going underneath them. This indicates that by forming the oxide-Au interface there is no longer an energetic advantage in compressing the top layer of Au atoms that results in the herringbone reconstruction and therefore the original Au(111) hexagonal lattice forms the template for film growth.

The phases obtained for the oxide films mainly include honeycomb, pinwheel, hexagonal, and row-like structures. The structure of the initial oxide monolayer of the film is strongly affected by the hexagonal symmetry of the Au(111) substrate. For the TiO$_x$/Au(111) system, STM reveals the co-existence of a honeycomb structure and a pinwheel structure as shown in Fig. 5.2 [18, 27]. The honeycomb

structure is formed with the Ti atoms occupying the three-fold hollow sites of the Au lattice and the O atoms located at the bridge sites of the Ti atoms, resulting in a stoichiometry of Ti_2O_3. The unit cell of the honeycomb structure aligns with the crystallographic directions of the Au substrate and corresponds to a (2 × 2) reconstruction. The pinwheel structure consists of six interlocking triangles. The atoms at the spokes occupy the Au bridge sites instead of the three-fold hollow sites of the lattice underneath. Consequently they are higher and appear brighter than the atoms within the triangles (Fig. 5.2b). The pinwheel structure originates from a Moiré pattern formed through the superposition of a metal/O lattice over the Au (111) surface [18]. The metal/O lattice is rotated by a certain angle with respect to the Au(111) lattice. Depending on the angle of rotation (whether clockwise or anticlockwise), two domains can be obtained for the pinwheel structure as shown in Fig. 5.2b. Two types of periodicities are observed by STM for the pinwheels: the unit cells by connecting the coincident points for the two lattices (Fig. 5.2b) and the atomic periodicity of the overlayer (Fig. 5.2c). The formation of the Moiré patterns may also lead to other appearances of the surface structure depending on the angle of rotation between the film and the substrate lattice. The most commonly observed Moiré patterns exhibit a hexagonal shape such as FeO(111) [34], CoO(111) [39, 41] and ZnO(0001) [47, 50] films on Au(111).

A hexagonal lattice has also been found for $V_2O_3(0001)$/Au(111) (Fig. 5.3), and for a number of years there were conflicting views concerning the detailed atomic structure of the film [51, 52]. While XPS and STM suggested a surface terminated with a vanadyl (V=O) group [37, 53], ion scattering investigations and ion beam triangulation supported the reconstructed O_3 model [35, 36, 38]. More recently, this controversy on the $V_2O_3(0001)$ termination has been revisited and resolved via a
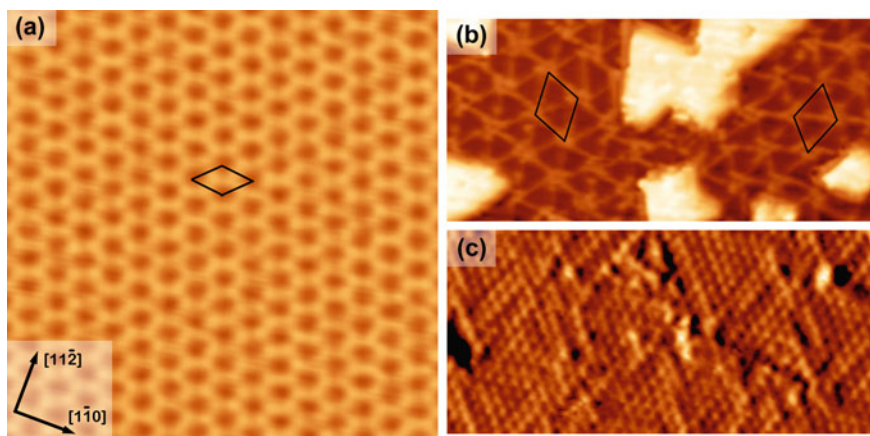
Fig. 5.2 STM images showing **a** the (2 × 2) honeycomb Ti_2O_3 structure on Au(111) (Image size: 8.5 × 8.5 nm^2; V_s = 0.98 V; I_t = 0.2 nA), **b** the pinwheel TiO monolayer with two domains indicated (Image size: 31 × 14 nm^2; V_s = 1.41 V; I_t = 0.18 nA) and **c** atomically resolved pinwheel structure on Au(111) (Image size: 11 × 5 nm^2; V_s = −0.12 V; I_t = 0.5 nA) [18]

Fig. 5.3 STM image showing the $V_2O_3(0001)$ surface on an Au(111) substrate (Image size: 20×20 nm^2; $V_s = -1.5$ V; $I_t = 0.2$ nA) [52]
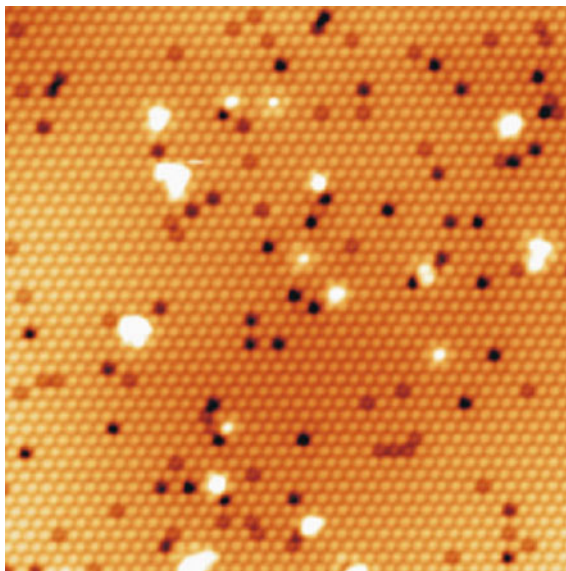
combination of I-V LEED, STM, fast atom scattering and DFT, indicating that the vanadyl termination is thermodynamically more stable [54]. It has also been reported that electron irradiation removes the O-involved termination, resulting in a vanadium terminated surface with three-fold symmetry and higher catalytic reactivity [55].

Other structures of vanadium oxide on Au(111) include $V_2O_5(001)$ and $V_6O_{13}(001)$ which exhibit row structures with rectangular or rectangular-like unit cells as shown in Fig. 5.4 [20, 21]. The $V_6O_{13}(001)$ phase grows as a double-layered film after completing the first layer of the $V_2O_5(001)$ structure. Both phases do not exist as a bulk termination and it is interesting that the second layer does not adopt the same unit cell as the first layer, demonstrating the significant influence of the Au (111) substrate on the structure of the first layer.

Monolayer MgO islands with both hexagonal (111) and rectangular-like (001) lattices exist on the Au(111) substrate depending on the deposition temperature and oxygen partial pressure [19, 44, 45]. The MgO(001) monolayer adopts a (6×1) superlattice with a stripe pattern, while triangular islands are seen for MgO (111) ultrathin films. Detailed total-energy calculations suggests that the MgO islands adopt the square lattice configuration with the perimeter formed by nonpolar [100] edges, while the MgO(111) islands are stabilized by hydroxylated polar zigzag edges [44, 46]. Different edges of the two types of oxide islands may be linked to molecular adsorption behavior and determine the catalytic reactivity. In the MoO_3/Au(111) system, the first monolayer of MoO_3 on Au(111) exhibits a c (4×2) structure [43, 49]. Increasing the Mo coverage gives rise to a bilayer MoO_3 film with a 11.6 Å $\times$ 5 Å rectangular unit cell. Beyond the bilayer structure,
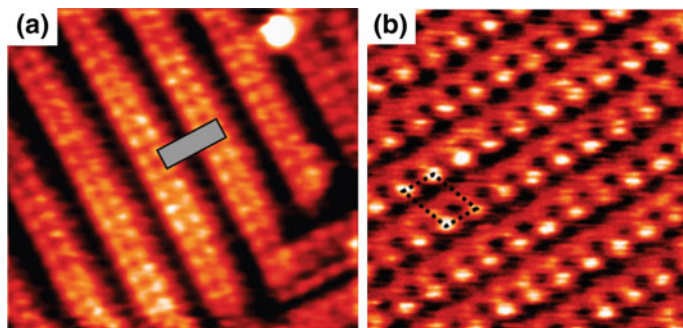
Fig. 5.4 STM images of **a** a V_2O_5 monolayer (Image size: 6.3 × 5.8 nm^2; V_s = 2 V; I_t = 0.2 nA) and **b** a V_6O_{13} ultrathin film (Image size: 3.4 × 3.4 nm^2; V_s = 2 V; I_t = 0.2 nA) on Au(111) prepared by oxidation of deposited vanadium [20, 21]

$MoO_3(010)$ crystallites grow as the Mo dose is further increased, similar to the case of $V_2O_5(001)$ on Au(111) [21].

The observed structures of ultrathin oxide films grown on Au(111) can be roughly divided into two categories. In the first category the structures possess three-fold symmetry, which can be attributed to the strong interaction between the film and the substrate lattice. The second category structures exhibit a stripe-pattern with rectangular (-like) unit cells. There are multiple reasons for the formation of these different phases, such as film stoichiometry, film thickness, and growth and processing conditions. These factors are discussed in turn in the following sections.

5.3.3 Structural Transitions of the Oxide Films

There are a number of factors that determine the growth behavior of ultrathin films, including the substrate-film lattice mismatch, the surface and interfacial energy of the system, the stoichiometry and thickness of the film, and the growth conditions of the oxide. These factors can interact with each other, making an understanding of the growth behavior even more challenging. Here we focus on the individual factors that can be manipulated in order to shed some light on how to influence the structure of oxide ultrathin films on Au(111).

5.3.3.1 Stoichiometry-Driven Structural Transitions

A significant variation of the chemical composition of a film inevitably leads to a change in its atomic structure. This is most easily achieved with metal elements that have multiple oxidation states, in which case the stoichiometry drives the formation of different structures of the oxide film. For example, for the first TiO_x monolayer grown on Au(111), a stoichiometry of Ti_2O_3 is obtained for the honeycomb

structure, whereas the pinwheel pattern corresponds to a stoichiometry of TiO [18, 56]. Another example are the rather different stoichiometry-driven phases observed for V_2O_3 (hexagonal), V_2O_5 (rectangular) and V_6O_{13} (rectangular-like) on Au(111) [20, 21, 35–38]. A change in the stoichiometry can be achieved by varying the growth conditions including the growth temperature, oxidation species, oxygen pressure and post-annealing process. For example, it has been found that increasing the growth temperature from 200 to 500 °C gives rise to preferential growth of 3D TiO_2 nanocrystals with rectangular unit cells rather than the 2D (2×2) honeycomb Ti_2O_3 lattice [27]. The oxidation method also plays an important role in the film stoichiometry. Ce metal nanoparticles on Au have limited reactivity toward molecular O_2 and NO_2 due to the formation of Ce–Au alloys, resulting in the formation of substoichiometric 3D CeO_x particles. Complete oxidation can be achieved by Ce deposition on to the Au substrate at elevated temperatures in an O_2 background pressure. This gives rise to ultrathin flat and ordered $CeO_2(111)$ nanoislands with a hexagonal surface structure [25]. For the FeO_x/Au(111) system, oxidation of Fe deposited on Au(111) with molecular O_2 at room temperature (RT) gives rise to the growth of an FeO monolayer, while the Fe_2O_3 phase forms by oxidation with NO_2 at elevated temperatures [22, 34]. STM images reveal a hexagonal Moiré pattern for the FeO(111) phase and an O-terminated α-$Fe_2O_3(0001)$ surface for the Fe_2O_3 phase. The oxygen pressure is also an important factor in the control of the stoichiometry of ultrathin oxide films on Au(111). It has been reported that Pb deposited on Au oxidizes to form PbO in an oxygen pressure (P_{O2}) less than 10^{-6} Torr. Increasing the P_{O2} to 10^{-4} Torr leads to the transition from PbO to PbO_2 [57]. Also, the ultrathin lead oxide film can be oxidized or reduced reversibly by thermal oxidation or vacuum annealing cycles. Similar effects of post-annealing on the stoichiometry have also been found for the CoO_x/Au(111) system [41] where the transition between the 2D CoO phase and the 3D Co_3O_4 phase can be tuned by oxidation and reduction annealing.

5.3.3.2 Lattice Mismatch-Driven Structural Transition

The degree of lattice mismatch between the film and substrate partially determines whether a wetting film with an ordered surface structure can be obtained. On the one hand, the lattice mismatch can be optimized by choosing an appropriate combination of oxide film and substrate to allow epitaxial growth to occur. On the other hand, a large lattice mismatch between the film and the substrate may be overcome by the formation of completely different structures from the bulk for the ultrathin films. For example, hexagonal Moiré patterns arise for the ZnO (0001)/Au (111) system due to the large lattice mismatch (approx. 12 %) [47]. The lattice mismatch may also give rise to the formation of different structures by varying the growth conditions. For MgO on Au(111), hexagonal symmetry arises with low temperature and O_2 partial pressure. MgO(001) with a stripe pattern forms with a higher temperature and oxygen pressure due to the symmetry mismatch of the square overlayer and the hexagonal substrate [19].

The influence of the lattice mismatch becomes weaker as the film grows thicker. For the TiO_x/Au(111) system, triangular islands start to grow as the second monolayer instead of the honeycomb Ti_2O_3 and pinwheel TiO wetting layer [18]. It is difficult to reveal the atomic structure of the second layer due to limited resolution of the STM images. One can however, infer that the second ML is still affected by the lattice of the Au(111) substrate because it nucleates as bright triangular islands that have inherited the three-fold symmetry of the substrate. Further increased Ti coverage results in the formation of a row structure on the triangular islands with a rectangular unit cell [18, 27], indicating a weakened influence of the substrate. Similarly, transitions between 2D Moiré-patterned CoO and 3D Co_3O_4 spinel clusters on Au(111) have also been reported by controlling the Co coverage [39, 41]. The strain introduced in the film by the substrate-film lattice mismatch can be relaxed with increased film thickness due to the introduction of crystal defects including point defects and misfit dislocations. Beyond a certain thickness the oxide film will tend to adopt its bulk structure. For example, a bulk-like CoO layer has been obtained for a coverage of 7 MLs on Au(111) [40]. This may even give rise to a different crystal orientation of the thicker film compared to the substrate in order to minimize the overall energy of the system. However, we will not discuss this phenomenon further in this chapter as it is devoted only to ultrathin films of thicknesses less than a few monolayers. A comprehensive understanding the influence of the film-substrate interaction, film stoichiometry and coverage on the stability of different oxide structures can be used to influence the oxide phase.

5.4   Interactions Between the Film and the Substrate

Apart from epitaxial effects of the substrate, interactions between the oxide ultrathin films and the substrate mainly consist of mass transport and charge redistribution [29]. In some instances ultrahigh vacuum (UHV) annealing of an Au substrate with a metal (M) deposited on it may lead to the formation of an M–Au alloy [25] in which case the oxide film can be grown by oxidation of the metal (M) extracted from the alloy [26]. The film-substrate mass exchange is usually neglected once the oxide has been formed due to the chemically inert nature of the Au substrate. The interfacial structure, however, needs to be considered for the first monolayer of the film on Au(111). Whether the oxide film starts with a densely packed layer of O or with one of the metal (M) atoms results in the different stacking sequences of Au–O–M or Au–M–O. The bonding energetics between Au and O or M need to be considered for the interfacial structure. Formation of M–Au alloys, the weak adsorption of O on Au and the fact that Au oxide easily decomposes indicate that Au prefers to bond with the metal (M) atoms, resulting in most cases in an Au–M–O interface [18, 40, 58].

Another important factor to consider for the film-substrate interactions is the charge transfer which is driven by the minimization of the system energy and the continuity of the electric potential in the solid [59]. For example, interfacial charge transfer between the oxide film and the electronegative gold surface, results in a

decreased work function of Au(111) following deposition of a MgO(001) monolayer [19]. A change in the work function is determined by the electronegativity of the substrate. A large decrease in work function has been reported for MgO/Au(111) compared with MgO/Mo(001) and MgO/Ag(001), indicating that Au substrates can be responsible for significant charge transfer between the adsorbates and the substrate [60]. For MgO/Au(111), DFT calculations indicate that the charge transfer compensates the polarity of the film [61]. Conversely, changes of the opposite sign can be induced in the work function of the substrate depending on the metal-oxide interface [60]. While MgO thin films decrease the substrate work function, growth of SiO_2 and TiO_2 films lead to raised work functions of the substrates. Consequently, a change in the work function of the substrate can be tuned by an appropriate choice of the metal-oxide interface. This can be explained by the electronegativity of the substrate which determines the sign and extent of the charge transfer at the metal-oxide interface [62]. These effects will be further discussed in the following section. Charge transfer is common for oxide-Au interfaces and has been reported for a number of systems including V_2O_3/Au(111) [53] and MoO_3/Au(111) [49, 63].

5.5 Properties and Potential Applications

Thin oxide films have applications in energy conversion, microelectronics and spintronics. Transition metal dopants such as Mn, Fe, Co and Ni have been predicted by DFT to induce magnetic moments in MgO films resulting in dilute magnetic semiconductors [64]. RT ferromagnetism has also been reported for various oxide systems including TiO_2, ZnO and SnO_2 [65]. The most important application is probably related to the catalytic properties of the oxide-metal systems. Most studies involve heterogeneous catalysts consisting of noble metal nanoparticles supported on oxides. The strong metal-support interaction (SMSI) proposed by Tauster et al. [66–68] has stimulated many investigations on the growth of oxide ultrathin films on metal substrates as an inverse catalyst model [18, 36, 47]. These models serve as excellent systems to allow the investigation of oxide-Au interactions and their influence on the catalytic performance.

Recent research demonstrating that the so-called inverse catalysts are reactive or catalytically active themselves has stimulated further interest in these systems. Enhanced catalytic reactivity has been found for CeO_x/Au(111) and TiO_x/Au(111) over Cu(111) and Cu(100) as the typical industrial catalysts towards the water-gas shift reaction [14, 15]. Also, reduced V_2O_3(0001) and V_2O_5(001) films on Au(111) enable oxidation of methanol into formaldehyde and/or methane [52, 69]. STM allows identification of the active sites and research has been conducted into methods for improving the catalytic activity. For example, oxygen vacancies serve as the absorption sites for CO, propane and propene molecules on V_2O_3(0001) and V_2O_5(001) films on Au(111), which can be created by electron irritation of the surface to promote a variety of reactions [51, 70, 71]. CO oxidation that may take

place at the Fe_2O_3/Au and titania/Au perimeter interface can be enhanced by optimization of the coverage of Fe_2O_3 or TiO_x [16, 17].

Thermal programmed desorption (TPD) experiments are usually employed to examine the chemical nature of the desorbing products, providing information on the reaction processes. Figure 5.5 shows the desorption species and their concentration (inserts) after depositing 2-propanol onto the TiO_2/Au(111) and the rutile TiO_2(110) surfaces [72]. The 2-propanol molecules attach to the Ti atoms on both surfaces and desorb at around 300 K. The tail of propanol desorption extends to 560 and 450 K for the TiO_2/Au(111) and the rutile TiO_2(110) surfaces respectively,

Fig. 5.5 TPD spectra taken from the TiO_2/Au(111) (*top*) and a rutile TiO_2(110) surface (*bottom*) deposited with 2-propanol molecules, showing the traces corresponding to the desorption rate of propanol, propene and acetone. The *inserts* show the distribution of the desorption products referred to the local surface concentration [72]
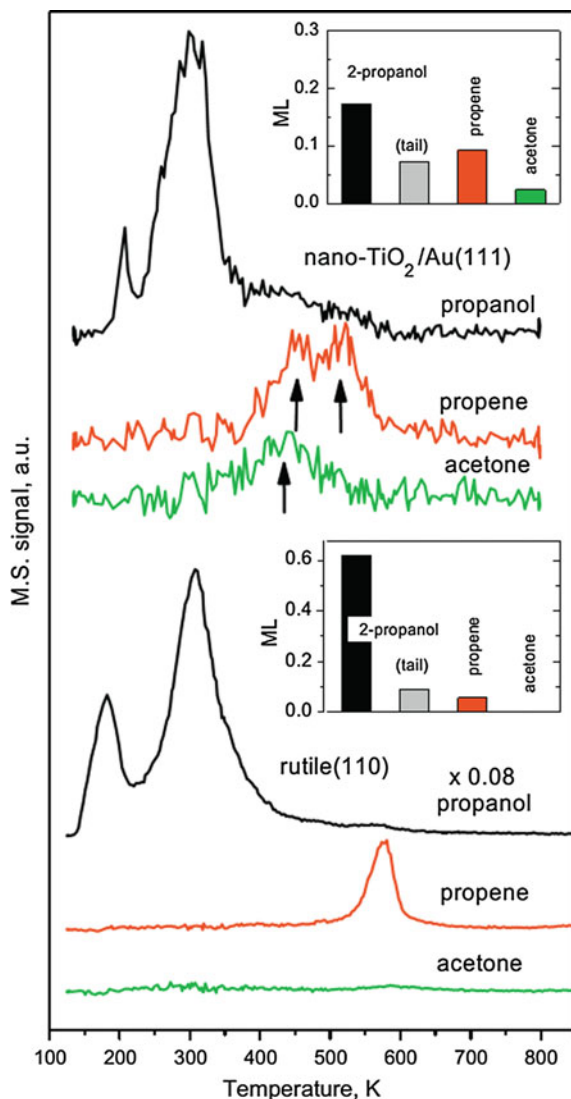
corresponding to the recombination of surface-bound propoxy and hydrogen. Propene is formed by removing a hydrogen atom from one of the methyl groups of a propoxy species adsorbed on the bridge-bonded oxygen vacancies. Propene desorption has been observed on both $TiO_2/Au(111)$ and the rutile $TiO_2(110)$ surface whereas an additional desorption peak at 450 K appears for the former. This may result from the under-coordinated atoms at the edges of the TiO_2 overlayer in addition to the oxygen vacancy-like defects as the adsorption sites. More importantly, acetone desorption has been observed on the $TiO_2/Au(111)$ surface which was not detected for the rutile $TiO_2(110)$ system. The acetone arises from α-hydride elimination, breaking the oxygen-surface bond and the formation of a double C=O bond. The production of acetone on the $TiO_2/Au(111)$ surface suggests the existence of sites which allow interactions for the α-hydrides. The enhanced reactivity of $TiO_2/Au(111)$ compared with the bulk rutile $TiO_2(110)$ surface may be due to changes in its electronic properties. Despite the picture of active sites and chemical process, many questions remain open, such as the function of Au during the reaction, and how the film-substrate interaction affects the reactivity. Further investigation on the electronic structure may be necessary to uncover the important mechanisms and to provide more information to allow tailoring of the catalytic properties of oxide-Au systems.

Ultrathin films can have crystal structures that are stabilized through the interaction with the substrate and where there are no bulk analogues. This opens the door to the opportunity of fabricating a rich class of oxide surface structures that do not exist in nature. Such novel structures are potentially of great importance in nanoengineering as templates for the self-assembly of adsorbed metal atoms, metal clusters, and molecules. Investigations on the adsorption behavior of metal atoms on ultrathin oxide films include Fe, Au, Pd and Ba on monolayers of MgO, TiO_x, FeO and CeO_x [62, 73–78]. The degree of charge exchange of the metal adsorbates is determined by their electronegativity and plays an important role in the adsorption behavior [62]. For neutral adatoms, e.g. Pd deposited on FeO/Pt(111), random adatom distributions are observed [74]. For the cases where charge transfer takes place, the adatoms tend to form regular arrays and can be either cationic or anionic. For example, electrons are transferred from Au adatoms to the support when deposited on FeO/Pt(111) [74], while conversely the Au adatoms acquire electrons from the support in the MgO/Ag(001) and TiO_x/Pt(111) systems [60, 76]. This charge transfer behavior is illustrated schematically in Fig. 5.6. The oxide film grown on a substrate with high electronegativity donates electrons to the metal substrate (Fig. 5.6a) while the negative charge goes in the opposite direction for the oxide film deposited on the substrate with low electronegativity (Fig. 5.6b). Similar effects come into play when depositing metal adatoms on the supported oxide monolayers. Electronegativity determines the charge state of the metal adatom, its adsorption mode, and it will either reinforce, reduce or even invert the rumpling of the supported oxide films as shown in Figs. 5.6c, d.

The charge transfer behavior is not only determined by the adatom/support species, but is also affected by the coverage of the adatoms. It has recently been reported that structural and electronic characteristics can be controlled by tuning the
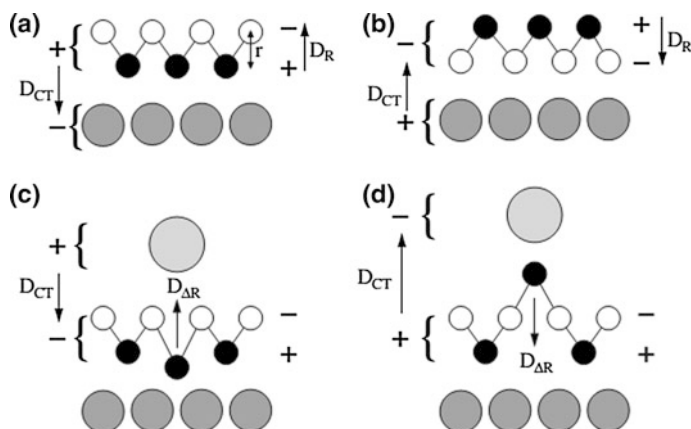
Fig. 5.6 **a** and **b** Sketches showing interfacial charge transfer (D_{CT}) and the film rumpling (D_R) dipole moments for an oxide monolayer (*small black circles* represent cations, *white circles* represent anions) grown on a metal substrate (*large grey circles*). Depending on the electronegativity of the substrate, charge can transfer from (**a**) or into (**b**) the film. The adatom can either (**c**) adsorb directly on the oxide surface, resulting in increased separation of the anion-cation planes, i.e. reinforce the rumpling, or (**d**) locally reduce or even invert the rumpling. Such structural changes are driven by charge transfer between the adatom and the support [62]

Ba deposition on Ti_2O_3 monolayers grown on Au(111) [78]. Figure 5.7 shows the evolution of Ba adsorption on Ti_2O_3/Au(111) with the Ba coverage increased from 0.07 to 0.62 ML. For low Ba doses (0.07 ML), the adatoms are randomly distributed, and have as their adsorption site the hollow location of the honeycomb Ti_2O_3 lattice (Fig. 5.7, 0.07 ML). Two well-ordered surface structures are generated at coverages of 1/3 and 2/3 ML. The 1/3 ML order arises when the Ba adatoms fill the six second nearest neighbor hollow sites (Fig. 5.7, 0.35 ML), whereas the 2/3 ML ordering occurs when the three first nearest hollow sites are occupied (Fig. 5.7, 0.62 ML). A labyrinth-like phase is observed for Ba coverages between 1/3 and 2/3 ML (Fig. 5.7, 0.43, 0.49 ML). The structural configurations are determined by Ba–Ba repulsion through dipole-dipole interactions induced by charge transfer. The overall charge transfer from Ba to the Au substrate increases with raised Ba dose, which also results in steadily increased Ti_2O_3 film rumpling and a decreased Au work function. The findings that the adsorption behavior can be tuned by choosing the combination of metal adatom species and the oxide thin film, as well as varying the adatom coverage, open up the possibility of designing metal-oxide interfaces with specific and novel properties.

Molecular self-assembly is another important area of nanostructure engineering where the surface structure of the substrate has a significant influence. For trimethyl acetic acid (TMAA) on the pinwheel reconstructions of TiO/Au(111), the molecules preferentially occupy sites near the centers of the pinwheels as shown in Fig. 5.8a [56]. With increased coverage, the adsorption pattern evolves into a triad
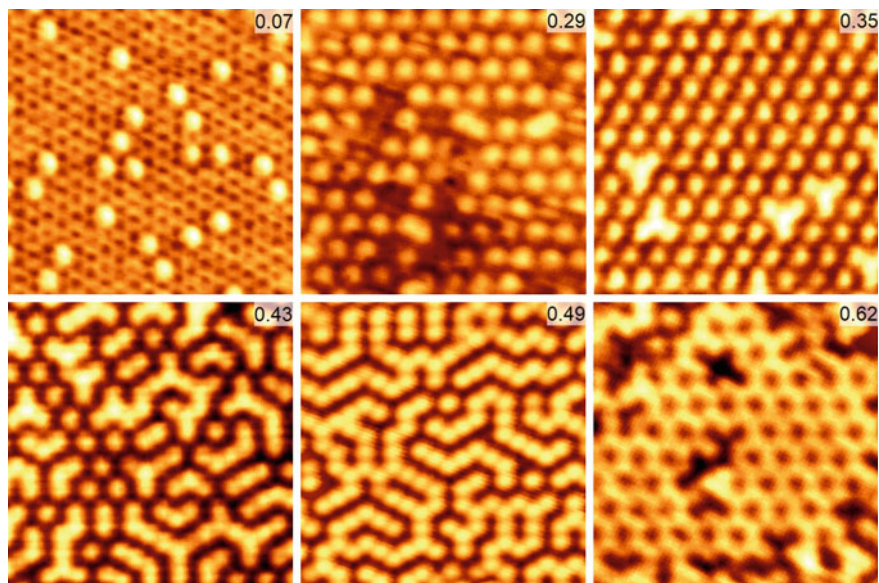
Fig. 5.7 STM images showing the Ba adsorption on the honeycomb Ti_2O_3 monolayer grown on Au(111). The Ba coverage is determined as 0.07, 0.29, 0.35, 0.43, 0.49 and 0.62 ML as indicated on each image. (Image sizes: 10×10 nm^2; $V_s = 0.35$–1.00 V; $I_t = 0.18$–0.28 nA) [78]
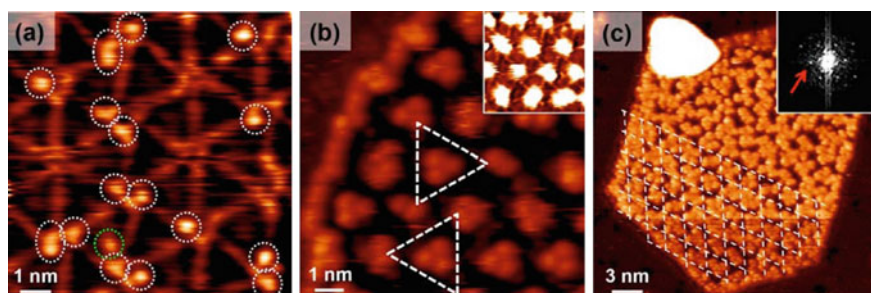
Fig. 5.8 Adsorption of TMAA on the pinwheel TiO/Au(111) surface at coverages of **a** 0.02 ML, **b** 0.06 ML and **c** 0.15 ML [56]

with three-fold symmetry (Fig. 5.8b). Further increasing the TMAA dose gives rise to an extended molecular network that avoids the sites at the centers of the triangles of the pinwheels (Fig. 5.8c). Apart from the pinwheel TiO/Au(111) system, many other ultrathin film structures may serve as templates for substrate-directed molecular self-assembly. Potential candidates include the honeycomb Ti_2O_3/Au (111) surface with hollow sites and the rectangular-like phases with gaps between the row structures. The richness of the various oxide structures on Au(111) provides a progressive step towards molecular engineering on the nanoscale.

5.6   Conclusions and Perspectives

This chapter has explored the rich variety of structures and properties observed in ultrathin oxide films on Au(111) surfaces. The ultrathin film structures may be divided into two categories, namely those which follow the hexagonal symmetry of the substrate and those that have row structures with rectangular-like surface unit cells. Multiple factors determine the surface structure of the oxide layers among which stoichiometry and substrate-film lattice mismatch tend to dominate. These factors can be controlled by selecting combinations of oxide and substrate materials, as well as optimizing the growth conditions such as the growth temperature, oxidation environment, post-process annealing steps and film thickness. The development of a comprehensive understanding of all the aspects that determine the film growth and properties will enable the future fabrication of precisely controlled oxide thin films. This is one of the critical materials challenges for nano-engineering of oxides.

References

1. Motoyama Y, Matsuzaki H, Murakami H (2001) A study of the secondary electron yield gamma of insulator cathodes for plasma display panels. IEEE Trans Electron Dev 48(8):1568–1574. doi:10.1109/16.936562
2. Matulevich YT, Vink TJ, van Emmichoven PAZ (2002) Low-energy ion-induced electron emission from a MgO(100) thin film: The role of the MgO-substrate interface. Phys Rev Lett 89(16):167601. doi:10.1103/PhysRevLett.89.167601
3. Shaikhutdinov S, Freund HJ (2012) Ultrathin oxide films on metal supports: structure-reactivity relations. Annu Rev Phys Chem 63:619–633. doi:10.1146/annurev-physchem-032511-143737
4. Chambers SA (2000) Epitaxial growth and properties of thin film oxides. Surf Sci Rep 39(5–6):105–180. doi:10.1016/s0167-5729(00)00005-4
5. Nilius N (2009) Properties of oxide thin films and their adsorption behavior studied by scanning tunneling microscopy and conductance spectroscopy. Surf Sci Rep 64(12):595–659. doi:10.1016/j.surfrep.2009.07.004
6. Goniakowski J, Finocchi F, Noguera C (2008) Polarity of oxide surfaces and nanostructures. Rep Prog Phys 71(1):55. doi:10.1088/0034-4885/71/1/016501
7. Huber H, McIntosh D, Ozin GA (1977) Metal atom model for oxidation of carbon-monoxide to carbon-dioxide-gold atom carbon monoxide dioxygen reaction and gold atom carbon dioxide reaction. Inorg Chem 16(5):975–979. doi:10.1021/ic50171a001
8. Green IX, Tang WJ, Neurock M, Yates JT (2011) Spectroscopic observation of dual catalytic sites during oxidation of CO on a Au/TiO$_2$ catalyst. Science 333(6043):736–739. doi:10.1126/science.1207272
9. Fu Q, Saltsburg H, Flytzani-Stephanopoulos M (2003) Active nonmetallic Au and Pt species on ceria-based water-gas shift catalysts. Science 301(5635):935–938. doi:10.1126/science.1085721
10. Fu Q, Weber A, Flytzani-Stephanopoulos M (2001) Nanostructured Au-CeO$_2$ catalysts for low-temperature water-gas shift. Catal Lett 77(1–3):87–95. doi:10.1023/a:1012666128812
11. Ueda A, Oshima T, Haruta M (1997) Reduction of nitrogen monoxide with propene in the presence of oxygen and moisture over gold supported on metal oxides. Applied Catalysis B-Environmental 12(2–3):81–93. doi:10.1016/s0926-3373(96)00069-0

12. Zheng N, Stucky GD (2006) A general synthetic strategy for oxide-supported metal nanoparticle catalysts. J Am Chem Soc 128(44):14278–14280. doi:10.1021/ja0659929

13. Hayashi T, Tanaka K, Haruta M (1998) Selective vapor-phase epoxidation of propylene over Au/TiO$_2$ catalysts in the presence of oxygen and hydrogen. J Catal 178(2):566–575. doi:10.1006/jcat.1998.2157

14. Rodriguez JA, Ma S, Liu P, Hrbek J, Evans J, Perez M (2007) Activity of CeO$_x$ and TiO$_x$ nanoparticles grown on Au(111) in the water-gas shift reaction. Science 318(5857):1757–1760. doi:10.1126/science.1150038

15. Senanayake SD, Stacchiola D, Evans J, Estrella M, Barrio L, Pérez M, Hrbek J, Rodriguez JA (2010) Probing the reaction intermediates for the water–gas shift over inverse CeO$_x$/Au(111) catalysts. J Catal 271(2):392–400. doi:10.1016/j.jcat.2010.02.024

16. Yan T, Redman DW, Yu W-Y, Flaherty DW, Rodriguez JA, Mullins CB (2012) CO oxidation on inverse Fe$_2$O$_3$/Au(111) model catalysts. J Catal 294:216–222. doi:10.1016/j.jcat.2012.07.024

17. Magkoev TT (2007) Interaction of carbon monoxide and oxygen at the surface of inverse titania/Au model catalyst. Surf Sci 601(14):3143–3148. doi:10.1016/j.susc.2007.05.015

18. Wu C, Marshall MSJ, Castell MR (2011) Surface structures of ultrathin TiO$_x$ films on Au (111). J Phys Chem C 115(17):8643–8652. doi:10.1021/jp111385n

19. Pan Y, Benedetti S, Nilius N, Freund H-J (2011) Change of the surface electronic structure of Au(111) by a monolayer MgO(001) film. Phys Rev B 84(7):075456. doi:10.1103/PhysRevB.84.075456

20. Guimond S, Goebke D, Romanyshyn Y, Sturm JM, Naschitzki M, Kuhlenbeck H, Freund H-J (2008) Growth and characterization of ultrathin V$_2$O$_y$ (y approximate to 5) films on Au(111). J Phys Chem C 112(32):12363–12373. doi:10.1021/jp8011365

21. Guimond S, Sturm JM, Goebke D, Romanyshyn Y, Naschitzki M, Kuhlenbeck H, Freund H-J (2008) Well-ordered V$_2$O$_5$(001) thin films on Au(111): growth and thermal stability. J Phys Chem C 112(31):11835–11846. doi:10.1021/jp8011156

22. Deng X, Matranga C (2009) Selective growth of Fe$_2$O$_3$ nanoparticles and islands on Au(111). J Phys Chem C 113(25):11104–11109. doi:10.1021/jp9021954

23. Potapenko DV, Hrbek J, Osgood RM (2008) Scanning tunneling microscopy study of titanium oxide nanocrystals prepared on Au(111) by reactive-layer-assisted deposition. ACS Nano 2 (7):1353–1362. doi:10.1021/nn800169y

24. Song D, Hrbek J, Osgood R (2005) Formation of TiO$_2$ nanoparticles by reactive-layer-assisted deposition and characterization by XPS and STM. Nano Lett 5(7):1327–1332. doi:10.1021/nl0505703

25. Ma S, Rodriguez J, Hrbek J (2008) STM study of the growth of cerium oxide nanoparticles on Au(111). Surf Sci 602(21):3272–3278. doi:10.1016/j.susc.2008.08.021

26. Potapenko DV, Osgood RM (2009) Preparation of TiO$_2$ nanocrystallites by oxidation of Ti-Au(111) surface alloy. Nano Lett 9(6):2378–2383. doi:10.1021/nl900904s

27. Ragazzon D, Schaefer A, Farstad MH, Walle LE, Palmgren P, Borg A, Uvdal P, Sandell A (2013) Chemical vapor deposition of ordered TiO$_x$ nanostructures on Au(111). Surf Sci 617:211–217. doi:10.1016/j.susc.2013.07.019

28. Biener MM, Friend CM (2004) Heteroepitaxial growth of novel MoO$_3$ nanostructures on Au (111). Surf Sci 559(2–3):L173–L179. doi:10.1016/j.susc.2004.01.021

29. Fu Q, Wagner T (2007) Interaction of nanostructured metal overlayers with oxide surfaces. Surf Sci Rep 62(11):431–498. doi:10.1016/j.surfrep.2007.07.001

30. Bach CE, Giesen M, Ibach H, Einstein TL (1997) Stress relief in reconstruction. Phys Rev Lett 78(22):4225–4228. doi:10.1103/PhysRevLett.78.4225

31. Barth JV, Brune H, Ertl G, Behm RJ (1990) Scanning tunneling microscopy observations on the reconstructed Au(111) surface-atomic-structure, long-range superatructure, rotational domains, and surface-defects. Physical Review B 42(15):9307–9318. doi:10.1103/PhysRevB.42.9307

32. Lauritsen JV, Besenbacher F (2006) Model catalyst surfaces investigated by scanning tunneling microscopy. In: Gates BC, Knozinger H (eds) Advances in catalysis, vol 50. Advances in catalysis. Elsevier Academic Press Inc, San Diego, pp 97–147. doi:10.1016/s0360-0564(06)50003-3

33. Morgenstern K, Kibsgaard J, Lauritsen JV, Laegsgaard E, Besenbacher F (2007) Cobalt growth on two related close-packed noble metal surfaces. Surf Sci 601(9):1967–1972. doi:10.1016/j.susc.2007.02.018

34. Khan NA, Matranga C (2008) Nucleation and growth of Fe and FeO nanoparticles and films on Au(111). Surf Sci 602(4):932–942. doi:10.1016/j.susc.2007.12.027

35. Window AJ, Hentz A, Sheppard DC, Parkinson GS, Woodruff DP, Unterberger W, Noakes TCQ, Bailey P, Ganduglia-Pirovano MV, Sauer J (2012) The structure of epitaxial V_2O_3 films and their surfaces: a medium energy ion scattering study. Surf Sci 606(21–22):1716–1727. doi:10.1016/j.susc.2012.07.015

36. Seifert J, Meyer E, Winter H, Kuhlenbeck H (2012) Surface termination of an ultrathin V_2O_3-film on Au(111) studied via ion beam triangulation. Surf Sci 606(9–10):L41–L44. doi:10.1016/j.susc.2012.02.004

37. Dupuis AC, Abu Haija M, Richter B, Kuhlenbeck H, Freund HJ (2003) V_2O_3(0001) on Au(111) and W(110): growth, termination and electronic structure. Surf Sci 539(1–3):99–112. doi:10.1016/s0039-6028(03)00752-0

38. Window AJ, Hentz A, Sheppard DC, Parkinson GS, Niehus H, Ahlbehrendt D, Noakes TCQ, Bailey P, Woodruff DP (2011) V_2O_3(0001) surface termination: Phase equilibrium. Phys Rev Lett 107(1):016105. doi:10.1103/PhysRevLett.107.016105

39. Li M, Altman EI (2014) Cluster-size dependent phase transition of Co oxides on Au(111). Surf Sci 619:L6–L10. doi:10.1016/j.susc.2013.09.029

40. Sindhu S, Heiler M, Schindler KM, Neddermeyer H (2003) A photoemission study of CoO-films on Au(111). Surf Sci 541(1–3):197–206. doi:10.1016/s0039-6028(03)00917-8

41. Li M, Altman EI (2014) Shape, morphology, and phase transitions during Co oxide growth on Au(111). J Phys Chem C 118(24):12706–12716. doi:10.1021/jp411375w

42. Biener MM, Biener J, Schalek R, Friend CM (2004) Growth of nanocrystalline MoO_3 on Au(111) studied by in situ scanning tunneling microscopy. J Chem Phys 121(23):12010–12016. doi:10.1063/1.1808422

43. Guimond S, Göbke D, Sturm JM, Romanyshyn Y, Kuhlenbeck H, Cavalleri M, Freund HJ (2013) Well-ordered molybdenum oxide layers on Au(111): preparation and properties. J Phys Chem C 117(17):8746–8757. doi:10.1021/jp3113792

44. Pan Y, Benedetti S, Noguera C, Giordano L, Goniakowski J, Nilius N (2012) Compensating edge polarity: A means to alter the growth orientation of MgO nanostructures on Au(111). J Phys Chem C 116(20):11126–11132. doi:10.1021/jp302302v

45. Benedetti S, Nilius N, Torelli P, Renaud G, Freund HJ, Valeri S (2011) Competition between polar and nonpolar growth of MgO thin films on Au(111). J Phys Chem C 115(46):23043–23049. doi:10.1021/jp207901a

46. Nilius N, Benedetti S, Pan Y, Myrach P, Noguera C, Giordano L, Goniakowski J (2012) Electronic and electrostatic properties of polar oxide nanostructures: MgO(111) islands on Au(111). Phys Rev B 86(20):205410. doi:10.1103/PhysRevB.86.205410

47. Stavale F, Pascua L, Nilius N, Freund H-J (2013) Morphology and luminescence of ZnO films grown on a Au(111) support. J Phys Chem C 117(20):10552–10557. doi:10.1021/jp401939x

48. Wu C, Castell MR (2012) Ba and BaO_x surface structures on Au(111). Surf Sci 606(3–4):181–185. doi:10.1016/j.susc.2011.09.013

49. Quek SY, Biener MM, Biener J, Friend CM, Kaxiras E (2005) Tuning electronic properties of novel metal oxide nanocrystals using interface interactions: MoO_3 monolayers on Au(111). Surf Sci 577(2–3):L71–L77. doi:10.1016/j.susc.2005.01.012

50. Deng X, Yao K, Sun K, Li W, Lee J, Matranga C (2013) Growth of single- and bilayer ZnO on Au(111) and interaction with copper. J Phys Chem C 117(21):11211–11218. doi:10.1021/jp402008w

51. Kuhlenbeck H, Shaikhutdinov S, Freund HJ (2013) Well-ordered transition metal oxide layers in model catalysis–a series of case studies. Chem Rev 113(6):3986–4034. doi:10.1021/cr300312n

52. Romanyshyn Y, Guimond S, Gobke D, Sturm JM, Kuhlenbeck H, Dobler J, Ganduglia-Pirovano MV, Sauer J, Freund HJ (2011) Methanol adsorption on V_2O_3(0001). Top Catal 54(10–12):669–684. doi:10.1007/s11244-011-9685-y

53. Simic-Milosevic V, Nilius N, Rust HP, Freund HJ (2008) Local band gap modulations in non-stoichiometric V_2O_3 films probed by scanning tunneling spectroscopy. Phys Rev B 77(12):125112. doi:10.1103/PhysRevB.77.125112

54. Feiten FE, Seifert J, Paier J, Kuhlenbeck H, Winter H, Sauer J, Freund H-J (2015) Surface Structure of V_2O_3(0001) Revisited. Phys Rev Lett 114(21). doi:10.1103/PhysRevLett.114.216101

55. Guimond S, Abu Haija M, Kaya S, Lu J, Weissenrieder J, Shaikhutdinov S, Kuhlenbeck H, Freund HJ, Dobler J, Sauer J (2006) Vanadium oxide surfaces and supported vanadium oxide nanoparticles. Top Catal 38(1–3):117–125. doi:10.1007/s11244-006-0076-8

56. Li ZS, Potapenko DV, Osgood RM (2014) Using moire patterning to map surface reactivity versus atom registration: Chemisorbed trimethyl acetic acid on TiO/Au(111). J Phys Chem C 118(51):29999–30005. doi:10.1021/jp5103302

57. Bouzidi L, Slavin AJ (2005) Ultrathin films of lead oxide on gold: dependence of stoichiometry, stability and thickness on O_2 pressure and annealing temperature. Surf Sci 580 (1–3):195–206. doi:10.1016/j.susc.2005.01.056

58. Barcaro G, Cavaliere E, Artiglia L, Sementa L, Gavioli L, Granozzi G, Fortunelli A (2012) Building principles and structural motifs in TiOx ultrathin films on a (111) substrate. J Phys Chem C 116(24):13302–13306. doi:10.1021/jp303730j

59. Tung RT (2001) Recent advances in Schottky barrier concepts. Mater Sci Eng R-Reports 35(1–3):1–138. doi:10.1016/s0927-796x(01)00037-7

60. Giordano L, Cinquini F, Pacchioni G (2006) Tuning the surface metal work function by deposition of ultrathin oxide films: density functional calculations. Phys Rev B 73(4):045414. doi:10.1103/PhysRevB.73.045414

61. Goniakowski J, Giordano L, Noguera C (2010) Polarity of ultrathin MgO(111) films deposited on a metal substrate. Phys Rev B 81(20):205404. doi:10.1103/PhysRevB.81.205404

62. Goniakowski J, Noguera C, Giordano L, Pacchioni G (2009) Adsorption of metal adatoms on FeO(111) and MgO(111) monolayers: effects of charge state of adsorbate on rumpling of supported oxide film. Phys Rev B 80(12):125403. doi:10.1103/PhysRevB.80.125403

63. Song Z, Cai TH, Chang ZP, Liu G, Rodriguez JA, Hrbek J (2003) Molecular level study of the formation and the spread of MoO_3 on Au (111) by scanning tunneling microscopy and X-ray photoelectron spectroscopy. J Am Chem Soc 125(26):8059–8066. doi:10.1021/ja034862m

64. Wu P, Cao G, Tang F, Huang M (2014) Electronic and magnetic properties of transition metal doped MgO sheet: a density-functional study. Comput Mater Sci 86:180–185. doi:10.1016/j.commatsci.2014.01.052

65. Coey JMD (2006) Dilute magnetic oxides. Curr Opin Solid State Mater Sci 10(2):83–92. doi:10.1016/j.cossms.2006.12.002

66. Tauster SJ, Fung SC, Garten RL (1978) Strong metal-support interactions-group-8 noble-metals supported on TiO_2. J Am Chem Soc 100(1):170–175. doi:10.1021/ja00469a029

67. Tauster SJ, Fung SC, Baker RTK, Horsley JA (1981) Strong-interactions in supported-metal catalysts. Science 211(4487):1121–1125. doi:10.1126/science.211.4487.1121

68. Tauster SJ (1987) Strong metal-support interactions. Acc Chem Res 20(11):389–394. doi:10.1021/ar00143a001

69. Sturm JM, Goebke D, Kuhlenbeck H, Doebler J, Reinhardt U, Ganduglia-Pirovano MV, Sauer J, Freund HJ (2009) Partial oxidation of methanol on well-ordered V_2O_5(001)/Au(111) thin films. Phys Chem Chem Phys 11(17):3290–3299. doi:10.1039/b822384j

70. Abu Haija M, Guimond S, Uhl A, Kuhlenbeck H, Freund HJ (2006) Adsorption of water on thin V_2O_3(0001) films. Surf Sci 600(5):1040–1047. doi:10.1016/j.susc.2005.12.035

71. Bandara A, Abu-Haija M, Höbel F, Kuhlenbeck H, Rupprechter G, Freund H-J (2007) Molecular adsorption on $V_2O_3(0001)$/Au(111) surfaces. Top Catal 46(1–2):223–230. doi:10. 1007/s11244-007-0332-6

72. Potapenko DV, Li Z, Lou Y, Guo Y, Osgood RM (2013) 2-Propanol reactivity on in situ prepared Au(111)-supported TiO_2 nanocrystals. J Catal 297:281–288. doi:10.1016/j.jcat.2012. 10.020

73. Barcaro G, Fortunelli A (2009) Adsorption and Diffusion of Fe on a Titania Ultrathin Film. J Phys Chem A 113(52):14860–14866. doi:10.1021/jp904998c

74. Giordano L, Pacchioni G, Goniakowski J, Nilius N, Rienks EDL, Freund H-J (2008) Charging of metal adatoms on ultrathin oxide films: Au and Pd on FeO/Pt(111). Phys Rev Lett 101 (2):026102. doi:10.1103/PhysRevLett.101.026102

75. Cavaliere E, Kholmanov I, Gavioli L, Sedona F, Agnoli S, Granozzi G, Barcaro G, Fortunelli A (2009) Directed assembly of Au and Fe nanoparticles on a TiO_x/Pt(111) ultrathin template: the role of oxygen affinity. Phys Chem Chem Phys 11(47):11305–11309. doi:10. 1039/b915641k

76. Barcaro G, Fortunelli A, Granozzi G (2008) Metal adsorption on oxide polar ultrathin films. Phys Chem Chem Phys 10(14):1876–1882. doi:10.1039/b719346g

77. Baron M, Bondarchuk O, Stacchiola D, Shaikhutdinov S, Freund HJ (2009) Interaction of gold with cerium oxide supports: $CeO_2(111)$ thin films vs CeO_x nanoparticles. J Phys Chem C 113(15):6042–6049. doi:10.1021/jp9001753

78. Wu C, Castell MR, Goniakowski J, Noguera C (2015) Stoichiometry engineering of ternary oxide ultrathin films: $Ba_xTi_2O_3$ on Au(111). Phys Rev B 91(15):155424. doi:10.1103/ PhysRevB.91.155424

Chapter 6
Phonons in Thin Oxide Films

Luca Vattuone, Letizia Savio and Mario Rocca

Abstract Thin oxide films have physical and chemical properties which may be significantly different from those of the corresponding bulk materials. For their complete characterization the information on the lattice dynamics which can be retrieved by vibrational spectroscopy is mandatory. Here we show that the number of observed phonon modes and their frequencies can indeed provide relevant information about stoichiometry, structure and thickness of the film.

6.1 Introduction

In recent years an increasing number of studies has been devoted to the characterization of the properties of thin oxide films. A film can be considered to be "thin" as long as the size of its single crystalline domains in the plane of the surface strongly exceeds its thickness. The term "ultrathin" is used, on the other hand, when the latter goes from one to just a few atomic layers. In the opposite limit, when the extension along all three dimensions is comparable, it is more appropriate to consider the film as an agglomeration of nanoparticles. The interest in thin and ultrathin films is motivated by the following considerations:

(a) A thin oxide film is usually grown epitaxially on an appropriate single or poly-crystalline substrate, chosen so that the lattice mismatch with the corresponding bulk oxide is minimized. One could thus expect the thin film to be very close to what one could ideally obtain by cutting a slab from the bulk

L. Vattuone (✉) · M. Rocca
Dipartimento di Fisica dell'università di Genova, Via Dodecaneso 33, 16146 Genoa, Italy
e-mail: vattuone@fisica.unige.it

M. Rocca
e-mail: rocca@fisica.unige.it

L. Vattuone · L. Savio · M. Rocca
IMEM-CNR Unità Operativa di Genova, Via Dodecaneso 33, 16146 Genoa, Italy
e-mail: savio@fisica.unige.it

solid. Reality is, however, often more complex. There is inevitably a few percent difference between the lattice spacing of the most appropriate substrate and the one of the bulk oxide. In the ultrathin limit the film is thus either slightly compressed or slightly strained, i.e. different from the ideal bulk-like slab depicted above. Such a difference may cause the film to show different electronic and chemical properties with respect to those expected for a surface layer obtained by cutting a bulk oxide [1]. Only after reaching thicknesses of some tens of layers, the lattice spacing attains the bulk limit value releasing the stress and reducing it to negligible values. In this limit we expect our film to behave in the same way as the bulk solid, except possibly for just the very first layers at the interface with the underlying substrate, and its surface to have properties quite similar to those of the one obtained by cutting the bulk oxide.

(b) The electronic structure of the substrate may directly affect the one of the thin film on top of it. For the most reactive cases, the deposition of the film can also modify the substrate by causing its reconstruction. The film itself or the atoms, the molecules and the clusters deposited on the surface can conversely behave differently depending on the influence of the substrate, i.e. on film thickness [2]. In some cases, charge transfer to particles supported on the oxide films may occur. Such charging depends on the electronic properties of the substrate and of the film and decreases with increasing film thickness. It has been shown that charging can affect the equilibrium shape of the nanoparticle as well as its chemical reactivity.

(c) Thin oxide films deposited on a conductive substrate still allow to use the powerful electron based spectroscopic tools typical of surface science, like X-ray photoelectron spectroscopy (XPS), Ultra violet Photoelectron Spectroscopy (UPS), High Resolution Electron Energy Loss Spectroscopy (HREELS) and Low Energy Electron Diffraction (LEED), just to mention the most widely employed. Since a large set of information regarding stoichiometry and oxidation state can be inferred only by such techniques, thin films represent an appealing model system for the characterization of the surfaces of insulating bulk oxides [3].

The aim of the present review is to show and discuss the vibrational spectra of thin films, from which a large amount of information on structure, stoichiometry and even morphology of the oxide layer can be inferred. To this purpose, we will not provide a comprehensive review but we will rather focus our attention on a few paradigmatic cases taken from the recent literature in the field. Since for an oxide film the number of observable vibrational modes, and hence the complexity of the spectra, is determined by its stoichiometry, we will firstly address simple oxides with only two atoms/cell such as MnO, MgO and NiO. We will then consider more complex materials such as TiO_2 and SiO_2 and move eventually to Al_2O_3 and Fe_3O_4. Whenever possible, we will present data obtained for different thicknesses of the films and try to correlate them with structural and stoichiometric information.

We will see that some modes have a microscopic character while other ones are macroscopic in nature. The former, addressed as Wallis modes, depend on the local

structure and force constants and can be predicted only using methods taking into account the real atomic structure and the actual forces between the atoms in the film. The latter, also called Fuchs-Kliewer (FK) modes [4], correspond to the relative motion of macroscopic cationic and anionic sub-lattices with respect to each other, and can be described in the frame of dielectric theory.

6.2 Power and Limits of Dielectric Theory

Dielectric theory enables one to predict the energy of vibrational modes for a bulk solid as well as for a film of given thickness [5]. For a single crystal and for a thick enough film, i.e. in the limit of bulk oxide surfaces, the energy of the FK mode (ω_{FK}) reads:

$$\hbar\omega_{FK} = \sqrt{\frac{\epsilon_0 + 1}{\epsilon_\infty + 1}}\hbar\omega_{TO} \tag{6.1}$$

where ω_{TO} is the frequency of the TO (i.e. zone centre transverse optical) phonon, ε_0 the static dielectric constant and ϵ_∞ the high frequency limit of the dielectric function.

For a film the energy of the FK mode depends on thickness. It is possible to define [6] an effective dielectric constant, $\xi_o(\boldsymbol{q}_\parallel, \omega, d)$ for a two layer system of thickness d in terms of the (frequency dependent) dielectric function of the oxide layer $\varepsilon(\omega)$ and of the substrate $\xi_s(\boldsymbol{q}_\parallel; \omega)$, which can be written as:

$$\xi_o(\boldsymbol{q}_\parallel, \omega, d) = \epsilon \coth(q_\parallel d) - \frac{\left(\frac{\epsilon}{\sinh(q_\parallel d)}\right)^2}{\epsilon \coth(q_\parallel d) + \xi_s(\boldsymbol{q}_\parallel, \omega)} \tag{6.2}$$

The dielectric function of the oxide layer is

$$\epsilon(\omega) = \epsilon_\infty + \frac{(\epsilon_0 - \epsilon_\infty)\omega_{TO}^2}{\omega_{TO}^2 - \omega^2 - i\gamma\omega\omega_{TO}} \tag{6.3}$$

where γ is the appropriate damping constant, while the dielectric function of the substrate can be written in a simplified Drude form (neglecting the dependence on the wavevector)

$$\xi_s(\omega) = \frac{-\omega_p^2}{\omega^2 + i\gamma_p\omega\omega_p} \tag{6.4}$$

where ω_p is the surface plasmon energy of the substrate and γ_p the damping factor. Using dielectric theory it is possible to compute also the loss function. Peaks are expected whenever $\xi = -1$ as shown in Fig. 6.1 [7, 8].
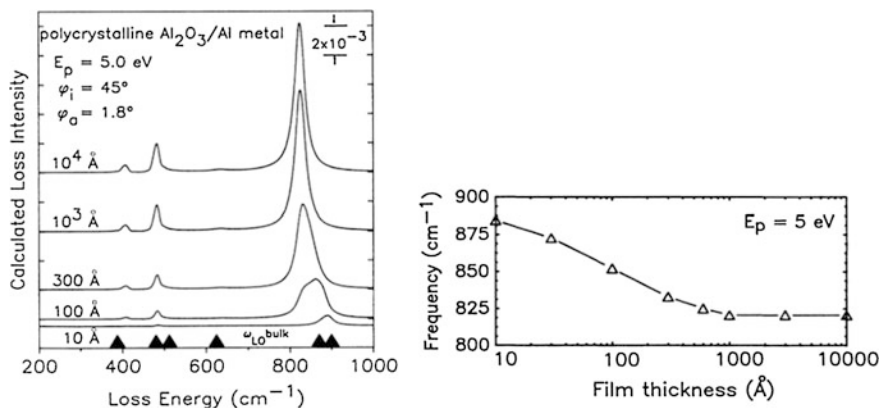
Fig. 6.1 *Left* Calculated HREEL spectra for polycrystalline Al_2O_3 films grown on Al for different thicknesses. *Right* Dependence of frequency on film thickness for the higher energy phonon. Taken with permission from [7]. Copyright by APS

As pointed out already in 1991 [8], dielectric theory becomes inadequate for thin films since the contribution of microscopic phonons is then no longer negligible and a microscopic theory becomes mandatory in order to reproduce the experimental results. In this limit also the distinction between macroscopic modes (predicted by dielectric theory) and microscopic ones may become fuzzy.

6.3 Brief Resume of Selection Rules for Vibrational Spectroscopy

Before showing selected results for a few systems of increasing complexity it is worth to briefly summarize the selection rules which are operative for HREELS and Infra-Red Absorption Spectroscopy (IRAS) on a metal substrate. The reader is referred to more specialized books [9] or reviews (see e.g. [10]) for a more comprehensive treatment [9].

According to quantum mechanics the vibrational transition probability is proportional to the square of the transition dipole moment:

$$\langle \mu \rangle = \int \Psi_f^*(Q_k) \mu \, \Psi_i(Q_k) dQ_k \tag{6.5}$$

where μ is the dipole moment operator of the molecule, Ψ_I and Ψ_f are the initial and final vibrational wave functions for the given normal mode with wavevector k and Q_k is the corresponding normal mode coordinate [10]. By expressing the dipole moment μ into its x, y and z coordinates we can easily conclude that at least one of these components must be non-vanishing for this mode to be IR active. We could

otherwise state that only vibrational transitions with a change in the dipole moment are IR active. The intensity I_k of band k will thus be proportional to $\left(\frac{d\mu}{dQ_k}\right)^2$. Using the general language of group theory it is necessary that the product $\Gamma_f \times \Gamma_\mu \times \Gamma_i$ of the representations of Ψ_f, μ and Ψ_i contains the totally symmetric representation.

For transitions from fundamental to first excited vibrational state (the most common case), since the initial state belongs to the totally symmetric representation [11], it is necessary that the final state belongs at least to the same representation of one of the components of μ. In less formal words, only vibrational modes which transform as one of the coordinates x, y or z can be excited by IR light.

If the substrate is a metal and if z is the coordinate normal to the surface, the selection rule is more restrictive and only dipole moments which transform as z can be active. This is the so-called metal selection rule which is usually shortly stated saying that only vibrational modes with a component of the dynamical dipole moment perpendicular to the metal surface will contribute to the IR absorbance. This rule can be understood qualitatively since the electric field parallel to the metal surface must vanish at least for frequencies lower than the plasma frequency of the metal, i.e. whenever a dipole parallel to the surface can be screened by the image dipole created by the conducting electrons in the metal.

In general, for any given space group it is possible to infer by inspection of the character table which modes are totally symmetric and then to know the number of expected IR active modes. Conversely, if the structure is not known or if there are alternative possibilities, the number of observed modes at least restricts the possible choices.

The situation is more complicated for HREELS. Under dipole scattering conditions, i.e. when the excitation of the surface vibration is caused by the electric field of the incoming electron, the same selection rules as for RAIRS apply. This is the usual case when inspecting spectra recorded in-specular, i.e. when the angle of incidence and of reflection of the electron beam are identical, so that the parallel momentum transfer is small compared to that of the incoming electrons. However for HREELS other scattering mechanisms are possible, namely impact and resonance scattering: such mechanisms are not affected by the dipole selection rule and allow to observe also vibrations which are not IR active. When these mechanisms dominate, the intensity may change with scattering angle non-monotonically and be significant for off-specular geometries. The use of impact and resonant scattering in the study of thin oxide films is limited since detailed theoretical calculations are needed to account for the angle and energy dependence of the scattering cross section. For this reason we will not discuss them further in this review [12, 13].

Finally, vibrational information can be obtained also by Surface Enhanced Raman Scattering, SERS. Similarly to RAIRS (and contrary to HREELS!) SERS does not require UHV conditions and can thus be employed also at atmospheric pressure and in reactive environments. At variance with RAIRS, the inelastic scattering of light has an inherently low cross section which severely limits its sensitivity except under special conditions associated to surface roughness. The selection rules for SERS are quite different from the ones of RAIRS and dipolar

HREELS: in order to be Raman active a vibrational transition must indeed cause a change in the polarizability (rather than a change in the dipole moment as for IRAS). Using the same formalism introduced above, for a transition from the fundamental to the first excited state to be Raman active it is necessary that the vibrational mode transforms as the product of two coordinates (e.g. xx, xy, xz, etc). The operator in (6.5) is now the polarizability tensor, while it was the dipole moment in the case of RAIRS. For this reason and with the only exception of crystals without center of inversion, a Raman active mode is inactive in RAIRS and viceversa [11].

Finally, we mention that the most common unit when dealing with IRAS and RS is the cm^{-1}, while for HREEL spectra are often expressed in meV. Since using a uniform notation would require to modify some of the original data, we recall here that the conversion factor between the two units is 1 meV = 8.065 cm^{-1}. We will report in the following the converted value in parenthesis next to the original value every time we feel it is necessary for an easier comparison between different experiments.

6.4 MeO Oxides Thin Films

6.4.1 MnO

Bulk MnO has a rock-salt structure with a lattice constant of 0.444 nm. MnO is an insulator with band gap between 3.6 and 4.3 eV and with antiferromagnetic behaviour below the Néel temperature of 118 K. Vibrational spectra for the bulk material show a transverse optical phonon (TO) at the $\bar{\Gamma}$ point having an energy of 265 cm^{-1} [14], which splits below 118 K due to the occurrence of magnetic ordering [15].

MnO films have been grown on different substrates (see [6] and references therein). In Fig. 6.2 we show the HREEL spectrum for MnO grown on Pt(111) by deposition of Mn in O_2 atmosphere at 375 K, parametric in film thickness (expressed in oxide monolayers, ML). Below the completion of the first ML, only one peak at 367 cm^{-1} (46 meV) is present. It shifts to higher energy with increasing thickness saturating at 382 cm^{-1} (47 meV). It is assigned to the Wallis mode, in which the first layer O atoms vibrate against the Mn lattice along the surface normal. The small change of the mode frequency with film thickness indicates its local character. A second peak at an energy of 547 cm^{-1} (68 meV) shows up only after completion of the first monolayer. Its intensity increases linearly with coverage and does not seem to saturate. This loss has been identified with the FK mode, a surface phonon polariton responsible for the dielectric response of MnO. The negatively charged oxygen lattice and the positively charged Mn lattice vibrate thereby with respect to each other in counter-phase. The FK mode frequency shows a slight decrease with increasing thickness, as predicted by dielectric theory.
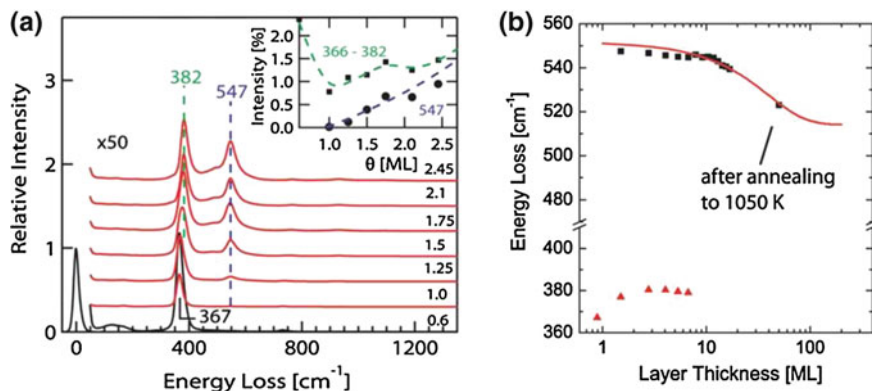
Fig. 6.2 *Left* HREEL spectra for MnO films on Pt(111). The *inset* shows the dependence of the peak intensities on thickness. The *dashed lines* are guide for the eye. *Right* Dependence of the frequency of the FK (*black squares*) and Wallis (*red triangles*) modes on the thickness of the oxide layer. Taken with permission from [6]. Copyright by APS

It is remarkable that the frequency of the FK mode depends not only on the MnO film thickness (i.e. number of layers, otherwise addressed as coverage) but also on its morphology. This result is evident from inspection of Fig. 6.3 showing the change in the HREEL spectra after annealing a 17 ML thick film of MnO/Pt(111). Up to 850 K, no qualitative changes occur in the HREEL spectra except for the decrease of the FK peak width, indicating a reordering of the film. On the contrary,
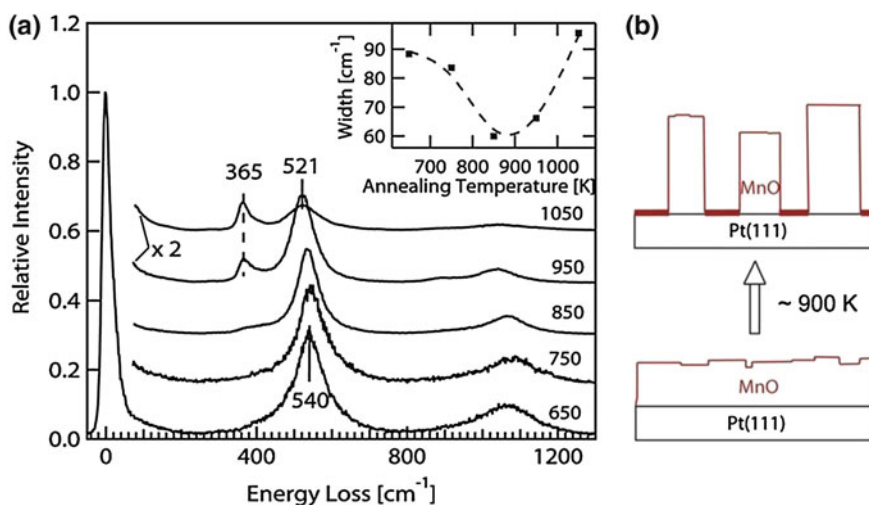
Fig. 6.3 *Left* HREEL spectra recorded after annealing a 17 ML thick film of MnO grown on Pt (111) at different temperatures. The *inset* shows the width of the FK peak while in the right part of the picture a schematic of the restructuring of films is shown. Taken with permission from [6]. Copyright by APS

annealing at higher temperature causes an increase in the width and a relatively large redshift (from 547 to 521 cm^{-1}, i.e. from 68 to 64 meV) of the FK mode, indicating a substantial restructuring of the MnO layer.

We note that the Wallis mode is not visible in the spectra of films thicker than 10 ML (see Figs. 6.2 and 6.3). In such conditions the mode is still there but its loss is embedded in the tail of the FK peak. It reappears only after annealing, when the intensity of the FK loss has decreased significantly. This behaviour is indicative of a restructuring of the surface (schematized in Fig. 6.3b). A large part of it is now covered by one monolayer thick MnO islands and, since the total amount of MnO cannot decrease, the remaining oxide must have reorganized in relatively thick clusters of 40–50 ML height. The authors estimate that, under the investigated experimental conditions, 2/3 of the surface is covered by monolayer MnO and 1/3 by thick clusters.

The oxidation of Mn can lead to the formation of oxides having a higher oxygen content than MnO. We will present vibrational data relative to them in paragraph 1.6.

6.4.2   MgO

In the case of MgO/Ag(100) the correlation between the vibrational frequencies and the morphology of the film is preserved and even amplified in the low coverage limit [16, 17]. We present the growth of MgO films of different thicknesses at the growth temperature T_g = 453 K in Fig. 6.4.
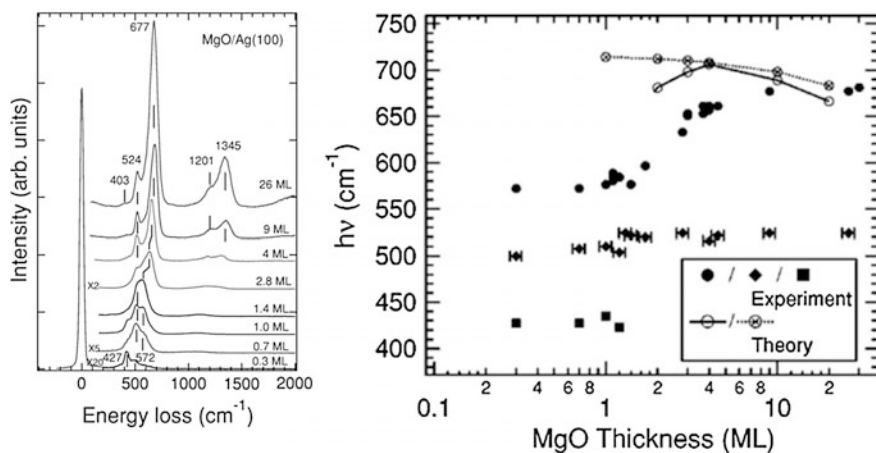
Fig. 6.4 *Left* HREEL spectra recorded after growing MgO films of different thicknesses on Ag (100) at 453 K. *Right* Dependence of observed vibrational frequencies on film thickness and comparison with the value predicted by theory for the FK mode. The *open circles* refer to the theoretical values for FK calculated using a microscopic approach (see [16] for details) while the crossed circles refer to the forecasts of dielectric continuum theory. Taken with permission from [16]. Copyright by APS

The spectra show a mode at 427 cm^{-1} (53 meV), which disappears upon the completion of the first layer, a mode around 524 cm^{-1} (64 meV), present for all films at the same frequency, and a mode around 670 cm^{-1} (83 meV), appearing only after completion of the monolayer and increasing in intensity with film thickness.

The low energy loss is assigned to a vibration at MgO sites at the edges of the islands in contact with Ag, since it disappears above 1 ML. Indeed STM inspection will show that, under the growth conditions applied in this experiment, sub-monolayer films consist of single layer islands of MgO with a quite irregular shape and thus a high density of borders. The loss at 524 cm^{-1} (64 meV) is identified with the Wallis mode, which is indeed expected to be little affected by thickness due to its microscopic nature. Finally, the mode at the highest frequency is assigned to the FK mode. In the thickness range between 0.7 and 1.4 ML, intensity is also present in the frequency range between 572 cm^{-1} (71 meV) and 605 cm^{-1} (75 meV).

Several growth procedures for monolayer MgO films on Ag(100) were tested, monitoring the film morphology by low temperature STM. It was found that both the usual growth parameters (T_g, oxygen pressure, Mg flux) and after growth treatments are important in determining the film structure [17], as evidenced in Fig. 6.5. When the film is grown at T_g = 450 K and the sample rapidly cooled down below room temperature (fast cooling procedure, FC), single layer MgO islands of irregular shape form (see line scans in Fig. 6.5e). If the growth temperature is increased to 773 K and the sample is again cooled down rapidly after growth, multilayer (mainly bilayer) islands with nice straight borders along the $\langle 001 \rangle$ direction are observed. Finally, if the film is grown at 773 K and subsequently cooled down slowly (slow cooling protocol, SC), flat terraces limited in size only by substrate steps are formed. This result can be explained by thermodynamic arguments: the surface energy of MgO and Ag(100) are respectively 1.15 and 1.20 J/m^2 so that entropy determines the favoured growth mode. At the lowest temperature a layer by layer growth is expected and in the low coverage limit islands of single layer thickness form to minimize the area of the uncovered Ag surface. At T_g = 773 K, due to entropy, a multilayer island growth mode is preferred: when the sample is rapidly cooled down, the morphology which is energetically favoured at this T_g is quenched and double or multilayer islands are observed. On the contrary, if the system is slowly cooled down, thus allowing it to attain its thermodynamically favoured morphology, nearly perfect single layer terraces are obtained.

It is interesting to see how the morphological information provided by STM correlates with the vibrational information obtained by HREELS (see Fig. 6.5f). The Wallis mode is always present, as expected. The mode at 53 meV (427 cm^{-1}) is best visible for T_g = 450 K and FC. In accord to its assignment to an MgO localised at the edges of the islands in contact with the substrate [16], it has a lower intensity when the film grown at 450 K is slowly cooled down, thus allowing the islands to attain a more regular shape and minimize the edge length. The mode at 75 meV (605 cm^{-1}), the intensity of which is largest for FC, i.e. when irregular edges are
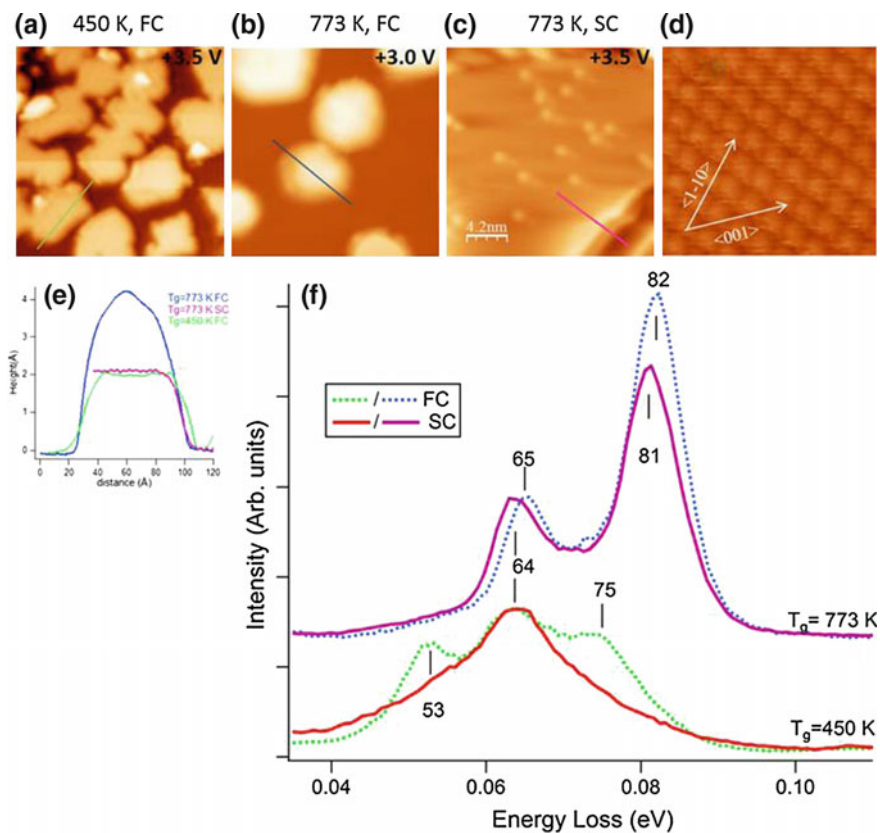
Fig. 6.5 *Top* (**a**–**c**) STM images recorded for different growth temperatures (450 and 773 K) and for different post growth treatments (*FC* fast cooling; *SC* slow cooling). Image size: 21×21 nm^2, I = 0.2 nA. We note that images are recorded at a bias voltage V $\geq$ 3.0 V, i.e. under topographical conditions. They are thus fully representative of the MgO layer geometry. **d** Atomically resolved image of clean Ag(100), used for calibration. High symmetry directions are marked by *arrows*. Image size 2.4×2.4 nm^2, V = 0.1 V, I = 0.2 nA. *Bottom* **e** Line scans along the directions marked in panels **a**, **b** and **c**. **f** HREEL spectra recorded for the different growth conditions. Taken with permission from [17]. Copyright by APS

present, has been assigned to microscopic modes different from the Wallis one and involving the motion of oxygen at the border of the islands. Indeed its width is indicative for the presence of several different contributions in the range of frequencies between 71 and 75 meV (572–605 cm^{-1}), whose weight depends on the details of the local environment.

More importantly, the FK mode, expected around 82 meV (661 cm^{-1}), is not observed here since it can only exist in areas covered by at least one layer. This mode is, indeed, well evident for the only case in which bilayer islands formation occurs, i.e. $T_g = 773$ K and FC.

There remains to explain why for T_g = 773 K and SC, when STM inspection shows only extended and nearly perfect single layer terraces, the FK mode persists, although with a slightly red shifted frequency (81 meV, 653 cm^{-1}). The reason is that in these conditions the film is over-stoichiometric in oxygen, as demonstrated by XPS [18]. The excess oxygen atoms accumulate at the interface and allow to release the stress present at the interface, definitely favouring the formation of the large single layer terraces observed by STM images. The 81 meV mode can thus be assigned to the counter-phase vibration of the Mg sub-lattice against the O atoms of the oxide film plus those of the incomplete interface oxygen layer, resulting in a FK-like motion.

MgO is usually grown on Ag(100) or Mo(100) but growth on TiC(100) has been tried, too [19]. For a two layer film, frequencies of 65 meV (524 cm^{-1}) and 86 meV (694 cm^{-1}) have been observed for the Wallis and FK modes, respectively. The Wallis mode has thus the same frequency observed for the other substrates, while the frequency of the FK mode is slightly higher than for MgO double layers on Ag (100). The better agreement with dielectric theory indicates a very good quality of the film structure.

6.4.3   NiO

Similar experiments have been performed for NiO thin films grown on Pd((100) or on Ni(111) [20, 21]. On Pd(100) the first layer consists thereby of a slightly distorted NiO(100) sheet with Ni vacancies arranged in an ordered $c(4 \times 2)$ array resulting in a Ni_3O_4 stoichiometry. Oxygen sits on-top of the Pd atoms, while Ni occupies the FFH sites. In such conditions only a single loss at 46 meV is observed in-specular with HREELS, see Fig. 6.6 bottom spectrum. When increasing the coverage, a peak at 64 meV (shifting to 68 meV with film thickness) appears as soon as the second layer forms, corresponding to the FK mode of NiO (to be compared with 69.5 meV for the bulk crystal) [22]. The loss at 46 meV redshifts to 42 meV and becomes hardly visible. Another (weak) peak is present at 52 meV, the origin of which is still unclear [20, 21]. The decrease in the FK frequency with film thickness predicted by dielectric theory becomes evident only at higher coverage.

NiO has been grown also on Ni(111) [21]. In such case the FK mode appears at 510 cm^{-1} (63 meV) in the low thickness limit.

6.5   MeO$_2$ and Me$_2$O$_3$ Thin Films

When considering oxides with more atoms per unit cell, the picture becomes more complex since the number of normal modes increases. We will consider here two examples: TiO_2 and SiO_2.
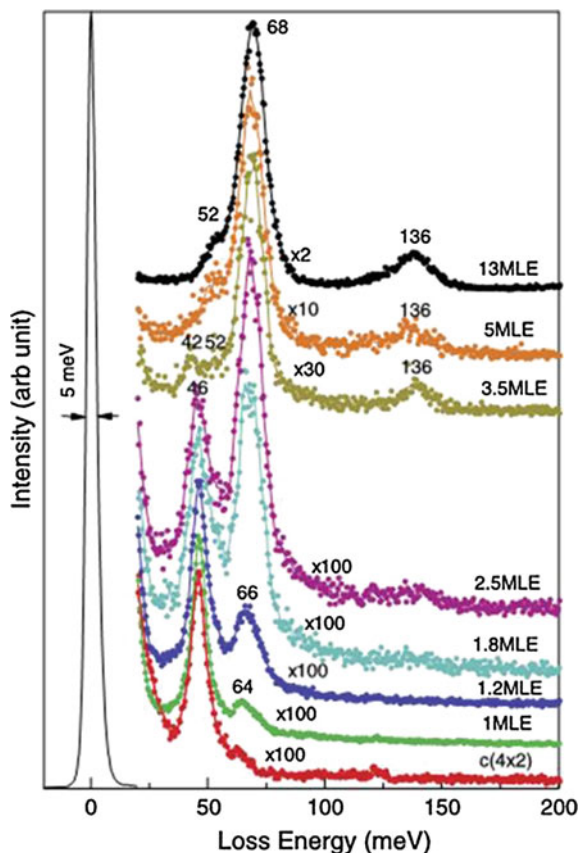
6.5.1 TiO$_2$ and Ti$_2$O$_3$

The interest for titania films has been boosted by the relevance of this material in several applications because of its biocompatibility. Titanium oxide exists in different stoichiometries and structures:

(a) TiO, having NaCl structure and lattice constant of 0.423 nm;
(b) TiO$_2$, which can have three different structures:

    1. brookite: orthorombic with lattice constants of 0.916 and 0.513 nm;
    2. rutile: tetragonal with lattice constants of 0.459 and 0.296 nm;
    3. anatase: tetragonal as well, but with lattice constants of 0.378 and 0.952 nm.

(c) Ti$_2$O$_3$, which has corundum structure with lattice constant 0.515 nm.
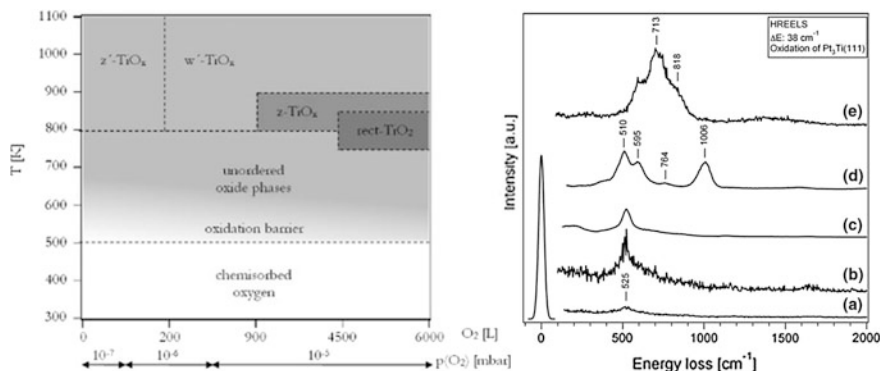
Fig. 6.7 *Left* Experimental phase diagram of the system $O_2/Pt_3Ti(111)$. Note that the abscissa is not linear. *Right* HREEL spectra recorded for different oxygen exposures: **a** 5 L O_2 at 1000 K, **b** 55 L O_2 at 1000 K, **c** 200 L O_2 at 1000 K, **d** 900 L O_2 at 900 K and **e** 4500 L O_2 at 800 K. The spectra **a** and **b** correspond to the $(6 \times 3\sqrt{3})$ phase, spectrum **c** to the $(7 \times 7)R21.8°$ layer, spectra **d** and **e** to the incommensurate rectangular and rotated rectangular structures, respectively. Taken with permission from [23]. DOI:

The right panel of Fig. 6.7 shows HREEL spectra recorded during the oxidation of a $Pt_3Ti(111)$ surface [23]. Four different phases are observed (see also phase diagram in Fig. 6.7 left panel): the $(6 \times 3\sqrt{3})$ phase (also addressed as z' because of its zig zag shape) and the $(7 \times 7)R21.8°$ phase (indicated as w', where w stands for wagon wheel), obtained upon oxidation at 1000 K, are the most stable ones; the two incommensurate rectangular phases obtained at lower temperature and higher oxygen doses are, on the contrary, metastable.

Notably the commensurate z' and w' phases exhibit a similar phonon spectrum characterised by a single prominent loss at 525 cm^{-1} (65 meV). The presence of one single loss is indicative that both of them have a TiO stoichiometry. A single loss with close values of vibrational frequency is indeed observed for MnO (572 cm^{-1}, 71 meV [24]), NiO (569 cm^{-1}, 71 meV [25]) and CoO (560 cm^{-1}, 69 meV, [26]).

The incommensurate phases exhibit more complex spectra with losses at 510 cm^{-1} (63 meV), 595 cm^{-1} (74 meV), 764 cm^{-1} (95 meV) and 1066 cm^{-1} (132 meV) (rectangular phase) and at 595 cm^{-1} (74 meV), 713 cm^{-1} (88 meV) and 818 cm^{-1} (101 meV) (rotated rectangular phase), respectively. The vibrational spectrum rules out a TiO stoichiometry for these phases. The observed frequencies, however, cannot be assigned (or assimilated) to any of the existing bulk structures, since they are different from those reported for bulk Ti_2O_3 (379 cm^{-1} and 709 cm^{-1} (47 and 88 meV), [27]) and for both phases of TiO_2 (rutile: 365, 445 and 755 cm^{-1} (45, 55 and 93 meV), respectively [28]; anatase: 355 and 790 cm^{-1} (44 and 98 meV), respectively [29]). This result supports the widely accepted idea that new phases having no direct bulk equivalent do form at surfaces and that vibrational spectroscopy provides a nearly unique tool to identify such novel oxides with potentially unexpected and useful properties.
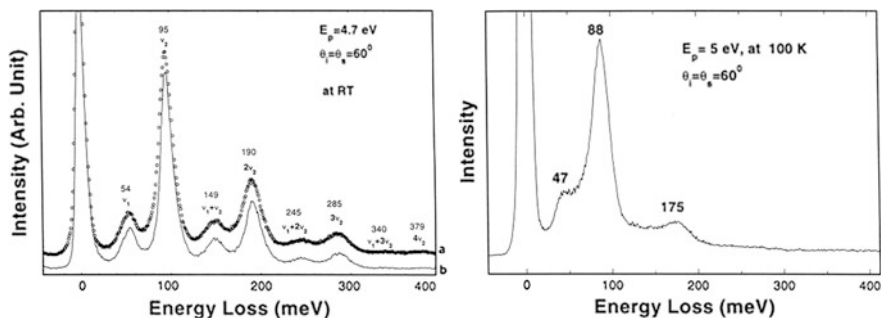
Fig. 6.8 HREEL spectra of titanium oxide films grown on Mo(110). *Left panel* Growth procedure with protocol I (30 ML thickness, recorded at RT, *upper trace*). The spectrum is compared to the one of a TiO_2(110) single crystal recorded at the same primary beam energy of 4.7 eV (*lower trace*). *Right panel* Film grown with protocol II (40 ML thickness, annealed to 1100 K, recorded at 100 K with primary energy of 5 eV). Taken with permission from [27]. Copyright by Elsevier

Titanium oxide films can also be grown on Mo(110) [27]. Films with different stoichiometry are obtained depending on the growth protocol. TiO_2 is obtained by evaporation of Ti under O_2 pressure (2.6×10^{-7} mbar) while keeping the substrate at 600–700 K and subsequent annealing to 800 K first in oxygen atmosphere and then in vacuum (protocol I). If, alternatively, some Ti (less than 1 ML) is deposited on the substrate in vacuum, continuing thereafter to grow the film following protocol I, an oxide layer with Ti_2O_3 stoichiometry forms (protocol II). The assignments of the structures was based on LEED, XPS and Auger Electron Spectroscopy, but valuable information is also provided by vibrational spectroscopy. Figure 6.8 shows HREEL spectra for films obtained with protocols I and II. Using protocol I, the HREEL spectrum is dominated by phonons at 54 and 95 meV and by their overtones. Such values are close to those measured [28] for rutile, which are reported for comparison. For protocol II the spectrum is dominated by losses at 47 and 88 meV and by one of their overtones. Such values are different both from those of films grown with protocol I and from those of bulk rutile [28] and anatase [29] samples; they are, however, similar to the peaks found for an ordered V_2O_3 film having corundum structure (see [27], main loss at 78 meV at 100 K and at 82 meV at 300 K). The frequencies obtained for Ti_2O_3 are thereby lower than for V_2O_3 because of the lower mass of Ti.

6.5.2 SiO₂

SiO_2 has also been widely investigated because of its technological importance. Single crystal SiO_2 films have been grown succesfully on Mo(112) [30–32]. Vibrational spectra, recorded both by HREELS and IRAS, show a main peak at 1048 cm^{-1} (130 meV), for which controversial assignments have been given. Chen

et al. [30] attributed it to the Si-O-Mo stretching vibration and, due to the absence of the Si–O–Si peak expected at 1176 cm^{-1} (146 meV), they concluded that the film consisted mainly of SiO$_4$ clusters. Kaya et al. [32] used the dipole selection rules to demonstrate that, for a 2D network of SiO$_2$, the Si–O–Si stretching vibration is not dipole active and thus cannot be detected by IRAS. Therefore, the absence of such mode in IRAS does not imply automatically the absence of Si–O–Si bonds. By using the same selection rules they could conclude that a 2D network can account for all the observed modes: indeed there are only three vibrations observable under dipole scattering conditions, namely the in-phase Si–O–Mo asymmetric mode (1061 cm^{-1}, 132 meV), and the out of phase and in phase couplings of symmetric Si–O–Si stretching modes (at 779 and 672 cm^{-1}, 97 and 83 meV respectively) as shown in Fig. 6.9. This result stems from the elegant application of the concepts of group theory described above.

Joining the vibrational information with STM and photoemission data, Kaya et al. further concluded that ultrathin silica film on Mo(112) consists of a two dimensional network of SiO$_4$ tetrahedra sharing the corner with one oxygen atom bonded with the substrate. For oxygen rich films a further oxygen moiety bonded directly to the substrate may be also present (see Fig. 6.10).

Modes (cm^{-1})	E	C$_2$	σ(xz)	σ(yz)	1/2τ	C$_2'$	σ'(xz)	σ'(yz)
Asymmetric Si–O–Si								
$v_1 = 1195$	1	−1	−1	1	−1	1	1	−1
$v_2 = 1137$	1	−1	−1	1	1	−1	−1	1
$v_3 = 1092$	1	1	1	1	−1	−1	−1	−1
$v_4 = 1018$	1	−1	−1	1	1	−1	−1	1
$v_5 = 1010$	1	−1	1	−1	1	−1	1	−1
$v_6 = 1008$	1	1	−1	−1	−1	−1	1	1
Asymmetric Si–O–Mo								
$v_1 = 1061$	1	1	1	1	1	1	1	1
$v_2 = 912$	1	−1	−1	1	−1	1	1	−1
$v_3 = 881$	1	1	1	1	−1	−1	−1	−1
$v_4 = 863$	1	−1	−1	1	1	−1	−1	1
Symmetric Si–O–Si								
$v_1 = 821$	1	−1	1	−1	−1	1	−1	1
$v_2 = 817$	1	1	−1	−1	1	1	−1	−1
$v_3 = 779$	1	1	1	1	1	1	1	1
$v_4 = 695$	1	−1	−1	1	−1	1	1	−1
$v_5 = 676$	1	1	1	1	−1	−1	−1	−1
$v_6 = 672$	1	1	1	1	1	1	1	1

E: identity; *C$_2$*: twofold symmetry axis; *σ(xz)*: symmetry plane; *σ'(xz)*: glide plane; *τ*: translational period.

Fig. 6.9 *Left* Schematics of the eigenvectors of the three IR active modes of SiO$_2$/Mo discussed in the text (frequency in cm^{-1}). *Right* Table showing the symmetry properties of each mode with respect to the elements of the *cmm* group. Only totally symmetric vibrations (having thus "1" for all the columns of the same row) are IR active. Taken with permission from [32]. Copyright by Elsevier
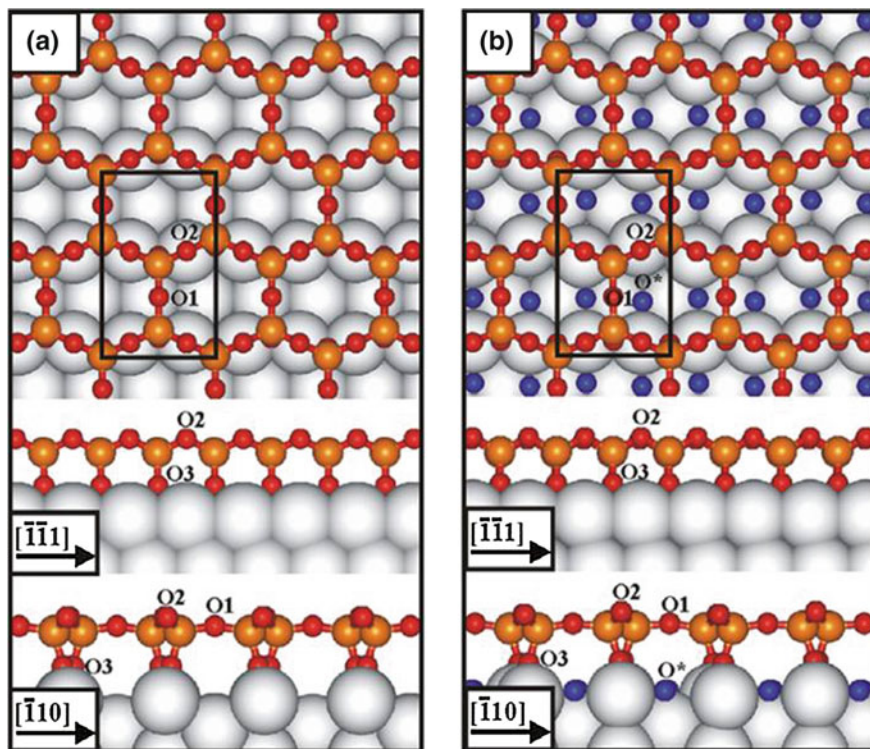
Fig. 6.10 Schematic of the 2D network model for the monolayer silica film grown on Mo(112). **a** O poor film and **b** O rich film. The additional O atoms (in *blue*) end up at the interface. Taken with permission from [32]. Copyright by Elsevier

The evolution of the vibrational spectra during growth and the subsequent annealing are shown in Fig. 6.11 [33]. We note that the modes expected according to the previous analysis definitely show up only after annealing the film (spectrum 8), i.e. when an ordered film has formed. The spectra recorded during growth are more complex. The mode at 675 cm^{-1} (84 meV) has been assigned to a Mo–O vibration involving oxygen atoms at the metal-oxide interface. The small band around 850 cm^{-1} (105 meV) corresponds to the symmetric Si–O stretch, while the asymmetric stretch modes in the region between 950 and 1250 cm^{-1} (i.e. between 118 and 155 meV) are intense and dominate the spectrum. The sharp peak at 987 cm^{-1} (122 meV) is assigned to the bending of Si–OH groups, as testified by the presence of the OH stretch mode at 3748 cm^{-1} (465 meV) (lower panel). The mode at 1022 cm^{-1} is assigned to a pseudomorphic SiO$_2$ layer at the interface. During growth the intensity of the high frequency shoulder at 1190 cm^{-1} increases and blue-shifts to 1218 cm^{-1} (151 meV). This effect was attributed to a decreased coupling of the film with the substrate due to the increased thickness. Another not identified shoulder shows up at 1155 cm^{-1} (143 meV). The richness of asymmetric
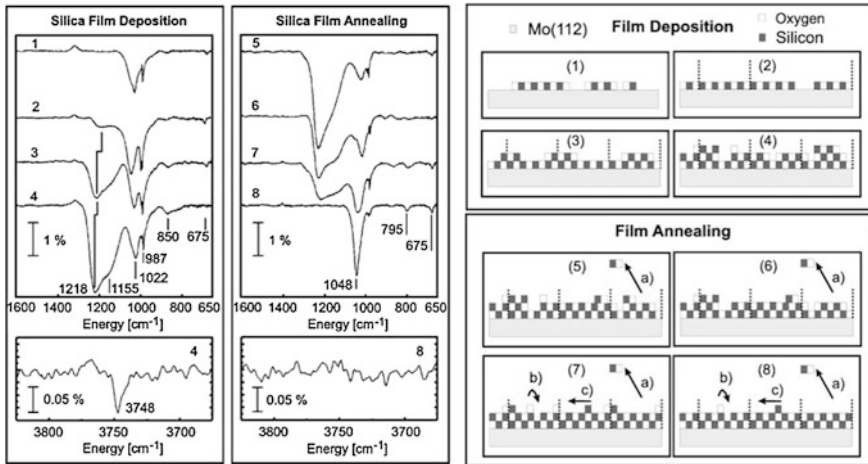
Fig. 6.11 *Left* IRA spectra recorded during growth of a silica film (1–4) and during annealing (5–8). The *bottom spectra* correspond to the frequency range of OH vibrations which indicate some OH contamination before annealing. *Right* Schematic of the suggested evolution of the layer during deposition and annealing. Taken with permission from [33]. Copyright by APS

Si–O modes is strongly indicative of the presence of different sites and thus of an increased corrugation of the film.

Upon annealing, the bands at 1155 cm^{-1} and at 1218 cm^{-1} disappear (see right panel, spectrum 8), leaving only an intense feature at 1048 cm^{-1} (130 meV) and small features in the low frequency region of the spectrum. Inspection of vibration spectra provides important hints about the growth mode, which are confirmed by LEED and Spot Profile Analysis-LEED investigations in the same multi-technique study [33].

The potential of vibrational spectroscopy is nicely demonstrated in Fig. 6.12 where the vibrational spectrum recorded for the 2D silica film is compared to the one of 1D stripes [34]. The mode at 1059 cm^{-1} (131 meV) is slightly red-shifted for the latter system, in agreement with the theoretical prediction (see bars in the highest part of Fig. 6.12). More important for the present context, the mode at 770 cm^{-1} (95 meV) blue-shifts to 875 cm^{-1} (108 meV) while the mode at 675 cm^{-1} (84 meV) remains almost unaffected. This result can be explained by the fact that in 1D stripes the Si–O–Si mode at 875 cm^{-1} is essentially a symmetric stretch vibration and has thus a higher frequency than the mode observed at 770 cm^{-1} for the 2D film, in which bending of the Si–O bond occurs. On the contrary, the Mo–O stretch vibration at 675 cm^{-1} does not change appreciably when changing the dimensionality of the layer.
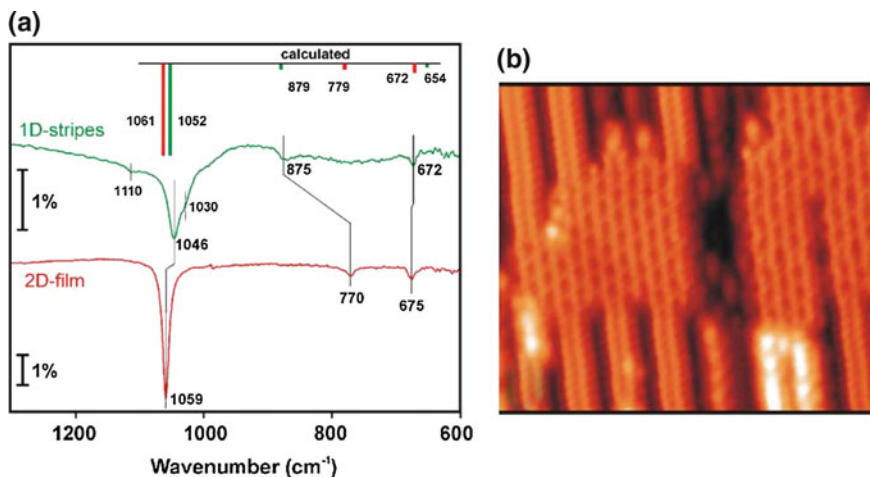
Fig. 6.12 a IRA spectra comparing 1D and 2D silica films. 1D stripes are obtained at submonolayer Si coverage [32]. When the silica stripes coalesce, particularly at increasing Si coverage, islands exhibiting a honeycomb-like structure are formed [34]. **b** STM image showing both stripes and island of silica film with atomic resolution (12.5×10.5 nm^2, -0.4 V, 0.4 nA). Taken with permission from [34]. Copyright by Elsevier

6.5.3   Al$_2$O$_3$

Together with titanium oxide, Al$_2$O$_3$ (alumina) is one of the most widely studied oxides because of its use as a support in catalysis. As already noted by Frank et al. [35], by monitoring frequency and intensity of the transverse optical (TO) and longitudinal optical (LO) phonons with IRAS it is possible to gather information on thickness and stoichiometry of such films. The ultimate reason for this is the so-called 'Berreman effect': in bulk dielectrics infrared adsorption occurs only at the frequencies corresponding to the TO phonon modes because of the transverse nature of electromagnetic waves. For films, on the contrary, also features close to the LO phonon modes are excited, provided that spectra are recorded using *p* polarized light at an oblique angle of incidence [36], thanks to the coupling to the component of the electric field normal to the surface.

For a dielectric slab on a metallic substrate it is therefore expected to observe IRAS features close to the LO frequencies of the related bulk solid. Transverse modes cannot be excited for a very thin film on a metal substrate since at a metal surface the electric field in the direction parallel to the interface vanishes. When measuring a vibrational spectrum by HREELS under dipole scattering conditions we expect to observe the same modes as in IRAS.

Al$_2$O$_3$ films can be grown on NiAl surfaces as shown first by Franchy [37]. The main information about FK modes and film structure are reported in Table 6.1. Depending on the phase formed, three to four FK modes are present.

Table 6.1 Vibrational frequencies of Fuchs-Kliewer modes and structure for alumina films on different NiAl surfaces. Data taken from [37].

Oxide and substrate	Fuchs Kliewer modes cm^{-1}	Structure
Al_2O_3/NiAl(100)	420, 603, 718, 896	θ-Al_2O_3
Al_2O_3/NiAl(110)	410, 620, 850	γ-Al_2O_3
Al_2O_3/NiAl(111)	427, 637, 887	γ-Al_2O_3 for T < 1000 K
		α-Al_2O_3 for T > 1100 K

In Fig. 6.13 IRA and HREEL spectra are compared for an alumina film grown on NiAl(110) [35]. A main feature at 860–870 cm^{-1} (107−108 meV) is observed in IRAS together with lower intensity features at 622 cm^{-1} (77 meV) and 660 cm^{-1} (82 meV). The HREEL spectrum is richer. Another intense mode is present at 419 cm^{-1} (52 meV), while additional fainter losses corresponding to microscopic modes are apparent, too. Such modes, not predicted by macroscopic dielectric theory, are expected to become more and more important with decreasing film thickness. Their assignment is, however, still controversial [38, 39].

In general, different phases can be obtained by oxidising a given substrate using different protocols. Vibrational spectroscopy can be used to distinguish among them. As summarized in Table 6.1, the γ phase is evidenced by the presence of three losses. It forms on NiAl(110) (frequencies at 410, 620 and 850 cm^{-1} (51, 77, 105 meV,
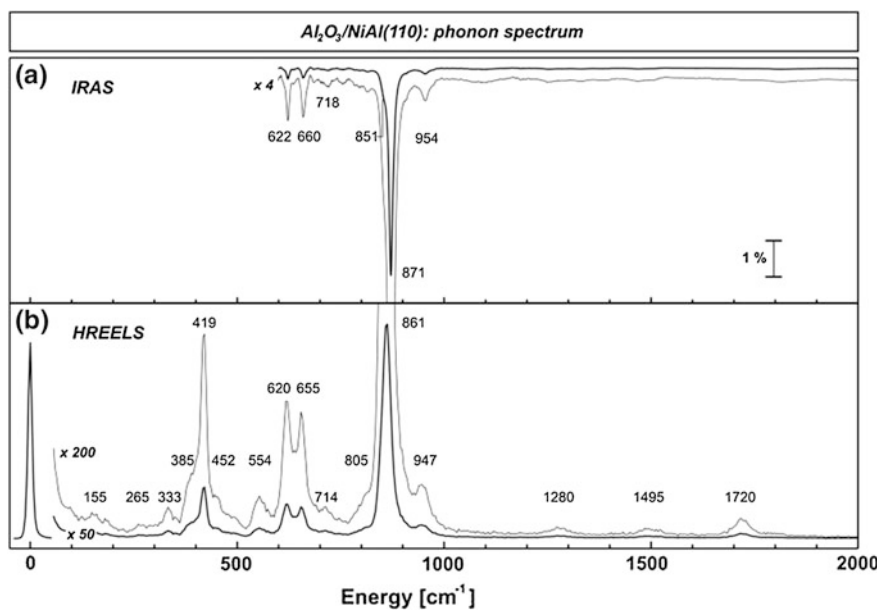
Fig. 6.13 IRA and HREEL spectra recorded at 90 K for alumina films grown on NiAl(110). Taken with permission from [35]. Copyright by Elsevier

respectively)) and on on NiAl(111) below 1000 K [frequencies at 427, 637 and 887 cm^{-1} (53, 79, 110 meV, respectively)]. The θ phase is, on the contrary, characterised by four losses. It forms on NiAl(100) where peaks at 420, 603, 718 and 896 cm^{-1} (52, 75, 89 and 111 meV, respectively) are observed. Annealing the γ phase grown on NiAl(111) above 1100 K the α-phase is obtained, characterised by losses at 78 and 113 meV [40]. Such phase forms also by oxidising NiAl(100) at 1400 K [41]. Losses at 638 and 913 cm^{-1} (79 and 113 meV, respectively) are then observed.

6.5.4 V_2O_3

Moving to vanadia, V_2O_3 thin films have been grown both on Rh(111) [42] and on TiO_2(110) (1 × 1) and (1 × 2) surfaces [43, 44]. Surface terminations for the (0001) surface of V_2O_3 with corundum structure have also been investigated by DFT [45], finding that three ideal bulk terminations are possible for the (0001) surface: (a) oxygen termination by an O_3 layer, (b) vanadium termination by a V_2 bilayer and (c) vanadium termination by a single V layer. According to DFT, termination (a) is favoured under oxygen rich conditions, termination (b) is highly unstable and (c) can occur only under highly reducing conditions. The thermodynamically stable
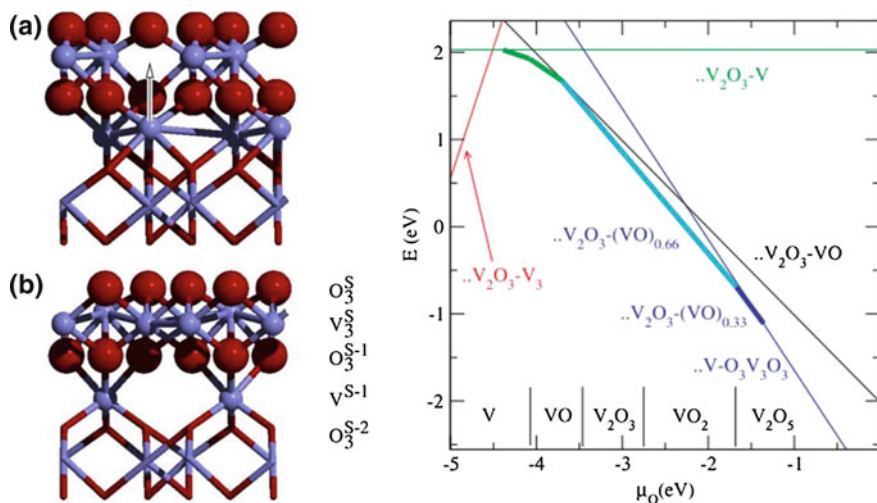
Fig. 6.14 *Left* Schematics showing the ideal V_2O_3 termination (**a**) and the energetically most stable termination (**b**) obtained by moving a vanadium atom from the second V_2 layer (S − 1) to the surface V_2 layer. *Right* Surface energy per primitive surface cell versus chemical potential μ_0 of oxygen for the (0001) surface of rhombohedral V_2O_3. *Thin lines* correspond to calculations for the primitive unit surface cell, *thick shorter lines* correspond to reconstructed cells with a periodicity of $(\sqrt{3} \times \sqrt{3})R30°$. The *thick lines* between V_2O_3V and V_2O_3VO indicate mixed $V_2O_3V_x(VO)_{1-x}1$ phases. The stability range of the bulk oxides are indicated at the *bottom* of the graph. Taken with permission from [45]. Copyright by Elsevier

O_3 termination is, however, not simply a continuation of the bulk corundum structure and a complex relaxation resulting into a—V_2O_3–V–$O_3V_3O_3$ stacking sequence occurs at the surface (see Fig. 6.14).

Over a wide range of oxygen chemical potentials the most favoured structure is, however, a surface terminated with vanadyl V=O groups. Such termination consists of a (1×1) unit cell with respect to the bulk structure with a further oxygen atom bonded to the outermost vanadia atom. Experiments confirm this theoretical prediction [42]. Figure 6.15 shows vibrational spectra of different vanadia films deposited on Rh(111). Spectrum (a) is recorded for a film exhibiting the (1×1) structure: it is characterised by features at 47, 78, and 129 meV, a weak shoulder at 92 meV and a weak structure at 156 meV. The losses at energies lower than 100 meV are associated to the phonons of V_2O_3. Theory predicts modes of relevant intensity under dipole scattering conditions at 46.2 and 63.3 meV (motion orthogonal to the hexagonal planes), a mode at 82 meV (originating from three oxygen atoms below the V=O group, vibrating nearly normally to the surface) and a mode at 135 meV (due to the vanadyl stretching mode, as suggested also by its high energy). The presence of the 129 meV vibration, close to the value predicted for the vanadyl stretch, provides a strong evidence for the presence of V=O groups. The spectrum is analogous to the one observed for a 5 ML thick film of vanadium oxide grown on Pd(111) [46].

Exposing the vanadyl terminated (1×1) surface to oxygen $(5 \times 10^6$ mbar) at 500 °C leads to the formation of a well ordered $(\sqrt{3} \times \sqrt{3})R30°$ surface (see model
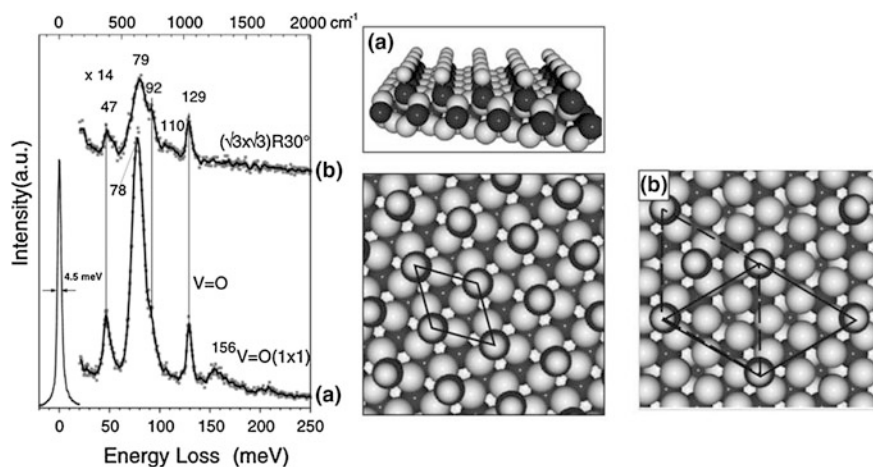
Fig. 6.15 *Left* HREEL spectra of the: **a** V_2O_3 (0001)(1×1) and **b** $(\sqrt{3} \times \sqrt{3})R30°$ surfaces recorded at 300 K. *Center* Model of the (1×1) surface: *dark spheres* indicate vanadium atoms while *bright ones* represent oxygen atoms. *Right* Model of the $(\sqrt{3} \times \sqrt{3})R30°$ structure with unit cells containing one (*dashed*) or two (*solid*) missing vanadyl groups. Taken with permission from [42]. DOI: 10.1088/0953-8984/17/26/004 © IOP Publishing. Reproduced with permission. All rights reserved

in the right part of Fig. 6.15). Due to the removal of V=O groups the surface layer is now oxygen richer. The corresponding vibrational spectrum is not very different from the one proper of the (1 × 1) structure, except for the overall lower intensity and for an additional loss at 110 meV which is not assigned. The similarity is explained by the close values of the vibrational modes of the O_3 terminated surface and to the residual presence of V=O groups [45].

Vanadium oxide films were grown also on TiO_2 [44]. In this case the vibrational spectra are complicated by the presence of the phonon modes of titania. The data analysis is therefore based on difference spectra, which confirm the assignments given above (see Fig. 6.16). The major difference is the observation of a peak at 111 meV rather than at 129 meV. The smaller frequency indicates the formation of a reactive oxygen species (VO_r bond rather than V=O), which is present on VO_x strands as well as on nanoislands.
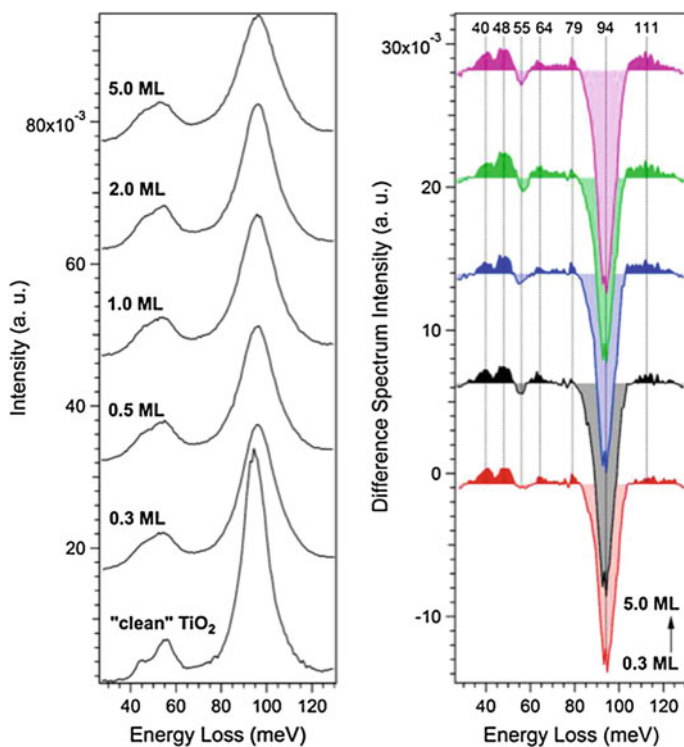
Fig. 6.16 VO_x (0.3–5.0 ML)/TiO_2(110) thin films. **a** HREELS data (recorded in specular) and **b** HREELS difference spectra calculated by subtracting the clean TiO_2(110) spectrum. Taken with permission from [44]. Copyright by ACS
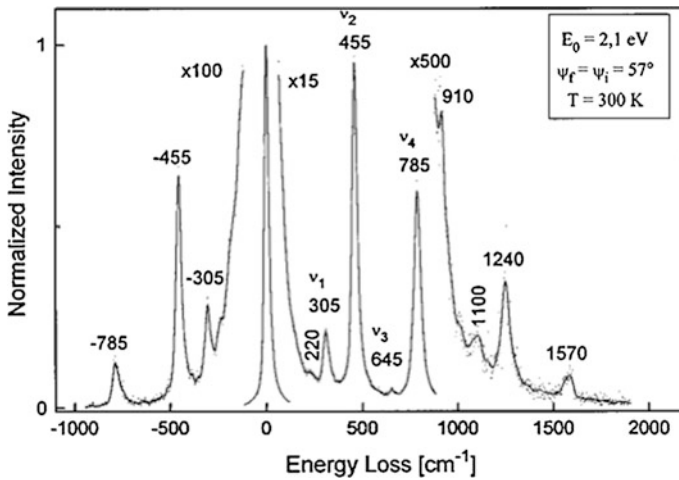
Fig. 6.17 HREEL spectra of β-Ga$_2$O$_3$ grown on CoGa(100). Taken with permission from [47]. Copyright by AIP

6.5.5 Ga$_2$O$_3$

In Fig. 6.17 we show HREEL spectra recorded for a 15 Å thick film of Gallium oxide (β-Ga$_2$O$_3$) grown on CoGa(100) (an intermetallic alloy, similar to NiAl) [47]. Losses at 220 cm^{-1} (27 meV) (extremely faint), 305 cm^{-1} (38 meV, v_1), 455 cm^{-1} (56 meV, v_2), 645 cm^{-1} (80 meV, v_3) and 785 cm^{-1} (97 meV, v_4) are observed together with the corresponding gain peaks and losses due to multiple excitation. Such losses correspond to the FK modes and are in good agreement with the values estimated theoretically on the base of dielectric theory.

The parameters used in this calculation are close to those of bulk Ga$_2$O$_3$ with the only exception of $\omega_{TO,3}$ (620 cm^{-1} (77 meV) in the model used in [47] to be compared with 450 cm^{-1} (56 meV) for the bulk oxide). The discrepancy may be due do the low thickness of the film, in which the top and bottom layers are slightly distorted with respect to their bulk counterpart.

6.5.6 CeO$_2$

Vibrational spectroscopy has also been used to assess the stoichiometry of cerium and chromium oxide films. Three cerium oxide bulk structures of defined stoichiometry are known: CeO$_2$, hexagonal h-Ce$_2$O$_3$ and cubic c-Ce$_2$O$_3$ [48].

CeO$_2$, which is the most common phase also known as ceria, crystallizes in a fluorite type structure with a lattice constant of 5.41 Å. The left panel of Fig. 6.18 shows the HREEL spectrum recorded after oxidising at 1000 K a Pt$_x$Ce-Pt(111)
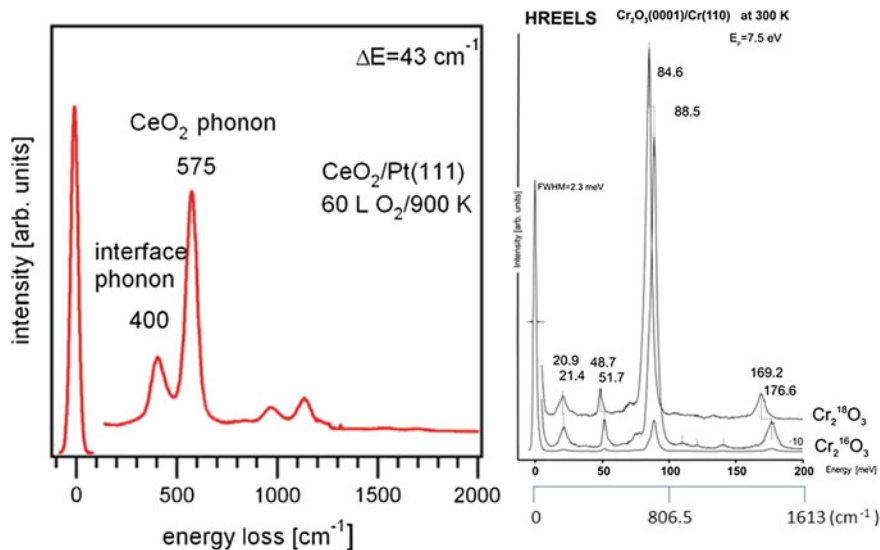
Fig. 6.18 *Left* HREEL spectra recorded for a ceria film (see text for details). *Right* HREEL spectra recorded for a Cr_2O_3 film of thckness $\approx$40 Å grown on Cr(110). Taken with permission from [48, 49]. Copyright by Elsevier

surface alloy, obtained evaporating Ce on a Pt(111) single crystal. Films of thickness between 1 and 5 layers were obtained. Two modes are evident: at 400 cm^{-1} (50 meV) and 575 cm^{-1} (72 meV). The former loss is due to an interface phonon while the latter is a phonon of the overlayer. This assignment is supported by the fact that the intensity of the high frequency mode increases with increasing thickness.

The comparison with vibrational data recorded for Cr_2O_3 grown on Cr(110) [49] (right panel of the same figure) allows to exclude the formation of h-Ce_2O_3 : in this case similar spectra should be obtained, contrary to experimental evidence.The film has thus a fluorite type $CeO_2(111)$ structure.

6.5.7 Cr_2O_3

For Cr_2O_3 the main modes are observed at 417 cm^{-1} (51.7 meV), 634 cm^{-1} (78.6 meV) and 714 cm^{-1} (88.5 meV) and correspond to three of the six expected dipole active modes [50] of the bulk oxide surface. They are thus identified with FK modes. The shoulder of the peak at 88.5 meV was tentatively ascribed to a further FK mode. The mode at 21.4 meV was assigned to a vertical in-phase vibration of the outermost O layer and the two Cr layers below while the higher frequency modes are due to combination losses.

6.6   Me₃O₄ and More Complex Oxides

6.6.1   Fe₃O₄

Fe_3O_4 films grown on alumina have been investigated by Raman Spectroscopy [51]. Iron oxides exist in different stoichiometry and structures: magnetite, hematite (α-Fe₂O₃), maghemite (γ-Fe₂O₃) and würstite ($Fe_{1-x}O$). Distinguishing among them is not straightforward: e.g. magnetite and maghemite have a similar crystal structure and close lattice constants.

Although the selection rules for RS and IR spectroscopy are quite different, vibrational information obtained from RS can also be used to distinguish between such crystallographic phases. By using group theory, it is indeed possible to predict
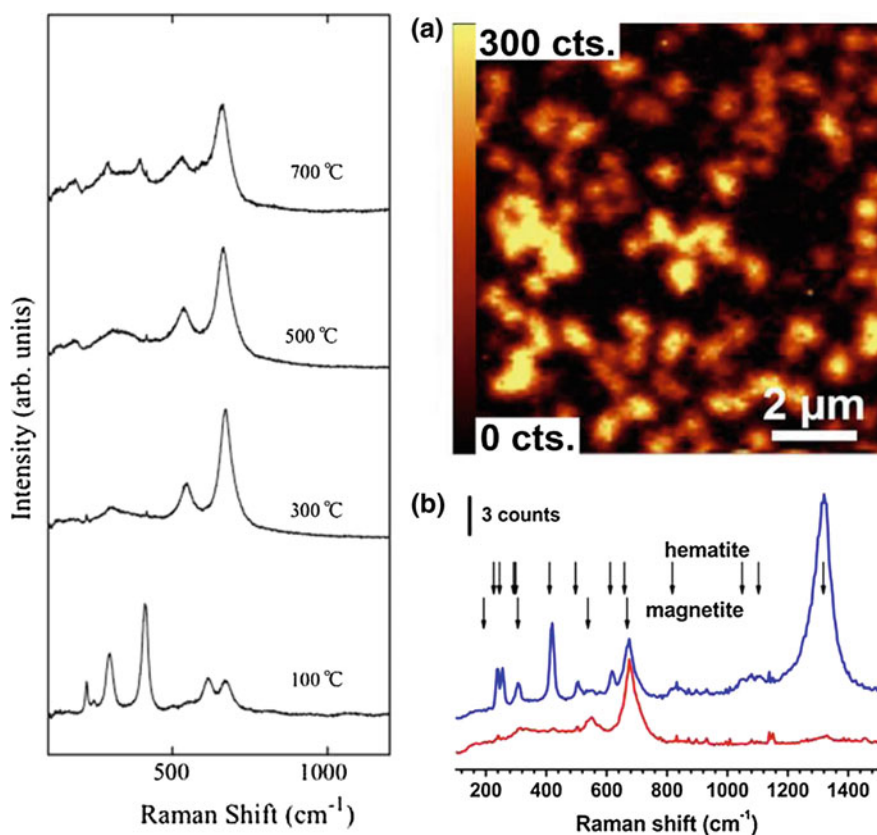
Fig. 6.19 *Left* Raman shift for Fe₃O₄ film grown on α-Al₂O₃. Taken with permission from [51]. Copyright by Elsevier. *Right* Raman image (**a**) and Raman shift (**b**) distinguishing bright areas (*blue line*, hematite) from dark ones (*red line*, magnetite). Taken with permission from [52]. Copyright by Elsevier

the number and symmetry of Raman active modes while the comparison with literature provides the frequency of the modes observed for magnetite and hematite [52].

Figure 6.19 shows the evolution of Raman spectra obtained growing the Fe_3O_4 film on the same substrate at different temperatures. In the film grown at 100 °C the vibrational features of both magnetite and hematite are present while at higher temperatures (300 and 500 °C) the intensities of the modes due to hematite decrease in favour of those due to magnetite. Only at 700 °C the features associated to hematite appear again.

At the lowest temperature adatom migration is slow and then crystals of poor quality are obtained. Increasing the temperature the quality improves. The negative effect of a further increase in the substrate temperature was explained as due to re-evaporation of the adatoms of the substrate.

6.6.2 Mn_3O_4

Mn_3O_4 thin films have been grown on Rh(111) [53]. Mn is thereby first evaporated on the Rh(111) substrate at RT and then oxidised at different temperatures. The corresponding HREEL spectra, shown in Fig. 6.20, should be compared with those of *MnO* reported in Figs. 6.2 and 6.3. Independently of the thickness of the film, peaks at ≈47 and 80 meV (379 and 645 cm^{-1}, respectively) appear already at the lowest temperature and slightly upshift in energy with increasing oxidation temperature. Such peaks are indicative of a trilayer O–Mn–O structure. For thicknesses of 2 and 3 ML, new loss peaks show up at 13, 39, 68 and 83 meV (105, 315, 548 and 669 cm^{-1}, respectively), such peaks being better resolved when oxidising Mn at 700 K or at 800 K. Since these peaks are indicative of a Mn_3O_4 structure, we can conclude that the latter forms only for films thicker than 1 ML.
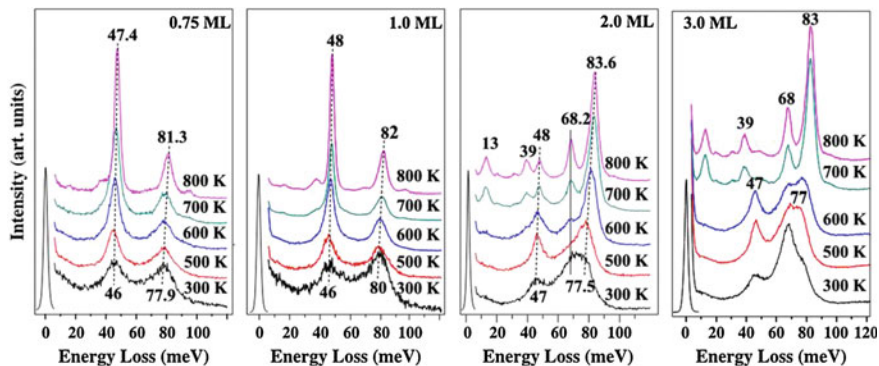
Fig. 6.20 HREEL spectra recorded for manganese oxide films of different thicknesses (0.75, 1, 2 and 3 ML) obtained by oxidising at the indicated temperature a Mn film deposited at RT. Taken with permission from [53]. Copyright by Elsevier

Fig. 6.21 HREEL spectra recorded for **a** a NbO thin film (3 ML), **b** a Nb_2O_5 thin film (3 ML) and **c** after bombarding Nb_2O_5 film with Ar ions to remove one layer. Taken with permission from [54]. Copyright by Elsevier
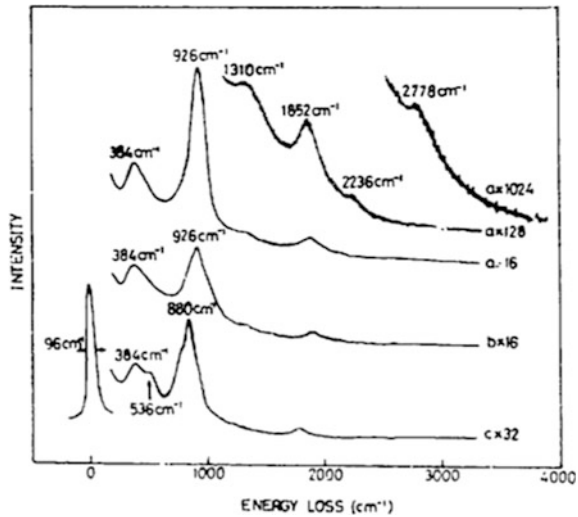
6.6.3 Niobium Oxide

As an example of more complex oxides, we show in Fig. 6.21 the HREEL spectra recorded for films of niobia with different stoichiometry, obtained by depositing Nb on Pt(111) and oxidising it [54]. Niobia may indeed grow in at least three possible stoichiometries: NbO, NbO_2 and Nb_2O_5.

NbO_x is obtained after an exposure of 500 L oxygen per 0.1 monolayer of Nb. Nb_2O_5 forms for an exposure of 1200 L O_2 at the same Nb coverage. The spectra for these films exhibit similar frequencies suggesting the presence of a common building block. The comparison of HREELS data for the film with data for the bulk crystal surface lead Xie et al. to conclude that the crystal structure(s) of the film do not correlate with the structures of bulk terminated oxides of niobium. The peak at 928 cm^{-1} (115 meV) was assigned to terminal Nb=O surface sites of highly distorted NbO_6 octahedra.

After Ar bombardment the film is characterized by the appearance of a new loss feature at 536 cm^{-1} (66 meV), which indicates the presence of a still different phase, explained by the formation of oxygen vacancies with the reduced niobium atoms.

6.6.4 Ternary Oxides

Little work is present in literature on thin films of ternary oxides. Tungstates ($MeWO_4$) have been recently studied because of their high potential in optics, optoeletronics and photochemistry. Denk et al. [55] succeeded recently to grow

films of such compound with atomic control by depositing $(WO_3)_3$ clusters on Cu
$(110) - (2 \times 1)O$ at cryogenic crystal temperatures. A morphologically flat and well
ordered W oxide overlayer is then obtained upon annealing a full monolayer of
such molecules at 600 K. As shown in Fig. 6.22 HREELS losses are apparent at
≈ 860 and 960 cm^{-1}. In bulk WO_3 the W–O–W groups cause bands at 711 and
806 cm^{-1} (88 and 100 meV, respectively) while a band at 987 cm^{-1}, (122 meV) is
indicative of the presence of W=O (tungstyls). DFT calculations indicate, however,
that for the oxide film the highest observed frequency may correspond to the W–O
stretching of WO_4 tetrahedra (found theoretically at 935 cm^{-1}, 116 meV) rather
than to tungstyl. The eigenvectors of this vibration are reported in Fig. 6.22b.
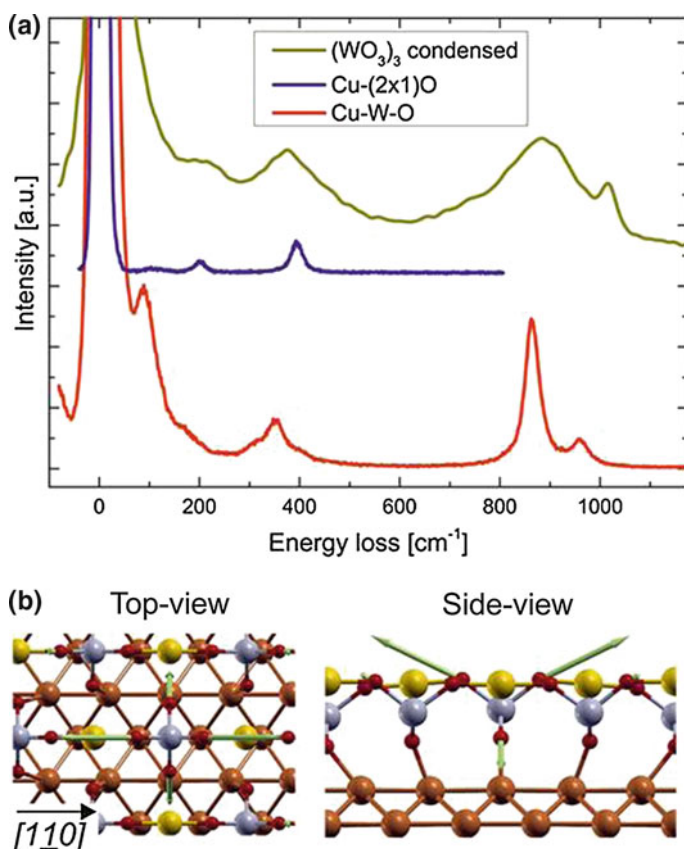
Fig. 6.22 **a** HREEL spectrum of the 2-D $CuWO_4$ system (Cu–W–O, in *red*), compared to the
Cu - $(2 \times 1)O$ bare substrate (in *blue*) and to a thick film of $(WO_3)_3$ clusters (in *green*). **b** Top and
side views of the high-frequency vibrational mode at 935 cm^{-1} as predicted by DFT. The *green
arrows* indicate the direction of atomic displacements. Taken with permission from [55].
Copyright by ACS

Ultrathin films of $BaTiO_3(001)$ were recently grown on Pt(001) by the group of Widdra [56, 57], who also performed HREELS investigations which are, however, still unpublished.

6.7 Conclusions

We have presented selected examples showing how vibrational spectroscopy has been used to determine the nature (stoichiometry and symmetry) and in some cases even the morphology of thin oxide films. The assignment of the observed vibrational signatures is non trivial and is ultimately based on symmetry arguments and on the selection rules operative for the probe particles (electrons or photons), for the particular substrate (metallic or not) and for the given scattering geometry.

While for thick enough thin films the predictions of macroscopic dielectric theory are generally confirmed by experiments, in the ultrathin limit microscopic modes are also observed and for their assignment a theory is usually required.

Once the more general properties of the film have been established, comparison of the frequencies and of the intensities of the modes for different growth conditions can provide information about the morphology of the film and about the different phases which may form. Vibrational analysis can highlight, moreover, the growth mode (layer by layer vs. 3D), thus complementing the information provided by microscopy.

References

1. Honkala K (2014) Tailoring oxide properties: an impact on adsorption characteristics of molecules and metals. Surf Sci Rep 69:366–388
2. Freund HJ, Pacchioni G (2008) Oxide ultra-thin films on metals: new materials for the design of supported metal catalysts. Chem Soc Rev 37:2224–2242
3. Goodman W (1995) Model studies in catalysis using surface science probes. Chem Rev 95:523–536
4. Fuchs R, Kliewer KL (1965) Optical modes of vibration in an ionic crystal slab. Phys Rev 140:A2076–A2088
5. Cox PA, Hill MD, Peplinskii F et al (1984) 2D surface phonons in high-resolution electron-energy-loss spectra of metallic oxides. Surf Sci 141:13–30
6. Sachert S, Polzin S, Kostov K et al (2010) Thickness dependent vibrational and electronic properties of MnO(100) thin films grown on Pt(111). Phys Rev B 81:195424-1–195424-7
7. Frederick BG, Apai G, Rhodin TN (1991) Surface phonons in thin aluminum oxide films: thickness, beam-energy, and symmetry-mixing effects. Phys Rev B 44:1880–1890
8. Lambin Ph, Senet P, Lucas AA (1991) Validity of the dielectric approximation in describing electron-energy-loss spectra of surface and interface phonons in thin films of ionic crystals. Phys Rev B 44:6416–6428

9. Ibach H, Mills DL (1982) Electron energy loss specroscopy and surface vibrations. Academic Press, New York
10. Hoffmann FM (1983) Infrared reflection-absorption spectroscopy of adsorbed molecules. Surf Sci Rep 3:109–192
11. Siebert F, Hildebrandt P (2008) Vibrational spectroscopy in life sciences. Wiley-VCH Verlag GmbH and Co. KGaA, Weinheim. doi:10.1002/9783527621347.ch2
12. Xu ML, Hall BM, Tong SY et al (1985) Energy dependence of inelastic electron scattering cross section by surface vibrations: experimental measurement and theoretical interpretation. Phys Rev Lett 54:1171–1174
13. Rocca M, Ibach H, Lehwald S et al (1986) Surface phonon dispersion of surface and adsorbate layers. In: Von Blanckenhagen P, Schommers W (eds) Structure and dynamics of surfaces. Topics in current physics, vol 41. Springer, Berlin, pp 245–276
14. Agarwal SK (1979) Lattice-dynamics of transition metal oxides MnO and NiO. Solid State Comm 29:197–200
15. Rudolf T, Kant Ch, Mayr F et al (2008) Magnetic-order induced phonon splitting in MnO from far-infrared spectroscopy. Phys Rev B 77:024421-1–024421-5)
16. Savio L, Celasco E, Vattuone L et al (2003) MgO/Ag(100): confined vibrational modes in the limit of ultrathin films. Phys Rev B 67:075420-1–075420-5
17. Pal J, Smerieri M, Celasco E et al (2014) Morphology of monolayer MgO films on Ag(100): switching from corrugated islands to extended flat terraces. Phys Rev Lett 112:126102-1–126102-5
18. Pal J, Smerieri M, Celasco E et al (2014) How growing conditions and interfacial oxygen affect the final morphology of MgO/Ag(100) films. J Phys Chem C 118:26091–26102
19. Hwang Y, Souda E, Aizawa T et al (1997) Surface phonon of MgO layer on TiC(100) surface. Jpn J Appl Phys 36:5707–5708
20. Schoiswohl J, Agnoli S, Xu B et al (2005) Growth and thermal behaviour of NiO nanolayers on Pd(1 0 0). Surf Sci 599:1–13
21. Tyuliev GT, Kostov KL (1999) XPS/HREELS study of NiO films grown on Ni(111). Phys Rev B 60:2900–2907
22. Cox PA, Williams AA (1985) The observation of surface optical phonons and low-energy electronic transitions in NiO single crystals by electron energy loss spectroscopy. Surf Sci 152 (153):791–796
23. Le Moal S, Moors M, Essen JM et al (2013) Structural and compositional characterization of ultrathin titanium oxide films grown on $Pt_3Ti(111)$. J Phys Cond Matt 25:045013-(1–11)
24. Langell MA, Hutchings CW, Carson GA et al (1996) High resolution electron energy loss spectroscopy of MnO(100) and oxidized MnO(100). J Vac Sci Technol A 14:1656–1661
25. Wulser KW, Langell MA (1994) Fuchs-Kliewer phonon structure and surface integrity of NiO (100). Surf Sci 314:385–397
26. Carson GA, Nassir MH, Langell MA (1996) Epitaxial growth of Co_3O_4 on CoO(100). J Vac SciTechnol A 14:1637–1642
27. Guo Q, Oh WS, Goodman DW (1999) Titanium oxide films grown on Mo(110). Surf Sci 437:49–60
28. Henderson MA (1996) An HREELS and TPD study of water on $TiO_2(110)$: the extent of molecular versus dissociative adsorption. Surf Sci 355:151–166
29. Gunrick G, Poelman H, Clauws P et al (1991) Observation of surface phonons on the (001) and (100) surfaces of anatase minerals. Solid State Comm 80:579–581
30. Chen MS, Santra AK, Goodman DW (2004) Structure of thin SiO_2 films grown on Mo(112). Phys Rev B 69:155404-1–155404-7)
31. Wendt S, Ozensoy E, Wei T et al (2005) Electronic and vibrational properties of ultrathin SiO_2 films grown on Mo(112). Phys Rev B 72:115409-1–115409-9
32. Kaya S, Baron M, Stacchiola D et al (2007) On the geometrical and electronic structure of an ultra-thin crystalline silica film grown on Mo(1 1 2). Surf Sci 601:4849–4861
33. Schroeder T, Giorgi JB, Bäumer M et al (2002) Morphological and electronic properties of ultrathin crystalline silica epilayers on a Mo(112) substrate. Phys Rev B 66:165422-1–165422-11

34. Lu JL, Kaya S, Weissenrieder J et al (2006) Formation of one-dimensional crystalline silica on a metal substrate. Surf Sci 600:L164–L168
35. Frank M, Wolter K, Magg N et al (2001) Phonons of clean and metal-modified oxide films: an infrared and HREELS study. Surf Sci 492:270–284
36. Berreman DW (1963) Infrared absorption at longitudinal optic frequency in cubic crystal films. Phys Rev 130:2193–2198
37. Franchy R (2000) Growth of thin, crystalline oxide, nitride and oxynitride films on metal and metal alloy surfaces. Surf Sci Rep 38:195–294
38. Strong RL, Firey B, de Wette FW et al (1982) Surface-site determination using electron-energy-loss spectroscopy and lattice-dynamical models. Phys Rev B 26:3483(R)-3486 and its Erratum Phys Rev B 27:3896
39. Lee MB, Lee JH, Frederick BG et al (2000) Surface structure of ultra-thin Al_2O_3 films on metal substrates. Surf Sci 448:L207–L212
40. Franchy R, Masuch J, Gassmann P (1996) The oxidation of the NiAl(111) surface. App Surf Sci 93:317–327
41. Gassmann P, Franchy R, Ibach H (1994) Investigations on phase transitions within thin Al_2O_3 layers on NiAl(001) HREELS on aluminum oxide films. Surf Sci 319:95–109
42. Pfuner F, Schoiswohl J, Sock M et al (2005) The metalinsulator transition in V_2O_3(0001) thin films: surface termination effects. J Phys Cond Matt 17:4035–4047
43. Guo K, Lee S, Goodman DW (1999) Vanadium oxides thin films grown on rutile TiO_2(110)-(1 1)and(1 × 2) surfaces. Surf Sci 437:38–48
44. Artiglia L, Agnoli S, Savio L et al (2014) From Vanadia nanoclusters to ultrathin films on TiO_2(110): evolution of the yield and selectivity in the ethanol oxidation reaction. ACS Catal 4:3715–3723
45. Kresse G, Surnev S, Schoiswohl J et al (2004) V_2O_3(0001) surface terminations: a density functional study. Surf Sci 555:118–134
46. Surnev S, Kresse G, Sock M et al (2001) Surface structures of ultrathin vanadium oxide films on Pd(1 1 1. Surf Sci 495:91–106
47. Schmitz G, Gassmann P, Franchy R (1998) A combined scanning tunneling microscopy and electron energy loss spectroscopy study on the formation of thin, well-ordered β-Ga_2O_3 films on CoGa(001). J Appl Phys 83:2533–2538
48. Breinlich C, Essen JM, Barletta E et al (2011) Growth, structure and electronic properties of ultrathin cerium oxide films grown on Pt(111). Thin Solid Films 519:3752–3755
49. Wolter K, Scarano D, Fritsch J et al (2000) Observation of a localized surface phonon on an oxide surface. Chem Phys Lett 320:206–211
50. Renneke DR, Lynch DW (1965) Infrared lattice vibrations and dielectric dispersion in single-crystal Cr_2O_3. Phys Rev 138:A530–A533
51. Ding J, Zhang D, Arita M et al (2011) Growth and characterization of Fe_3O_4 films. Mat Res Bull 46:2212–2216
52. Lübbe M, Gigler A, Stark R et al (2010) Identification of iron oxide phases in thin films grown on Al_2O_3(0001) by Raman spectroscopy and X-ray diffraction. Surf Sci 604:679–685
53. Zhang L, Tang Z, Wang S et al (2012) Growth and vibrational properties of MnO_x thin films on Rh(111). Surf Sci 606:1507–1511
54. Xie L, Wang D, Zhong C et al (1994) The preparation of and water adsorption on thin films of niobium oxide on Pt(111). Surf Sci 320:62–76
55. Denk M, Kuhness D, Wagner M et al (2014) Metal tungstates at the ultimate two-dimensional limit: fabrication of a $CuWO_4$ nanophase. AcsNano 8:3947–3954
56. Förster S, Meinel K, Hammer R et al (2013) Quasicrystalline structure formation in a classical crystalline thin-film system. Nature 502:215–218
57. Widdra W, Schumann F, Christl M et al (2015) Surface phonons and ferroelectric coupling in ultrathin perovskite oxides. ECOSS 31 Book of abstract, 129, available at: http://www.ecoss2015.org

Chapter 7
Electrostatics and Polarity in 2D Oxides

Claudine Noguera and Jacek Goniakowski

Abstract We review the manifestations of electrostatic interactions, and in particular polarity effects, in oxide ultra-thin films and two-dimensional nano-objects. We discuss the efficiency of various compensation mechanisms such as overall structural transformations, strong lattice relaxations, inhomogeneous charge redistributions, support effects, and/or the formation of 2D or 1D electron/hole gases.

7.1 Introduction

Due to its relevance in mineralogy, geochemistry, catalysis, electrochemistry, electronics, magnetic recording, etc., in the past 25 years the field of oxide surfaces has enormously evolved. While the characteristics and properties of most binary oxide surfaces are now well-established, in the last decade, the main focus has been on ultra-thin oxide films. Usually grown on metallic supports, these systems may represent oxygen reservoirs, inverse catalysts, patterned supports for the formation of catalytically active size-selected clusters, or device constituents in the emerging field of all-oxide electronics. When the film thickness is no more than one or two atomic layers, depending upon preparation conditions, these two-dimensional (2D) oxides may display structures, stoichiometries and properties that are not seen in bulk crystals [1–6]. The same is expected in 2D small objects, such as nano-ribbons or nano-islands, whose controlled fabrication and growth nowadays remain a difficult challenge.

C. Noguera (✉) · J. Goniakowski
CNRS, Institut Des Nanosciences de Paris, UMR 7588, 4 place Jussieu,
75005 Paris, France
e-mail: claudine.noguera@insp.jussieu.fr

J. Goniakowski
e-mail: jacek.goniakowski@insp.jussieu.fr

C. Noguera · J. Goniakowski
Institut des NanoSciences de Paris, Sorbonne Universités, UPMC Univ Paris 06,
75005 Paris, France

The present chapter focuses on the manifestations of electrostatic interactions in oxide ultra-thin films and 2D nano-objects, and in particular on polarity effects. Indeed, numerous oxide properties cannot be understood without taking into account the strong Coulomb interactions which result from their ionic character. Along certain crystallographic directions, a macroscopic polarization induces a surface instability. These *polar* orientations have been thoroughly studied at semi-infinite surfaces [7, 8]. But in polar ultra-thin films, especially when their thickness reaches the monolayer (ML) limit, new questions arise, which are related to the role of electrostatic interactions and dimensionality. Compared to semi-infinite surfaces, new mechanisms of polarity compensation exist at the nanoscale, involving, among others, complete changes of structures, strong lattice relaxations, inhomogeneous charge redistributions. The interplay between polarity and substrate effects, interfacial charge transfers, and lattice mismatch, have also to be considered since most 2D-objects are grown on (metallic or insulating) sub-strates. Finally, the possibility to stabilize 2D or 1D electron or hole gases (2DEG, 2DHG, 1DEG, 1DHG) at polar interfaces or at polar island edges in new layered materials has recently generated excitement in the physics community.

The aim here is to present an overview of the consequences of the strong Coulomb interactions and polarity effects which exist in low dimensional oxide structures. We will outline how polarity concepts, which have been developed for surfaces and which are recalled in Sect. 7.2, apply or have to be modified at the nanoscale. For this purpose, they will be successively reviewed in the cases of ultra-thin films (Sect. 7.3), interfaces (Sect. 7.4), and 2D ribbons or islands (Sect. 7.5).

7.2 Polarity Concepts

In Tasker's classification [9], compound surfaces are differentiated according to whether or not the structural repeat unit starting from vacuum bears a non-vanishing dipole moment. The presence of a dipole moment is characteristic of *polar* surfaces.

In the simplest capacitor-type representation of a crystal cut along a polar orien-tation (Fig. 7.1), with alternating positively and negatively charged plates (charge densities $\pm\sigma$, successive inter-plate distances R_1 and R_2), an electrostatic instability—sometimes called polar catastrophe—develops due to the existence of a macroscopic electric field perpendicular to the surface. According to Gauss law, this instability can be healed by an excess charge density $\pm\delta\sigma$ on the external plates, such that:

$$\delta\sigma = \sigma\mathscr{R} \tag{7.1}$$

with $\mathscr{R} = R_1/(R_1 + R_2)$ [7–9]. $\sigma\mathscr{R}$ represents the dipole moment per unit volume of the repeat unit. The electrostatic field due to $\delta\sigma$ precisely cancels the average macroscopic electric field in the bulk of the material.
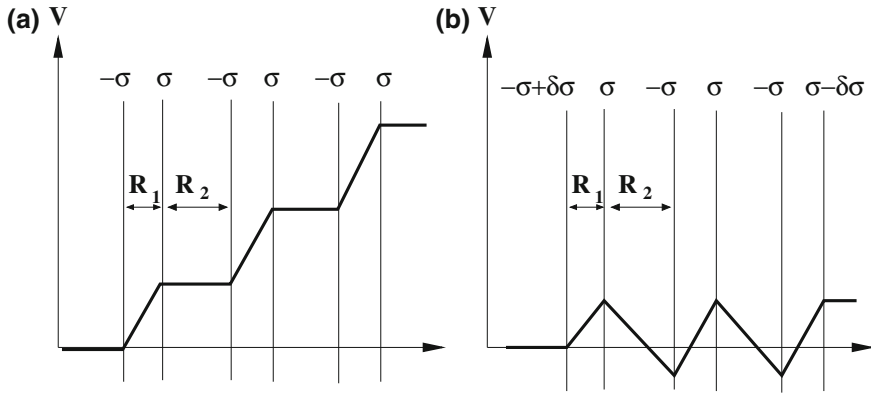
Fig. 7.1 a Capacitor model of a polar surface with alternating layers of charge densities $\pm\sigma$ and spatial variation of its electrostatic potential V. **b** Same but with excess charges $\pm\delta\sigma = \sigma R_1/(R_1 + R_2)$ on the outer layers which suppress the monotonic variation of V

Beyond this simplistic picture, in realistic compounds, the charge density σ of the atomic layers is delocalized and differs from the value Σ obtained by assigning formal charges to the atoms. It involves an electronic contribution σ_{el} due to covalent effects, so that $\sigma = \Sigma + \sigma_{el}$. Whatever the partitioning scheme adopted to define σ and σ_{el}, the electrostatic criterion, (7.1), defines the modification of surface charge density $\delta\sigma$ required for surface stability, which is then the sum of two contributions $\delta\sigma = \delta\sigma_{el} + \delta\sigma_{comp}$. The first one, $\delta\sigma_{el}$, comes from the modification of covalent effects at surfaces, due to the change in local environment of the atoms, associated, for example, to bond breaking. It exists whatever the surface orientation and is not specific to polarity. The second contribution, $\delta\sigma_{comp}$, represents the compensating charge which has to be provided by processes other than covalency effects, for example partial filling of surface bands, surface adsorbates, vacancies, non-stoichiometric reconstructions, or non-isoelectronic substitutions, in order to stabilize the surface. It is specific to polarity and, using (7.1), its value has to be equal to:

$$\delta\sigma_{comp} = \Sigma\mathscr{R} + (\mathscr{R}\sigma_{el} - \delta\sigma_{el}) \qquad (7.2)$$

It consists of an ionic term $\Sigma\mathscr{R}$ plus an electronic one $\mathscr{R}\sigma_{el} - \delta\sigma_{el}$.

The Modern Theory of Polarization [10–12] provides a formal derivation of this result. It relates the compensating charge, $\delta\sigma_{comp}$ to the bulk polarization P_{bulk} of the system, i.e. its dipole density, and writes the latter as:

$$\delta\sigma_{comp} = P_{bulk}; \quad P_{bulk} = \Sigma\mathscr{R} + P_{el} \qquad (7.3)$$

The electronic contribution P_{el}, which depends on the center-of-gravity positions of the valence band (VB) Wannier functions, corresponds to the terms $\mathscr{R}\sigma_{el} - \delta\sigma_{el}$

written in (7.2). P_{el} is non-zero in non-centro-symmetric structures in which the electronic density presents an asymmetry [10, 12–14].

Some qualitative insight into P_{el} is given by a simple tight-binding approach which accounts for electron delocalization through inter-layer transfers T_1 and T_2 per 2D unit cell (T_1 and T_2 positive), as shown in Fig. 7.2. In this particular partitioning of space, the electronic contribution to σ is thus $\sigma_{el} = -T_1 - T_2$. At the surface T_2 is missing, which yields $\delta\sigma_{el} = -T_2$. Local charge redistributions modifying the mixed ionic and covalent character of the bonding in the surface region, and thus T_1 and T_2, are irrelevant, since they induce no global charge variation. In this simple scheme, $\delta\sigma_{comp}$ and the electronic contribution to P thus read:

$$P_{el} = \sigma_{el}\left(\mathscr{R} - \frac{T_2}{T_1 + T_2}\right) \tag{7.4}$$

This expression, not intended to be used for quantitative evaluation, shows that symmetry considerations alone can tell whether or not $P_{el} = 0$. Indeed, the key issue for its cancellation is in the difference between $T_2/(T_1 + T_2)$ and $\mathscr{R}$. It vanishes, for example, in rock salt (111) or zinc blende (100) compounds where layers are equidistant ($R_1 = R_2$ and $\mathscr{R} = 1/2$) and $T_1 = T_2$ by symmetry. Similarly, it vanishes in zinc blende (111) compounds where $R_2 = 3R_1$ and, by symmetry $T_1 = 3T_2$.

In wurtzite compounds, whether or not their structure is ideal, a spontaneous polarization of electronic origin exists, due to the absence of inversion symmetry in their lattice. Whenever $\Sigma\mathscr{R} \neq 0$, the electronic contribution P_{el} is often negligible, so that relying on a formal charge analysis most of the time allows a correct assignment of polarity. However, when $\Sigma\mathscr{R} = 0$, either because $\Sigma = 0$ or because $\Sigma\mathscr{R}$ is exactly canceled out by external charges, P_{el} remains the sole factor which drives polarity effects. An illustration of the case $\Sigma = 0$ is given in Fig. 7.3, which displays the value of P_{el} and its consequences on surface polarity, in an hypothetical distorted ($R_1 \neq R_2$) perovskite bulk. In thin films or nano-objects, interfacial strain and global symmetry lowering may also induce non-vanishing and non-negligible P_{el}, so that a formal charge analysis may not always be sufficient to assess the polar character of these nanoscale objects.
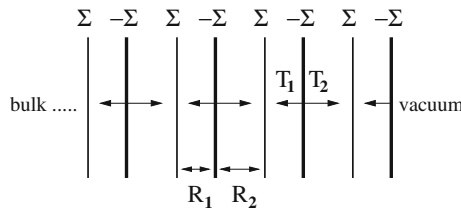
Fig. 7.2 Succession of layers along a direction perpendicular to a polar surface. T_1 and T_2 represent the interlayer electron transfers associated to R_1 and R_2 interlayer distances, respectively. $\pm\Sigma$ are the layer formal charge densities. Due to bond breaking, T_2 is missing at the surface
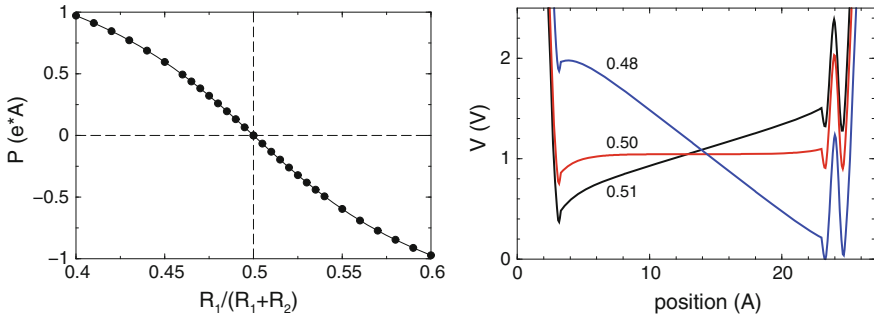
Fig. 7.3 *Left* polarization in an hypothetical distorted SrTiO$_3$ bulk with flat, formally-neutral (001) layers, for various values of $\mathcal{R}$. Only when $\mathcal{R} = 0.5$ does the polarization vanish. When $\mathcal{R} \neq 0.5$, since $\Sigma = 0$, its non-zero value solely comes from its electronic contribution P_{el}. *Right* electrostatic potential profile across a distorted SrTiO$_3$(001) slab for $\mathcal{R} = 0.48$, 0.5 and 0.51. The non-zero slope when $\mathcal{R} \neq 0.5$ is the signature of polarity

One can remark that polar semi-infinite surfaces are characterized by a *polarization discontinuity* δP between a polar compound ($P_{bulk} \neq 0$) and vacuum, which is a medium with zero polarization ($P = 0$). The same is true for polar surfaces in contact with any non-polar medium [15], to which all previous considerations apply.

In order to provide the compensating charge densities $\delta\sigma_{comp} = P_{bulk}$ required for surface stabilization, several mechanisms may be at work, whose relative efficiency is strongly dependent on the oxide, the surface atomic structure, the chemical environment or the thermodynamic conditions (temperature, oxygen or water partial pressures). As reviewed in [7, 8], a modification of the surface region composition by an adequate density of charged vacancies, or the adsorption of an adequate density of charged foreign species, in particular protons or hydroxyl groups resulting from the dissociation of water molecules, are the most commonly met. Whenever $P_{el} \neq 0$, it should be kept in mind that these required densities are close to, but not equal to $\mathcal{R}$. This is for example the case at wurtzite (0001) surfaces, whether ideal or not. There are also examples of surface configurations consistent with a metallization mechanism, sometimes called electronic reconstruction, in which a modification of the surface band filling (Zener breakdown) induces the presence of 2DEG/2DHG at the surface.

7.3 Polarity Scenarios in Thin Films

As reviewed in [8, 16], the physics of polar thin films is very rich in new electronic and structural features, due to finite size effects, structural flexibility, softening of the electrostatic interactions and interaction with the substrate. In particular, at variance with semi-infinite surfaces, the stability of polar film does not necessarily

require $\delta\sigma_{comp} = P_{bulk}$. We will successively describe several scenarios that may take place.

7.3.1 Electronic Reconstruction in Polar Films

As evidenced for example in MgO(111) [17, 18], CoO(111) [19] or ZnO(0001) [20, 21] films, two qualitatively different thickness regimes may be differentiated. At large thicknesses, the polarity stabilization mechanisms are qualitatively similar to those occurring at semi-infinite surfaces. However, the electronic reconstruction scenario displays finite size characteristics, that are specified below.

Simulations of the electronic structure of thick polar films evidence metallization and spin polarization at their surfaces (Fig. 7.4a). The local VB on one side of the film and the local conduction band (CB) on the other side intersect the Fermi level. This allows a reduction of charge density $\pm\delta\sigma$ on both terminations, through electron exchange between them (Zener breakdown) . More precisely, the local densities of states (LDOS) are monotonically shifted across the film, due to a residual polarization coming from the opposing effect of the film polarization P and $\delta\sigma$ (Fig. 7.4b). The associated total band shift ΔV, no longer proportional to the film thickness, remains of the order of the surface gap (G) to allow band overlap and electron transfer.

The self-consistent relationship between ΔV and $\delta\sigma$ constrains the latter to vary with the film thickness $N(R_1 + R_2)$ (N the number of repeat units), according to the asymptotic law [22, 23] (ε^∞ the film dielectric constant):
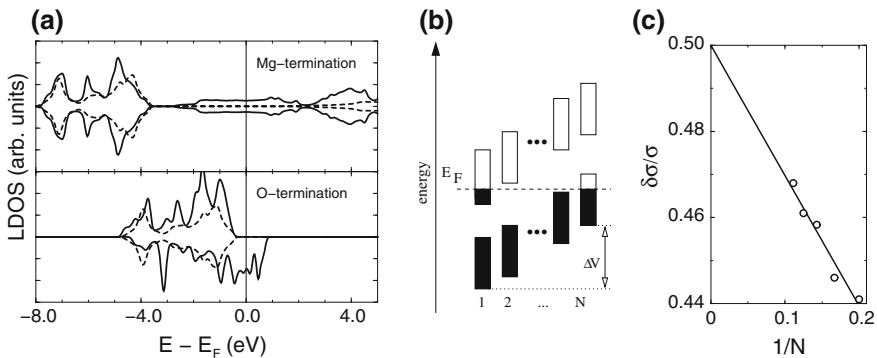
Fig. 7.4 a Spin resolved LDOS on the magnesium (*top*) and oxygen (*bottom*) terminations of a MgO(111) film, highlighting the metallization of both surfaces and the magnetic moment on the oxygen termination. **b** Sketch of the electronic structure across a polar thick film. **c** Thickness dependence of $\delta\sigma/\sigma$, deduced from a Bader analysis, in thick MgO(111) films, evidencing its $1/N$ asymptotic behavior

$$\delta\sigma_{comp}(N) \approx P_{bulk} - \frac{\Delta V \varepsilon^\infty}{4\pi N(R_1 + R_2)} \tag{7.5}$$

An example of the $1/N$ dependence of $\delta\sigma$, found in MgO(111) films, is shown in Fig. 7.4c. Thus, in these finite size systems, $\delta\sigma_{comp}$ differs from the bulk polarization P_{bulk}:

$$\delta\sigma_{comp}(N) \neq P_{bulk} \tag{7.6}$$

whenever G is non-zero. Only in the $N \to \infty$ limit is the equality recovered.

7.3.2 Uncompensated Polarity

Under specific conditions, the total shift of electrostatic potential ΔV may be insufficient to induce band overlap. This happens, either at extremely low thickness without much structural distortion ($P \approx P_{bulk}$), or at low thickness if the film structure is flexible enough to strongly reduce its polarization with respect to the bulk value ($P \ll P_{bulk}$). Whatever the case, $\delta\sigma_{comp} \neq P$ since

$$\delta\sigma_{comp} = 0 \tag{7.7}$$

For this reason, this regime has been called "uncompensated polarity" [18]. In another context, it is referred to as the subcritical regime [24]. The associated electronic structure is sketched in Fig. 7.5a.
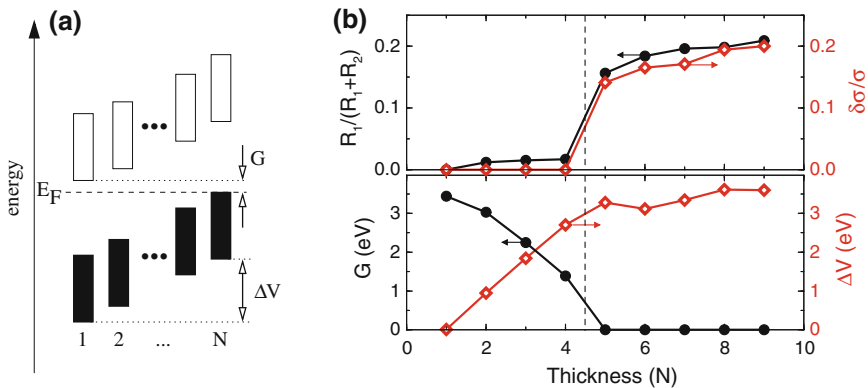
Fig. 7.5 a Sketch of the electronic structure across a polar uncompensated film for $N < N_C$; **b** thickness dependence of unsupported MgO (111) film properties in the metastable zinc blende phase. *Top panel* $\mathcal{R} = R_1/(R_1 + R_2)$ (*black symbols*) and excess Bader charge densities $\delta\sigma/\sigma$ (*red open symbols*); *Bottom panel* gap G (*black symbols*) and total voltage ΔV (*red open symbols*)

This scenario was discovered in a theoretical study of stoichiometric MgO(111), ZnO(0001) and NaCl(111) ultra-thin films, which display a metastable zinc blende phase at low thickness with strongly size-dependent properties [18]. As shown in Fig. 7.5b, $\mathscr{R}$ is extremely reduced thanks to a drastic decrease of the inter-layer distance R_1. The total dipole moment grows linearly with N and simultaneously, G decreases. The electronic structure remains insulating but only up to a critical thickness N_c. At N_c, a metal-insulator transition takes place with a strong discontinuity in $\mathscr{R}$ and $\delta\sigma$. Above N_c, all film properties follow the general trends of compensation by metallization described in the previous section.

Kaolinite films have also been predicted to display the same scenario, although the uncompensated mechanism was not referred to [25]. Kaolinite $Al_2Si_2O_5(OH)_4$ is a layered silicate compound, whose (0001) layers are composed of two sublattices, made of a silica and a gibbsite sheet, respectively. Due to this asymmetry, the repeat unit along the (0001) orientation bears a finite dipole moment, making this orientation polar. According to the simulation, kaolinite (0001) films display a metal insulator transition when the thickness reaches about three repeat units.

A nearly identical scenario has been invoked in $LaAlO_3(100)$ and $KTaO_3(100)$ films grown on a $SrTiO_3$ substrate to rationalize experimental results [26–30]. It gave rise to an intense debate on whether the 2DEG originates from polarity or/and from the presence of oxygen vacancies [31, 32]. Indeed, these oxides are insulating, but the $LaAlO_3(100)$ and $KTaO_3(100)$ orientations are polar. For example, in $LaAlO_3$, a metal-insulator transition occurs at a critical thickness of four repeat units [24, 26]. This transition was assigned to the shift of the $LaAlO_3$ bands, which, beyond N_c, allows its top of VB to overlap the $SrTiO_3$ CB minimum.

7.3.3 Structural Transformation

The literature review on polar ultra-thin films [8, 16] evidences another scenario at low thickness, in which a global structural transformation takes place in order to make the film orientation non-polar. In that case, the equality $\delta\sigma_{comp} = P$ is fulfilled, but in the specific limit where:

$$P = 0 = \delta\sigma_{comp} \tag{7.8}$$

Such transformation results from a competition between surface and bulk energy terms, in which the surface term wins. The new structure being different from the bulk ground state, there is a cost of energy for each additional repeat unit when the thickness N increases. However, as long as N remains small, the gain in surface energy in having a non-polar orientation is able to overcome this cost. Thus, up to a critical thickness, ultra-thin polar films may sustain a structure which is not their bulk ground state but allows a non-polar termination.

This generic scenario was first proposed in [17], accompanying simulations of MgO(111) films (Fig. 7.6a). It rationalizes theoretical or experimental findings
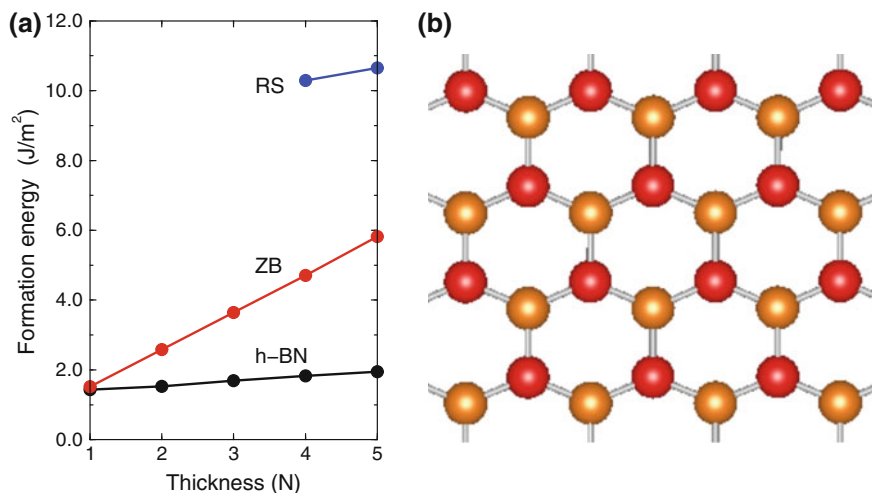
Fig. 7.6 a Structural phase diagram of MgO(111) unsupported films as a function of thickness, indicating the relative stability of the rock salt (RS), zinc blende (ZB) and h-BN phases. **b** *Top view* of the honeycomb structure of the h-BN ML

made in many polar binary oxide films, such as MgO [33], FeO [34, 35], CoO [36, 37], ZnO [38, 39], BeO [40, 41], other wurtzite type compounds [42], and AlO$_x$ [43], which evidence nearly flat repeat units and expanded in-plane lattice parameters compared to bulk. Among the reported results, a frequently-met feature is the existence of flat layers with a graphene-like honeycomb structure made of six-member rings with equal number of cations and oxygens (Fig. 7.6b). When such layers are stacked together, a non-polar (0001) film of an hexagonal boron nitride structure (h-BN) is produced. This scenario is relevant for binary compounds which, in the bulk, crystallize in the rock salt, zinc blende or wurtzite structures. More generally, the stabilization of polar films by a strong transformation of the bulk equilibrium structure appears to be a quite general scenario at extremely low thickness, due to the structural flexibility of ultra-thin films.

7.3.4 Support Effects

While previous scenarios are intrinsic to (unsupported) polar thin films, the inter-action with a support can significantly modify the film structure, their stability and their electronic characteristics, depending on their thickness.

At the interface between a thick polar film and a metal substrate, the cost of polarity is strongly reduced by a transfer of the compensating charge from the oxide to the metal [44, 45]. The interfacial oxide bands recover their normal filling, and it is the filling of the metal bands in contact with the oxide which changes with

respect to that of the clean metal surface. This transfer avoids electron excitations across the oxide gap and replaces them by low-energy excitations in the vicinity of the metal Fermi level. The associated gain of energy is reflected in a strong interfacial adhesion. This process was invoked to support the experimental evidence of a structurally and chemically abrupt Cu/MgO(111) interface [46, 47].

When the oxide film is thin and especially when polarity effects are weak or absent (case of uncompensated polarity or structural transformation), an interfacial charge transfer of a different origin takes place between the film and the metal substrate, which is no longer driven by the requirement of polarity compensation. Due to interfacial hybridization and/or penetration of the MIGS (Metal Induced Gap States), its amount and sign depend on the relative position of the metal Fermi level and the oxide point of zero charge. The associated dipole moment contributes to the Schottky barrier height [48–50]. For example, deposition of a MgO(111) film on a simple metal (Mg, Al) of low electronegativity results in an electron transfer from the substrate to the film, while on transition metal substrates (Ag, Mo, Pt) an opposite transfer occurs. Such charge transfer is unrelated to polarity as it may also occur at the interface between a metal and a non-polar surface.

As a *response* to the electrostatic field produced by the interfacial charge transfer, thin films undergo a structural distortion as schematized in Fig. 7.7 in the case of an oxide ML of honeycomb structure deposited on a metal substrate. While perfectly flat when unsupported, the ML gets rumpled upon deposition, in such a way that the dipoles associated to charge transfer and rumpling have opposite sign and thus partially compensate each other [51]. This argument based on a generic electrostatic coupling between charge transfer and structural distortion rationalizes the small and large rumpling values in MgO/Ag(111) and FeO/Pt(111) ML films, respectively.

A similar electrostatic coupling between charge transfer and structural distortion applies to adsorbates on thin oxide films supported on a metal support. Upon deposition, the adsorbates become charged, in a way which is mainly determined by the electronic characteristics (e.g. the work function) of the oxide-on-metal support [52–62]. In response to this charge transfer, especially at low film thickness, a polaronic distortion of the oxide film takes place around the charged adsorbates,
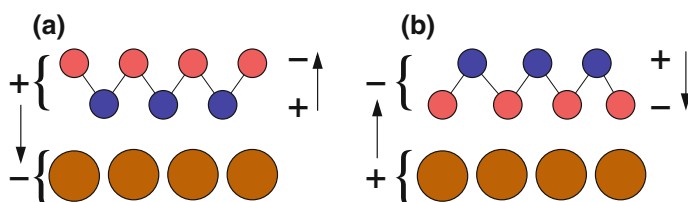
Fig. 7.7 Schematic representation of the two dipoles associated to the charge transfer between an oxide film and its metal support and to the rumpling inside the oxide film (shown by *arrows*), for the two cases of a negative (**a**) and a positive (**b**) metal charging. In the first case, oxygen atoms of the oxide film are repelled by the negative charge of the metal and pushed outwards. In the second case, they are attracted by the substrate. Cations, oxygens, and metal atoms are represented as *blue*, *red* and large *brown balls*, respectively

which significantly stabilizes them [63] and has implications on the growth, chemical, optical, and magnetic properties of adsorbed metal particles, their self-organization [3, 64] and their wetting on the oxide film [54, 58].

It has furthermore been demonstrated that this mechanism allows to incorporate oxygen atoms into ultra-thin oxide films supported on a metal, producing oxygen-rich oxide phases, with no bulk equivalent, which may serve as oxygen reservoirs in low temperature oxidation reactions [65, 66]. A prototypical example is the FeO ML on Pt(111) which, upon interaction with an oxygen atmosphere, transforms into O-Fe-O trilayer islands stabilized by a strong interfacial charge transfer [67, 68]. A similar mechanism is also likely active for other O–M–O trilayers, such as IrO_2 [69], PdO_2 [70], RhO_2 [71], RuO_2 [72] and MnO_2 [73, 74].

7.4 Interface Polarity

Oxide/oxide interfaces have recently focused the attention of the research community, due to the entirely new properties they display compared to their parent materials, and to their much wider variety of behaviors compared to traditional semiconductor/semiconductor interfaces [75, 76]. The possibility of producing a confined 2DEG/2DHG, subject of enhanced correlation effects, and magnetic or even superconducting instabilities, represents a particularly exciting issue. This section focuses on the compensation scenarios which may take place at polar/polar interfaces.We will not consider polar/non-polar interfaces for which, as stated in Sect. 7.2, the absence of polarization in one of the compounds makes their polarity characteristics similar to those described at the interface between polar films and vacuum.

7.4.1 Criterion of Compensation

A straightforward extension of (7.1) and (7.3) to polar/polar interfaces in the large thickness limit (Fig. 7.8), yields the following electrostatic criterion for the stability of the interface:

$$\delta\sigma = \mathcal{R}\sigma; \quad \delta\sigma' = \mathcal{R}'\sigma' \tag{7.9}$$

The excess charge densities $\delta\sigma$ and $\delta\sigma'$ are required at the polar terminations of each medium, leading to an excess interface charge density:

$$\delta\sigma^I = \delta\sigma - \delta\sigma' \tag{7.10}$$
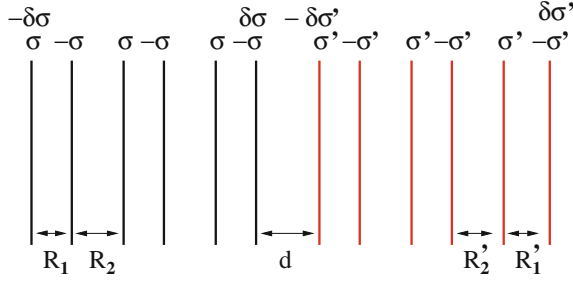
Fig. 7.8 Capacitor model of a polar/polar interface, assuming contact between two layers of opposite character. In an heterostructure, the two outer layers (extreme *left* and *right* layers) are free surfaces in contact with vacuum. In superlattices, they are in contact with each other, via the application of periodic boundary conditions. In that case, the outer interface charge density is equal and opposite to that in the central interface

Aside from those provided by covalent contributions, the remaining compensating charges leading to the cancellation of the polarizations P and P' present in the core of each subsystem read:

$$\delta\sigma_{comp} = P = \mathscr{R}\Sigma + P_{el}; \quad \delta\sigma'_{comp} = P' = \mathscr{R}'\Sigma' + P'_{el} \qquad (7.11)$$

The interfacial compensating charge densities $\pm\delta\sigma^I_{comp}$ are equal to the polarization discontinuity $\delta P = P - P'$ between the two media:

$$\delta\sigma^I_{comp} = \delta\sigma_{comp} - \delta\sigma'_{comp} = \delta P \qquad (7.12)$$

At a polar/polar interface, both polarizations P and P' are different from zero. Using (7.11), the polarization discontinuity can be written under the following form [77]:

$$\delta P = P - P' = \mathscr{R}(\Sigma - \Sigma') + \Sigma'(\mathscr{R} - \mathscr{R}') + \delta P_{el} \qquad (7.13)$$

which highlights its three contributions:

- the term $\mathscr{R}(\Sigma - \Sigma')$ depends on the difference of formal charge densities $\Sigma - \Sigma'$ between the two parts of the system. It represents the contribution from *valence discontinuity*.
- the term $\Sigma'(\mathscr{R} - \mathscr{R}')$ represents the contribution from *structural discontinuity*.
- the term δP_{el} depends on the difference of the electronic contributions to P and P'. It thus represents the *electronic discontinuity*. It is non-zero when one or both compounds are non-centro-symmetric.

Polarity compensation mechanisms at polar/polar interfaces may be extrapolated from those already mentioned at polar surfaces. They may involve interface

non-stoichiometry (including charged vacancies or interfacial mixing [78]), structural reconstructions [79] or electronic reconstruction. In the field of oxide/oxide interfaces, the latter mechanism has been experimentally evidenced at the polar/polar $ZnO(0001)/Zn_x Mg_{1-x} O(0001)$ interface [80].

7.4.2 Electronic Reconstruction at Polar/Polar Interfaces

In this section, we specify the conditions under which a 2DEG may exist at the interface between two stoichiometric polar compounds [77].

A first situation arises when $\delta P = 0$. Although, in that case, $\delta\sigma^I_{comp} = 0$, non-negligible charge modifications may take place at the interface, which reveal the electronic contribution to $\delta\sigma^I$. There is no need of electronic or structural reconstruction at the interface, which remains insulating. The profile of the electrostatic potential across the system is flat and there is no residual electric field on both sides of the interface. The interface is thus *non polar*, although each sub-system on its own is polar. For this condition to be fulfilled, there needs to be no structural discontinuity, no valence discontinuity and no electronic contribution to polarization on both sides of the interface. $\delta P = 0$ occurs at ideal zinc blende/zinc blende interfaces when the two compounds have the same valency, at ideal rock salt/rock salt (RS) interfaces (as exemplified in Fig. 7.9 in the particular case of $MgO(111)/CaO(111)$ interface [77]), at ideal perovskite/perovskite interface such as $KSbO_3(001)/KNbO_3(001)$ [81]. The $SrTiO_3(110)/LaAlO_3(110)$ interface studied in [82, 83] between two perovskites aligned along the polar (110) direction represents a special case. If stoichiometric, this interface is non-polar, since no polarization discontinuity exists between the two materials. However, in the experiment, a metal-insulator transition was evidenced and assigned to polarity effects induced by an interfacial mixing.

A second type of polar/polar interfaces is characterized by $\delta P \neq 0$, when one or several of its three contributions (structural, valence, or electronic discontinuity) are non zero. Such interfaces are *polar*, with a strong voltage across the system, which has to be canceled out, either by interface non-stoichiometry, as in the ZnO/FeO interface [84], or by the formation of a 2DEG, depending upon experimental preparation conditions. For the latter to exist, an overlap between the top of the VB of one compound and the bottom of the CB of the other compound has to take place, as illustrated in Fig. 7.9 in the case of wurtzite $ZnO(0001)$/rock salt $MgO(111)$interface [77] and recently recognized in [15]. The $ZnO(0001)/Zn_xMg_{1-x}O(0001)$ interface, in which Shubnikov-de Haas oscillations and the quantum Hall effect have been observed [80], also belongs to the family of *polar compensated* interfaces.
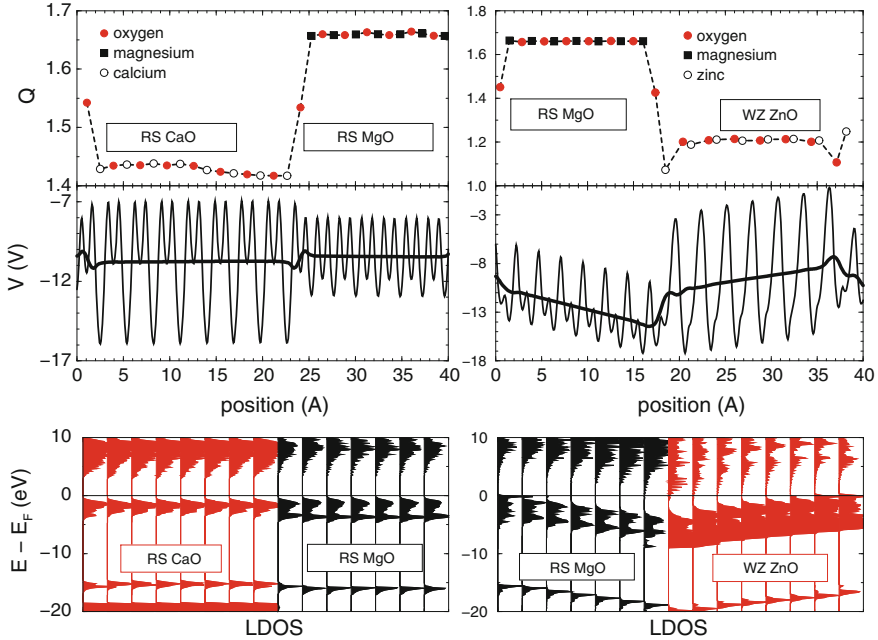
Fig. 7.9 Electronic properties of rock salt CaO(111)/rock salt MgO(111) (*left panels*) and rock salt MgO(111)/wurtzite ZnO(0001) (*right panels*) superlattices. From *top* to *bottom*: Bader charges Q (absolute values), electrostatic potential profiles V, and LDOS. The *thin line* in the potential profiles represent its lateral average $\overline{V}$, while the thick one corresponds to its cell average $\overline{\overline{V}}$

7.4.3 Finite Size Effects

Similarly to what occurs in polar ultra-thin films, polar/polar heterostructures or superlattices involving compounds of finite thickness may display properties modified by finite size effects. The latter may lead to the existence of a subcritical regime or to a structural transformation to avoid polarity.

An uncompensated polarity regime may take place at low thickness, either without much structural distortion (case of a small polarization discontinuity between the two bulk compounds δP_{bulk}), or when the film structure is flexible enough to strongly reduce the polarization discontinuity ($\delta P \ll \delta P_{bulk}$). Under these circumstances, the voltage ΔV due to δP is too small to induce an overlap of the VB of one compound with the CB of the other one at the interface and $\delta \sigma_{comp}^{I} = 0$. Equation (7.12) is thus not fulfilled in this regime ($\delta \sigma_{comp}^{I} \neq \delta P$). The interface remains insulating up to a critical thickness d_c of the order of $\Delta V / \delta \sigma_{comp}^{I}$ and displays a metal-insulator transition at d_c [77].

If δP results from a valence discontinuity or a strong structural discontinuity, the critical thickness will be extremely small and the pre-critical regime will likely not

be observable. If, however, the polarization discontinuity and thus $\delta\sigma_{comp}^{I}$ are small enough, d_c may involve up to several tens of repeat units. This may happen at the interface between e.g. two wurtzite compounds with $\Sigma = \Sigma'$. As an example, Fig. 7.10 displays the interfacial characteristics of an AlN(0001)/GaN(0001) superlattice [77]. Both compounds crystallize in a non-ideal wurzite structures with slightly different $\mathcal{R}$. δP thus results from a weak structural discontinuity and from an electronic contribution δP_{el} due to the non-centro-symmetric wurtzite structure. The average potential $\overline{\overline{V}}$ profile presents a small slope, which yields small band shifts. Below a critical thickness of about twenty repeat units, $\Delta\overline{\overline{V}}$ is insufficient to induce a band overlap and the interfaces remain insulating. A similar behavior has been found in a simulation of the polar/polar ZnO(0001)/MgO(0001) interface at low thickness, assuming wurtzite structure for MgO [85]. Above d_c, VB and CB overlap, which provides the compensating interfacial charges, and an interfacial 2DEG occurs, as found experimentally in ZnO(0001)/ZnMgO(0001) superlattices in the regime of low Mg doping [80, 86].

Aside from the existence of a subcritical regime, other finite size effects may occur. At small thickness, atomic layers are flexible and may depart from the bulk geometry, either intrinsically or in order to accommodate the interfacial strain. As described in the thin film section, a layer flattening towards a honeycomb structure may allow to avoid polarity at low thickness in thin rock salt or wurtzite films.
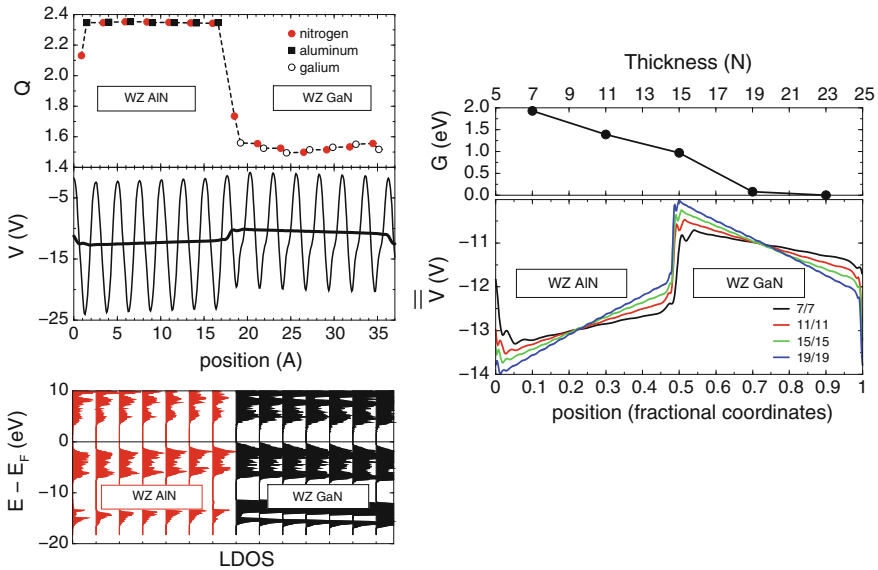
Fig. 7.10 *Left panels* same as in Fig. 7.9 for a wurtzite AlN(0001)/wurtzite GaN(0001) superlattice. At the thickness under consideration, the interfaces are insulating. Right panels, from *top* to *bottom*: thickness dependence of the gap width G and cell-averaged electrostatic potential profiles (in fractional coordinates), in superlattices of increasing thicknesses

These remarks stress that, in superlattices or heterostructures made of thin layers, predicting polarity character from the bulk properties of the two materials may lead to erroneous results. In the case of interfaces with large polarization discontinuity, finite size effects are not likely to alter the polar character of the interface, except if a structural transformation towards non-polar orientations takes place. In other systems, they may modify the structural and the electronic contributions to the polarization discontinuity, and thus the critical thickness of the metal-insulator transition. They may also induce a finite polarization discontinuity in systems in which bulk considerations predict $\delta P = 0$.

7.5 Polarity in 2D Nano-ribbons and Nano-Islands

While polarity concepts in ultra-thin films are rather well-established, the same is not true in 2D nano-ribbons and nano-islands [16]. A surge of interest in this field has taken place after the discovery of edge states at the Fermi level of graphene zigzag (ZZ) nano-ribbons [87, 88], although, as it will appear clearly, their physical origin is different. It is not often well-recognized that, depending upon the orientation of their edges, 2D objects may have a non-vanishing in-plane polarization. Experimentally, the difficulty in producing them in a well-characterized and reproducible way explains why most information that we have come from atomistic simulations.

7.5.1 Electrostatic Characteristics

Nano-ribbons with infinite edges are the 2D equivalents of thin films. When their 2D repeat unit bears a dipole moment perpendicular to their edges, the latter are polar. The polarity characteristics then depend on the charge density per unit length of the atomic rows $\pm \lambda$, the geometric factor associated to inter-row distances $\mathscr{R} = R_1/(R_1 + R_2)$ and the ribbon width $H = N(R_1 + R_2)$ (N the number of repeat units perpendicular to the edge).

Nano-ribbons may be produced from (001) ML of rock salt structure. Edges along the [110] direction ($\mathscr{R} = 1/2$) are polar, while those along [100] directions are non-polar. Alternatively, starting from the honeycomb-like (0001) ML of the h-BN structure, ribbons with ZZ or armchair (AC) edges can be obtained. The former are polar ($\mathscr{R} = 1/3$) and the latter non-polar. Ribbons cut out of a 1H (0001) trilayer of transition metal dichalcogenides (TMD) may also have ZZ or AC edges. Figure 7.11a, b display top views of polar [110] and ZZ ribbons.

The main electrostatic difference between polar thin films and polar ribbons lies in the logarithmic variation of the electrostatic potential $V(z)$ across a ribbon and the logarithmic dependence of the potential jump ΔV as a function of its width H (Fig. 7.11c) [89]. Contrary to thin films in which ΔV and the total dipole moment
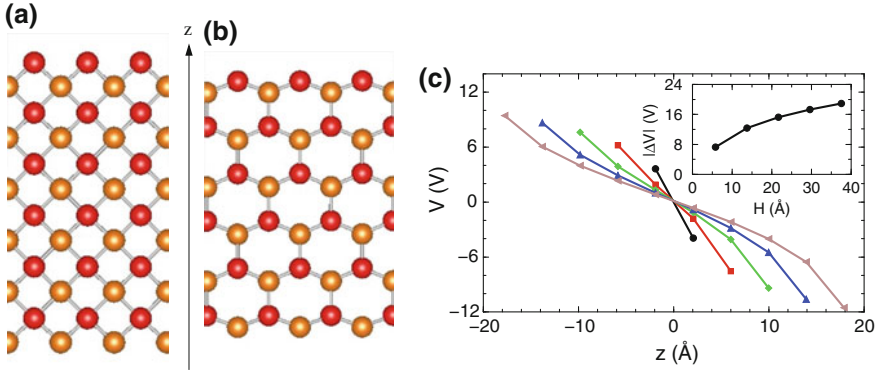
Fig. 7.11 *Top view* of polar nano-ribbons cut out of **a** a rock salt (001) ML with [110] edges or **b** an h-BN(0001) ML with ZZ edges. **c** Variations of the electrostatic potential across polar ribbons of increasing width H = 6, 14, 22, 30, and 38 Å. The *inset* highlights the logarithmic dependence of $|\Delta V|$ as a function of H

scale linearly with N, in polar ribbons in the absence of compensating charges, ΔV grows as $\ln N$ while the total dipole moment diverges linearly with N. Such logarithmic asymptotic behavior of ΔV and the absence of proportionality between ΔV and the total dipole moment are characteristic of electrostatic fields in 2D.

In the large width limit, the stability of polar ribbons requires edge excess charge densities $\delta\lambda$ (per unit length), whose expression is formally similar to that for $\delta\sigma$ in polar films:

$$\delta\lambda = \mathscr{R}\lambda \tag{7.14}$$

and the expression of the compensating charges $\delta\lambda_{comp}$, as a function of the 2D polarization P_{ML} (now referred to the full ML) and the formal charge densities Λ borne by the rows, reads:

$$\delta\lambda_{comp} = P_{ML} = \Lambda\mathscr{R} + P_{el}. \tag{7.15}$$

7.5.2 Unsupported Polar Ribbons

Considering the similarities of the electrostatic properties between polar thin films and polar ribbons, it is not surprising that the range of possible behaviors displayed by the latter largely overlaps those described in Sect. 7.3. In the following, we will nevertheless highlight some distinctive features of polar ribbons.

In the electronic reconstruction mechanism, due to the increase of ΔV with N, eventually an overlap of the outermost row VB and CB takes place, yielding the compensating charges $\delta\lambda_{comp}$ and edge metallization(1DEG). The LDOS narrowing

on edge atoms, due to their reduced coordination number, which is particularly strong on the anion terminations, favors the stabilization of spin polarization together with the edge metallization, as at thin film polar surfaces. ΔV does not vanish but stabilizes at a value of the order of the ribbon gap. This finite value constrains $\delta\lambda_{comp}$ to depart from P_{ML}:

$$\delta\lambda_{comp}(N) \neq P_{ML} \tag{7.16}$$

and to vary with the ribbon width N according to the following asymptotic law [90]:

$$\delta\lambda_{comp}(N) \approx P_{ML} - \frac{\Delta V \varepsilon^\infty}{4 \ln N} \tag{7.17}$$

This expression bears a close resemblance to the corresponding expression for thin films, (7.5), except for the logarithmic function of size in the denominator which replaces the linear function in films.

Such scenario has been found in polar ribbons of various oxides, such as MgO [90, 91], ZnO [92–95], BeO [41], V_2O_5 [96], as well as in non-oxide compounds MoS_2 [90, 97–103], ZnS [104], BN [105–107], AlN, GaN and SiC [108, 109]. In most cases, the authors did not make reference to polarity. In MgO ZZ ribbons, however, the LDOS and the size variation of the excess charges, displayed in Fig. 7.12, clearly exemplify the electronic reconstruction scenario and the validity of (7.17) [90]. By a detailed comparison between ZZ ribbons of MgO and MoS_2, it was also shown that polar signatures depend only marginally on the degree of ionicity of the compound [90]. It is important to stress that edge metallicity in these polar ribbons results from polarity compensation and is associated to an effective
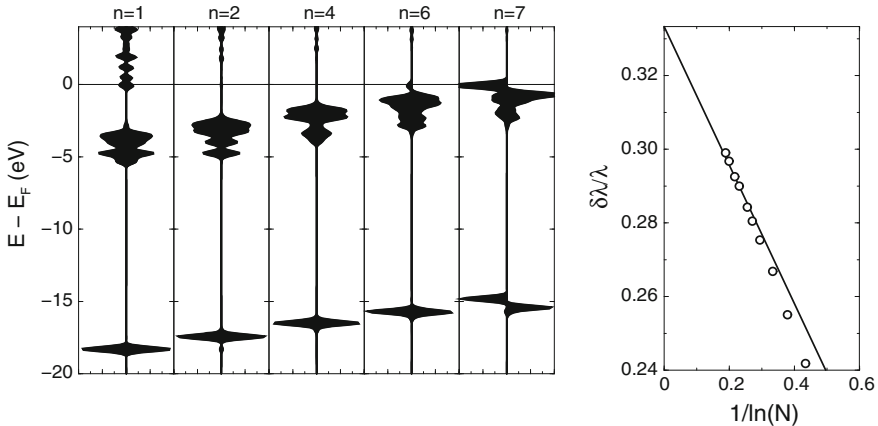
Fig. 7.12 *Left* LDOS through an MgO ZZ ribbon of width $N = 7$, highlighting the metallization of the edges and the band shifts across the ribbon. Row $n = 1$ is a cationic row. For simplicity, LDOS of rows $n = 3$ and $n = 5$ are not plotted. *Right* width dependence of $\delta\lambda/\lambda$ represented as a function of $1/\ln N$ to highlight its asymptotic behavior

charge transfer between the two opposite edges. This is not the case in graphene ZZ nano ribbons, which are non-polar and in which states at the Fermi level are non-bonding π states localized at low coordinated edge atoms, with no correlation to charge transfer processes across the ribbon.

Compensating charges may also be provided by non-stoichiometry in the outermost rows, or adsorption of charged species such as protons or hydroxyl groups issued from water dissociation. As in polar thin films, these mechanisms are generally more efficient than electronic reconstruction. In Fig. 7.13, the stability diagrams of MgO(111) polar surfaces [110, 111] and MgO ZZ polar ribbons [91] highlight their similar behavior, despite the difference in dimensionality.

Edge energies of infinite ribbons enable the determination of large island shapes on the basis of the Wulff construction. Results for unsupported MgO islands (Fig. 7.13) at increasing values of water chemical potential show a progressive transition from dry non-polar [100] to hydroxylated polar [110] edges [91]. This trend is the 2D equivalent of the transition from cubic shapes with dry (100) facets to octahedral shapes with hydroxylated (111) facets found in 3D MgO particles [110, 111].

Interestingly, according to simulations of ZnO ZZ ribbons [92], the metallic character of their edges disappears at 2ML-thickness. Due to the h-BN(0001) stacking sequence in which oxygen atoms are located on-top cations and vice versa, there is a cancellation of polarity effects between the two layers, the potential difference induced by the top layer being equal and opposite to that of the bottom
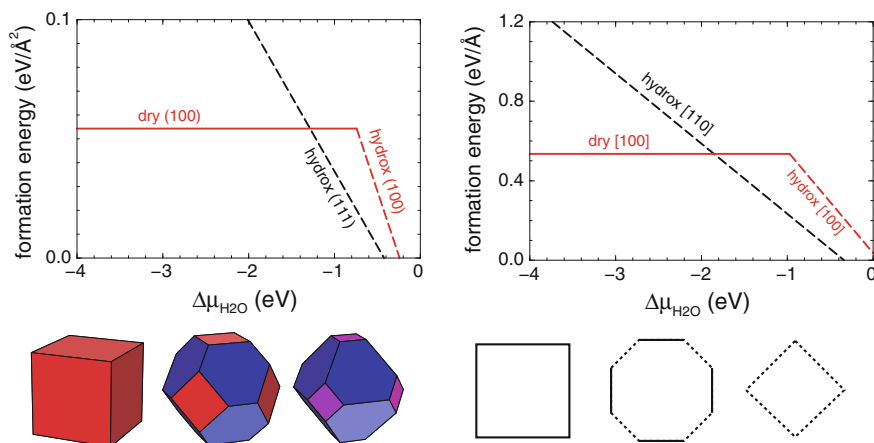
Fig. 7.13 *Left* formation energies (eV/Å^2) of polar MgO(111) and non-polar MgO(001) surfaces as a function of water chemical potential μ_{H_2O}. *Right* formation energies (eV/Å) of polar MgO [110] and non-polar MgO [100] ribbons, as a function of μ_{H_2O}. *Bottom panels* display the corresponding Wulff shapes at low, medium and high water chemical potentials, from *left* to *right*. Dry (100) facets, hydroxylated (100) facets and hydroxylated (111) facets of 3D particles are represented in *red*, *purple* and *blue*, respectively. Dry [100] and hydroxylated [110] edges of 2D islands are represented by *plain* and *dashed lines*, respectively

layer. No compensating charges are then needed and the ribbons keep their insulating or semi-conducting character. This reasoning may be extended to other compounds displaying the h-BN structure and to thicker ribbons in which an odd-even alternation of the electronic structure takes place as a function of thickness. It has no equivalent in the case of polar thin films.

7.5.3 Finite Size Effects

Polarity compensation cannot be avoided in large width polar ribbons. However, similarly to ultra-thin films, different scenarios may be expected at small width, in which charge compensation $\delta\lambda_{comp}$ may substantially differ from the actual polarization P and/or P may differ from P_{ML}.

A spontaneous transformation towards a structure with non-polar edges pertains to the case where $\delta\lambda_{comp} = P = 0$ and thus $P \neq P_{ML}$. It may occur in small width ribbons due to their important edge-to-central atom ratio. The new structure being different from the ML ground state, there is a cost of energy for each additional 2D repeat unit when the width N increases. However, as long as N remains small, the gain in edge energy in having a non-polar orientation is able to overcome this cost. Thus, up to a critical width, ultra-thin polar ribbons may sustain a structure which is not their ML ground state but allows non-polar edges.

This scenario has been invoked in ZZ ribbons of MoS_2, WS_2 and $MoSe_2$ [112]. In the infinite trilayer, their structural ground state, labeled 1H, is such that each TM has a trigonal prismatic coordination with the nearby S/Se atoms. Higher in energy, is a metastable 1T phase, in which each TM is octahedrally coordinated to its neighbors. ZZ edges of 1T ribbons are non-polar, while ZZ edges of 1H ribbons are polar (Fig. 7.14). The 1T phase is thus stabilized in narrow ZZ ribbons up to a critical width N_c of the order of a few repeat units. Such structural transformation does not take place in ZrS_2 ZZ ribbons since the ML ground state is already 1T. An interesting outcome of the 1H-to-1T transformation, which is expected to drastically change the ribbon transport as well as optical properties, is the existence of a sound modification in their electronic properties at N_c, due to the different electronic character of the 1T and 1H MLs: metallic in the 1T phase and semiconducting in the 1H phase.

To our knowledge, there is presently no example of uncompensated polarity (in which $\delta\lambda_{comp} = 0$ and $\delta\lambda_{comp} \neq P$), in polar nano-ribbons. The flexibility of these nano-structures, much stronger than thin films, may give hints for the absence of this regime. For example, in our study of ZZ MgO ribbons [91], we found that below $N = 6$, there is a spontaneous transformation of ZZ ribbons towards a non-polar [100] configuration, preventing the occurrence of uncompensated polarity.
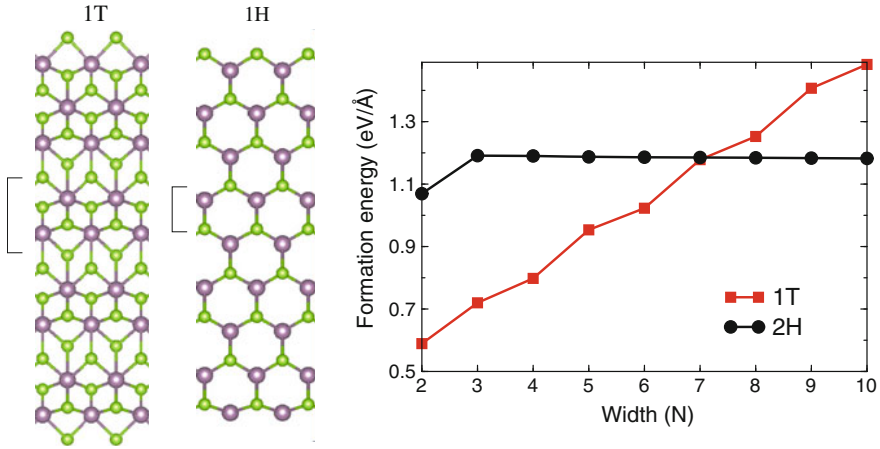
Fig. 7.14 *Left panels* top views of 1T and 1H MoS_2 ZZ ribbons. Mo and S atoms are represented by *large purple* and *small green balls*, respectively. Note that the 1T repeat units bears no dipole moment at variance with the 1H one. *Right panel* formation energy of 1T and 1H MoS_2 ZZ ribbons as a function of their width N

7.5.4 Interfaces Between Polar Ribbons

In line with the similarities of behaviors between polar films and polar ribbons, the interface characteristics between two polar ribbons are driven by the strength of the polarization discontinuitys δP, which, in 2D, reads:

$$\delta P = P - P' = \mathscr{R}(\Lambda - \Lambda') + \Lambda'(\mathscr{R} - \mathscr{R}') + \delta P_{el} \qquad (7.18)$$

In the absence of polarization discontinuity ($\delta P = 0$), the interface will remain insulating, while a finite discontinuity ($\delta P \neq 0$) will lead either to electronic reconstruction at large width or to uncompensated polarity below a critical width.

Such polar/polar interfaces between 2D ribbons have been predicted to accommodate fully spin-polarized 1DEG or 1DHG in the case of AlN/SiC and ZnO/SiC ZZ ribbons [113]. Indeed these interfaces exemplify cases in which the polarization discontinuity is driven by the valence discontinuity with $\Lambda - \Lambda' = 1$ in the former and 2 in the latter, per unit cell length. Consistently, the interfacial compensating charge density is nearly twice larger in ZnO/SiC than in AlN/SiC, the small discrepancy with respect to the ratio 2 being due to the electronic contribution to δP in these non-centro-symmetric honeycomb lattices. Considering the fact that these compounds have not been isolated as ML, the authors of [114] have suggested several pathways to engineer polar discontinuities, involving selective functionalization of a BN ML or total functionalization of graphene/BN interfaces.

7.5.5 Support Effects

The scenarios described previously apply to (unsupported) polar ribbons. Although interesting because they allow to point out the intrinsic effect of polarity, they can only represent a preliminary step towards a full understanding of the behavior of supported polar ribbons.

Similarly to what happens at the interface between a polar thin film and its metallic support (Sect. 7.3.4), compensation of polarity in supported ribbons involves screening effects by the support. A large part of the compensating charges is transferred from the oxide edges to the metal support, thus allowing the oxide ions to recover charges closer to their ML values. In that way, the polar instability is healed and the interfacial electron transfer leads to strong adhesion along the ribbon edges. The efficiency of the metal screening is even stronger for polar ribbons than for polar films, since both ribbon edges interact with the support, while screening occurs at a single film termination, the one in contact with the support.

The few theoretical works which have considered metal-supported polar ribbons [90, 91, 115, 116] support this picture. For example, Fig. 7.15 compares the charge distribution in unsupported and Au-supported MgO ZZ ribbons [91]. It evidences an electron excess in the metal below the ribbon cation edge and an electron depletion under its oxygen edge.

The relative efficiency of electronic reconstruction, non-stoichiometry and hydroxylation in compensating polarity may be strongly influenced by the support. In particular, since the stabilization due to the screening of the compensating charges by the metal on both sides of supported polar ribbons is very efficient, electronic reconstruction becomes competitive with respect to non-stoichiometry and
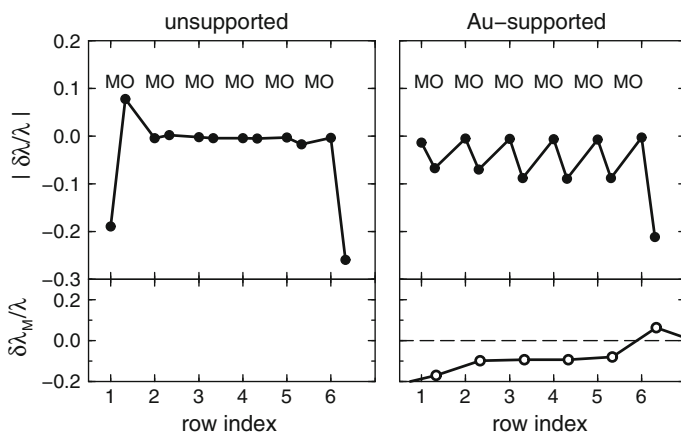
Fig. 7.15 Bader excess charge $\delta\lambda/\lambda$ at anion and cation sites across unsupported and Au-supported MgO ZZ ribbons. *Bottom panels* represent the modification of charge $\delta\lambda_M/\lambda$ in the metal substrate underneath the ribbon. Note that screening at the Mg edge (row #1) is more efficient than at the O edge, due to the large electronegativity of gold
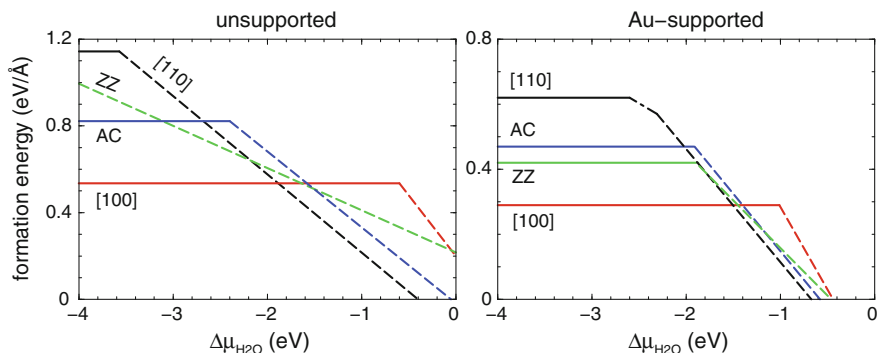
Fig. 7.16 Formation energies (eV/Å) of unsupported and Au-supported polar and non-polar MgO ribbons as a function of water chemical potential μ_{H_2O}. Bare or fully hydroxylated states of the ribbons are represented with full and dashed lines, respectively [91]

hydroxylation, allowing polar ribbons to remain dry and unreconstructed in a large range of water chemical potentials. These general features are exemplified in the case of Au-supported MgO ZZ ribbons (Fig. 7.16) [91]. It turns out that, at variance with unsupported ribbons, supported dry and unreconstructed ZZ ribbons are more stable than AC ones. At intermediate water chemical potential, where differences between [100, 110], ZZ, and AC edge energies are tiny, islands of different symmetries may coexist. This is consistent with the recent experimental findings of shape transitions in MgO islands grown on the Au(111) surface [117–119].

To our knowledge, there are no experimental results on infinitely long polar ribbons. There are however hints of edge polarity in polar 2D islands in non-oxide compounds such as MoS_2 [120, 121], or BN [105–107, 122], although no relation to polarity was invoked. For example, STM experiments [120, 121] have evidenced the growth of MoS_2 (0001) islands of triangular shape on Au(111), with edges displaying a pronounced contrast which was interpreted as due to the presence of metallic states [97, 123]. The observation of MgO and NiO mono- or bi-layer islands with [110] polar edges, grown on Ag(001) [124–126] as well as simulations [115, 116] have suggested that these islands might be embedded in the substrate grooves. Let us note that an excess of oxygen in 2D islands stabilized under specific preparation conditions, such as observed in MgO/Ag(100) [127, 128] or FeO_x/Pt (111) [65, 66], may alter the relative stability of the various island edges.

This discussion proves that a metallic support may drastically change the properties of polar ribbons—atomic structure, electronic properties and stability—compared to those expected when the ribbons are unsupported. In particular, in the electronic reconstruction scenario, the exciting electronic and magnetic properties of the 1DEG disappear, since the compensating charge, mainly localized in the support, becomes mixed with its metallic states.

7.5.6 Polar Nano-Islands

The previous analysis has mainly focused on (infinitely long) ribbons, but also applies to 2D large islands with polar edges, as long as their shape may be predicted from edge formation energies by the Wulff theorem. However, electrostatic considerations predict some specific finite size effects, driven by the finite length L of the island edges.

Across an island, such as the one represented in Fig. 7.17, the voltage ΔV depends on both the island width H and the edge length L in the following way (a an atomic length) [89]:

$$\Delta V = 2\delta\lambda \ln\left(\frac{LH}{a(L+\sqrt{L^2+4H^2})}\right) \tag{7.19}$$

When $L \gg H$, the behavior of infinite ribbons is recovered, with ΔV increasing as $\ln H$. In the opposite limit $L \ll H$, relevant for nano-islands, ΔV grows as the logarithm of the lateral size L of the polar termination:

$$\Delta V = 2\delta\lambda \ln\left(\frac{L}{2a}\right) \tag{7.20}$$

It is thus the smallest of the two shape parameters, the width H of the polar island or the length L of its polar edge, which drives the electrostatic behavior. Ultimately, when the size of the polar edge is reduced to a single atom (1D wire), $\Delta V = 2\lambda \ln 2$ remains finite and independent of H.

Another finite size effect affects the potential profile along polar edges. In infinite ribbons, the average potential $V(x)$ along an edge is flat. This is no longer true in
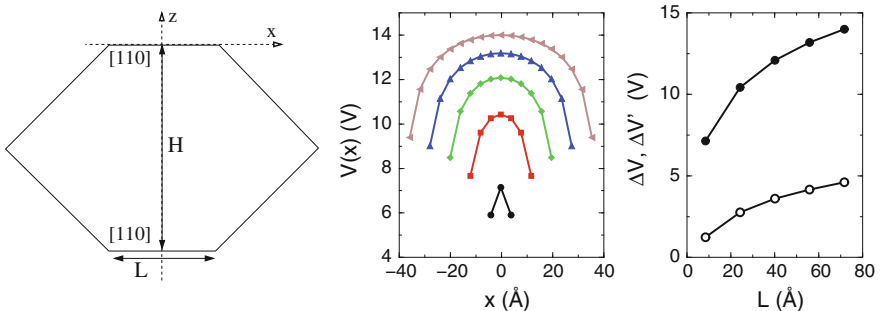
Fig. 7.17 *Left panel* a 2D (001) island with two [110] polar edges. *Middle panel* potential profile $V(x)$ along a polar edge in the limit $L \ll H$, for different values of L ($L = 8, 34\ 40, 55,$ and 71 Å). *Right panel* potential difference ΔV between the center of the objects and the center of gravity of their polar termination (*black symbols*), and maximal potential variation $\Delta V'$ within their polar terminations (*open symbols*)

finite size islands in the limit $L \ll H$ (Fig. 7.17). $V(x)$ presents large variations $\Delta V'$ between the corners and the center of the edge, which scale as $\ln L$.

From these considerations, one could anticipate that polarity effects are less crucial in islands with small polar edges, and that the compensating charge density $\delta \lambda_{comp}$ in the regime $L \ll H$ might not be homogeneously distributed. As a consequence, vacancy formation energies might drastically depend on the edge length and on the location of the vacancy on the edge. Similarly, adsorption energies of charged species might depend on the precise adsorption site on the edge. However, these arguments remain speculative and need further confirmation whether by experiment or by simulation.

7.6 Conclusion

As reviewed in this chapter, electrostatic interactions and polarity effects are key driving forces behind many new compositions, structures and morphologies that oxides may display in the 2D limit. Most of the time, these new oxides have nothing to do with bulk oxides. While an intense activity has been devoted to polar thin films during the last decade, the synthesis of 2D polar nano-objects, such as ribbons or islands, is not as well-controlled and their properties not as well-understood. Several major challenges have to be taken up, such as defining preparation protocols, mastering the kinetics of the first steps of their formation, characterizing their composition and simulating their properties. The importance of the field has long been recognized in chemistry, due to the novel reactivity and selectivity properties displayed by these 2D oxides. Physical properties are nowadays also scrutinized, with a specific interest towards the consequences of confinement on the electronic degrees of freedom: edge/interface metallization, magnetism, and, in some cases, superconductivity. No doubt that a convergent effort of interdisciplinary nature will allow a deeper understanding and mastering of these objects in a near future.

References

1. Weiss W, Ranke W (2002) Surface chemistry and catalysis on well-defined epitaxial iron-oxide layers. Prog Surf Sci 70:1–151
2. Chen MS, Goodman DW (2008) Ultrathin, ordered oxide films on metal surfaces. J Phys: Condens Matter 20:264013
3. Freund H-J, Pacchioni G (2008) Oxide ultra-thin films on metals: new materials for the design of supported metal catalysts. Chem Soc Rev 37:2224–2242
4. Nilius N (2009) Properties of oxide thin films and their adsorption behavior studied by scanning tunneling microscopy and conductance spectroscopy. Surf Sci Rep 64:595–659
5. Wu Q-H, Fortunelli A, Granozzi G (2009) Preparation, characterisation and structure of Ti and Al ultrathin oxide films on metals. Int Rev Phys Chem 28:517–576

6. Netzer FP, Allegretti F, Surnev S (2010) Low-dimensional oxide nanostructures on metals: hybrid systems with novel properties. J Vac Sci Technol B 28:1–16

7. Noguera C (2000) Polar oxide surfaces. J Phys Cond Matter 12:R367–R410

8. Goniakowski J, Finocchi F, Noguera C (2008) Polarity of oxide surfaces and nanostructures. Rep Prog Phys 71:016501

9. Tasker PWJ (1979) Stability of ionic crystal surfaces. J Phys C 12:4977–4984

10. King-Smith RD, Vanderbilt D (1993) Theory of polarization of crystalline solids. Phys Rev B 47:1651–1654

11. Stengel M, Vanderbilt D (2009) Berry-phase theory of polar discontinuities at oxide-oxide interfaces. Phys Rev B 80:241103

12. Stengel M (2011) Electrostatic stability of insulating surfaces: theory and applications. Phys Rev B 84:205432

13. Garcia A, Cohen ML (1993) 1st principles ionicity scales. 1 Charge asymmetry in the solid-state. Phys Rev B 47:4215–4221

14. Belabbes A, Furthmüller J, Bechstedt F (2013) Relation between spontaneous polarization and crystal field from first principles. Phys Rev B 87:035305

15. Bristowe NC, Ghosez P, Littlewood PB, Artacho E (2014) The origin of two-dimensional electron gases at oxide interfaces: insights from theory. J Phys: Condens Matter 26:143201

16. Noguera C, Goniakowski J (2013) Polarity in oxide nano-objects. Chem Rev 113:4073–4105

17. Goniakowski J, Noguera C, Giordano L (2004) Using polarity for engineering oxide nanostructures: structural phase diagram in free and supported MgO(111) ultrathin films. Phys Rev Lett 93:215702

18. Goniakowski J, Noguera C, Giordano L (2007) Prediction of uncompensated polarity in ultrathin films. Phys Rev Lett 98:205701

19. Gragnaniello L, Agnoli S, Parteder G, Barolo A, Bondino F, Allegretti F, Surnev S, Granozzi G, Netzer FP (2010) Cobalt oxide nanolayers on Pd(100): the thickness-dependent structural evolution. Surf Sci 604:2002–2011

20. Weirum G, Barcaro G, Fortunelli A, Weber F, Schennach R, Surnev S, Netzer FP (2010) Growth and surface structure of zinc oxide layers on a Pd(111) surface. J Phys Chem C 114:15432

21. Schennach R, Weber F, Piffl M, Weirum G, Surnev S (2012) Growth and reactivity of Zn and ZnO on Pd(111). Surf Eng 28:87–90

22. Noguera C, Goniakowski J (2008) Polarity in oxide ultrathin films. J Phys: Condens Matter 20:264003

23. Kresse G, Dulub O, Diebold U (2003) Competing stabilization mechanism for the polar ZnO (0001)-Zn surface. Phys Rev B 68:245409

24. Thiel S, Hammerl G, Schmehl A, Schneider CW, Mannhart J (2006) Tunable quasi-two-dimensional electron gases in oxide heterostructures. Science 313:1942–1945

25. Hu XL, Michaelides A (2010) The kaolinite (001) polar basal plane. Surf Sci 604:111–117

26. Ohtomo A, Hwang HY (2004) A high-mobility electron gas at the $LaAlO_3/SrTiO_3$ heterointerface. Nature 427:423–426

27. Nakagawa N, Hwang HY, Muller DA (2006) Why some interfaces cannot be sharp. Nat Mater 5:204–209

28. Pentcheva R, Pickett WE (2006) Charge localization or itineracy at $LaAlO_3/SrTiO_3$ interfaces: Hole polarons, oxygen vacancies, and mobile electrons. Phys Rev B 74:035112

29. Reyren N, Thiel S, Caviglia AD, Kourkoutis LF, Hammerl G, Richter C, Schneider CW, Kopp T, Rüetschi A-S, Jaccard D, Gabay M, Muller DA, Triscone J-M, Mannhart J (2007) Superconducting interfaces between insulating oxides. Science 317:1196–1199

30. Gabay M, Gariglio S, Triscone JM, Santander-Syro AF (2013) 2-Dimensional oxide electronic gases: interfaces and surfaces. Eur Phys J Special Topics 222:1177–1183

31. Segal Y, Ngai JH, Reiner JW, Walker FJ, Ahn CH (2009) X-ray photoemission studies of the metal-insulator transition in $LaAlO_3/SrTiO_3$ structures grown by molecular beam epitaxy. Phys Rev B 80:241107

32. Slooten E, Zhong Z, Molegraaf HJA, Eerkes PD, de Jong S, Massee F, van Heumen E, Kruize MK, Wenderich S, Kleibeuker JE, Gorgoi M, Hilgenkamp H, Brinkman A, Huijben M, Rijnders G, Blank DHA, Koster G, Kelly PJ, Golden MS (2013) Hard x-ray photoemission and density functional theory study of the internal electric field in $SrTiO_3$/$LaAlO_3$ oxide heterostructures. Phys Rev B 87:085128

33. Kiguchi M, Entani S, Saiki K, Goto T, Koma A (2003) Atomic and electronic structure of an unreconstructed polar MgO(111) thin film on Ag(111). Phys Rev B 68:115402

34. Ritter M, Ranke W, Weiss W (1998) Growth and structure of ultrathin FeO films on Pt(111) studied by STM and LEED. Phys Rev B 57:7240–7251

35. Ranke W, Ritter M, Weiss W (1999) Crystal structures and growth mechanism for ultrathin films of ionic compound materials: FeO(111) on Pt(111). Phys Rev B 60:1527–1530

36. Gubo M, Ebensperger C, Meyer W, Hammer L, Heinz K (2009) Substoichiometric cobalt oxide monolayer on Ir(100)-(1 × 1). J Phys: Condens Matter 21:474211

37. Ebensperger C, Gubo M, Meyer W, Hammer L, Heinz K (2010) Substrate-induced structural modulation of a CoO(111) bilayer on Ir(100). Phys Rev B 81:235405

38. Tusche C, Meyerheim HL, Kirschner J (2007) Observation of depolarized ZnO(0001) monolayers: formation of unreconstructed planar sheets. Phys Rev Lett 99:026102

39. Claeyssens F, Freeman CL, Allan NL, Sun Y, Ashfold MN, Harding JH (2005) Growth of ZnO thin films—experiment and theory. J Mat Chem 15:139–148

40. Baumeier B, Krüger P, Pollmann J (2007) Structural, elastic, and electronic properties of SiC, BN, and BeO nanotubes. Phys Rev B 76:085407

41. Wu W, Lu P, Zhang Z, Guo W (2011) Electronic and magnetic properties and structural stability of BeO sheet and nanoribbons. ACS Appl Mater Interfaces 3:4787–4795

42. Freeman CL, Claeyssens F, Allan NL, Harding JH (2006) Graphitic nanofilms as precursors to wurtzite films: theory. Phys Rev Lett 96:066102

43. Kresse G, Schmid M, Napetschnig E, Shishkin M, Kohler L, Varga P (2005) Structure of the ultrathin aluminum oxide film on NiAl(110). Science 308:1440–1442

44. Goniakowski J, Noguera C (1999) Characteristics of Pd deposition on the MgO(111) surface. Phys Rev B 60:16120–16128

45. Goniakowski J, Noguera C (2002) Microscopic mechanisms of stabilization of polar oxide surfaces: transition metals on the MgO(111) surface. Phys Rev B 66:085417

46. Muller DA, Shashkov DA, Benedek R, Yang LH, Silcox J, Seidman DN (1998) Atomic scale observations of metal-induced gap states at {222}MgO/Cu interfaces. Phys Rev Lett 80:4741–4744

47. Imhoff D, Laurent S, Colliex C, Backhaus-Ricoult M (1999) Determination of the characteristic interfacial electronic states of {111}Cu-MgO interfaces by ELNES. Eur Phys J A 5:9–18

48. Tejedor C, Flores C, Louis E (1977) Metal-semiconductor interface- Si (111) and zincblende (110) junctions. J Phys C 10:2163–2177

49. Bordier G, Noguera C (1991) Electronic structure of a metal-insulator interface—towards a theory of nonreactive adhesion. Phys Rev B 44:6361–6371

50. Goniakowski J, Noguera C (2004) Electronic states and Schottky barrier height at metal/MgO(100) interfaces. Interf Sci 12:93–103

51. Goniakowski J, Noguera C (2009) Polarization and rumpling in oxide monolayers deposited on metallic substrates. Phys Rev B 79:155433

52. Pacchioni G, Giordano L, Baistrocchi M (2005) Charging of metal atoms on ultrathin MgO/Mo(100) films. Phys Rev Lett 94:226104

53. Giordano L, Pacchioni G (2006) Charge transfers at metal/oxide interfaces: a DFT study of formation of K^+ and Au^- species on MgO/Ag(100) ultra-thin films from deposition of neutral atoms. Phys Chem Chem Phys 8:3335–3341

54. Ricci D, Bongiorno A, Pacchioni G, Landman U (2006) Bonding trends and dimensionality crossover of gold nanoclusters on metal-supported MgO thin films. Phys Rev Lett 97:036106

55. Honkala K, Häkkinen H (2007) Au adsorption on regular and defected thin MgO(100) films supported by Mo. J Phys Chem C 111:4319–4327

56. Frondelius P, Hellman A, Honkala K, Häkkinen H, Grönbeck H (2008) Charging of atoms, clusters, and molecules on metal-supported oxides: a general and long-ranged phenomenon. Phys Rev B 78:085426

57. Sterrer M, Risse T, Pozzoni UM, Giordano L, Heyde M, Rust H-P, Pacchioni G, Freund H-J (2007) Control of the charge state of metal atoms on thin MgO films. Phys Rev Lett 98:096107

58. Sterrer M, Risse T, Heyde M, Rust H-P, Freund H-J (2007) Crossover from three-dimensional to two-dimensional geometries of Au nanostructures on thin MgO(001) films: a confirmation of theoretical predictions. Phys Rev Lett 98:206103

59. Barcaro G, Fortunelli A, Granozzi G (2008) Metal adsorption on oxide polar ultrathin films. Phys Chem Chem Phys 10:1876–1882

60. Grönbeck H (2006) Mechanism for NO_2 charging on metal supported MgO. J Phys Chem B 110:11977–11981

61. Hellman A, Klacar S, Grönbeck H (2009) Low temperature CO oxidation over supported ultrathin MgO films. J Am Chem Soc 131:16636

62. Gonchar A, Risse T, Freund H-J, Giordano L, Di Valentin C, Pacchioni G (2011) Activation of oxygen on MgO : O_2^- radical ion formation on thin, Metal-Supported MgO(001) Films. Angew Chem Int Ed 50:2635–2638

63. Goniakowski J, Noguera C, Giordano L, Pacchioni G (2009) Adsorption of metal adatoms on FeO(111) and MgO(111) monolayers: effects of charge state of adsorbate on rumpling of supported oxide film. Phys Rev B 80:125403

64. Benedetti S, Stavale F, Valeri S, Noguera C, Freund H-J, Goniakowski J, Nilius N (2013) Steering the growth of metal Ad-particles via Interface Interactions between a MgO thin film and a Mo support. Adv Funct Materials 23:75–80

65. Sun YN, Qin ZH, Lewandowski M, Carrasco E, Sterrer M, Shaikhutdinov S, Freund H-J (2009) Monolayer iron oxide film on platinum promotes low temperature CO oxidation. J Catal 266:359–368

66. Sun YN, Giordano L, Goniaksowski J, Lewandowski M, Qin ZH, Noguera C, Shaikhutdinov S, Pacchioni G, Freund H-J (2010) The interplay between structure and CO oxidation catalysis on metal-supported ultrathin oxide films. Angew Chem Int Ed 49:4418–4421

67. Giordano L, Lewandowski M, Groot IMN, Sun YN, Goniakowski J, Noguera C, Shaikhutdinov S, Pacchioni G, Freund H-J (2010) Oxygen-induced transformations of an FeO(111) film on Pt(111): a combined DFT and STM study. J Phys Chem C 114:21504–21509

68. Giordano L, Pacchioni G, Noguera C, Goniakowski J (2014) Identification of active sites in a realistic model of strong metal-support interaction catalysts: the case of platinum (111)-supported iron oxide film. ChemCatChem 6:185–190

69. He YB, Stierle A, Li WX, Farkas A, Kasper N, Over H (2008) Oxidation of Ir(111): from O-Ir-O trilayer to bulk oxide formation. J Phys Chem C 112:11946–11953

70. Rogal J, Reuter K, Scheffler M (2008) CO oxidation on Pd(100) at technologically relevant pressure conditions: first-principles kinetic Monte Carlo study. Phys Rev B 77:155410

71. Gustafson J, Mikkelsen A, Borg M, Lundgren E, Köhler L, Kresse G, Schmid M, Varga P, Yuhara J, Torrelles X, Quirós C, Andersen JN (2004) Self-limited growth of a thin oxide layer on Rh(111). Phys Rev Lett 92:126102

72. Flege JI, Hrbek J, Sutter P (2008) Structural imaging of surface oxidation and oxidation catalysis on Ru(0001). Phys Rev B 78:165407

73. Franchini C, Podloucky R, Allegretti F, Li F, Parteder G, Surnev S, Netzer FP (2009) Structural and vibrational properties of two-dimensional Mn_xO_y layers on Pd(100): experiments and density functional theory calculations. Phys Rev B 79:035420

74. Martynova Y, Soldemo M, Weissenrieder J, Sachert S, Polzin S, Widdra W, Shaikhutdinov S, Freund H-J (2013) CO oxidation over monolayer manganese oxide films on Pt(111). Catal Lett 143:1108–1115

75. Hwang HY, Iwasa Y, Kawasaki M, Keimer B, Nagaosa N, Tokura Y (2012) Emergent phenomena at oxide interfaces. Nature Mater 11:103–113
76. Mannhart J, Blank DHA, Hwang HY, Millis AJ, Triscone J-M (2008) Two-dimensional electron gases at oxide interfaces. MRS Bull 333:1027–1034
77. Goniakowski J, Noguera C (2014) Conditions for electronic reconstruction at stoichiometric polar/polar interfaces. J Phys: Condens Matter 26:485010
78. Harrison A, Kraut EA, Waldrop JR, Grant RW (1978) Polar heterojunction interfaces. Phys Rev 18:4402–4410
79. Martin RM (1980) Atomic reconstruction at polar interfaces of semiconductors. J Vac Sci Technol 17:978–981
80. Tsukazaki A, Ohtomo A, Kita T, Ohno Y, Ohno H, Kawasaki M (2007) Quantum Hall effect in polar oxide heterostructures. Science 315:1388–1391
81. Das H, Spaldin NA, Waghmare UV, Saha-Dasgupta T (2010) Chemical control of polar behavior in bicomponent short-period superlattices. Phys Rev B 81:235112
82. Annadi A, Zhang Q, Wang XR, Tuzla N, Gopinadhan K, Lü WM, Barman AR, Liu ZQ, Srivastava A, Saha S, Zhao YL, Zeng SW, Dhar S, Olsson E, Gu B, Yunoki S, Maekawa S, Hilgenkamp H, Venkatesan T, Ariando (2013) Anisotropic two-dimensional electron gas at the LaAlO$_3$/SrTiO$_3$ (110) interface. Nature Comm 4:1838
83. Herranz G, Sánchez F, Dix N, Scigaj M, Fontcuberta J (2012) High mobility conduction at (110) and (111) LaAlO$_3$/SrTiO$_3$ interfaces. Sci Rep 2:758
84. Xue M, Guo Q, Wu K, Guo J (2009) Epitaxial growth of ZnO films on thin FeO(111) layers. J Cryst Growth 311:3918–3923
85. Betancourt J, Saavedra-Arias JJ, Burton JD, Ishikawa Y, Tsymbal EY, Velev JP (2013) Polarization discontinuity induced two-dimensional electron gas at ZnO/Zn(Mg)O interfaces: a first-principles study. Phys Rev B 88:085418
86. Ohtomo A, Kawasaki M, Ohkubo I, Koinuma H, Yasuda T, Segawa Y (1999) Structure and optical properties of ZnO/Mg$_{0.2}$Zn$_{0.8}$O superlattices. Appl Phys Lett 75:980–982
87. Dutta S, Pati SK (2010) Novel properties of graphene nanoribbons: a review. J Mater Chem 20:8207–8223
88. Acik M, Chabal YJ (2011) Nature of graphene edges: a review. Jap J Appl Phys 50:070101
89. Goniakowski J, Noguera C (2011) Polarity at the nanoscale. Phys Rev B 83:115413
90. Güller F, Llois AM, Goniakowski J, Noguera C (2013) Polarity effects in unsupported polar nanoribbons. Phys Rev B 87:205423
91. Goniakowski J, Giordano L, Noguera C (2013) Polarity compensation in low-dimensional oxide nanostructures: the case of metal-supported MgO nanoribbons. Phys Rev B 87:035405
92. Botello-Mendez AR, Martinez-Martinez MT, Lopez-Urias F, Terrones M, Terrones H (2007) Metallic edges in zinc oxide nanoribbons. Chem Phys Lett 448:258–263
93. Botello-Mendez AR, Lopez-Urias F, Terrones M, Terrones H (2008) Magnetic behavior in zinc oxide zigzag nanoribbons. Nano Lett 8:1562–1565
94. Topsakal M, Cahangirov S, Bekaroglu E, Ciraci S (2009) First-principles study of zinc oxide honeycomb structures. Phys Rev B 80:235119
95. Wang Y, Wang B, Zhang Q, Shi D, Yunoki S, Kong F, Xu N (2012) A simple capacitor model and first-principles study of carbon-doped zigzag ZnO nanoribbons. Solid State Comm 152:534–539
96. Tang Q, Li F, Zhou Z, Chen Z (2011) Versatile electronic and magnetic properties of corrugated V$_2$O$_5$ two-dimensional crystal and its derived one-dimensional nanoribbons: a computational exploration. J Phys Chem C 115:11983–11990
97. Bollinger MV, Lauritsen JV, Jacobsen KW, Nørskov JK, Helveg S, Besenbacher F (2001) One-dimensional metallic edge states in MoS$_2$. Phys Rev Lett 87:196803
98. Li Y, Zhou Z, Zhang S, Chen Z (2008) MoS$_2$ nanoribbons: high stability and unusual electronic and magnetic properties. J Am Chem Soc 130:16739–16744
99. Botello-Mendez AR, Lopez-Urias F, Terrones M, Terrones H (2009) Metallic and ferromagnetic edges in molybdenum disulfide nanoribbons. Nanotechnology 20:325703

100. Ataca C, Sahin H, Akturk E, Ciraci S (2011) Mechanical and electronic properties of MoS_2 nanoribbons and their defects. J Phys Chem C 115:3934–3941
101. Erdogan E, Popov IH, Enyashin AN, Seifert G (2012) Transport properties of MoS_2 nanoribbons: edge priority. Eur Phys J B 85:33
102. Pan H, Zhang YW (2012) Edge-dependent structural, electronic and magnetic properties of MoS_2 nanoribbons. J Mater Chem 22:7280–7290
103. Yang SQ, Li DX, Zhang TR, Tao ZL, Chen J (2012) First-principles study of zigzag MoS_2 nanoribbon as a promising cathode material for rechargeable Mg batteries. J Phys Chem C 116:1307–1312
104. Zhang S, Ma J (2011) Width- and edge-dependent stability, electronic structures, and magnetic properties of graphene-like and wurtzite ZnS nanoribbons. J Phys Chem C 115:4466–4475
105. Ding Y, Wang Y, Ni J (2009) The stabilities of boron nitride nanoribbons with different hydrogen-terminated edges. Appl Phys Lett 94:233107
106. Chen W, Li Y, Yu G, Li C-Z, Zhang SB, Zhou Z, Chen Z, Chen J (2010) Hydrogenation: a simple approach to realize semiconductor-half-metal-metal transition in boron nitride nanoribbons. J Am Chem Soc 132:1699–1705
107. Lopez-Bezanilla A, Huang J, Terrones H, Sumpter BG (2011) Boron nitride nanoribbons become metallic. Nano Lett 11:3267–3273
108. Wu M, Wu X, Pei Y, Zeng XC (2011) Inorganic nanoribbons with unpassivated zigzag edges: half metallicity and edge reconstruction. Nano Res 4:233–239
109. Li H, Dai J, Li J, Zhang S, Zhou J, Zhang L, Chu W, Chen D, Zhao H, Yang J, Wu Z (2010) Electronic structures and magnetic properties of GaN sheets and nanoribbons. J Phys Chem C 114:11390–11394
110. Finocchi F, Goniakowski J (2007) The effects of exchange and correlation on the computed equilibrium shapes of wet MgO crystallites. Surf Sci 601:4144–4148
111. Geysermans P, Finocchi F, Goniakowski J, Hacquart R, Jupille J (2009) Combination of (100), (110) and (111) facets in MgO crystals shapes from dry to wet environment. Phys Chem Chem Phys 11:2228–2233
112. Güller F, Llois AM, Goniakowski J, Noguera C (2015) Prediction of structural and metal-to-semiconductor phase transitions in nanoscale MoS_2, WS_2, and other transition metal dichalcogenide zigzag ribbons. Phys Rev B 91:075407
113. Bristowe NC, Stengel M, Littlewood PB, Artacho E, Pruneda JM (2013) One-dimensional half-metallic interfaces of two-dimensional honeycomb insulators. Phys Rev B 88:161411
114. Gibertini M, Pizzi G, Marzari N (2014) Engineering polar discontinuities in honeycomb lattices. Nature Comm 5:5157
115. Ferrari AM, Casassa S, Pisani C (2005) Electronic structure and morphology of MgO submonolayers at the Ag(001) surface: an ab initio model study. Phys Rev B 71:155404
116. Ferrari AM, Casassa S, Pisani C, Altieri S, Rota A, Valeri S (2005) Polar and non-polar domain borders in MgO ultrathin films on Ag(001). Surf Sci 588:160–166
117. Benedetti S, Nilius N, Torelli P, Renaud G, Freund H-J, Valeri S (2011) Competition between polar and nonpolar growth of MgO thin films on Au(111). J Phys Chem C 115:23043
118. Pan Y, Benedetti S, Noguera C, Giordano L, Goniakowski J, Nilius N (2012) Compensating edge polarity: a means to alter the growth orientation of MgO nanostructures on Au(111). J Phys Chem C 116:11126
119. Nilius N, Benedetti S, Pan Y, Myrach P, Noguera C, Giordano L, Goniakowski J (2012) Electronic and electrostatic properties of polar oxide nanostructures: MgO(111) islands on Au(111). Phys Rev B 86:205410
120. Helveg S, Lauritsen JV, Lægsgaard E, Stensgaard I, Nørskov JK, Clausen BS, Topsøe H, Besenbacher F (2000) Atomic-scale structure of single-layer MoS_2 nanoclusters. Phys Rev Lett 84:951–954

121. Lauritsen JV, Bollinger MV, Lægsgaard E, Jacobsen KW, Nørskov JK, Clausen BS, Topsøe H, Besenbacher F (2004) Atomic-scale insight into structure and morphology changes of MoS_2 nanoclusters in hydrotreating catalysts. J Catal 221:510–522
122. Liu Y, Bhowmick S, Yakobson BI (2011) BN white graphene with "Colorful" edges: the energies and morphology. Nano Lett 11:3113–3116
123. Schweiger H, Raybaud P, Kresse G, Toulhoat H (2002) Shape and edge sites modifications of MoS_2 catalytic nanoparticles induced by working conditions: a theoretical study. J Catal 207:76–87
124. Valeri S, Altieri S, del Pennino U, di Bona A, Luches P, Rota A (2002) Scanning tunnelling microscopy of MgO ultrathin films on Ag(001). Phys Rev B 65:245410
125. Caffio M, Atrei A, Cortigiani B, Rovida G (2006) STM study of the nanostructures prepared by deposition of NiO on Ag(001) J Phys : Condens Matter 18:2379–2384
126. Steurer W, Allegretti F, Surnev S, Barcaro G, Sementa L, Negreiros F, Fortunelli A, Netzer FP (2011) Metamorphosis of ultrathin Ni oxide nanostructures on Ag(100). Phys Rev B 84:115446
127. Cabailh G, Lazzari R, Cruguel H, Jupille J, Savio L, Smerieri M, Orzelli A, Vattuone L, Rocca M (2011) Stoichiometry-dependent chemical activity of supported MgO(100) films. J Phys Chem A 115:7161–7168
128. Pal J, Smerieri M, Celasco E, Savio L, Vattuone L, Ferrando R, Tosoni S, Giordano L, Pacchioni G, Rocca M (2014) How growing conditions and interfacial oxygen affect the final morphology of MgO/Ag(100) films. J Phys Chem C 118:26091–26102

Chapter 8
CeO$_x$(111)/Cu(111) Thin Films as Model Catalyst Supports

Iva Matolínová, Josef Mysliveček and Vladimír Matolín

Abstract An important part of fundamental research in catalysis is based on theoretical and modelling foundations which are closely connected with studies of single-crystalline model catalyst surfaces. These so-called model catalysts are often prepared in the form of epitaxial thin films, and characterized using advanced material characterization techniques. This concept is providing the fundamental understanding and the knowledge base needed to tailor the design of new heterogeneous catalysts with improved catalytic properties. The present contribution is devoted to development of a model catalyst system of CeO$_2$ on a Cu(111) substrate.

8.1 Introduction

Complex model catalysts are developed using a rigorous surface-science approach in ultrahigh vacuum (UHV). Starting from metal single crystals as reference systems, novel oxide-based model systems were explored using epitaxial oxide thin films grown on suitable, mostly metallic substrates. Preparation of such model systems permitted to develop new preparation strategies for metal-doped and metal-loaded model systems at nanometre scale mimicking a large spectrum of industrially relevant catalysts. In-depth studies of reaction mechanisms and microscopic kinetics on model systems are mostly performed in ideal UHV conditions; however recent development of state of the art operando techniques permitted to extend the model studies closer to realistic reaction conditions, providing

I. Matolínová (✉) · J. Mysliveček · V. Matolín
Faculty of Mathematics and Physics, Charles University in Prague,
V Holešovičkách 2, Praha 8, 18000 Czech Republic
e-mail: iva.matolinova@mff.cuni.cz

J. Mysliveček
e-mail: josef.myslivecek@mff.cuni.cz

V. Matolín
e-mail: matolin@mbox.troja.mff.cuni.cz

an atomic scale understanding when aiming for improved activity, selectivity, and stability of the catalysts.

The present contribution is devoted to development of a model catalyst system of CeO_2 (ceria) on a Cu(111) substrate [1–7]. We propose ways how to experimentally characterize and control important parameters of the model catalyst—the coverage of the ceria layer, the influence of the Cu substrate, and the density of surface defects on ceria, particularly the density of step edges and the density and the ordering of the oxygen vacancies. The large spectrum of controlled parameters makes ceria on Cu(111) an interesting alternative to a more common model system ceria on Ru(0001) [8–10] that has served numerous catalysis studies, mainly as support for metal clusters.

Cerium oxide is well known for its ability to catalyse a number of chemical reactions. Interaction of ceria with various metals further promotes the catalytic activity. As an example, copper-ceria catalysts are highly active in CO oxidation [11–14], NO reduction [15, 16] and water-gas-shift (WGS) reaction [17]. It has been observed that small amounts of Cu can significantly increase catalytic properties of ceria [12, 14–16].

Adjustable morphology and degree of reduction represent desirable properties of model oxide substrates for heterogeneous catalysis [4]. The chemical reactivity of ceria on Cu(111) has been investigated for discontinuous layers (inverse model catalysts) [18–21], continuous layers [22, 23], and continuous layers activated with adsorbed metal clusters [24–27]. Many of the above cited works invoke the morphology of the ceria layers as an important factor determining the catalytic behaviour of the studied systems. The coverage of the metal substrate by ceria determines the presence or absence of activity of the model systems toward reactions like water-gas shift [18, 19] or oxidation of CO [21]. The density of atomic steps in the ceria layer determines the dispersion and the electron structure of ceria-supported metal clusters [28] because the atomic steps on ceria serve as preferential nucleation sites for many metals [28–31]. The catalytic behaviour of ceria layers is further determined by degree of reduction of ceria in the layer. Ceria reduction influences reaction pathways for most adsorbates [32, 33] and the accompanying surface oxygen vacancies may also serve as nucleation sites for metal clusters [28–31, 34].

As a very important parameter of a reducible oxide, the degree of reduction of ceria can be measured by the X-ray Photoelectron Spectroscopy (XPS), and, with a considerably higher sensitivity, by Resonant Photoelectron Spectroscopy (RPES) involving synchrotron activated photoemission of the ceria valence band [2]. Both techniques rely on the fact that while Ce^{4+} ions present in oxidized ceria feature an empty $4f$ state (configuration $4f^0$), in Ce^{3+} ions present in the reduced ceria the $4f$ band is occupied by one electron (configuration $4f^1$) [35, 36].

Partial reduction of ceria at the Cu/ceria interface was reported in [37–39]. Combined XPS and DFT (Density Functional Theory) studies presented in [39] showed that ultrathin Cu films (0.01–0.4 ML) deposited on a stoichiometric

CeO$_2$(111) film grown on the Ru(0001) substrate exhibit ceria reduction at the Cu/ceria interface. The Cu/ceria interaction was studied using the concept of so called inverse catalyst, i.e. ultrathin ceria islands on the Cu(111) substrate [1, 2, 18, 19]. By investigating the inverse catalysts prepared by depositing CeO$_2$ thin films on the Cu(111) single crystal surface it was found that after depositing more than 0.6 nm thick cerium oxide film Low Energy Electron Diffraction (LEED) indicated epitaxial growth of continuous CeO$_2$(111) on Cu(111) [2].

8.2   Stoichiometry of Cerium Oxide Measured by XPS and RPES

The main property of ceria in chemical reactions is the release and the uptake of lattice oxygen to/from the reaction atmosphere. Upon leaving the ceria lattice, the neutral O atom leaves behind two electrons that localize on two Ce atoms occupying the 4f state of Ce [37]. The changes in the occupation of the 4f state result in changes in both valence band spectra and XPS spectra of Ce 3d and Ce 4d core level states due to different final state effects. The stoichiometry of cerium oxide is usually determined by analyzing the Ce 3d XPS spectra. The spectra consist of three 3$d_{3/2}$–3$d_{5/2}$ spin-orbit-split doublets (f^0, f^1 and f^2) representing different 4f configurations in the photoemission final state and arising from 4f hybridization in both the initial and the final states [3]. The appearance of the high f^0 signal at binding energy (BE) of 917 eV, together with the f^1 peak (889 eV) which is less intense than the f^2 peak (882.5 eV), is evidence of the formation of CeO$_2$ oxide [40, 41]. Two spectral components that appear at binding energies BE = 880 and 885 eV correspond to the Ce^{3+} state. In order to estimate the Ce^{3+} state concentration the spectra must be decomposed to elementary doublets. However this is not a simple task because of the ambiguity of background subtraction (the energy interval of the Ce 3d spectrum is too large for correct Shirley background use), choice of elemental peak shape including asymmetry and insufficient spectrometer resolution in general [42]. A typical Ce 3d spectrum of cerium oxide, and the corresponding decomposition of the spectrum into the elementary doublets and the background are shown in Fig. 8.1. The spectra in Fig. 8.1 were obtained for 1.5 nm thick CeO$_2$(111) thin film grown epitaxially on the Cu(111) substrate [2, 4] at 523 K. The spectra were acquired at 300 K after preparation (upper curve) and annealing at 800 K (bottom curve). Vacuum annealing should lead to partial reduction of the film surface, however, by comparing both Ce 3d spectra any noticeable difference cannot be seen. The bottom spectrum is decomposed and one weak Ce^{3+} doublet at 885 eV is tentatively fitted. Detailed analysis reveals that fitting this type of spectra with Ce^{3+} features is not relevant because similarly good fit can be obtained for different Ce^{3+} intensities, even for zero intensity, showing that the Ce 3d spectrum analysis cannot be used in the case of weakly reduced ceria.

Fig. 8.1 XPS Ce
3d spectrum of as deposited
(523 K, *upper curve*) and
thermally annealed (800 K,
bottom curve) cerium oxide
thin film obtained using Al
Kα laboratory X-ray source
(1486 eV). Decomposition of
the Ce 3d spectrum yields
background contribution
(monotonously decreasing
curve), spectral peaks
belonging to Ce^{4+} doublets
(*thin lines*) and to Ce^{3+}
doublets (*thick lines*)
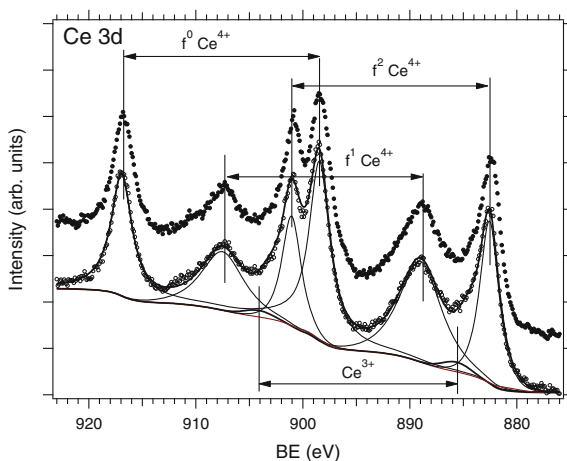
Employing tuneable soft X-ray synchrotron radiation, resonance effects in the Ce
4d–4f photoabsorption region can be used to distinguish between Ce^{3+} and Ce^{4+}
contributions with very high sensitivity using so called Resonance Photoelectron
Spectroscopy (RPES) [11, 43, 44], see Fig. 8.2. High sensitivity of RPES can be
demonstrated by comparing Figs. 8.1 and 8.2 showing the Ce 3d spectra (Fig. 8.1)
and the Ce 4d–4f resonance spectra (Fig. 8.2) of the same samples. An appearance
of the Ce^{3+} resonance at 1.4 eV for the annealed sample, which is distinguishably
higher than that of the as prepared sample, shows that RPES exhibits high sensi-
tivity. It permits to detect very low Ce^{3+} concentrations which cannot be determined
from the Ce 3d level analysis.

Fig. 8.2 Valence band
off-resonance (hν = 115 eV)
and on-resonance
(hν = 121.4 eV,
hν = 124.8 eV) spectra of as
prepared (523 K, *upper
curves*) and partially reduced
(800 K, *bottom curves*)
cerium oxide as in Fig. 8.1.
D stands for resonant intensity
enhancements obtained
by subtraction of the
off-resonance spectrum from
the on-resonance one.
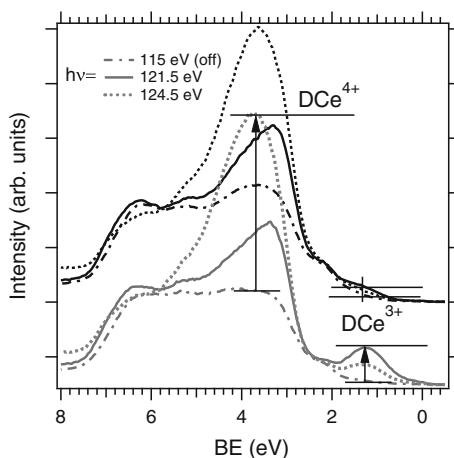
In RPES at the Ce 4*d*–4*f* absorption edge the photon energy is tuned in the proximity of the so called resonant energy corresponding to the energetic difference between the empty Ce 4*f* and filled Ce 4*d* levels. Photoelectrons from the Ce 4*f* level can be emitted by means of two mechanisms: (i) direct photoemission from the Ce 4*f* level, (ii) photoexcitation of a 4*d* electron to the 4*f* level and subsequent decay of the intermediate state followed by transfer of energy to a 4*f* electron. In consequence at the resonant energy we observe a resonant enhancement D of the Ce 4*f* photoemission [45]. The process of the resonant emission from 4f^1 systems, i.e. from Ce^{3+}, can be described as

$$4d^{10}4f^1 + h\nu \rightarrow 4d^94f^2 \rightarrow 4d^{10}4f^0 + e^-$$
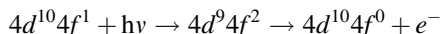
where hν and e^- stand for an incident photon and ejected photoelectron. In case of cerium oxide the maximum resonant emission from Ce^{3+} states is observed for photon energy between 121 and 122 eV as a photoemission peak rising at BE = 1.4 eV, see Fig. 8.2.

An example of series of valence band photoelectron spectra of CeO$_x$ in the Ce 4*d*–4*f* photoabsorption region for photon energies tuned from 115 to 130 eV is shown in Fig. 8.3 where variation of the Ce^{3+} resonance intensity with photon energy is highlighted.

The resonance process of the indirect emission from 4f^0 (Ce^{4+}) systems is

$$4d^{10}4f^0 + h\nu \rightarrow 4d^94f^1 \rightarrow 4d^{10}4f^0L + e^-,$$
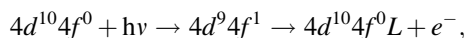
where *L* denotes a hole in the valence band. Variation of the Ce^{4+} resonance intensity with photon energy is highlighted in Fig. 8.3.

The density of 4*f* states can be obtained by subtracting the off-resonance spectrum (hν = 115 eV) from the on-resonance spectrum, i.e. by obtaining so called resonance enhancements DCe^{3+}, DCe^{4+}, see Fig. 8.2. Consequently the resonant enhancement ratio (RER) DCe^{3+}/DCe^{4+} can be used as a parameter sensitively indicating the degree of reduction of cerium oxide surface [2].

Fig. 8.3 Resonance Photoelectron Spectroscopy of the cerium 4*f* level: Ce^{3+} and Ce^{4+} resonant profiles were obtained for the photon energy interval 115–130 eV

CeO$_2$ film/Cu(111)
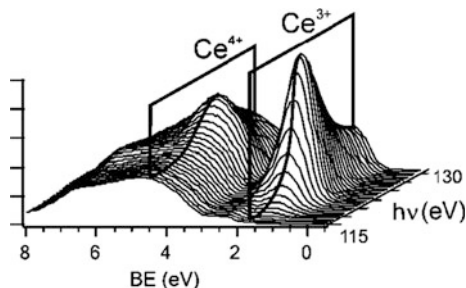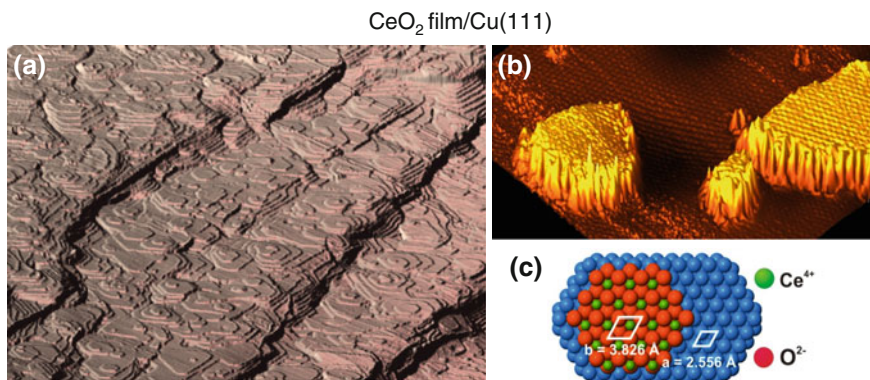
Fig. 8.4 3D rendered images of topography of CeO$_2$ thin films on Cu(111) obtained by Scanning Tunneling Microscopy. **a** 5 ML ceria on a vicinal Cu(111) surface. Apparent are ceria (111) terraces separated by monolayer-high step edges. **b** 2 ML ceria on the Cu(111) surface. The corrugation on the (111) terraces of ceria corresponds to the periodicity of the ceria crystal lattice. **c** Ball model of the epitaxy of CeO$_2$(111) on Cu(111)

8.3 Morphology of Cerium Oxide Measured by STM

Scanning Tunnelling Microscopy (STM) reveals terraces, atomic steps, surface atoms, and surface vacancies on a model catalyst surface which makes it an important characterisation tool. Local information of the morphology of the model catalysts combines favourably with the information on their chemical state obtained by photoelectron spectroscopy. Roughness and step structure of ceria on Cu(111) have been characterized in a study devoted to preparing thin continuous layers of ceria on Cu(111) [3, 4, 46]. STM images of a discontinuous ceria layer [18] and a continuous ceria layer on Cu(111) with adsorbed Pt clusters [25] have appeared in recently published reactivity studies. Figure 8.4 shows examples of STM observations: the Cu(111) single-crystal coated with the CeO$_2$(111) film exhibiting ceria islands composed of CeO$_2$(111) terraces separated by 1 ML (O–Ce–O trilayer)-high steps (0.315 nm high) (a), isolated ceria islands of a discontinuous film (b) and corresponding ball model of ceria on Cu(111) (c).

8.4 Growth of CeO$_2$(111) Continuous Films on the Cu(111) Substrate

A basic approach to prepare the epitaxial ultra-thin CeO$_2$(111) films on the Cu(111) substrate is deposition of Ce metal on clean Cu(111) substrate kept at the temperature of 523 K in a background pressure of 5×10^{-5} Pa of O$_2$ [2]. This approach yields continuous films of ceria as evidenced by the LEED diffraction patterns

showing no contribution of Cu(111) spots for the films with equivalent thickness above 2.5 ML as can be seen in Fig. 8.5b, c. RPES measurements at the Ce $4d \rightarrow 4f$ resonance confirm a good CeO$_2$ stoichiometry with 5 ML continuous film having predominantly a Ce^{4+} character indicating a negligible concentration of Ce^{3+} surface defects (see Fig. 8.2, upper spectrum). Discontinuous CeO$_2$(111) layers as on Fig. 8.5 a exhibit a higher concentration of Ce^{3+} (RPES spectra not shown) and defects than continuous layers grown at the same conditions.

The LEED diffraction pattern presented in Fig. 8.5 can be interpreted as indicating formation of a CeO$_2$(111)/Cu(111) epitaxial overlayer with the morphological relationship

$$2a_{CeO_2} = 3a_{Cu}; CeO_2(111)||Cu(111); CeO_2[0\,1]||Cu[0\,1]$$

where a is the surface lattice parameter. The bulk lattice parameter of copper is 0.360 nm, determining the length of the [10-1] lattice vector in the Cu(111) plane $a_{Cu} = 0.255$ nm. The bulk lattice parameter of cubic cerium dioxide is 0.54 nm which corresponds to a [10-1] lattice vector length in the CeO$_2$(111) plane of $a_{CeO2} = 0.382$ nm. Thus the expected a_{CeO2}/a_{Cu} ratio is 1.50 indicating very good lattice matching with negligible strain (<0.6 %) for the observed (1.5 × 1.5) commensurate superstructure. Epitaxial growth and practically negligible lattice mismatch made the preparation of very thin continuous CeO$_2$ film using reactive vapour deposition feasible and it opened a new promising field of model studies of cerium oxide surfaces. The reactive evaporation of Ce on Cu(111) provides films of superior quality compared to other approaches as e.g. proposed in [20] where cerium oxide on Cu(111) was grown by depositing 10 ML of Ce at room temperature. Freshly deposited cerium was oxidized at room temperature by oxygen exposure resulting in Ce$_2$O$_3$, cerium trioxide. Annealing in oxygen to 930 K led to the formation of discontinuous Ce^{4+} oxide layers, however Ce $3d$ X-ray photoelectron spectrum still showed a significant contribution of the Ce^{3+} species.
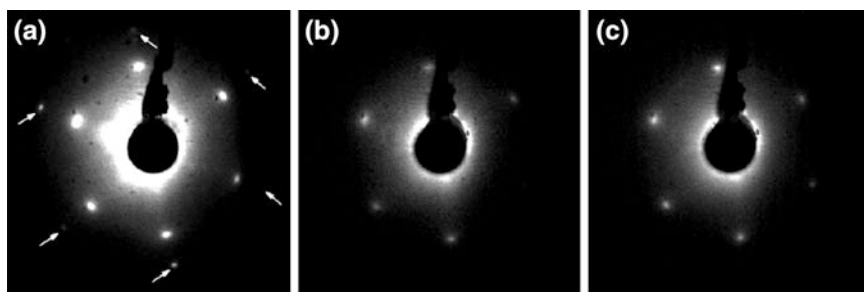
Fig. 8.5 LEED patterns taken at the electron energy of 98 eV for various coverage of CeO$_2$ on Cu (111): **a** discontinuous film; **b** 2.5 ML; **c** 5 ML. Weak Cu(111) (1 × 1) spots are marked by the *arrows* [2]

Suitability of the $CeO_2(111)/Cu(111)$ very thin films for mimicking the cerium oxide single-crystal surface depends on the substrate—oxide interaction that can strongly influence the chemical properties of the ceria/Cu systems as demonstrated in many studies of Cu—ceria inverse catalysts. DFT + U calculations of systems consisting of Cu atoms supported by stoichiometric and reduced $CeO_2(111)$ surfaces show that Ce^{3+} species are always present underneath the Cu particles supported by stoichiometric and reduced ceria (111) surfaces [47]. The calculations predict a substantial charge transfer across the coherent $Cu(111)/CeO_2$ interface leading to the full reduction of the first ceria monolayer underneath the supported Cu particles. Therefore the emerging question concerning the physicochemical properties of the $CeO_2(111)/Cu(111)$ thin films was related to the ceria—copper interaction and the extent to which this interaction determines the properties of ceria/Cu(111). Scanning Tunnelling Microscopy and ab initio calculations allowed to determine the unusual properties of the first ceria monolayer in contact with the Cu(111) substrate showing finite size effects when the limiting thickness of the oxide monolayer and the proximity of the metal substrate cause significant rearrangement of charges and oxygen vacancies compared to thicker and/or bulk ceria [3], see Fig. 8.6.

The finite size effects in the 1st ML of ceria on Cu(111) cause a compressive strain with respect to bulk ceria and (2×2) surface reconstruction indicating the presence of oxygen vacancies in the ceria—copper interface (Fig. 8.6) which is confirmed by evaluating the stability of the vacancies and simulating STM images in the calculation. The extraordinary behaviour of oxygen vacancies is a consequence of proximity of the metal substrate when all Ce atoms in 1st ML ceria are Ce^{3+}. Electrons left after creation of oxygen vacancies must then localize in the Cu substrate. Both Ce^{3+} and oxygen vacancies relieve the intrinsic compressive strain in ultrathin ceria. Metal—oxide interactions determining the properties of oxygen vacancies in ultrathin ceria influence not more than 1 ML in the oxide. Indeed,

Fig. 8.6 STM image showing (2×2) atom pattern in the 1st ML ceria on Cu (111). (2×2) reconstruction on ceria surface is indicative of subsurface oxygen vacancies **a**. Unreconstructed 2nd ML ceria surface **b**. The (1×1) and (2×2) unit cells are highlighted *white*. Image width is 2 nm. Sample bias and tunnelling current: **a** 1 V, 0.3 nA; **b** 2.3 V, 0.15 nA
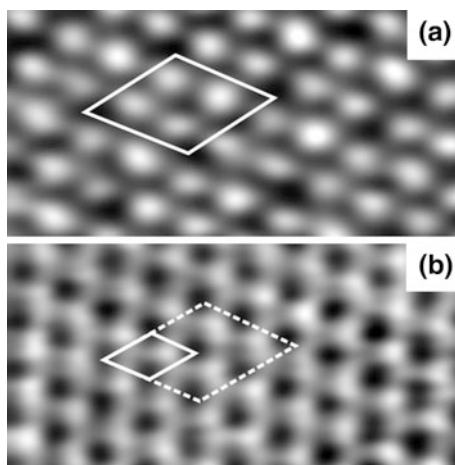
already 2nd ML ceria shows a bulk like termination in experiment and a standard behaviour of oxygen vacancies in the calculation. The distinct physicochemical properties of the first ceria monolayer likely play a significant role in the enhanced reactivity of inverse model ceria/Cu catalysts where 1st ML ceria represents the most extended surface phase.

8.5 Adjusting the Morphology of CeO$_2$(111) Films on Cu(111)

For obtaining control over the morphological parameters of the ceria layers on Cu (111), mainly the coverage of the Cu(111) substrate by the oxide, and the density of monolayer-high steps on the surface of the oxide, a knowledge of the growth mechanisms of ceria layers on Cu(111) becomes necessary. Growth mechanisms of ceria on Cu(111) have been identified in [4]. Ceria forms an incomplete oxide interfacial layer. On top of the interfacial layer, ceria growth proceeds by growing three-dimensional ceria pyramids composed of stacks of monolayer-high islands. It was shown that the coverage, the number of open monolayers, the step density and degree of reduction of ceria thin films on Cu(111) can be controlled by changing parameters of the deposition and by annealing of the deposited films.

The shape and the density of the interfacial layer islands are temperature-dependent, indicating that both are determined by the diffusion rate of cerium and/or oxygen species on the oxidized Cu surface. At lower temperature of 573 K, the interfacial layer islands have open dendrite-like shapes and nucleate with higher density than the interfacial layer islands at 723 K that are compact with step edges oriented in high-symmetry substrate directions [4]. This corresponds to a classical picture of the diffusion-limited nucleation [48]. Figure 8.7 shows STM images of 5 ML thick CeO$_2$(111)/Cu(111) prepared by reactive evaporation of Ce in 5×10^{-5} Pa oxygen at 423, 523, 723, and 850 K.

5 ML thick ceria films grown at substrate temperatures of 423 and 523 K cover the whole substrate; however at 423 K the layer is composed of very small ceria islands with diameters below 10 nm. At 523 K larger islands with diameters 10–15 nm are formed. The height profile of the layer shows that 3–4 ceria monolayers are open. After deposition at 723 K, ceria does not cover the whole substrate. As a practical, well defined and easy to prepare continuous ceria layer, the 5 ML ceria deposited at 523 K on Cu(111) has since publication in [2] served as a model ceria substrate in a number of model catalytic studies [3, 4, 22–27].

At higher substrate temperature, ceria layers on Cu(111) tend to be discontinuous and maximize the number of open ceria monolayers. However, with decreasing the substrate temperature, the amount of ceria needed to prepare a continuous film decreases, together with the number of open ceria monolayers in the film. This fact has been used in recipes for continuous ceria films on Cu(111) [46] and Ru(0001) [29] which proposed starting ceria deposition at low substrate
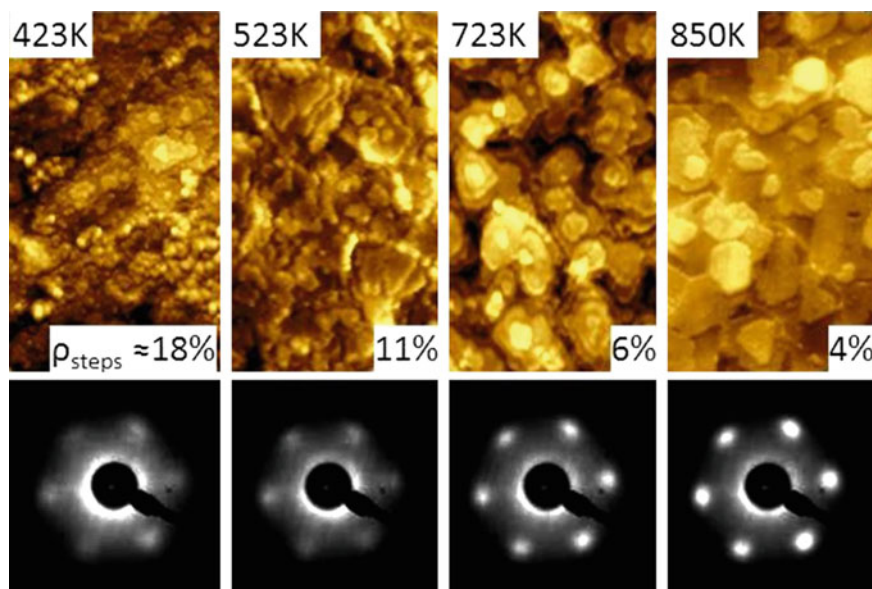
Fig. 8.7 STM micrographs, LEED diffraction pattern, and density of surface steps for stoichiometric 5 ML thick ceria layers on the Cu(111) surface. Change of the substrate temperature during preparation allows changing the step density ρ_{steps} on the surface from 4 to 18 %. Growth at constant temperature at 423 and 523 K, growth at gradient temperature from RT at 723 and 850 K

temperature (100 K) and increasing the substrate temperature in later stages of growth. Adopting a less stringent condition for the growth of ceria at gradient substrate temperature starting the deposition at room temperature (RT) and increasing the substrate temperature from room temperature to 723 K after depositing 1 ML ceria, the growth resulted in the morphology of ceria films shown in Fig. 8.7. The obtained high degree of surface ordering and 2–3 open ceria monolayers represent a morphology that is resembling ideal layer-by-layer growth. A further improvement of the ordering of the ceria layer can be obtained by growing the ceria layer at gradient temperature from RT to 850 K (Fig. 8.7). Ceria growth at gradient substrate temperature thus represents a way to gain control over the coverage of the ceria films on Cu(111).

Different substrate temperatures during growth of ceria layers result in different density of monolayer-high surface steps on ceria. Quantification of the coverage of the step sites on the ceria surface reveals that using the above mentioned approach the step density of stoichiometric and fully oxidized ceria layers can be adjusted between approximately 4 and 18 %, representing a significant change by the factor of 4 between preparations at substrate temperatures 423 and 850 K (Fig. 8.7) [4].

Control of degree of ceria reduction is, beside adjustment of the film morphology, an attractive possibility of tailoring model catalyst properties because

Fig. 8.8 Degree of reduction of the ceria layers prepared at 423 K (*square*), 523 K (*rhombus*), and 723 K (*circle*) during subsequent annealing in vacuum to higher temperatures. The onset of reduction of the layers is marked with *arrows* and coincides with the maximum temperature reached during the preparation of the layers
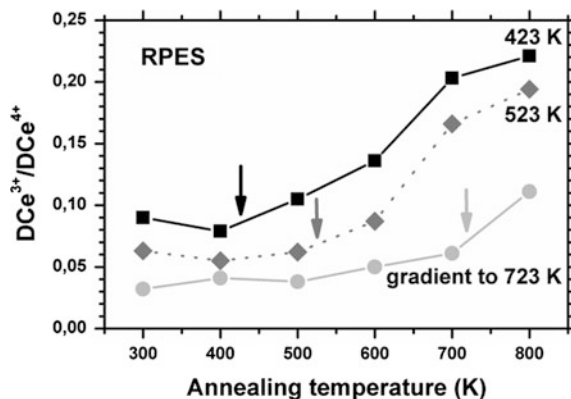
Ce^{3+} ions are considered catalytically active sites in ceria. Most commonly, Ce^{3+} ions are referred to as accompanying bulk [35, 38] and surface [49, 50] oxygen vacancies. Reduction of ceria surface can be obtained by vacuum annealing, and therefore by measuring an increase of amount of surface Ce^{3+} ions the temperature stability of layers can be determined. In Fig. 8.8 an evaluation of thermal stability of the samples shown in Fig. 8.7 is presented as a variation of resonance enhancement ratio (cf. Fig. 8.2) as a function of the annealing temperature. It can be clearly seen that changes in ceria stoichiometry are most pronounced with layers prepared at lower temperatures. The layer grown at variable temperature up to 723 K (Fig. 8.7) exhibits the highest stability which can be correlated with the highest layer ordering and absolutely the lowest concentration of defects [4]. For oriented and stoichiometric thin films of ceria on Cu(111) prepared at temperatures of 423 and 523 K both the morphology and the surface reduction of these layers readily change with increasing temperature. This must be accounted for in considering temperature-programmed experiments with ceria on Cu(111).

8.6 Adjusting the Stoichiometry of CeO$_2$(111) Films on Cu(111)

For obtaining a broader range of reduction of ceria layers on Cu(111) than can be obtained by annealing in vacuum, an alternative method to prepare well-defined reduced ceria has been proposed [5–7]. The method is based on physical vapour deposition of metallic Ce onto a stoichiometric CeO$_2$(111) film, i.e. on using metallic Ce as a reducing species. We demonstrated that upon reactive interaction of the two components according to

$$3CeO_2 + Ce \rightarrow (900\,K)2Ce_2O_3$$
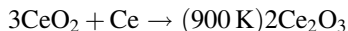
it is possible to obtain highly ordered films of Ce_2O_3 on Cu(111) [5, 6] as well as on the Ru(0001) [7] substrate.

The morphology of the ceria film undergoing reaction with metallic Ce is shown in Fig. 8.9. As a starting point, an ordered 4 ML thick CeO_2 buffer layer (a continuous layer of $CeO_2(111)$ on Cu(111)) was prepared at 523 K. Upon deposition of metallic Ce, the surface becomes disordered (see Fig. 8.9b). A much improved ordering, however, is re-established after annealing of the buffer with the Ce deposit to 900 K for 30 min in vacuum. In Fig. 8.9c the resulting morphology of a flat film with an average terrace width of 30 nm is shown.

On the newly formed surface, STM reveals a characteristic surface reconstruction shown in the inset of Fig. 8.9c. The unit cell of the reconstruction is 1.5 nm, i.e., about 4 times the size of the unit cell of the unreconstructed $CeO_2(111)$ (1×1) surface. The (4×4) reconstruction of ceria after reaction with metallic Ce at 900 K is confirmed by Low Energy Electron Diffraction in Fig. 8.9d. For comparison, a LEED pattern of the ordered CeO_2 buffer layer is shown in Fig. 8.9d, too.

The stoichiometry of the films was analysed by XPS before and after the reaction. The Ce $3d$ spectra of the ordered $CeO_2(111)$ buffer reveal pure Ce^{4+} spectrum (as in CeO_2), while the film after reaction with Ce (Fig. 8.10) reveals pure Ce^{3+} spectrum (as in Ce_2O_3). Measuring the XPS at different emission angles 20° and 60° off normal reveals no change in the stoichiometry of the layers with the emission angle, which indicates that both before and after reaction the films are bulk-terminated CeO_2 and Ce_2O_3, respectively. Transformation of CeO_2 into Ce_2O_3 is accompanied by a shift of O $1s$ level from 529.25 eV to higher binding energy 530.20 eV. Also the extremely sensitive RPES reveals no Ce^{3+} contribution in the
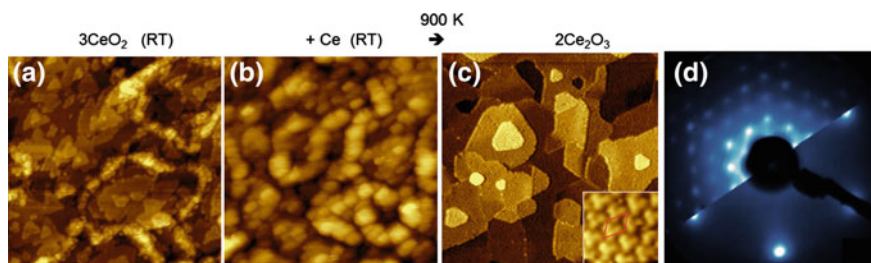
Fig. 8.9 STM images of the interfacial reaction between Ce and the CeO_2 buffer layer: **a** the ordered CeO_2 buffer, **b** the disordered surface upon Ce deposition, **c** the ordered layer upon annealing in vacuum at 900 K. *Inset* a high-resolution image and surface unit cell (*red rhombus*) of the reacted layer. Images **a–c** are in scale: image width (**a**, **b**) 60 nm, **c** 120 nm, (*Inset*) 6 nm. **d** LEED patterns of the reaction between Ce and the CeO_2 buffer layer: (upper half of the image) reacted layer, (bottom half of the image) starting CeO_2 buffer. Electron energy 55 eV
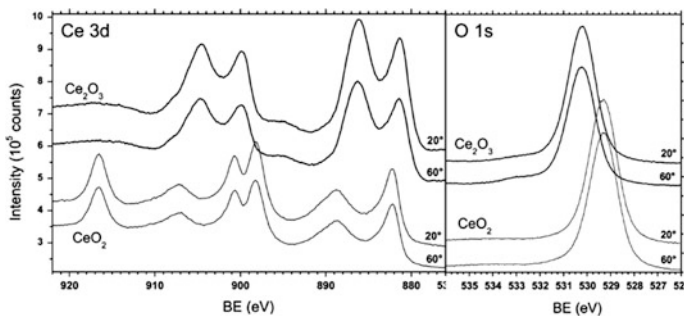
Fig. 8.10 Photoelectron spectroscopy of cerium oxide (Ce 3d) and lattice oxygen ions (O 1s) after the interfacial reaction between Ce and the CeO$_2$ buffer layer (*black lines*) and the starting CeO$_2$ buffer (*grey lines*)

CeO$_2$ buffer layer and no Ce^{4+} contribution (at 3.56 eV) in the Ce$_2$O$_3$ layer after reaction [5].

Reduction of ceria by metallic Ce yields highly ordered layer of cubic bixbyite c-Ce$_2$O$_3$(111) [5] with the surface structure corresponding to bulk-terminated c-Ce$_2$O$_3$(111), see Fig. 8.9c, d. Ce$_2$O$_3$ contains ordered O vacancies in the concentration of 25 % compared to CeO$_2$. The vacancies occupy O positions of the fluorite lattice of CeO$_2$ and group together in objects that can be considered as vacancy clusters, each consisting of four oxygen vacancies [5]. Within vacancy clusters the O vacancies are next-neighbour coordinated in an arrangement not observed in less reduced ceria. The c-Ce$_2$O$_3$(111) film represents a unique model experimental system for highly reduced ceria surfaces. It provides an atomically well-defined surface exposing exclusively Ce^{3+} ions and a high density of oxygen vacancies with a precisely defined environment.

Upon partial reduction of CeO$_2$(111) by metallic Ce, LEED investigations reveal intermediate surface reconstructions which can be characterised as ($\sqrt{7} \times \sqrt{7}$) R19.1° and (3 × 3) [6]. The observed reconstructions represent ordered phases of reduced ceria with stoichiometry between CeO$_2$ and Ce$_2$O$_3$. The morphology and the structural characteristics of these phases, together with CeO$_2$ and Ce$_2$O$_3$ are shown in Fig. 8.11. RPES analysis showing degree of surface reduction is presented in Fig. 8.12. Extremely sensitive RPES reveals no Ce^{3+} contribution in the CeO$_2$ buffer and no Ce^{4+} contribution in the c-Ce$_2$O$_3$ layer after the interfacial reaction. Photoemission data analysis of the Ce 3d core-level spectra gives relative concentration of Ce^{3+} of 0, 0.35, 0.55 and 1 for all reconstructions shown in Fig. 8.11 (values 0 and 1 correspond to limiting stoichiometry of CeO$_2$ and Ce$_2$O$_3$). The ($\sqrt{7} \times \sqrt{7}$) R19.1° and (3 × 3) reconstructions are identified as surface terminations of ordered bulk phases of reduced ceria, the t-Ce$_7$O$_{12}$ or CeO$_{1.71}$ phase for the ($\sqrt{7} \times \sqrt{7}$) R19.1° reconstruction, and the CeO$_{1.67}$ phase for the (3 × 3) reconstruction. These bulk reduced phases representing distinct regular arrangements of oxygen vacancies in cubic ceria are established in the three or more topmost monolayers of the ceria films reduced by Ce.
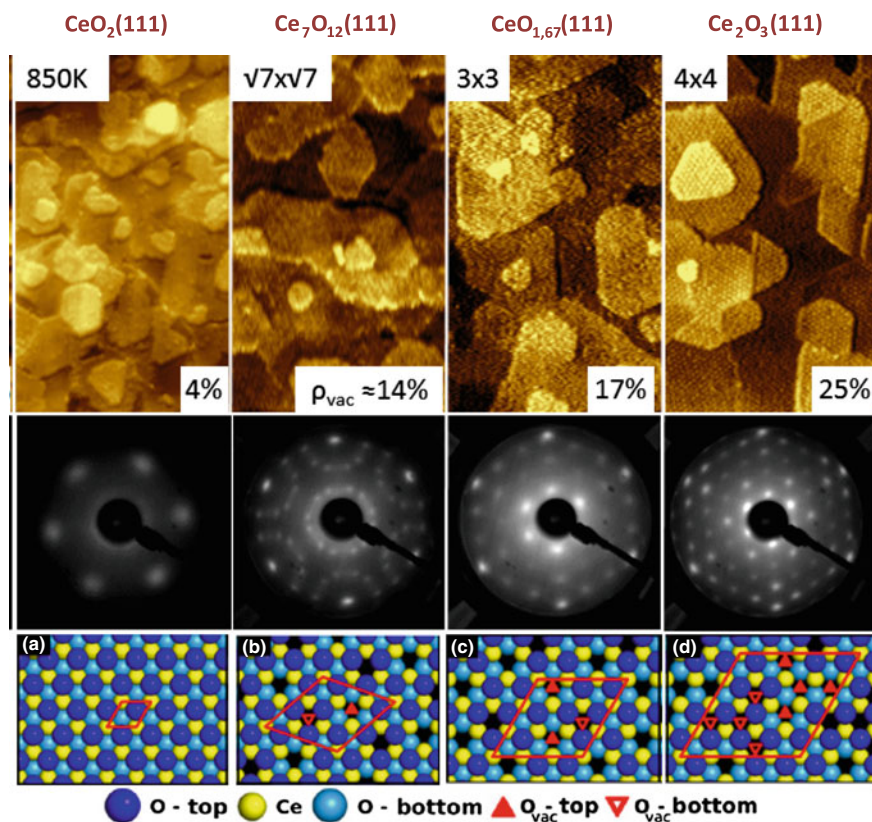
Fig. 8.11 STM micrographs, LEED patterns and corresponding models illustrating the structure and morphology of cerium oxide films during reduction via interfacial reaction of metallic Ce with CeO$_2$ buffer layer: **a** as-prepared fully oxidized buffer layer of CeO$_2$. **b** ceria layer with ($\sqrt{7} \times \sqrt{7}$) R19.1° surface reconstruction, **c** ceria layer with (3 × 3) surface reconstruction, **d** c-Ce$_2$O$_3$ layer with (4 × 4) surface reconstruction. Reduction of ceria with metallic Ce allows to adjust the concentration of oxygen vacancies ρ_{vac} between 0 and 25 %

By combining ceria reduction by Ce and oxidation by annealing in oxygen it was shown that both processes are fully reversible [6]. Annealing of the reduced ceria layers in oxygen preserves the morphology of the reduced ceria layer; in particular, the low step density of the Ce$_2$O$_3$ thin films shown in Fig. 8.13a is preserved upon oxidation to CeO$_2$ (Fig. 8.13b). CeO$_2$ layers obtained by oxidation of Ce$_2$O$_3$ exhibit the smallest step density and the highest degree of oxidation from the above described model systems of CeO$_2$/Cu(111). However, the contraction of the lattice constant of ceria upon oxidation causes cracking of the ceria layer revealing up to 2 % of the Cu substrate on reoxidized Ce$_2$O$_3$/Cu(111) samples (Fig. 8.13c). Still, the highly ordered ceria surface represents a suitable substrate for STM experiments that can be further modified e.g. by homoepitaxy and high-temperature annealing of
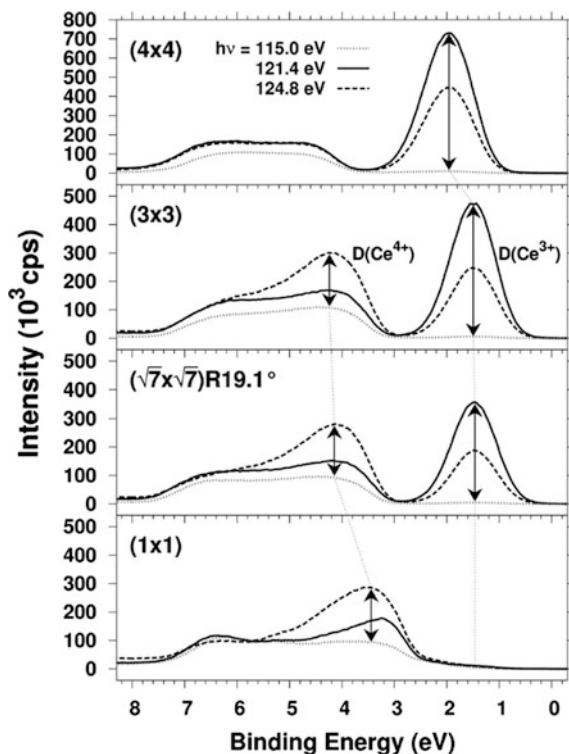
Fig. 8.12 RPES spectra of the valence band of stoichiometric ceria (*bottom curves*) and the ordered phases of reduced ceria grown on Cu(111). The spectra are measured off-resonance (photon energy 115 eV, *dotted lines*), in the Ce^{4+} resonance (124.8 eV, *dashed lines*), and in the Ce^{3+} resonance (121.4 eV, *full lines*). The resonance enhancements DCe^{3+} and DCe^{4+} are indicated by *arrows*
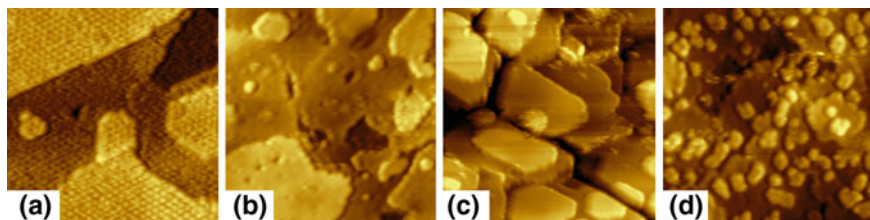
Fig. 8.13 STM micrographs of oxidation of Ce$_2$O$_3$ layer on Cu(111): **a** the starting Ce$_2$O$_3$ layer. **b**, **c** The morphology upon reoxidation. **c** Reoxidation causes cracking of the ceria layer revealing up to 2 % of the Cu substrate. **d** Upon homoepitaxy of 0.3 ML ceria on sample (**b**) at RT and annealing in oxygen at 800 K. Unlike the procedures in Figs. 8.8 and 8.9 resulting surface in (**d**) exhibits both the high density of surface steps and high temperature stability. Image width (**a**, **b**, **d**) 45 nm, (**c**) 90 nm

CeO_2 for increasing the step density on the ceria surface without destabilizing the surface thermally (Figs. 8.7, 8.8, 8.13d, cf.).

Practically, ceria layers reduced by the interfacial reaction with metallic Ce represent a realization of the ideal scenario of reduction and reoxidation of ceria by removing/adding oxygen from/to the fluorite CeO_2 lattice without largely modifying the structure of the Ce sub-lattice [35]. This, accompanied by the preference of oxygen vacancies to arrange in regular structures, makes the ceria layers reduced by the interfacial reaction with metallic Ce a unique experimental playground for studying the influence of the oxygen vacancy concentration and coordination on the chemical properties of ceria.

References

1. Matolin V, Sedlacek L, Matolinova I, Sutara F, Skala T, Smid B, Libra J, Nehasil V, Prince KC (2008) Photoemission spectroscopy study of Cu/CeO_2 systems: Cu/CeO_2 nanosized catalyst and $CeO_2(111)/Cu(111)$ inverse model catalyst. J Phys Chem C 112:3751–3758
2. Sutara F, Cabala M, Sedlacek L, Skala T, Skoda M, Matolin V, Prince KC, Chab V (2008) Epitaxial growth of continuous $CeO_2(111)$ ultra-thin films on Cu(111). Thin Solid Films 516:6120–6124
3. Szabova L, Stetsovych O, Dvorak F, Camellone MF, Fabris S, Myslivecek J, Matolin V (2012) Distinct physicochemical properties of the first ceria monolayer on Cu(111). J Phys Chem C 116:6677–6684
4. Dvorak F, Stetsovych O, Steger M, Cherradi E, Matolinova I, Tsud N, Skoda M, Skala T, Myslivecek J, Matolin V (2011) Adjusting morphology and surface reduction of $CeO_2(111)$ thin films on Cu(111). J Phys Chem C 115:7496–7503
5. Stetsovych V, Pagliuca F, Dvorak F, Duchon T, Vorokhta M, Aulicka M, Lachnitt J, Schernich S, Matolinova I, Veltruska K, Skala T, Mazur D, Myslivecek J, Libuda J, Matolin V (2013) Epitaxial cubic Ce_2O_3 films via $Ce–CeO_2$ interfacial reaction. J Phys Chem Lett 4:866–871
6. Duchon T, Dvorak F, Aulicka M, Stetsovych V, Vorokhta M, Mazur D, Veltruska K, Skala T, Myslivecek J, Matolinova I, Matolin V (2014) Ordered phases of reduced ceria as epitaxial films on Cu(111). J Phys Chem C 118:357–365
7. Duchon T, Dvorak F, Aulicka M, Stetsovych V, Vorokhta M, Mazur D, Veltruska K, Skala T, Myslivecek J, Matolinova I, Matolin V (2014) Comment on "ordered phases of reduced ceria as epitaxial films on Cu(111)". J Phys Chem C 118:5058–5059
8. Mullins D, Radulovic P, Overbury S (1999) Ordered cerium oxide thin films grown on Ru (0001) and Ni(111). Surf Sci 429:186–198
9. Lu J-L, Gao H-J, Shaikhutdinov S, Freund H-J (2006) Morphology and defect structure of the $CeO_2(111)$ films grown on Ru(0001) as studied by scanning tunneling microscopy. Surf Sci 600:5004–5010
10. Kaemena B, Senanayake SD, Meyer A, Sadowski JT, Falta J, Flege JI (2013) Growth and morphology of ceria on ruthenium (0001). J Phys Chem C 117:221–232
11. Liu W, Flytzani-Stephanopoulos M (1995) Total oxidation of carbon monoxide and methane over transition metal fluorite oxide composite catalysts: I. Catalyst composition and activity. J Catal 153:304–316
12. Liu W, Flytzani-Stephanopoulos M (1996) Transition metal-promoted oxidation catalysis by fluorite oxides: a study of CO oxidation over $Cu-CeO_2$. Chem Eng J Biochem Eng J 64: 283–294

13. Liu W, Flytzani-Stephanopoulos M (1995) Total oxidation of carbon-monoxide and methane over transition metal fluorite oxide composite catalysts: II. Catalyst characterization and reaction-kinetics. J Catal 153:317–332
14. Jung CR, Han J, Nam SW, Lim T-H, Hong S-A, Lee H-I (2004) Selective oxidation of CO over CuO–CeO$_2$ catalyst: effect of calcination temperature. Catal Today 93–95:183–190
15. Wen B, He M (2002) Study of the Cu–Ce synergism for NO reduction with CO in the presence of O$_2$, H$_2$O and SO$_2$ in FCC operation. Appl Catal B 37:75–82
16. Bera P, Aruna ST, Patil KC, Hegde MS (1999) Studies on Cu/CeO$_2$: a new NO reduction catalyst. J Catal 186:36–44
17. Djinovic P, Batista P, Pintar A (2008) Calcination temperature and CuO loading dependence on CuO–CeO$_2$ catalyst activity for water-gas shift reaction. Appl Catal A 347:23–33
18. Rodriguez JA, Graciani J, Evans J, Park JB, Yang F, Stacchiola D, Senanayake SD, Ma S, Pérez M, Liu P, Sanz JF, Hrbek J (2009) Water-gas shift reaction on a highly active inverse CeO$_x$/Cu(111) catalyst: unique role of ceria nanoparticles. J Angew Chem Int Ed 48:8047–8050
19. Rodriguez JA, Hrbek J (2010) Inverse oxide/metal catalysts: a versatile approach for activity tests and mechanistic studies. Surf Sci 604:241–244
20. Siokou A, Nix RM (1999) Interaction of methanol with well-defined ceria surfaces: reflection/absorption infrared spectroscopy, X-ray photoelectron spectroscopy, and temperature-programmed desorption study. J Phys Chem B 103:6984–6997
21. Wrobel R, Suchorski Y, Becker S, Weiss H (2008) Cerium oxide layers on the Cu(111) surface: substrate-mediated redox properties. Surf Sci 602:436–442
22. Matolin V, Libra J, Skoda M, Tsud N, Prince KC, Skala T (2009) Methanol adsorption on a CeO$_2$(111)/Cu(111) thin film model catalyst. Surf Sci 603:1087–1092
23. Staudt T, Lykhach Y, Tsud N, Skala T, Prince KC, Matolin V, Libuda J (2010) Ceria reoxidation by CO$_2$: a model study. J Catal 275:181–185
24. Skoda M, Cabala M, Matolinova I, Prince KC, Skala T, Sutara F, Veltruska K, Matolin V (2009) Interaction of Au with CeO2(111): a photoemission study. J Chem Phys 130:034703
25. Lykhach Y, Staudt T, Lorenz MPA, Streber R, Bayer A, Steinruck H-P, Libuda J (2010) Microscopic insights into methane activation and related processes on Pt/Ceria model catalysts. ChemPhysChem 11:1496–1504
26. Skala T, Sutara F, Skoda M, Prince KC, Matolin V (2009) Palladium interaction with CeO$_2$, Sn–Ce–O and Ga–Ce–O layers. J Phys-Condens Matter 21:055005
27. Vayssilov GN, Lykhach Y, Migani A, Staudt T, Petrova GP, Tsud N, Skala T, Bruix A, Illas F, Prince KC, Matolin V, Neyman KM, Libuda J (2011) Support nanostructure boosts oxygen transfer to catalytically active platinum nanoparticles. Nat Mater 10:310–315
28. Weststrate CJ, Westerstroem R, Lundgren E, Mikkelsen A, Andersen JN (2009) A influence of oxygen vacancies on the properties of ceria-supported gold. J Phys Chem C 113:724–728
29. Baron M, Bondarchuk O, Stacchiola D, Shaikhutdinov S, Freund H-J (2009) Interaction of gold with cerium oxide supports: CeO$_2$(111) thin films vs CeO$_x$ nanoparticles. J Phys Chem C 113:6042–6049
30. Senanayake SD, Zhou J, Baddorf AP, Mullins DR (2007) The reaction of carbon monoxide with palladium supported on cerium oxide thin films. Surf Sci 601:3215–3223
31. Lu J-L, Gao H-J, Shaikhutdinov S, Freund H-J (2007) Gold supported on well-ordered ceria films: nucleation, growth and morphology in CO oxidation reaction. Catal Lett 114:8–16
32. Mullins DR, Robbins MD, Zhou J (2006) Adsorption and reaction of methanol on thin-film cerium oxide. Surf Sci 600:1547–1558
33. Gordon WO, Xu Y, Mullins DR, Overbury SH (2009) Temperature evolution of structure and bonding of formic acid and formate on fully oxidized and highly reduced CeO$_2$(111). Phys Chem Chem Phys 11:11171–11183
34. Wilson EL, Grau-Crespo R, Pang CL, Cabailh G, Chen Q, Purton JA, Catlow CRA, Brown WA, de Leeuw NH, Thornton G (2008) Redox behavior of the model catalyst Pd/CeO$_{2−x}$/Pt(111). J Phys Chem C 112:10918–10922

35. Skorodumova NV, Simak SI, Lundqvist BI, Abrikosov IA, Johansson B (2002) Quantum origin of the oxygen storage capability of ceria. Phys Rev Lett 89:166601
36. Fabris S, de Gironcoli S, Baroni S, Vicario G, Balducci G (2005) Taming multiple valency with density functionals: a case study of defective ceria. Phys Rev B 71:041102
37. Barrio L, Estrella M, Zhou G, Wen W, Henson JH, Hungria AB, Hornes A, Fernandez-Garcia M, Martínez-Arias A, Rodríguez JA (2010) Unraveling the active site in copper-ceria systems for the water-gas shift reaction. In situ characterization of an inverse powder CeO2−x/CuO–Cu catalyst. J Phys Chem C 114:3580–3587
38. Wang X, Rodríguez JA, Hanson JC, Gamarra D, Martínez-Arias A, Fernández-García M (2006) In situ studies of the active sites for the water gas shift reaction over Cu–CeO$_2$ catalysts: complex interaction between metallic copper and oxygen vacancies of ceria. J Phys Chem B 110:428–434
39. Szabova L, Skala T, Matolinova I, Fabris S, Camellonec MF, Matolin V (2013) Copper-ceria interaction: a combined photoemission and DFT study. Appl Surf Sci 267:12–16
40. Fujimori A (1983) Mixed-valent ground state of CeO$_2$. Phys Rev B 28:2281–2283
41. Mullins DR, Overbury SH, Huntley DR (1998) Electron spectroscopy of single crystal and polycrystalline cerium oxide surfaces. Surf Sci 409:307–319
42. Skala T, Sutara F, Prince KC, Matolin V (2009) Cerium oxide stoichiometry alteration via Sn deposition: influence of temperature. J Electron Spectrosc Relat Phenom 169:20–25
43. Matsumoto M, Soda K, Ichikawa K, Tanaka S, Taguchi Y, Jouda K, Aita O, Tezuka Y, Shin S (1994) Resonant photoemission study of CeO$_2$. Phys Rev B 50:11340–11346
44. Kucherenko Y, Molodtsov SL, Herber M, Laubschat C (2002) 4f-derived electronic structure at the surface and in the bulk of alpha-Ce metal. Phys Rev B 66:155116
45. Hüfner S (2003) Photoelectron spectroscopy, principles and applications. Springer, Berlin
46. Staudt T, Lykhach Y, Hammer L, Schneider MA, Matolin V, Libuda J (2009) A route to continuous ultra-thin cerium oxide films on Cu(111). Surf Sci 603:3382–3388
47. Szabova L, Camellone MF, Huang M, Matolin V, Fabris S (2010) Thermodynamic, electronic and structural properties of Cu/CeO$_2$ surfaces and interfaces from first-principles DFT+U calculations. J Chem Phys 133:234705
48. Michely T, Hohage M, Bott M, Comsa G (1993) Inversion of growth speed anisotropy in 2-dimensions. Phys Rev Lett 70:3943–3946
49. Zhou J, Baddorf AP, Mullins DR, Overbury SH (2008) Growth and characterization of Rh and Pd nanoparticles on oxidized and reduced CeO$_x$(111) thin films by scanning tunneling microscopy. J Phys Chem C 112:9336–9345
50. Esch F, Fabris S, Zhou L, Montini T, Africh C, Fornasiero P, Comelli G, Rosei R (2005) Electron localization determines defect formation on ceria substrates. Science 309:752–755

Chapter 9
Catalytic Chemistry on Oxide Nanostructures

**Aravind Asthagiri, David A. Dixon, Zdenek Dohnálek, Bruce D. Kay,
José A. Rodriguez, Roger Rousseau, Darío J. Stacchiola
and Jason F. Weaver**

Abstract In this chapter we review distinct well-defined planar models to illustrate the unique chemical properties that can be realized by oxide nanostructuring in the form of continuous ultra-thin films, extended islands and/or supported nanoclusters. The highlighted systems include metastable PdO films for C–H bond activation, multifunctional catalytic sites at copper/cerium-oxide island interfaces for water-gas shift reactions, and $(WO_3)_3$ and $(MoO_3)_3$ nanoclusters with active dioxo, O=M=O, moieties for dehydration and partial oxidation of alcohols.

A. Asthagiri
William G. Lowrie Department of Chemical and Biomolecular Engineering,
The Ohio State University, Columbus, OH 43210, USA
e-mail: asthagiri.1@osu.edu

D.A. Dixon
Department of Chemistry, The University of Alabama, Shelby Hall,
Box 870336, Tuscaloosa, Alabama 35487, USA
e-mail: dadixon@ua.edu

Z. Dohnálek (✉) · B.D. Kay · R. Rousseau
Institute for Integrated Catalysis, Pacific Northwest National laboratory,
PO Box 999, Richland, Washington 99352, USA
e-mail: zdenek.dohnalek@pnnl.gov

B.D. Kay
e-mail: bruce.kay@pnnl.gov

R. Rousseau
e-mail: riger.rousseau@pnnl.gov

J.A. Rodriguez · D.J. Stacchiola (✉)
Chemistry Department, Brookhaven National Laboratory, Upton, NY 11973, USA
e-mail: djs@bnl.gov

J.A. Rodriguez
e-mail: rodriguez@bnl.gov

J.F. Weaver (✉)
Department of Chemical Engineering, University of Florida, Gainesville, FL 32611, USA
e-mail: jweaver@che.ufl.edu

9.1 Introduction

Metal oxides represent one of the most important and widely employed materials in catalysis. Extreme variability of their surface chemistry provides a unique opportunity to tune their properties and utilize them for the design of highly active and selective catalysts. For bulk oxides, this can be achieved by varying their stoichiometry, crystallographic structure, exposed surface facets, defects, dopant densities and numerous other ways. Further, distinct properties from those of bulk oxides can be attained by restricting the oxide dimensionality and preparing them in the form of ultrathin films and nanoclusters as discussed throughout this book. In this chapter we focus on demonstrating such unique catalytic properties brought about by oxide nanoscaling. In the highlighted studies planar models are carefully designed to achieve minimal dispersion of structural motifs and attain detailed mechanistic understanding of targeted chemical transformations. The detailed level of morphological and structural characterization necessary to achieve this goal is accomplished by employing both high-resolution imaging via scanning probe methods and ensemble-averaged surface sensitive spectroscopic methods. Three prototypical examples illustrating different properties of nanoscaled oxides in different classes of reactions are selected.

In the first example we show how in oxidation catalysis the surfaces of late transition metals can oxidize to form metal oxide films with catalytic properties that are distinct from the parent metals. Advances in preparing crystalline oxide films of the late transition-metals have enabled researchers to apply state-of-the-art experimental and computational methods to gain new insights into the surface chemistry of this class of oxides. Of particular significance is the finding that late transition-metal oxide surfaces with undercoordinated metal and oxygen atoms can readily promote the C–H bond activation and complete oxidation of alkanes, with reactivity that exceeds that of many metal surfaces. We discuss investigations of alkane adsorption and activation on the PdO(101) surface, focusing on the formation of adsorbed alkane σ-complexes and the critical role of these species in serving as precursors for alkane C–H bond cleavage on late transition-metal oxides.

In the second example we demonstrate the importance of multifunctional active sites at metal/oxide interfaces. While their role has long been recognized, the molecular level understanding of their function based on concrete experimental evidence has only recently started to emerge. In a metal-oxide interface, one can have adsorption/reaction sites with complementary chemical properties, truly bifunctional sites which would be very difficult to generate on the surface of pure metal or alloy systems. We show how model systems can be prepared to highlight and study the activity of metal-oxide interfaces in relation to the water-gas shift reaction by combining in situ studies with theoretical calculations.

In the third example we focus on the properties of early transition metal oxide clusters prepared in a monodispersed form. Their metal center (W, Mo) dependent acid/base and redox properties are compared and contrasted while keeping the cluster structure the same. Their catalytic activity is assessed by quantitatively

following the conversion of small aliphatic alcohols in dehydration reactions to alkenes and ethers and dehydrogenation reactions to aldehydes and ketones. High level correlated electronic structure coupled clusters theory methods are employed to uncover complex details of the underlying reaction mechanisms. The structure–activity relationships are subsequently explored by comparing the activity of unsupported clusters with that of clusters supported on surfaces of other oxides and with that of nanoporous thin films. The catalytic activity of a range of studied cluster motifs further sheds light onto the role that structure and binding of clusters with the support play in determining their catalytic properties.

9.2 Alkane Adsorption and Activation on PdO(101)

Alkane activation on metal oxide surfaces is a critical step in the catalytic processing of alkanes in applications such as the catalytic combustion of natural gas, exhaust gas remediation and the selective oxidation of alkanes to value-added products. Advances in alkane catalysis are important for realizing technologies that more effectively utilize hydrocarbon resources and would indeed have significant economic and environmental benefits. Relatively few studies of alkane activation on well-defined oxide surfaces have been reported, mainly because alkanes interact weakly with many oxides and thus investigating alkane activation on such surfaces is challenging in typical experiments conducted under ultrahigh vacuum (UHV) conditions. Palladium oxide (PdO) appears to be an exceptional case as recent studies demonstrate that PdO(101) thin films are highly active toward alkanes and readily promote the activation and oxidation of propane and higher *n*-alkanes under UHV conditions [1–5]. These observations are consistent with reports that PdO formation is responsible for the exceptional activity of high surface-area Pd catalysts in applications of the catalytic combustion of methane under oxygen-rich conditions [6]. Recent in situ investigations have also shown that the PdO(101) facet develops preferentially during the oxidation of Pd(100) [7, 8], and that PdO(101) formation coincides with increased rates of methane oxidation during reaction at millibar pressures [9, 10].

Experimental and computational investigations with well-defined PdO(101) surfaces have provided new understanding about alkane activation on oxide surfaces that may have broad implications for alkane catalysis. These studies show that alkane C–H bond activation occurs on PdO(101) by a precursor-mediated mechanism wherein a molecularly-adsorbed state serves as the precursor to initial dissociation. A particularly significant finding is that the molecular precursor to dissociation corresponds to adsorbed alkane σ-complexes that form through dative bonding interactions between alkane molecules and coordinatively unsaturated (cus) Pd atoms at the PdO(101) surface. Alkane σ-complexes represent a type of coordination compound that is well known in organometallic chemistry and thought to serve as a key intermediate in alkane activation by various transition metal compounds [11–14]; however, experimental evidence for the formation of adsorbed

alkane σ-complexes has only been reported for the PdO(101) surface. Notably, recent density functional theory (DFT) studies predict that the formation and facile C-H bond activation of alkane σ-complexes occurs on late transition-metal oxide surfaces other than PdO(101) [15]. The prediction that alkane activation is facile on several late transition-metal oxides is quite interesting because it suggests the possibility of generating oxide surfaces that exhibit both high activity and selectivity for transforming alkanes to value-added products.

9.2.1 Structure of the PdO(101) Surface

Experimentally, PdO(101) surfaces have been generated as thin films by oxidizing Pd(111) using O-atom beams in UHV under conditions discussed previously [16–19]. The PdO(101) thin films are stoichiometrically-terminated, contain between 3 and 4 monolayers (ML, 1 ML is equal to the surface atom density of Pd(111)) of oxygen atoms and are 10 to 15 Å thick. A model representation of the stoichiometric PdO(101) surface is shown in Fig. 9.1. Bulk crystalline PdO has a tetragonal unit cell and consists of square planar units of Pd atoms fourfold coordinated with oxygen atoms [20]. The bulk-terminated PdO(101) surface is defined by a rectangular unit cell, where the a and b lattice vectors coincide with the [010] and [$\bar{1}$01] directions of the PdO crystal, respectively. The stoichiometric PdO(101) surface consists of alternating rows of threefold or fourfold coordinated Pd or O atoms that run parallel to the a direction shown in Fig. 9.1. Thus, half of the surface O and Pd atoms are coordinatively unsaturated (cus). The side view of PdO(101) shows that
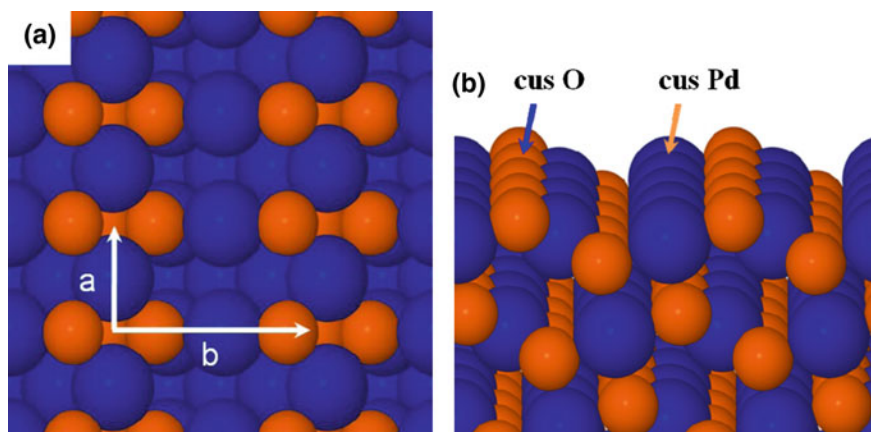
Fig. 9.1 Model representation of the stoichiometric PdO(101) surface identifying coordinatively saturated (4f) and coordinatively unsaturated (cus) Pd and O atoms. The a and b directions correspond to the [010] and [$\bar{1}$01] crystallographic directions of PdO. Reprinted from [15]

the coordinative environment associated with each cus-Pd atom resembles a square planar Pd complex with a coordination vacancy directed away from the surface and three oxygen ligands, one of which is a cus-O atom. The areal density of each type of coordinatively-distinct atom of the PdO(101) surface is equal to 35 % of the atomic density of the Pd(111) surface. Hence, the coverage of cus-Pd atoms is equal to 0.35 ML, and each PdO(101) layer contains 0.7 ML of Pd atoms and 0.7 ML of O atoms. The presence of cus-Pd/O pairs is responsible for the high reactivity of the PdO(101) surface toward alkanes [5].

9.2.2 Facile C–H Bond Activation of Propane on PdO(101)

The original discovery of strongly-bound molecular precursors and facile alkane dissociation on PdO(101) was made through experiments of the adsorption and oxidation of propane on a PdO(101) thin film that is grown on Pd(111) in UHV [1]. Figure 9.2 shows the results of temperature programmed desorption (TPD) experiments performed after saturating the PdO(101) surface with propane at 85 K. The data reveals that a fraction of the molecularly adsorbed propane desorbs without reacting, generating two main TPD features centered at 120 and 190 K. The remaining propane is completely oxidized by the surface during heating to produce H_2O and CO_2 which desorb simultaneously in reaction-limited peaks at ~ 465 K. A small fraction of H_2O also evolves in a desorption-limited peak near 350 K during the TPD measurement.

Fig. 9.2 TPD spectra of m/z ratios equal to 29 (propane), 28 (propane + CO), 44 (propane + CO_2), 18 (H_2O) and 2 (H_2) obtained after saturating a PdO(101) surface with propane at 85 K. Reprinted with permission from [1]
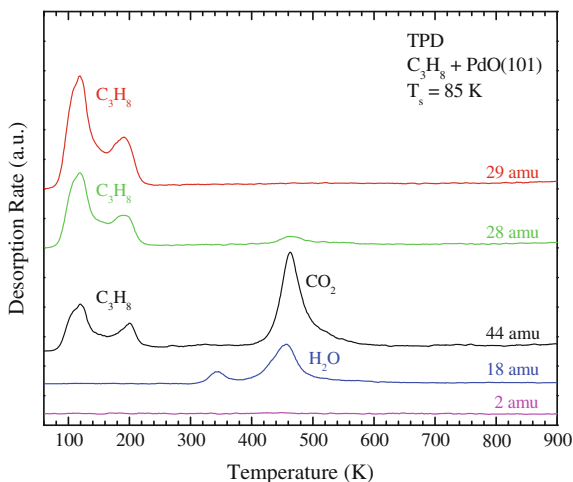
The behavior observed during TPD is consistent with a facile pathway for the precursor-mediated dissociation of propane on PdO(101). In particular, the data shows that a significant fraction of the molecularly adsorbed propane dissociates rather than desorbing during TPD, and that the initial dissociation occurs before the molecularly-adsorbed propane desorbs from the surface at temperatures below about 200 K. The data further suggests that initial dissociation occurs by cleavage of a single C–H bond and that the resulting propyl fragments remain stable on the surface up to about 400 K. Support for this interpretation comes from the relative yields of the desorption and reaction-limited H_2O TPD features. Analysis of the data shows that about seven times as much water desorbs in the reaction-limited peak compared with the desorption-limited peak, which implies that C_3H_8 dissociates below 200 K to liberate a H-atom which reacts with the surface to generate the H_2O peak at 350 K, and that the resulting C_3H_7 species undergoes negligible dehydrogenation until about 400 K, at which point this species is rapidly oxidized by the surface to generate the reaction-limited H_2O and CO_2 peaks at 465 K. The high reactivity of propane on PdO(101) represents the first example in which an alkane molecule was found to undergo facile dissociation on an oxide surface under UHV conditions. This observation suggests that the PdO(101) surface engages in a strong interaction with propane, the likes of which had not been identified for other oxides.

To test the idea that propane dissociates on PdO(101) from a molecularly-adsorbed state, Weaver et al. [1] performed measurements to estimate the initial dissociation probability S_o of propane on PdO(101) as a function of the surface temperature T_s, where S_o is defined as the dissociation probability in the limit of zero surface coverage of propane. These measurements show that the initial dissociation probability of propane on PdO(101) decreases with increasing surface temperature from 250 to 300 K, and thus that the apparent activation energy for propane dissociation is negative on the oxide surface. The authors showed that a simple kinetic model for precursor-mediated C–H bond cleavage accurately reproduces the measured dependence of S_o on T_s. The model assumes that a molecularly-adsorbed state of propane serves as the precursor for dissociation and that a kinetic competition between dissociation and desorption of the precursor determines the net dissociation probability. From the model, the initial dissociation probability is given by the equation $S_o = \alpha k_r/(k_r + k_d)$ where α is the probability for molecular adsorption, and is close to unity for the conditions studied, and k_r and k_d represent rate coefficients for dissociation ("r = reaction") and desorption ("d = desorption"), respectively. Analysis of the data using the precursor-mediated model gives values of $E_r - E_d = -16.2$ kJ/mol and $\nu_r/\nu_d = 3.9 \times 10^{-4}$ for the so-called apparent activation energy and the apparent pre-factor for propane dissociation on PdO(101), respectively, where the quantities E_r and E_d represent the activation energies for dissociation and desorption of the molecularly-adsorbed precursor. The results of the kinetic analysis support the conclusion that propane dissociation on PdO(101) occurs by a facile, precursor-mediated mechanism. Additional studies have provided insights into the nature of the molecular precursor and the reasons that this species readily dissociates on PdO(101) [3, 5, 15, 21, 22].

9.2.3 Molecular Precursor for Propane Dissociation on PdO(101)

A comparison of propane TPD spectra obtained from PdO(101) versus Pd(111) indeed demonstrates that propane molecules bind strongly on the oxide surface. Figure 9.3 shows propane TPD spectra obtained from PdO(101) and Pd(111) as a function of the initial propane coverage generated at 85 K. Propane physically adsorbs on Pd(111) and desorbs in a single TPD peak centered at 155 K, with a small amount of second layer propane desorbing in a shoulder at 120 K. Propane dissociates on Pd(111) to an immeasurable extent during the TPD experiments, in contrast to the significant reactivity that propane exhibits on the PdO(101) surface. The propane TPD spectra obtained from PdO(101) exhibit a broad desorption feature that consists of two distinct maxima centered at ~ 120 and 190 K, and denoted as the α_2 and α_1 states, respectively. Assuming that the propane which reacts, and desorbs as CO_2 and H_2O, originates from the α_1 state, one estimates that propane adsorbs in equal quantities in the α_1 and α_2 states when the propane monolayer on PdO(101) is saturated at 85 K. A likely interpretation is that the α_1 and α_2 states correspond to propane molecules adsorbed on the cus versus $4f$ Pd sites, respectively, since these sites are also present in equal concentrations on the PdO(101) surface.

Significantly, the propane TPD data reveals that propane adsorbed in the α_1 state on PdO(101) has a higher binding energy than propane which is physically adsorbed on Pd(111). This result was rather surprising because one generally expects higher binding energies when alkanes are physically adsorbed on a metal versus a metal oxide. The high binding energy associated with the α_1 state caused the authors to speculate that propane molecules experience a chemical bonding interaction in the α_1 state on PdO(101) that occurs negligibly on Pd(111) and enhances the α_1 propane binding energies on PdO(101) beyond that of physically adsorbed propane on Pd(111) [1].
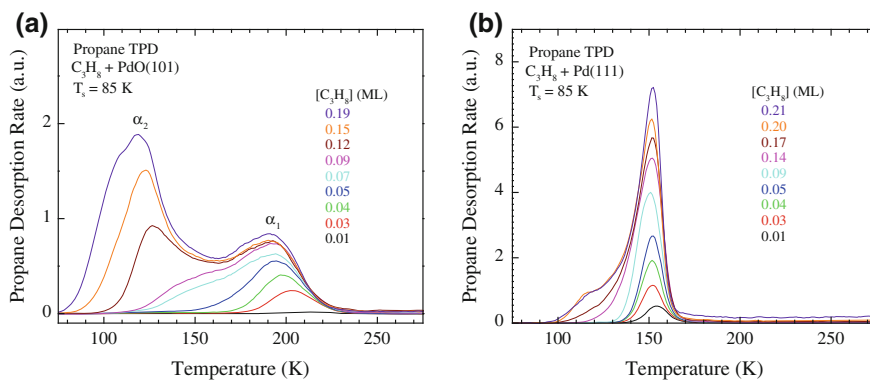
Fig. 9.3 Propane TPD spectra obtained from **a** PdO(101) and **b** Pd(111) as a function of the initial propane coverage prepared at 85 K. Reprinted with permission from [1]

Experiments have established that the α_1 state of adsorbed propane and higher *n*-alkanes serves as the precursor for alkane C–H bond cleavage on the PdO(101) surface. For example, the yield of dissociated propane correlates with the amount of propane which desorbs in the α_1 state, but is independent of the coverage of propane in the more weakly-bound α_2 state [1]. Site blocking experiments, in which compounds such as O_2 and H_2O are adsorbed on the Pd_{cus} sites prior to alkane adsorption, provide particularly convincing evidence that the α_1 state serves as the precursor for alkane dissociation on PdO(101) and that the precursor binds to the Pd_{cus} sites of the surface [3, 20].

9.2.4 Adsorbed Alkane σ-Complexes on PdO(101)

The binding of *n*-alkanes adsorbed in the strongly-bound α_1 state on PdO(101) has been investigated extensively both experimentally and computationally. Figure 9.4 shows a plot of molecular binding energies as a function of the chain length for *n*-alkanes (C_1 to C_5) adsorbed on both Pd(111) and in the α_1 state on PdO(101), where the binding energies were determined from an analysis of experimental TPD data [3, 21]. It is important to mention that neither methane nor ethane measurably dissociate on PdO(101) during TPD experiments in UHV, but that the C_3 to C_5 *n*-alkanes dissociate readily during TPD. Dispersion-corrected DFT calculations reproduce these trends in *n*-alkane reactivity on PdO(101) [22]. The plot in Fig. 9.4 shows that the binding energies are enhanced by a nearly constant amount for *n*-alkanes adsorbed on PdO(101) versus Pd(111), and that the E_d versus N relation for PdO(101) is linear but exhibits an intercept on the *y*-axis that is significantly larger than zero ($\sim$25 kJ/mol). Indeed, this comparison demonstrates that the enhanced

Fig. 9.4 Desorption energy as a function of the molecular chain length for *n*-alkanes adsorbed on PdO(101) and Pd (111). The desorption activation energies were estimated from TPD data and the energies reported for PdO (101) correspond to alkanes adsorbed as σ-complexes (α_1 TPD peak). Reprinted with permission from [15]
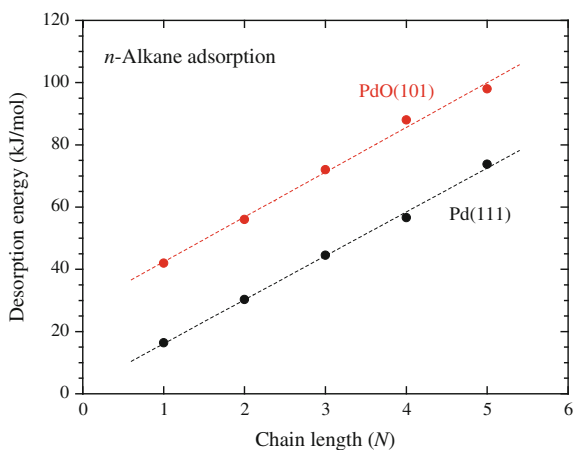
binding on PdO(101) relative to Pd(111) is a common feature in the binding of *n*-alkanes on the oxide surface.

The authors suggested that two main energetic contributions can explain the nature of the E_d versus N relation for *n*-alkanes adsorbed on PdO(101). The linear increase was attributed to a chain-length dependent contribution that arises from molecule-surface dispersion interactions, which is analogous to the explanation given previously of the linear E_d versus N relations for *n*-alkanes that are physically adsorbed on close-packed surfaces [23]. The non-zero intercept was attributed to dative bonding interactions between the alkanes and the cus-Pd atoms of the PdO (101) surface, which enhance the alkane-surface binding on PdO(101) beyond that afforded by only dispersion interactions. The constant enhancement suggests that the molecule-surface dative bonding produces a similar contribution to the total binding energy for the *n*-alkanes studied (C_1 to C_5).

DFT calculations support the interpretation that *n*-alkanes datively bond with the cus-Pd atoms of PdO(101), resulting in adsorbed alkane σ-complexes [3, 5, 9, 21, 22, 24–26]. A dative (or coordinate) bond is a covalent bond in which the shared electrons originate from only one species that is involved in the bonding. In an alkane σ-complex, one or more C–H bonds of the alkane donate electrons into empty *d*-states of the transition metal atom [13]. Back-donation of charge from filled *d*-states into unoccupied molecular orbitals of the alkane can also contribute to the bonding in an alkane σ-complex. According to DFT predictions, CH_4 adopts an η^2 configuration on PdO(101) in which the CH_4 molecule straddles a cus-Pd atom and places the two Pd-coordinated C–H bonds in a plane that is parallel to the cus-Pd row [3, 21, 22, 25]. DFT calculations also predict that CH_4 binds more strongly on PdO(101) than Pd(111) by about 15 kJ/mol [21], which can be associated with additional covalent bonding due to σ-complex formation.

Fig. 9.5 Difference charge density plot determined by DFT for the CH_4 η^2(H, H) complex adsorbed on a Pd_{cus} site of PdO(101). Reprinted with permission from [21]
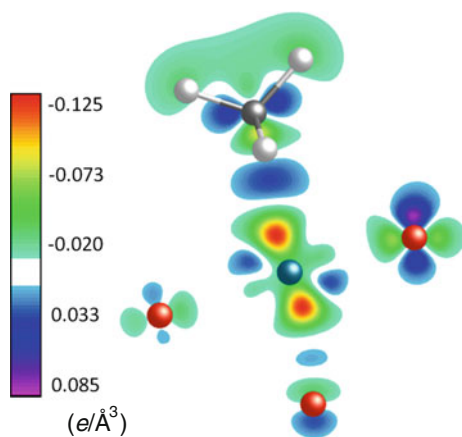
DFT-derived changes in the charge distribution and electronic structure that are induced by CH_4 adsorption on PdO(101) demonstrate that the methane molecule experiences a donor-acceptor interaction with the cus-Pd atom. Figure 9.5 shows a charge-density difference plot that is obtained by subtracting the charge distribution of the isolated CH_4 molecule plus the clean PdO(101) surface from that predicted for the η^2 CH_4 complex on PdO(101) [21]. The plot reveals that electrons accumulate between the CH_4 molecule and the cus-Pd atom and that the electron density is depleted near the cus-Pd atom. The latter feature is characteristic of back-bonding in which electrons from filled *d*-states of the cus-Pd atom occupy anti-bonding orbitals of the CH_4 molecule that are empty when the molecule is isolated from the surface. Such back-donation of charge is expected to strengthen the molecule-surface binding while weakening intramolecular bonds of the adsorbed species. Consistent with this idea, normal mode analysis predicts that vibrational modes which involve motions of the Pd-coordinated C–H bonds are redshifted by as much as 200 cm^{-1} from their gas-phase values, thus confirming that the dative bonding interaction with the surface softens C–H bonds [3].

To investigate the role of alkane-surface dative bonding in promoting C–H bond cleavage on PdO(101), Weaver et al. [3] calculated energy barriers for the cleavage of a Pd-coordinated C–H bond versus a "non-activated" C–H bond of the CH_4 η^2 complex, where the latter bond corresponds to one of the C–H bonds that is directed away from the surface and is not directly involved in the dative interaction. These calculations predict that the energy barrier for breaking one of the Pd-coordinated C–H bonds is lower by more than 100 kJ/mol than the barrier for breaking a non-activated C–H bond of the CH_4 complex on PdO(101), demonstrating that the dative bonding interaction significantly weakens alkane C–H bonds. Using DFT, Hellman et al. [9] have further shown that the population of filled 5*s* states is low on the cus-Pd atoms of PdO(101) and consequently promotes a bonding interaction with the CH_4 molecule in addition to reducing the C–H bond cleavage barrier.

Overall, prior studies demonstrate that the formation of adsorbed alkane σ-complexes is critical to achieving facile C–H bond cleavage on the PdO(101) surface. The formation of an adsorbed σ-complex enhances alkane binding to the surface relative to that achieved by physisorption alone, and thereby increases the desorption activation energy E_d. In addition, σ-complex formation weakens the Pd-coordinated C–H bonds and thus acts to lower the intrinsic activation energy for reaction E_r. Both of these effects serve to lower the apparent energy barrier ($E_r - E_d$) for alkane C–H bond cleavage on PdO(101), making PdO(101) highly reactive toward alkane dissociation. DFT calculations also predict the formation and facile C–H bond activation of alkane σ-complexes on RuO_2 and IrO_2 surfaces [15]. An implication is that a high activity toward alkane dissociation is not limited to the PdO(101) surface, but is a property of other late transition-metal oxide surfaces as well, provided that under-coordinated metal and oxygen atoms are available.

9.3 Reaction Pathway for the Water-Gas Shift Reaction on Copper-Based Catalysts

In this section we present results highlighting how different model assemblies can be used to emphasize the importance or effect of various components or local environments in a complex heterogeneous catalyst involved in the water-gas shift (WGS) reaction. The WGS reaction ($CO + H_2O \rightarrow CO_2 + H_2$) is an industrial chemical process used to remove carbon monoxide from hydrogen streams. It has been extensively debated if the most active sites on the industrial catalyst used for the low temperature WGS reaction ($Cu/ZnO/Al_2O_3$) are either Cu or Cu^+ sites. There is consensus in the fact that the rate limiting step on top of copper particles is the dissociation of water. The studies described here show that an alternative reaction pathway involving multifunctional active sites present at the metal-oxide interface of catalysts containing a more reducible oxide could yield more efficient catalysts.

Extensive experimental and theoretical studies relating to the WGS reaction have led to hotly debated competing reaction mechanisms and intermediates [27–33]. From these studies, mainly two mechanisms (redox and associative) have been considered as most probable for the WGS reaction over Cu based catalysts.

Redox mechanism

$$H_2O(gas) + {}^* \rightarrow H_2O(ads)^*$$
$$H_2O(ads)^* + {}^* \rightarrow OH(ads)^* + H(ads)^*$$
$$OH(ads)^* + OH(ads)^* \rightarrow O(ads)^* + H_2O(ads)^*$$
$$CO + {}^* \rightarrow CO(ads)^*$$
$$CO(ads)^* + O(ads)^* \rightarrow CO_2(gas) + 2^*$$
$$H(ads)^* + H(ads)^* \rightarrow H_2(gas) + 2^*$$

Associative mechanism

$$H_2O(gas) + {}^* \rightarrow H_2O(ads)^*$$
$$H_2O(ads)^* + {}^* \rightarrow OH(ads)^* + H(ads)^*$$
$$CO + {}^* \rightarrow CO(ads)^*$$
$$CO(ads)^* + OH(ads)^* \rightarrow HOCO(ads)^* + {}^*$$
$$HOCO(ads)^* \rightarrow CO_2(gas) + H(ads)^*$$
$$H(ads)^* + H(ads)^* \rightarrow H_2(gas) + 2^*$$
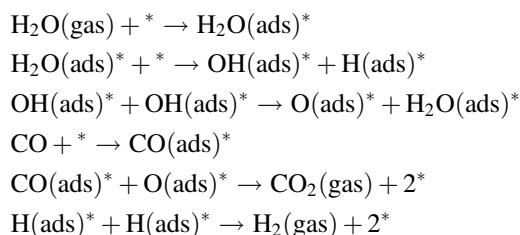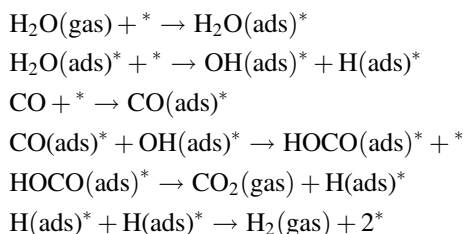
In the redox mechanism water fully dissociates and the resulting adsorbed atomic oxygen reacts with CO to form CO_2. The dissociation of molecular H_2O also leads to

the production of H_2 by the recombination of adsorbed H. In the associative process a stable CO_yH_x intermediate species, produced by the reaction of CO with OH groups derived from the dissociation of water, must precede the formation of H_2 and CO_2. It has been proposed with some controversy that the predominant intermediate species for this associative reaction pathway is either a surface bound formate ($HCOO^-$) or a carbonate (CO_3^{2-}) species. In addition, electronic structure calculations also suggest the possibility of a weakly bound carboxyl (HOCO) [31, 33] intermediate as the most efficient pathway for the WGS reaction, but this species remains experimentally elusive and difficult to detect. Open questions still remain about the reaction mechanism, key intermediates and oxidation state of the metal centers, which hinders the design and optimization of catalysts. One method to seek answers to these questions is to combine the in situ characterization of the active state of the catalyst and adsorbed surface species under catalytic WGS reaction conditions with theoretical modeling of alternative reaction pathways.

9.3.1 WGS Activity Measurements for Cu-Based Catalysts

Figure 9.6 compares the activities for the WGS reaction among different copper-based model catalysts, including representative scanning tunneling micro-copy (STM) images for each system [34]. The testing of catalytic activity was carried out in an ultrahigh vacuum (UHV) chamber that has attached a high-pressure cell or batch reactor. The sample could be transferred between the
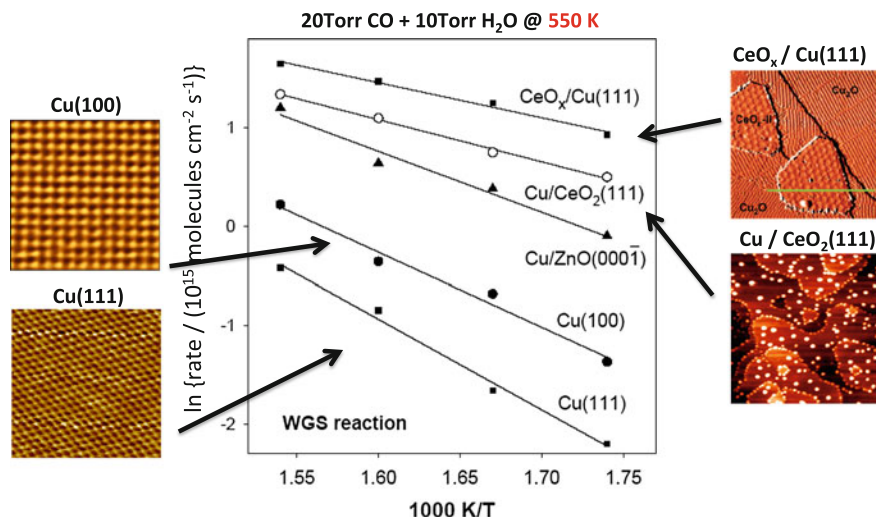
Fig. 9.6 Arrhenius plot for the WGS reaction rate on different Cu-based catalysts. Representative STM images of the corresponding model catalysts are included at each side of the Arrhenius plot. Reprinted with permission from [34]

reactor and vacuum chamber without exposure to air. Bare Cu(111) can be used as a benchmark for fundamental studies on the WGS, presenting the lowest activity of all of the model catalysts. Single crystals with more open surfaces such as Cu(100) or Cu(110) slightly increase the catalytic efficiency with respect to Cu(111). A significant improvement is observed when nanoparticles of copper are deposited on an oxide substrate. For comparison, results obtained under the same reaction conditions for 0.5 ML of Cu deposited on ZnO(000$\bar{1}$), the system modeling the industrial catalyst, and on a more reactive reducible oxide such as CeO$_2$(111) are also included. Control measurements on both oxide support model systems, ZnO (000$\bar{1}$) and CeO$_2$(111), indicate that they present no activity on their own for the WGS reaction, showing the critical importance of the presence of a metallic component in the catalyst. A model system with a 20 % coverage of CeO$_x$ nanoparticles deposited on Cu(111) generated a better model catalyst, being 8 (at 650 K) to 23 times (at 575 K) more active than the clean Cu(111) substrate. A fully covered oxide film CeO$_x$/Cu(111) surface displayed negligible WGS activity.

The data in Fig. 9.6 were collected at temperatures between 575 and 650 K. Arrhenius plots for all the model catalysts were constructed. The WGS on Cu(111) has the highest apparent activation energy (0.78 eV) among all systems studied, which is 0.1–0.2 eV larger than that found on Cu(100) and Cu(110). In contrast, the apparent activation energy for the WGS on CeO$_x$/Cu(111) is only 0.31 eV. This value is considerably smaller than the corresponding value found for Cu nanoparticles supported on the industrial model ZnO(000$\bar{1}$) of 0.54 eV. In order to gain insight into the catalytic reaction mechanism associated with our best model system, the CeO$_x$/Cu(111) surface, we will present in the next section results from in situ studies of the WGSR.

9.3.2 In Situ Studies of the WGS Reaction on CeO$_x$/Cu(111)

Figure 9.7 presents spectra obtained during ambient pressure X-ray photoelectron spectroscopy (AP-XPS) experiments on the CeO$_x$/Cu(111) catalyst under WGS reaction conditions (CO: 90 mTorr, H$_2$O: 30 mTorr). The O 1s spectra include features due to gas-phase CO and H$_2$O [35]. For comparison, the corresponding data for bare Cu(111) is also included. On Cu(111), a broad peak at 533.4 eV in the O 1s spectrum and the main peak in the C 1s spectrum at 286.2 eV are assigned to chemisorbed molecular CO. Features at 285 eV or lower energies in the C 1s spectra can be associated with carbonaceous C$_x$H$_y$ species (referred as C^0) formed from residual gases, a common occurrence in ambient pressure studies. No other features are observed at higher temperatures in the presence of CO and H$_2$O. Therefore, the absence of carbonaceous species other than the original reactant molecule on the surface of the pure metallic catalyst does not support an associative mechanism for the WGS on Cu(111), being consistent with a redox process.

On the other hand, a very different picture emerges on the CeO$_x$/Cu(111) model system. When CeO$_x$ nanoparticles are deposited on Cu(111), changes in the O and
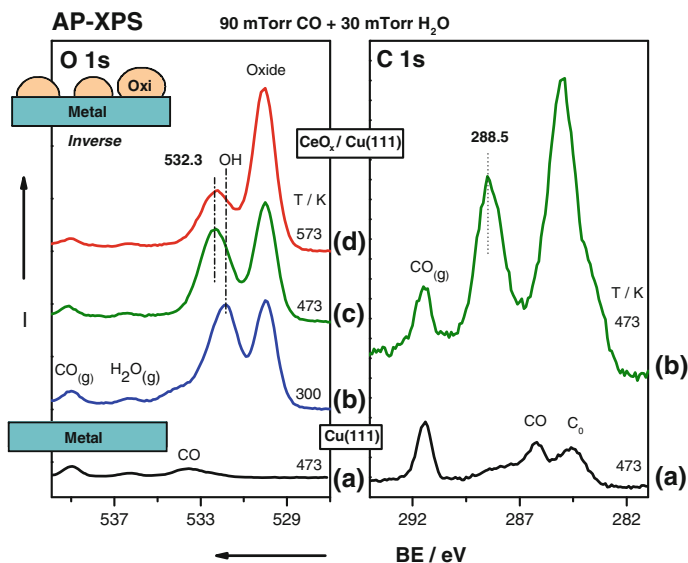
Fig. 9.7 AP-XPS from Cu(111) and CeO$_x$/Cu(111) under WGS reaction. Reprinted with permission from [35]

C 1s regions are observed under WGS conditions. The O 1s peak at 530.0 eV in Fig. 9.7b corresponds to lattice oxygen in the CeO$_x$ nanoparticles. The broad peak at 531.8 eV is associated with OH groups which could be bonded to the ceria nanoparticles or the copper substrate, and a shoulder at a higher binding energy corresponds to adsorbed CO. As the sample temperature was increased, several changes were observed. In the O 1s spectrum (Fig. 9.7c), the shoulder due to chemisorbed CO and the peak at 531.8 eV decreased in intensity, and a peak at 532.3 eV became dominant. The peak at 532.3 eV results from the potential contribution from numerous adsorbed species, including CO$_3^{2-}$, HCOO$^-$, CO$_2^{\delta-}$, and OH on CeO$_x$.

The C 1s spectrum presented in Fig. 9.7b shows a peak at 288.5 eV and a C^0 peak at approximately 285 eV. The assignment of the peak at 288.5 eV is very challenging. Formate (HCOO) is ruled out based on control experiments, since its C 1s binding energies on CeO$_x$/Cu(111) are 289.2 and 287.5 eV on CeO$_x$ and Cu (111), respectively. Carbonate (CO$_3$) species, which have a C 1s binding energy of about 289.5 eV can be also ruled out. Carbonate species are detected when ceria films are exposed to similar WGS reaction conditions, without production of hydrogen as described above. Therefore the peak at 288.5 eV has been tentatively assigned to a CO$_2^{\delta-}$ or HOCO species. The presence of a CO$_2^{\delta-}$ species is consistent with additional complimentary studies using ambient pressure infrared reflection absorption spectroscopy (AP–IRRAS) and DFT calculations presented below. In the case of the AP-IRRAS data, the detection of both symmetric and asymmetric stretches in the spectra points to the breaking of the symmetry in the CO$_2^{\delta-}$ adsorbed

molecule, based on surface selection rules, indicating its presence in a heterogeneous environment such as the interface between the metal substrate and the oxide nanoparticle.

9.3.3 DFT Results for the WGS Reaction on CeO$_x$/Cu(111)

Figure 9.8 presents results from DFT calculations for the energy profile of the WGS reaction on a simulated model of the CeO$_x$/Cu(111) catalyst [35]. While the activation energy for water dissociation on Cu(111) is very high (more than 1 eV), water can be easily dissociated on the reduced ceria nanoparticles. The adsorption of CO on Cu sites near the interface with the ceria nanoparticles is favored with respect to sites on the flat Cu(111) terraces. A carboxyl (HOCO) intermediate can be generated by the reaction of CO with OH species at the metal-oxide interface. The electronic structure calculations indicate that the CO$_2^{\delta-}$ detected experimentally is a consequence of the decomposition of a HOCO intermediate. The interaction of molecular CO$_2$ with a ceria film leads to the formation of strongly adsorbed carbonate species, while it only weakly physisorbs on a Cu(111) surface. Since the CO$_2^{\delta-}$ species are not observed on either fully oxidized or reduced CeO$_2$(111) films or clean Cu(111) surfaces, the interfacial sites formed on the CeO$_x$/Cu(111) system appear to be critical for the formation and stabilization of activated CO$_2^{\delta-}$.

The most abundant surface species on bare Cu(111) under WGSR conditions is adsorbed CO, suggesting that the prevailing reaction path is not related to an associative mechanism. Under the mild WGSR conditions investigated during the AP-XPS experiments, trapped CO$_2^{\delta-}$ species are identified over both CeO$_x$/Cu (111) and CeO$_x$/Au(111) systems and reduction of Ce^{4+} to Ce^{3+} is observed. AP-XPS and DFT calculations show that CO$_2^{\delta-}$ species derived from a *carboxyl* intermediate are stabilized at the interfaces of CeO$_x$/Cu(111) and CeO$_x$/Au(111).

Fig. 9.8 Proposed pathway for the WGS reaction on CeO$_x$/Cu(111) including intermediate species and transition state structures and energies. Reprinted with permission from [35]
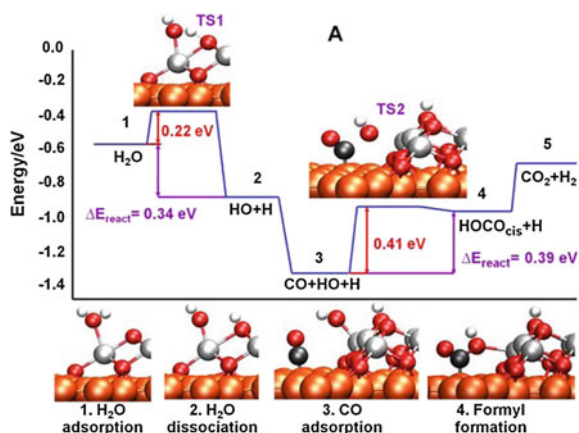
Even though the WGSR over CeO$_x$/Cu catalysts can occur via both redox and associative mechanisms, the study presented here shows that the presence of the oxide/metal interface activates the more efficient associative mechanism pathway and leads to a more than one order of magnitude increase in the activity of the CeO$_x$/Cu(111) system compared with Cu(111). The synthesis and catalytic testing of a model system that incorporates both components, the oxide and metal phases, in the form of nanoparticles are discussed in the next section.

9.3.4 WGS Reaction on a Cu/CeO$_x$/TiO$_2$(110) Surface

The combination of two reactive metals in a common oxide matrix can produce materials with novel structural and/or electronic properties [36]. It has been found that when ceria nanoparticles are deposited on a reducible oxide such as TiO$_2$(110), the titania substrate imposes on the ceria nanoparticles non-typical coordination modes leading to a subsequent change in the relative stability of the Ce^{3+}/Ce^{4+} oxidation states that translates into a significant enhancement in chemical activity. An STM image of ceria nanoparticles stabilized on TiO$_2$(110) is shown in Fig. 9.9. The image was taken with a bias of +1.2 V, and the angle of the diagonal array is close to 42° with respect to the [1$\bar{1}$0] direction. When this feature was imaged at +0.4 V, the individual bright features appeared as dimers. Each ceria dimer is located between two rows of oxygen atoms protruding from the surface. Ce 3d XPS spectra indicated that the oxidation state of the Ce atoms in the dimers was +3. On the other hand, in the Ti 2p XPS region mainly Ti^{4+} is observed, with a small amount (<5 %) of Ti^{3+}, comparable to that found on clean TiO$_2$(110). The presence of O$_2$ in the background during the deposition of Ce for the synthesis of the ceria nanoparticles prevented the reduction of the titania support by Ce.

Fig. 9.9 STM image for the ordering of Ce$_2$O$_3$ dimers on a TiO$_2$(110) surface (7 nm × 7 nm image size). Reprinted with permission from [36]
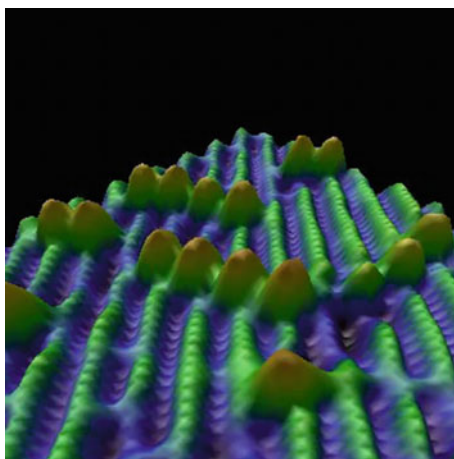
When metals such as Au, Pt or Cu are deposited on top of the $Ce_2O_3/TiO_2(110)$ surface, they form three-dimensional nanoparticles [37]. The ceria nanoparticles act as nucleation centers and favor the dispersion of both Au and Cu. In the case of the latter metal, a substantial number of Cu particles remain on the terraces of $Cu/CeO_x/TiO_2(110)$ even after annealing to 625 K, where they easily sinter when adsorbed on bare $TiO_2(110)$. For low coverages of both Cu and CeO_x nanoparticles, the $Cu/CeO_x/TiO_2(110)$ system is ~ 10 times more active than the model for the Cu/ZnO industrial catalysts.

In the $Cu/CeO_x/TiO_2(110)$ system, there is a strong coupling of the chemical properties of the admetal and the mixed-metal oxide: The adsorption and dissociation of water can easily take place on the reducible oxide nanoparticles, CO adsorbs on the admetal nanoparticles, and all subsequent reaction steps occur at the oxide-admetal interface. Powder catalysts of ceria-modified titania can be prepared for practical applications. The high catalytic activity of the $Cu/CeO_x/TiO_2(110)$ surfaces reflects the unique properties of the mixed–metal oxide at the nanometer level. The titania substrate imposes on the ceria nanoparticles non-typical coordination modes enhancing their chemical reactivity. This phenomenon leads to a larger dispersion of supported metal nanoparticles and at the same time makes possible the direct participation of the oxide in the rate limiting step in the catalytic WGS reaction, the dissociation of water.

In summary, synergistic effects between metal and oxide sites have being discussed in the catalysis literature since the middle of the 20th century, in particular the formation of special multifunctional sites at metal/oxide interfaces [38–40]. But interrogating these special interfacial sites experimentally is challenging. Our study illustrates the power of combining DFT electronic structure calculations with in situ mechanistic studies on well-defined catalysts and the important role that metal-oxide interfaces can play in catalysis. The simultaneous participation of atoms present in the metal and oxide make possible the formation and stabilization of weakly adsorbed *carboxyl* (HOCO) species, favoring a reaction mechanism for hydrogen production that is more effective than on either pure copper or ceria sites. Thus, when optimizing this type of catalysts one should pay special attention to the properties of metal-oxide interfaces.

9.4 Conversion of Alcohols on Model Systems Based on $(WO_3)_3$ and $(MoO_3)_3$ Clusters

Clusters of early transition metal oxides (e.g. WO_x, MoO_x and VO_x), supported on high surface area oxide scaffolds (i.e. ZrO_2, Al_2O_3, SiO_2, and TiO_2) are an important class of catalytic materials with applications in a broad range of chemical transformations. Dehydration and partial oxidation of alcohols, isomerization of alkanes and alkenes, dehydration and metathesis of alkenes, and selective reduction of nitric oxide, are just few examples illustrating their broad applicability [41, 42].

As a result of the complexity of these materials our mechanistic understanding of such reactions on their various structural motifs is far from complete. As such, the design, preparation and characterization of well-defined structural models are critical tasks for advancing our fundamental understanding of structure-function relationships on complex oxide catalysts.

Unfortunately, the preparation of well-defined oxide clusters is a rather challenging task. Traditional simple methods generally employ deposition of metal and/or volatile organometallic precursor followed by their oxidation. While fairly simple, these procedures generally result in a range of poorly defined cluster sizes with a broad distribution of sites. The deposition of mass-selected oxide clusters, on the other hand, offers an extreme level of control over cluster sizes and composition, but the applications have been rather limited due to the complexity of cluster sources and low yields [44, 45]. Below we discuss an alternative simple method which is based on a sublimation of oxide powders yielding nearly monodispersed oxide clusters of a specific but not variable size. The simplicity of this approach allows for extensive detailed studies of the structure and catalytic activity of a number of model catalytic systems [46]. Conversion of alcohols to alkenes, aldehydes, ketones, and ethers is used as a model set of reactions to probe both the acid/base (Lewis and Brønsted) and redox properties of different structural motifs prepared using this technique.

9.4.1 Preparation of $(WO_3)_3$ and $(MoO_3)_3$ Clusters

While sublimation of oxides has been used extensively in matrix isolation experiments, surprisingly it has not been widely employed in the preparation of supported oxide clusters in the surface science studies of planar model catalysts. The studies illustrated here focus on the preparation, characterization and reactivity of $(WO_3)_3$ and $(MoO_3)_3$ clusters [46]. The main limitation of this approach is that for most oxides only monomer-like units such as MgO, TiO, SiO, Al_2O_3 are expected to be the dominant gas phase species that result from the sublimation. Sublimation of WO_3 and MoO_3 powders, which leads primarily to cyclic $(WO_3)_3$ and $(MoO_3)_3$ trimers (schematically shown in Fig. 9.10, left) is rather an exception to this rule. This is demonstrated by the IRRAS experiments of the isolated clusters deposited into a krypton matrix that are shown in Fig. 9.10 [43]. Theoretical studies further reveal that in gas phase both $(WO_3)_3$ and $(MoO_3)_3$ trimers are structurally similar and have D_{3h} symmetry [47]. Each metal (M) atom is tetrahedrally coordinated with two bridging oxygen atoms ($M–O_b–M$) and two terminal oxygen atoms ($M=O_t$).

Before we focus on the catalytic activity of such clusters, we summarize their most relevant thermodynamic properties that determine their reactivity with organic species, namely, the Lewis and Brønsted acid/base and redox properties of different sites. These properties have been calculated with high accuracy using high level correlated electronic structure methods such as coupled clusters theory (CCSD(T))
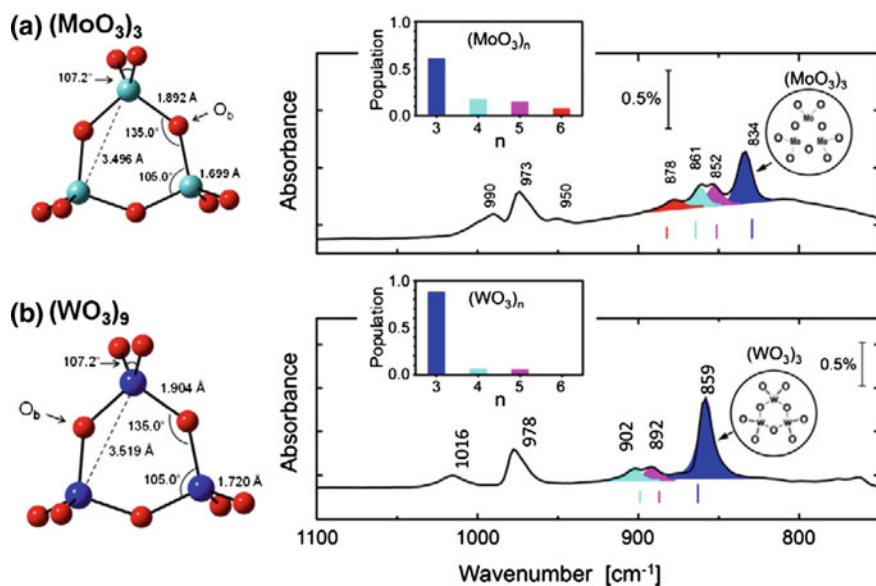
Fig. 9.10 IRRAS spectra for **a** $(MoO_3)_n$ and **b** $(WO_3)_n$ suspended in a Kr matrix on an inert graphene substrate supported on Pt(111). Predicted vibrational frequencies for different types of clusters are shown as "stick" spectra under the experimental peaks. The "stick" spectra for MoO_3 clusters were red-shifted by 29 cm^{-1} in order to match the experimental spectra. The insets show the population as a function of cluster sizes, n, as determined from the area of the $M–O_b–M$ stretching mode peaks for various cluster sizes assuming identical oscillator strengths. Adapted with permission from [43]

with correlation-consistent basis sets [48, 49]. Both $(WO_3)_3$ and $(MoO_3)_3$ clusters possess strongly Lewis acidic metal sites. It has been predicted that $(WO_3)_3$ has a Lewis acidity of 117.9 kcal/mol (computed in terms of its fluoride affinity) which is comparable to that of SbF_5. The Lewis acidity of $(MoO_3)_3$ of 105.3 kcal/mol is only slightly smaller. On the opposite end, both O_b and O_t atoms are only weakly basic, with proton affinities of 146.4 and 175.1 kcal/mol for $(WO_3)_3$ and 160.8 and 176.3 kcal/mol for $(MoO_3)_3$, respectively, not much higher than that of H_2O. Consequently, the expected site for Lewis acid attack is the metal and for Brønsted acid attack is the O_t for both Mo and W clusters with W being the stronger Lewis acid of the two. Further, the reducibility of the metal centers is also of fundamental importance as it affects redox reactions. It can be quantified in terms of the adiabatic electron detachment energy (equivalent to the electron affinity of the neutral) for cyclic $(MO_3)_3^-$ anions. For the cyclic $(MO_3)_3^-$ species, values of 3.29 and 3.03 eV were obtained for Mo and W, respectively, indicating easier reducibility of the $(MO_3)_3$. The implications are that Mo is not only a mildly weaker Lewis acid but that it can be reduced easier (i.e. stronger oxidizing agent) than W to a lower oxidation state.

9.4.2 Alcohol Chemistry on Unsupported $(WO_3)_3$ and $(MoO_3)_3$

With these general properties in mind one can now compare the inherent catalytic activity of both $(WO_3)_3$ and $(MoO_3)_3$ towards small C1-C4 aliphatic alcohols in the absence of support effects [43, 50]. This can be accomplished by direct sublimation of $(MoO_3)_3$ and $(WO_3)_3$ into the reactive matrices of alcohols at low temperatures. Several competing reaction pathways, dehydration to alkanes, dehydrogenation to aldehydes/ketones and condensation to ethers are available and allow to probe different acid/base and redox properties as summarized above. Product formation can be followed as a function of increasing temperature using temperature programmed desorption (TPD) in concert with in situ spectroscopic studies and concomitant electronic structure calculations can provide detailed quantification of the reaction energetics.

The TPD spectra in Fig. 9.11 illustrate the observed desorption products from OD-labeled ethanol (C_2H_5OD) adsorbed on both $(WO_3)_3$ (upper black traces) and $(MoO_3)_3$ (lower gray/red traces) clusters. The desorbing species are divided into three categories, (A) excess unreacted ethanol between 135 and 200 K, (B) water as the only observed carbon-free product and (C) carbon containing products. The quantified yields of the products for all C1–C4 aliphatic alcohols are further summarized in Fig. 9.12 [50].

Fig. 9.11 Desorption rates of **a** CH_3CH_2OD, **b** D_2O and H_2O, and **c** CH_3CH_2OH, CH_2CH_2, CH_3CHO, and $(CH_3CH_2)_2O$ as a function of linearly increasing temperature (2 K/s) obtained during the TPD experiment following co-adsorption of 2.0×10^{15} WO_3/cm^2 (*black traces*) and MoO_3/cm^2 (*gray/red traces*) with 20×10^{15} of CH_3CH_2OD/cm^2 on graphene/Pt(111) at 24 K. Adapted with permission from [43]
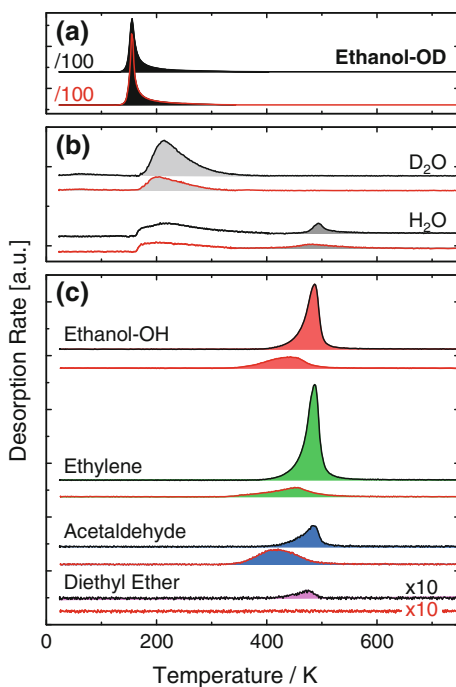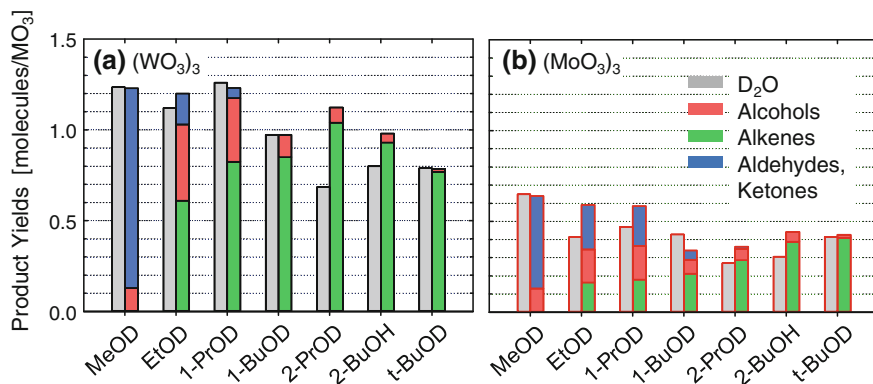
Fig. 9.12 Quantified yields of D_2O (measure of the total alcohol–OD conversion) and major carbon-containing products (alcohols, alkenes, aldehydes/ketones) following coadsorption of 20×10^{15} alcohol/cm^2 with **a** 2.0×10^{15} WO$_3$/cm^2 and **b** MoO$_3$/cm^2 on graphene/Pt(111) at 25 K. Reprinted with permission from [50]

The evolution of D_2O at low temperatures (170–300 K) demonstrate that a fraction of C_2H_5OD dissociated and since this is the only observed D-containing product that deuterium was utilized to solely form D_2O. Electronic structure calculations at the CCSD(T) level further reveal that water formation is a result of the deprotonation of ethanol molecules on the dioxo moieties as illustrated in (9.1) below.

$$O=M=O + 2C_2H_5OD_{(a)} \rightleftharpoons DO-M-OD \rightleftharpoons O=M-OC_2H_5 + D_2O_{(a)} \tag{9.1}$$
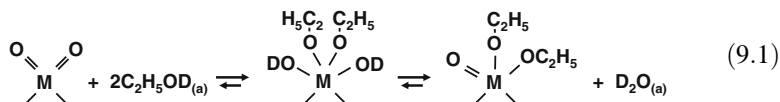
A detailed quantitative analysis of product yields showed that on average 0.56 D_2O molecules formed per W^{6+} center. On (MoO$_3$)$_3$, a significantly reduced yield of 0.21 D_2O/Mo^{6+} was observed. The factor of two reduction in the D_2O yields on (MoO$_3$)$_3$ is common to all C1–C4 alcohols that were studied (Fig. 9.12). The more considerable shift in (9.1) towards the products for W^{6+}, is a consequence of its higher Lewis acidity which stabilizes the initial alcohol/cluster complex, lowers the alcohol dissociation barrier on the dioxo species and increases the thermodynamic stability of the products. The absence of H_2O further indicates that C–H bonds are not being cleaved in this temperature range.

This initial desorption of low temperature water has been found to be a critical step kinetically driving forward the formation of other organic products which are endothermic in the overall reaction energy scheme. As such, the amount of deuterium in D_2O directly corresponds to the sum of the carbon containing products as evident from (9.1). The electronic structure calculations at the CCSD(T) level have further shown that if only a single alcohol is dissociated on each dioxo, O=M=O center, the alcohol recombination is favored over the formation of reaction products.

As the temperature is further increased in the TPD experiments, the diethoxy coordinated clusters yield five products that can be seen in Fig. 9.11 at 400–500 K, namely water, ethylene, acetaldehyde, non-deuterated ethanol, and diethyl ether. These products arise from ethoxy dehydration to $CH_2=CH_2$ and H_2O, dehydrogenation to CH_3CHO, recombination to CH_3CH_2OH, and condensation to $(CH_3CH_2)_2O$. It should be noted that the H atom bound to the hydroxyl group must have initially arisen from a C–H bond breaking process. The similar temperature range at which all of these reactions are observed implies that all three reaction channels are in competition and it is notable that the branching ratios show a pronounced difference for W versus Mo. For the former, dehydration is the preferred channel whereas dehydrogenation is preferred for the latter.

Reaction energetics calculated at the CCSD(T) level for dehydration shows similar reaction energy barrier of 35–36 kcal/mol on both W and Mo as expected based on similar desorption temperatures observed in the TPD of Fig. 9.11. The transition state for the ethoxy (and alkoxy in general) dehydration has been postulated to involve the concerted breaking of the C_α–O and C_β–H bond and involves a carbo-cationic character in the C_2H_5 fragment as illustrated in (9.2) below [51, 52].

$$(9.2)$$
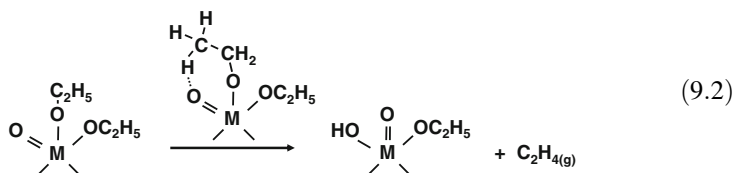
Several reaction pathways are subsequently available for the hydroxyl and ethoxy coordinated clusters: (1) the dehydration of the second ethoxy (over similar energy barrier) followed by H_2O evolution and/or (2) recombination of the hydroxyl and ethoxy yielding protonated ethanol. Both water and protonated ethanol, C_2H_5OH, are observed in the TPD experiments (Figs. 9.11 and 9.3).

In contrast with dehydration, dehydrogenation shows an appreciably lower net reaction barrier of 34 kcal/mol for Mo^{6+} relative to 43 kcal/mol for W^{6+} as predicted at the CCSD(T) level. This is a direct consequence of easier reducibility of Mo^{6+} as compared to W^{6+}. Interestingly, the difference in Mo^{6+} and W^{6+} reducibility lead to differences in the calculated reaction mechanisms. Reaction proceeds via heterolytic breaking of a C_α–H bond on both types of clusters. For W^{6+}, the H transfer leads to the formation of a transient hydride species as shown in (9.3):

$$(9.3)$$
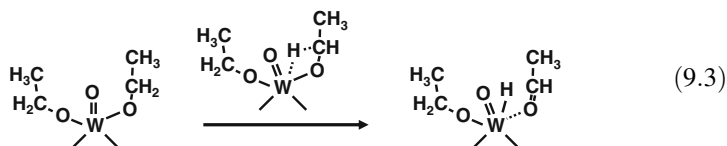
This hydride formation avoids the energetically costly reduction of W^{6+} centers. In contrast, on more reducible Mo^{6+}, transient reduction represents the lowest energy paths. While the reduction can involve one or two neighboring Mo^{6+} centers on the cluster, for simplicity only the single site example is illustrated in (9.4).

$$
\text{(9.4)}
$$
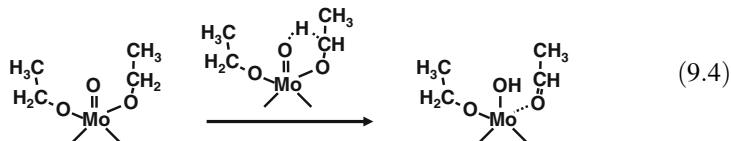
As a result of the lower reaction energy for dehydrogenation on Mo than W, dehydrogenation thus becomes the dominant channel on $(MoO_3)_3$ clusters as opposed to the dehydration route observed on $(WO_3)_3$ clusters. Ethers are also found but under the employed reaction conditions have been shown to be only minor products. The calculated reaction mechanism [50] shows that three alcohol molecules are required for the low energy ether formation pathway with one being sacrificed to generate a highly basic Brønsted OH group, which is unlikely under the employed reaction conditions.

The observed alcohol-dependent trends further show that the formation temperature of C-containing products on both $(WO_3)_3$ and $(MoO_3)_3$ decreases with increasing alkyl chain length (e.g. from methanol to 1-butanol) and chain number (e.g. from 1-butanol to 2- and t-butanol). This effect has been attributed to the increased inductive effect of the alkyl chains [51, 53] that lead to stabilization of carbo-cationic transition state and barrier lowering of the β-hydrogen elimination in the course of the dehydration reaction. The comparison of the overall alcohol conversion and relative yields of different reaction products for all alcohols is shown in Fig. 9.12. As already stated, the D_2O yields (gray bars) directly represent the total conversion yield on a per MO_3 basis. The obtained D_2O yield should be therefore identical with the sum of yields of all carbon-containing products (green + red + blue bars) and generally a good agreement is indeed seen. Dehydration is the major channel for all alcohols (except methanol) on $(WO_3)_3$. In contrast, on $(MoO_3)_3$, all channels (dehydration, dehydrogenation, and recombination) remain competitive for all primary alcohols. For secondary and tertiary alcohols, dehydration is dominant on both $(WO_3)_3$ and $(MoO_3)_3$.

9.4.3 Model Supported Catalytic Systems Based on $(WO_3)_3$ Clusters

The straightforward accessibility of such monodispersed clusters affords an excellent opportunity to utilize them as building blocks in the synthesis of well-defined supported model catalytic systems. These systems can in turn be used in model reactivity studies and yield valuable information about how the binding of
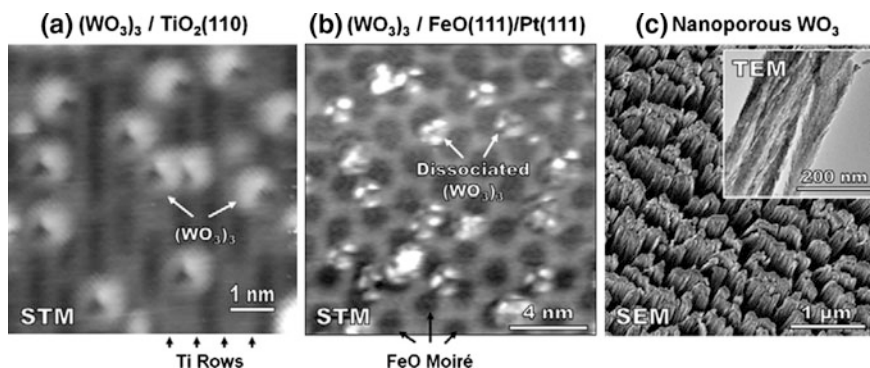
Fig. 9.13 a Empty-state scanning tunneling micrograph (STM) of isolated $(WO_3)_3$ nanoclusters following the $(WO_3)_3$ deposition on rutile $TiO_2(110)$ at 300 K and annealing to 600 K. The underlying rows (running vertically) of Ti and O ions that form troughs and ridges are imaged *bright* and *dark*, respectively. **b** Empty state STM image of dissociated $(WO_3)_3$ clusters deposited on FeO(111)/Pt(111) at 300 K. The underling honeycomb like structure is a moiré due to difference in the surface lattice constants of the FeO(111) bilayer and the underlying Pt(111) substrate. **c** Scanning (SEM) and transmission (TEM) electron micrographs of a ~ 1 μm thick nanoporous WO_3 film deposited at an incident angle of 85° and a substrate temperature of 20 K on a graphene monolayer on Pt(111). **a**, **b**, and **c** adapted with permission from [54, 56, 58], respectively

such identical building blocks on different substrates influence their activity. This approach is illustrated by a series of thermally robust models for $(WO_3)_3$ deposited in dispersed form on rutile $TiO_2(110)$ [54, 55] and FeO(111)/Pt(111) [56] and as a nanoporous WO_3 film on graphene/Pt(111) [57, 58]. The micrographs of these model systems are depicted in Fig. 9.13.

Figure 9.13a shows the appearance of $(WO_3)_3$ clusters on rutile $TiO_2(110)$ surface as revealed by high-resolution scanning tunneling microscopy (STM) [54, 55]. The supported clusters are prepared by room temperature deposition of $(WO_3)_3$ followed by annealing to 450-600 K. The images are dominated by very bright isolated $(WO_3)_3$ features that have a crescent-like appearance. The alternating bright and dark rows of low-and high-lying titanium and bridging oxygen rows, respectively, of the underlying corrugated $TiO_2(110)$ surface can be also recognized. The number of observed features were directly correlated with the total deposited mass of WO_3 as determined by a quartz crystal microbalance demonstrating that each bright feature indeed contains three WO_3 units as expected for cyclic $(WO_3)_3$. The atomistic structure of the $(WO_3)_3$ on $TiO_2(110)$ system was subsequently explored in theoretical studies using DFT based ab initio molecular dynamics (AIMD) [59, 60]. The calculations have shown a number of structures that were very close in energy with all structures forming multiple bonds that can be described in terms of Lewis acid–base interactions with electrons being donated from basic O_t to acidic surface titanium and from acidic W^{6+} to basic surface bridging oxygen sites.

The catalytic studies of 2-propanol on $(WO_3)_3$ on $TiO_2(110)$ have shown that the dehydration to propene is the primary reaction channel, similar to that observed for 2-propanol on unsupported $(WO_3)_3$ clusters (Fig. 9.12). In the TPD experiments, the propene yield dropped by a factor of three for clusters deposited at 100 K (relative to unsupported $(WO_3)_3$ clusters) and another factor of four following the cluster preannealing to 600 K. While the yield decreased significantly, the propene evolution temperature remained the same. The yield decrease was interpreted in terms of decreasing number of available dioxo, $O=W=O$, species as the temperature is increased and the clusters bound more strongly/reacted with the underlying $TiO_2(110)$. Sustained catalytic activity and propene yield was observed in isothermal reactive scattering experiments [46] demonstrating a true catalytic nature of this system.

Strong interactions of the $(WO_3)_3$ clusters with the substrate are observed on polar, oxygen terminated FeO(111) bilayer on Pt(111) which has been employed in numerous studies both as active catalysts and as supports for metal clusters [61, 62]. Due to the lattice mismatch between FeO(111) and Pt(111), a periodic hexagonal Moiré pattern (bright and dark areas) is formed as clearly visible in the high resolution STM image shown in Fig. 9.13b [56]. The combined STM, IRRAS, XPS and DFT-AIMD studies have shown that the $(WO_3)_3$ clusters dissociate already at 300 K to their monomeric WO_3 units. The theoretical studies further reveal that the highly oxophilic Fe^{2+} ions of the FeO interact strongly with electron rich $W=O$ bonds of the clusters and that each W^{6+} site possesses only a single terminal monoxo, $W=O$, moiety.

The 2-propanol conversion studies on this system have yielded only negligible amount of propene showing very low activity of the monoxo, $W=O$, species [56]. The propene desorption temperature was practically identical with that observed for $(WO_3)_3$ on $TiO_2(110)$ further indicating that the cluster binding to different substrates does not significantly influence the energetics of the dehydration reaction.

Further evidence for high activity of dioxo, $O=W=O$, relative to monoxo, $W=O$, moieties was obtained from alcohol reactivity studies on nanoporous WO_3 films that were prepared by ballistic deposition of $(WO_3)_3$ [57, 58]. This method is based on a deposition at low substrate temperatures under limited surface diffusion conditions. Under such conditions the species impinging from the vapor phase are incorporated at and/or very near the site where they initially land (hit and stick) which results in the formation of nanoporous films [63, 64]. Surface area of the films further increases with increased incident angle of the deposited material (here $(WO_3)_3$) due to shadowing and leads to the formation of columnar film structure such as the one shown for WO_3 in Fig. 9.13c.

The dehydration of 1-propanol was studied on such nanoporous films as a function of annealing temperature. The propane yield was compared with the surface area (from physisorbed amount of krypton) and the integrated intensity of $W=O$ stretch (from IRRAS) as a function of annealing which induced densification [57]. Interestingly, the integrated $W=O$ stretching band in IRRAS which here represents the sum of both monooxo and dioxo species decreased in the same

fashion as the film surface area. In contrast, the propene yield decreased significantly faster than the sum of the monooxo and dioxo species. The faster decrease in the reactivity as compared with the surface area or the intensity of the W=O stretch was interpreted to be a result of thermal conversion of the dioxo species (dehydration active) to monooxo species (dehydration inactive), as schematically shown in (9.5) below.

$$O_{\diagdown}\,\,_{\diagup}O \quad \xrightarrow{\text{T}} \quad \overset{O}{\underset{\diagup \, \diagdown}{\parallel}} \quad \xrightarrow{\text{T}} \quad _{\diagup} W_{\diagdown} \tag{9.5}$$
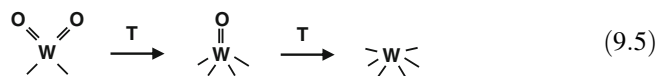
The studies have shown that the propene yield correlates well with the coverage of dioxo, O=W=O species obtained from a simple model assuming random annihilation of W=O bonds independent of whether they are in dioxo and/or monoxo species. The interpretation was further supported by DFT-AIMD calculations of the reaction mechanisms on both types of species [57].

In summary, in this section we have illustrated how studies of $(MO_3)_3$ in reactive matrices and on planar model supports can provide a wealth of insight on the details of the structure, reactivity and energetics of these catalysts. In general, reactivity of these species towards organic molecules is found to be governed by the terminal M=O oxo groups with dioxo species shown to be necessary for catalytic reactions such as alcohol hydration and dehydrogenation. The stronger Lewis acidity of the W^{6+} sites relative to the Mo^{6+} analogue enhances the overall reactivity of these centers but the more easily reducible Mo^{6+} leads to a higher selectivity towards oxidation reactions (e.g. ethanol to acetaldehyde). Interestingly, the reaction yields on different substrates have been found to vary dramatically, primarily due the annihilation of dioxo groups as a result of differences in cluster binding. Surprisingly, no substrate induced changes have been observed in the overall energetics of observed reactions.

9.5 Summary

In summary, in this chapter we illustrated the unique chemical properties that can be realized by oxide nanostructuring in the form of continuous ultra-thin films, extended islands and/or supported nanoclusters. Such structures allow for stabilization of distinct structural motifs that can be exploited in desired catalytic transformations. Properties of such complex systems are challenging to understand and predict. As such, they require the use of model systems that allow us to unravel the key descriptors defining the structure-activity relationships. Planar models employed in the studies highlighted here are ideally suited to address such fundamental questions. We have demonstrated their importance on (a) metastable PdO films that promote facile C–H bond activation and oxidation of alkanes, (b) multifunctional catalytic sites at copper/cerium-oxide island interfaces that are highly

active in water-gas shift reactions, and (c) $(WO_3)_3$ and $(MoO_3)_3$ nanoclusters with active dioxo, O=M=O, moieties that efficiently catalyze dehydration and partial oxidation of alcohols. Despite the unparalleled level of structural and chemical characterization provided by detailed imaging and spectroscopic studies of such model systems, close coupling with theoretical studies is critical if one strives to achieve detailed understanding of underlying reaction mechanisms.

References

1. Weaver JF, Devarajan SP, Hakanoglu C (2009) Facile C–H bond cleavage and deep oxidation of propane on a PdO(101) thin film. J Phys Chem C 113(22):9773–9782
2. Weaver JF, Hakanoglu C, Antony A, Asthagiri A (2011) High selectivity for primary C–H bond cleavage of propane σ-complexes on the PdO(101) surface. J Am Chem Soc 133 (40):16196–16200
3. Weaver JF, Hinojosa JA Jr, Hakanoglu C, Antony A, Hawkins JM, Asthagiri A (2011) Precursor-mediated dissociation of n-butane on a PdO(101) thin film. Catal Today 160 (1):213–227
4. Hakanoglu C, Zhang F, Antony A, Asthagiri A, Weaver JF (2013) Selectivity in the initial C–H bond cleavage of n-butane on PdO(101). Phys Chem Chem Phys 15(29):12075–12087
5. Weaver JF (2013) Surface chemistry of late transition metal oxides. Chem Rev 113(6):4164–4215
6. McCarty JG (1995) Kinetics of PdO combustion catalysis. Catal Today 26(3–4):283–293
7. Westerström R, Messing ME, Blomberg S, Hellman A, Grönbeck H, Gustafson J, Martin NM, Balmes O, van Rijn R, Andersen JN, Deppert K, Bluhm H, Liu Z, Grass ME, Hävecker M, Lundgren E (2011) Oxidation and reduction of Pd(100) and aerosol-deposited Pd nanoparticles. Phys Rev B 83(11):115440
8. van Rijn R, Balmes O, Resta A, Wermeille D, Westerstrom R, Gustafson J, Felici R, Lundgren E, Frenken JWM (2011) Surface structure and reactivity of Pd(100) during CO oxidation near ambient pressures. Phys Chem Chem Phys 13(29):13167–13171
9. Hellman A, Resta A, Martin NM, Gustafson J, Trinchero A, Carlsson PA, Balmes O, Felici R, van Rijn R, Frenken JWM, Andersen JN, Lundgren E, Grönbeck H (2012) The active phase of palladium during methane oxidation. J Phys Chem Lett 3(6):678–682
10. Martin NM, Van den Bossche M, Hellman A, Grönbeck H, Hakanoglu C, Gustafson J, Blomberg S, Johansson N, Liu Z, Axnanda S, Weaver JF, Lundgren E (2014) Intrinsic ligand effect governing the catalytic activity of pd oxide thin films. ACS Catal 4(10):3330–3334
11. Crabtree RH (1993) Transition metal complexation of σ bonds. Angew Chem Int Ed 32 (6):789–805
12. Crabtree RH (1995) Aspects of methane chemistry. Chem Rev 95(4):987–1007
13. Hall C, Perutz RN (1996) Transition metal alkane complexes. Chem Rev 96(8):3125–3146
14. Bercaw JE, Labinger JA (2007) The coordination chemistry of saturated molecules. Proc Natl Acad Sci USA 104(17):6899–6900

15. Weaver JF, Hakanoglu C, Antony A, Asthagiri A (2014) Alkane activation on crystalline metal oxide surfaces. Chem Soc Rev 43(22):7536–7547
16. Kan HH, Shumbera RB, Weaver JF (2008) Adsorption and abstraction of oxygen atoms on Pd (111): characterization of the precursor to PdO formation. Surf Sci 602(7):1337–1346
17. Kan HH, Weaver JF (2008) A PdO(101) thin film grown on Pd(111) in ultrahigh vacuum. Surf Sci 602(9):L53–L57
18. Kan HH, Weaver JF (2009) Mechanism of PdO thin film formation during the oxidation of Pd (111). Surf Sci 603(17):2671–2682
19. Hinojosa JA Jr, Weaver JF (2011) Surface structural evolution during the thermal decomposition of a PdO(101) thin film. Surf Sci 605(19–20):1797–1806
20. Rogal J, Reuter K, Scheffler M (2004) Thermodynamic stability of PdO surfaces. Phys Rev B 69(7):075421
21. Weaver JF, Hakanoglu C, Hawkins JM, Asthagiri A (2010) Molecular adsorption of small alkanes on a PdO(101) thin film: Evidence of σ-complex formation. J Chem Phys 132 (2):024709
22. Antony A, Hakanoglu C, Asthagiri A, Weaver JF (2012) Dispersion-corrected density functional theory calculations of the molecular binding of n-alkanes on Pd(111) and PdO(101). J Chem Phys 136(5):054702
23. Tait SL, Dohnálek Z, Campbell CT, Kay BD (2005) n-alkanes on MgO(100). II. Chain length dependence of kinetic desorption parameters for small n-alkanes. J Chem Phys 122:164708
24. Antony A, Asthagiri A, Weaver JF (2012) Pathways for C–H bond cleavage of propane σ-complexes on PdO(101). Phys Chem Chem Phys 14(35):12202–12212
25. Antony A, Asthagiri A, Weaver JF (2013) Pathways and kinetics of methane and ethane C–H bond cleavage on PdO(101). J Chem Phys 139(10):104702
26. Kinnunen NM, Hirvi JT, Suvanto M, Pakkanen TA (2011) Role of the interface between pd and pdo in methane dissociation. J Phys Chem C 115(39):19197–19202
27. Nakamura J, Campbell JM, Campbell CT (1990) Kinetics and mechanism of the water-gas shift reaction catalysed by the clean and Cs-promoted Cu(110) surface: a comparison with Cu (111). J Chem Soc Faraday Trans 86(15):2725–2734
28. Campbell CT, Daube KA (1987) A surface science investigation of the water-gas shift reaction on Cu(111). J Catal 104(1):109–119
29. Campbell CT, Koel BE (1987) A model study of alkali promotion of water-gas shift catalysts: Cs/Cu(111). Surf Sci 186(3):393–411
30. Jakdetchai O, Nakajima T (2002) Mechanism of the water–gas shift reaction over Cu(110), Cu (111) and Cu(100) surfaces: an AM1-d study. J Mol Struct (Thoechem) 619(1–3):51–58
31. Lin C-H, Chen C-L, Wang J-H (2011) Mechanistic studies of water–gas-shift reaction on transition metals. J Phys Chem C 115(38):18582–18588
32. Tang Q-L, Chen Z-X, He X (2009) A theoretical study of the water gas shift reaction mechanism on Cu(111) model system. Surf Sci 603(13):2138–2144
33. Gokhale AA, Dumesic JA, Mavrikakis M (2008) On the mechanism of low-temperature water gas shift reaction on copper. J Am Chem Soc 130(4):1402–1414
34. Rodriguez JA, Graciani J, Evans J, Park JB, Yang F, Stacchiola D, Senanayake SD, Ma S, Pérez M, Liu P, Sanz JF, Hrbek J (2009) Water-gas shift reaction on a highly active inverse CeOₓ/Cu(111) catalyst: unique role of ceria nanoparticles. Angew Chem 121(43):8191–8194
35. Mudiyanselage K, Senanayake SD, Feria L, Kundu S, Baber AE, Graciani J, Vidal AB, Agnoli S, Evans J, Chang R, Axnanda S, Liu Z, Sanz JF, Liu P, Rodriguez JA, Stacchiola DJ (2013) Importance of the metal-oxide interface in catalysis: in situ studies of the water-gas shift reaction by ambient-pressure x-ray photoelectron spectroscopy. Angew Chem Int Edit 52 (19):5101–5105
36. Stacchiola DJ, Senanayake SD, Liu P, Rodriguez JA (2013) Fundamental studies of well-defined surfaces of mixed-metal oxides: special properties of MOₓ/TiO₂(110) {M = V, Ru, Ce, or W}. Chem Rev 113(6):4373–4390
37. Park JB, Graciani J, Evans J, Stacchiola D, Senanayake SD, Barrio L, Liu P, Sanz JF, Hrbek J, Rodriguez JA (2010) Gold, copper, and platinum nanoparticles dispersed on CeOₓ/TiO₂(110)

surfaces: high water-gas shift activity and the nature of the mixed-metal oxide at the nanometer level. J Am Chem Soc 132(1):356–363

38. Schwab GM (1967) Boundary-layer catalysis. Angew Chem Int Edit 6(4):375

39. Schwab GM, Siegert R (1966) Inverse Mischkatalysatoren. I. Kohlenmonoxid-Oxydation an Nickeloxid Auf Silber. Z Phys Chem Neue Fol 50(3–4):191-&

40. Hayek K, Kramer R, Paal Z (1997) Metal-support boundary sites in catalysis. Appl Catal A Gen 162(1–2):1–15

41. Kung HH (1989) Transition metal oxides: surface chemistry and catalysis. Studies in surface science and catalysis, vol 45. Elsevier, New York

42. Jackson DS, Hargreaves JSJ (2009) Metal oxide catalysis, vol 2. Wiley, Weinheim

43. Li Z, Fang Z, Kelley MS, Kay BD, Rousseau R, Dohnalek Z, Dixon DA (2014) Ethanol conversion on cyclic $(MO_3)_3$ (M = Mo, W) clusters. J Phys Chem C 118(9):4869–4877

44. Yang Y, Zhou J, Nakayama M, Nie L, Liu P, White MG (2014) Surface dipoles and electron transfer at the metal oxide-metal interface: a 2PPE Study of size-selected metal oxide clusters supported on Cu(111). J Phys Chem C 118(25):13697–13706

45. Tang X, Bumueller D, Lim A, Schneider J, Heiz U, Ganteför G, Fairbrother DH, Bowen KH (2014) Catalytic dehydration of 2-propanol by size-selected $(WO_3)_n$ and $(MoO_3)_n$ metal oxide clusters. J Phys Chem C 118(50):29278–29286

46. Rousseau R, Dixon DA, Kay BD, Dohnalek Z (2014) Dehydration, dehydrogenation, and condensation of alcohols on supported oxide catalysts based on cyclic $(WO_3)_3$ and $(MoO_3)_3$ clusters. Chem Soc Rev 43(22):7664–7680

47. Li SG, Dixon DA (2006) Molecular and electronic structures, Bronsted basicities, and Lewis acidities of group VIB transition metal oxide clusters. J Phys Chem A 110(19):6231–6244

48. Li SG, Guenther CL, Kelley MS, Dixon DA (2011) Molecular structures, acid-base properties, and formation of group 6 transition metal hydroxides. J Phys Chem C 115(16):8072–8103

49. Li S, Dixon DA (2013) Structural and electronic properties of group 6 transition metal oxide clusters. In: Suib S (ed) new and future development in catalysis: catalysis by nanoparticles. Elsevier, Amsterdam, pp 21–61

50. Fang Z, Li Z, Kelley MS, Kay BD, Li S, Hennigan JM, Rousseau R, Dohnálek Z, Dixon DA (2014) Oxidation, reduction, and condensation of alcohols over $(MO_3)_3$ (M = Mo, W) nanoclusters. J Phys Chem C 118(39):22620–22634

51. Kim YK, Dohnálek Z, Kay BD, Rousseau R (2009) Competitive oxidation and reduction of aliphatic alcohols over $(WO_3)_3$ clusters. J Phys Chem C 113(22):9721–9730

52. Kim YK, Rousseau R, Kay BD, White JM, Dohnálek Z (2008) Catalytic dehydration of 2-propanol on $(WO_3)_3$ clusters on $TiO_2(110)$. J Am Chem Soc 130(15):5059–5061

53. Kim YK, Kay BD, White JM, Dohnálek Z (2007) Alcohol chemistry on rutile $TiO_2(110)$: the influence of alkyl substituents on reactivity and selectivity. J Phys Chem C 111(49):18236–18242

54. Bondarchuk O, Huang X, Kim J, Kay BD, Wang LS, White JM, Dohnálek Z (2006) Formation of monodisperse $(WO_3)_3$ clusters on $TiO_2(110)$. Angew Chem Int Ed 45(29):4786–4789

55. Kim J, Bondarchuk O, Kay BD, White JM, Dohnálek Z (2007) Preparation and characterization of monodispersed WO_3 nanoclusters on $TiO_2(110)$. Catal Today 120(2):186–195

56. Li SC, Li Z, Zhang Z, Kay BD, Rousseau R, Dohnalek Z (2012) Preparation, characterization, and catalytic properties of tungsten trioxide cyclic trimers on FeO(111)/Pt(111). J Phys Chem C 116(1):908–916

57. Li ZJ, Šmíd B, Kim YK, Matolín V, Kay BD, Rousseau R, Dohnálek Z (2012) Alcohol dehydration on Monooxo W=O and Dioxo O=W=O species. J Phys Chem Lett 3(16):2168–2172

58. Šmíd B, Li Z, Dohnálková A, Arey BW, Smith RS, Matolin V, Kay BD, Dohnálek Z (2012) Characterization of nanoporous WO_3 films grown via ballistic deposition. J Phys Chem C 116(19):10649–10655

59. Zhu J, Jin H, Chen WJ, Li Y, Zhang YF, Ning LX, Huang X, Ding KN, Chen WK (2009) Structural and electronic properties of a W_3O_9 cluster supported on the $TiO_2(110)$ surface. J Phys Chem C 113(40):17509–17517
60. Di Valentin C, Rosa M, Pacchioni G (2012) Radical versus nucleophilic mechanism of formaldehyde polymerization catalyzed by $(WO_3)_3$ clusters on reduced or stoichiometric $TiO_2(110)$. J Am Chem Soc 134(34):14086–14098
61. Shaikhutdinov SK, Meyer R, Lahav D, Baumer M, Kluner T, Freund HJ (2003) Determination of atomic structure of the metal-oxide interface: Pd nanodeposits on an FeO(111) film. Phys Rev Lett 91(7):076102
62. Fu Q, Li W-X, Yao Y, Liu H, Su H-Y, Ma D, Gu X-K, Chen L, Wang Z, Zhang H, Wang B, Bao X (2010) Interface-confined ferrous centers for catalytic oxidation. Science 328 (5982):1141–1144
63. Barabasi AL, Stanley HE (1995) Fractal concepts in surface growth. Cambridge University Press, Cambridge
64. Stevenson KP, Kimmel GA, Dohnálek Z, Smith RS, Kay BD (1999) Controlling the morphology of amorphous solid water. Science 283(5407):1505–1507

Chapter 10
Charge Transfer Processes on Ultrathin Oxide Films

Thomas Risse

Abstract This chapter is concerned with charge transfer processes on ultrathin oxide films. The discussion is centered around Au deposited on ultrathin single crystalline oxide films as model systems to illustrate the different effects associated with charge transfer processes. Apart from Au atoms and 1- or 2-dimensional Au particles the behavior of oxygen (O_2) as an example for a molecule with high electron affinity will be discussed.

10.1 Introduction

Charge transfer is ubiquitously found in nature and is, hence, very important to all natural sciences, which may be illustrated by the fact that every oxidation or reduction reaction involves charge transfer. Consequently, it is at the heart of many important technological as well as natural systems. There is a countless number of examples such as electrochemical electrodes, photovoltaic devices, or complex natural processes such as photosynthesis to name only few. Photosystem II is a beautiful example to illustrate the complex interplay between geometric and electronic structure that is required to enable the transfer of four electrons needed for the reduction of water to molecular oxygen. Tremendous advances have been achieved over the years to understand charge transfer processes in various branches of science including surfaces in general and oxide surfaces in particular [1–4]. These processes may be classified into transient charge transfer states as created e.g. after photo excitation and processes, which create metastable charge transfer products such as molecular radicals. One of the first observations proving the charge transfer from an oxide surface to an adsorbate goes back to work by Lunsford, who

T. Risse (✉)
Institute for Chemistry and Biochemistry, Freie Universität Berlin, Takustreet 3, 14195 Berlin, Germany
e-mail: risse@chemie.fu-berlin.de

T. Risse
Berlin Joint EPR Laboratory, FU Berlin, Germany

employed electron paramagnetic resonance (EPR) spectroscopy showing that defect sites on MgO can serve as electron donor sites for electron transfer. This was exemplified by the spontaneous formation CO_2^- radicals upon adsorption onto so-called color center at the surface of MgO [5]. Within this chapter we will restrict the discussion to spontaneous charge transfer processes only and will not discuss induced charge transfer processes any further.

Conceptually charge transfer involves a donor and an acceptor of the charge. The nature of these species at solid surfaces and interfaces depend crucially on the properties of the system under investigation. The theoretical framework used to describe such processes has been reviewed in detail in various articles and will not be presented here in detail again [6, 7]. In brief, if an electron is transferred from a donor state D into an acceptor state A the appropriate description of the system depends on the strength of the electron-nuclear coupling. If the coupling is strong, electron transfer is controlled by nuclear motion. The rate of electron transfer in such a strongly coupled system may be conveniently described by classical Marcus theory in which the nuclear motion is described by harmonic oscillators for both the reactant as well as the product states. On the contrary, if electron-nuclear coupling is weak a nonadiabatic description in the potential energy surfaces of the initial and the final state may be used and the transition rate can be approximated within a perturbative treatment to depend to first-order on the matrix element describing the electronic coupling between the initial and the final state and the overlap of the nuclear wave functions, so-called Franck-Condon factors, of educts and products corresponding to the same electronic energy.

From this discussion it is readily clear that a proper description of charge transfer processes at surfaces requires detailed knowledge about the potential energy hypersurfaces. Such information can only be gathered for systems characterized at the atomic level. Epitaxial, single crystalline oxide films grown on metal surfaces allow for such an atomic level characterization employing modern surface science tools [8, 9]. These films may serve as suitable models for bulk oxides, which might be intended if such systems are considered as supports for heterogeneous model catalysts. In case ultrathin films of a few monolayer thickness are used the coupling of the oxide surface to the metal support may alter the properties of the surface significantly, however, it depends crucially on the system under consideration whether or not significant changes occur. Hence, detailed investigations are required to elucidate this aspect. Charge transfer processes being the central topic of this chapter can serve as an example for such a change of surface properties if comparing thin films with bulk single crystals. It should be noted in passing that charge transfer processes on wide band gap semiconductor surfaces are not limited to ultrathin films, but may also be found for bulk systems if these have been appropriately modified e.g. by doping with appropriate transition metal ions [10, 11].

Within this chapter we will not try to give an exhaustive review on the topic of charge transfer on ultrathin oxide films but rather focus on few examples that can be used to illustrate the different effects to be considered. In particular we will use Au deposited onto oxide surfaces as a prototype system, which will be complemented by discussing the adsorption of oxygen molecules onto ultrathin MgO film to

illustrate that several of the concepts are not restricted to metals. This chapter is focusing on experimental results, however, it needs to be stressed that the microscopic understanding of the processes are largely driven by the intimate interplay between experiment and theory and particular care has been taken to highlight the important contributions of theory throughout the discussion. The interested reader may, however, be referred to recent, more theory oriented reviews on this topic for a more detailed discussion of theses aspects [12, 13].

10.2   Adsorption of Atoms and Molecules

Atoms and simple molecules are a good starting point for the discussion of charge transfer processes at ultrathin oxide films as they already show many of the effects that are important to understand these processes. We will start the discussion with molecular oxygen as an example for a molecular adsorbate with high electron affinity and then turn to Au atoms, which will be the first step towards the understanding of more complex Au particles being discussed in the following.

10.2.1 O_2 on Ultrathin MgO

Molecular oxygen adsorbes weakly on the stoichiometric (001)-surface of bulk MgO. This is in line with expectations based on the ionic nature of MgO with a band gap of more than 7 eV. The band gap of MgO converges to the bulk value already for a very thin film, however, the Fermi level of the metal support is located within the band gap of the oxide [14]. Electron transfer will be possible if the film is thin enough to allow for a tunneling of an electron provided that the total energy of the system decreases. Charge transfer onto an adsorbate is expected in a simple band structure model if the affinity level of the adsorbate is located below the Fermi level of the support, which will occur to first approximation if the electron affinity of the adsorbate exceeds the work function of the support. Therefore charge transfer was predicted for molecules with high electron affinities such as NO_2 or O_2 adsorbed on ultrathin MgO(001) films grown on Ag(001) or Mo(001), which show a reduction of the work function as compared to the clean metal surfaces [15–17].

As compared to the weak adsorption on the (001) surface of bulk MgO, theory predicts a strongly enhanced adsorption energy of −0.82 and −1.5 eV on thin MgO (001) films grown on Ag(001) or Mo(001), respectively [16, 17]. The chemisorbed molecules are negatively charged and adopt a flat adsorption geometry on the MgO surface with the oxygen molecule bridging between two Mg cations. A detailed analysis of the adsorption complex shows, that a so-called polaronic distortion of the MgO lattice contributes significantly the adsorption energy of the molecule. In particular the Mg cations are lifted out of the surface plane (Fig. 10.1c). From an experimental point of view the characterization of the superoxide anion can be
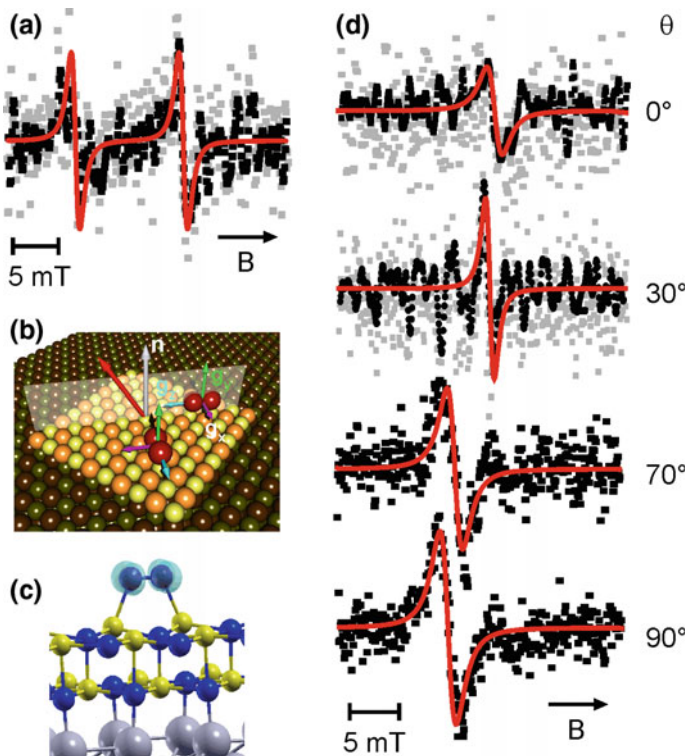
Fig. 10.1 a EPR spectrum of 20 L O_2 adsorbed at 40 K on a 4 ML thick MgO(001) film on Mo (001) with the magnetic field in the surface plane along a [110] equivalent direction. **b** sketch of oxygen molecules adsorbed on 2 ML MgO films as predicted by theory. The transparent plane indicates the plane in which the magnetic field was lying in (**a**). The orientation of the three principal components of the g-matrix of the two symmetry equivalent molecules are shown as color coded *arrows*. As an EPR experiment probes the g-value oriented along the static magnetic field it readily clear that both molecules are not identical for the magnetic field lying in the surface plane. **c** result of a DFT calculation of O_2 on a 2 ML thin MgO(001) film on Mo(001) showing the polaronic distortion of the MgO lattice. **d** EPR spectra taken for 20 ML O_2 adsorbed at 30 K on a 4 ML MgO(001) grown on Mo(001) as a function of the polar angle θ. The magnetic field was oriented in a plane spanned by a [100] equivalent direction in the surface and the surface normal ([001] direction). Adapted from [20]

approached using EPR spectroscopy as the superoxide anion is a radical with a doublet ground state. EPR spectroscopy is a powerful tool to characterize paramagnetic systems and was shown to have the required sensitivity to detect radicals on planar single crystal surfaces with less than a per mill of a monolayer [18]. On the one hand it has to be kept in mind that the method requires paramagnetic species and as such will be blind for all other species on the surface. In addition spin physics may hamper the detection of paramagnetic species. A well-known example is the so-called Korringa exchange between a paramagnetic center and the conduction band electrons of a metal, which leads to very broad lines and renders the detection

of EPR signals impossible on planar metal surfaces [19]. On the other hand EPR has a very high energetic resolution as compared to other spectroscopies used in surface science, which allows to discriminate centers with very similar properties. On single crystal surfaces it is even more important that the magnetic interactions such as the Zeeman interaction (electron spin with magnetic field) or the hyperfine interaction (electron spin with nuclear spins) are anisotropic. Symmetric interaction matrices having a principal axis system, which is uniquely defined for each system, describe these anisotropic interactions. Angular dependent measurements allow determining the orientation of theses interaction matrices and by that provides direct access to geometric properties of the systems. Concomitantly, these measurements provide the values of the principal components of the matrices, which encode information on the electronic properties as well as the local chemical environment of the paramagnetic species. To illustrate this strategy we will now return to the discussion of the superoxide anion radical. The spectrum of the $^{16}O_2{}^-$ radical is determined by an anisotropic Zeeman interaction. For systems with sufficiently high symmetry such as the $O_2{}^-$ radical the principal axis system of the g-matrix is linked to the high symmetry directions of the system. In case of the theoretically predicted adsorption geometry of the superoxide radical on ultrathin MgO(001) films, one of the principle axis is aligned with molecular axis, one is the surface normal and the third one is mutual perpendicular on the two others as shown in Fig. 10.1b. An EPR spectrum obtained after adsorbing 20 L molecular oxygen at 40 K on a 4 ML thick MgO(001) film grown on Mo(001) is shown in Fig. 10.1a [20]. The magnetic field was oriented in the surface plane collinear with a [110] equivalent direction (see Fig. 10.1b). The spectrum consists of a doublet of lines at g-values of 2.072 and 2.002, respectively. The signal positions are well in line with the expectations for $O_2{}^-$ species as found on chemically modified MgO powder for which two g-matrix (g_{xx}, g_{yy}) components were found between 2.0023 and 2.007 while the third one (g_{zz}) varies between 2.062 and 2.091 depending on the adsorption site of the $O_2{}^-$ radical [21–23]. It is important to note that the signal is only observed for thin films and vanishes for film thickness above 15 ML. In line with the theoretical predictions the radicals are bound strongly to the support showing a desorption temperature of approximately 350 K.

As mentioned above a detailed analysis of the properties of the $O_2{}^-$ radical requires the determination of the principal components of the g-matrix as well as its orientation with respect to the surface. To determine the orientation of the tensor as well as its principal values angular dependent measurements are required, both in as well as out of the surface plane. The lowest trace in Fig. 10.1d shows the spectrum taken after rotating the crystal 45° in the surface plane, hence, with the magnetic field along a [100] equivalent direction. A single line at g = 2.0037 is observed. This is in perfect agreement with the expectation based on the theoretically predicted adsorption geometry. Spectra taken with the magnetic field oriented out the surface plane (Fig. 10.1d) show a $\cos^2$ dependence of the resonance position as a function of the out-of-plane angle θ with the extreme values found at 90° and 0°, respectively. Thus, two tensor components are oriented in the surface plane and the third component is oriented perpendicular to the surface. The two orthogonal components in plane are aligned to [110] equivalent directions as inferred from the

collapse of the splitting if the magnetic field is aligned along a [100] equivalent direction, which renders the two symmetry equivalent adsorption sites on the fourfold symmetric (001) surface also magnetically equivalent. Therefore, the EPR results prove on the one hand the formation of O_2^- radicals on ultrathin MgO films and on the other hand confirm the adsorption geometry as predicted by theory.

Additional insight into the adsorption properties can be obtained from a comparison of the g-tensor components with those found on bulk MgO powder, which are given in Table 10.1. Please note that the assignment on the powders is based on a detailed comparison between theory and experiment [24]. On powders the g_{zz} component is found to vary strongly for different adsorption sites. Theory shows that the value of the g_{zz} component reduces with decreasing coordination number. From a comparison between the experimental results on bulk MgO powder and the ultrathin film it is readily clear that the g_{zz} component observed on the film are much closer to the one observed for O_2^- adsorbed at edges of MgO powder, while the adsorption at terrace sites, which would correspond to the adsorption site of on the thin film, shows a significantly larger g_{zz} component on the powder. How is this apparent discrepancy reconciled? It is the polaronic distortion of the MgO lattice in case of the ultrathin film (see Fig. 10.1c) that is the origin of this effect and which have been elucidated in detail by quantum chemical calculations [20]. The essence of the effect may be described by a simple physical picture: the polaronic distortion increases the local electric field at the O_2^- radical as compared to an unperturbed flat terrace with little buckling of the ions. The same effect is found when moving the radical from the terrace to a low coordinated site such as an edge site. The increase of the electric field is also reflected in the adsorption geometry as extracted from the theoretical calculations. According to expectations the O_2^-–Mg distances shrinks, if comparing the adsorption on the terrace of a thin film with the terrace of a bulk oxide (Table 10.1). The resulting increased electric field, gives rise to an increase of the energy splitting between the two π^* orbitals of the oxygen radical being degenerate in the gas phase. In a simple crystal field picture the shift of g_{zz} component away from the free electron value is given by $g_{zz} = g_e + 2\left[\lambda^2/(\lambda^2 + \Delta^2)\right]^{1/2}$ [25], with λ being the spin orbit coupling constant and $\Delta = 2\pi_g^y - 2\pi_g^x$. The increase of Δ due to

Table 10.1 Measured and computed g-matrix components as well as computed distances for O_2^- adsorbed on the surface of MgO(001)/Mo(001) films and MgO powders

		g_{xx}	g_{yy}	g_{zz}	d(O–Mg)	d(O–O)
MgO/Mo(001) exp. [20]	Terrace	2.002	2.012	2.072	–	–
MgO powders exp. [22]	Terrace	2.002	2.008	2.091	–	–
MgO powders exp. [21]	Edge	2.002	2.008	2.077	–	–
MgO(001) theory [24][a]	Terrace	2.0022	2.0092	2.0639	2.329	1.345
MgO(001) theory [24][a]	Edge	2.0021	2.0096	2.0527	2.158	1.353
MgO(001) with polaronic distortion theory [20]	Terrace	2.0025	2.0093	2.0560	2.075	1.345

[a]Please note that the labelling of the axis is different in [24]

the increased electric field will lead to the expected reduction in the g_{zz} component. Consequently, the observed reduction of the g_{zz} component for the ultrathin film results can be taken as direct experimental evidence for the polaronic distortion of the MgO-film, which is an effect that plays an important role for the stabilization of the charge transfer states found on ultrathin ionic oxides as illustrated further below.

10.2.2 An Ultrathin FeO$_{2-X}$ Film on Pt(111)

The observed charge transfer onto the oxygen molecule is the initial step to activate the molecule and it is an obvious extension to look for the possibility to use this system as a catalyst for oxidation reactions. The ability to catalyze CO oxidation on ultrathin MgO films grown on Ag(001) was predicted theoretically [16], however, an experimental verification of this prediction is still lacking. The problem is that the Ag support is even more active towards CO oxidation, which renders it difficult to provide univocal evidence for the catalytic oxidation on the ultrathin MgO surface. There is, however, an ultrathin oxide film that exhibits surprising catalytic activity towards CO oxidation namely an ultrathin iron oxide film on Pt(111) [26]. As shown in Fig. 10.2 the pristine FeO(111)-film, which consists of a single layer of Fe and oxygen, forms a well-ordered film exhibiting a pronounced Moire structure due to the lattice mismatch between FeO and the Pt support [27–32]. This film is not reactive towards CO oxidation under ultrahigh vacuum conditions [27]. However, in case the film is exposed to a stoichiometric mixture of CO and oxygen at elevated pressures (40 and 20 mbar, respectively, filled to 1 bar with helium) significant CO oxidation activity is observed for temperatures above 430 K (Fig. 10.2b) [26, 33]. At this temperature the FeO/Pt(111) system is about an order of magnitude more reactive than clean platinum.

The microscopic origin of the catalytic activity for this particular iron oxide film has been elucidated combining experiments and density functional calculations [26]. Figure 10.2c summarizes the scenario. At elevated pressures molecular oxygen interacts with the pristine double layer FeO film on Pt(111) by pulling an iron atom to the surface of the film. The rearrangement causes a local reduction of the work function at the interface, which allows to transfer an electron onto the oxygen molecule. In contrast to MgO the O_2^- radical is only a transition state, which further reacts by accepting another electron to from a peroxide and finally dissociates to form more strongly oxidized Fe layer. For high enough oxygen partial pressure this process transforms the entire FeO film into an O–Fe–O trilayer system, whose STM image is shown in the center of Fig. 10.1c. The theoretical calculations reveal that the trilayer system if exposed to carbon monoxide can transform incoming CO to CO_2 via an Eley Rideal mechanism leaving behind an oxygen vacancy in the film. If oxygen pressure is sufficiently high the oxygen vacancies are filled again and the trilayer is sustained, which renders this trilayer film a heterogeneous catalyst.
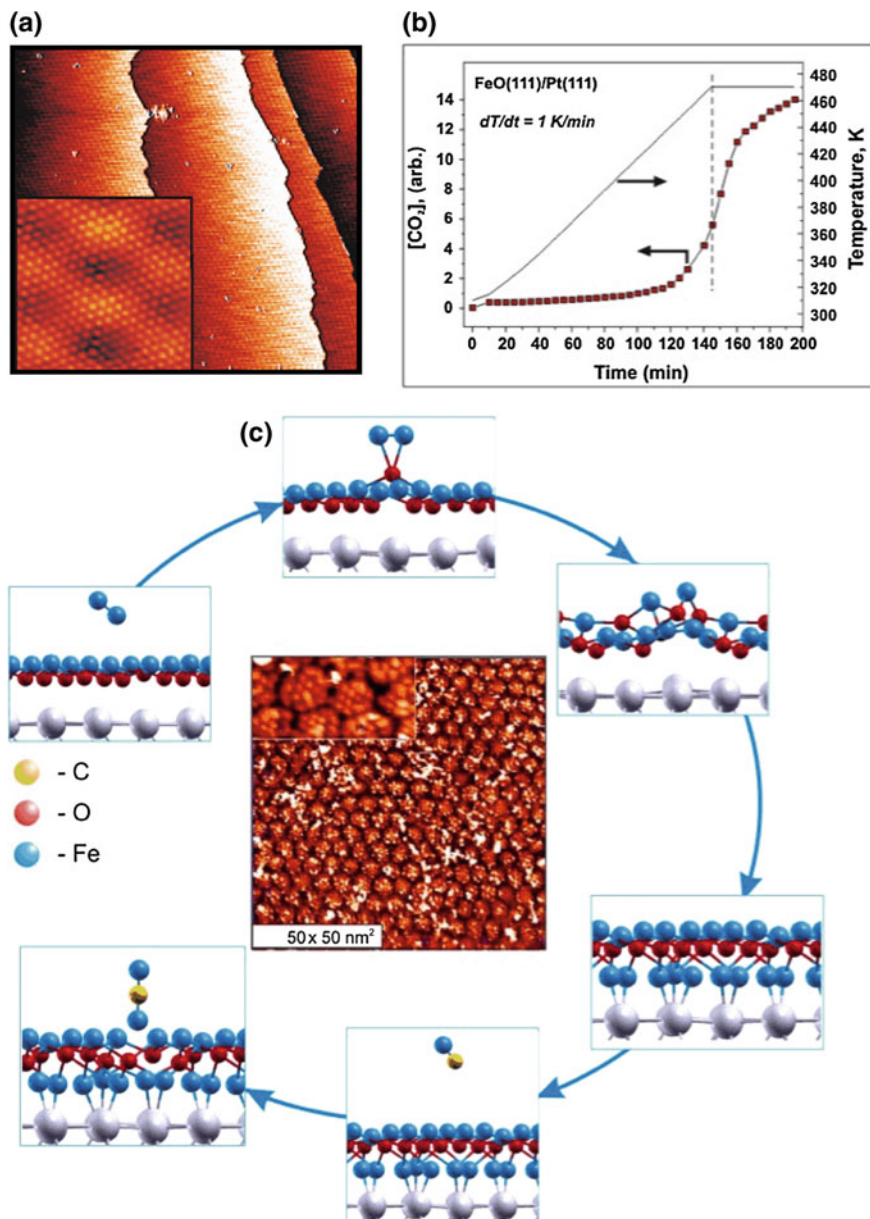
Fig. 10.2 a STM image of a pristine FeO(111) on Pt(111). The *inset* shows an atomically resolved image showing the Moire pattern between the film and the Pt support. **b** CO oxidation on FeO(111)/Pt(111) as a function of time and temperatures (1 K/min). The *dotted line* indicates the time when the temperature was held constant. **c** STM images of the FeO_{2-x}-phase. *Inset* higher resolution image of one of the islands. *Sketches* depict some of the steps as revealed by DFT calculations to from the trilayer (1–3) and its reaction with CO to form CO_2 (4,5). Adapted from [26, 94]

With respect to the central topic of this chapter it is important to stress that it is the initial electron transfer onto molecular oxygen the allows to transform the unreactive FeO(111) film into a catalyst for CO oxidation. Electron transfer to molecular adsorbates on ultrathin oxide films has to be considered a general concept provided that the system obeys the general requirements outlined above.

10.2.3 Single Gold Atoms Supported on Oxide Films

The interaction of individual Au atoms with stoichiometric oxide surfaces is typically weak as compared to the bond between Au atoms. Hence, Au atoms tend to aggregate on the surface and investigations on individual supported Au atoms require low temperature as well as low coverage. Deposition of Au atoms on ultrathin oxide films may alter this behavior, however, significant differences are observed depending on the nature of the oxide film. In the following we exemplify the changes that can occur discussing the adsorption of gold atoms on MgO(001)-films being a good starting point as these films have a simple geometric as well as electronic structure.

The preparation of single crystalline MgO(001) films on Mo(001) [34–36] and Ag(001) [37, 38] is well established and leads to well-defined, long-ranged ordered films. Prior to a discussion of the properties of Au atoms on ultrathin films it is instructive to discuss theses species on thicker, 15–20 monolayer (ML) MgO(001)-films on Mo(001). Au atoms were deposited on the pristine films at 35 K by physical vapor deposition (PVD). A singly occupied 6s orbital and correspondingly a ^{2}S ground state characterize Au atoms in the gas phase. Therefore, EPR spectroscopy is a suitable technique to investigate such species. The EPR spectrum of 0.01 ML equivalent Au is characterized by a quartet of lines (Fig. 10.3a) [39]. The
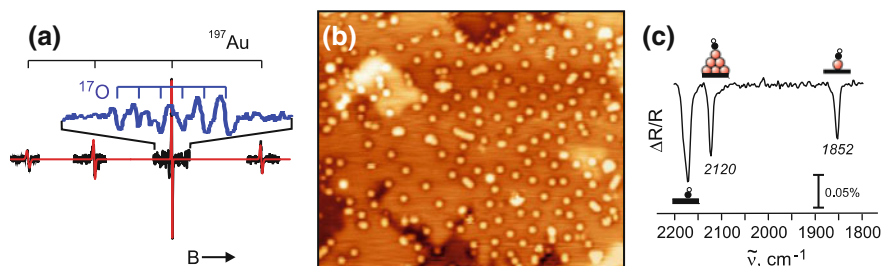
Fig. 10.3 a Experimental and simulated EPR spectra of 0.01 ML Au atoms adsorbed on a 20 ML thick MgO(001)film on Mo(001). Positions of the four expected ^{197}Au (I = 3/2) hyperfine lines are indicated above the spectrum. Please note that the splitting is not symmetric due to the fact that the hyperfine interaction is not small as compared to the Zeeman interaction. EPR spectrum of Au atoms on an ^{17}O enriched MgO film is shown in *blue*. **b** STM image (30 × 25 nm^2) of Au atoms (0.035 ML) deposited at 8 K on ∼8 ML thick MgO(001)/Ag(001) film. **c** IR-spectrum of CO adsorbed on Au atoms and clusters on a MgO(001) film. Adapted from [39, 44]

single line that is expected from transitions between the two spin states of the ^2S ground state is split by hyperfine interaction of the electron spin with the nuclear spin of the associated gold atom. As Au is an isotopically pure element (I (^{197}Au) = 3/2; 100 % natural abundance) each of the two energy levels of the electron spin state is split into four states due to hyperfine interaction, resulting in four resonance lines as the nuclear spin state is preserved in an EPR experiment. Along the lines discussed above for the superoxide radicals the orientation and the principal components of the g- and hyperfine-matrices can be determined from an analysis of angular dependent EPR spectra, which allows to conclude that Au atoms are located on terrace sites of the MgO(001) islands. This is in perfect agreement with low temperature STM results (Fig. 10.3b) [39]. The adsorption site of the Au atoms can be determined from EPR spectroscopy taking spectra of Au atoms deposited on ^{17}O enriched (about 90 %) MgO films (Fig. 10.3a, blue trace). As illustrated the most intense of the hyperfine lines of the Au atoms splits into six resonances due to the hyperfine interaction with ^{17}O. This is in line with expectations for the interaction of Au atoms with a single oxygen ion (I(^{17}O) = 5/2) and allows to conclude that the Au atom adsorb on-top of oxygen ions in agreement with theoretical predictions [40–42]. Apart from this qualitative analysis interesting information on the electronic properties is encoded in the values of the hyperfine tensor components. As compared to Au atoms in the gas phase the isotropic part of the gold hyperfine interaction, which is associated with the spin density at the nucleus due to so-called Fermi contact interaction, is reduced by about 50 %. There are two possibilities how such a reduction can come about. One is a charge transfer into or from the Au atom, which reduces the spin density. Alternatively, there might by a redistribution of the electron density upon binding to the surface. A discrimination of the two scenarios is not possible based on the experimental results only. However, it is possible to differentiate between them using theory. DFT calculations showed that the reduction of the isotropic hyperfine interaction is due to a polarization of the singly occupied 6s orbital of neutral Au atoms away from the MgO surface. In a simple orbital picture the polarization can be rationalized as an admixture of contributions with higher angular momentum to the wave function leading to a reduction of the spin density at the nucleus [39].

Another technique often used to investigate the properties of adsorbed species is infrared (IR) spectroscopy. For deposited metal atoms usually the stretching frequency of simple probe molecules such as CO are used to elucidate the properties of the system. Gold catalysts were extensively investigated using this approach ([43] and references therein). The adsorption of CO onto these systems results in two IR bands centered at 2120 and 1852 cm^{-1} (Fig. 10.3c) [44]. The signal at 2120 cm^{-1} is due to CO adsorbed on small Au clusters. If larger amounts of Au are deposited, hence, larger Au clusters are produced this band shifts towards lower frequencies to be found around 2100 cm^{-1}. The line at 1852 cm^{-1} is associated with single Au atoms. It is red-shifted by 291 cm^{-1} as compared to the value found for gas-phase CO and by 180 cm^{-1} as compared to the Au–CO complex in the gas-phase [45], respectively. The large red-shift, indicating a significant charge transfer into the π*-orbital of the CO, is usually thought to be indicative of charge

transfer, namely the formation of negatively charged Au atoms, which would, however, be inconsistent with the results from EPR spectroscopy discussed above. Again a theoretical analysis of this system allows reconciling these observations. Form the theoretical analysis it is concluded that the large polarization of Au 6s valence electron renders a partial transfer of electron density to the adsorbed CO molecule possible leading to a $Au^{\delta+}CO^{\delta-}$ complex on the surface. This shows that particularly for atoms or very small clusters probe molecules such as CO may fail to properly report on the properties of the underlying metal [44].

From these investigations on relatively thick MgO(001) films it is concluded that Au atoms are neutral entities, however, it became already clear that the deposited Au atoms are strongly polarized and allow for charge transfer if appropriate acceptors such as CO adsorb. The question arises if it is possible to manipulate the interaction between the oxide surface and gold atoms by changing the properties of the oxide. There are various ways of doing so. One possibility is to create reactive centers on the surface. To this end point defects are particularly interesting and in can be shown that is oxygen vacancies also known as color centers are suitable centers to induce a charge transfer between these centers and deposited Au atoms. Using a combination of STM/STS and EPR spectroscopy it is possible to show that oxygen vacancies intentionally created by electron bombardment are located on edges and corners of the MgO islands [46, 47]. If Au atoms are nucleating to these color centers they become negatively charged, as verified by a combination of IR spectroscopy and theoretical calculations [46].

In this section we will focus on the effect of ultrathin films of only a few monolayer in thickness. Theory had proposed that Au deposited onto ultrathin MgO films get negatively charged due to a charge transfer from the metal substrate onto gold [48]. Qualitatively this can be understood by the fact that the unoccupied part of the Au 6s level found in the band gap on thick films is located below the Fermi-energy of the support for the thin film system. As discussed above there are different contributions to this effect. First, the deposition of MgO onto the metal substrate reduces the work function of the system, which has been confirmed both theoretically as well as experimentally [14, 49, 50]. Second, charged Au atoms adsorbed on the surface of the ultrathin MgO film are stabilized by polaronic distortions of the oxide lattice [15, 51].

Experimental evidence for the charging of Au atoms on ultrathin MgO(001) films comes from low-temperature scanning tunneling microscopy (STM) experiments. As seen from the STM images shown in Fig. 10.4a, b Au atoms deposited 3 ML and 8 ML thin MgO films (T = 5–10 K) form an ordered structure indicating significant repulsion between the Au atoms [52]. In contrast to that adsorption of Pd atoms under the same condition on a 3 ML MgO film (Fig. 10.4c) reveals no evidence for the formation of an ordered structure. The observation for Pd is in perfect agreement with expectations based on a statistical distribution of the atoms as shown by the radial distance distribution (Fig. 10.4e), while the same quantity for the Au atoms exemplarily shown for Au atoms on 3 ML MgO reveal maxima indicative for an ordered arrangement of the atoms (Fig. 10.4d) [53]. The formation of the ordered structure observed for Au atoms requires lateral mobility of the
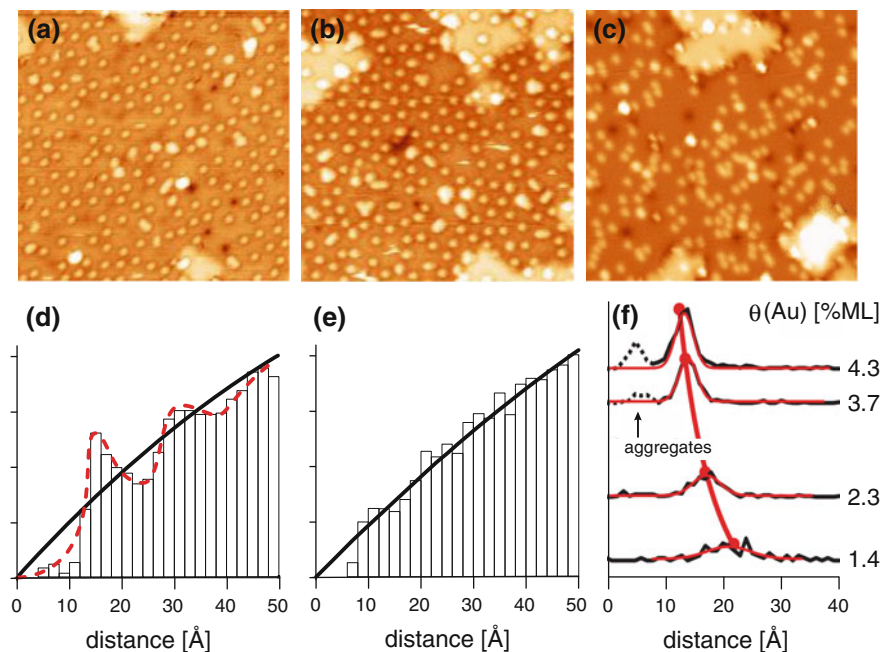
Fig. 10.4 STM images (30 nm × 30 nm) of **a** Au atoms adsorbed on a 3 ML thin MgO film; **b** Au atoms adsorbed on an 8 ML thin MgO film; **c** Pd atoms adsorbed on a 3 ML thin MgO film; **d** radial pair distribution of Au atoms on a 3 ML MgO film; **e** radial pair distribution of Pd atoms on a 3 ML MgO film; **f** nearest neighbor distance distribution of Au atoms on a 8 ML MgO film. *Red dots* mark the distance expected for a perfect hexagonal lattice for the corresponding coverage. *Red lines* are Gaussian fits to the data. Adapted from [52, 53]

adatoms subsequent to the adsorption even at low temperature being consistent with the low diffusion barrier ($E_d = 0.08$ eV) [54]. The effect can be characterized in more detail by looking into the nearest-neighbor distance distribution of Au adatoms as a function of coverage as shown in Fig. 10.4f. The maximum as well as the width of the nearest-neighbor distance distribution decreases with increasing coverage, which is in line with a repulsive interaction between the Au atoms. Charge transfer from the substrate to the Au atoms is an obvious possibility suggested by theory to be efficient for ultrathin films [51, 55].

The electron affinity of Pd is much lower compared to Au, thus, it is expected that Pd will not get charged as evidenced by DFT calculations showing that the Pd 5s level to remain above the Fermi energy [48]. In turn, Pd does not show an ordered arrangement on the surface. Further evidence for the difference in charge state can be found from the STM experiments. To this end it is interesting to compare the experimental STM signatures of single Au and Pd atoms with simulated ones applying the Tersoff-Hamann approximation [56] (Fig. 10.5). The appearance of the Au atoms showing a protrusion surrounded by a depression is different from that of the Pd atoms imaged as protrusions only (Fig. 10.5a–e) [53]. The theoretically
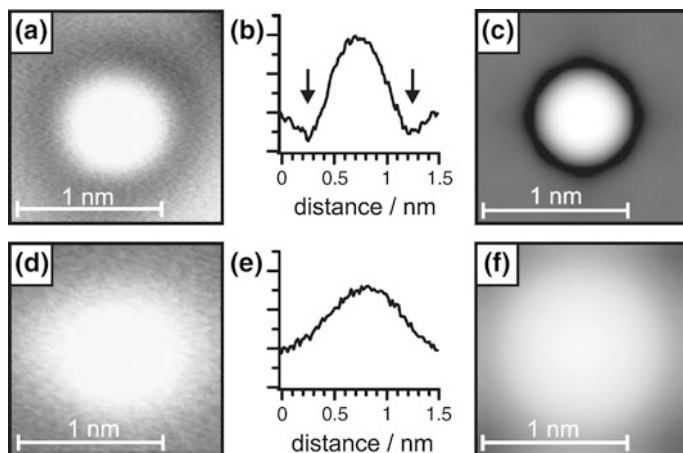
Fig. 10.5 Experimental STM image (**a**, **d**), line profile (**b**, **e**) and calculated STM image (**c**, **f**) shown from *left* to *right*. *Top row* Au atoms on 3 ML MgO/Ag(001), *bottom row* Pd atoms on 3 ML MgO/Ag(111). (With permission from [53]. Copyright 2007 American Physical Society)

calculated images reflect this behavior very nicely and it is important to stress that the "sombrerolike" appearance of charged Au atoms disappears if images of neutral gold atoms are calculated. Such depressions around charged Au atoms are found for other systems such as Au on ultrathin NaCl films as well [57].

It should be kept in mind that Au atoms on thick films (20 ML) or bulk single crystals are highly polarized but essentially neutral [39]. Hence it is not clear that the order observed on 3 and 8 ML thick films has the same origin. To elucidate this question in more detail it is interesting to note that on bulk MgO or thick films Au atoms nucleate on top of oxygen ions [39, 48]. In contrast to that charged Au atoms on thin films adsorb preferably on Mg sites or hollow sites in combination with an increased absolute binding energy [48, 51, 58]. STM can provide evidence for the change in the distribution of the adsorption sites as shown in Fig. 10.6. To this end the lattice of the MgO film determined on a clean film (Fig. 10.6a) is superimposed on the STM images of Au atoms deposited onto 3 ML (Fig. 10.6b) and 8 ML thick films. While in case of the 8 ML film more than 80 % of the atoms occupy one adsorption site, this changes for the 3 ML film where at least two different adsorption sites are populated with almost equal probability. A unique assignment to specific adsorption sites is, however, difficult. A direct comparison of the observed distribution with expectations based on the calculated binding energies for different adsorption sites is hampered by the fact that the metal deposits are not in thermodynamic equilibrium. Hence, the occupancy of the adsorption sites depends on the details of the dynamics of the adsorption process, which renders a quantitative comparison difficult. Based on the abovementioned knowledge that Au atoms nucleate on top of oxygen on the surface of thick MgO films or bulk MgO single crystals, it is inferred that the majority of Au atoms adsorbed on the 8 ML thin MgO film nucleate on oxygen ions. In addition, it is straightforward to deduce that the
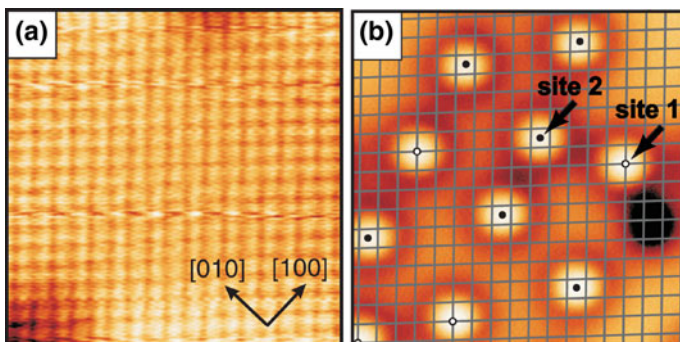
Fig. 10.6 a Atomically resolved STM image (5 nm × 5 nm) of 3 ML MgO/Ag(001); please note that only one ionic sublattice is resolved. **b** STM image (5 nm × 5 nm) of Au atoms on 3 ML MgO/Ag(001); the *grey* lattice is the ionic sublattice extracted from (**a**). Adapted from [52]

adsorption sites are changing for the 3 ML film, which indicates that the adsorption behavior of Au atoms is significantly altered for film thicknesses between 3 and 8 ML. Therefore, it is concluded that the ordered arrangement of the Au atoms observed on the 3 ML thick film is due to the repulsion between the charged metal atoms. On the other hand Au atoms on 8 ML films resemble at least the adsorption site of those on thick MgO films. In turn, the observed order is expected to be induced by the dipole-dipole interaction of the strongly polarized atoms [52].

The strongly polarized adsorption of Au atoms on top of oxygen anions of a bulk MgO surface can be understood in a straightforward manner keeping in mind the large polarizability and the high electronegativity of Au atoms. The question arises whether these effects can be used to probe the properties of ultrathin oxide films. An interesting class of systems, where this concept might be used, is polar oxide surfaces characterized by a divergence of the Madelung potential in case of thick film. The Madelung instability occurs if charged planes of ions alternate perpendicular to the surface [59, 60]. One of the main questions is the mechanism by which the film reduces its electrostatic potential. There are various examples for polar oxide films. Here we want to focus the ultrathin FeO(111) film grown on Pt(111), which has already been discussed above concerning its activity towards CO oxidation at elevated pressures. This film, which consists of one Fe and one oxygen layer, forms a Moire pattern with a periodicity of ~ 25 Å due to the lattice mismatch between FeO (111) and Pt(111). Deposition of Au atoms onto this surface at low temperature (5 K) results in the formation of a well-ordered superstructure of Au atoms, which maps the Moire pattern of the underlying surface [61]. The registry analysis of the single Au atoms within the Moire unit cell (Fig. 10.7a) revealed that Au adsorbs preferentially on the so-called hcp domain, which exhibits the largest dipole moment. The latter is determined by the distance between the $Fe^{\delta+}$ and $O^{\delta-}$ layers being governed by the registry with the underlying Pt substrate [62]. The adsorption of gold atoms on the sites with the largest dipole moment results in the largest polarization of the adatoms in the dipole field of the oxide and therefore strengthens the Au-oxide bond.
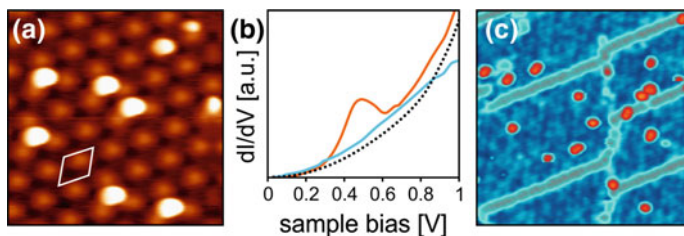
Fig. 10.7 **a** STM image (15×15 nm^2) of single Au atoms deposited on FeO(111)/Pt(111) at 5–10 K; *romb* indicated the Moiré unit cell with lattice constant of ~ 25 Å. **b** conductance spectra of bare FeO (*black trace*) and on *top* of Au atoms on FeO (*orange* hcp site; *blue* fcc site). **c** STM image (30×30 nm^2) of single Au atoms on $Al_{10}O_{13}$/NiAl(110) at 5–10 K. Adapted from [61, 67]

The Au adatoms appear in the STM images as large protrusions (Fig. 10.7a) [61]. The size of the protrusion is of electronic origin and is basically determined by the extension of the Au 6s wave function above the surface. The electronic properties of the Au atoms can be further elucidated using tunneling spectroscopy. The spectra of Au atoms located on the most stable adsorption sites so-called hcp sites exhibit a state ~ 0.5 eV above the Fermi level, while atoms bound at fcc sites lack this feature (Fig. 10.7b) [61]. The unoccupied state observed for Au atoms on the hcp sites is attributed to a Au 6s derived state. Together with the lack of states in the occupied region of the electronic structure this observation suggests positive charging of the adatom in agreement with theoretical predictions [63]. Such unusual charge state of Au adatoms is explained by the high work function of Pt(111), which is further increased by the polar FeO(111) film and inverts the direction of the charge transfer as compared to the ultrathin MgO film [64].

The situation is considerably different for Au atoms on a thin alumina film grown on NiAl(110) [65]. The film consists of two O–Al layers (O_s–Al_s–O_i–Al_i–NiAl…) with a rather complex structure, which exhibits an overall $Al_{10}O_{13}$ stoichiometry [66]. Figure 10.7c shows low temperature STM images of single Au atoms deposited on $Al_{10}O_{13}$/NiAl(110) [67, 68]. In contrast to FeO, the tunneling spectra of the Au atoms lack an unoccupied state of Au 6s character. Also the appearance of Au adatoms as faint protrusions in STM images, taken at positive bias, indicates the absence of unoccupied states below the alumina conduction band and therefore suggests a completely filled Au 6s orbital located below the Fermi level of the system. DFT calculations further corroborate the presence of a negative excess charge. In addition, these calculations provide a detailed picture for the binding characteristics [68]. The Au atoms adsorb on top of so-called Al_{surf} sites of the oxide, which are located above an Al atom in the topmost layer of the NiAl(110) substrate. Au adsorption induces the rupture of an Al_{surf}-O_{int} bond within the alumina film. The Au 6s hybridizes with the 3s orbital of the Al_{surf} and abstracts an electron to form a negatively charged Au atom. The coordinatively unsaturated interface oxygen (O_{int}) restores its preferred valence by a new bond to an Al atom of the NiAl substrate. Chemically speaking the Au atoms oxidize the NiAl surface.

For more covalent oxides the interaction with Au due to polarization will decrease and Au is expected to bind only weakly as long as the oxide-film is chemically inert. However, as seen from the discussion above, additional effects may complicate such a simple picture. A system that follows this expectation almost perfectly is an ultrathin single crystalline silica film grown on Mo(112) [69]. The film consists of a monolayer network of corner sharing [SiO$_4$] tetrahedra with one oxygen atom bonded to the Mo substrate [70]. The interaction of Au with this silica surface is found to be very weak. Even at 10 K, Au atoms diffuse to the antiphase domain boundaries present in the film, where stronger binding sites are available. The adsorption properties of metal atoms on this silica surface as well as a double layer silica film grown e.g. on Ru(0001) [71] vary significantly and are controlled by the possibility that some atoms can penetrate the silica-rings of the film, however, a detailed discussion goes beyond the scope of this contribution.

10.3 1-D Au Chains on Ultrathin Oxide Films

The charge transfer through a thin oxide spacer is not limited to Au atoms but is also found for larger Au aggregates. We will start the discussion by looking into Au chains on ultrathin MgO(001)-films [72, 73]. The two low-temperature STM images (T = 5 K) taken after deposition of ∼0.03 ML Au atoms onto a 3 ML MgO/Ag(001)-film (Fig. 10.8a, b) show bright protrusions related to Au species on the terraces of the MgO film [73]. About 90 % of these protrusions can be assigned
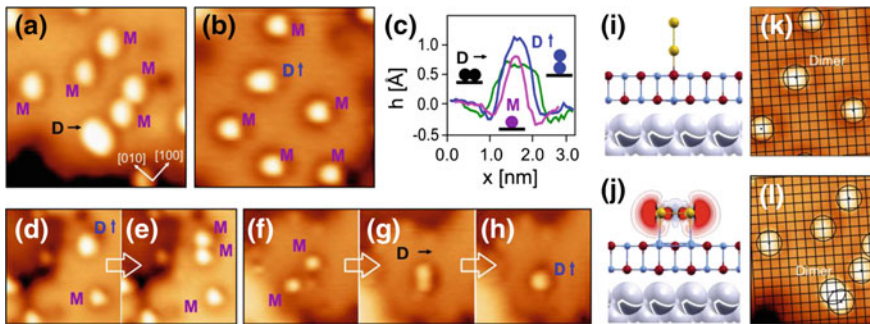
Fig. 10.8 a and **b** STM images (6 nm × 6 nm) of Au on 3 ML MgO/Ag(001); protrusions as marked (M) for single Au atoms and "D→" and "D↑" for Au dimers; **c** corresponding line profiles. **d** STM image with Au atom "M" and Au dimer "D↑". **e** same area as in **d** after applying a voltage pulse. **f–h** series of STM images of the same area starting from two monomers **f** showing the transformation into a flat dimer "D→" and subsequently into an upright dimer "D↑". **i** Structure of an *upright* Au$_2$ (singlet ground state) adsorbed on an O site of 2ML MgO/Ag(001). **j** Structure of flat Au$_2^-$ on 2ML MgO/Ag(001) (doublet ground state); Au atoms are nearly on-top of Mg cations. The contour plot depicts the spin density. **k** and **l** STM images overlaid with a grid of one ionic sublattice showing the relative position of an upright and a flat lying isomer with respect to Au monomers. Adapted from [73]

to Au atoms (monomers "M") according to their height and lateral dimensions. The properties of the latter have been discussed above. Apart from single Au atoms, circular features with increased height (20 %) as compared to the atoms indicated by "D↑" and elongated protrusions named "D→" were observed. A typical line profile of the species called "D→" is shown in Fig. 10.8c. The Au features called "D↑" can be dissociation into two single Au atoms (assigned by the line profile) by a voltage pulse (Fig. 10.8d, e) and were, hence, assigned to dimers. Conversely, Fig. 10.8f–g show the formation of an elongated dimer ("D→") out of two atoms, which was subsequently manipulated into a circularly shaped dimer ("D↑") as shown in Fig. 10.8h. DFT calculations reveal the most stable configuration of Au dimers on 2 ML MgO/Ag(001) to be standing upright, while flat lying dimers have about 0.4 eV higher energy (Fig. 10.8i, j). The most stable adsorption site of the upright configuration was found on-top of oxygen anions, while the flat lying dimers exhibits a very flat potential energy surface with many almost isoenergetic isomers [73]. Information on the experimental registry of the Au dimers can be obtained using the same approach already discussed for Au atoms using an experimentally determined grid of one sublattice (Fig. 10.8k, l). The upright dimer is centered on the same ionic sublattice as the Au atoms, while the particular flat lying dimer shown in Fig. 10.8l was found to be oriented along the [100] direction of the MgO lattice. However, flat lying clusters were also observed with orientation along the [110] directions. The centers of gravity of these species are located in hollow as well as on ionic lattice sites in line with the theoretical prediction. The theoretical analysis of the different isomers reveal that the flat lying ones on the ultrathin film have an increased bond length (0.12 Å) as compared to the upright dimer, an elongation also found with respect to the flat-lying counterpart on bulk MgO [41, 42]. The elongation was found to be due to a charge transfer of an electron into the antibonding σ* orbital of the Au dimer resulting in a doublet ground state as illustrated in Fig. 10.8j showing the corresponding spin density. In contrast to that, the upright isomer on the ultrathin film is found to be neutral and characterized by a singlet ground state as found on bulk MgO(001) surfaces.

Larger Au oligomers containing with up to 7 atoms are found to adopt linear configurations on ultrathin MgO/Ag(001) films, as well [72]. While oligomers of up to 7 atoms were observed trimers and tetramers were the most frequently found species, which is not only due to statistical reasons, but was also suggested by the lower energy of formation theoretically predicted for the longer oligomers. It may be noted in passing that these oligomers have no counterpart to Au clusters in the gas-phase, where non-linear isomers are preferred due to the gain in energy achieved by forming additional Au–Au bonds. The reason for the tendency to form linear chains on the ultrathin film is due to charge transfer onto the Au oligomers. Experimentally, it is not simple to find prove for the charging as the oligomers are minority species and fragile in nature. The latter hampers in particular the investigation of the clusters by means of scanning tunneling spectroscopy (STS), which is a very powerful technique to unravel the electronic structure of individual metal cluster. For the small linear Au oligomers on ultrathin MgO/Ag(001)-films STS is only possible in a window of ±1 V around the Fermi energy. Within this window no
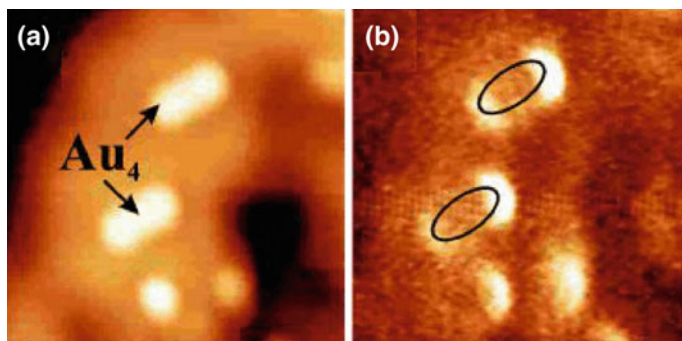
Fig. 10.9 **a** topographic STM image (6.5×6.5 nm^2) of two Au$_4$ chains on 3 ML MgO/Ag(001). **b** Corresponding differential conductance dI/dV image both taken at -0.4 V. Adapted from [72]

additional peaks were found in the dI/dV spectra taken on top of the different oligomers. Figure 10.9 shows the topographic as well as the corresponding conductance map for two tetramers, which indicates states, which enhance the tunneling probability at the end of theses clusters in the occupied part of the electronic structure [72]. The formation of linear chains is in line with DFT investigations on ultrathin MgO/Ag (001). Theory predicts a charge transfer from the support onto the Au chains, which stabilizes the linear adsorption configuration as compared to the more compact structures on bulk MgO. It may be noted that other configuration such as a Y-shaped configuration of Au$_4$ were found to be more stable on ultrathin MgO/Mo(001) [74]. The amount of charge transferred onto the cluster increases with increasing chain length. For the trimer a single electron is transferred leading to a closed shell ground state, while two electrons are found on chains with 4–6 Au atoms [72]. While linear Au$_6$ and Au$_7$ chains were observed, these oligomers already coexist with 2D clusters. This transition between 1D and 2D growths is also found for Au aggregates on alumina/NiAl(110). The similarity between the two systems suggests that crossover, which is driven by the balance between the surplus of energy gained by delocalizing the excess charge and the formation of additional Au–Au bonds in more compact aggregates, is rather independent of the details of the bonding to the surface.

In contrast to the Au oligomers on ultrathin MgO/Ag(001), which were found to be sensitive to electron induced modifications e.g. by STM investigations, corresponding species on the ultrathin alumina film on NiAl(110) are much more stable and allow a detailed characterization of the species by STS [68]. Figure 10.10 shows the topographic STM images together with the shape of the highest occupied state for Au$_3$–Au$_7$ except for the hexamer. The highest occupied states for chains larger than three show nodal planes, which are purely electronic in origin as exemplified by the topographic images taken at different bias voltages. The nodal planes can be readily understood within a particle in the box model, however, a direct assignment of the observed structures to Au oligomers is hampered by charge transfer, which renders the number of electrons present in the cluster unknown. The latter information is extracted from theoretical calculations. While dimers to tetramers
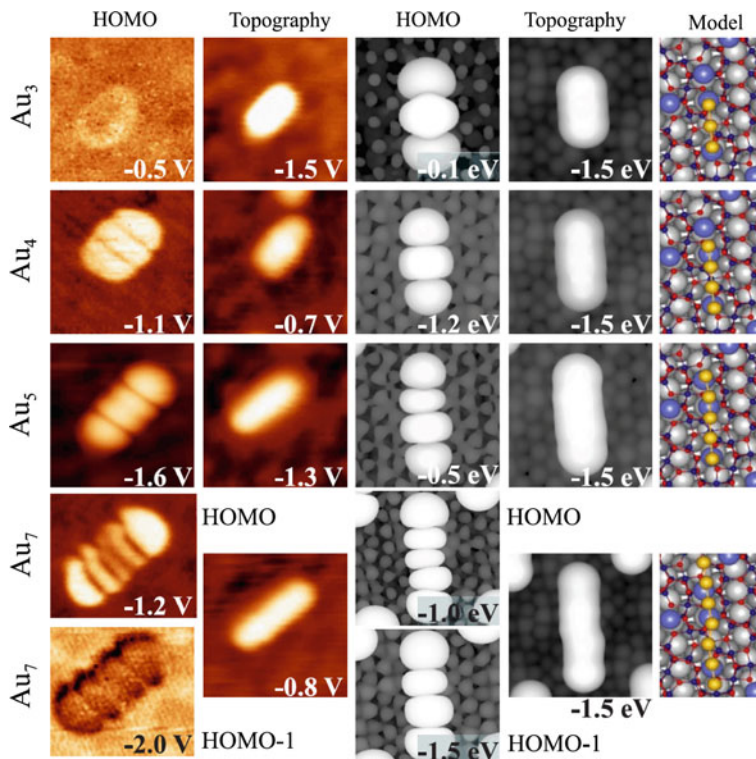
Fig. 10.10 Experimental and calculated shapes of the HOMO (column 1 and 3) and the corresponding topography (column 2 and 4) are shown together with the calculated structure model for Au_3, Au_4, Au_5 and Au_7 chains on alumina/NiAl(110). Images are 5×5 nm^2 in size. For Au_7 the HOMO-1 is additionally shown. With permission from [68]. Copyright 2008 American Physical Society

were found to have two extra charges, the larger oligomers up to a length of seven atoms have three extra electrons. With this information it is possible to compare the nodal structure of the highest occupied state to the expectations for the different oligomers, which allows to assign the images to Au clusters as given in Fig. 10.10. The experimentally observed images fit very nicely the theoretical counterparts, which corroborates the assignment further. The different stability of the Au chains on the alumina surface can be understood along the lines already discussed for the Au atoms above. In particular, it is found that the number of electrons transferred to the Au oligomers corresponds to the number of Al_{sur}–O_{int} bonds disrupted upon binding of the Au chains of the alumina surface. Correspondingly, the Au atoms have to have well defined adsorption sites to facilitate this bond cleavage, which explains the observed registry of the Au chains on the alumina surface [68].

10.4   2-D Au Particles on Ultrathin MgO Films

As discussed in the preceding chapter the stability window for linear Au chains on ultrathin MgO films is limited to about 6 atoms and the question arises how do larger clusters behave. Apart from the structure of the clusters on the ultrathin films it is also interesting to determine if the crossover between the expected 3-dimensional growth found on most bulk oxides as well as oxide films and the regime of charge transfer is the same as found for the single Au atoms. The electrons are transferred onto the particles by tunneling from the Fermi level of the metal substrate through the oxide layer. The tunneling probability depends exponentially on the oxide thickness, and to a smaller extent on the gap size, as discussed earlier by Cabrera and Mott [75, 76]. Consequently, it could be naively expected that simply increasing the film thickness to the point where tunneling transport becomes impossible will alter the growth of Au on thin oxide films. Theory provided the first insight into the effects expected for larger clusters showing that clusters of 8–20 atoms will form 2-dimensional islands on ultrathin MgO films in contrast to expectations on bulk MgO, where 3-dimensional particles are expected [75, 77, 78]. The planar Au_8 cluster on a 2 ML MgO-film turned 3D on an eight layer film in order to increase the number of Au–Au bonds and to counterbalance the loss in interfacial adhesion by the reduced charge transfer. Please note that the theoretical picture does not involve the tunneling process itself as it assumes it to be fast enough to form the charged final state even for experiments in which neutral Au atoms are deposited. Consequently, the crossover is not dictated by tunneling probability. The reduced stability goes back to a reduction of the stabilizing effect due to the image charge as well as the increased cost for the polaronic distortion. The latter is caused by a stiffening of the MgO lattice due to the long-range nature of the Coulomb interaction, which renders the Madelung potential to be not yet converged for ultrathin films. Some account of this effect can be found in the development of the phonon spectrum of MgO films as a function of thickness [79]. A low temperature STM study provided experimental evidence for the predicted crossover in growth mode. For an 8 ML MgO/Ag(001)-film 3-dimensional particles are observed after annealing to room temperature, whereas the Au-particles on 3 ML MgO/Ag(001) stay 2-dimensional after the corresponding annealing step (Fig. 10.11) [52]. An increase of the contact area between metal and oxide film allows to optimize the charge transfer. For a close-packed Au layer on an ultrathin MgO (001)/Ag(001) an average charge transfer of about $-0.2|e|$ per adatom has been calculated [80]. As discussed for Au chains it is not expected that the charge distribution within Au islands is homogeneous. Experimentally, this distribution can be interrogated using the STM as a local probe [81]. From a naive point of view it would be expected that the negative charges on the island repel each other, which would imply that an accumulation of charges should be found at the perimeter of the particles along the lines found for the linear chains (see above). Conduction maps already provide evidence for this effect as shown in Fig. 10.12 [81]. Around the Fermi level enhanced dI/dV contrast is observed at the island edges, which indicates a higher density of states at these sites. Semi-empirical tight-binding DFT calculations,
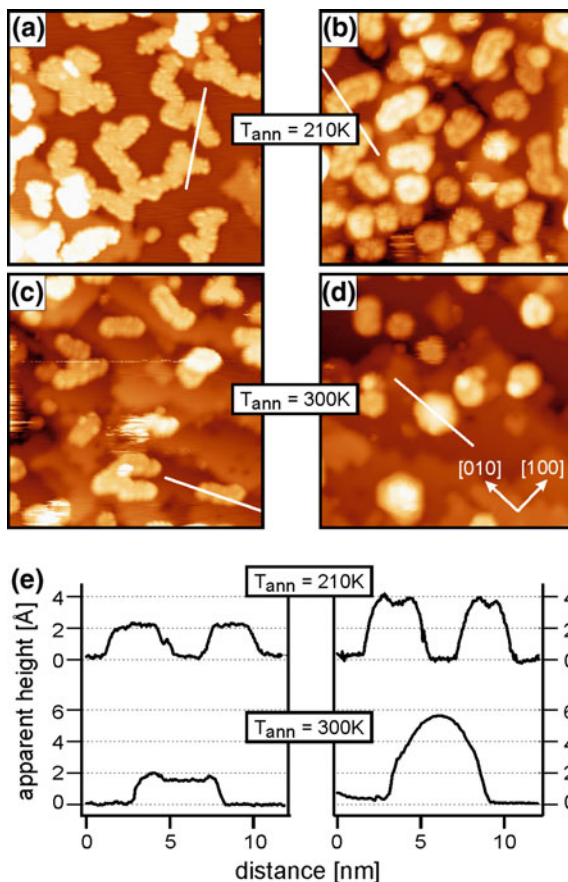
which allows to account for the structure of such large islands shown in Fig. 10.12 explicitly, including the structure of the perimeter, reveals an increase of charges at the perimeter of the particles as well (Fig. 10.12c) [81].

A more detailed picture on the electronic structure of the adsorbed Au particles can be obtained if the particles exhibit well-defined, so-called quantum well states (QWS). The analysis of such states is, however, more complex for 2-dimensional particles as compared to linear chains, because the potential confining the valence electrons is sensitive to the shape and in particular to structural irregularities. In turn, the analysis of the QWS of large, arbitrarily shaped particles is challenging. Figure 10.13a shows three STM images providing information on topography as well as electronic structure of occupied as well as unoccupied states of a small Au cluster with ∼10 Å diameter grown on a 2 ML MgO/Ag(001) film [80]. The image taken around the Fermi energy reveals mainly cluster morphology as no states are available in that energy range probed by the STM experiment. At higher bias both in the occupied as well as in the unoccupied region the appearance of the clusters
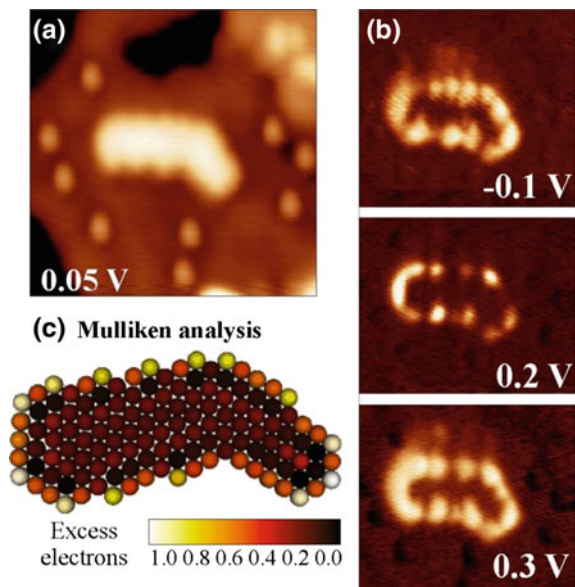
Fig. 10.12 a, **b** STM topographic image and dI/dV maps of a planar Au island on 2 ML MgO/Ag (001) taken at the indicated bias voltage (25×25 nm^2). **c** Corresponding charge distribution derived from a Mulliken analysis of the DFTB calculation. Adapted from [81]
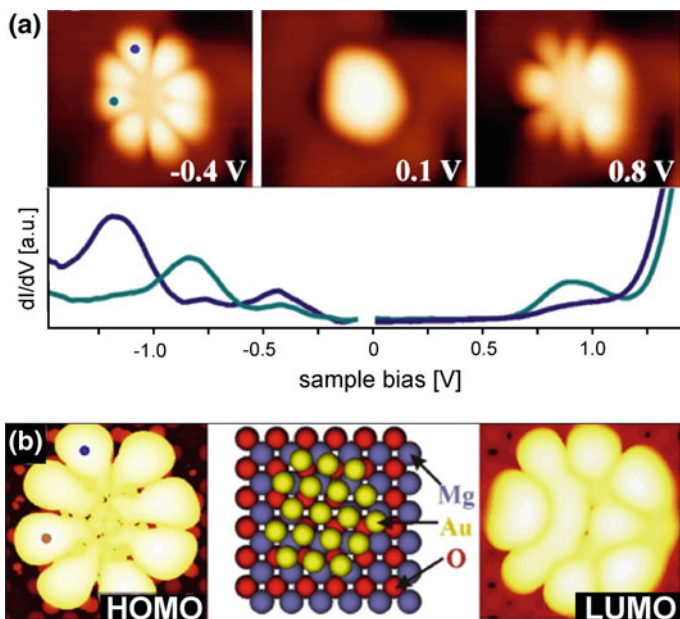
Fig. 10.13 a *Top* STM images of a symmetric Au cluster on 2 ML MgO/Ag(001) taken at the given sample bias. *Bottom* dI/dV spectra of top (*blue*) and left (*cyan*) part of the cluster. **b** Calculated images of the HOMO and LUMO as well as structure model of an Au$_{18}$ cluster on MgO/Ag(001). Adapted from [80]

change to flowerlike protrusions. The bias-dependent contrast is clear evidence for tunneling governed by the electronic and not the topographic properties of the island. Both observed QWS probed by STM resemble the eigenstates of a free-electron gas in a 2-dimensional parabolic potential [82]. The states within such a potential can be characterized by the angular momentum quantum number m. The latter is a direct measure of the number of nodes in the 2-dimensional electron density probability [83]. Both states shown in Fig. 10.13a exhibit four nodal planes (m = 4), which corresponds to a state of G-symmetry. The simplifying discussion above, and hence the ability to deduce the symmetry of the QWS directly from the STM image, holds as the QWS of the Au clusters are derived from 6s orbitals of the Au atoms, which does not mix with states of the oxide or with orbitals of higher angular momentum of the Au atom (5d, 6p) [84].

Combining the images with spectroscopic information as shown in Fig. 10.13a the energetic position of the highest occupied as well as lowest unoccupied state could be derived to be −0.4 and +0.8 V, respectively. The next two lower lying occupied states are found at −0.8 and −1.2 V, which both exhibit of P-symmetry with orthogonal nodal planes (data not shown) with respect to each other. A detailed analysis of the electronic structure of this Au cluster including its charge state was achieved by comparing the experimental results to DFT calculations [80]. However, an extensive search of the parameter space is required to determine the number of atoms, the geometric structure as well as the charge state of the cluster. The degree to which theory is able to reproduce the experimental results is nicely shown in Fig. 10.13b assuming a planar Au_{18} cluster lacking one corner atom of a Au_{19} cluster, the latter being a so-called magic-size. In agreement with the experiment, the highest occupied as well as the lowest unoccupied state are of G symmetry being located in the 5th shell of the harmonic potential, whereas the highest states of 4th shell of this potential are of P symmetry in line with the experimental results. The charge state is readily determined by counting the filled states in the potential. There are 11 doubly occupied orbitals, hence, 22 electrons. The 18 Au atoms contribute 18 electrons, which leads to a 4-fold negatively charged cluster being provided by charge transfer from the support within this model. A Bader analysis of the DFT calculation yields a value of −3.54|e| for the Au_{18} cluster. Please note that this amounts to an average transfer of almost 0.2|e| per atom as calculated for closed-packed Au layers on the MgO thin film [80].

Along the same lines many other Au aggregates on the MgO/Ag(001) system have been evaluated [80]. In all cases, a negative charging of the particles was found, which corroborates the charge-mediated binding concept for Au islands on ultrathin MgO films [13, 85, 86]. The number of transferred electrons was found to be proportional to the number of atoms in the 2D cluster. Please note that the accumulated charge per Au atom is found to be lower in 2D aggregates as compared to 1D chains. The observation may be rationalized by the reduced Coulomb repulsion due to the possibility to increase the average distance between the charges in case of chains [72]. It may be noted in passing that the HOMO-LUMO gap is strongly dependent on the atom number per cluster, as well. For Au clusters containing 10–15 atoms experimental gap sizes of around 1.5 eV were measured,

which is inversely proportional to the cluster area as expected assuming a 2-dimensional harmonic potential [82, 83]. For clusters containing more than 100 atoms a closing of the gap is observed, in line with earlier results for Au clusters on TiO_2 [87].

10.5 Molecules on Charged Au Particles

The importance of the charge state of metal nano particles for the catalytic properties of the system is discussed in the heterogeneous catalysis literature for a long time. IR spectroscopy using appropriate probe molecules such as CO were used to elucidate the charge state e.g. of Au nano particles [43]. On MgO(001) it could be shown that Au particles nucleating at color centers located at the edges of MgO (001) islands are negatively charged [46, 47]. In case of ultrathin oxide films scanning probe microscopy and spectroscopy allows to go a step further and elucidate the role of the anisotropic charge distribution on the adsorption properties. It is tempting to predict that the excess charge available at the perimeter of the Au islands will modify the adsorption properties of molecules in particular Lewis acids, which in turn will also change their chemical properties [88]. Using appropriate tunneling conditions it is possible to visualize CO adsorbed on Au islands, which have been saturated with CO (Fig. 10.14a) [89]. As seen from the STM image the CO-induced features are exclusively localized at the perimeter of the islands, while
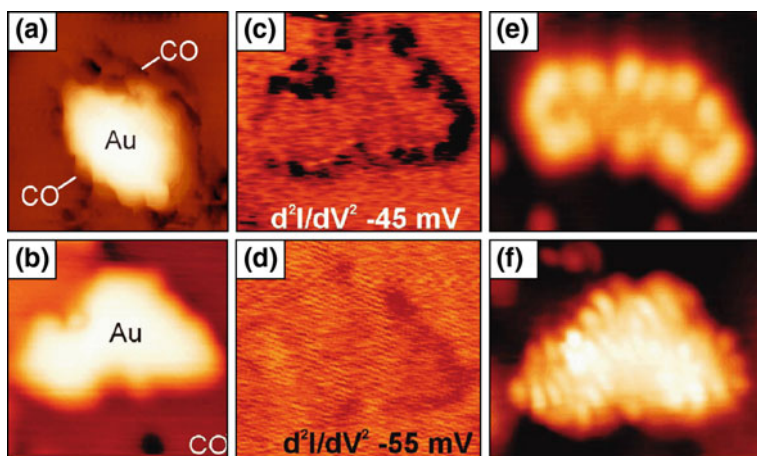
Fig. 10.14 a STM image of a CO-saturated Au island on 2 ML MgO/Ag(001) taken with a CO-covered tip (4×4 nm^2, 100 mV, 3 pA). CO-induced contrast is only revealed at the perimeter of the Au Island. **b** STM topographic image of a planar Au island saturated with CO (5.5×5.5 nm^2, 10 pA). Due to the metallic tip state, the CO molecules are not resolved. **c**, **d** second-derivative maps of **b** (6.2×5.5 nm^2); **e** bare and **f** a CO-saturated Au island (7.0×5.5 nm^2, 150 mV). Adapted from [89]

the inner part of the islands remain empty. It would, however, be important to find additional evidence for the adsorption of the molecules at the perimeter of the islands. This can be achieved by inelastic-electron-tunneling spectroscopy (IETS), which probes inelastic transport channels [90, 91]. Vibrational modes of CO are possible inelastic channels and the one with the highest excitation cross section in STM-IETS is the frustrated rotation [90]. Figure 10.14c, d show the conductance images of a Au particle at −45 and −55 mV, respectively. The former value is chosen, because it is located on the peak of the inelastic tunneling spectrum of Au mono-carbonyls on MgO/Ag(001). As nicely seen additional contrast is seen at −45 mV which is missing at −55 mV. Please note that a corresponding feature is also seen at +45 mV (data not shown). It has been shown above that the clean Au particles exhibit a bright rim reflecting electronic states at the perimeter of the particles available to accommodate the extra charges (Fig. 10.14e). The question arises whether the binding strength of CO at the perimeter is enhanced by the presence of extra charges. According to calculations that is not the case [92]. The calculation reveal that the coordination of the Au atoms is the important factor that determines the bonding strength and hence favor binding to the perimeter of the particles. The binding of CO on 3-fold coordinated sites is much stronger than the one on 5-fold coordinated sites in the center of the islands. However, the binding energy is reduced if CO is bound to a negatively charged cluster as compared to a neutral one, which is due to the reduced ability of the CO molecule to form a bond through σ-donation [92]. The Au particles adopts to the perturbation by reducing the charge at the perimeter, which leads to a reduction of the Pauli-repulsion with the CO and hence a stronger bond at the expense of the charge distribution within the cluster. That is to say the CO molecules bind to the perimeter of the particles not because of the extra charge but despite the extra charge. Experimental evidence for this picture is found in the STM images observed after CO adsorption (Fig. 10.14f). The bright contrast at the rim of the particle disappears and standing wave pattern appears in the interior of the particle, which is in line with the picture that electrons are pushed out of localized states at the perimeter into delocalized states in the interior of the particle. Very recently the effect of the adsorbates onto the QWS of the particles have been elucidated in more detail comparing chemisorbed and physisorbed adsorbates, which show that the confinement of the QWS is reduced for strongly bound ligands, while the opposite is found for weakly interaction adsorbates [93].

10.6   Conclusions

In this chapter we have discussed charge transfer effects on ultrathin oxide films focusing on Au deposited on ultrathin oxide films. Using MgO films as a prototype example of an ionic crystal it was shown that Au atoms as well as clusters get charged if adsorbed to films thinner than 8 ML. This is due to low work function of the oxide film and the large electron affinity of Au. Consequently, an increasing

work function of the film for a given electron affinity of the ad-metal renders charge transfer to the ad-metal more difficult and may result in charge transfer from the ad-metal to the support. Hence, the question whether ultrathin film alter the adsorption properties of metal particle or not depends on the details of the system. For small oligomeric Au clusters charging leads to the stabilization of linear chains. However, this stabilization, which is driven by electrostatic repulsion, will be overcompensated by additional Au–Au bonds in case the particles are larger than about 6 Au atoms. The larger particles remain 2-dimensional even close to monolayer coverage showing the effect of the enhanced adhesion energy for the charged Au atoms. For larger clusters it could be shown that the charge is accumulated at the perimeter of the particle. These are also the sites were molecules adsorb preferentially, however, the detailed analysis of CO adsorption revealed that the preference in case of Au is due to the lower coordination of the atoms at the perimeter and not because of the charge transfer. Charge transfer is not restricted to metal atoms or clusters. It was shown that molecules with sufficiently high electron affinity such as molecular oxygen are subject to charging on ultrathin MgO films, as well. Here, clear experimental evidence for a polaronic distortion of the MgO lattice could be derived from the g-tensor components deduced from the EPR results.

Finally it should be stressed that the understanding of the microscopic details associated to the charge transfer processes on ultrathin oxide films goes beyond the ability to interpret a series of experimental evidences on the system at hand. The tools and concepts that have been established to arrive at this point provide a basis, which can be transferred to wider class of oxide systems.

References

1. Chiesa M, Giamello E, Che M (2010) EPR characterization and reactivity of surface-localized inorganic radicals and radical ions. Chem Rev 110:1213–1808
2. Diebold U (2003) The surface science of titanium dioxide. Surf Sci Rep 48:53–229
3. Osgood R (2006) Photoreaction dynamics of molecular adsorbates on semiconductor and oxide surfaces. Chem Rev 106:4379–4401
4. Zhao J, Li B, Onda K, Feng M, Petek H (2006) Solvated electrons on metal oxide surfaces. Chem Rev 106:4402–4427
5. Lunsford JH, Jayne JP (1965) Formation of CO_2^- radical ions when CO_2 is adsorbed on irradiated magnesium oxide. J Phys Chem 69:2182
6. Newton MD, Sutin N (1984) Electron-transfer reactions in condensed phases. Annu Rev Phys Chem 35:437–480

7. Mikkelsen KV, Ratner MA (1987) Electron-tunneling in solid-state electron-transfer reactions. Chem Rev 87:113–153
8. Freund H-J, Goodman DW (2008) Ultrathin oxide films. In: Ertl G, Knözinger H, Schüth F, Weitkamp J (eds) Handbook of heterogeneous catalysis, vol 1, 2nd edn. Wiley VCH, Weinheim, pp 1298–1309
9. Surnev S, Fortunelli A, Netzer FP (2013) Structure-property relationship and chemical aspects of oxide-metal hybrid nanostructures. Chem Rev 113:4314–4372
10. McFarland EW, Metiu H (2013) Catalysis by doped oxides. Chem Rev 113:4391–4427
11. Nilius N, Freund H-J (2015) Activating nonreducible oxides via doping. Acc Chem Res 45:1532–1539
12. Honkala K (2014) Tailoring oxide properties: an impact on adsorption characteristics of molecules and metals. Surf Sci Rep 69:366–388
13. Pacchioni G, Freund H (2013) Electron transfer at oxide surfaces. The MgO paradigm: from defects to ultrathin films. Chem Rev 113:4035–4072
14. Schintke S, Messerli S, Pivetta M, Patthey F, Libioulle L, Stengel M, De Vita A, Schneider W-D (2001) Insulator at the ultrathin limit: MgO on Ag(001). Phys Rev Lett 87:276801
15. Grönbeck H (2006) Mechanism for NO_2 charging on metal supported MgO. J Phys Chem B 110:11977–11981
16. Hellman A, Klacar S, Grönbeck H (2009) Low temperature CO oxidation over supported ultrathin MgO films. J Am Chem Soc 131:16636–16637
17. Frondelius P, Häkkinen H, Honkala K (2010) Adsorption and activation of O_2 at Au chains on MgO/Mo thin films. Phys Chem Chem Phys 12:1483–1492
18. Schlienz H, Beckendorf M, Katter UJ, Risse T, Freund H-J (1995) Electron-spin-resonance investigations of the molecular-motion of NO_2 on Al_2O_3(111) under ultrahigh-vacuum conditions. Phys Rev Lett 74:761–764
19. Farle M, Zomack M, Baberschke K (1985) ESR of adsorbates on single crystal metal surfaces under UHV conditions. Surf Sci 160:205
20. Gonchar A, Risse T, Freund H-J, Giordano L, Di Valentin C, Pacchioni G (2011) Activation of oxygen on MgO: O_2^- radical ion formation on thin, metal-supported MgO(001) films. Angew Chem Int Ed 50:2635–2638
21. Chiesa M, Giamello E, Paganini MC, Sojka Z, Murphy DM (2002) Continuous wave electron paramagnetic resonance investigation of the hyperfine structure of $^{17}O_2$ adsorbed on the MgO surface. J Chem Phys 116:4266–4274
22. Pacchioni G, Ferrari AM, Giamello E (1996) Cluster model of O_2^- adsorption on regular and defect sites and F_s centers of the MgO(100) surface. Chem Phys Lett 255:58–64
23. Sterrer M, Diwald O, Knözinger E (2000) Vacancies and electron deficient surface anions on the surface of MgO nanoparticles. J Phys Chem B 104:3601–3607
24. Napoli F, Chiesa M, Giamello E, Preda G, Di Valentin C, Pacchioni G (2010) Formation of superoxo species by interaction of O_2 with Na atoms deposited on MgO powders: a combined continuous-wave EPR (CW-EPR), hyperfine sublevel correlation (HYSCORE) and DFT study. Chem Eur J 16:6776–6785
25. Känzig W, Cohen MH (1959) Paramagnetic resonance of oxygen in alkali halides. Phys Rev Lett 3:509–510
26. Sun YN, Giordano L, Goniakowski J, Lewandowski M, Qin ZH, Noguera C, Shaikhutdinov S, Pacchioni G, Freund HJ (2010) The interplay between structure and CO oxidation catalysis on metal-supported ultrathin oxide films. Angew Chem Int Ed 49:4418–4421
27. Galloway HC, Benítez JJ, Salmeron M (1993) The structure of monolayer films of FeO on Pt (111). Surf Sci 298:127–133
28. Weiss W, Barbieri A, Vanhove MA, Somorjai GA (1993) Surface-structure determination of an oxide film grown on a foreign substrate—Fe_3O_4 multilayer on Pt(111) identified by low-energy-electron diffraction. Phys Rev Lett 71:1848–1851
29. Vurens GH, Maurice V, Salmeron M, Somorjai GA (1992) Growth, structure and chemical properties of FeO overlayers on Pt(100) and Pt(111). Surf Sci 268:170

30. Vurens GH, Salmeron M, Somorjai GA (1988) Structure, composition and chemisorption studies of thin ordered iron oxide films on platinum (111). Surf Sci 201:129–144
31. Kim YJ, Westphal C, Ynzunza RX, Galloway HC, Salmeron M, Van Hove MA, Fadley CS (1997) Interlayer interactions in epitaxial oxide growth: FeO on Pt(111). Phys Rev B 55:R13448–R13551
32. Ritter M, Ranke W, Weiss W (1998) Growth and structure of ultrathin FeO films on Pt(111) studied by STM and LEED. Phys Rev B 57:7240–7251
33. Qin ZH, Lewandowski M, Sun YN, Shaikhutdinov S, Freund HJ (2008) Encapsulation of Pt nanoparticles as a result of strong metal-support interaction with Fe_3O_4 (111). J Phys Chem C 112:10209–10213
34. Wu MC, Corneille JS, He JW, Estrada CA, Goodman DW (1992) Preparation, characterization, and chemical-properties of ultrathin MgO films on Mo(100). J Vac Sci Technol A 10:1467–1471
35. Sterrer M, Risse T, Freund H-J (2005) Low temperature infrared spectra of CO adsorbed on the surface of MgO(001) thin films. Surf Sci 596:222–228
36. Benedetti S, Benia HM, Nilius N, Valeri S, Freund HJ (2006) Morphology and optical properties of MgO thin films on Mo(001). Chem Phys Lett 430:330–335
37. Wollschläger J, Viernow J, Tegenkamp C, Erdös D, Schröder KM, Pfnür H (1999) Stoichiometry and morphology of MgO films grown reactively on Ag(100). Appl Surf Sci 142:129–134
38. Pal J, Smerieri M, Celasco E, Savio L, Vattuone L, Rocca M (2014) Morphology of monolayer MgO films on Ag(100): switching from corrugated islands to extended flat terraces. Phys Rev Lett 112:126102
39. Yulikov M, Sterrer M, Heyde M, Rust HP, Risse T, Freund H-J, Pacchioni G, Scagnelli A (2006) Binding of single gold atoms on thin MgO(001) films. Phys Rev Lett 96:146804
40. Yudanov I, Pacchioni G, Neyman K, Rösch N (1997) Systematic density functional study of the adsorption of transition metal atoms on the MgO(001) surface. J Phys Chem B 101:2786–2792
41. Del Vitto A, Pacchioni G, Delbecq FO, Sautet P (2005) Au atoms and dimers on the MgO (100) surface: a DFT study of nucleation at defects. J Phys Chem B 109:8040–8048
42. Barcaro G, Fortunelli A (2005) The interaction of coinage metal clusters with the MgO(100) surface. J Chem Theory Comput 1:972–985
43. Meyer R, Lemire C, Shaikhoutdinov SK, Freund HJ (2004) Surface chemistry of catalysis by gold. Gold Bull 37:72–124
44. Sterrer M, Yulikov M, Risse T, Freund H-J, Carrasco J, Illas F, Di Valentin C, Giordano L, Pacchioni G (2006) When the reporter induces the effect: unusual IR spectra of CO on Au_1/MgO(001)/Mo(001). Angew Chem Int Ed 45:2633–2635
45. Jiang L, Xu Q (2005) Reactions of gold atoms and small clusters with CO: infrared spectroscopic and theoretical characterization of Au_nCO (n = 1 − 5) and $Au_n(CO)_2$ (n = 1, 2) in solid argon. J Phys Chem A 109:1026–1032
46. Sterrer M, Yulikov M, Fischbach E, Heyde M, Rust HP, Pacchioni G, Risse T, Freund HJ (2006) Interaction of gold clusters with color centers on MgO(001) films. Angew Chem Int Ed 45:2630–2632
47. Sterrer M, Fischbach E, Risse T, Freund H-J (2005) Geometric characterization of a singly charged oxygen vacancy on a single-crystalline MgO(001) film by electron paramagnetic resonance spectroscopy. Phys Rev Lett 94:186101
48. Pacchioni G, Giordano L, Baistrocchi M (2005) Charging of metal atoms on ultrathin MgO/Mo(100) films. Phys Rev Lett 94:226104
49. Giordano L, Cinquini F, Pacchioni G (2005) Tuning the surface metal work function by deposition of ultrathin oxide films: density functional calculations. Phys Rev B 73:045414
50. Goniakowski J, Noguera C (2004) Electronic states and Schottky barrier height at metal/MgO (100) interfaces. Interface Sci 12:93–103

51. Giordano L, Pacchioni G (2006) Charge transfers at metal/oxide interfaces: a DFT study of formation of $K^{\delta+}$ and $Au^{\delta-}$ species on MgO/Ag(100) ultra-thin films from deposition of neutral atoms. Phys Chem Chem Phys 8:3335–3341
52. Sterrer M, Risse T, Heyde M, Rust H-P, Freund H-J (2007) Crossover from three-dimensional to two-dimensional geometries of Au nanostructures on thin MgO(001) films: a confirmation of theoretical predictions. Phys Rev Lett 98:206103
53. Sterrer M, Risse T, Martinez Pozzoni U, Giordano L, Heyde M, Rust H-P, Pacchioni G, Freund H-J (2007) Control of the charge state of metal atoms on thin MgO films. Phys Rev Lett 98:096107
54. Giordano L, Baistrocchi M, Pacchioni G (2005) Bonding of Pd, Ag, and Au atoms on MgO (100) surfaces and MgO/Mo(100) ultra-thin films: a comparative DFT study. Phys Rev B 72:11
55. Frondelius P, Hellman A, Honkala K, Häkkinen H, Grönbeck H (2008) Charging of atoms, clusters, and molecules on metal-supported oxides: a general and long-ranged phenomenon. Phys Rev B 78:085426–085427
56. Tersoff J, Hamann DR (1985) Theory of the scanning tunneling microscope. Phys Rev B 31:805–813
57. Repp J, Meyer G, Olsson FE, Persson M (2004) Controlling the charge state of individual gold adatoms. Science 305:493–495
58. Honkala K, Hakkinen H (2007) Au adsorption on regular and defected thin MgO(100) films supported by Mo. J Phys Chem C 111:4319–4327
59. Tasker PW (1984) Surfaces of magnesia and alumina. Adv Ceram 10:176
60. Goniakowski J, Finocchi F, Noguera C (2008) Polarity of oxide surfaces and nanostructures. Rep Prog Phys 71:016501
61. Nilius N, Rienks EDL, Rust HP, Freund HJ (2005) Self-organization of gold atoms on a polar FeO(111) surface. Phys Rev Lett 95:066101
62. Rienks EDL, Nilius N, Rust HP, Freund HJ (2005) Surface potential of a polar oxide film: FeO on Pt(111). Phys Rev B 71:241404
63. Giordano L, Pacchioni G, Goniakowski J, Nilius N, Rienks EDL, Freund H-J (2008) Charging of metal adatoms on ultrathin oxide films: Au and Pd on FeO/Pt(111). Phys Rev Lett 101:026102–026104
64. Giordano L, Pacchioni G, Goniakowski J, Nilius N, Rienks EDL, Freund HJ (2007) Interplay between structural, magnetic, and electronic properties in a FeO/Pt(111) ultrathin film. Phys Rev B 76:075416
65. Jaeger RM, Kuhlenbeck H, Freund H-J, Wuttig M, Hoffmann W, Franchy R, Ibach H (1991) Formation of well-ordered aluminium oxide overlayer by oxidation of NiAl(110). Surf Sci 259:235–252
66. Kresse G, Schmid M, Napetschnig E, Shishkin M, Köhler L, Varga P (2005) Structure of the ultrathin aluminum oxide film on NiAl(110). Science 308:1440–1442
67. Kulawik M, Nilius N, Freund HJ (2006) Influence of the metal substrate on the adsorption properties of thin oxide layers: Au atoms on a thin alumina film on NiAl(110). Phys Rev Lett 96:036103
68. Nilius N, Ganduglia-Pirovano MV, Brazdova V, Kulawik M, Sauer J, Freund HJ (2008) Counting electrons transferred through a thin alumina film into Au chains. Phys Rev Lett 100:096802
69. Schroeder T, Adelt M, Richter B, Naschitzki M, Bäumer M, Freund HJ (2000) Epitaxial growth of SiO_2 on Mo(112). Surf Rev Lett 7:7–14
70. Todorova TK, Sierka M, Sauer J, Kaya S, Weissenrieder J, Lu JL, Gao HJ, Shaikhutdinov S, Freund HJ (2006) Atomic structure of a thin silica film on a Mo(112) substrate: a combined experimental and theoretical study. Phys Rev B 73:165414
71. Löffler D, Uhlrich JJ, Baron M, Yang B, Yu X, Lichtenstein L, Heinke L, Buchner C, Heyde M, Shaikhutdinov S, Freund HJ, Wlodarczyk R, Sierka M, Sauer J (2010) Growth and structure of crystalline silica sheet on Ru(0001). Phys Rev Lett 105:146104

72. Simic-Milosevic V, Heyde M, Lin X, Konig T, Rust H-P, Sterrer M, Risse T, Nilius N, Freund H-J, Giordano L, Pacchioni G (2008) Charge-induced formation of linear Au clusters on thin MgO films: scanning tunneling microscopy and density-functional theory study. Phys Rev B 78:235426–235429

73. Simic-Milosevic V, Heyde M, Nilius N, König T, Rust HP, Sterrer M, Risse T, Freund HJ, Giordano L, Pacchioni G (2008) Au dimers on Thin MgO(001) films: flat and charged or upright and neutral? J Am Chem Soc 130:7814–7815

74. Frondelius P, Häkkinen H, Honkala K (2007) Adsorption of small Au clusters on MgO and MgO/Mo: the role of oxygen vacancies and the Mo-support. New J Phys 9:339

75. Ricci D, Bongiorno A, Pacchioni G, Landman U (2006) Bonding trends and dimensionality crossover of gold nanoclusters on metal-supported MgO thin films. Phys Rev Lett 97:036106

76. Cabrera N, Mott NF (1949) Theory of the oxidation of metals. Rep Prog Phys 12:163–184

77. Bäumer M, Freund H-J (1999) Metal deposits on well-ordered oxide films. Prog Surf Sci 61:127–198

78. Henry CR (1998) Surface studies of supported model catalysts. Surf Sci Rep 31:235–325

79. Savio L, Celasco E, Vattuone L, Rocca M, Senet P (2003) MgO/Ag(100): confined vibrational modes in the limit of ultrathin films. Phys Rev B 67:075420

80. Lin X, Nilius N, Freund HJ, Walter M, Frondelius P, Honkala K, Häkkinen H (2009) Quantum well states in two-dimensional gold clusters on MgO thin films. Phys Rev Lett 102:206801–206804

81. Lin X, Nilius N, Sterrer M, Koskinen P, Häkkinen H, Freund HJ (2010) Characterizing low-coordinated atoms at the periphery of MgO-supported Au islands using scanning tunneling microscopy and electronic structure calculations. Phys Rev B 81:153406

82. Kittel C (1996) Introduction to solid state physics. Wiley, New York

83. de Heer WA (1993) The physics of simple metal clusters: experimental aspects and simple models. Rev Mod Phys 65:611–676

84. Walter M, Frondelius P, Honkala K, Häkkinen H (2007) Electronic structure of MgO-supported Au clusters: quantum dots probed by scanning tunneling microscopy. Phys Rev Lett 99:096102–096104

85. Giordano L, Pacchioni G (2011) Oxide films at the nanoscale: new structures, new functions, and new materials. Acc Chem Res 44:1244–1252

86. Nilius N (2009) Properties of oxide thin films and their adsorption behavior studied by scanning tunneling microscopy and conductance spectroscopy. Surf Sci Rep 64:595–659

87. Valden M, Lai X, Goodman DW (1998) Onset of catalytic activity of gold clusters on titania with the appearance of nonmetallic properties. Science 281:1647–1650

88. Andersin J, Nevalaita J, Honkala K, Häkkinen H (2013) The redox chemistry of gold with high-valence doped calcium oxide. Angew Chem Int Ed 52:1424–1427

89. Lin X, Yang B, Benia HM, Myrach P, Yulikov M, Aumer A, Brown MA, Sterrer M, Bondarchuk O, Kieseritzky E, Rocker J, Risse T, Gao HJ, Nilius N, Freund HJ (2010) Charge-mediated adsorption behavior of CO on MgO-supported Au clusters. J Am Chem Soc 132:7745–7749

90. Ho W (2002) Single-molecule chemistry. J Chem Phys 117:11033–11061

91. Wallis TM, Nilius N, Ho W (2002) Electronic density oscillations in gold atomic chains assembled atom by atom. Phys Rev Lett 89:236802

92. Sicolo S, Giordano L, Pacchioni G (2009) CO adsorption on one-, two-, and three-dimensional au clusters supported on MgO/Ag(001) ultrathin films. J Phys Chem C 113:10256–10263

93. Stiehler C, Calaza F, Schneider W-D, Nilius N, Freund H-J (2015) Molecular adsorption changes the quantum structure of oxide-supported gold nanoparticles: chemisorption versus physisorption. Phys Rev Lett 115:036804

94. Sun YN, Qin ZH, Lewandowski M, Carrasco E, Sterrer M, Shaikhutdinov S, Freund HJ (2009) Monolayer iron oxide film on platinum promotes low temperature CO oxidation. J Catal 266:359–368

Chapter 11
Characterizing Defects Responsible for Charge Transport Characteristics at Interfaces of Nano-Thick Materials Stacks

Gennadi Bersuker, Matthew B. Watkins and Alexander L. Shluger

Abstract Major functioning blocks in modern devices employed in a variety of applications (electronics, energy harvesting, sensors, etc.) comprise of stacks of nm-thin layers of dielectric materials in contact with conductive electrodes (semiconductors, metals). The performance and reliability of these devices are affected by charge transfer characteristics of these multilayer stacks. We discuss collaboration between electrical measurements and computational modeling leading to identification of defects responsible for degradation phenomena in nm-thin dielectric films employed as gate dielectrics in metal oxide field effect transistors.

11.1 Introduction

Ultrathin dielectric films employed in various device structures as isolation layers in transistors, capacitors and memory cells, electroluminescent and spintronic devices, gas sensors, etc. represent one of the most critical components of these devices. The primary role of the gate dielectric, in particular, in transistors is to enable modulating the carrier concentration in the semiconductor channel, by applying a voltage to the control gate electrode. Such dielectric films need to satisfy a strict set of requirements to ensure the performance and reliability of devices, while not com-

G. Bersuker (✉)
The Aerospace Corporation, Los Angeles, CA 90009-2957, USA
e-mail: gennadi.bersuker@aero.org

M.B. Watkins
School of Mathematics and Physics, University of Lincoln, Brayford Pool,
Lincoln LN6 7TS, UK
e-mail: matthew.watkins@ucl.ac.uk

M.B. Watkins · A.L. Shluger
Department of Physics and Astronomy, University College London,
London WC1E 6BT, UK
e-mail: a.shluger@ucl.ac.uk

311

promising their fabrication process. The density of carriers in the semiconductor channel in metal oxide field effect transistors (MOSFETs) depends on the capacitance of the electrode/dielectric/substrate gate stack, that is, proportional to k/t, where t is the dielectric thickness and k is its dielectric constant. Achieving higher performance, thus, requires employing very thin dielectric films comprised of high-dielectric-constant materials (high-k dielectrics) [1, 2]. On the other hand, the dielectric has to form an effective electrically insulating barrier in order to keep parasitic leakage current between the electrodes/substrate as low as possible. These requirements set restrictions on the thickness of a dielectric film and its conductivity band offsets value (with respect to electrodes) [1, 2]. Furthermore, while operating under relatively high bias (under electric fields of up to 15 MV cm^{-1} and above) and temperatures (up to 100 °C for conventional applications or higher) the electrical characteristics, in particular threshold voltage and gate leakage current, must remain stable to meet reliability criteria.

Analysis of a charge transport through the dielectric film in a stack is therefore crucial for developing and evaluating such devices. Such analysis should achieve two major objectives: determine the time dependency of electrical parameters and identify the "weak links" and their origins in the dielectric film structures in order to provide directions to materials stack modification and define a range of electrical use-conditions meeting performance/reliability requirements. Reaching this goal relies on establishing a relation between the material's structure and electrical characteristics of a stack. This requires employing atomistic models explicitly considering the physical processes responsible for electrical properties. The critically important demand to the physics-based models is their predictive capability—knowing which specific material features affect each given electrical parameter allows for targeted efforts to reach the performance goals and a quicker turnaround.

Specific features of advanced dielectric stacks:

(a) Multi-layers structure: stacks may be comprised of metals, various oxides, crystalline silicon, etc: interactions between these materials can be expected to result in inter-diffusion and atoms incorporation into adjacent layers.
(b) Ultra-thin layers: stack properties are dominated by the materials interfaces.
(c) Characterization complexity: Traditional experimental techniques for defect characterization in bulk materials are limited due to low defect concentration (optical absorption), shielding by metal electrodes (EPR), and other factors. Defects can be more effectively probed by certain electrical measurements, such as Deep-level transient spectroscopy (DLTS), charge pumping electrically detected magnetic resonance to mane a few.

Features (a) and (b) may result in high density of (as-grown) structural defects in the dielectric stacks [3]. Some of these defects are shown to be capable of trapping charge carriers injected into the dielectrics under operation conditions. This leads to a instability of dielectric characteristics caused by the charge trapping/de-trapping at these pre-existing defects [4–6]. Characteristic times of the carrier trapping processes can be expected to be much shorter than those associated with the generation of new defects, which requires a rather significant energy in order to break chemical bonds.

Therefore, as-fabricated (time-zero) dielectric properties may determine both short- and long- term reliability characteristics of modern stacks [7].

The electron transport can proceed via intermediate steps—bandgap electronic states where the carrier can (temporarily) localize (so-called trap assisted tunneling mechanism, TAT, Fig. 11.1). Such electronic states are usually associated with defects in the dielectric structure, such as vacancies and impurities. It has been demonstrated that oxygen vacancies in specific charge states are representatives of the typical intrinsic charge transporting defects in a variety of oxides. The "elementary act" of such transport consists of the carrier tunneling to (from) and its localization (de-localization) at the defect site, Fig. 11.1.

The charge carrier localization (trapping) at the defect site generally requires overcoming an activation barrier that is associated with often significant displacements of the atoms surrounding the defect into thier new equilibrium positions (see Fig. 11.1). The magnitude of the activation barrier, which determines the characteristic time of the carrier trapping by the defect, depends on the defect ionization and relaxation energies and, therefore, serves as an identifier of the defect atomic configuration [5–7]. The trapping time, along with the time of the carrier tunneling between the substrate/gate and defect controls the rate of the carrier transport through the dielectric. By matching the measured and calculated carrier transfer rates one can extract the tunneling distance and activation barrier, thus determining the defect structure and its distance from the injecting electrode (substrate).
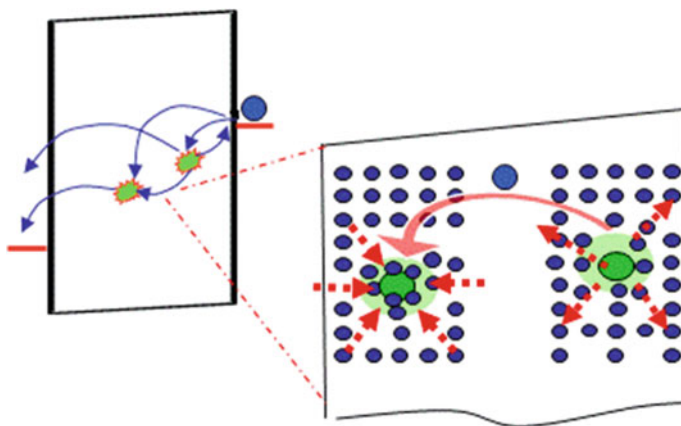
Fig. 11.1 Schematics of the charge carrier transport process via dielectric defects (non-elastic trap assisted tunneling) and structural re-arrangements in the dielectric associated with each trapping/de-trapping event (in the case of an electron transport). The *right-hand panel* shows schematically the displacements (*red arrows*) of atoms (*blue dots*) surrounding the defect site (*green dot*) caused by electron trapping/de-trapping. The *left-hand panel* illustrates schematically an electron (*blue sphere*) tunneling from the electrode Fermi level into a defect state in the band gap of an oxide and then tunneling into an appropriately located available defect state and finally into an unoccupied state in the electrode (Color figure online)

Below we present an example of linking electric measurements and computational modelling data that allowed to identify plausible defects responsible for degradation phenomena in nm-thin dielectric films employed as gate dielectrics in metal oxide field effect transistors. First, we briefly describe the charge trapping/de-trapping mechanisms and electrical techniques used for defect probing. Then we focus on a particular example of charging/discharging in HfO_2/SiO_2 nano-layers stacks illustrating the application of electrical measurements to characterizing defects in this complex system and describing the results of ab initio modelling of defect candidates at the HfO_2/SiO_2 interface. We discuss the state of the art multi-phonon statistical carrier transport simulations of the temperature dependent leakage current and their relation with in electrical measurements and atomistic simulations that determine possible atomic structures of the electrically active defects in dielectric stacks.

11.2 Charge Transport Through Metal Oxide/Silicon Dioxide Stacks

We focus on the dielectric stacks fabricated by growing high-k metal oxide films (HfO_2, ZrO_2, $HfSiO_x$, etc.) over a semiconductor substrate (Si, III–V). As discussed below, these oxide films tend to contain various types of defects and the gate stacks may include a thin SiO_2 layer at the metal oxide/substrate interface. The structure and electronic properties of high-k metal oxide materials are influenced by d-electrons of Zr(Hf), that differs significantly high-k films from a conventional SiO_2 gate dielectric [2]. One of the consequences of the d-electron bonding in these dielectrics is a relatively high density of as-grown defects, specifically oxygen vacancies [3, 4]. As shown by ab initio calculations [8, 9], oxygen vacancies in monoclinic HfO_2, may exist in five charge states, from −2 to +2, and may function as both transient electron/hole traps and fixed charges. Thus, the contribution to electrical instability from charge trapping/de-trapping at *pre-existing* structural defects in metal oxide devices may be significant and even dominate the stress-induced *defect generation* traditionally considered as the major cause of instability in SiO_2 gate dielectrics.

Understanding the fundamental charge trapping/de-trapping mechanisms is complicated by the fact that high-k metal oxide stacks formed using Hf and Zr oxide (or their silicates) thin films are usually multilayer structures that include a SiO_2-layer either spontaneously or intentionally formed at the interface with the substrate [3]. This interfacial layer (IL) exhibits a rather non-uniform elemental composition due to its interaction with the overlaying high-k film, the gate electrode, and the substrate. While SiO_2 is known to form an oxygen-deficient transitional layer near the interface with the Si substrate to accommodate the lattice constant mismatch between these materials, data from high resolution chemical and spectroscopic analyses suggest that the SiO_2 film adjacent to a high-k dielectric is also oxygen-deficient [7, 10, 11]. This deficiency is driven by the energetically

advantageous diffusion of oxygen vacancies out of the metal oxide into the silicon dioxide [12]. Therefore the IL in the high-*k* gate stack can be expected to contain a high density of electrically active defects and defect precursors.

A high density of as-grown process-related electrically active defects in the dielectric stacks induce *electrical* properties linked to charge trapping/de-trapping at these defects. The effect of trapping process on device parameters is determined by its characteristic time with respect to that of test measurements and stress-induced defect generation. When the characteristic time of the charge trapping at pre-existing defects is much shorter than that of the test measurement, the effect of this fast trapping manifests itself in intrinsic (rather than time-dependent) device characteristics. In other words, the contribution of the fast process is included in the time-zero value of a parameter. However, under certain actual use conditions, for instance, when employed as a high frequency switch, the device may experience much shorter bias pulses than those used in the test measurements (in particular, in DC measurements), which would lead to not only different time-zero values of device parameters but also to a drift of these values with the total actual time of device operation.

On the other hand, slower charge trapping/de-trapping at the pre-existing defects may add to the overall as-tested time-dependent dielectric stack instability. When the characteristic time of these slow processes is shorter than that of new defect generation, the contribution from the charge trapping at pre-existing defects may dominate device instability, resulting in a time dependency of the electrical parameters. This is traditionally interpreted as, and thus could erroneously be assigned to, a dielectric degradation caused by the generation of new defects. Importantly, the presence of a large fast instability component may affect the evaluation of slower, long-term instability processes that are responsible for time-dependent degradation. Separating contributions of the fast and slow processes to total device instability is thus critically important to obtain correct reliability estimations.

The above considerations indicate that characterization of such complex multi-layer, multi-component, ultra-thin dielectric stacks raises new issues that were not significant for conventional silicon dioxide-based gate stacks:

– Where are the defects contributing to instability located: in the metal oxide film or silicon dioxide layer
– Are these pre-existing (process-related) defects? Or are they stress-generated?
– How can device lifetime projection be affected by the contributions of fast charging/discharging processes to the total instability?

These issues, in turn, define requirements for electrical measurements, which should provide both high time and spatial resolutions to address fast charge transport processes and differentiate signals from different regions through the depth of the dielectric stack.

11.3 Electrical Techniques for Defect Probing

11.3.1 Requirements for Electrical Measurements and Analysis

The above mentioned features necessitate quite stringent requirements for the electrical measurements and data analysis. The measurements should be able to resolve fast processes involving carrier exchange between the substrate/electrode and dielectric [10], while the analysis of electrical data should determine defect spatial and energy distributions and help to identify the defect atomic structure [5, 6, 11]. Achieving this goal requires employing an electron transfer model that explicitly considers the electron-phonon coupling between a charge carrier and the lattice atoms constituting the defect, since this process was shown to primarily control the characteristic times of the charge transport via the defects.

Electrical measurements on the materials stacks reflect the transport of injected charge carriers (electrons and/or holes) through the dielectrics. In particular, in the case of transistor gate stacks, the oxide defects charging by the injected channel carriers and subsequently discharging back into the transistor channel exhibit a wide range of time constants; the system remains, however, in dynamic equilibrium. These charge trapping/de-trapping processes are controlled by multi-phonon emission rates. Application of extra positive or negative bias results in the trapping of excess charge (electrons or holes) on oxide defects. After switching off the extra bias, the system returns to dynamic equilibrium via a process of charge de-trapping where individual defects can be characterized by their charge capture and emission rates.

Defect probing can be done using a variety of electrical techniques measuring different aspects of charge trapping/de-trapping at defect states: Charge Pumping (CP) [3, 4], Low Frequency Noise (LFN) [5], pulse current-voltage (IV) [6], pulse capacitance-voltage (CV) [7], and Stress Induced Leakage Current (SILC) [10] measurements. Each technique has its limitations in sensitivity and energy/spatial ranges it can probe, and therefore comprehensive defect evaluation requires applying a combination of these techniques.

Defect identification is done using the trap energy characteristics extracted by matching the experimental data to the modeling results based on the physical processes involved in each particular measurement method. The underlying physical mechanism describing the carrier exchange between the traps and substrate involves the phonon-assisted structural relaxation of the lattice surrounding the defect [5, 7, 10, 11], which is the trap type specific. The trap capture rates $\alpha(x_T, E_T)$ can be expressed as follows [7, 13]:

$$\alpha(x_T, E_T) = \sigma_0 n v_t \exp\left(-\frac{x_T}{\lambda}\right) \exp\left(-\frac{(E_C - E_T - e \cdot x_T F + E_{rel})^2}{4E_{rel} \cdot k_B T}\right). \quad (11.1)$$

Here σ_0 is the trap electronic capture cross-section (see, for instance, [7]), n and v_t are the carrier density and thermal velocity in the semiconductor substrate, respectively, λ is the characteristic electron (hole) tunneling distance in the oxide. E_C is the conduction band edge energy, E_T is the trap ionization energy, E_{rel} is the trap relaxation energy, x_T is the trap position in the oxide with respect to the interface with the substrate, F is the magnitude of the electric field in the oxide, $k_B T$ is the thermal energy. Due to a strong dependency of the calculated σ_0 value on the employed approximations, σ_0 is often considered as a fitting parameter. In this expression, the first and second exponent describe the electron tunneling and the lattice relaxation associated with the electron capture, respectively. E_{rel} character-izes the amount of energy dissipated into phonons as a result of electron tunneling.

As charges are trapped in the gate dielectric, the threshold voltage of the tran-sistor increases due to the built-in voltage in the gate capacitor; therefore, the drain current decreases. It appears that charge trapping and de-trapping times strongly depend on the composition of the gate stacks, i.e., physical thickness of the interfacial SiO_2 layer and high-k film, as well as on film processing techniques [13]. The time scale varies from several microseconds to tens of milliseconds. The de-trapping of the charges is also strongly gate voltage and polarity dependent. A wide dynamic range of charge trapping and the voltage dependent trapping and de-trapping, makes it ineffective applying only a single characterization technique to analyze the processes inside the stacked gate dielectric.

Traditionally, discharging from the dielectric layer is assessed by the shift in conventional $C-V$ measurements [14] on capacitors and transfer characteristics in transistors. These measurements generally take from several seconds to tens of seconds and are too slow for probing traps in thin dielectric layers. To gain a better understanding of these traps, several charge pumping methods (CP) are used to probe the traps in metal oxide (high-κ) layers [7, 15, 16]. However, charge pumping can usually reach the traps within a distance of about 1 nm into the high-κ (counting from its substrate side) layer when the thickness of interfacial SiO_2 layer (located in between the metal oxide and substrate) is around 1 nm [16]. while the thickness of metal oxide films in transistors is generally within 1.5–5 nm. The CP current is directly proportional to the number of oxide traps, which can contribute to the carrier exchange with the transistor channel under the given CP pulse frequency and amplitudes [7]. The trapping/de-trapping times depend exponentially on the tun-neling distance (11.1). This requires lower frequency in order to be able to probe traps situated farther from the Si substrate.

On the other hand, the pulsed $C-V$ technique [17, 18] is used to measure the flatband voltage, V_{FB}. Flatband voltage separates the accumulation regime from the depletion regime. It is the voltage at which there is no charge on the plates of the capacitor and hence there is no electric field across the oxide. Its numerical value depends on the doping of the semiconductor and on any residual interface charge that may exist at the interface between the semiconductor and the insulator. Similar to the conventional $C-V$ measurements, the rising and falling slopes of a pulse signal applied to the gate will give rise to a displacement current proportional to the capacitance and the pulse ramp rate. Since there is a minimum 4-s delay between

each measurement due to equipment initialization, single-pulse C–V cannot be used to accurately measure the discharging-induced V_{FB} shift. A two-pulse C–V technique was therefore developed to measure the flatband voltage shift caused by charging and discharging the traps in dielectric. A two-pulse signal is generated by the pulse generator so that the delay between two pulses can be accurately controlled down to milliseconds [18].

Below we demonstrate by comparing the pulse C–V and LFN analysis results of the data collected on HfO_2-based stacks with different SiO_2 interfacial layer thicknesses within the frame of phonon assisted trapping/de-trapping kinetics, the way to correlate the data obtained by different techniques.

11.3.2   Pulse C–V Technique

By applying a voltage pulse, the device can be switched from depletion into accumulation for the duration of time determined by the pulse width, during which period carriers are injected into the oxide. This changes the capacitance of the device, C. A pulse base of an opposite polarity is used to discharge the traps prior to the charging pulse. Charging and discharging transient currents associated with the rising and falling portions of the pulse are utilized to calculate the C-V dependency before and after the pulse (Fig. 11.2).

If there is no charge present in the oxide or at the oxide-semiconductor interface, the flat band voltage, $V_{FB,}$ equals the workfunction difference between the gate metal and the semiconductor. By monitoring the relative V_{FB} shift at the trailing edge caused by the charging of the dielectric traps, one obtains the trapped charge versus pulse duration dependency. The modeling (using phonon-assisted trap kinetics) yields the trap density profile in the gate stack by tracing the charge trapped in the portion of the dielectric located in between the depth fronts corresponding to pulses of different durations (and/or amplitudes), in Fig. 11.3.

The trap profiling can be done separately for the holes and electrons depending on the substrate type (p- or n-) used. In the case of the p-capacitors, the pulse C–V probing range is within of ~ 1 nm interfacial layer of the stack and is comparable to that accessible by the multi frequency CP measurements where the probing depth is also limited by the hole tunneling [3, 4].

11.3.3   Extraction of Trap Profile

Figure 11.3 shows the experimentally observed V_{FB} shifts in the MOS with a thin (1 nm) IL versus the pulse duration for the n-type substrate and the theoretical fit. Trap parameters previously extracted by modeling CP [3, 4], SILC [10] data, and pulsed IV analysis [6] were used for the theoretical fitting of the measured dependencies. Using pulses of 1.5 μs < T < 1 ms duration and gate biases of
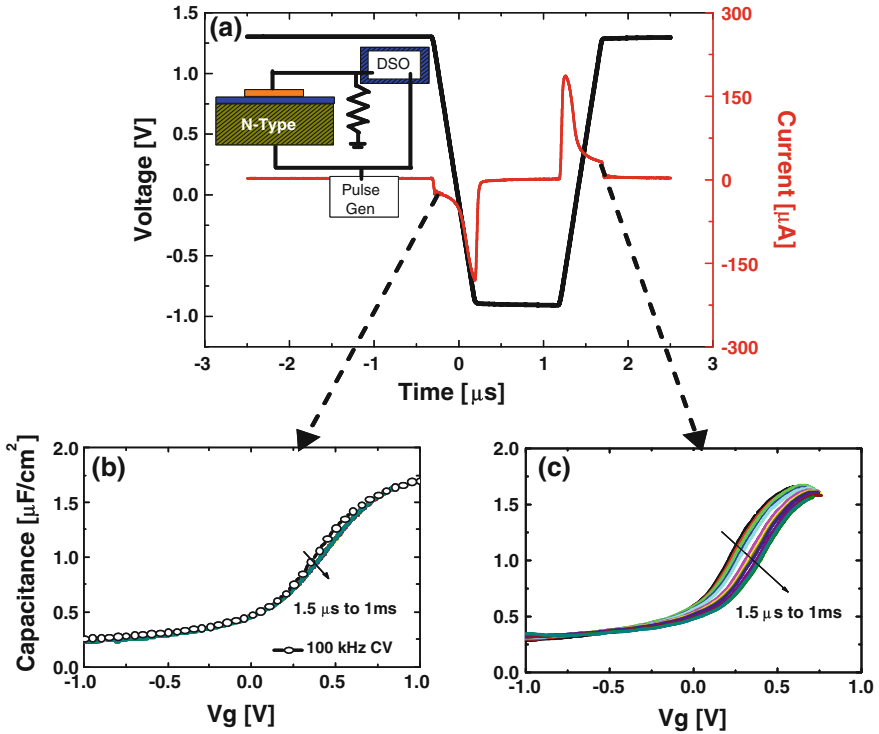
Fig. 11.2 **a** An example of the voltage pulse (*black*) and displacement current, $I = C \cdot dV/dt$, trace (*red*) measured on the n-capacitor. Inset shows an equivalent circuit for the pulse CV setup; **b** extracted CV at the pulse leading edge, and **c** trailing edge for different pulse durations (Color figure online)

0.6–1.0 V, the relative V_{FB} shift for the n-type samples was found to be caused primarily by the trap band in the high-k dielectric: its energy is centered above the Si conduction band edge, with the width $\Delta E \sim 0.4$ eV and a uniform spatial trap distribution with the density $N_T \sim 7 \times 10^{19}$ cm^{-3}. In the p-type samples, the traps in the IL layer (primarily a midgap centered trap band with the trap density exponentially increasing toward the IL/high-k interface [4]) can be probed. In the n-type samples, the ΔV_{FB} was found to increase monotonically with temperature. A significantly weaker temperature dependency was observed in the p-type samples. This points to a larger energy barrier for phonon-assisted trapping in high-k materials, as well as a larger relaxation energy. The relaxation energies used in our simulations correlate with the CP [3, 4] and SILC [10] modeling results, where the traps in the high-k layer were identified as neutral oxygen vacancies having relaxation energy, $E_{rel} \sim 1.2$ eV, while the traps in the SiO$_2$ IL were characterized by $E_{rel} \sim 0.36$ eV. It has been also observed that the additional, post-stress V_{FB} shift in the n-type devices was very small, which indicates a low rate of trap generation in the high-k dielectric.

Fig. 11.3 a The V_{FB} shifts measured (*symbols*) and simulated (*lines*) on the n-substrate capacitors, at different pulse amplitudes, V_g. **b** The simulated trap filling front profile for two pulse durations $T_{pulse} = 0.3$ and 0.5 ms. The *red rectangles* illustrate the spatial range of the trap distribution affected by the difference in the pulse duration (Color figure online)
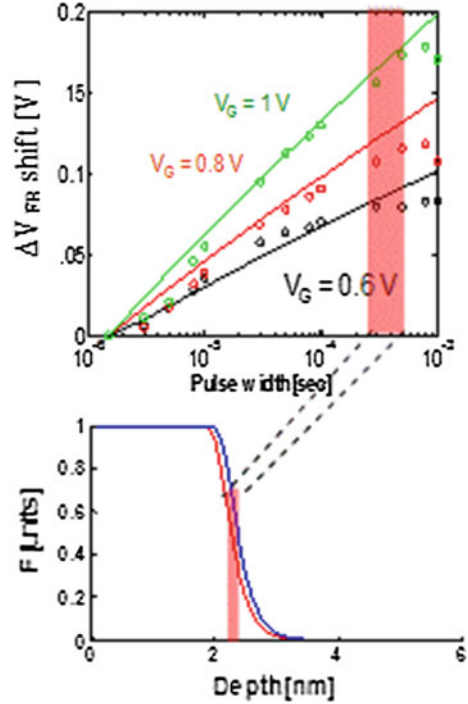
The calculated energy characteristics and extracted spatial distributions of the oxygen vacancies in the HfO$_2$ dielectric and SiO$_2$ interfacial layer allow reproducing the current-voltage dependency in the entire temperature range, Fig. 11.4.

A proposed methodology combines the pulsed *C–V* profiling technique (which is shown to be effective for evaluation of the charge trapping defects in the multilevel dielectrics stacks using a simple capacitor structure) and LFN technique. The described analysis allows extracting the defects' characteristics and their spatial distribution throughout the dielectric. Combination of different characterization techniques enables calibrating the extracted metal oxide and IL trap parameters, which are shown to correlate with those obtained by modeling the SILC [10] and CP [3] measurement data.

The procedure described above for extracting defect characteristics is implemented in a software, which provides, for a selected gate stack and measurement conditions, full Monte Carlo multi-phonon calculations for all possible carrier paths via the pre-existing defects, Fig. 11.4, presumed to be distributed either randomly or in accord with the collected physical characterization data [21]. The program accounts for the properties of the gate stack materials and defect characteristics as obtained by ab initio calculations; the defect density is used as a fitting parameter for each considered type of defects. Uniqueness of the defect characteristics extraction is ensured by employing a wide range of measurement conditions (reproducing entire *I-V* curves at different voltages and temperatures) and cross-correlating results for a
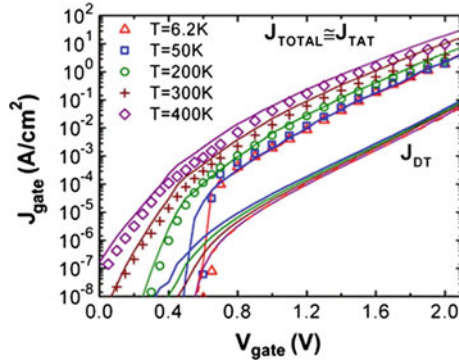
Fig. 11.4 Measured data (*symbols*) and simulations (*lines*) of the leakage current in the 1 nm SiO_2/3 nm HfO_2 NMOS/TiN gate dielectric stack in inversion at different temperatures [5]. The simulations are performed employing the multiphonon trap-assisted tunneling model and defect characteristics of the oxygen vacancies in SiO_2 and HfO_2 as calculated by the ab initio methods [8, 9, 19, 20]

variety of measurement techniques (e.g., the same set of defect parameters fits leakage current in the entire voltage range at several temperatures, flatband voltage shift, $V_{FB,}$ CP current, etc.). The program was demonstrated to successfully reproduce, using a predefined set of defect parameters, electrical data collected by a variety of measurement techniques on a wide range of transistor, capacitor, charge trapping and resistive memory stacks.

11.4 Charging/Discharging of HfO_2/SiO_2 Nano-Layers Stacks

As follows from the above discussion, under applied voltages, metal/dielectric stacks may experience gradual changes of their electrical characteristics. Below we consider in detail the case of defect activation by electron trapping in dielectric stacks grown over semiconductor substrates. The measured samples in this study are nMOSFETs with TiN (top gate electrode)/3 nm HfO_2/1.1 nm SiO_2 (dielectrics films)/Si (bottom substrate) stack. The SiO_2 interlayer is thermally grown on the 200 mm Si-substrate and etched back to the desired thickness, followed by the O_3-based ALD of HfO_2 layer and TiN electrode [7, 22].

Figure 11.5 shows variations of the threshold voltage (minimum applied voltage required to form a layer of charge carriers in the transistor channel, V_T) and leakage current (current through the dielectric stack, I_g) during the application of a voltage to the gate electrode of this stack ($V_{gs} = 2.3$ V at 100 °C for 2 ks), and after the recovery phase at $V_{gs} = -0.8$ V bias for 5 ks. The stress-induced changes in I_g, V_T correlate.

Fig. 11.5 Stress/recovery voltage, V_{gs} (*top panel*), V_T (*middle panel*), and I_g (*bottom panel*) evolution versus time for two consecutive stress/recovery cycles. 3 nm HfO$_2$/1.1 nm SiO$_2$ nMOSFET. $V_{gs} = 2.3$ V stress/-0.8 V for recovery, $T = 375$ K. I$_g$ is plotted @$V_{gs} = 0.9$ V. Both V_T and I_g experience "fast" jump: rise/drop during the first 10 s of stress/recovery, and monotonic increase/decrease on a longer timescale, marked with the *dashed ellipses* [7] (Color figure online)
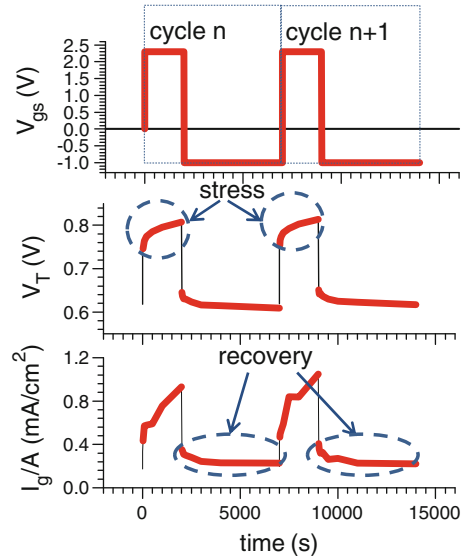
The time dependencies of I_g and V_T in Fig. 11.5 have two timescales. At a short timescale, during the first 10 s of stress/recovery, these two parameters exhibit characteristic large increase. Such a fast component was previously attributed to rapid electron trapping/de-trapping in the HfO$_2$ layer [23]. The long-timescale variation of these parameters is monotonic and smooth. The latter is near-identical in two sequential stress/recovery cycles, indicating that no additional defect generation, which would lead to an accumulation of parameter changes with each stress cycles, occurred. A similar repeatable variation of electrical parameters during repeated cycles of charging/discharging of this dielectric stack is observed by other electrical measurement techniques. In particular, interrupting stress to perform multi-frequency charge pumping (CP) measurements on these transistors demonstrated the increase (with the stress duration) and reduction (during recovery—de-trapping phase) of the cumulative trap density in the SiO$_2$ interlayer [7]. Measurements and modeling data for this dielectric stack were interpreted as controlled by accumulation of the charges trapped by the defects.

The critical question is whether new structural defects were *generated* by the electrons injected under the applied voltage conditions or whether the pre-existing defects were electrically *activated* by trapping injected electrons, which enables subsequent electron transport via the newly activated defects?

Creation of new defects in SiO$_2$ films is associated with structural changes in the oxide involving Si–O bond breaking, which requires significant energy [24] and is unlikely at the stress voltage used here. On the other hand, partial reversibility of degradation, points to a possibility that the stress-induced instability might be, at least partially, caused by the activation of electrically "silent" pre-existed defects rather than by bond breaking. These defects should become activated when they

capture injected charge carriers. Upon activation, such a defect can contribute to the further transport of charge carriers, which contributes to a variety of electrical measurements. Trap activation may be associated with a large multi-phonon assisted structural relaxation of the lattice in the proximity of the defect. Accordingly, a large energy barrier can cause the activation and de-activation of a defect to be slow processes. The following capture and emission of a subsequent charge carrier by an activated trap, which contributes to electrical measurements, may, however, be a relatively fast process, associated with a significantly smaller structural relaxation. Further analysis of electrical measurements suggests that traps responsible for these processes are most likely located in the SiO_2 IL layer at the interface with HfO_2 [7].

The feasibility of such a trap activation process was explored by informing the activation concept with the defect parameters obtained by ab initio calculations described below [22].

11.5 Modeling Defect Activation in HfO_2/SiO_2 Nano-Layers Stacks

To produce a model of a defect responsible for electrical behaviour described above we need to construct a model of a $Si/SiO_2/HfO_2$ stack and consider a number of plausible candidates. To narrow down our search, we consider that prior to activation, the precursor defects should be "silent", i.e. not able to participate in a sufficiently fast electron exchange with the electrode and substrate observed by the chosen measurement technique(s). A relatively slow activation under the applied bias points to low rates of the electron capture by the precursor defects in the interlayer. This suggests that the electron trapping should be associated with a large structural change of the defect lattice surroundings, which defines the energy barrier of the trapping process [11, 25]. After activation, on the other hand, the defect should be in the energy range allowing fast exchange of injected carriers with the substrate and gate electrode (in order to contribute to the above mentioned electrical measurements). The defect deactivates by losing trapped electron under the recovery conditions (that is under an applied negative gate bias) and reactivate (upon the reapplied stress bias). To satisfy these requirements, we may consider the following scenario for the defect activation process:

(i) Prior to capturing an electron, the precursor defect has two possible stable configurations of different energies. We will refer to this pre-activation state as the initial state.

(ii) Upon capturing an electron, the energy ordering between the two configurations reverses: the energy of the configuration with the localized electron rises prompting the system to transition into the second (deeper) energy minimum, which corresponds to a new lattice configuration (see also Fig. 11.10). When the stress bias is applied, the energy of this configuration falls below the gate Fermi-level.

(iii) Based on the estimated activation rates, the energy barrier between the two defect configurations after electron trapping is of the order ~ 1.5 eV

(iv) When the stress is removed, the defect energy level is above the Fermi level, enabling electron emission and the defect reverting to its initial configuration.

To identify the candidate defects meeting the above requirements, we employed ab initio simulations using the CP2K program suite [26]. The Quickstep DFT module was used to carry out hybrid density functional calculations using the PBE0-TC-LRC-ADMM hybrid density functional [27, 28], containing 25 % exact exchange. The primary basis sets were the DZVP-MOLOPT-SR-GTH basis distributed with the code along with the corresponding GTH pseudo-potentials (with 12, 4, 6, and 1 electrons treated as valence for Hf, Si, O and H) [29–31]. The auxiliary Gaussian basis for the ADMM method was pFIT3, as detailed in [19], and a FIT3 basis for Hf was optimized using a variant of the procedure outlined in the same paper. Wave-function optimizations are performed using the orbital transformation method [32].

The procedure used for constructing an $HfO_2/SiO_2/Si$ stack has been described in detail in [33]. In this work, the number of Si layers has been increased with respect to the original structure to converge the band gap of the Si substrate (to 1.2 eV). The geometric structure of the whole stack has been optimized using the hybrid density functional and basis sets described above. The electronic structure of the stack was analysed using a real-space projection of the density of states with energy resolution of 0.1 eV (Fig. 11.6). The stack has no obvious defect energy levels within the energy ranges of interest. The respective band gaps and offsets of the components of the model stack are in reasonable agreement with available experimental data, allowing ready interpretation of the location of defect energy levels without additional adjustments.

The defect candidates include oxygen vacancies in different positions in the gate stack and various charge states. Oxygen vacancies in amorphous SiO_2 are known to have several configurations connected via potential barriers [19, 34]. However, an interface defect satisfying the criteria outlined above cannot be based on the double well puckering model of a positively charged O vacancy, the so called E' center, because the barrier for the transformation between the two configurations is too small and non-existent after the electron trapping [34]. The only oxygen deficient center in bulk a-SiO_2 having two configurations, stable in two charge states, and having a large barrier between these states is a so-called back-projected configuration of neutral or negatively charged oxygen vacancies [19]. Therefore, we considered three plausible families of defects that could address all the above listed requirements, all based around the oxygen vacancy, but extended to consider its proximity of the HfO_2/SiO_2 interface:

(a) Oxygen vacancies located directly at the HfO_2/SiO_2 interface (Fig. 11.7a). These defects could have a back-projected configuration with a Si ion neighboring the vacancy moving back into the silica, leaving space near HfO_2 that could accept additional electrons.
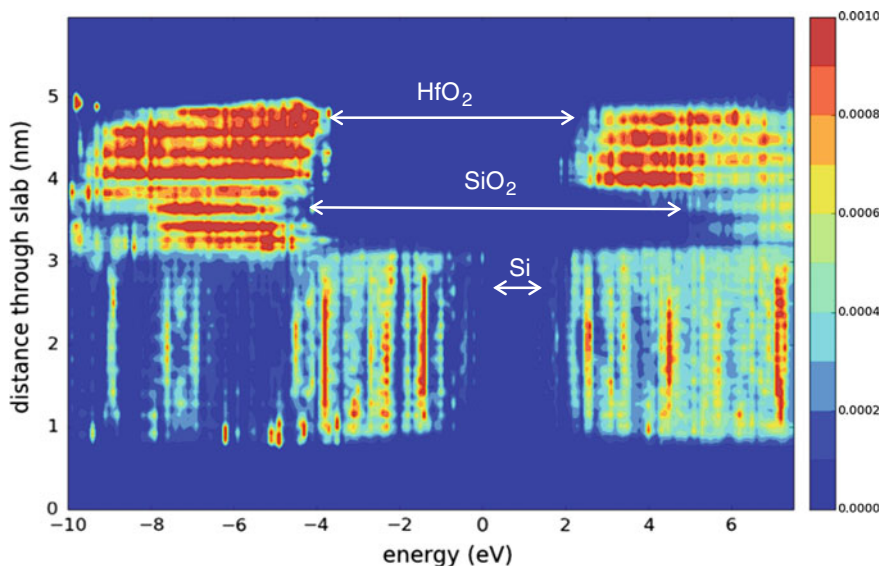
Fig. 11.6 Electronic denisty of state of the HfO$_2$/SiO$_2$/Si stack. The maximum energy of the Si valence band is arbitrarily set zero as the reference. The *y*-axis is the direction perpendicular to the interfaces. The *color scale* shows the density of electron states/Å^3. *Arrow bars* show the band gaps of corresponding materials

(b) Oxygen vacancies separated from the HfO$_2$/SiO$_2$ interface by one Si–O bond, i.e. just inside the SiO$_2$ (Fig. 11.7b). These defects could have back-projected configuration where the more highly charged Hf ions at the interface (compared to Si) could help stabilize additional electrons on the Si that is displaced away from the vacancy.

(c) A hybrid of the first two, where upon electron addition, the vacancy site could migrate towards the interface forming a more HfO$_2$-like vacancy that would stabilize the added electron (Fig. 11.7c).

In each of these cases the barriers between the configurations would be expected to be of the correct order (1–1.6 eV) due to the motion of an O or Si ion by around 2 Å and we can suggest mechanisms that stabilize the rearranged electron attached state [22]. The transitions between these configurations showing the activation and regeneration states are also schematically illustrated in Fig. 11.7.

To locate possible defects that satisfy our criteria, we first calculated the formation energies of a sample of O vacancy defects at sites throughout the SiO$_2$ part of our model interface. The results are shown in Fig. 11.8. It can be seen that there is considerable spread in the formation energies of oxygen vacancies at different sites within the stack. A similarly large distribution of energies is expected for the negatively charged vacancies and the electron affinities of the different vacancy sites do not necessarily correlate strongly with the formation energies of the neutral defect (this is the rationale behind the 3rd suggested family of defects, Fig. 11.7c).

Fig. 11.7 Schematics of the configuration transitions associated with the activation of the defect for 3 different defect types: **a** Oxygen vacancy directly at the interface between the HfO$_2$ and SiO$_2$ with the vacancy moving into SiO$_2$ after the transition; **b** Oxygen vacancy is one Si–O bond distant from the HfO$_2$/SiO$_2$ interface; **c** An oxygen vacancy in SiO$_2$ moving into the HfO$_2$/SiO$_2$ interface. In each case we also show the activated trap state of the defect that would occur after electron trapping, and atomic rearrangment. The *dots* in the atomic diagrams schematically show the number and possible locations of localized electrons related to the defect
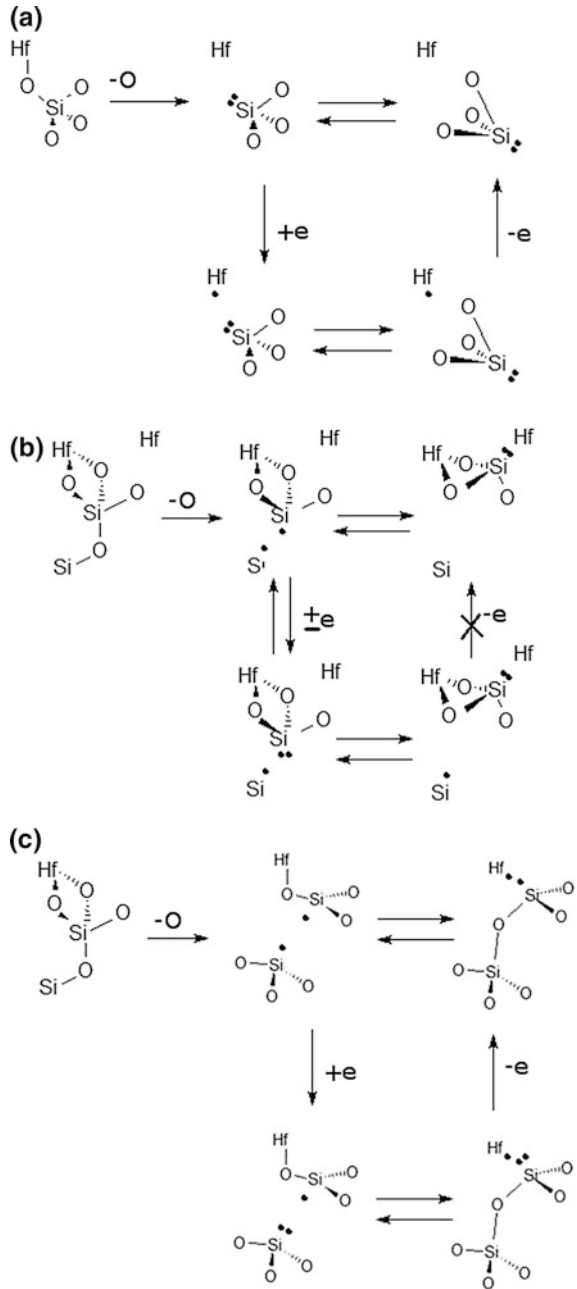
Fig. 11.8 Formation energies of 43 neutral oxygen vacancies at various positions between the Si and HfO$_2$ parts of the stack (i.e. nominally within SiO$_2$). The right-most defects are directly at the HfO$_2$/SiO$_2$ interface and the left-most directly at the SiO$_2$/Si interface
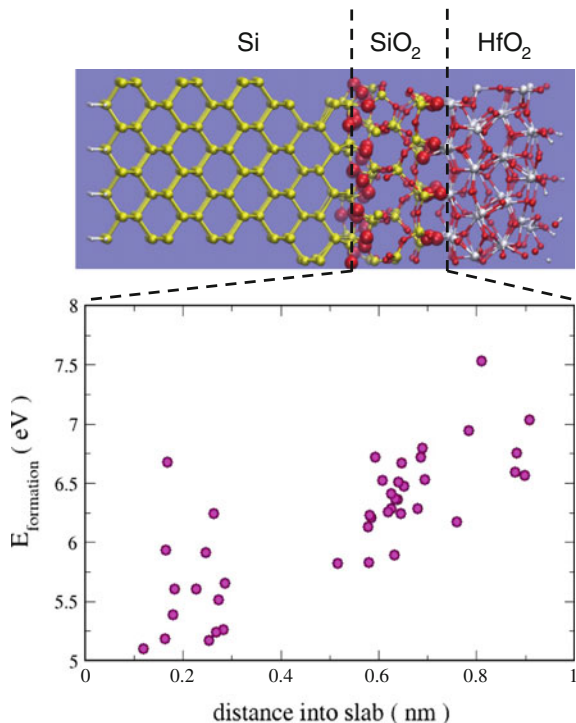
An example of the possible configurations of the system is shown in Fig. 11.9. Starting from a neutral vacancy separated from the HfO$_2$/SiO$_2$ interface by one Si–O bond, we move clockwise round in Fig. 11.9. The Si atom nearest to the HfO$_2$ film can relax away from the vacancy towards the Hafnia, forming a back-projected oxygen vacancy. This state is found to be high in energy and a shallow local minimum on the potential energy surface. It would however, rapidly relax back to the original vacancy configuration.

When an electron is added to form a negatively charged oxygen vacancy, the back-projected configuration is strongly stabilized compared to the neutral back-projected one. The stabilization of this defect configuration is caused by the presence of the HfO$_2$ layer through a combination of electrostatics and covalent bonding, as can be seen in the simulated adiabatic potential energy surfaces (Fig. 11.10). This confirms the suggestion that the interface can act to stabilize otherwise unlikely [22] configurations of negatively charged vacancies in a-SiO$_2$.

Figure 11.10 shows the adiabatic potential energy surfaces corresponding to the configurations 1–4 in Fig. 11.9. Red curves represents negatively charged configurations (configurations 2 and 3) with (solid red curve) and without (dotted red curve) the inclusion of the correction for the stress voltage bias.

As can be seen, for the *particular* defect in Fig. 11.7b, the negative charge in the back projected vacancy state is closer to the HfO$_2$/SiO$_2$ interface than the charge in

Fig. 11.9 Configurations of a
vacancy at/near the HfO$_2$/
SiO$_2$ interfaces corresponding
to the scheme in Fig. 11.7b.
The *black dotted line*
indicates the two silicon ions
flanking the removed oxygen
ion, the number indicates their
seperation in Å. Silicon,
oxygen ions and hafnium
atoms are shown as *yellow*,
red, and *grey*, respectively

configuration 1
neutral O vacancy

configuration 4
neutral back-projected

configuration 2
charged O vacancy

configuration 3
charged back-projected
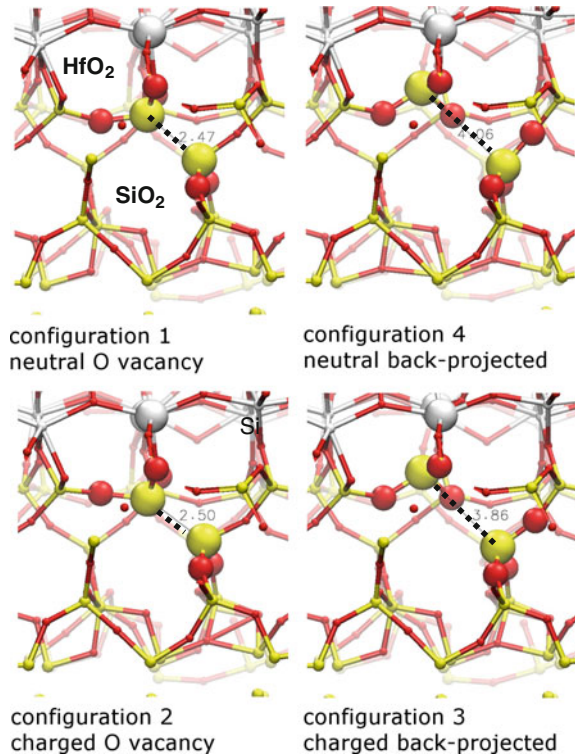
the negative state of the unreconstructed vacancy by ~ 2 Å. The latter assists the
stabilization of the back projected defect configuration by the potential gradient
across the interface, making it closer in energy (within about 0.2 eV) to that of the
undistorted charged configuration. When stress bias is applied, the energy of the
charged back-bonded configuration becomes equal to the energy of the undistorted
configuration of a negatively charged oxygen vacancy.

The charged back-projected configuration is seen to be stable against emitting an
electron to the electrode—the vertical transition energy to the neutral state at
configuration 3 of Fig. 11.10 is calculated to be 5.2 eV when the bias at the gate
electrode during stress is kept at 2.3 V. Thus, the configuration 3 can only relax
back to the ground state (to the configuration 1 in Figs. 11.7 and 11.10) by first
overcoming the barrier required to switch back to configuration 2.

While attempting to find defects that fit the experimental data quantitatively, we
have confirmed that the sequences of defect transformations suggested in Fig. 11.7
are locally stable within state-of-the-art DFT and that they can support varying
charge states within the Si band-gap. This also indicates that oxygen vacancies near
the interface may have complex potential energy surfaces capable of having several
local minima in each charge state. This picture emerges from the known flexibility
of a-SiO$_2$ and its ability to host a range of defects combining with the new
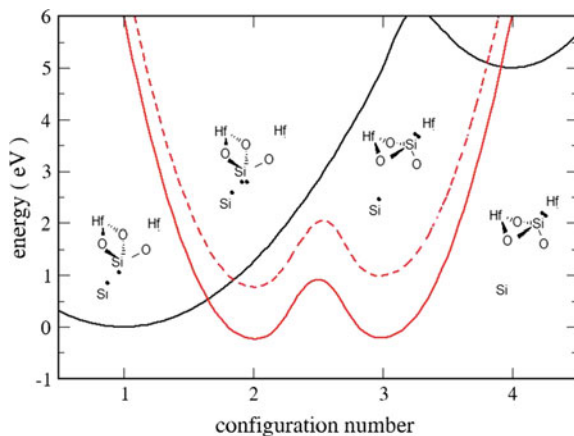
Fig. 11.10 Potential energy diagram for the defect shown in Fig. 11.9. The *black curve* shows the adiabatic energy for the neutral configurations of the defect. The *red dashed curve* shows potential energy profile for the system with an added electron at zero applied bias. The *solid red curve* includes the approximate effect of the applied stress bias of 2.3 V. For comparison to Fig. 11.7b cartoons are shown for the four atomic configurations of the system. Relative energies of the different configurations come from simulation, the distance between configurations and the energy barriers are only schematic. Energies are compared to electrons occupying the bottom of the silicon conduction band

environment in close proximity to the HfO_2 material. The large spread of relative vacancy formation energies in Fig. 11.8 suggests that, allowing for a similar variation in the energies of the other configurations, a subset of vacancies may have the charged back-projected state stabilized more strongly than is shown for this particular case.

These results confirm that changes of electrical characteristics of the nFETs high-*k* gate stacks under low voltage stresses of practical interest can be induced by a reversible electron capture at the pre-existing defects rather than generation of new structural defects. By utilizing the multi-phonon assisted charge transport description it is demonstrated that the trap activation concept allows reproducing a variety of experimental results including stress time dependency of the threshold voltage, leakage current, CP current, and low frequency noise [7, 22]. Continuous, long-term degradation (e.g., described by the power law time dependency in the case of V_T) is shown to be caused by the activation of defects located in the interfacial SiO_2 layer of the high-k gate stacks. Ab initio calculations suggest a plausible candidate—an oxygen vacancy in the SiO_2 region adjacent to the high-*k* film, which can reversibly change their atomic configuration upon capturing/emitting an electron. These electron trapping properties are directly related to the proximity of the oxygen vacancy to the HfO_2, which stabilizes its negatively charged back-projected atomic configuration. The characteristic time of the vacancy transformation into this configuration determines the defect activation rates controlling the rates of degradation of device electrical characteristics.

These results also serve to illustrate the process of collaboration between electrical measurements on fabricated devices and ab initio modelling of defect candidates through the model extraction procedure. They highlight several challenges: (i) limited data provided by electrical measurements to inform defect modelling; (ii) statistical nature of both the experimental data and theoretical results related to disorders in amorphous structure and interfaces of the oxide stacks; (iii) complexity of identifying which defects are involved—in most cases they remain 'most plausible candidates' until new experimental data emerge.

11.6 Summary and Outlook

In this chapter we briefly discussed the charge transfer phenomena, which determine the performance and reliability of electronic device stacks of nm-thin layers of dielectric materials in contact with the conductive electrodes (semiconductors, metals). By employing multi-phonon statistical carrier transport simulations of the temperature dependent leakage currents we linked electrical measurements to possible atomic structures of the electrically active defects in dielectric stacks. Comparing modeling results with the measurement data allows one to extract the critical defect characteristics, specifically their ionization and relaxation energies, which were combined with the ab initio modelling data to identify contributing defects. Knowing the defect structures enables considering specific physical processes responsible for the defects generation and activation. We also discussed a possibility that the stress-induced instability might be primarily caused by the activation of electrically "silent" pre-existed defects rather than by bond breaking leading to generation of new defects. These pre-existing defects become activated after capturing injected charge carriers, and upon activation they can contribute to trap assisted transport of charge carriers affecting a variety of electrical characteristics. Although the activation and deactivation of a pre-existing defect might proceed rather slowly, the subsequent capture and emission of a charge carrier by an activated trap can be a relatively fast process associated with a significantly smaller structural relaxation.

Future work will need to take into account that the current through the dielectric accompanied by the carrier trapping/de-trapping events may substantially increase the probability of generating new defects which we did not consider in this discussion. Indeed, carrier localization can weaken chemical bonds [35] while the excess of the carrier energy (the energy difference between the Fermi level and defect ground state) dissipated into the surrounding lattice tends to rise the local temperature. This excitation of atomic vibrations increases the possibility that the participating atoms (oxygens) overcome the binding energy barrier and displace out of their regular lattice positions, thus creating new defects, which are also capable of contributing to the carrier transport (TAT) process. The widely accepted statistical description, which has successfully reproduced many aspects of the electrical degradation phenomenon resulting in the formation of a permanent highly

conductive path [aka dielectric breakdown (BD)], is based on the premises that the defects are randomly generated in the dielectric subjected to electrical stress, and the BD occurs as soon as the defects form a percolation path connecting the electrodes through the dielectric film. This description, while being attractive due to its intuitive simplicity, does not necessarily accurately reflect physical processes governing the BD mechanism. Treating defects as unspecified black boxes hampers addressing a number of critical issues, for instance, whether an accelerated (high) voltage stress is an adequate approach for estimating device life time under use-conditions or how fabrication-related changes in the gate stack composition might affect device reliability.

References

1. Wilk GD, Wallace RM, Anthony JM (2001) High-k gate dielectrics: current status and materials properties considerations. J Appl Phys 89:5243–5275
2. Robertson J (2006) High dielectric constant gate oxides for metal oxide Si transistors. Rep Progr Phys 69:327–396
3. Bersuker G, Lysaght PS, Park CS, Barnett J, Young CD, Kirsch PD, Choi R, Lee BH, Foran B, van Benthem K, Pennycook SJ, Lenahan PM, Ryan JT (2006) The effect of interfacial layer properties on the performance of Hf-based gate stack devices. J Appl Phys 100:094108–094108–10
4. Bersuker G (2013) Reliability implications of fast and slow degradation processes in high-k gate stacks. In: Kar S (ed) High permittivity gate dielectric materials. Springer, Berlin, pp 309–342
5. Vandelli L, Padovani A, Larcher L, Southwick RG III, Knowlton WB, Bersuker G (2011) A physical model of the temperature dependence of the current through SiO_2/HfO_2 stacks. IEEE Trans El Dev 58:2878–2887
6. Vandelli L, Padovani A, Larcher L, Bersuker G (2013) Microscopic Modeling of electrical stress-induced breakdown in poly-crystalline hafnium oxide dielectrics. IEEE Trans El Dev 60:1754–1762
7. Veksler D, Bersuker G (2014) Gate dielectric degradation: pre-existing vs. generated defects. J Appl Phys 115:034517–034517–11
8. Gavartin JL, Muños Ramo D, Shluger AL, Bersuker G, Lee BH (2006) Negative oxygen vacancies in HfO_2 as charge traps in high-k stacks. Appl Phys Lett 88:082901–082901–3
9. Broqvist P, Pasquarello A (2006) Oxygen vacancy in monoclinic HfO_2: A consistent interpretation of trap assisted conduction, direct electron injection, and optical absorption experiments. Appl Phys Lett 89:262904–262904–3

10. Young CD, Zhao Y, Heh D, Choi R, Lee BH, Bersuker G (2009) Pulsed I_d–V_g methodology and its application to electron-trapping characterization and defect density profiling. IEEE Trans El Dev 56:1322–1329
11. Veksler D, Bersuker G, Koudymov A, Liehr M (2013) Analysis of charge pumping data for identification of dielectric defects. IEEE Trans El Dev 60:1514–1522
12. Li X, Yajima T, Nishimura T, Nagashio K, Toriumi A (2014) Effect of Si substrate on interfacial SiO_2 scavenging in $HfO_2/SiO_2/Si$ stacks. Appl Phys Lett 105:182902–182902–4
13. Choi R, Rhee SJ, Lee JC, Lee BH, Bersuker G (2005) Charge trapping and detrapping characteristics in Hafnium silicate gate stack under static and dynamic stress. IEEE El Dev Lett 26:197–199
14. Zhang JF, Taylor S, Eccleston W (1992) A comparative study of the electron trapping and thermal detrapping in SiO_2 prepared by plasma and thermal oxidation. J Appl Phys 72:1429–1439
15. Heh D, Young CD, Brown GA, Hung PY, Diebold A, Vogel EM, Joseph B, Bersuker G (2007) Spatial distributions of trapping centers in HfO_2/SiO_2 gate stack. IEEE Trans El Dev 54:1338–1345
16. Wang Y, Lee V, Cheung KP (2006) Frequency dependent charge-pumping, how deep does it probe? IEDM Tech Digest 491–494
17. Weinberg ZA, Fischetti MV (1986) SiO_2-induced substrate current and its relation to positive charge in field-effect transistors. J Appl Phys 59:824–832
18. Zhang WD, Govoreanu B, Zheng XF, Ruiz Aguado D, Rosmeulen M, Blomme P, Zhang JF, Van Houdt J (2008) Two-pulse C-V : a new method for characterizing electron traps in the bulk of SiO2/high-κ dielectric stacks. IEEE El Dev Lett 29:1043–1048
19. Kimmel AV, Sushko PV, Shluger AL, Bersuker G (2009) Positive and negative oxygen vacancies in amorphous silica. ECS Trans 19:3–17
20. Muñoz Ramo D, Gavartin JL, Shluger AL, Bersuker G (2007) Intrinsic and defect-assisted trapping of electrons and holes in HfO_2: an ab initio study. Microel Eng. 84:2362–2365
21. www.mdlab-software.it
22. Veksler D, Bersuker G, Watkins MB, Shluger AL (2014) Activation of electrically silent defects in the high-k gate stacks. In: IEEE international reliability physics symposium (IRPS) 5B. 3.1–5B. 3.7
23. Vandelli L, Larcher L, Veksler D, Padovani A, Bersuker G (2015) A charge-trapping model for the fast component of positive bias temperature instability (PBTI) in high-k gate stacks (submitted)
24. Mukhopadhyay S, Sushko PV, Stoneham AM, Shluger AL (2005) Correlation between the atomic structure, formation energies, and optical absorption of neutral oxygen vacancies in amorphous silica. Phys Rev B 71:235204–235204–10
25. Fowler WB, Rudra JK, Zvanut ME, Feigl FJ (1990) Hysteresis and Franck-Condon relaxation in insulator-semiconductor tunneling. Phys Rev B 41:8313–8320
26. VandeVondele J, Krack M, Mohamed F, Parrinello M, Chassaing T, Hutter J (2005) Quickstep: fast and accurate density functional calculations using a mixed Gaussian and plane waves approach. Comput Phys Commun 167:103–128
27. Guidon M, Hutter J, VandeVondele J (2009) Robust periodic Hartree-Fock exchange for large-scale simulations using Gaussian basis sets. J Chem Theory Comput 5:3010–3021
28. Guidon M, Hutter J, VandeVondele J (2010) Auxiliary density matrix methods for Hartree-Fock exchange calculations. J Chem Theory Comput 6:2348–2364
29. VandeVondele J, Hutter J (2007) Gaussian basis sets for accurate calculations on molecular systems in gas and condensed phases. J Chem Phys 127:114105–114105–9
30. Goedecker S, Teter M, Hutter J (1996) Separable dual-space Gaussian pseudopotentials. Phys Rev B 54:1703–1710
31. Krack M (2005) Pseudopotentials for H to Kr optimized for gradient-corrected exchange-correlation functionals. Theor Chem Accounts 114:145–152
32. VandeVondele J, Hutter J (2003) An efficient orbital transformation method for electronic structure calculations. J Chem Phys 118:4365–4369

33. Gavartin JL, Shluger AL (2007) Modeling $HfO_2/SiO_2/Si$ interface. Microel Eng 84: 2412–2415
34. Mukhopadhyay S, Sushko PV, Stoneham AM, Shluger AL (2004) Modeling of the structure and properties of oxygen vacancies in amorphous silica. Phys Rev B 70:195203–195203–15
35. Bradley SR, Shluger AL, Bersuker G (2015) Electron injection assisted generation of oxygen vacancies in monoclinic HfO_2. Phys Rev Appl 4:064008

Chapter 12
Two-Dimensional Electron Gas at Oxide Interfaces

Alexander A. Demkov, Kristy J. Kormondy and Kurt D. Fredrickson

Abstract In this chapter, we provide an overview of the growing field of the two-dimensional electron gas in oxide heterostructures. The discovery of the high mobility electron gas at the oxide-oxide interface has spurred subsequent investigations which draw from the large body of work on polar oxide surfaces and thin films. We discuss the three main mechanisms of electronic reconstruction, oxygen vacancy formation, and cation exchange in order to address the question, "How can the interface between two insulators be conducting?" Throughout the chapter, in addition to the model $LaAlO_3/SrTiO_3$ system, we provide the reader with a sampling of what has been learned from other oxide heterostructures through both experiment and theory.

12.1 Introduction

A recently discovered revolutionary class of polar oxide heterostructures [67] holds tremendous promise for exploiting the physical properties of the novel quasi two-dimensional electron gas (2DEG) formed at the oxide/oxide interface. The polar catastrophe mechanism has a historic relation to a problem of polar oxide surfaces. The subject has been in the spotlight of the intense investigation for years, and there are several excellent reviews summarizing the main results [66]. To give the reader a flavor of that field we now briefly sketch the main ideas. In general, oxide surfaces are more complicated than those of semiconductors, where the problem has been recognized for almost 40 years [32]. Three different types of insulating surfaces can be identified. The type 1 surface has neither charge or dipole

A.A. Demkov (✉) · K.J. Kormondy · K.D. Fredrickson
Department of Physics, University of Texas, Austin, TX 78712, USA
e-mail: demkov@physics.utexas.edu

K.J. Kormondy
e-mail: kkormond@physics.utexas.edu

K.D. Fredrickson
e-mail: kdfred@physics.utexas.edu

moment, the type 2 surface has charge but does not possess the dipole, and the type 3 surface has both, the unbalanced charge in the surface layer and a non-zero dipole in the repeated unit in the direction normal to the surface.

Polarity of the oxide surface can be cancelled in different ways depending on how severe it is. In ultra-thin films ionic screening may be enough [81]. However, for fully polar surface the surface states must be created and filled, to provide the compensating field. This in turn can be achieved either though electronic reconstruction or by removal of atoms from the surface layers.

Similarly, in the case of oxide heterostructures, the fundamental scientific understanding is of significant fundamental importance. The origin of the 2DEG is still widely investigated and can be attributed to at least three interfacial phenomena, as illustrated in Fig. 12.1: (i) electronic reconstruction, as suggested for the original $LaAlO_3/SrTiO_3$ (LAO/STO) structure [67]; (ii) electrically active defects [44, 76, 84]; or (iii) stoichiometry deviations [61, 76].

Many exciting results reported to date have been discovered in heterostructures based on oxides of transition metals with perovskite crystal structure [15, 35, 38, 41, 72, 92, 99]. Owing to the exquisite, atomic level control of layer design, afforded by new developments in oxide epitaxy, these systems are expected to enable militarily significant and commercially valuable products. The unprecedented richness of physical phenomena observed in these materials systems, stems from the delicate balance of multiple interactions that control the quantum behavior of d- and sometimes f-electrons in the unfilled shells of the transition metal ion. In bulk materials, this is the origin of magnetism, superconductivity, ferroelectricity and several other related effects [57]. On the other hand, the properties of epitaxial interfaces are controlled by strain, band alignment, and crystal imperfections that may affect the long-range as well as the short-range order. Symmetry lowering at the interface creates entirely new environments for the electrons of the "active" atomic species that are not realizable in the bulk environments.

Although the 2DEG is usually thought of as localized at the interface, the spatial extent of the gas has been found to vary from a depth of a few nanometers to hundreds of micrometers. [5] The varying spread of the 2DEG is due to many factors, including oxygen vacancy concentration, [5] temperature of the system,
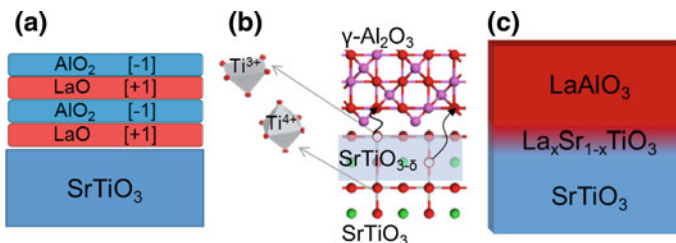
Fig. 12.1 Highly conductive interfaces can be formed between two insulating oxides due to **a** electronic reconstruction, **b** Oxygen vacancies (Modified from [48]), and **c** Stoichiometry deviations

[84] charge density of the gas, [46] amount of cationic exchange, [89] and ionic relaxation at the interface [68, 69, 73].

Experiment and theory show that the 2DEG at the oxide/oxide interface has many exotic features. It can be paramagnetic, ferromagnetic or even superconducting, [12, 50, 62, 63, 74, 79] with strong Rashba splitting leading to a controllable magnetic moment. [11, 45, 58]. It has been demonstrated that various modifications of the LAO/STO heterostructure also lead to a variety of interesting effects. Arras et al. used density functional theory (DFT) to calculate the effect of metallic layers on LAO/STO heterostructures. For a thin STO substrate (2.5 unit cells (UC)), 1 monolayer (ML) of Ti deposited on LAO lead to the vanishing of the electric field in LAO; even given this, the LAO/STO interface is still conducting, due to the migration of charge to the lowest unoccupied states that exist at the bottom of the STO conduction band; moreover, the Ti metallic layer and the interface are both magnetic. For thicker STO (6.5 UC), the system is the same, except that the interface is nonmagnetic; the authors ascribe the magnetization of the interface for thinner STO to quantum confinement effects. Upon the addition of more MLs of Ti metal on the LAO surface, the conducting states do not change appreciably, but the magnetization of the Ti metal is reduced; by 3 ML of Ti, the surface metal (and thus the entire system) is nonmagnetic. The authors also tried different metallic contacts (single ML of Na, Al, Fe, Co, Cu, Ag, Pt and Au). The field in LAO was not always reduced to zero; in fact, for the Au contact, the electric field was enhanced! This is due to the large work function of Au, which places the Fermi energy mid-gap in STO; therefore, no charge is transferred to the STO/LAO surface and the field in LAO is not destroyed [3].

Although most of the experiments were done on LAO grown on bulk STO, there have also been reports of the 2DEG found in LAO/STO heterostructures deposited on Si, paving the way for semiconducting devices utilizing the properties of the oxide 2DEG. [71] Levy and co-authors used atomic force microscope lithography to induce a reversible metal/insulator transition of the interface [13, 14].

In this chapter, we identify oxide systems which exhibit interfacial conductivity (often two dimensional) stemming from (one or more of) three separate origins: electronic reconstruction, cation exchange, and oxygen vacancies.

12.2 Electronic Reconstruction

Discussions of the origins of the oxide 2DEG often start with polar catastrophe and electronic reconstruction. [28, 32, 39, 40] Whenever there is an abrupt change in polarization, in order to satisfy Maxwell's equations, there must be a free charge density σ_f:

$$D_{1,n} - D_{2,n} = \sigma_f \qquad (12.1)$$

where D_n is the electric displacement normal to the surface or the interface. This equation is always satisfied, whether at a surface of a material, or at the interface between two dissimilar materials. It has been shown that true polar surfaces are impossible; any excess charge due to polar terminations must be compensated by a free charge density provided by holes or electrons, or possibly by adsorbed molecules or vacancies. [87] In ferroelectrics, free charge carriers can form due to uncompensated charge at the surface [33, 47, 83, 94, 96], and at head-to-head or tail-to-tail domain walls [30, 85, 86, 93] where there is a relatively abrupt change in polarization. In pure $BaTiO_3$ (BTO), a positively poled system was measured to have 10 times higher surface conductance than a negatively or randomly polarized sample, which is ascribed to accumulation of electrons at the BTO surface. The surface is also seen to have an Ohmic relation upon performing I-V measurements, consistent with a conducting state [95]. (12.1) must also be satisfied at interfaces; at oxide-oxide interfaces, the system will do its best to reduce the jump in polarization, and thus reduce σ_f [88]. For interfaces between two polar materials, the situation is even more complex; depending on the relative valence charge of the interface, structural distortions, and symmetry breaking of the interface, the system may have an insulating interface, a metallic interface due to two-dimensional gas formation, or it may even exhibit a thickness-dependent metal-insulator transition [29].

Left uncompensated, a large electric field is built-up in a polar oxide such as LAO; the alternating positively charged LaO and negatively charged AlO_2 layers lead to a ramping up of the electrostatic potential that grows without limit (Fig. 12.2). Due to the large energy cost of this internal field, and to avoid dielectric breakdown, the heterostructure must find a way to compensate this diverging electrostatic potential. One way to avoid the polar catastrophe is electronic reconstruction, where the electronic charge migrates to the interface to eliminate the field once a critical thickness is reached (Fig. 12.2). In this case, (12.1) is satisfied by the migration of electrons to the surface, which is caused by the abrupt change of polarization between the polar LAO and nonpolar STO.

In this section, we summarize theoretical and experimental results on the phenomenon of electronic reconstruction in LAO, $LaTiO_3$ (LTO), several other polar oxides, and ferroelectric oxides.

12.2.1   LAO/STO

The phenomenon of electronic reconstruction has received extensive consideration since the initial discovery of the conducting layer at the interface of polar LAO and nonpolar STO (001) [67]. Here, the thickness of LAO is an important factor; the interface undergoes an insulator-metal transition at a critical thickness of four unit
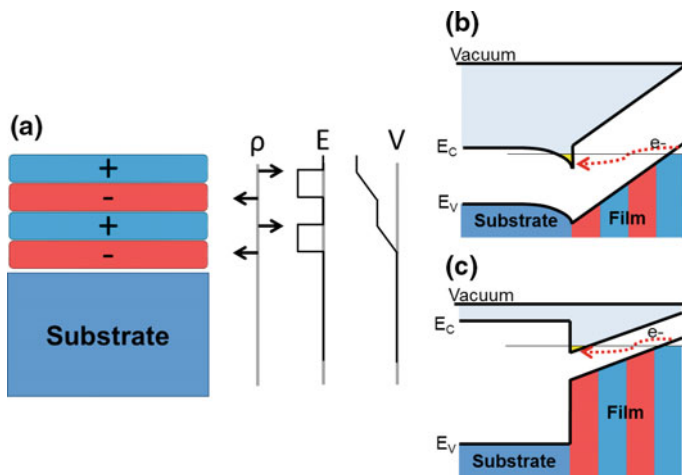
Fig. 12.2   a Illustration of electrostatic model for the polar catastrophe. **b** and **c** Illustrate critical thickness for electronic reconstruction

cells (UC) of LAO [90] for an LAO/STO heterostructure and six UC's in LAO/STO multilayer structures. [37] It was also found that even when the LAO thickness is less than the critical thickness of 4 UC, the interface could still be made conducting by applying a gate voltage [90].

Spatial confinement of charge at the interface has also been investigated. Experimentally, measured charge densities are lower than the expected 0.5 e per unit cell. [10, 44, 84, 90]. Popović et al. used DFT to investigate a LAO/STO supercell and examined the sub-bands that the 2DEG occupied. The d_{xy} state of the interfacial Ti, which forms the lowest sub-band, have strong 2D character (as they are parallel to the interface), and are expected to become Anderson localized for disordered systems; therefore, they would not be expected to conduct very well in realistic interfaces where disorder must be considered. The occupied d_{xz} and d_{yz} states have high effective masses parallel to the interface, and thus also should not be expected to contribute strongly to conductance measurements. The bands that are expected to conduct are the d_{xy} states in the neighboring TiO_2 layers; these are not nearly as two-dimensional as the interface TiO_2 states, and therefore will experience far less Anderson localization in the presence of disorder [75].

Lee et al. used DFT calculations to research LAO/STO/LAO heterostructures (capped with 20 Å of vacuum) in order to accurately capture the transfer of charge from the surface of LAO to the LAO/STO interface. In supercell calculations, if a symmetrically terminated TiO_2/LaO (AlO_2/SrO) interface is desired, an additional LaO (AlO_2) must be included in the system, and the LAO will not be stoichiometric. This will automatically dope the system with an additional electron (hole), and therefore the system must be metallic, regardless of thickness, in contrast with experiment, which shows that the conducting layer does not form for LAO under a critical thickness. In contrast, with a mirror-symmetric heterostructure calculation

that includes vacuum, no extra LaO (AlO$_2$) layer is needed to satisfy the periodic boundary conditions and the system will be insulating if electronic reconstruction does not occur. With 3 UC of LAO, the system does not experience electronic reconstruction, but in the calculation with 5 UC of LAO, electronic reconstruction does indeed occur. Interestingly, the interface induces the d_{xy} band to split off and is separated from the remainder of the t_{2g} states by $\sim$ 1–2 eV; it is the only occupied state. Although the symmetry in the z-direction is broken by the interface, other calculations without electronic reconstruction show that this effect is very small (on the order of 0.01 eV). Another explanation could be the chemical effect; the Al-O bond is shorter than that of Ti-O, so it is expected that Ti should be pulled closer to the interface; however, the opposite is found to be true, so the change energy of the d_{xy} state cannot be due to the chemical effect. Finally, the result of the splitting in energy is concluded to be due to the pseudo-Jahn-Teller effect, which breaks the electrical degeneracy and lowers the energy of the d_{xy} state [50].

Compressive strain has been shown to decrease the conductivity of the 2DEG and increase the critical LAO thickness for formation of the 2DEG; however, tensile strain was shown to result in an insulating interface. DFT calculations showed that, in unstrained LAO/STO heterostructures, polar Ti-O displacements are small; but for heterostructures with 1.2 % compressive strain, a non-switchable, polar displacement with a polarization of 18 μC/cm^2 is formed, which points away from the interface. This increases the critical thickness of LAO needed to from the 2DEG by decreasing the effective field induced in LAO (the formed polarization opposes the internal field of LAO) [4]. In STO/LaTiO$_3$ superlattices, the initial unrelaxed structure localizes the charge heavily in the center TiO$_2$ plane of LaTiO$_3$, but the relaxation of ions spreads the electron nearly evenly through the entire heterostructure. This shows the importance of ionic polarization in determining the localization of electron gas in this system [31].

Much of the theoretical work has been to determine why the p-type (hole doped) LAO/STO interface is insulating, and the n-type (electron doped) interface is conducting. Density functional theory calculations show that the n-type LaO/TiO$_2$ interface has charge localized on the interfacial Ti sites, which order ferromagnetically. Although this interface was calculated to be insulating, it has been argued that large two-dimensional hopping will cause the interface to be conducting even at very low temperatures. It has been shown that for the p-type AlO$_2$/SrO interface, the hole localizes as a charge polaron at the O in the interfacial AlO$_2$ layer; the interface is insulating when these polarons order antiferromagnetically [74].

12.2.2 Other Polar Oxides

In contrast to wide band gap LAO, the Mott–Hubbard insulator LaTiO$_3$ (LTO) exhibits metallic behavior for even a single unit cell [6, 7, 13, 68, 78, 100]. The confinement of the LTO/STO 2DEG has been studied by photoemission [18, 89] and optical techniques [82]. The *n*-type LaVO$_3$/STO interface was also found to be

conducting at a critical thickness of 5 UC. [36] The combination of two polar materials ($Mg_xZn_{1-x}O/ZnO$) led to a 2DEG at the interface due to charge being driven there by the polarization of the materials [91]; however, these materials are not switchable [49].

Other theoretical work has shown that the Ti-O bond length at the interface is very important. Comparing LAO on $CaTiO_3$, STO, and BTO, it was found that the electron gas is more localized with increasing the in-plane Ti-O bond length (in this case, the BTO/LAO interface had the longest bond length) (Fig. 12.3). The longer Ti-O bond lengths cause the d_{xy} orbital to be able to hold more charge, so the longer the bond, the more charge can fit in the interfacial layer, and thus the charge is more localized [63]. This is consistent with prior theory that compressive strain decreases the localization of the 2DEG and tensile strain increases the localization of the 2DEG at the LAO/STO interface. Biaxial strain reduces the O_h symmetry of the TiO_6 octahedra to D_{4h}, which breaks the degeneracy of the t_{2g} states. Under compressive strain, the in-plane Ti-O bond length is reduced and d_{xy} state cannot hold as many electrons, resulting in less electrons per layer. On the contrary, tensile strain increases the Ti-O bond length and increases the capacity of the interfacial d_{xy} state, increasing the localization of the electrons at the interface. Tensile strain also increases the magnetic moment and conductivity of the 2DEG located at the interface [62].

Using GGA+U, Lee et al. modeled LAO/EuO heterostructures with different thicknesses of EuO. Of note is that the LAO in this system is stoichiometric; the transfer of charge to the interface is due to electronic reconstruction, and not the additional charge that must be present from nonstoichiometric LAO. At the LAO/EuO interface, a 2DEG is created at the interface that extends ~ 10 Å into the system; the confinement is due to the band bending of the EuO d_{xy} states near the interface (Fig. 12.4). Due to the strong spin-splitting of EuO, the 2DEG is located only in the spin-up channel in EuO and thus is completely spin-polarized. Using different thicknesses of LAO (3, 4 and 5 unit cells), the charge density of the 2DEG can be controlled; for the 3 UC case, electronic reconstruction does not occur. As the exchange coupling constants vary with charge density, the charge transfer from
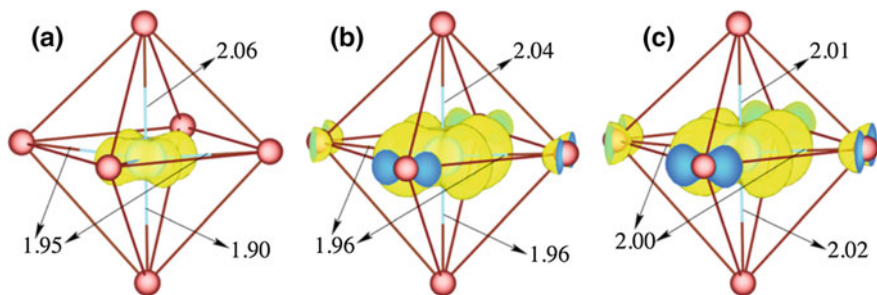
Fig. 12.3 Locally distorted TiO_6 octahedra and calculated three-dimensional charge density projected on the bands forming 2DEG at the **a** LAO/CaTiO$_3$ **b** LAO/STO and **c** LAO/BTO interface. From [63]
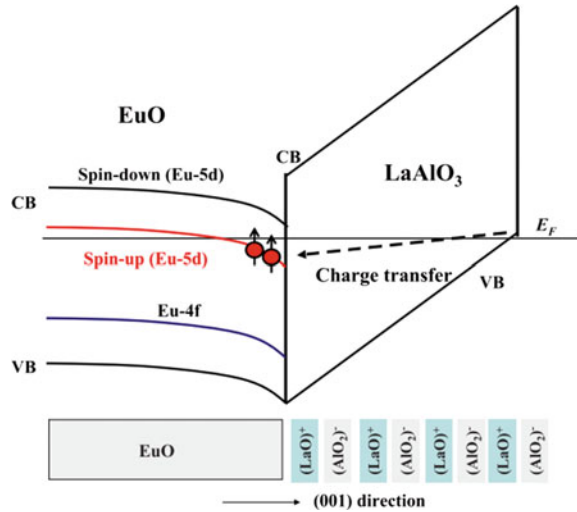
LAO to EuO also changes the critical temperature of ferromagnetism of the closest EuO cells to the interface, with the 2DEG increasing the critical temperature of the LAO/EuO interface to 105 K [53].

The NdAlO$_3$/STO interface has been theoretically shown to have a built-in field, causing a 2DEG at the n-type interface; O vacancies at the surface kill the electric field in NdAlO$_3$, but the interface is still insulating, due to the defect energy level being located at the bottom of the STO conduction band [98]. The GdTiO$_3$/STO interface also has a 2DEG located at the interface, but this 2DEG is present even in symmetrically terminated STO/GdTiO$_3$/STO structures that contain no internal field; the presence of the 2DEG is ascribed to band bending [8, 9, 43].

12.2.3 Ferroelectrics

There is evidence that ferroelectrics may allow for the creation of surface charge. In the bulk of a ferroelectric, the material cannot be metallic, due to screening of the polarization due to conduction electrons. [2] However, there is experimental and theoretical evidence of the formation of a two-dimensional conducting layer on the surface of clean ferroelectrics, which is attributed to the uncompensated surface charge due to the ferroelectric nature of the material [33, 47, 83, 94, 96].

Ferroelectrics also have the capability to control the charge density of 2DEGS at the interface of the ferroelectric and its substrate. A recent study has shown that a PbZr$_{0.2}$Ti$_{0.8}$O$_3$/LaNiO$_3$ heterostructure allows a switchable conduction layer at the interface, although in this case the substrate is already metallic [59]. Theoretically, a YMnO$_3$/GaN heterostructure was shown to have a spin-dependent conduction band offset due to a spin-polarized metallic interface [80]. Pt/BTO/Fe and Pt/PbTiO$_3$/Fe

superlattices have also been shown to have a magnetic interfacial conducting layer, and the strength of the magnetism can be controlled via the polarization of BTO or $PbTiO_3$ [52].

In a recent theoretical study, Niranjan et al. studied $ATiO_3$ (ATO)/$KNbO_3$ (KNO) superstructures (where A = Sr, Ba or Pb). They studied heterostructures that were either paraelectric (un-polarized) or ferroelectric (polarized); in all cases, the interface was NbO_2/AO. In the paraelectric case, a 2DEG forms at the KNO/ATO interface, due to an additional electron provided by the extra NbO_2 layer; each interface contains 0.5 e. In the ferroelectric case, however, the system behaves differently depending on the A ion. For the KNO/BTO superstructure, the polarization of BTO is nearly the same KNO, which greatly reduces the free surface charge that satisfies (12.1), and thus the charge density at both interfaces is nearly equal. For the KNO/STO interface, a small polarization is induced in STO. Due to the imbalance of charge due to the differing polarization, the charge density at the right interface is much higher than that of the left interface. In the KNO/PTO superstructure, the polarization of PTO is much higher than KNO, and one of the interfaces is insulating, as all the free charge migrates to the other interface in order to satisfy (12.1) (Fig. 12.5). This shows that the polarization of KNO can be used to change the charge density of the 2DEG, and in the KNO/PTO case, even make it insulating [65]. While the charge density of the 2DEG at the KNO/STO interface can be modified by switching the polarization of KNO (provided it is a single domain film), the origin of the 2DEG is in the polar nature of KNO, which is clear as the 2DEG is still seen even when KNO is in a paraelectric state with no polarization present. In other words, although the 2DEG responds to the change in the polarization of the sample, the polarization does not *create* the 2DEG.

Recently, however, using the ability of ferroelectrics to transfer charge from the oxide surface, it was found that a 2DEG can be found at the interface of polarized
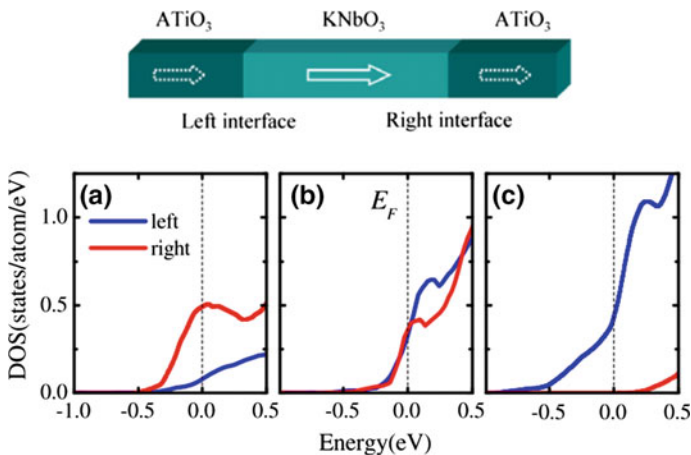
Fig. 12.5 Density of states near the fermi level (E_F) for KNO/ATO superstructures, where **a** A = Sr, **b** A = Ba and **c** A = Pb. The top panel shows the geometry of the unit cell with polarization indicated by *arrows*. From [65]
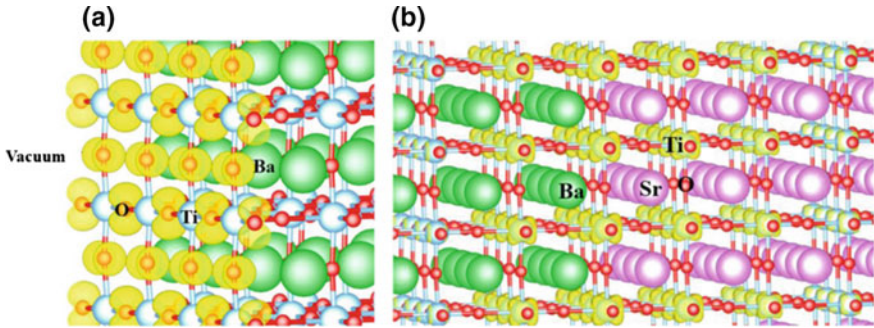
Fig. 12.6 Charge density at the fermi level. The pictured isosurface is for a charge density of 0.1203 e/Å^3. **a** The hole gas at the surface of BTO. Note the p character of the charge density. **b** The electron gas at the STO/BTO interface. Note the d character of the charge density. From [27]

BaTiO$_3$ (BTO)/STO heterostructure. Theoretically, the BTO has been shown to have two stable polarization states; one is polarized inward, away from vacuum and toward the BTO/STO interface, and one is un-polarized. When there is a difference in the polarization between the BTO and STO, free charge must be localized there in order to satisfy (12.1). Indeed, in the polarized heterostructure, the migration of the surface electron states to the interface satisfies this, and is the source of the 2DEG which occupies the Ti d states at the bottom of the conduction band (a corresponding hole gas of equal charge is localized at the surface O p states) (Fig. 12.6). In the un-polarized heterostructure, where there is no change in polarization between BTO and STO, the 2D gases do not form. LDA+U calculations show that the increase of the band gap localized the electron gas even further, essentially limiting them to only the first interfacial TiO$_2$ layer. This gives the opportunity for a 2DEG that can be turned on or off via ferroelectric switching [27].

12.2.4 Conclusions

The development of novel methods of deposition of highly crystalline oxide thin films has enabled investigation of electronic reconstruction at the 2D oxide interface. In addition to LAO/STO, electronic reconstruction has also been studied in other polar perovskite oxides and predicted in ferroelectrics. These studies open the possibility of future all-oxide devices.

12.3 Oxygen Vacancies

Surprisingly, conductivity has been demonstrated at the interfaces between the STO surface and oxide thin films of polar, nonpolar, epitaxial and amorphous varieties. [24, 34, 56] These studies have highlighted a need to investigate the role of defects

in the formation of the oxide 2DEG and its corresponding transport properties. In particular, interfacial redox reaction of STO can n-dope the material to stabilize a confined conducting layer. As a result, interfacial defect formation has been studied alongside electronic reconstruction the LAO/STO system.

12.3.1 LAO/STO

An alternative explanation for the conductivity at the n-type interface is due to surface O vacancy formation. These O defects introduce electrons to the system, which settle at the STO conduction band bottom and kill the polar field in LAO, creating the interfacial 2DEG. The enthalpy of formation for these vacancies decreases with increasing LAO thickness, spontaneously forming at the LAO critical thickness, which shows why the system is not insulating under the critical thickness but becomes insulating suddenly at the critical thickness. In contrast, at the p-type interface, the enthalpy of formation of surface O vacancies never becomes negative, so the 2DEG does not form at any thickness [101]. O vacancies at the p-type interface create a defect state just above the Fermi energy, which also causes the interface to become insulating [74]. Slabs of pure LAO that show electronic reconstruction can also be made insulating by the addition of O vacancies at the surface that donate electrons to the system [81].

Ferrari et al. examined the less-traditionally studied AlO_2/TiO_2 interface for a LAO/STO heterostructure, which has been found to be more stable when O vacancies are included [97]. The heterostructure consisted of 10 UC of both LAO and STO, with 10 ML of vacuum to prevent slab-slab interactions; the lateral size of the cell was ($\sqrt{2}\times\sqrt{2}$) in order to include more O to perform O vacancy studies. For 50 % and 25 % O vacancies at the AlO_2/TiO_2 interface, the AlO_2/TiO_2 interface contained a 2DEG that was found occupied the interfacial Ti d states, and the O at the LAO surface contained 2D hole states [25].

Kalabukhov et al. experimentally investigated optical, electrical, and microstructural properties of heterointerfaces between two thin-film perovskite insulating materials, STO and LAO, deposited at different oxygen pressure conditions. Cathode and photoluminescence experiments suggested that oxygen vacancies were formed in the bulk STO substrate during the growth of LAO films, resulting in high electrical conductivity and mobility values. In both high and low oxygen pressure interfaces, the electrical Hall mobilities followed a similar power law dependence as observed in oxygen reduced STO bulk samples. The results were confirmed on a microscopic level by local strain fields at the interface reaching 10 nm into the STO substrate [44]. Electrical measurements were made in a four-point van der Pauw configuration in the temperature range 2–300 K and in magnetic field up to 5 T. Gold contact pads were fabricated by sputtering using a Ti adhesion layer. The temperature dependence of the sheet resistance R_{XX}, the Hall mobility μ_H, and the charge-carrier density n_S are presented in Fig. 12.7. The results

Fig. 12.7 Sheet resistivity R_{XX}, charge-carrier density n_S, and hall mobility μ_H for STO substrates annealed in deposition conditions (10^{-6} mbar O2, 800 °C) and Ar-ion bombarded (U = 300 eV, J = 0.2 mA/cm^2) (*open* and *solid circles*); LAO/STO heterointerfaces prepared at low oxygen pressure (10^{-6} mbar) as well as annealed at 500 mbar during cooling (*open* and *solid diamonds*); LAO/STO heterointerfaces prepared at high oxygen pressure (10^{-4} mbar) and annealed at 500 mbar during cooling (*open* and *solid triangles*). From [44]
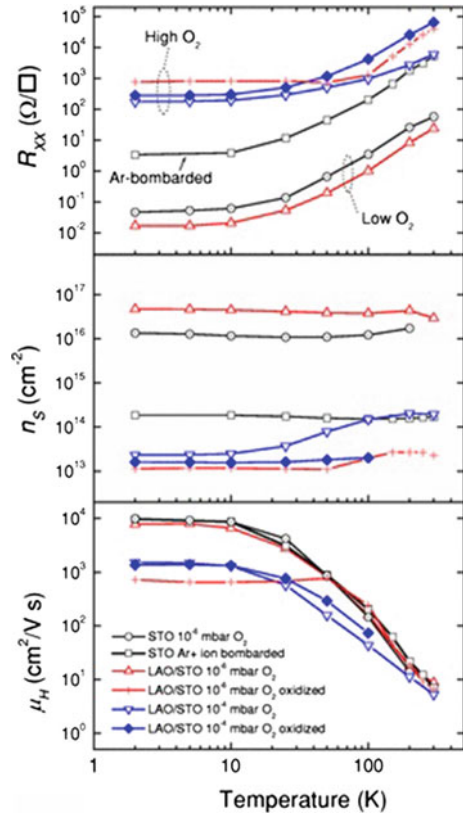
strongly suggest that oxygen vacancies in STO are responsible for the conductivity in LAO/STO heterostructures prepared even at high oxygen pressures.

Similarly, based on transport, spectroscopic, and oxygen-annealing experiments, Siemons et al. concluded that extrinsic defects in the form of oxygen vacancies introduced by the pulsed laser deposition (PLD) process were the source of the large carrier densities [84]. Annealing experiments showed a limiting carrier density. In addition, a model was introduced that explains the high mobility based on carrier redistribution due to an increased dielectric constant. Measurement of the electronic properties of the interfaces created by depositing LAO on STO showed electronic properties similar to those found originally by Ohtomo and Hwang [67]. Also, ultraviolet photoelectron spectroscopy (UPS) spectra showed states at the Fermi level, indicating a conducting interface. The number of these states was reduced when the sample was oxidized, suggesting that oxygen vacancies played an essential role in supplying the charge carriers. This was further confirmed by near-edge X-ray absorption spectroscopy (NEXAS) and vacuum ultraviolet spectroscopic ellipsometry (VUV-SE) measurements, which showed more Ti^{3+} for samples made at lower pressures. It appeared that the vacancies were created by the PLD process itself

where relatively high energy particles sputter off oxygen [1]. Annealing samples in atomic oxygen reduced the number of carriers but kept the mobility the same. The dependence of sheet carrier density as a function of temperature was changed dramatically. To determine the electron location, the authors calculated the potential and the carrier density in the STO as a function of distance from the interface and concluded that electrons moved into the pristine STO over large distances, mainly due to the high dielectric constant of STO at low temperatures.

12.3.2   Alumina/STO

To isolate the role of oxygen vacancies, nonpolar and amorphous oxides have also been studied. For example, alumina (in its amorphous or nonpolar gamma phase) has received attention. Thin alumina films have been deposited on STO by PLD [20, 21], molecular beam epitaxy (MBE) [48], atomic layer deposition (ALD) [54, 55, 64], and electron beam evaporation [23]. During deposition of alumina on STO, two reactions take place: reduction of STO and oxidation of aluminum metal. Alumina's large negative enthalphy of formation $\left(\Delta H_f \sim -1600 kJ/mol\right)$ encourages formation of oxygen vacancies at the STO surface [60].

The presence of oxygen vacancies at the STO/alumina interface has been verified by x-ray photoemission spectroscopy (XPS). After alumina deposition, XPS of the Ti $2p$ core level in STO reveals the presence of reduced Ti in the 3+ oxidation state at the interface (Fig. 12.8) [20, 48, 64]. STO surfaces exposed only to ALD precursor trimethylaluminum also form oxygen vacancies [54, 55, 64]. Characteristically, conductivity vanishes upon oxygen atmospheric anneal. This vacancy-based 2DEG demonstrates that electronic reconstruction is not essential for formation of the oxide 2DEG. No special preparation of the STO surface is necessary, nor is crystallinity of alumna a prerequisite for conductivity. Notably, highly conductive interfaces can be formed using room-temperature fabrication methods [20].

Once the presence of interfacial vacancies has been verified, electrical characterization has been used to characterize the conducting layer. In some cases, a critical or threshold thickness is identified below which the STO vacancies only patches rather than a continuous conducting layer [54]. The highest mobilities are measured for crystalline samples grown at high temperature (Fig. 12.9), and 2D conduction is revealed by angle-dependent Shubniov-de-Haas quantum oscillations. It is worth noting that in principle, a thin conductive layer is not necessarily a 2DEG in the traditional sense of the term. The two dimensional character comes from confinement in the direction normal to the interface. That results in the two dimensional density of states manifested in oscillations in transport measurements such as Shubniov-de-Haas.

Fig. 12.8 From [48]. **a** After alumina deposition on STO, gaussian decomposition of the XPS Ti 2*p* core level reveals a Ti3+ shoulder at lower binding energies, confirming the presence of oxygen vacancies. **b** Reduction of Ti is localized at the interface
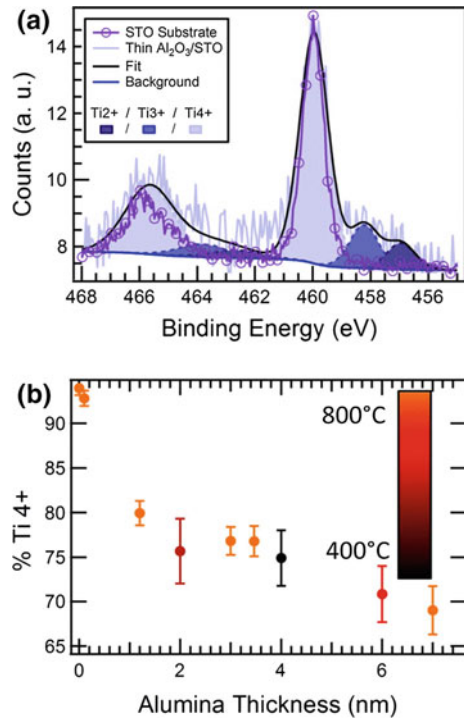
12.3.3 Other Oxides

Chen et al. deposited several insulating amorphous oxide thin films by PLD [19].
While amorphous LAO, STO, yttria-stabilized zirconia (YSZ) films deposited on
STO rendered a metallic interface, $La_{7/8}Sr_{1/8}MnO_3$ interfaces remained highly
insulating. Along with the thickness-dependence of conductivity, this suggests that
sputtering due to the high energy of incident ions cannot account solely for the
formation of oxygen vacancies. Therefore, interfacial chemical reactions play an
important role in the formation of the STO oxygen vacancy 2DEG, with possible
enhancement due to the sputtering effect. This is consistent with studies of amor-
phous LAO, alumina, and $YAlO_3$ deposited by ALD [55].

12.3.4 Conclusions

In conclusion, interfacial oxygen vacancies in STO contribute to the formation of a
conducting layer. The confinement of this layer depends on the chemical reactivity
of the film. The demonstration of room-temperature 2DEG formation based on
oxygen vacancies is particularly promising for future applications.
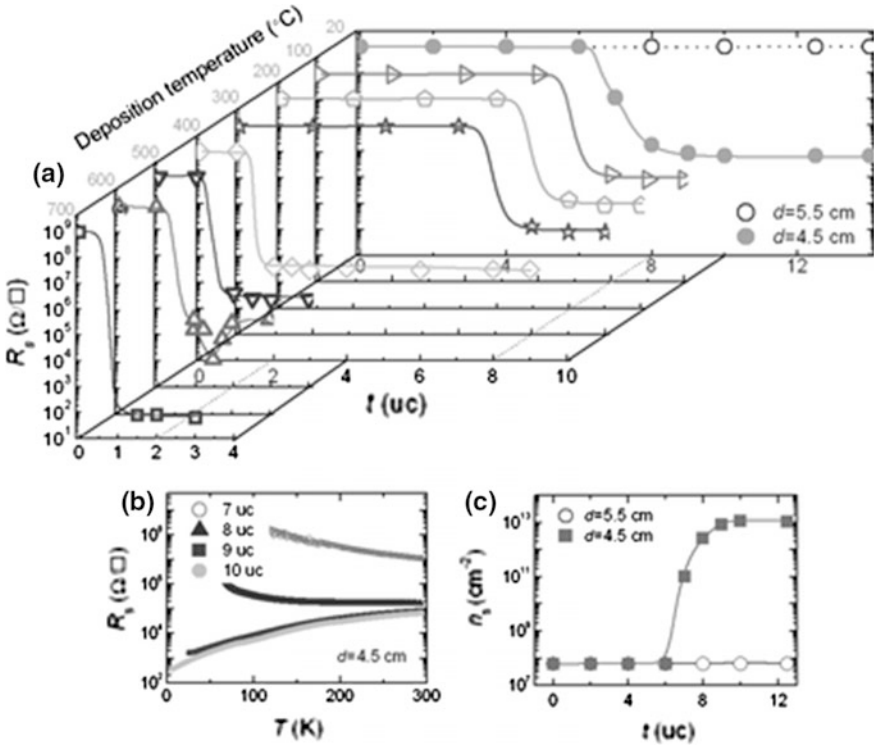
Fig. 12.9 From [20]. **a** Phase diagram for the conduction of GAO/STO interfaces grown at different temperatures. The room-temperature-formed interface shows a unique dependence of conduction on target-substrate distance, d, (*open symbol* for $d = 5.5$ cm, and *solid symbol* for $d = 4.5$ cm); **b** Temperature dependence of sheet resistance, R_s, at different film thicknesses, t, for $d = 4.5$ cm; **c** Thickness dependence of the carrier density, n_s, measured at 300 K. High-mobility 2DEGs are obtained once t is above 8 uc at $d = 4.5$ cm for room temperature deposition

12.4   Cation Intermixing

In addition to oxygen vacancies, cation exchange cannot be ignored, particularly considering the high temperature of typical film deposition. In pure STO, replacing a SrO layer with a rare earth-oxide (RO) ML leads to an additional donated electron in the system. Using pulsed layer deposition, Jang et al. inserted a single layer of RO for a variety of rare earth atoms: La, Pr, Nd, Sm and Y. They found that LaO, PrO and NdO layers create a 2DEG localized near the RO layer in the TiO$_2$ planes, but SmO and YO layers remain insulating. DFT calculations show that STO with a single LaO layer become conducting, but STO with a single YO layer remain insulating, in agreement with experiment. The YO layer induces a spin-polarized state to form directly below the conduction band in STO; this completely-filled state prevents the system from becoming metallic [42]. Inserting sub-monolayer doping

levels of La in pure STO induces a change from 3D to 2D conducting states, depending on the concentration of the La dopant levels [70].

12.4.1 LAO/STO

In addition to polar catastrophe and oxygen vacancies, instability against diffusional mixing or cationic exchange has been identified as a possible mechanism of conductivity at the LAO/STO interface [12, 61]. Chambers and co-workers, using several independent analytical methods, have shown that there is a strong tendency for the LAO/STO interface, as prepared by on-axis PLD, to intermix rather than form an atomically abrupt configuration [77] (Fig. 12.10) .

Although the intermixing is approximately correlated, which means that A-site exchanges (La ⇔ Sr) occur to the same extent as B-site exchanges (Al ⇔ Ti), there is preferential diffusion of La into the STO, which leads to n-type doping of the STO and the formation of itinerant electrons within the STO [16, 17, 22, 25, 26, 61, 76, 89]. Ferrari et al. found that, at the AlO_2/TiO_2 interface, swapping of one Al and Ti across the interface led lowered the energy of the system by 1.8 eV, making this substitution very energetically favorable. Interestingly, the combination of 25 % interfacial O vacancies and Al–Ti swapping led to an insulating interface [25].
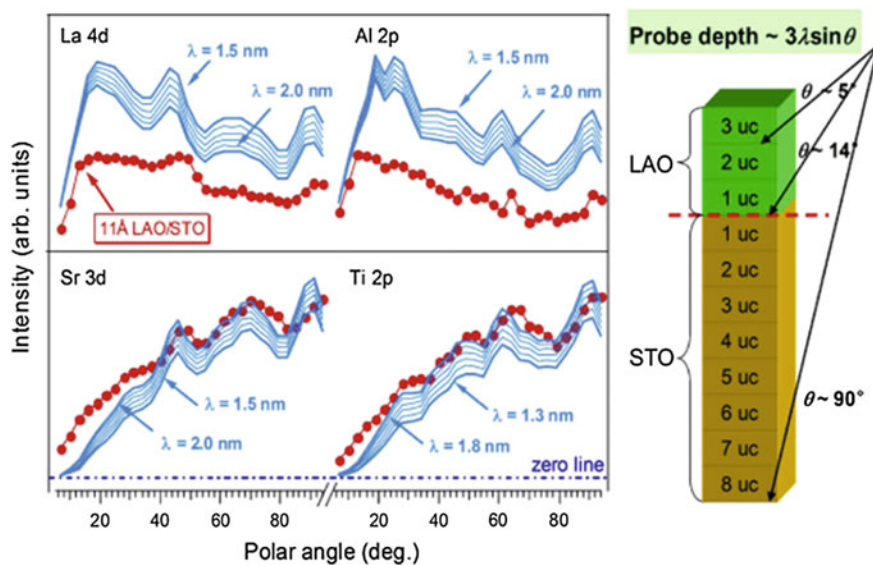
Fig. 12.10 Angle-resolved XPS from [77]. Polar scans in the (100) azimuth of La 4d, Al 2p, Sr 3d and Ti 2p intensities for a 11 Å LAO film, along with analogous scans for a 196 Å LAO film and bulk STO. The bulk or bulk-like STO and LAO polar scans were scaled by factors of exp(–d/λsinθ) and 1—exp(–d/λsinθ), respectively. A range of λ values was used, as discussed in the text. *Left*—schematic illustration of how the XPD probe depth varies with angle

In a combination experimental/theoretical study on the subject of ionic inter-mixing, Chambers et al. used Rutherford backscattering spectrometry (RBS), time-of-flight secondary ion mass spectrometry (TOF-SIMS), high-angle dark field scanning transmission electron microscopy (HAADF-TEM), and electron energy loss spectroscopy (EELS) to investigate ionic intermixing in LAO/STO heterostructures. Although each method on its own was inconclusive, a combination of all the methods support that there is large ionic intermixing within the first few UC of each oxide, leading to a complex mixed oxide at the interface. They also used DFT to calculate the effects of ionic mixing, with a $(\sqrt{2} \times \sqrt{2})$ lateral cell and varying thicknesses of LAO. It was found that, for swapping of Ti in STO and Al in LAO, Ti preferred to swap with an Al atom in LAO, and it lowered its energy by being as far from the interface as possible. Also, the hole caused by the Al^{3+} impurity in STO and the electron caused by the Ti^{4+} impurity in LAO both prefer to migrate to the interface and recombine, regardless of the original positions of the ions before they were swapped. This consideration is important, because this reduces the field in LAO, as does the electronic reconstruction, but the swapping of ions is energetically favored at any LAO thickness, whereas the electron reconstruction has a minimum critical thickness before it occurs. Although the swapping of La for Sr is not ener-getically favorable, the simultaneous swapping of Al/La in the interfacial cell with Ti/Sr was found to be always energetically favorable, no matter the initial positions of the Sr/Ti atoms or the thickness of LAO. Classical shell model calculations based on the DFT studies showed that the most stable structures contain large amounts of ionic mixing [17].

These results call into question the original interpretation of conductivity based on an electronic reconstruction to alleviate the polar catastrophe resulting from the growth of polar LAO on nonpolar STO and abrupt interface formation. Moreover, XPS-based measurements of the valence band offset and band bending near the interface revealed a much smaller band offset than was predicted based on an abrupt interface model and the absence of electric fields on both the STO and LAO sides of the interface. Good agreement between the measured and calculated band offset could be obtained if intermixing was included in the physical model of the inter-face. Perhaps the most puzzling result was the absence of measurable electric fields in LAO.

12.4.2 Stoichiometry Deviations

Fix et al. reported a systematic study of the transport properties of LAO/STO interfaces doped at the nanoscale with different atoms substituting Ti and with different concentrations [26]. They show that the electronic reconstruction model is compatible with the results obtained. Interestingly, although doping was found useful to induce additional properties such as ferromagnetism, undoped interfaces provide the highest carrier density.
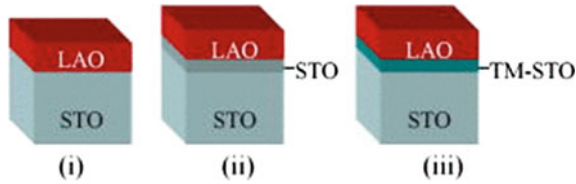
Fig. 12.11 Schematic diagrams of the samples grown for these experiments. **a** Layers of homoepitaxial STO grown between the substrate and the LAO cap; **b** Layers of M–STO grown between the substrate and the LAO cap; **c** STO/Mn–STO layers grown on the STO substrate so that the LAO/STO interface is formed between LAO and undoped homoepitaxial STO. From [26]

Films were grown on Ti-terminated single-crystal STO substrates by pulsed laser deposition. Commercial LAO and STO targets were used. For doping, M–STO targets, where M was Sc, V, Cr, Mn, Fe, Co, Nb, and In, were made by milling, presintering at 900 °C for 6 h, pressing and sintering at 1300 °C for 6 h a stoichiometric mixture of high purity (99.99 %) $SrCO_3$, TiO_2, and M-oxide powders. Figure 12.11 shows the different architectures used in the study as follows: LAO/STO/STO$_{substrate}$ (a) where a few unit cells of homoepitaxial STO was used for comparison with M–STO in LAO/M–STO/STO$_{substrate}$ (b), and finally, LAO/STO/SrTi$_{1-x}$Mn$_x$O$_3$/STO$_{substrate}$, where a STO monolayer was placed on top of SrTi$_{1-x}$Mn$_x$O$_3$ (Mn–STO) (c).

The authors found that even low dopant concentrations have a profound impact on the carrier density. Thus for the case of Mn, they considered LAO (15 uc)/SrTi$_{1-x}$Mn$_x$O$_3$ (1 uc)/STO$_{substrate}$ with $x = 0$, 0.0003, 0.001, 0.003, and 0.01. A nonlinear decrease of the carrier density by a factor 100 was observed when x varied from 0 to 0.01. Samples with $x = 0.04$ were insulating. However, inserting just a single unit cell of STO on top of the 3 UC of Mn–STO for $x = 0.003$ (Fig. 12.11c), allowed the carrier density recovery from insulating to values of around 4×10^{13} cm^{-2}, similar to the undoped case. Similar results were obtained for other metals. Interestingly, the authors found that for the dopants from Sc to Co, the evolution of the carrier density follows that of the ionization energy, and argued that the ionization energy is the driving force of the electronic reconstruction. In other words, the higher the ionization energy, the larger the energy gain from the electronic reconstruction.

12.4.3 Cs/STO

The Cs/STO interface was shown to cause a strong hybridization of the interfacial Ti $4p$ and $3d$ states, leading to a metallic hybridization state that pins the Fermi level. This leads to a creation of a 2DEG which is highly localized at the first two layers of TiO_2 at the interface. There approximately 0.2 e in this 2DEG (ten times higher than that of the LAO/STO interface) due to the larger reservoir of electrons from the metal. Interestingly, the real-shape space of the 2DEG depends strongly on
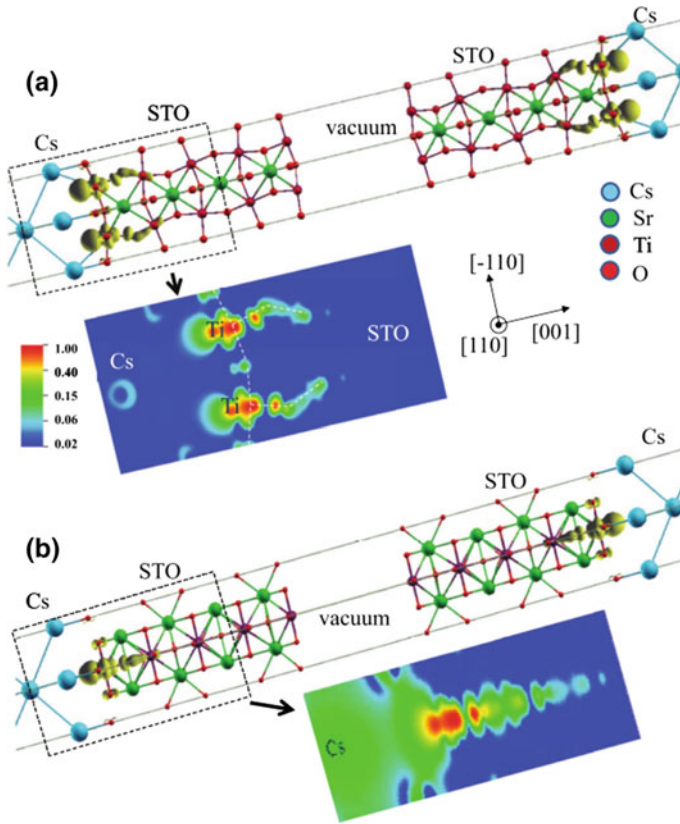
Fig. 12.12 The isosurface plot of transferred charge distribution for the Cs/STO slab with **a** The Cs atoms on the O sites and **b** The Cs atoms on the hollow sites. In both cases, the interfacial charge distributions inside STO are dumbbell-like, indicating the $3d_z2$ orbital order. From [51]

the atomic structure of the Cs/TiO_2 interface Fig. 12.12; this is because the location of the Cs atoms in the interface changes the relaxations in the STO substrate. For Cs atoms placed on the "hollow" sites (the empty sites located between the Ti and O on the TiO_2-terminated surface), the STO experiences ferroelectric-like distortions. When the Cs atoms are placed on top of the O sites, however, the STO experiences antiferrodistortive relaxation. In the ferroelectric case, the distortion in STO is directly due to the charge density transferred into the STO bulk. However, in the antiferrodistortive case, the charge is localized only in the first two layers of STO, whereas the distortion permeates the entire STO; therefore, it is argued that the distortion is not due to charge transfer [51].

12.4.4 Conclusions

Ionic intermixing is an important factor in the prevention of the polar catastrophe. Even with experimental setups that allow exceptional control over the deposition of thin films, high-growth temperatures allow ion mobility, which gives the system an intrinsic ability to reduce the inner electric field without the advent of electronic reconstruction.

12.5 Summary

Thin conductive layers have been demonstrated at the interfaces of several oxide systems. In many cases the two dimensional nature of the carriers (two dimensional electron gas or 2DEG) has been clearly demonstrated in transport measurements. For the 2DEG at the oxide/oxide interface, several factors, including electronic reconstruction, oxygen vacancy concentration, and level of cationic exchange, have been shown to influence the localization of charge at the interface to varying degrees. The phenomenon of electronic reconstruction has been investigated in LAO/STO heterostructures, as well as other polar and ferroelectric oxides. Study of amorphous and nonpolar oxides on STO has highlighted the role of oxygen vacancies. Cation intermixing can also lead to the formation of thin conductive layers. Rapid advances in experiment and theory alike, promise to provide new insights and discoveries in this fast-growing field.

References

1. Amoruso S, Aruta C, Aurino P (2012) Oxygen background gas influence on pulsed laser deposition process of $LaAlO_3$ and $LaGaO_3$. Appl Surf Sci 258:9116–9122. doi:10.1016/j.apsusc.2011.09.078
2. Anderson P, Blount E (1965) Symmetry considerations on martensitic transformations: "Ferroelectric" metals 14:217–219
3. Arras R, Ruiz VG, Pickett WE, Pentcheva R (2012) Tuning the two-dimensional electron gas at the $LaAlO_3/SrTiO_3$ (001) interface by metallic contacts. Phys Rev B 85:125404. doi:10.1103/PhysRevB.85.125404
4. Bark CW, Felker DA, Wang Y (2011) Tailoring a two-dimensional electron gas at the $LaAlO_3/SrTiO_3$ (001) interface by epitaxial strain. Proc Natl Acad Sci 108:4720–4724. doi:10.1073/pnas.1014849108
5. Basletic M, Maurice JL, Carrétéro C (2008) Mapping the spatial distribution of charge carriers in $LaAlO_3/SrTiO_3$ heterostructures. Nat Mater 7:621–625. doi:10.1038/nmat2223
6. Biscaras J, Bergeal N, Hurand S (2012) Two-dimensional superconducting phase in $LaTiO_3/SrTiO_3$ heterostructures induced by high-mobility carrier doping. Phys Rev Lett 108:247004. doi:10.1103/PhysRevLett.108.247004

7. Biscaras J, Bergeal N, Kushwaha A (2010) Two-dimensional superconductivity at a Mott insulator/band insulator interface LaTiO₃/SrTiO₃. Nat Commun 1:89. doi:10.1038/ncomms1084

8. Boucherit M, Shoron O, Jackson CA (2014) Modulation of over 10^{14} cm^{-2} electrons in SrTiO3/GdTiO3 heterostructures. Appl Phys Lett 104:182904. doi:10.1063/1.4875796

9. Boucherit M, Shoron OF, Cain TA (2013) Extreme charge density SrTiO₃/GdTiO₃ heterostructure field effect transistors. Appl Phys Lett 102:242909. doi:10.1063/1.4811273

10. Brinkman A, Huijben M, van Zalk M (2007) Magnetic effects at the interface between non-magnetic oxides. Nat Mater 6:493–496. doi:10.1038/nmat1931

11. Caviglia AD, Gabay M, Gariglio S (2010) Tunable Rashba spin-orbit interaction at oxide interfaces. Phys Rev Lett 104:126803. doi:10.1103/PhysRevLett.104.126803

12. Caviglia AD, Gariglio S, Reyren N (2008) Electric field control of the LaAlO₃/SrTiO₃ interface ground state. Nature 456:624–627. doi:10.1038/nature07576

13. Cen C, Thiel S, Hammerl G (2008) Nanoscale control of an interfacial metal-insulator transition at room temperature. Nat Mater 7:298–302. doi:10.1038/nmat2136

14. Cen C, Thiel S, Mannhart J, Levy J (2009) Oxide nanoelectronics on demand. Science 323:1026–1030. doi:10.1126/science.1168294

15. Chakhalian J, Freeland JW, Habermeier H-U (2007) Orbital reconstruction and covalent bonding at an oxide interface. Science 318:1114–1117. doi:10.1126/science.1149338

16. Chambers SA (2011) Understanding the mechanism of conductivity at the LaAlO₃/SrTiO₃ (001) interface. Surf Sci 605:1133–1140. doi:10.1016/j.susc.2011.04.011

17. Chambers SA, Engelhard MH, Shutthanandan V (2010) Instability, intermixing and electronic structure at the epitaxial LaAlO₃/SrTiO₃ (001) heterojunction. Surf Sci Rep 65:317–352. doi:10.1016/j.surfrep.2010.09.001

18. Chang YJ, Moreschini L, Bostwick A (2013) Layer-by-layer evolution of a two-dimensional electron gas near an oxide interface. Phys Rev Lett 111:126401. doi:10.1103/PhysRevLett.111.126401

19. Chen Y, Pryds N, Kleibeuker JE (2011) Metallic and insulating interfaces of amorphous SrTiO₃-based oxide heterostructures. Nano Lett 11:3774–3778. doi:10.1021/nl201821j

20. Chen YZ, Bovet N, Kasama T (2014) Room temperature formation of high-mobility two-dimensional electron gases at crystalline complex oxide interfaces. Adv Mater 26:1462–1467. doi:10.1002/adma.201304634

21. Chen YZ, Bovet N, Trier F (2013) A high-mobility two-dimensional electron gas at the spinel/perovskite interface of γ-Al2O₃/SrTiO₃. Nat Commun 4:1371. doi:10.1038/ncomms2394

22. Colby R, Qiao L, Zhang KHL (2013) Cation intermixing and electronic deviations at the insulating LaCrO₃/SrTiO₃ (001) interface. Phys Rev B 88:155325. doi:10.1103/PhysRevB.88.155325

23. Delahaye J, Grenet T (2012) Metallicity of the SrTiO₃ surface induced by room temperature evaporation of alumina. J Phys D: Appl Phys 45:315301. doi:10.1088/0022-3727/45/31/315301

24. Eckstein JN (2007) Oxide interfaces: Watch out for the lack of oxygen. Nat Mater 6:473–474. doi:10.1038/nmat1944

25. Ferrari V, Weissmann M (2014) Tuning the insulator-metal transition in oxide interfaces: An ab initio study exploring the role of oxygen vacancies and cation interdiffusion. Phys status solidi 251:1601–1607. doi:10.1002/pssb.201451050

26. Fix T, MacManus-Driscoll JL, Blamire MG (2009) Delta-doped LaAlO₃/SrTiO₃ interfaces. Appl Phys Lett 94:172101. doi:10.1063/1.3126445

27. Fredrickson KD, Demkov AA (2015) Switchable conductivity at the ferroelectric interface: Nonpolar oxides. Phys Rev B 91:115126. doi:10.1103/PhysRevB.91.115126

28. Goniakowski J, Finocchi F, Noguera C (2008) Polarity of oxide surfaces and nanostructures. Reports Prog Phys 71:016501. doi:10.1088/0034-4885/71/1/016501

29. Goniakowski J, Noguera C (2014) Conditions for electronic reconstruction at stoichiometric polar/polar interfaces. J Phys: Condens Matter 26:485010. doi:10.1088/0953-8984/26/48/485010

30. Gureev MY, Tagantsev AK, Setter N (2011) Head-to-head and tail-to-tail 180° domain walls in an isolated ferroelectric. Phys Rev B 83:184104. doi:10.1103/PhysRevB.83.184104

31. Hamann DR, Muller DA, Hwang HY (2006) Lattice-polarization effects on electron-gas charge densities in ionic superlattices. Phys Rev B 73:195403. doi:10.1103/PhysRevB.73.195403

32. Harrison W, Kraut E, Waldrop J, Grant R (1978) Polar heterojunction interfaces. Phys Rev B 18:4402–4410. doi:10.1103/PhysRevB.18.4402

33. He J, Stephenson GB, Nakhmanson SM (2012) Electronic surface compensation of polarization in $PbTiO_3$ films. J Appl Phys 112:054112. doi:10.1063/1.4750041

34. Herranz G, Sánchez F, Dix N (2012) High mobility conduction at (110) and (111) $LaAlO_3$/$SrTiO_3$ interfaces. Sci Rep 2:758. doi:10.1038/srep00758

35. Hoffman J, Pan X, Reiner JW (2010) Ferroelectric field effect transistors for memory applications. Adv Mater 22:2957–2961. doi:10.1002/adma.200904327

36. Hotta Y, Susaki T, Hwang H (2007) Polar discontinuity doping of the $LaVO_3$/$SrTiO_3$ interface. Phys Rev Lett 99:3–6. doi:10.1103/PhysRevLett.99.236805

37. Huijben M, Rijnders G, Blank DHA (2006) Electronically coupled complementary interfaces between perovskite band insulators. Nat Mater 5:556–560. doi:10.1038/nmat1675

38. Hwang HY (2006) Tuning interface states. Science 313:1895–1896. doi:10.1126/science.1133138

39. Hwang HY (2006) Applied physics: Tuning interface states. Science 313:1895–1896. doi:10.1126/science.1133138

40. Hwang HY, Iwasa Y, Kawasaki M (2012) Emergent phenomena at oxide interfaces. Nat Mater 11:103–113. doi:10.1038/nmat3223

41. Jang HW, Baek SH, Ortiz D (2008) Epitaxial (001) $BiFeO_3$ membranes with substantially reduced fatigue and leakage. Appl Phys Lett 92:062910. doi:10.1063/1.2842418

42. Jang HW, Felker DA, Bark CW (2011) Metallic and insulating oxide interfaces controlled by electronic correlations. Science 331:886–889. doi:10.1126/science.1198781

43. Janotti A, Bjaalie L, Gordon L, Van de Walle CG (2012) Controlling the density of the two-dimensional electron gas at the $SrTiO_3$/$LaAlO_3$ interface. Phys Rev B 86:241108. doi:10.1103/PhysRevB.86.241108

44. Kalabukhov A, Gunnarsson R, Börjesson J (2007) Effect of oxygen vacancies in the $SrTiO_3$ substrate on the electrical properties of the $LaAlO_3$/$SrTiO_3$ interface. Phys Rev B 75:121404. doi:10.1103/PhysRevB.75.121404

45. Khalsa G, Lee B, MacDonald AH (2013) Theory of t_{2g} electron-gas Rashba interactions. Phys Rev B 88:041302. doi:10.1103/PhysRevB.88.041302

46. Khalsa G, MacDonald AH (2012) Theory of the $SrTiO_3$ surface state two-dimensional electron gas. Phys Rev B 86:125121. doi:10.1103/PhysRevB.86.125121

47. Kolodiazhnyi T, Tachibana M, Kawaji H (2010) Persistence of ferroelectricity in $BaTiO_3$ through the insulator-metal transition. Phys Rev Lett 104:147602. doi:10.1103/PhysRevLett.104.147602

48. Kormondy KJ, Posadas AB, Ngo TQ (2015) Quasi-two-dimensional electron gas at the epitaxial alumina/$SrTiO_3$ interface: Control of oxygen vacancies. J Appl Phys 117:095303. doi:10.1063/1.4913860

49. Kozuka Y, Tsukazaki A, Kawasaki M (2014) Challenges and opportunities of ZnO-related single crystalline heterostructures. Appl Phys Rev 1:011303. doi:10.1063/1.4853535

50. Lee J, Demkov AA (2008) Charge origin and localization at the n-type $SrTiO_3$/$LaAlO_3$ interface. Phys Rev B 78:193104. doi:10.1103/PhysRevB.78.193104

51. Lee J, Lin C, Demkov AA (2013a) Metal-induced charge transfer, structural distortion, and orbital order in $SrTiO_3$ thin films. Phys Rev B 87:165103. doi:10.1103/PhysRevB.87.165103

52. Lee J, Sai N, Cai T (2010a) Interfacial magnetoelectric coupling in tricomponent superlattices. Phys Rev B 81:144425. doi:10.1103/PhysRevB.81.144425

53. Lee J, Sai N, Demkov AA (2010b) Spin-polarized two-dimensional electron gas through electrostatic doping in LaAlO$_3$/EuO heterostructures. Phys Rev B 82:235305. doi:10.1103/PhysRevB.82.235305

54. Lee SW, Heo J, Gordon RG (2013b) Origin of the self-limited electron densities at Al$_2$O$_3$/SrTiO$_3$ heterostructures grown by atomic layer deposition—oxygen diffusion model. Nanoscale 5:8940–8944. doi:10.1039/c3nr03082b

55. Lee SW, Liu Y, Heo J, Gordon RG (2012) Creation and control of two-dimensional electron gas using Al-based amorphous oxides/SrTiO$_3$ heterostructures grown by atomic layer deposition. Nano Lett 12:4775–4783. doi:10.1021/nl302214x

56. Liu ZQ, Li CJ, Lü WM (2013) Origin of the two-dimensional electron gas at LaAlO$_3$/SrTiO$_3$ interfaces: The role of oxygen vacancies and electronic reconstruction. Phys Rev X 3:021010. doi:10.1103/PhysRevX.3.021010

57. Maekawa S, Tohyama T, Barnes SE (2004) Physics of transition metal oxides. Springer, Berlin

58. Manchon A, Zhang S (2008) Theory of nonequilibrium intrinsic spin torque in a single nanomagnet. Phys Rev B 78:212405. doi:10.1103/PhysRevB.78.212405

59. Marshall MSJ, Malashevich A, Disa AS (2014) Conduction at a ferroelectric interface. Phys Rev Appl 2:051001. doi:10.1103/PhysRevApplied.2.051001

60. Medvedev VA, Wagman DD, Cox JD (1989) CODATA key values for thermodynamics. Hemisphere Publishing Corporation, New York

61. Mundy J, Fitting Kourkoutis L, Warusawithana M (2011) Probing stoichiometry in LaAlO$_3$/SrTiO$_3$ interfaces by aberration-corrected STEM. Microsc Microanal 17:1450–1451

62. Nazir S, Behtash M, Yang K (2014) Enhancing interfacial conductivity and spatial charge confinement of LaAlO$_3$/SrTiO$_3$ heterostructures via strain engineering. Appl Phys Lett 105:141602. doi:10.1063/1.4897626

63. Nazir S, Behtash M, Yang K (2015) Towards enhancing two-dimensional electron gas quantum confinement effects in perovskite oxide heterostructures. J Appl Phys 117:115305. doi:10.1063/1.4915950

64. Ngo TQ, McDaniel MD, Posadas A (2015) Oxygen vacancies at the γ-Al$_2$O$_3$/STO heterointerface grown by atomic layer deposition. In: MRS Proceedings, vol 1730. pp. mrsf14–1730. doi: 10.1557/opl.2015.294

65. Niranjan M, Wang Y, Jaswal S, Tsymbal E (2009) Prediction of a switchable two-dimensional electron gas at ferroelectric oxide interfaces. Phys Rev Lett 103:016804. doi:10.1103/PhysRevLett.103.016804

66. Noguera C (2000) Polar oxide surfaces. J Phys: Condens Matter 12:R367

67. Ohtomo A, Hwang HY (2004) A high-mobility electron gas at the LaAlO$_3$/SrTiO$_3$ heterointerface. Nature 427:423–426. doi:10.1038/nature02308

68. Ohtomo A, Muller DA, Grazul JL, Hwang HY (2002) Artificial charge-modulation in atomic-scale perovskite titanate superlattices. Nature 419:378–380. doi:10.1038/nature00977

69. Okamoto S, Millis A, Spaldin N (2006) Lattice relaxation in oxide heterostructures: LaTiO$_3$/SrTiO$_3$ superlattices. Phys Rev Lett 97:056802. doi:10.1103/PhysRevLett.97.056802

70. Ong PV, Lee J, Pickett WE (2011) Tunable two-dimensional or three-dimensional electron gases by submonolayer La doping of SrTiO$_3$. Phys Rev B 83:193106. doi:10.1103/PhysRevB.83.193106

71. Park JW, Bogorin DF, Cen C (2010) Creation of a two-dimensional electron gas at an oxide interface on silicon. Nat Commun 1:94. doi:10.1038/ncomms1096

72. Pauli SA, Willmott PR (2008) Conducting interfaces between polar and non-polar insulating perovskites. J Phys: Condens Matter 20:264012. doi:10.1088/0953-8984/20/26/264012

73. Pentcheva R, Pickett W (2009) Avoiding the polarization catastrophe in LaAlO$_3$ overlayers on SrTiO3 (001) through polar distortion. Phys Rev Lett 102:107602. doi:10.1103/PhysRevLett.102.107602

74. Pentcheva R, Pickett WE (2006) Charge localization or itineracy at LaAlO$_3$/SrTiO$_3$ interfaces: Hole polarons, oxygen vacancies, and mobile electrons. Phys Rev B 74:035112. doi:10.1103/PhysRevB.74.035112

75. Popović Z, Satpathy S, Martin R (2008) Origin of the two-dimensional electron gas carrier density at the $LaAlO_3$ on $SrTiO_3$ interface. Phys Rev Lett 101:1–4. doi:10.1103/PhysRevLett.101.256801

76. Qiao L, Droubay T, Varga T (2011) Epitaxial growth, structure, and intermixing at the $LaAlO_3/SrTiO_3$ interface as the film stoichiometry is varied. Phys Rev B 83:085408. doi:10.1103/PhysRevB.83.085408

77. Qiao L, Droubay TC, Shutthanandan V (2010) Thermodynamic instability at the stoichiometric $LaAlO_3/SrTiO_3$(001) interface. J Phys: Condens Matter 22:312201. doi:10.1088/0953-8984/22/31/312201

78. Rastogi A, Pulikkotil JJ, Auluck S (2012) Photoconducting state and its perturbation by electrostatic fields in oxide-based two-dimensional electron gas. Phys Rev B 86:075127. doi:10.1103/PhysRevB.86.075127

79. Reyren N, Thiel S, Caviglia AD (2007) Superconducting interfaces between insulating oxides. Science 317:1196–1199. doi:10.1126/science.1146006

80. Sai N, Lee J, Fennie CJ, Demkov AA (2007) Spin-filtering multiferroic-semiconductor heterojunctions. Appl Phys Lett 91:202910. doi:10.1063/1.2814961

81. Seo H, Demkov AA (2011) First-principles study of polar $LaAlO_3$ (001) surface stabilization by point defects. Phys Rev B 84:045440. doi:10.1103/PhysRevB.84.045440

82. Seo SSA, Choi WS, Lee HN (2007) Optical study of the free-carrier response of $LaTiO_3/SrTiO_3$ superlattices. Phys Rev Lett 99:266801. doi:10.1103/PhysRevLett.99.266801

83. Shi Y, Guo Y, Wang X (2013) A ferroelectric-like structural transition in a metal. Nat Mater 12:1024–1027. doi:10.1038/nmat3754

84. Siemons W, Koster G, Yamamoto H (2007) Origin of charge density at $LaAlO_3$ on $SrTiO_3$ heterointerfaces: Possibility of intrinsic doping. Phys Rev Lett 98:196802. doi:10.1103/PhysRevLett.98.196802

85. Sluka T, Tagantsev AK, Bednyakov P, Setter N (2013) Free-electron gas at charged domain walls in insulating $BaTiO_3$. Nat Commun 4:1808. doi:10.1038/ncomms2839

86. Sluka T, Tagantsev AK, Damjanovic D (2012) Enhanced electromechanical response of ferroelectrics due to charged domain walls. Nat Commun 3:748. doi:10.1038/ncomms1751

87. Stengel M (2011) Electrostatic stability of insulating surfaces: Theory and applications. Phys Rev B 84:205432. doi:10.1103/PhysRevB.84.205432

88. Stengel M, Vanderbilt D (2009) Berry-phase theory of polar discontinuities at oxide-oxide interfaces. Phys Rev B 80:241103. doi:10.1103/PhysRevB.80.241103

89. Takizawa M, Wadati H, Tanaka K (2006) Photoemission from buried interfaces in $SrTiO_3/LaTiO_3$ superlattices. Phys Rev Lett 97:057601. doi:10.1103/PhysRevLett.97.057601

90. Thiel S, Hammerl G, Schmehl A (2006) Tunable quasi-two-dimensional electron gases in oxide heterostructures. Science 313:1942–1945. doi:10.1126/science.1131091

91. Tsukazaki A, Ohtomo A, Kita T (2007) Quantum Hall effect in polar oxide heterostructures. Science 315:1388–1391. doi:10.1126/science.1137430

92. Ueda K, Tabata H, Kawai T (1998) Ferromagnetism in $LaFeO_3$-$LaCrO_3$ superlattices. Science 280:1064–1066

93. Vul BM, Guro GM, Ivanchik II (1973) Encountering domains in ferroelectrics. Ferroelectrics 6:29–31. doi:10.1080/00150197308237691

94. Wang Y, Liu X, Burton JD (2012) Ferroelectric instability under screened coulomb interactions. Phys Rev Lett 109:247601. doi:10.1103/PhysRevLett.109.247601

95. Watanabe Y (1998) Theoretical stability of the polarization in a thin semiconducting ferroelectric. Phys Rev B 57:789–804. doi:10.1103/PhysRevB.57.789

96. Watanabe Y, Okano M, Masuda A (2001) Surface conduction on insulating $BaTiO_3$ crystal suggesting an intrinsic surface electron layer. Phys Rev Lett 86:332–335. doi:10.1103/PhysRevLett.86.332

97. Weissmann M, Ferrari V (2009) Ab initio study of a $TiO_2/LaAlO_3$ heterostructure. J Phys: Conf Ser 167:012060. doi:10.1088/1742-6596/167/1/012060

98. Xiang X, Qiao L, Xiao HY (2014) Effects of surface defects on two-dimensional electron gas at $NdAlO_3/SrTiO_3$ interface. Sci Rep 4:5477. doi:10.1038/srep05477

99. Yamada H, Ogawa Y, Ishii Y (2004) Engineered interface of magnetic oxides. Science 305:646–648. doi:10.1126/science.1098867
100. You JH, Lee JH (2013) Critical thickness for the two-dimensional electron gas in LaTiO$_3$/SrTiO$_3$ superlattices. Phys Rev B 88:155111. doi:10.1103/PhysRevB.88.155111
101. Yu L, Zunger A (2014) A unified mechanism for conductivity and magnetism at interfaces of insulating nonmagnetic oxides. Nat Commun 5:5118. doi:10.1038/ncomms6118

Chapter 13
Ultrathin Perovskites: From Bulk Structures to New Interface Concepts

Stefan Förster and Wolf Widdra

Abstract The growth of ultrathin films of ternary oxides on metal substrates enables a precise control of a variety of surface structures with particular properties. For the class of perovskite oxides, this is demonstrated with a specific focus on barium titanate ($BaTiO_3$) in the following.

13.1 Introduction

13.1.1 Structure and Properties of Perovskite Oxides

Perovskite oxides are ternary oxides represented by the sum formula ABO_3. They consist of two different types of cations A and B. Cation A formally carries a charge of 2+ or 3+ and is combined with cation B with a charge of 4+ or 3+, respectively. Together with three O^{2-} anions, they form a cubic or pseudo-cubic structure as depicted in Fig. 13.1. The corners of the cubic or pseudo-cubic unit cell are occupied with the A cations, the B cations are located at the body-centered position of the cubes, and the oxygen anions occupy the face-centered sites. In this structure, the oxygen forms an octahedral cage around the B cations. In the family of perovskites, a great diversity in the combination of different A and B site cations can be found. It leads to a wide range of different physical properties. Typical A site cations are alkaline earth or rare earth elements whereas at the B sites 3d, 4d, or 5d

S. Förster · W. Widdra (✉)
Surface Science Group, Institute of Physics, Martin-Luther-Universität Halle-Wittenberg, 06120 Halle, Germany
e-mail: wolf.widdra@physik.uni-halle.de

S. Förster
e-mail: stefan.foerster@physik.uni-halle.de

Fig. 13.1 The cubic
perovskite unit cell which
includes the oxygen
octahedron. Oxygen atoms
occupy the face-centered
positions in the cubic
structure. The cations A are
located at the corners and the
cations B are located in the
center of each cell. In the
family of perovskites, the
cations A and B are
exchangeable within a broad
range of elements resulting in
a great diversity of physical
properties
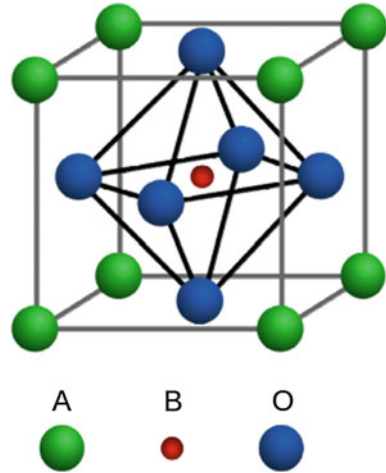
transition metals are most common. In general, a combination of two metals is expected to form a stable perovskite if the tolerance factor t calculated from the ionic radii of the three components R_A, R_B, and R_O,

$$t = \frac{R_A - R_O}{\sqrt{2}(R_B - R_O)}$$

ranges between 0.75 and 1.

This freedom in combining different elements is the reason why the class of perovskite oxides contains insulators, metals, semiconductors, and superconductors. Some are ferroelectrics, ferroelastics, or ferromagnets, and many are catalytically active.

The combination of different chemical species in the structural framework of the perovskite unit cell can lead to slight distortions of the ideally cubic structure. In most cases, different stable phases are observed. Very common are rhombohedral and tetragonal phases with structural distortions in the percentage range which are associated with changes of the physical properties of the material. These different phases and their transitions are of great interest with regard to the fabrication of functional materials where one would like to use external parameters like temperature, pressure, or magnetic fields to control the materials properties. One very prominent example of this structure-property relation is the ferroelectric to paraelectric phase transition of $BaTiO_3$ when changing the phase from tetragonal to cubic at 400 K as depicted in Fig. 13.2 (adapted from [1]). Polarization data are from the early work of Merz [2].

Beyond that, the properties of individual perovskites can be altered in a controlled fashion by substitution of ions at the A or B sites or incorporation of defects. In addition, due to the structural equivalence perovskites with different properties can be stacked together in multilayer systems to produce functional materials with
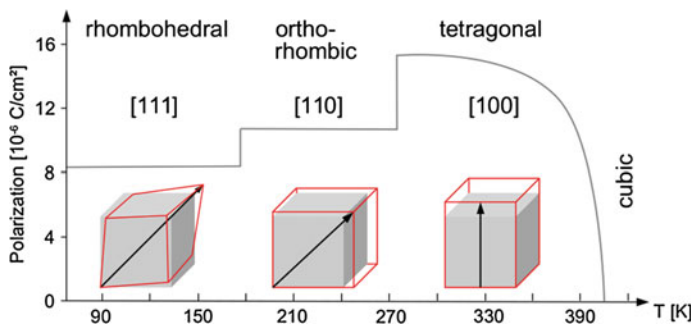
Fig. 13.2 Phase diagram of BaTiO$_3$ for the temperature range from 60 to 420 K. The *arrows* in the unit cells indicate the direction of the spontaneous ferroelectric polarization, which corresponds to the direction of the unit cell distortion

unique properties [3–5]. In such multilayer systems, different ferroic properties are combined across the internal interfaces to realize complex multiferroic materials in which one uses the structural coupling to change the properties from one species by stimulating changes of a different species. In magnetoelectric multiferroics for example, one takes advantage of the magnetoelectric coupling at the interface between a ferromagnetic and a ferroelectric material. A magnetic field can switch the ferroelectric polarization of the system, or even better, electric fields can be used to induce magnetic ordering. Conceptually this could open the way to new memory devices in which the magnetically stored information is read or manipulated using electric fields instead of currents. This concept would increase the speed and reduce the energy consumption and thus the heat production of the device.

13.1.2 Surface and Interface Properties

Surfaces and interfaces are exposed places of a solid due to the breaking of the translational symmetry here. The energy minimization of the system induces modifications from the truncated bulk structure. Consequently, the outermost atomic layers are forced to rearrange. The atomic displacements are accompanied by changes in the distribution of charges, which can significantly alter the materials properties. Exemplarily one can take the case of SrTiO$_3$ which is one of the most popular perovskite oxides used, e.g., as high-k dielectrics, in optoelectronics, or as substrate for epitaxial growth of functional oxide heterostructures. Although stoichiometric SrTiO$_3$ is a band insulator with a 3.2 eV band gap, early photoemission experiments have found a metallic behavior at (001) single crystal surfaces [6, 7]. Recent experiments revealed that the charge carriers are mainly confined in quasi two-dimensional bands of d$_{xy}$ symmetry [8, 9]. Several experimental and theoretical studies, carried out in the past 25 years, determined three major structural and

electronic changes at the surface. At first, a pronounced rumpling of the atoms in the top layer: The metal atoms of the terminating layer relax towards the bulk whereas the oxygen atoms do not significantly change their positions. Secondly, a deviation of the interlayer distance of the three outermost layers from the bulk value is found. Finally, a strongly enhanced covalent character of the Ti-O bonds needs to be included [10–12]. As consequence of these changes, a dipole is formed at the surface that might be the driving force for the surface accumulation of charges of different origin, as e.g. Sr adatoms or O vacancies.

For the thin film regime, the situation becomes even more complex, because additional to the outer surface also the internal interface to the substrate will affect the thin film structure and properties. Comparable relaxation phenomena are expected at the interface. The understanding of the interface relaxation eventually leads to tunable materials by controlling interface strain and chemical boundary conditions. The range of tunability of the thin film properties will depend on the film thickness. For several tens of atomic layers the influence of the surface and the interface might be weak. However in the ultrathin regime of only few atomic layers, the surface and interface mediated changes will dictate the overall structure [13, 14]. A prominent recent example for unexpected properties are ultrathin films of the band-insulator $LaAlO_3$ grown on $SrTiO_3(001)$ substrates. In this system, the charge neutral SrO and TiO_2 substrate planes are combined with LaO and AlO_2 layers with a net charge of ± 1 in the ionic limit. Consequently, a polar discontinuity arises at the interface. Depending on the substrate termination, this system can be either insulating or conductive, where the charge carrier density and mobility depends on the $LaAlO_3$ thickness and the growth conditions [15–19]. Although a large number of complementary method have been applied to investigate the system, the reason for its unusual behavior is still under debate. Possible explanations are an electronic reconstruction, doping by oxygen vacancies, intermixing of cations of the film and the substrate, or interface reconstructions [20–25].

In artificially grown multilayer systems, one nowadays applies the knowledge about the thickness and strain dependence of physical properties of different thin film materials to combine them to heterostructures with unique properties [4, 5]. This is especially attractive for functional oxides in all oxide perovskite systems because due to the structural equivalence and the small deviations in the lattice parameters a particularly precise control is given.

13.1.3 Ferroelectricity at the Limit

To give a deep insight in the dedicated changes of properties of ultrathin films, we will focus from now on to the prototypical ferroelectric perovskite $BaTiO_3$. Already one year after solving the crystal structure in 1945 by *Megaw* [26], the ferroelectric properties of this material have been proven [27]. With an easily accessible

temperature range of the tetragonal ferroelectric phase between 275 and 400 K, $BaTiO_3$ became the drosophila among the ferroelectric materials that exposes a rich phase diagram as depicted in Fig. 13.2.

The stable polarization at room temperature makes $BaTiO_3$ interesting for use in functional oxide heterostructures as well as in magnetoelectric multilayer systems. However for the surface and internal interfaces, the ferroelectric properties might change due to the reduced dimensionality and structural as well as electronic relaxations. For the $BaTiO_3$ surface, an inward relaxation of the outermost metal atoms is observed as similarly also found for $SrTiO_3$. It goes in hand with an increased covalency of the Ti-O bond perpendicular to the surface normal. Ab initio calculations showed that the resulting surface dipole suppresses the intrinsic fer-roelectricity by about 30 % [28]. For $BaTiO_3$, the atomic displacements of the surface atoms depend on the direction of the ferroelectric polarization of the bulk. In the case of an inward (P↓) polarization, there is only a weak net surface relax-ation as compared to bulk-like positions, since the displacement is a continuation of the underlying bulk behavior. For the paraelectric phase and in-plane (P→) polarization, the surface layer exhibits only a minor rumpling. However, in the case of an outward (P↑) polarization, stronger deviations from the bulk structure are found because the surface relaxation is antiparallel to the ferroelectric displacement in the bulk. These different configurations result in a polarization dependent local work function, which is largest for P↓ and smallest for P↑ polarization. These local work function differences can be used to image the ferroelectric domain structure at the nanoscale by photoelectron emission microscopy (PEEM). In a temperature-dependent PEEM study, *Höfer* et al. could demonstrate that the domain contrast is preserved at the surface of a $BaTiO_3$(001) single crystal up to a temperature of 510 K, which is nearly 100 K above the bulk ferroelectric to paraelectric phase transition temperature T_C [29]. Their calculations revealed that the surface relax-ation stabilizes the tetragonal distortion of the surface-near domains on top of a paraelectric bulk. This example demonstrates the influence of surface and interface relaxation also on the ferroelectric properties. Therefore, strong modifications of the properties are expected when going to the thin film regime. From the beginning of the characterization of ferroelectric thin films during the past decades, there was frequently the potential existence of a critical minimum thickness for a stable ferroelectric phase discussed. The thickness of the assumed dead layer decreased with the advancement of surface preparation techniques and time as is shown in Fig. 13.3 [30]. *Tenne* et al. were the first to show that such a critical thickness in general does not exist [31]. They studied $SrTiO_3/BaTiO_3$ superlattices in which the thickness of the $BaTiO_3$ layer was reduced to the ultimate two-dimensional limit of a single unit cell. The strain promoted by the surrounding $SrTiO_3$ layers, which have a slightly smaller lattice parameter as compared to $BaTiO_3$, stabilizes the tetragonal distortion of the $BaTiO_3$. Furthermore, by varying the thickness of both the $BaTiO_3$ and $SrTiO_3$ layers, the critical temperature T_C could be tuned from below to 230 K above the bulk T_C [31]. Their results show that under favorable electrical and mechanical boundary conditions, ferroelectricity is robust down to

Fig. 13.3 Evolution of reported critical thickness of a stable ferroelectric phase in perovskites with time. The curve nowadays approached the unit cell limit. The ultimate minimum of a single unit cell has been realized in a superlattice only. Adapted from Kohlstedt [30]
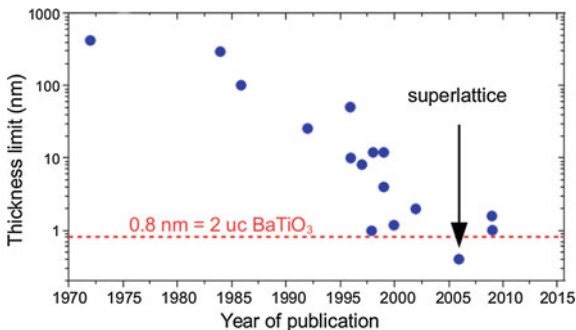
unit cell dimensions in film thickness. Besides stabilizing the ferroelectric phase by sandwiching the ferroelectric layer in an all oxide superstructure, one can also grow ultrathin layers on a support, which has the advantage that the powerful methods of surface science can be applied directly. *Garcia* et al. demonstrated for an ultrathin $BaTiO_3$ film that the ferroelectric phase could be stabilized at room temperature down to a film thickness of 1 nm for the growth on a $La_{0.67}Sr_{0.33}MnO_3$/ $NdGaO_3(001)$ substrate which imposes a compressive strain of 3.2 % on the $BaTiO_3$ thin film [32]. For ultrathin films of $BaTiO_3$, it is theoretical predicted that the ferroelectric to paraelectric phase transition temperature will increase substantially by several 100 K when applying in-plane strain [33]. As schematically illustrated in Fig. 13.4, the upshift scales nearly linear with compressive as well as tensile strain. Therefore, the pseudomorphic growth of $BaTiO_3$ on substrates with a lattice misfit in the range between −3 and 3 % might offer the chance to engineer the ferroelectric properties to a large extend. Suitable metallic substrate in this range are Pt(001) and Au(001) which offer lattice misfits of about −2 and +2 %, respectively.

Fig. 13.4 Ferroelectric phase diagram of $BaTiO_3$ as function of temperature and in-plane lattice strain, adapted from Li et al. [33]. In the ferroelectric state, the direction of the electric polarization is indicated. Epitaxial films of $BaTiO_3$ on Pt and Au single crystals are candidates for perovskite films with strong compressive and strong tensile strain, respectively
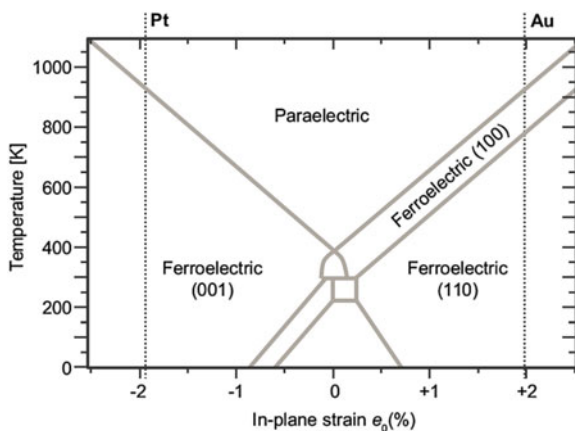
13.2 Structure and Growth of Ultrathin BaTiO$_3$ Films

Ultrathin films of BaTiO$_3$ have been grown on a variety of different substrates using different techniques. The use of pulsed laser deposition (PLD) is nowadays very common to deposit BaTiO$_3$ on various other perovskite substrates to produce all oxide heterostructures. Most frequently, SrTiO$_3$ substrates are used in different crystal orientations—often combined with a variety of capping layers, as e.g., SrRuO$_3$ or La$_x$Sr$_{1-x}$MnO$_3$—to engineer the substrate promoted strain [34–36]. A second very successful route is the use of molecular beam epitaxy (MBE) which in case of a high degree of automation can provide the possibility to grow complex multilayer systems with a high level of accuracy [5, 37].

Besides the growth on all oxide substrates, also metal single crystals serve as substrate for the deposition of ultrathin oxide films. Often metal substrates offer a smoother surface with larger average terrace widths as compared to oxide substrates. Furthermore, they have the advantage that their chemically different nature simplifies the analysis of the thin film composition and the identification of possible defects in the film. In addition, their metallic conductivity allows the investigation of ultrathin oxide films by electron-based techniques.

13.2.1 General Growth on Metal Substrates

For offering good growth conditions for ultrathin BaTiO$_3$ films, a metal substrate has to meet three important criteria. At first, the mismatch of the lattice constant to the value of 4.00 Å for cubic BaTiO$_3$ has to be small to facilitate a pseudomorphic layer-by-layer growth. Secondly, it has to be stable at high temperatures that are required for oxygen diffusion for enhancing long-range order. Finally, it has to be stable against high oxygen partial pressures, which are mandatory for the growth of stoichiometric oxide films. From this perspective, the late transition metals Ru, Rh, Pd, Ir, and Pt are good choices. Their lattice parameters with respect to BaTiO$_3$ can be found in Fig. 13.5.

So far ultrathin BaTiO$_3$ films have been grown on Ru(0001), Pd(001), Fe(001), Pt(001), and Pt(111) substrates [38–42]. Although Fe does not meet the criteria of high temperature and oxygen partial pressure stability it has been tested since its potential technological relevance as a ferromagnetic substrate. Thin films can be grown layer-by-layer at 900–1000 K [42]. However frequently, the growth is conducted in two steps: BaTiO$_3$ is deposited by PLD, MBE, or RF magnetron sputtering at room temperature and the deposited material is subsequently annealed to temperatures in the range of 850 K. The annealing step is important to initiate diffusion and to achieve long-range ordering in the amorphously deposited material. To prevent the formation of oxygen vacancies, the growth or the subsequent annealing is often conducted under high oxygen partial pressures up to 10^{-4} mbar. As a result ultrathin epitaxial BaTiO$_3$ films of bulk-like composition are formed,
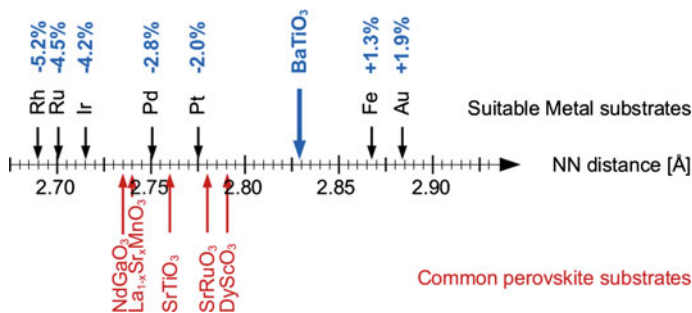
Fig. 13.5 Next-neighbor distances of hexagonal top-layer forming metal substrates favorable for the preparation of $BaTiO_3$ thin films and their lattice mismatch with respect to $BaTiO_3$. For comparison, values for typical perovskite substrates are added

which grow commensurate on the metal support as can be deduced from low-energy electron diffraction (LEED) (see Figs. 13.6 and 13.7). As discussed above, the observation of a commensurate growth implies the growth of strained $BaTiO_3$. The misfit and different surface free energies might lead to altered growth modes on different substrates. Whereas for $BaTiO_3(111)$ films grown on Pt(111) a Stranski-Krastanov like growth is revealed by scanning tunneling microscopy (STM) (see Fig. 13.6), measurements on $BaTiO_3(001)$ films on Pt(001) indicate instead a layer-by-layer growth (see Fig. 13.7). This is interesting because the strain mediated by the substrate is the same for both cases. The 2.0 % compressive misfit strain can be easily adopted for (001) oriented films by a relaxation along the surface normal. In other words, the strain favors a tetragonal distortion of the ultrathin $BaTiO_3(001)$ film perpendicular to the surface. A LEED I–V analysis for
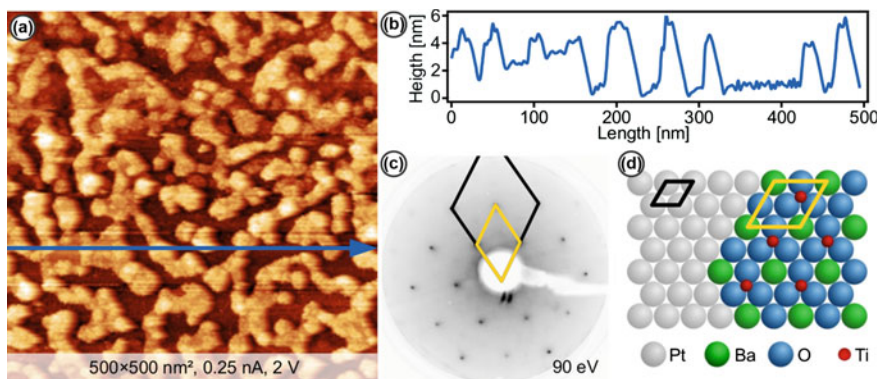
Fig. 13.6 Ultrathin films of $BaTiO_3$ grown on Pt(111) exhibit a Stranski-Krastanov-like structure as derived from STM as shown in (**a**). The line profile in (**b**) taken along the *blue arrow* in (**a**) reveals islands heights of several nm above a rough wetting layer. The LEED pattern in (**c**) confirms the commensurate growth of $BaTiO_3(111)$ on Pt(111) as sketched in the ball model of (**d**). The pseudomorphic oxide structure with the substrate produces a strain of 2 % in the $BaTiO_3$ film
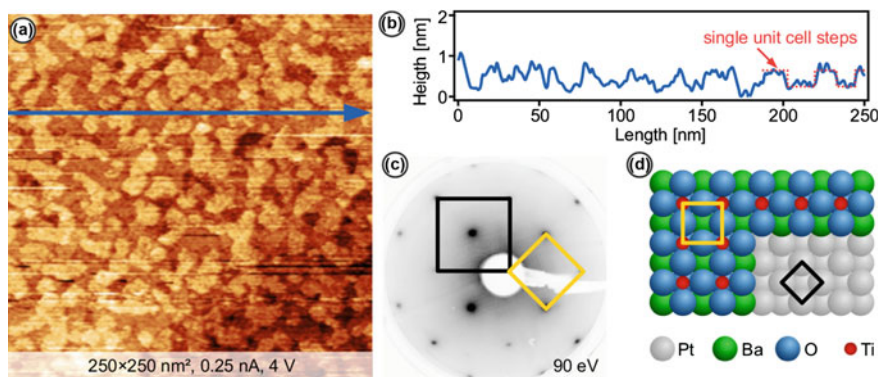
Fig. 13.7 Ultrathin films of $BaTiO_3$ grown on Pt(001) exhibit a layer-by-layer growth as derived from STM (**a**). In the line profile of (**b**), single unit cell high steps are measured. The LEED data in (**c**) demonstrates that well-ordered $BaTiO_3$(001) films can be grow pseudomorphically on Pt(001). The non-trivial relation of the $BaTiO_3$(001) lattice and the substrate is sketched in (**d**)

$BaTiO_3$(001) films in the thickness range of 2–4 unit cells on Pt(001) and on $SrRuO_3$(001) shows identical results on both substrates, for which the lattice mismatch is very similar and a DFT calculation favors a tetragonal out-of-plane relaxation [39, 43, 44]. For a tensile strain like on Fe(001), a Stranski-Krastanov growth is observed again as argued above [40].

The analysis of surface x-ray diffraction on metallic (001) substrates revealed that ultrathin $BaTiO_3$(001) films are TiO_2 terminated at the metal-oxide interface [41]. However, at the surface the termination varies between a TiO_2 termination for Pt(001), a BaO termination in case of Fe(001), and a mixed termination in case of Pd(001) [39, 41, 43]. However, the details of the termination are sensitive to interfacial carbon as well as oxygen [41].

Focusing on the $BaTiO_3$ growth on Pt substrates, a pronounced long-range order of ultrathin (001)-oriented oxide films develops upon annealing in UHV starting from 900 K within a temperature window of 150 K. For annealing temperatures above 1050 K, such initially continuous films restructure by formation of rectangular vacancy islands [39]. These vacancy islands are aligned along the (100) direction which corresponds to the high-symmetry directions of $BaTiO_3$(001). At these vacancy islands, the Pt substrate is covered by a $BaTiO_3$ wetting layer with a (4×4) or, at even higher annealing temperatures, a (3×3) superstructure. The absence of bare Pt(001) areas is proven by the absence of the well-known quasi-hexagonal surface reconstruction of Pt(001). There have been attempts to grow ultrathin $BaTiO_3$ films by RF magnetron sputtering directly at the optimal ordering temperature of 900 K. However as it is shown in Fig. 13.8, this leads to substantial changes in the morphology of the surface. The $BaTiO_3$ forms the bulk-like (001) structure in thick patches at the Pt(001) step edges only. On the terraces in-between, a (4×4) structured wetting layer is again observed. This morphology results from the competition of several processes. A fast diffusion allows $BaTiO_3$
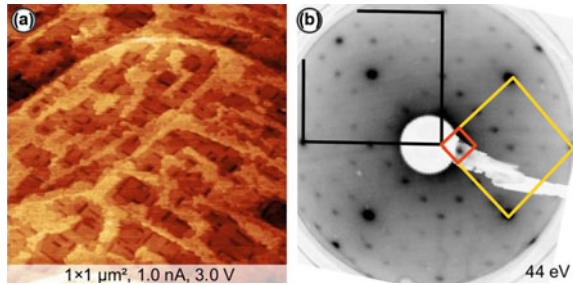
Fig. 13.8 The high-temperature deposition of BaTiO$_3$ on Pt(001) by RF magnetron sputtering causes substantial changes in the film morphology. At 900 K, the STM image in (**a**) reveals a morphology that is typical for strong re-sputtering which leads also to a lower total deposition rate. BaTiO$_3$ concentrates at the step edges, whereas a thin wetting layer covers the terraces. The LEED pattern in (**b**) shows the formation of a BaTiO$_3$(001)-(4 × 4) superstructure related to the wetting layer

nucleation at preferred substrate step sites. The intrinsic re-sputtering at the surface due to the high kinetic energy of the arriving ions during the sputter deposition process reduces the sticking of material on the terraces.

For the growth of BaTiO$_3$ on the hexagonal Pt(111) substrate about 100 K higher annealing or growth temperatures as compared to Pt(001) are needed. BaTiO$_3$ shows remarkable structural changes between the onset of growth and the formation of thicker films. For thicknesses up to 0.7 nm which corresponds to three BaTiO$_3$(111) lattice planes, a hexagonal structure is formed which is by 10 % compressed as compared to bulk BaTiO$_3$(111), despite a Pt-BaTiO$_3$ lattice mismatch of only 2.0 %. This initial layer grows 30° rotated with respect to the substrate lattice [38]. For thicknesses above 1 nm, BaTiO$_3$(111) films grow 2.0 % strained in registry with the substrate and without any rotation. For film thicknesses well above 3 nm, the BaTiO$_3$(111) films tend to relax to the bulk BaTiO$_3$ lattice. This is accompanied by a rotation of the BaTiO$_3$ by 30 ± 10° against the substrate lattice. Figure 13.9 shows LEED data for such 2.8 and 4.2 nm thick films upon annealing to 1150 K in 10^{-4} mbar O$_2$. Despite an O$_2$ background pressure of 10^{-4} mbar during annealing, the oxide layer is slightly reduced as revealed by the formation of a ($\sqrt{3}$ × $\sqrt{3}$)$R30°$ vacancy reconstruction (marked by arrows in the LEED pattern of Fig. 13.9). For compensation of oxygen desorption at these high temperatures, a larger O$_2$ background pressure is required. The sickle-shaped segments in the LEED data of Fig. 13.9b indicate the rotation of the thicker BaTiO$_3$ film at similar annealing temperatures in a 20° interval around the 30° position. These results with respect to film rotation and relaxation emphasize a significantly weaker interface coupling on Pt(111) as compared to Pt(001). By changing from annealing in O$_2$ environment to reducing UHV conditions, BaTiO$_3$ islands form at these temperatures. In most cases their (111) structure is preserved but also the formation of rectangular structures in registry with the Pt(111) substrate have been observed, another indication of a high level of structural flexibility [38].
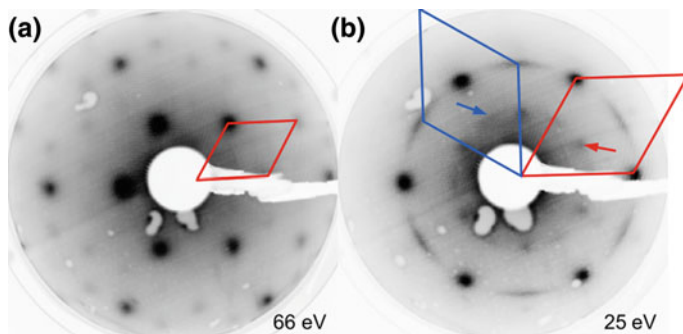
Fig. 13.9 LEED image of 2.8 nm (**a**) and 4.2 nm (**b**) thick BaTiO$_3$(111) on Pt(111) upon annealing at 1150 K. Besides BaTiO$_3$(111) islands in registry with the substrate (indicated in *black*), BaTiO$_3$(111) islands rotated by 30 ± 10° are formed for higher BaTiO$_3$ thicknesses. All islands exhibit the typical ($\sqrt{3} \times \sqrt{3}$)*R30°* superstructure of reduced BaTiO$_3$(111) (marked by *arrows*)

13.2.2 Oxide Growth by MBE Versus Magnetron Sputtering

A major difference between MBE and magnetron sputter deposition is the magnitude of the kinetic energy of the atoms impinging on the sample surface. In the case of MBE, the average kinetic energy is below 1 eV and corresponds to the thermal energy k$_B$T at the materials evaporation temperature. For the radio-frequency assisted magnetron sputter process, the typical energies are about two orders of magnitude larger and in the range of tens of eV up to 100 eV, as has been determined experimentally [45]. The resulting differences for the thin film growth are illustrated in the following. The XPS spectrum in Fig. 13.10a right after room temperature deposition of BaTiO$_3$ via RF magnetron sputtering shows two different Pt 4f doublets. A first 4f$_{5/2}$ 4f$_{7/2}$ doublet corresponds to metallic Pt (marked gray in Fig. 13.10a); whereas an intense second doublet that is shifted by 2.3 eV to higher binding energies (hatched in Fig. 13.10a) corresponds to PtO$_2$ [46]. Note the high formation energy of PtO$_2$ in the range of 1 eV [47]. Oxidation of platinum usually requires larger O$_2$ pressures and temperatures above 1100 K [48]. In addition, oxidation by exposition to atomic oxygen at room temperature has been reported [46]. Upon magnetron sputtering, the amount of Pt transformed into PtO$_2$ exceeds one monolayer of Pt, which rules out a simple surface oxidation. Instead, a strong intermixing of the interfacial layers occurs where the impinging atoms possess enough kinetic energy to form PtO$_2$. Upon annealing to 900 K, excess oxygen is released from the platinum substrate and an ultrathin BaTiO$_3$ film is formed. The Pt 4f spectrum in Fig. 13.10b now contains only a single metallic component. Any incorporation of Pt in the oxide thin film or a Pt oxidation are ruled out upon annealing.

The oxide growth by magnetron sputtering as well as by PLD introduces an intrinsic interface roughening due to the high kinetic energy of impinging atoms
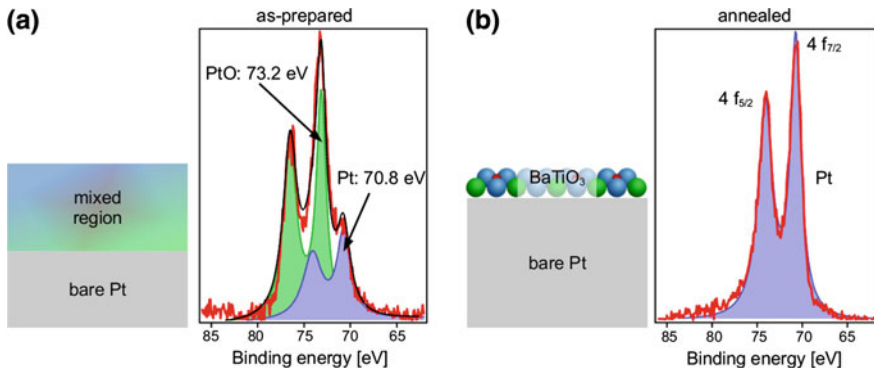
Fig. 13.10 XPS spectra of the Pt 4f region upon RF magnetron sputter deposition at room temperature (**a**) and upon annealing the sample to 750 K (**b**). The high kinetic energies involved in the sputter deposition process cause a roughening of the vacuum interface and the formation of PtO in this amorphous region. Upon annealing, the mixed Pt-BaTiO$_3$ region separates in a continuous BaTiO$_3$ film on a flattened Pt substrate as indicated by the presence of a single doublet of bulk-like Pt only in (**b**)

and ions. Whereas this intermixing can deteriorate the growth interface, it might help to improve the growth by surmounting structural barriers as is discussed for Pt (001) in the following. The bare Pt(001) surface exhibits the famous (5 × 20) surface reconstruction that is closely related to the Au(001) surface reconstruction [49, 50]. Pt(001) forms a close-packed quasi-hexagonal Pt top layer on the fcc(001) square lattice. The induced Moiré-like rumpling gives rise to the (5 × 20) surface reconstruction visible by STM and LEED. The hexagonal top Pt layer might induce an (111)-oriented growth of BaTiO$_3$. However, if the Pt top-layer reconstruction is destroyed during deposition, the square lattice of platinum bulk can dictate an (001)-oriented BaTiO$_3$ growth instead. Indeed, only the growth of (001)-oriented BaTiO$_3$ films has been reported on Pt(001) for deposition by RF magnetron sputtering or PLD [39, 41]. However for MBE oxide growth, the orientation of the BaTiO$_3$ films can be tuned to (001) or (111) by either lifting or preserving the Pt (001) surface reconstruction. For the deposition of at least 2 nm thick layers, the growth of (111)-oriented BaTiO$_3$ films is observed on the hexagonally reconstructed Pt(001) surface as shown in Fig. 13.11a. The twelve spots in the LEED pattern of Fig. 13.11a correspond to the two rotational domains of BaTiO$_3$(111). Clearly, the growth of the first BaTiO$_3$ layer does not destroy the quasi-hexagonal Pt reconstruction. It is further stabilized underneath a continuous BaTiO$_3$ layer as soon as it is formed. The unreconstruction of the interfacial Pt layer into the bulk-like Pt square lattice requires the release of one fifth of the top layer Pt atoms. This would cause a roughening of the interface, which requires additionally a BaTiO$_3$ film restructuring. Both lead to the stabilization of the reconstruction at the interface.

However, MBE growth on an *unreconstructed* Pt(001) leads to (001)-oriented BaTiO$_3$ films. The Pt(001) (5 × 20) reconstruction can be lifted by, e.g., oxygen
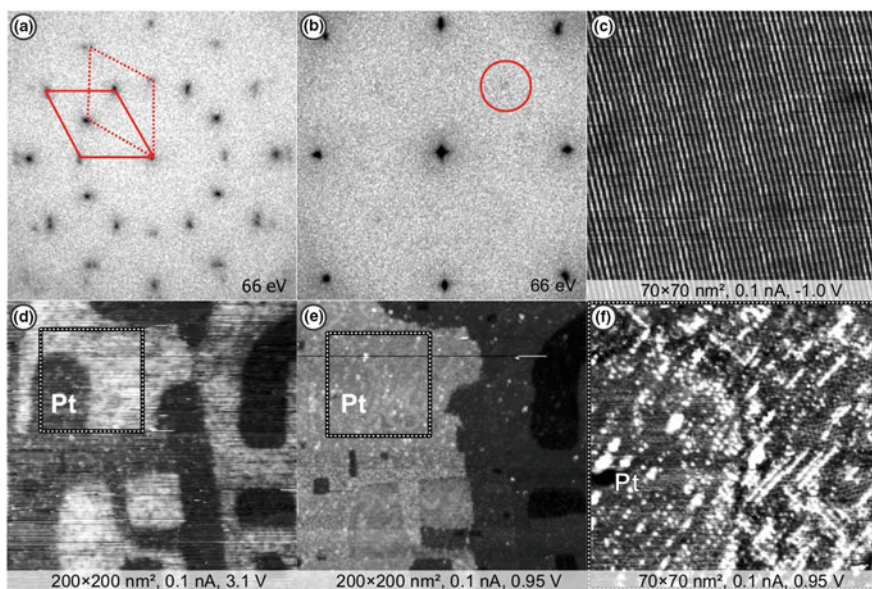
Fig. 13.11 For BaTiO$_3$ films grown by MBE on Pt(001), the film orientation can be switched between (001) and (111) by either preserving or lifting the platinum surface reconstruction. The SPALEED image in (**a**) shows two rotational domains of a 2.0 nm thick BaTiO$_3$(111) film on the reconstructed surface. The SPALEED image of (**b**) exhibits the onset of BaTiO$_3$(001) growth for submonolayer coverage upon lifting the reconstruction. To test the substrate structure underneath the BaTiO$_3$ islands, STM imaging in the band gap has been performed (**d**–**f**). The islands of (**d**) become transparent at 0.95 V as shown in (**e**). The structure underneath the islands (**f**) does not exhibit the stripe-like pattern of the (111)-reconstructed surface, as shown in (**c**) on identical scale for comparison

adsorption. This is demonstrated in Fig. 13.11b by LEED. The atomic structure at the metal-oxide interface can also be imaged by STM. It requires a bias voltage that corresponds to tunneling inside the oxide gap as illustrated in Fig. 13.11. Underneath the film, a smooth substrate is found, which does not show the stripe-like pattern that is characteristic for the (5 × 20) reconstructed Pt(001) surface.

13.3   New Concepts of Aperiodic Oxides at the 2D Limit

The structure and the properties of oxide thin films can differ from the related bulk materials when approaching the 2D limit, which is the fascinating topic of this book. However as is discussed in the following section, completely new structural concepts can develop which go beyond a periodic interface modification. The interface frustration might drive an oxide into a new form of aperiodic order [51].

13.3.1 2D Oxide Quasicrystals

Ultrathin films of $BaTiO_3$ on Pt(111) can be converted by simple annealing steps into a two-dimensional quasicrystal structure which exhibits brilliant 12-fold rotational symmetric diffraction patterns. The sharp diffraction spots visible in LEED and in SXRD witness a well-developed long-range order of the oxide film [51]. On the other hand, the 12-fold symmetry is a "forbidden" symmetry for any *periodic lattice* and corresponds to the aperiodic order of a dodecagonal quasicrystal. The long-range order that is necessary for sharp diffraction peaks is based on a self-similar hierarchical structure. This 2D building concept is often explained in terms of a self-similar tiling pattern as has been discovered by Sir Roger Penrose [52]. Figure 13.12 illustrates this for the dodecagonal quasicrystal of the Stampfli-Gähler type [53]. The tiling consists of three basic tiling motives: A square, an equilateral triangle, and a rhombus with interior angles of 30° and 150°. In the dodecagonal quasicrystal these motives are arranged in a hierarchy of self-similar tilings with a scaling factor of $(2 + \sqrt{3})^n$ ($n \in \mathbb{N}$). This concept is highlighted in Fig. 13.12 for the first higher order of self-similarity. An alternative concept to create a quasicrystal is based on recursion rules. Consequences of the recursive rules are the self-similarity and the absence of translational symmetry in the 2D arrangement, both are characteristic properties of quasicrystals.

The atomically-resolved structure of the oxide quasicrystal that is derived from a $BaTiO_3$ thin film on Pt(111) is shown in the STM image of Fig. 13.13. As described in the previous sections, a ultrathin $BaTiO_3$ film tends to form periodic $BaTiO_3$(111) islands on the Pt(111) substrate upon high-temperature annealing in O_2 atmosphere.
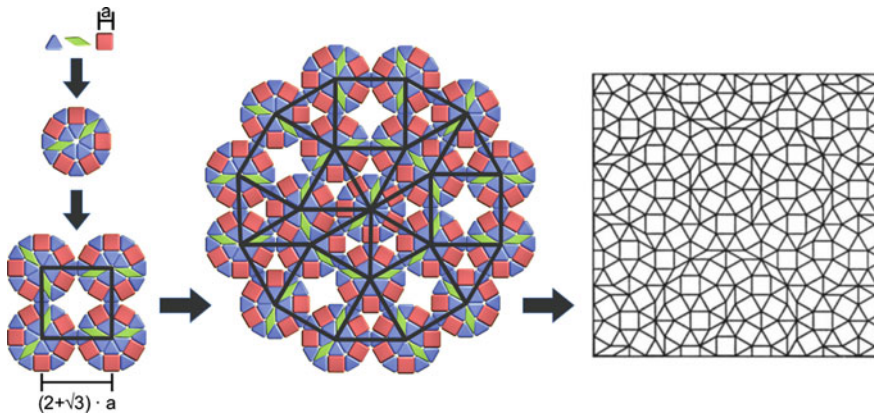
Fig. 13.12 Building principle of the Stampfli-Gähler tiling in a 2D dodecagonal lattice. *Triangles, squares* and *rhombi* with a common edge length are combined in the typical Stampfli-Gähler *dodecagon*. By combining these basic units, the same geometrical objects are formed on a $(2 + \sqrt{3})$ times larger scale. These larger elements are again assembled to *dodecagons*. The quasicrystalline dodecagonal lattice is formed by an infinite repetition of this inflation. The result is a hierarchical self-similar lattice

If the annealing is performed in UHV conditions instead, a 2D wetting layer spreads on the entire substrate surface in-between the BaTiO$_3$(111) islands. In this wetting layer, the quasicrystalline structure forms [51]. In the atomically resolved STM image of Fig. 13.13, one of the Stampfli-Gähler dodecagons is highlighted in the top left corner of the image. Twelve triangles, five squares and two rhombi, all with a characteristic length scale of 0.685 nm, form it. Together with the adjacent dodecagons the self-similar structure on $2 + \sqrt{3}$ larger scale is developed. Unfortunately, the higher-hierarchical structures are hard to identify due to the existence of some structural disorder that might be interpreted as atomic phason flips in the 2D quasicrystal. Phason flips are known lattice excitations for a quasicrystal, which superimpose positional changes onto the original tiling. A detailed description of common phenomena related to quasicrystals can be found in [54].

In the Fourier-transforms of the large-scale STM image, the 12 central sharp spots according to the first order diffraction of the quasicrystal are clearly visible and also higher order reflections can be well identified. This characteristic 12-fold set of diffraction spots is identically reproduced in the LEED experiment. Note that this observation rules out any explanation of the 12-fold LEED pattern on the basis of a superposition of different rotational domains of three or fourfold symmetry each. It shows further that the local atomic arrangement as observed in STM is present over the full sample surface. The two-dimensionality of the oxide structure is concluded from the XPS measurements [51].

The well-defined orientation of the quasicrystalline LEED pattern with respect to the Pt(111) substrate implies that the oxide quasicrystal is perfectly oriented along the high-symmetry directions of the metal substrate. This observation is nontrivial,
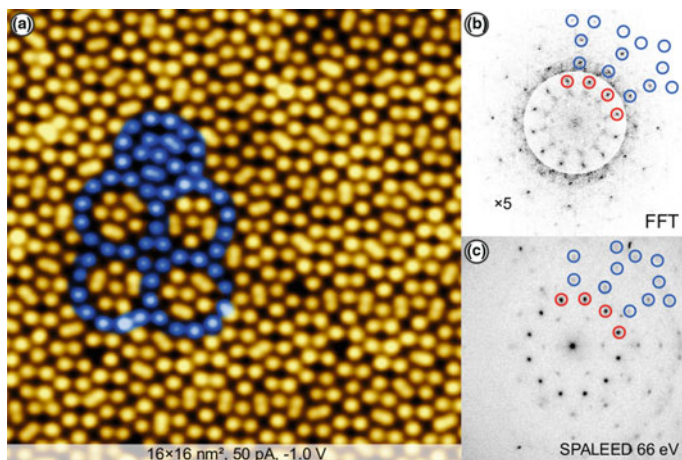
Fig. 13.13 The detailed structure of the 2D oxide quasicrystal is determined by STM (**a**, **b**) and LEED (**c**). On local scale, Stampfli-Gähler dodecagons are found everywhere and higher-hierarchical elements can be identified as indicated in (**a**) in *blue*. The Fourier-transform of the STM image in (**b**) obtained on local scale is in excellent agreement with the global structure measured with SPALEED as shown in (**c**)

since the edge length of the atomic motifs of 0.685 nm does not match any distance of the underlying lattice as, e.g., the next-neighbor distance of 0.277 nm. The reason for this epitaxial growth is still not known. More general concepts of epitaxial relationships like point-on-line symmetries (see [55]) also fail to explain in this case.

13.3.2 Transition Between Periodic and Aperiodic Oxide: The Role of Approximants

Approximants are *periodic* structures formed by the same characteristic building blocks as the parent quasicrystal. They can exhibit different degrees of complexity. They range from simple structures, which are far from the original arrangement of the quasicrystal but made of the same building blocks, to large unit cells that periodically resemble small patches of the aperiodic structure. Such approximant structures exist also for the oxide quasicrystal that is derived from a $BaTiO_3$ thin film on Pt(111). Figure 13.14 depicts the STM image of such a complex approximant. It is formed by the same building blocks of squares, triangles, and rhombi. Even the arrangement of the characteristic dodecagonal ring structure (marked blue) by twelve triangles, five squares and two rhombi is present in the approximant. However, they are hexagonally ordered in the long range, which leads to a hexagonal diffraction pattern. In the parent quasicrystal tiling, adjacent dodecagons are sharing edges, which is not the case for the approximant. Instead, the space between three adjacent dodecagons is filled by three additional atoms and, in most cases, a fourth atom on top. The latter appears bright in the STM image in Fig. 13.14a, b.
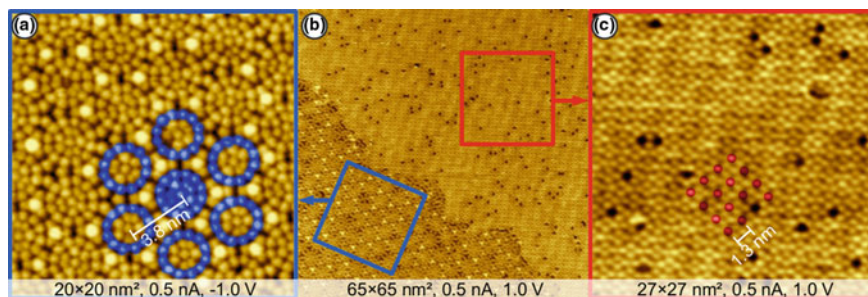
Fig. 13.14 Two examples of periodic approximant structures of the 2D oxide quasicrystal. The structure in (**a**) is the most complex approximation to the quasicrystal observed so far. It is formed by a hexagonal arrangements of Stampfli-Gähler dodecagons separated by 3.8 nm. In contrast, the second structures in (**c**) exhibits the smallest unit cell observed, consisting of triangles and squares only. It is almost quadratic with a lattice vector of about 1.3 nm. Both structures can meet in neighboring domains as shown in (**b**) for submonolayer coverages of $BaTiO_3$ upon high-temperature UHV annealing

A second *periodic* approximant with a nearly quadratic unit cell can be also prepared in a similar way. It can coexist with the hexagonal structure described above as shown in Fig. 13.14b, or it can be prepared as single phase. With respect to the tiling pattern, it consists of triangles and squares only. Three triangles and two squares form, in the same local arrangement as they are present in quasicrystal structure (compare Fig. 13.12), the periodic unit cell of about 1.3×1.3 nm^2. It is the smallest possible approximant from these two tiles.

The *periodic* approximants and the *aperiodic* quasicrystal, all three develop from a BaTiO$_3$ thin film on Pt(111) upon high-temperature UHV annealing. Details of the preparation decide which structure is formed. The existence of approximants with respect to the oxide quasicrystal is of great interest for a comprehensive structure determination, the development of aperiodic growth concepts, and for comparison of properties of aperiodic versus periodic structures. Due to their periodicity, the approximants can serve as less complex systems, which are theoretically describable by a large variety of methods that rely on periodic boundary conditions.

13.4   Summary

Ultrathin Perovskite films can be grown epitaxially on many different substrates as is shown here for the cases of BaTiO$_3$ films on metal substrates. Controlled by the substrate surface orientation and reconstruction, either BaTiO$_3$(001) or BaTiO$_3$(111) films grow pseudomorphically with a sharp interface on the Pt substrate. For oxygen-deficient ultrathin films, several competing monolayer structures exist. Most prominently, the formation of a long-range ordered but aperiodic perovskite-derived structure has been demonstrated. It opens the field of oxide-based two-dimensional quasicrystals.

References

1. Fesenko OE, Popov VS (1981) Phase T, E-diagram of barium titanate. Ferroelectrics 37:1–4
2. Merz WJ (1949) The electric and optical behavior of BaTiO$_3$ single-domain crystals. Phys Rev 76(8)
3. Vrejoiu I, Alexe M, Hesse D, Goesele U (2008) Functional perovskites—From epitaxial films to nanostructured arrays. Adv Func Mat 18(24)
4. Tsymbal EY, Dagotto ERA, Eom CB, Ramesh R (2012) Multifunctional oxide heterostructures. Oxford University Press, Oxford, U.K
5. Schlom DG, Chen LQ, Fennie CJ, Gopalan V, Muller DA, Pan X, Ramesh R, Uecker R (2014) Elastic strain engineering of ferroic oxides. MRS Bull 39
6. Courths R, Cord B, Saalfeld H (1989) Bulk and surface Ti3d valence and defect states in SrTiO$_3$(001) from resonant photoemission. Sol Stat Comm 70(11)
7. Aiura Y, Hase I, Bando H, Yasue T, Saitoh T, Dessau DS (2002) Photoemission study of the metallic state of lightly electron-doped SrTiO$_3$. Surf Sci 515(1)

8. Santander-Syro AF, Copie O, Kondo T, Fortuna F, Pailhes S, Weht R, Qiu XG, Bertran F, Nicolaou A, Taleb-Ibrahimi A, Le Fevre P, Herranz G, Bibes M, Reyren N, Apertet Y, Lecoeur P, Barthelemy A, Rozenberg MJ (2011) Two-dimensional electron gas with universal subbands at the surface of $SrTiO_3$. Nature 469(7329)
9. Plumb NC, Salluzzo M, Razzoli E, Månsson M, Falub M, Krempasky J, Matt CE, Chang J, Schulte M, Braun J, Ebert H, Minár J, Delley B, Zhou KJ, Schmitt T, Shi M, Mesot J, Patthey L, Radović M (2014) Mixed dimensionality of confined conducting electrons in the surface region of $SrTiO_3$. Phys Rev Lett 113(8)
10. Heifets E, Eglitis RI, Kotomin EA, Maier J, Borstel G (2001) Ab initio modeling of surface structure for $SrTiO_3$ perovskite crystals. Phys Rev B 64
11. Eglitis RI, Vanderbilt D (2008) First-principles calculations of atomic and electronic structure of $SrTiO_3$ (001) and (011) surfaces. Phys Rev B 77
12. Tétot R, Salles N, Landron S, Amzallag E (2013) $SrTiO_3$ (001) surface and strained thin films: Atomic simulations using a tight-binding variable-charge model. Surf Sci 616
13. Warusawithana MP, Cen C, Sleasman CR, Woicik JC, Li Y, Kourkoutis LF, Klug JA, Li H, Ryan P, Wang LP, Bedzyk M, Muller DA, Chen LQ, Levy J, Schlom DG (2009) A ferroelectric oxide made directly on silicon. Science 324(5925)
14. Eerenstein W, Wiora M, Prieto JL, Scott JF, Mathur ND (2007) Giant sharp and persistent converse magnetoelectric effects in multiferroic epitaxial heterostructures. Nat Mat 6(5)
15. Ohtomo A, Muller DA, Grazul JL, Hwang HY (2002) Artificial charge-modulationin atomic-scale perovskite titanate superlattices. Nature 419(6905)
16. Kalabukhov A, Gunnarsson R, Börjesson J, Olsson E, Winkler D, Claeson T (2008) Effect of various deposition conditions on the electrical properties of LAO/STO hetero interfaces. J Phys Conf Ser 100(8)
17. Thiel S, Hammerl G, Schmehl A, Schneider CW, Mannhart J (2006) Tunable quasi-two-dimensional electron gases in oxide heterostructures. Science 313(5795)
18. Huijben M, Rijnders G, Blank DHA, Bals S, Aert SV, Verbeeck J, Tendeloo GV, Brinkman A, Hilgenkamp H (2006) Electronically coupled complementary interfaces between perovskite band insulators. Nat Mat 5(7)
19. Siemons W, Koster G, Yamamoto H, Geballe TH, Blank DHA, Beasley MR (2007) Experimental investigation of electronic properties of buried heterointerfaces of $LaAlO_3$ on $SrTiO_3$. Phys Rev B 76
20. Okamoto S, Millis AJ (2004) Electronic reconstruction at an interface between a mott insulator and a band insulator. Nature 428(6983)
21. Pentcheva R, Pickett WE (2009) Avoiding the polarization catastrophe in $LaAlO_3$ overlayers on $SrTiO_3$(001) through polar distortion. Phys Rev Lett 102
22. Salluzzo M, Cezar JC, Brookes NB, Bisogni V, De Luca GM, Richter C, Thiel S, Mannhart J, Huijben M, Brinkman A, Rijnders G, Ghiringhelli G (2009) Orbital reconstruction and the two-dimensional electron gas at the $LaAlO_3/SrTiO_3$ interface. Phys Rev Lett 102
23. Ferrari V, Weissmann M (2014) Tuning the insulator–metal transition in oxide interfaces: An ab initio study exploring the role of oxygen vacancies and cation interdiffusion. phys stat sol b 251(8)
24. Segal Y, Ngai JH, Reiner JW, Walker FJ, Ahn CH (2009) X-ray photoemission studies of the metal-insulator transition in $LaAlO_3/SrTiO_3$ structures grown by molecular beam epitaxy. Phys Rev B 80
25. Kalabukhov AS, Boikov YA, Serenkov IT, Sakharov VI, Popok VN, Gunnarsson R, Börjesson J, Ljustina N, Olsson E, Winkler D, Claeson T (2009) Cationic disorder and phase segregation in $LaAlO_3\backslash SrTiO_3$ heterointerfaces evidenced by medium-energy ion spectroscopy. Phys Rev Lett 103
26. Megaw HD (1945) Crystal structure of barium titanate. Nature 155 (3938)
27. Wul B (1946) Barium titanate—A new ferroelectric. Nature 157(3998)
28. Fechner M, Ostanin S, Mertig I (2008) Effect of the surface polarization in polar perovskites studied from first principles. Phys Rev B 77

29. Höfer A, Fechner M, Duncker K, Hölzer M, Mertig I, Widdra W (2012) Persistence of surface domain structures for a bulk ferroelectric above T_C. Phys Rev Lett 108(8)

30. Kohlstedt H, Pertsev NA, Waser R (2002) Size effects on polarization in epitaxial ferroelectric films and the concept of ferroelectric tunnel junctions including first results. Mat Res Soc Symp Proc 688

31. Tenne DA, Bruchhausen A, Lanzillotti-Kimura ND, Fainstein A, Katiyar RS, Cantarero A, Soukiassian A, Vaithyanathan V, Haeni JH, Tian W, Schlom DG, Choi KJ, Kim DM, Eom CB, Sun HP, Pan XQ, Li YL, Chen LQ, Jia QX, Nakhmanson SM, Rabe KM, Xi XX (2006) Probing nanoscale ferroelectricity by ultraviolet raman spectroscopy. Science 313 (5793)

32. Garcia V, Fusil S, Bouzehouane K, Enouz-Vedrenne S, Mathur ND, Barthelemy A, Bibes M (2009) Giant tunnel electroresistance for non-destructive readout of ferroelectric states. Nature 460(7251)

33. Li YL, Chen LQ (2006) Temperature-strain phase diagram for $BaTiO_3$ thin films. Appl Phys Lett 88(7)

34. Kim YS, Kim DH, Kim JD, Chang YJ, Noh TW, Kong JH, Char K, Park YD, Bu SD, Yoon J-G, Chung J-S (2005) Critical thickness of ultrathin ferroelectric $BaTiO_3$ films. Appl Phys Lett 86(10)

35. Gruverman A, Wu D, Lu H, Wang Y, Jang HW, Folkman CM, Zhuravlev MY, Felker D, Rzchowski M, Eom CB, Tsymbal EY (2009) Tunneling electroresistance effect in ferroelectric tunnel junctions at the nanoscale. Nano Lett 9(10)

36. Lu H, Bark CW, Esque de los Ojos D, Alcala J, Eom CB, Catalan G, Gruverman A (2012) Mechanical writing of ferroelectric polarization. Science 336(6077)

37. Ramesh R (2013) Complex functional oxide heterostructures. Curr Sci 105(8)

38. Förster S, Widdra W (2010) Growth, structure, and thermal stability of epitaxial $BaTiO_3$ films on Pt(111). Surf Sci 60:423–24

39. Förster S, Huth M, Schindler K-M, Widdra W (2011) Epitaxial $BaTiO_3$(100) films on Pt(100): A low-energy electron diffraction, scanning tunneling microscopy, and x-ray photoelectron spectroscopy study. J Chem Phys 135(10)

40. Meyerheim HL, Klimenta F, Ernst A, Mohseni K, Ostanin S, Fechner M, Parihar S, Maznichenko IV, Mertig I, Kirschner J (2011) Structural Secrets of Multiferroic Interfaces. Phys Rev Lett 106

41. Meyerheim HL, Ernst A, Mohseni K, Maznichenko IV, Henk J, Ostanin S, Jedrecy N, Klimenta F, Zegenhagen J, Schlueter C, Mertig I, Kirschner J (2013) Tuning the structure of ultrathin $BaTiO_3$ films on Me(001) (Me = Fe, Pd, Pt) surfaces. Phys Rev Lett 111

42. Premper J, Sander D, Kirschner J (2015) In situ stress measurements during pulsed laser deposition of $BaTiO_3$ and $SrTiO_3$ atomic layers on Pt(001). Appl Surf Sci 335

43. Shin J, Nascimento VB, Borisevich AY, Plummer EW, Kalinin SV, Baddorf AP (2008) Polar distortion in ultrathin $BaTiO_3$ films studied by in situ LEED I\V. Phys Rev B 77

44. Stengel M, Vanderbilt D, Spaldin NA (2009) Enhancement of ferroelectricity at metal-oxide interfaces. Nat Mat 8(5)

45. Andersson JM, Wallin E, Münger EP, Helmersson U (2006) Energy distributions of positive and negative ions during magnetron sputtering of an Al target in Ar/O_2 mixtures. J Appl Phys 100(3)

46. Parkinson CR, Walker M, McConville CF (2003) Reaction of atomic oxygen with a Pt(111) surface: Chemical and structural determination using XPS, CAICISS and LEED. Surf Sci 545:1–2

47. Pedersen TM, Xue Li W, Hammer B (2006) Structure and activity of oxidized Pt(110) and alpha-PtO_2. Phys Chem Chem Phys 8

48. Krasnikov SA, Murphy S, Berdunov N, McCoy AP, Radican K, Shvets IV (2010) Self-limited growth of triangular PtO_2 nanoclusters on the Pt(111) surface. Nanotech 21(33)

49. Abernathy DL, Gibbs D, Grübel G, Huang KG, Mochrie SGJ, Sandy AR, Zehner DM (1993) Reconstruction of the (111) and (001) surfaces of Au and Pt: Thermal behavior. Surf Sci 283(1)

50. Hammer R, Sander A, Förster S, Kiel M, Meinel K, Widdra W (2014) Surface reconstruction of Au(001): High-resolution real-space and reciprocal-space inspection. Phys Rev B 90
51. Förster S, Meinel K, Hammer R, Trautmann M, Widdra W (2013) Quasicrystalline structure formation in a classical crystalline thin-film system. Nature 502(7470)
52. Penrose R (1979) Pentaplexity a class of non-periodic tilings of the plane. Math Intell 2(1)
53. Gähler F (1988) Quasicrystalline materials. Proceeding of the I. L. L./CODEST Workshop (Eds.: Ch. Janot, J.-M.Dubois), World Scientific, Singapore, pp 272–284
54. Steurer W, Deloudi S (2009) Crystallography of quasicrystals, springer series in materials science, Springer, Berlin
55. Franke KJ, Gille P, Rieder K-H, Theis W (2007) Achieving epitaxy between incommensurate materials by quasicrystalline interlayers. Phys Rev Lett 99

Index